NIST-GCR-94-645

BEHAVIOR OF CHARRING MATERIALS IN SIMULATED FIRE ENVIRONMENTS

E. M. Suuberg, I. Milosavljevic, W. D. Lilly
Division of Engineering
Brown University
Providence, RI 02912

Issued June 1994
January 1994

Sponsored by:
U.S. Department of Commerce
Ronald H. Brown, *Secretary*
Technology Administration
Mary L. Good, *Under Secretary for Technology*
National Institute of Standards and Technology
Arati Prabhakar, *Director*

Notice

This report was prepared for the Building and Fire Research Laboratory of the National Institute of Standards and Technology under grant number 60NANB0D1042. The statements and conclusions contained in this report are those of the authors and do not necessarily reflect the views of the National Institute of Standards and Technology or the Building and Fire Research Laboratory.

FINAL PROJECT REPORT

THE BEHAVIOR OF CHARRING MATERIALS IN SIMULATED FIRE ENVIRONMENTS

by

Eric M. Suuberg, Principal Investigator
Ivan Milosavljevic, Graduate Student
William D. Lilly, Senior Research Engineer

Division of Engineering, Box D
Brown University
Providence, Rhode Island 02912

Submitted to: **Dr. Thomas Ohlemiller, NIST Scientific Officer**
Building and Fire Research Laboratory
National Institute of Standards and Technology
Building 224
Gaithersburg, MD 20899

NIST Grant 60NANB0D1042
January 1994

Executive Summary

The complicated interplay of chemistry, heat and mass transfer serves to make the study of combustion phenomena generally quite difficult, particularly when a solid phase is also involved. If the solid phase consists of an organic macromolecular material, the complexity is compounded by the need to account for a host of pyrolytic phenomena in addition to the gas phase processes. This is unfortunately the situation in many real fire situations.

The general phenomena that govern fire behavior are qualitatively understood, and in some cases a reasonable quantitative understanding is emerging. Still, there are major unanswered questions in many areas, particularly related to the *chemistry* of the fire processes. This is particularly true with respect to the chemistry of the solid phase itself.

The focus of this study was the *behavior of thick charring solids in fire situations.* Clearly one of the most important parameters governing the fire phenomenon is the rate of release of combustible volatiles into the gas phase, in which they actually burn. Over the years, fire researchers have learned how to model the processes in the gas phase, so that the rate of heat feedback to the solid surface can be reasonably well predicted. Likewise, there exists the ability to model the heat transfer processes at the solid surface and within the solid itself. Finally, there is a large literature on the laboratory-scale pyrolysis of various charring polymers. It might appear that predicting the course of the fire would involve carefully coupling these different models together. There have unfortunately not been any successful demonstrations of the ability to do this, though in broad stroke, some models capture the key features of the processes.

This study was concerned with the possibility that the inability to come to complete closure on the charring polymer fire problem might derive from difficulties in applying laboratory scale kinetics to actual fire conditions. *Specifically, we were concerned about how well small scale laboratory experiments used to derive the kinetics of pyrolysis could be used to predict the behavior of charring solids in fire situations.*

Sample Selection

The complexity of the phenomena of interest led us to make an important decision early in the project. We could reasonably expect to make progress towards the goal of the project only by studying a material for which a large literature on pyrolysis kinetics already was available. This made it necessary to focus our attention on a single, relatively well-characterized model material - cellulose. This is not to claim that the kinetics of cellulose pyrolysis is well understood, even on a laboratory scale. In fact, we believe that we have helped to resolve a

long-standing dispute as to kinetic constants. Still, cellulose pyrolysis is much better understood than the pyrolysis of any other charring material.

We nevertheless felt compelled to work in a range of relevance to real fires, and selected the conditions to be as representative of the burning of a wood wall as we could. We worked with large samples (up to 1" thickness) of pressed cellulose powder, whose densities bracketed those of common woods. We verified that the simulated fire behavior of this model material was in most significant respects quite similar to that of wood (i.e. fuel release rates were quite similar). The advantage in use of the pressed cellulose model materials was that the degree of complexity of the pyrolytic phenomena was greatly reduced and the reproducibility of results greatly enhanced, relative to that observed with real woods. This is because the feedstock for our samples was highly purified analytical filter paper pulp, which could be pressed into relatively flawless samples.

The success that was achieved in capturing the key elements of fire-driven pyrolysis phenomena with "simulated wood" samples leads back to a key philosophical question in fire research - to what extent should idealized model systems should be studied, as opposed to actually testing "real" materials. *Our recommendation is that the fire community settle upon a well-characterized standard material (cellulose, though not necessarily the particular kind that we studied) which will serve as a benchmark for all studies and testing methods.* We feel this would be of enormous benefit in that this would enable establishing for the community a reliable property data base for a single material. Too often in fire modeling, there have been difficulties in finding relevant property values (this drove our own effort strongly in a direction of measuring many properties). If properties are unavailable, it becomes unclear which parameters are key in the failure of a particular modeling effort. Perhaps worse yet, the lack of data on certain parameters invites turning them into pseudo-adjustable parameters, sometimes not even acknowledged as such in the models. When many investigators work on a single material, anomalies become quickly apparent. It is then only with the confidence that comes from models that work well, with well-established property values, that generalized experimental testing methods themselves can be more quantitatively understood, from the results that they provide on the benchmark materials. At present, there is no material that can serve as a calibration benchmark for any testing method. Having a standard material that can serve in this role would represent an important step forward in fire research and testing.

Experimentally Important Variables

Any study of fire phenomena that involves the study of chemistry in an environment that is removed from that encountered in actual fire situations runs a significant risk of producing results that do not accurately model actual fire behavior; the concern is in our ability to predict a priori the key variables that must be controlled in order to accurately simulate conditions of

relevance. Studies of pyrolysis of organic solids have been performed under an enormous variety of conditions, and the question in the fire literature has been often raised as to which, if any, of the studies are of relevance to fire modeling? If the heating rate of the solid in controlled laboratory experiments were orders of magnitude different from that encountered in the fire situation, would the same products of pyrolysis obtain? What about the effect of sample size? Surface temperature or surface heat flux? Impurities? The care with which the choice of conditions must be made can be illustrated with one example.

The focus of the present work is on the behavior of charring solids during combustion in a fire environment. This defines a very different kind of environment would might be encountered in pulverized combustion, which would occur at higher heating rates due to better particle-flame heat transfer. The yield of char in cellulose pyrolysis has been long reported to be a function of heating rate, but recent work in this laboratory did not show this to be a large effect when small samples were used. It has turned out that the role of heating rate on volatiles yield is critical only in connection with a mass transfer limitation, as would exist in large samples. This perhaps unexpected coupling of two variables - heating rate and sample size - makes it clear that there is not yet an ability to confidently reduce the research to a simpler laboratory experiment, or to import results from other very different conditions.

The variables that affect the processes of pyrolysis are known, but their interplay remains unknown. For that reason, until there is greater ability to model the processes reliably, experimenters should as faithfully as possible simulate the conditions encountered in real fires. Our choice of a "simulated fire apparatus" for performing many key measurements was based upon this realization. We had at our disposal an enormous number of other ordinary laboratory devices for studying the pyrolysis of cellulose, all of which would have been much easier to use. Still, *it was only the simultaneous study of the phenomena in the simulated fire apparatus and the smaller laboratory scale devices, that allowed us to draw firm conclusions about certain aspects of the phenomena.* We would caution others who propose to study the pyrolysis of charring solids to keep this in mind.

Our experiments were all performed in an inert gas environment. Thus oxidative pyrolysis was not studied here, nor do we believe that it would be particularly important in real flaming combustion situations. If not screened by the outward flux of volatiles, the product cellulose char may itself react with oxygen, and become a local heat source, as in glowing combustion that often follows flaming combustion. Since our measurements did not involve adding any oxygen to the ambient gas, our work might be criticized as not yet providing a full enough description of the fire process. We accept the criticism, noting that there was so much that was poorly understood about the phase during which the oxygen is screened out by the flame that we felt compelled to focus mainly on that period of combustion.

The char itself may be highly catalytic in promoting certain reactions of volatiles. It can

catalyze cracking reactions of volatiles, changing the composition of the volatiles from that which exists in the active pyrolysis zone. The cracking may also result in additional carbon deposition in the char layer. Such possibilities have been often recognized, but generally not studied in a systematic manner. We have looked at these effects, by examining the gas phase volatiles composition, and believe that the effect is certainly there, though perhaps not as large as we might have originally believed. The analysis of the effect is made very difficult by the complicated nature of the volatiles transport processes seen in the charring material.

Experimental Approach

The simulated fire equipment allows bulk samples of several centimeters in diameter and length to be held in an insulating ceramic holder atop an electronic balance. The sample holder, balance, and heater assembly are held in a controlled gas environment, which can be purged with nitrogen or other inert gases. The environment simulates a diffusion flame environment, in which little or no oxygen reaches the surface of the sample. Heating of the sample is accomplished by use of radiant quartz heaters, which can provide a flux of up to about $100 kW/m^2$, which covers the range of relevance in ordinary fire situations. The critical role that the optical properties of the sample play was very apparent.

The mass of the sample was monitored continuously. The samples were fitted with thermocouples, to provide temperature profiles. The total yield of volatiles was provided by the data on mass loss of the sample. The analysis of the volatiles was provided by either gas chromatography (GC) or by mass spectrometry.

In addition to those in the simulated fire apparatus, measurements of pyrolysis behavior were made by using standard thermogravimetric (TGA) and differential scanning calorimetric (DSC) techniques, as well as by use of a "heated wire mesh" apparatus. The experiments in the TGA system were directed at establishing the global kinetics of mass loss, as well as determining the composition of gaseous products in the presence and absence of mass transfer limitations. The experiments in the DSC were aimed at establishing the heat effects of pyrolysis, and at providing an independent set of kinetic parameters for the decomposition processes. The experiments in the heated wire mesh apparatus were aimed at studying mass transfer of tars within the samples, since in that device external mass transfer limitations are negligible. Experiments in these laboratory scale devices were in all cases guided by the results obtained from the simulated fire apparatus. In particular, the choice of temperature history was dictated by what the samples in the simulated fire apparatus experienced.

In addition to experiments aimed at establishing the kinetics of pyrolysis, a separate set of experiments was performed to establish key thermal properties of the cellulose and its chars. The heat capacity was measured using the DSC. The surface reflectivity of the cellulose and

char were measured using FTIR (for the mid-IR region) and a broadband fluxmeter, in recognition of the broad spectral distribution in the incident flux. The thermal diffusivity was measured using a separate device, which permitted imposition of a sinusoidal temperature at the face of the sample. From the phase lag as a function of depth, the diffusivity could be calculated. From the measurements of the thermal diffusivity, heat capacity, and density, the thermal conductivity was also determined.

Key Results

Broadly speaking, the results from the simulated fire apparatus generally led to the conclusion that the pyrolysis process under ordinary fire conditions could be either conduction heat transfer limited or kinetics limited, depending upon the incident surface flux. Under high flux conditions (>40 kW/m^2), the pyrolysis *appears* to occur in a sharp reaction front that separates char from cellulose. The front propagates at a nearly constant velocity, as a result of the nature of the front surface boundary condition (constant flux). The temperature gradient is maintained, as the front propagates, by a continual rise in surface temperature with time, until a combination of front surface radiative and/or convection losses limit the rise. The pyrolysis in actuality does not occur in a thin zone, though it appears visually to do so. The mass loss that occurs outside of the thin zone is, however, small enough so as not to impact seriously on the overall mass loss rate.

At fluxes lower than 40 kW/m^2, the propagation of the pyrolysis wave into the solid cannot be maintained at a constant rate. This is because the temperature of the solid becomes generally low enough that the assumption of a thin pyrolysis zone breaks down.

The above conclusions suggest the importance of accurate knowledge of the thermal properties of the solid. It was this realization that forced us to engage in their measurement, since suitably accurate values could not be found in the literature. Information on the temperature dependence of the properties was particularly difficult to find. Moreover, there were subtle aspects of the process that required further direct measurements. For example, there is a significant shrinkage of the sample that could not be calculated from the mass loss a priori. This shrinkage makes a significant difference in the value of the temperature gradient that exists in the solid, and thus significantly affects the release rate of combustible volatiles. Again, this is an effect that would be difficult to establish without direct measurements under simulated fire conditions.

It was observed that no single set of kinetic parameters could fit the mass loss rates. This led to a reconsideration of the literature on the kinetics of cellulose pyrolysis. Reports of two different activation energies have been circulating for some time, and some workers have been seeking to establish which is the "correct" value. Based upon our work in the simulated fire apparatus and the additional TGA and DSC work that it inspired, it now appears that both

activation energies reflect "real" processes that dominate in different temperature regimes (the dividing line being somewhere around 600 K). Unfortunately for the fire modeler, both ranges are important, each distinct kinetic process controlling the mass loss rate at different times.

It was noted that the heat of pyrolysis and char yield upon pyrolysis were strongly correlated. Since the char yield was observed to be a strong function of position in the sample (due to the position dependence of the kinetic pathways that were followed), then the heat sink due to the normally endothermic pyrolysis process was also a strong function of position. Generally, the heat sink decreased strongly with depth into the sample.

It was also noted that the rate of volatiles release was strongly dependent upon the sample surface conditions. The dramatic change in emissivity that accompanied initial pyrolysis created a sudden jump in surface temperature. The oft-used assumption that the fully pyrolyzed char has a surface emissivity near unity was shown by direct measurements to be quite erroneous. The potentially important role of volatile aerosol interposed between the surface and the source of the incident heat flux was also demonstrated. The sensitivity of the mass loss rate to the surface heat transfer coefficient was also striking.

It may be concluded that earlier understanding of fire-induced volatiles release processes was, in broad outline, correct. What this study suggests, however, is that the actual prediction of combustible mass release rates has not been quantitatively reliable, given the paucity of relevant data available in the literature. *To progress beyond the current level of capability in prediction of fuel release rates, greater emphasis must be placed on experimental studies that provide the full range of data necessary for prediction of mass loss rates. This means that measurement of both kinetic and thermal transport properties is needed, under conditions relevant to fire situations*. This conclusion was confirmed by exploring the behavior of a very simple unidimensional pyrolysis model that incorporated the experimental findings of this study.

Acknowledgements

The body of this report is the doctoral dissertation of Dr. Ivan Milosavljevic. Dr. Milosavljevic holds a B.Sc. degree in Mechanical Engineering from Belgrade University and an M.Sc. degree in Engineering from Brown University.

We would like to acknowledge Professors Joseph Calo and Gerald Diebold who served as readers for the dissertation, and Professor Merwin Sibulkin for donation of key pieces of apparatus and generally very useful inputs. Also, the technical contributions of William Lilly and Jack Liang are acknowledged. Finally, the understanding of Dr. Milsavljevic's wife, Dragana, and children, Iva and Philip, during the preparation of this work deserve acknowledgement.

TABLE OF CONTENTS

LIST OF TABLES

LIST OF FIGURES

1. INTRODUCTION

According to a Greek myth, the first misunderstanding between the Gods and the Humans took place when Zeus decided to rule the Earth. At the meeting of two sides, Prometheus, a Human, managed to outwit Zeus, who got so angry that he decided to burn the Humans. Smart Prometheus went to the island Lemnos to find Hephaestus, the Blacksmith's God, to steal the Firebrand and give it to the Humans. Zeus was very angry and decided to punish the careless Humans. Hephaestus made the first woman, Pandora, and Hermes filled her heart with dishonesty and lies, while the rest of the Gods gave her a box full of sins. She was told not to open the box and was then sent to the Humans. She could not resist, and opened the box, and ever since sins flow freely among the Humans. That is how the Humans paid for the luxury of having fire.

Generally speaking, fire is a process that involves an exothermic chemical reaction between oxygen and combustible material, when a certain set of conditions is satisfied. Since energy is evolved from the process, fire has been in use by mankind from the dawn of time. If not confined, however, fire represents a significant danger, even nowadays, when technology is so well advanced for its control. Recent unfortunate examples are the "Los Angeles fire", where the Santa Ana winds fanned more than a dozen fires, charring 720 buildings, 152,000 acres and causing at least $500 million in damage (125), the "Oakland fire", where the two-day blaze took 24 lives and 2300 homes (182) and the "Kuwait fires" which had a tremendous impact on the environment. These three examples are representative of the damage that uncontrolled fire can cause: human lives, the environment and property are at risk.

One of the greatest minds of human race, Albert Einstein, to the question about his opinion

of the best product made by man, replied:"Matches". Indeed, if one considers how the matches work, one would find that several processes are involved: the phosphorous is heated in air by friction, its temperature rises to the point where the ignition is achieved, the phosphorous starts combustion with the evolution of heat, causing the stem of the match to pyrolyze, the volatiles are released and ignited. As the process proceeds, the stem is completely pyrolyzed, leaving a char residue. The process extinguishes when there is no more original stem material to be pyrolyzed and, therefore, no more volatile matter can be produced.

Matches represent a small, but controlled, fire. Another example of small controlled fire is wood charcoal (previously pyrolyzed wood) combustion for a barbecue. Everybody knows that when the match flame is no longer needed it can be extinguished by blowing the flame off. Likewise, everybody knows that when the barbecue's temperature is not high enough, it can be increased by blowing on the charcoal. What is the difference? In the case of matches the stream of air physically separates the flame from the pyrolyzing solid, if no heat were supplied to solid by the flame because it is blown away, no volatiles could be generated by thermal decomposition of the solid and the match is extinguished. On the contrary, in the case of burning charcoal, the stream of air supplies additional oxygen to the burning solid, the combustion rate within the charcoal increases, due to the increase in oxygen concentration, a flame cannot be blown away.

Although the fire phenomena has been extensively studied, it is still not well understood due to the complexity of the problem, which arises from the tight interconnection of the chemistry of the process, heat and mass transfer to and from the burning material. For example, the thermodynamics of relatively simple carbon combustion can be explained by a set of elementary chemical reactions. However, even in that simple case, it cannot be

positively said what the actual mechanism is. Furthermore, the chemistry of the process becomes more complex when the thermal decomposition (pyrolysis) of the material takes place. Since a flame is a gas phase process, the combustion of liquid or solid materials is preceded by evaporation and/or thermal decomposition, when the volatile matter, that can react with oxygen to produce the flame, is formed.

The study of fire phenomena can be significantly simplified by deconvoluting the participating processes, so that the processes can be analyzed separately. There is a possibility to study independently heat or mass transfer events by simulating similar conditions as occur in a real fire environment. Unfortunately, there is no possibility of separating chemical processes from the accompanying heat and mass transfer effects since the reactions always produce heat and involve changes in composition.

In terms of fire behavior, materials can be crudely classified into five categories:

- gaseous, that do not undergo any changes prior to combustion,
- liquids, that evaporate prior to combustion and enter a fire as a vapor,
- liquids, that undergo a decomposition upon heating and enter a fire as a mixture of lower molecular weight gases,
- solids, that melt and decompose upon heating, and enter a fire as a mixture of lower molecular weight gases, leaving no solid residue,
- solids, that decompose upon heating and enter a fire as a mixture of lower molecular weight gases and leave, in the case of organic solids, a carbonaceous residue (char)--charring materials

This work is focused on charring materials. The members of this group are "cured" thermosetting synthetic polymers and also several natural polymers, the best known of

which is cellulose. Wood, a mixture of natural polymers, is also a charring material. The study of charring materials has another difficulty associated with it, namely a char layer is being formed between the flame and the pyrolyzing material. The char layer changes the resistance to the heat flow through the sample. In addition to its heat flow resistance, it can influence the rate of escape and composition of the outgoing volatile matter and, consequently, the course of the fire process.

Deconvolution of the processes is the approach used in this work. The emphasis in this study is on behavior of charring materials during the pyrolysis process. The process that was left out of the study is the flaming combustion of volatile matter.

2. BACKGROUND

2.1 THE STRUCTURE AND PROPERTIES OF CELLULOSE

It is easy to find materials that are cellulose-related. Clothing, furniture, houses, books, newspapers etc. all contain cellulose in different forms and amounts. Metals do not contain cellulose, but the production of some metals might depend on it, since some coke used in metallurgical furnaces might be pyrolyzed wood that contained about 50% cellulose.

So what is cellulose? The answer really depends who is asked. It can be clothing, industrial or building material, it can be fuel, it can be dietary fiber or it can be food (for certain organisms).

Cellulose is the major constituent of the cell walls of the higher plants and the constituent of all plant life. It accounts for about 50% of a tree on average, depending on the species. Younger and older leaves have about 10% and 20% of cellulose, respectively; straw has about 35% and in the seed hair of cotton plant, the cellulose content is over 90% (141). It can be obtained from various plants by boiling in dilute alkali solution containing rosin soap for removing fatty material, washing repeatedly with hot water and dilute alkali. Following that procedure it is washed with cold water and bleached with dilute sodium hypochlorite solution, rewashed with distilled water and dried in air. Cellulose obtained in this way contains less than 0.05% ash and about 99.8% alpha cellulose. Alpha cellulose is the historical name for the fraction of cellulose that remains undissolved in 17.5% sodium hydroxide solution at room temperature. The other two "types" are called beta and gamma cellulose. Beta cellulose is dissolved, but can be precipitated under certain treatments and gamma cellulose remains in the solution. The differences among these three "types" of

cellulose are in the length of chain. Alpha cellulose has the longest chains, followed by beta and gamma cellulose.

Cellulose is a natural polymer. It is composed of 44.4% carbon, 6.2% hydrogen and 49.4% oxygen. The simplest empirical formula obtained from these ratios is $C_6H_{10}O_5$. Since it is a polymer, then its chemical formula is $(C_6H_{10}O_5)_n$. The quantity "n" represents the degree of polymerization, "the number of repeating units strung together like identical beads in the polymer chain (147)". The formula of cellulose is shown in Figure 2.1. It is a linear, condensation polymer of glucose. Characteristic for cellulose are its β-1,4 linkages. As opposed to cellulose, starch has the same formula except the linkages are α-1,4. The real meaning of different linkages is seen in the profoundly different behavior of cellulose and starch, the former can be characterized as an inert in most solvents and agents, whereas the latter can be acted upon in almost anything. As Kemp and Vellaccio state: "This is nature's way of ensuring that only the desired reaction occurs at a given site and a given time. Usually a biochemical process requires exactly the right molecule and exactly the right enzyme (catalyst) at the same site in the cell (93)". The differences in behavior arises from the arrangement of hydroxyl groups in the chain. In cellulose the hydroxyl groups form a spacial "zig-zag" pattern and in starch they are instead linearly arranged. Hydroxyl groups readily form hydrogen bonds, which together with its geometry results in cellulose chains being linked together via hydrogen bonds in close-packed, and consequently in very stiff configurations. Cellulose, as opposed to starch, exhibits high crystallinity. The stiff crystalline arrangement is the reason that cellulose, although linear, behaves as a thermosetting polymer. If the hydroxyls are reacted with acids the formed cellulose esters form weaker interchain linkages, and they behave as thermoplastic polymers (147).

The arrangement of the atoms of the four glucose anhydride units is shown schematically in

Figure 2.2 (195). The four form, the so called, unit cell of cellulose, the smallest perfectly repeating unit (the remaining two units in the figure belong to the diagonally adjacent unit cell). The carbon atoms are located at the intersections of solid lines, the oxygen atoms are represented as circles and the hydrogen atoms are omitted. The chains are oriented along the b axis, with the identical structure and symmetry, but with the opposite directions. The unit pair in the b direction is called a cellobiose unit (also shown in Figure 2.3). The bonds in the b direction are covalent between oxygen and carbon. In the a direction there are hydrogen bonds, which are holding the chains together and contribute to a "cross-linked-like" structure. The interactions in the c direction are the weakest, and the structural units are held together by dipole forces between hydroxyl groups and permanent electric moments between COC groups.

Native cellulose has a molecular weight more than 570,000 Daltons, which corresponds to degree of polymerization in excess of 3500 (141). Purified cotton has a molecular weight of about 112,000 to 120,000 (degree of polymerization 690 to 740), whereas sulfite wood pulp has a molecular weight of about 51,000 to 38,000 (degree of polymerization 315 to 235) (71). Table 2.1 shows a summary of molecular weights of different cellulosic materials.

Due to the presence of hydroxyl groups cellulose exhibits an affinity towards water. The exposure of cellulose to water vapor is followed by adsorption of vapor, up to complete saturation of hydroxyl groups, which can be achieved by cellulose water-soaking. Adsorption-desorption curves show a hysteresis, the desorption always shows higher moisture content values than adsorption, under the same equilibrium conditions. This is probably due to the different mechanism of hydrogen bonding between the adjacent molecules. Upon water-soaking all hydroxyl groups are satisfied with water and after

subsequent drying some of the freed hydroxyl groups bond to each other, which leads to decreased concentration of hydroxyl groups available for hydrogen bonding with water. If the relative humidity is increased, at some point close to the fiber saturation point more hydroxyl groups are freed and the rate of adsorption increases again. The affinity of cellulose for water is well represented by the fact that cotton dried in vacuum over phosphorous pentoxide still retains about 0.35% water, that can be removed by heating to 100°C. However, this amount will be readsorbed on cooling. This means that cellulose can be viewed as a more powerful dehydrating agent than phosphorous pentoxide (141).

Inert gases show little affinity for cellulose at room temperature. In general, it was observed that gases are adsorbed in the amount of few thousandths of a percent per weight. The situation is considerably different for the case of polar gases. Cellulose adsorbs about 1% per weight of carbon dioxide at room temperature and atmospheric pressure and 13.6% per weight of sulfur dioxide. Furthermore, the equilibrium of inert gases adsorption is reached within minutes, while the adsorption of polar gases reached the equilibrium after tens of hours (169). Sorption of nonaqueous vapors occurs to a lesser extent, but somewhat similar in mechanism, to water vapor. Alcohols exhibit a similar hysteresis loop and there is a tendency for small amounts of methyl alcohol to be retained even after prolonged evacuation. The saturated adsorption of normal aliphatic alcohols is observed to decrease by addition of CH_2 groups. It was noted that organic vapors that swell cellulose tend to be adsorbed so firmly that they cannot be removed by increasing the temperature above their boiling points. However, they can be subsequently washed with water, which indicates a similarity in adsorption mechanism.

The thermal properties of cellulose represent very important parameters in a study of its fire behavior and, for that reason, they will be treated in more depth below.

Cellulose flammability represents a considerable drawback in its use. There are various examples throughout history of man's attempts to decrease the flammability of wood. The Egyptians soaked wood in a solution of potassium aluminum sulfate. The Romans used wood impregnation with vinegar, originally recommended in 4th Century BC by Aeneas (44). The materials that reduce the flammability are known as fire (or flame) retardants. There are three ways in which fire retardation can be achieved: by physical protection of the material (coatings) with inert material, by altering the pyrolysis process and by introducing inert material within the flammable material that can decompose upon heating and release non-combustible gases (44, 169, 184). Probably the most important and safest fire retardation technique involves altering the pyrolysis process. Two mechanisms of action of fire retardants are well established: quenching the free-radical forming reactions (113, 147) (fire retardant upon heating produce radicals that attract more hydrogen and hydroxyl radicals than do the radicals produced by fuel decomposition) and producing an intermediate compound that can react with cellulose to produce large amounts of char and non-combustible gases (water and carbon dioxide). It has also been observed that fire retardants lower the temperature of decomposition (161). However, this issue is not critical, since the amounts of char and inert products of pyrolysis (water and carbon dioxide) increase, and the overall rate of heat release is reduced.

2.2 EXPERIMENTAL INVESTIGATIONS OF CELLULOSE PYROLYSIS

Cellulose pyrolysis has been of practical importance for a long time. Products of cellulose pyrolysis are a valuable source of secondary materials and chemicals. As one of the major constituents of wood, cellulose contributes a significant portion of char to wood-derived charcoals. The volatile products of pyrolysis are viewed as potential fuels, that, in some cases, can serve as a replacement for liquid fuels.

The high flammability of cellulose represents a potential hazard in the otherwise, very widespread use of cellulose as a clothing, building and office material. Therefore, the experimental studies on cellulose pyrolysis are needed for a better understanding of cellulose degradation mechanism, no matter whether the ultimate goal is fire protection or utilization of pyrolysis products.

2.2.1 PRODUCTS OF CELLULOSE PYROLYSIS

Globally speaking, pyrolysis of cellulose is a simple process. Upon degradation, cellulose will yield char, tars and liquids and gases. Unfortunately, yields of all of the products are condition dependent. The substance that is commonly referred to as char, can be pure carbon under one set of pyrolysis conditions and carbon with some residual hydrogen and oxygen under another set of conditions. The so called, tar, is a conveniently chosen name for a mixture of higher molecular weight compounds, condensable at room temperature. As one would expect, the composition of the tar depends heavily on the conditions that cellulose was exposed to. The third group of cellulose pyrolysis products are gases, easily identifiable with various techniques, and, of course, unpredictable in yield, since the previous two constituents of the pyrolysis products change with almost any change in

pyrolysis conditions. At this point, it is more than obvious that the statement made in the first sentence of this passage just represents wishful thinking, not really reflective of the complexity of the process.

Knowledge of cellulose pyrolysis products has a profound importance in terms of both obtaining mechanistic explanations of the phenomena and in predicting fire behavior. By identifying all the different cellulose products it is, at least in theory, possible to come closer to understanding the mechanism of cellulose pyrolysis and, subsequently, cellulose combustion. From the fire protection perspective, identification of cellulose pyrolysis products, under different conditions, can lead to measures to reduce hazards, since the tar, the main volatile component at pyrolysis temperature, is very flammable, has a high heating value and serves as a heat source to the pyrolyzing solid in a fire. The gaseous products of pyrolysis also represent a danger. How dangerous the gases are can be seen in Figure 2.4 (18). Carbon monoxide poisoning causes so called, visual agnosia, the failure to recognize visually presented material. What is even worse, it seems that visual agnosia does not go away, it is a permanent brain damage (168).

One of the first studies on decomposition products of cellulose was conducted by Pictet and Sarasin (140). They distilled cellulose at 210°C under reduced pressure and obtained 45% by mass of tars, 32% liquid water, 13% was described as gases and losses and 10% char. Later they identified that 70% of the tars (or about 30% of original cellulose) was levoglucosan (1,6-anhydro-β-D-glucopyranose). The liquid water they obtained contained small amounts of organic material, namely furfurol and acids.

In early work on pyrolysis of cellulose Schwenker and Pacsu (152) were interested in composition of the tarry aqueous solutions. They pyrolyzed cotton fabric in air at 350°C

and 375 °C. The heating rate was not reported. In that work, they obtained average condensables yield of 68.1% and the average char yield was 12.1% (85.42% carbon and 3.38% hydrogen content). By analyzing the aqueous solution by paper chromatography they found levoglucosan to be the major product (12.5% of the total pyrolyzate). The authors concluded that the cellulose pyrolyzate is a complex mixture of organic acids (formic, acetic, glycolic, lactic and dilactic), aldehydes, ketones, water and levoglucosan (14 or more different compounds). In their work there was no attempt to analyze gaseous products of pyrolysis. Also, Schwenker's group did a chromatographic study of pyrolysis products (151), using three different columns. They pyrolyzed purified cotton fabric (predried at 110°C) at 370°C (heating rate 15°C/min) in an atmosphere of air or purified nitrogen. The products were trapped at 75°C and -78°C. In another part of the study, small amounts of material were pyrolyzed directly within the injection port of the gas chromatograph on a hot wire loop. The authors indicated that a minimum of 37 different volatile products were obtained. The complexity of chromatograms, obtained in (151), are illustrated in Figure 2.5, which represents the original data from (151) as well as the peak identifications. The fixed gases were not separated, but they claimed that those were mainly carbon dioxide and carbon monoxide. Identified compounds were water and families of aldehydes, ketones, acids and small amounts of alcohol. Unlike other studies described so far here, they did not positively identify levoglucosan, although the conditions were such that levoglucosan could have not been withheld in a column (boiling point of levoglucosan is 180°C and the maximum operating temperature was 225°C).

Golova, Krylova and Nikolaeva (63) examined the behavior of cotton cellulose and cellulose hydrate (swollen cellulose) isothermally in vacuum at 305°C, achieving the final temperature in 5-10 min, and holding for residence times from 10 to 300 minutes. They found that the amount of tar, defined as percentage of total pyrolysis products, increased

with the amount of original cellulose decomposed (or with residence time) and the amount of gases decreased. Levoglucosan represented 56.7% to 71.6% of tars or 20% to 47% of original cellulose. Cellulose hydrate had a significantly lower yield of levoglucosan, at 44% cellulose decomposed the amount was only 0.9% of the original cellulose and at 76% cellulose decomposed levoglucosan yield was 5.7%. The char yield was found to be 15% after the mass loss was finished in 300 min, for cellulose, and 24% after 110 min for cellulose hydrate. The authors proposed two different stages of pyrolysis, the first up to 10-20% decomposed and the second up to 70-80%. The reason is that they observed steep changes in the amounts of pyrolysis products in first 20% of decomposition, which become rather moderate after 20%. The observed degree of polymerization sharply decreased during the first 2% of decomposition and after that remained relatively constant.

In a study aimed at identifying the action of flame retardants, Holmes and Shaw (75) pyrolyzed purified cotton cloth strips (pure, with various flame retardants and oxidized cellulose) in vacuum, at temperatures of 418°C (a few experiments at 318°C). They found that the amount of tar decreased and the amounts of water and gases increased for flame retarded samples. Three different temperature were used for collecting volatiles: at -190°C, at -80°C and room temperature. It was also found that fraction that remains volatile at -190°C was carbon monoxide, the fraction volatile at -80°C was mostly carbon dioxide, with small amounts of carbonyl compounds and other flame retardant related gases. The fraction volatile at room temperature was identified as water only. The room temperature non-volatile fraction consisted of tars, that were composed of levoglucosan (which was not found in oxycellulose products), carbonyl compounds and acids. Levoglucosan made up about 81.4% (62.9% of original material) of the total amount of tars for pure cellulose and about 53.9% (9.8% of original material) for fire retarded. Tables 2.2a and 2.2b represent a summary of the findings, taken from (75). In a continuation of the study, Holmes' group (33) in addition to the materials used in (75) used two more cotton materials and a few

more flame retardants. In that study they obtained significantly lower values for levoglucosan yield (from 27% at 350°C to 44% at 456°C on weight basis of dry cotton).

Berkowitz-Mattuck and Noguchi (19) studied the pyrolysis of untreated and flame retardant treated cellulose in helium under high heat flux conditions (210 kW/m^2 to 1050 kW/m^2), with exposure times between 0.5 and 2 seconds. Identified gases were carbon dioxide, carbon monoxide methane and ethylene. The identification of compounds that were present in the condensable fraction of pyrolysis products at -80°C was based only upon the boiling points and the authors indicate that their number is almost unlimited, but they suspect that there are twelve aldehydes, ketones, acids, esters, etc., containing three to six carbon atoms present, based on approximate boiling points (between 14°C and 178°C). The principal component of room temperature condensable fraction of pyrolysis was identified as levoglucosan and the results indicated a presence of an unidentified second component that contained a carbonyl group. It was also found that, generally, flame retarded cellulose gave higher char yields.

Martin (116) investigated the pyrolysis of α-cellulose sheets that contained about 2% carbon black in helium atmosphere under conditions of intense radiative heating (incident heat fluxes from 184 kW/m^2 to 670 kW/m^2). Total amounts of volatiles were 20% to 50%. The total number of compounds separated was 24. An example of analytical results for 184 kW/m^2 heat flux, obtained in (116) is shown in Table 2.3. He concluded that water and oxides of carbon make up the bulk of volatile material measured chromatographically and that the other determined components are decidedly minor (on a weight basis). Acids, esters, acetals and formaldehyde were missing from the chromatograms, apparently contrary to the authors expectations. The tars were not analyzed quantitatively, their infrared-absorption spectrum was compared to that of pure levoglucosan and it was found

that they compare well, except that there was another peak present at 5.7 μm, the same unidentified carbonyl group recorded by Berkowitz-Mattuck and Noguchi (19). An observation made by Martin was that the char yield in the case of low level heat fluxes was 25-30% and on higher level heat fluxes about 4%.

Decompositions of cellulose and levoglucosan were compared by Glassner and Pierce (62). They used α-cellulose pulp. The pyrolysis reaction chamber was a small oven directly connected to gas chromatograph. The temperature range was between 170°C and 360°C (the samples were dried at 110°C for 40 minutes and inserted into pre-heated oven) and the atmosphere was helium. Similar to the study of Schwenker and Beck (151) they found 34 different volatile products with three or four fixed gases peaks superimposed onto the air peak. Positively identified compounds were primarily aldehydes, ketones and acids. Also, they demonstrated that the cellulose pyrolysis products were essentially the same as levoglucosan pyrolysis products at temperatures above 242°C and that led them to the conclusion that cellulose decomposes through levoglucosan as an intermediate.

Lipska and Wodley (111) studied isothermal pyrolysis of pure and fire retardant treated α-cellulose in a fluidized bath in atmosphere of nitrogen and on temperatures between 298°C and 360°C (the sample temperature raised to pyrolysis temperature in 15 seconds). Their analytical technique (gas chromatography, with mass spectrometric confirmation) pertained only to the degradation products with molecular weights below 110 and did not include char and tar. A sample chromatogram, obtained by analyzing products of pyrolysis at 315°C is shown in Figure 2.6. The authors have identified 17 out of total of 34 peaks. They found water to be the predominant constituent of pyrolysis products. One of the conclusions from this work was that the flame retardant does not have an effect on the types of degradation products. However, it was shown that the amount of water and

carbon dioxide, relative to the rest of the products increases.

Untreated and flame retardant treated cellulose pyrolysis was a subject of a study by Tsuchiya and Sumi (185). The samples were made from Whatman No. 40 filter paper with ash content 0.018%. Pyrolyses were performed isothermally under vacuum, at temperatures from 320°C to 520°C for 20 minutes. An example of chromatogram obtained in that study is represented in Figure 2.7. The authors have concluded that the main decomposition products were large organic fragments such as the monomers (levoglucosan and 1,6-anhydro-b-D-glucofuranose), dimers, an unidentified product at a retention index of 2270, water, carbon monoxide and carbon dioxide. Also found, in smaller quantities, were many carbonyl compounds, organic acids and hydrocarbons, which are believed to be the products of secondary reactions.

Shafizadeh's group (26, 158, 162) studied pyrolysis of Whatman (CF 11) chromatographic cellulose powder (26, 158) and a variety of other cellulosic materials (162), under atmospheric pressure of nitrogen (158, 162), in vacuum (158, 162) and under 1.5 Torr pressure with nitrogen flow (26). The experiments were done isothermally, at several temperatures: 300°C (predried at 100°C for 2 hrs, residence time at 300°C 2.5 hrs) in (158), between 259°C and 341°C in (26) and between 300°C and 500°C, with various residence times, but shorter at higher temperatures (162). Table 2.4 shows a comparison of pyrolysis product yields at atmospheric and reduced pressures (158). As can be seen, the char yield increases with increasing pressure, whereas the yield of tar decreases. Also, the yields of levoglucosan, a major tar component, and 1,6-anhydro-β-D-glucofuranose decrease with pressure increase. It is shown in Tables 2.5a, b and c, for various cellulose materials, that the char yield increases and tar (and therefore, levoglucosan) decrease with increasing the pyrolysis temperature. From the same study (158), a chromatogram of cellulose pyrolysis tar is shown in Figure 2.8. It is confirmed there that the major

constituent of tar is levoglucosan, with another major portion of 1,6-anhydro-β-D-glucofuranose. There were detected small amounts of α-D-glucose, β-D-glucose, different tautomers of 3-deoxy-D-erythro-hexosulose and oligosaccharide derivatives. In one of the studies (162) the authors discuss the possible errors in determination of levoglucosan yields from tars. They argue that, based on reported analytical techniques, most of the studies prior to (162) have overestimated levoglucosan yields and that the part of the reported values is, "almost certainly", 1,6-anhydro-β-D-glucofuranose. As one of the proofs, they offer Holmes and co-workers correction (33) of levoglucosan content.

Basch and Lewin (13) investigated the effect of crystallinity on the pyrolysis of different materials derived cellulose. The pyrolyses were performed in air at 251°C. They found that levoglucosan made up to 35% of tar, depending on crystallinity. Their data is represented in Table 2.6 and Figure 2.9.

In a study of rapid cellulose pyrolysis Hajaligol et al. (68) used 0.101 mm thick strips of low ash (<0.007 wt %) filter paper. Pyrolyses were performed at heating rates from ≤100°C/s to 15,000°C/s, to the final temperatures between 300°C and 1100°C, with residence times up to 30 seconds in the atmosphere of helium, at pressure of 136 kPa. A summary of their data is represented in Table 2.7. The major component found in gaseous products of pyrolysis was carbon monoxide and the other two major gaseous products were water and carbon dioxide. Relatively smaller amounts of alkanes, hydrogen, ethylene, alcohols, acataldehyde, acetone, furan and carboxylic acids (mainly acetic) were detected. Elemental analyses of char and tar are provided, but tar composition is not reported. However, according to the unpublished work of Bhadha cited in (68) it is believed that tar contains at least several hundred compounds. They concluded that the increase in severity of pyrolysis conditions leads to smaller char and tar yields and higher yields of gases. The

explanation for that phenomena is that tars undergo secondary reactions during its relatively short residence time in the elevated temperature region in the sample surroundings and that those secondary reactions are source of production of hydrogen, carbon monoxide and light hydrocarbon gases.

Lipska-Quinn et al. (112) studied the pyrolysis of rice straw and its components and wood cellulose in atmospheres of dry air and nitrogen. It was noted that cellulose, prepared from rice straw, retained high ash content (9.3%, compared to the original ash content of rice straw of 15.9% of oven dry weight), while wood cellulose had an ash content of 0.1%. Heating rates were 5, 10, 20 and 40°C/min and the final temperature was 600°C. The complexity of pyrolysis product mixture can be judged from Figure 2.10. A comparison between rice straw derived cellulose and wood cellulose shows a qualitative agreement of compounds found. Quantitatively, it seems that the amounts of products are a little bit different. As expected, there are more products evolved in pyrolysis of non-treated rice straw (not shown here).

Cullis et al. (45) were interested in pyrolysis of Kipawa 97 cellulose, which is the basic component of cigarette paper. As the choice of cellulose implies they were concerned about its behavior during cigarette smoking. The heating rates were between 5°C/s and 25°C/s, in the atmosphere of helium and nitrogen. They investigated an effect of carrier gas flowrate on gaseous products of pyrolysis. The gas was sampled with a syringe up to 8 mm from the sample in downstream direction and up to 2 mm of the central axis of the sample. A summary of their findings is shown in Tables 2.8a and 2.8b for helium flow rates of 100 ml/min and 200 ml/min. The relative amounts of gases vary with the pyrolysis temperature, but it can be said that the main gaseous pyrolysis products were found to be carbon monoxide, carbon dioxide, hydrogen, methane and ethylene, and the minor, but measured,

components were ethane, propene, propyne, butane and butene. As expected, increasing the flowrate of carrier gas causes the concentrations of gases to decrease.

Agrawal et al. (2) investigated the pyrolysis of as received and acid washed newsprint (single edition of The New York Times) under conditions of reduced pressure (below 1 Torr), over the temperature range 260-340°C. They found that the major components of the product tars were levoglucosan and its stereoisomers. The main components of the gaseous pyrolysis products were carbon monoxide, carbon dioxide, water and methane. There were identified several trace compounds, such as formaldehyde, acetaldehyde, acetone, methanol, propanol, 2-methylfuran, acetic acid, furfural, 2,3-butanedione, methyl ethyl ketone, crotonaldehyde and cyclopentane. It was shown that an acid wash pretreatment increases tar yields largely at the expense of gaseous products. The same group (1) studied the effect of pressure on the pyrolysis of newsprint and found that the tar yield decreases with pressure increase (but still sub-atmospheric). Contrary to that observation, Radlein et al (142) did not find any yield variations with pressure.

Evans and Milne (55) used molecular-beam, mass spectrometric sampling of products from pyrolysis of wood and its principal isolated constituents. Pyrolyses were conducted in helium, at an estimated heating rates between 30°C/s and 50°C/s. The final temperature of the reactor was 550°C. They, however, point out that the actual sample temperature was not known due to the endothermic process. Table 2.9 shows a summary of their analyses. It was noted that the major product of pyrolysis of cellulose is levoglucosan, but that it is completely decomposed when vapor phase cracking is induced. During the vapor phase cracking, decomposition leads mostly to carbon dioxide and carbon monoxide with low molecular weight alkenes such as ethylene, propylene and butene. Some aromatic species were also detected, such as furan, benzene, toluene and phenol.

In a simultaneous thermogravimetric-mass spectrometric study, Varhegyi et al. (188) used Avicel cellulose with and without catalysts. The heating rate was 10°C/min and the atmosphere was argon. They estimated, by difference, that tars represented about 70%, by weight, of original material. The major gaseous products of pyrolysis were water (17%), carbon monoxide (4%) and carbon dioxide (1.5%). Also, they estimated the total amount of various aldehydes to be about few weight percent and the amount of furan and 2-furaldehyde to be less than 0.1%. Char accounted for about 5%, by weight at 450°C. An interesting observation was reported. The evolution of water, furan and 2-furaldehyde preceded the differential thermogravimetry curve by a few degrees Celsius. The authors argue that the dehydration reactions make a greater contribution to the weight loss during the early stages of decomposition. Sample preheating (at 260°C for two hours) did not produce any marked effect on subsequent sample yields or kinetics. When a closed sample holder (with a pinhole at the top) was used, however, they observed considerably higher yields of water, CO, CO_2 and char, with only a small impact on the overall differential thermogravimetry curve. Their explanation for that phenomena was that the increase in CO, CO_2 and char yields was due to the secondary reactions.

Julien et al. (79) studied the pyrolysis of untreated and acid washed Sigmacell α-cellulose in vacuum. The final temperature and heating range were varied between 210°C and 525°C, 2°C/min and 16°C/min, respectively. A summary of their data is shown in Table 2.10. They found that the acid wash treatment (reducing the amount of ash, but introducing the acid impurity) has an effect of increasing the yield of total organic liquid at the expense of water, char and gases yields. Up to temperatures of 325°C the composition of char changes slightly, whereas at temperatures above 325°C they observed disappearance of certain bands (in FTIR) and that the material is completely amorphous (by X-ray diffraction). The product correlations were made and it was found that most of the liquid products yields

(from Table 2.10) vary linearly with carbon monoxide yield. The total amounts of char, pyrolytic water, formic acid and levulinic acid also correlate well with carbon dioxide yield. In light of their results they propose a mechanism for cellulose pyrolysis, which will be discussed below.

In a recent study Kashiwagi and Nambu (87) were interested in global kinetic constants of cellulose pyrolysis. They used office supply black paper. Pyrolysis experiments were carried out in nitrogen, 0.28%, 1.08%, 5.2% oxygen concentrations and air. The heating rates employed were 0.5, 1, 1.5,3 and 5°C/min. It was found that water represents a major constituent of gaseous pyrolysis products, followed by carbon dioxide and then carbon monoxide. Concentrations of latter two gases indicated that the char degradation continues over a wide temperature range after the pyrolysis reaction, but the authors argue that the char degradation is negligible. The found that, under their conditions, the char yield is not affected by the heating rate.

2.2.2 EFFECTS OF VARIABLES ON PRODUCT YIELDS

Product yields are heavily influenced by a choice of pyrolysis conditions. Again, the yields of various (major) products of pyrolysis can be very crudely controlled. In a situation where the conditions are largely unknown, such as a fire, the prediction and, especially, control is very difficult task.

For a fire protection engineer, or a fire modeler, a knowledge of every single component present during the pyrolysis (and combustion, for that matter) of cellulose does not represent the most useful knowledge. More important is the "will it, or it will not burn?" question; if it will burn, how much heat or how much toxic gases, can one expect? For that

reason, this part of the background review will be structured slightly differently than the preceding. The purpose of this part is to outline the available information in such a way that it can be used by somebody interested in major products of pyrolysis, their yields and what the variables are that can cause the change of relative amounts of products. In this part, the products will be termed: char, tar and gases. Water will be separately treated to the extent possible.

Holmes group (33, 75) studied pyrolysis of different cellulose materials with and without flame retardants in vacuum. They found that with temperature increase (in isothermal experiments from 350°C to 500°C) the amount of tar increases. Addition of flame retardants resulted in increasing char yield and decreasing tar yield with increasing the amount of retardant added. Cellulose decomposition was divided in two stages by Golova et al. (63). During the first stage (up to 20% decomposition) the yield of tar sharply increases and then, in the second stage (additional 70-80%) remained a relatively constant fraction of mass loss up to the point where about 65% of the material is decomposed and then decreased, while the amount of gases sharply decreased and then remained relatively constant, followed by an increase at the same point where the concentration of tar decreased. For cellulose hydrate, it was found that the amount of tar increased steadily up to the point where about 65% of the material was decomposed and the amount of gases decreased, with no increase beyond 65% conversion.

A very important conclusion from the point of view of fire protection and modeling was drawn by Martin (116), who studied diffusion controlled ignition of cellulose, under conditions of intense radiative heating. He stated: "The persistence of ignition depends only upon the continued flow of flammable, volatile products, not on any unique composition of the mixture". In his work, he found that cellulose was spontaneously ignited, under a

diffusion controlled regime, when the surface reached a constant temperature of 600°C to 650°C. Interestingly enough, his data, as shown in Figures 2.11a and 2.11b for incident heat fluxes of 184 kW/m^2 and 486 kW/m^2, indicate that, in the pre-ignition period the amount of tar increased, gas amounts decreased and in the post-ignition period, the trend reversed. The trend is similar for other minor volatile products of pyrolysis. As noted above the char yield in the case of low level heat fluxes was 25-30% and for higher level heat fluxes about 4%.

The effect of the high intensity radiative heat flux on pyrolysis products of cellulose is shown in Figures 2.12a and 2.12b, adopted from Berkowitz-Mattuck and Noguchi (19). Again, it can be seen that the more severe pyrolysis conditions lead to more gases and less char. On the other hand, it does not seem that the addition of flame retardant has a profound effect on gas yields, which cannot be said for char yield, despite the data scatter.

In general, the studies can be divided, in terms of the nature of sample heating into three categories: isothermal, dynamic with isothermal hold, and purely dynamic. This distinction is necessary in order to compare the results from different studies. No matter how an experiment was performed it is common to all studies that the yield of char decreases with increasing severity, either temperature or heating rate. In a study by Hajaligol (65, 68) it was observed that the char yield very slightly increases (from 3.32% to 3.91%) at temperatures higher than 800°C, due to tar cracking, since there was not enough time provided for them to escape high temperature zone (see Figure 2.13). A study by Lewellen et al. (108) indicated that cellulose can be converted completely to volatiles, provided that the heating rate is very high, and no mass transfer limitations exist.

Isothermal studies have shown that at lower temperatures, tar yields increase with temperature. For Shafizadeh's group (26, 162) the low temperature region is up to 500°C.

Their data is conveniently plotted in a review paper by Shafizadeh (160) and it is shown in Figure 2.14. The work by Agrawal et al. (1, 2) showed a lower temperature region where the amount of tar yield increased up to 475°C. Tsuchiya and Sumi (185) had a low temperature region to approximately 460°C, after that temperature the tar yield decreased. A summary of their data is shown here in Figure 2.15. Dynamic studies show a similar trend. At lower temperatures the tar yield increases (65, 68, 79) and at higher temperatures a decrease was observed (65, 68, 153). Scott et al. (153) observed a decrease in liquid (which also included water) yield from cellulose pyrolysis at high heating rates throughout the temperature range they used (450°C to 900°C). However, they indicate that the maximum liquid yield occurs near 450°C, for the type of cellulose they used. In the same study (153) the liquid yield from pyrolysis of maple wood (included here for comparison only) increases up to about 520°C and after that temperature the yield decreases. In a study by Julien et al. (79) a maximum was not observed for tar yield, it remained rather constant, once the pyrolysis was completed up to about 550°C. The same result was obtained by Kojima et al. (98), who also found that the elemental composition of tar did not change in temperature range of 350°C to 550°C. Therefore, it can be concluded that the tar yield, depending on temperature, can increase to the maximum and then decrease unless quickly removed from the hot zone. In Hajaligol's study it is possible that the maximum of the tar yield is seen at higher temperature in cotrast to other studies due to the high heating rates used. It is quite plausible that Hajaligol's maximum tar yield temperature is also more indicative of primary tar yield since the system used in their study had almost no mass transfer limitations, which cannot be said for other studies. Mass transfer limitations can increase the probability for secondary, tar cracking, reactions, by providing sufficiently high residence times of tar in contact with char.

The amount of generated gases generally increases with temperature (65, 68, 79, 87, 98,

153, 185). In some studies (2, 45, 162 reviewed in 160) the amount of gases decreased. In a study by Agrawal et al. (2) the amount of gases decreased slightly, but steadily, in the temperature range between 250°C and 475°C, for non washed newsprint, while for acid washed newsprint it remained relatively constant in the same temperature range. Cullis et al. (45) observed a decrease in gas amount at temperatures above 350°C. Shafizadeh's group (160, 162) reported a decrease in gas amount at temperatures higher than 375°C (see Figure 2.14). It is not obvious why the amount of total gas should decrease above certain temperatures but it might well be due to the fact that the increase in tar yield removes gas precursors from the system, before cracking reactions release the gases.

Pressure affects the pyrolysis process in that with increasing pressure, the amount of char increases (1, 21, 65, 122, 158). Also it was observed that the amount of tar decreases (1, 65, 158) and that the amount of gases increase (65) with pressure increase. All these data are consistent with the hypothesis that the increased pressure reduces the ability of vaporized tars to flow out of the sample as fast as they would flow in a case of low pressure. That would promote secondary reactions of tar decomposition, which would reduce its amount and increase the amount of char and gases formed, which is, again, consistent with the data.

Impurities and flame retardants have an effect on cellulose pyrolysis. Generally the tar yield decreases, while char and gas yields increase, when impurities are present. Chen et al. (39, 40) and Byrne et al. (33) found that fire retardant concentration increases caused tar yield to decrease and gas and char yields to increase. Many studies (19, 29, 75, 111, 117, 158, 177, 185) have similarly found that addition of flame retardants has a similar effect; fire retarded cellulose gives lower tar yields, while char and gas yields increase. On the other hand, acid washing of newsprint (2) resulted in increased yield of tar and decreased

amounts of char and gases. Similar results were obtained by acid washing of cellulose, which reduced the amount of ash, but introduced an acidic impurity (79). Varhegyi et al. (188) used four inorganic salts (magnesium, sodium and zinc chlorides and iron sulfate) and found that the effect cannot be generalized. Addition of a salt to cellulose can result in gases and/or water yield increases, as compared to original cellulose, but addition of different salts can have completely different effects.

Crystallinity was shown to decrease with weight loss of pure cellulose held isothermally at 260°C and to slightly increase (75% to 77%) during the first 2% of weight loss and after that again slightly decreases (192). For ammonia treated cellulose heated isothermally at 250°C crystallinity also passes through a maximum. However, the reported crystallinity changes are so minute, about few percent, that there is a possibility that the data reflects an experimental artifact. In a study of pyrolysis of different celluloses in air at 251°C, Basch and Lewin (13) report that there is a correlation between levoglucosan content in tar and crystallinity, the amount of levoglucosan in tar increases from 13% in 41.6% crystalline cellulose to about 35% in 71.3% crystalline cellulose (see Figure 2.9).

2.2.3 PYROLYSIS OF "BULK" CELLULOSIC SAMPLES

Pyrolysis of "bulk" (large size) cellulosic samples is different from pyrolysis of small samples due to transport (heat and mass) limitations. In work in which large cellulose samples were used it was observed (120) that transport limitations play a significant role in overall behavior of the material. This is similar to what happens, for example, in coal (see refs. 173 and 174). In a fire, transport limitations often determine the course of the event. Within the pyrolyzing solid, transport limitations depend mostly on the thermal properties and the structure of materials used. These are general similarities among all charring

materials. Therefore, the intent this section is to outline the available information about the pyrolysis behavior of bulk charring solids, irrespective of geometry.

Lee, Chaiken and Singer (106) performed one-dimensional radiative heating experiments on bulk wood samples (0.62 g/cm^3 density) and found that a pyrolysis wave moves with a constant velocity through the sample during the first half of the heating period. The applied heat flux was 83.7 kW/m^2 and the grains were parallel with the direction of the heat flux. Different behavior was seen in the case when the heat flux was 31.8 kW/m^2, the pyrolysis wave was thicker than in the higher heat flux case. When the grain orientation was perpendicular to the direction of 83.7 kW/m^2 heat flux, the velocity of a pyrolysis wave was not constant, but the temperature profile was more reminiscent of the same heat flux and different grain orientation than in the lower heat flux case. Although the authors found a constant velocity of a pyrolysis wave they did not find a constant mass loss rate. The closest to the constant mass loss rate were the low flux cases of 22.2 kW/m^2 and 31.8 kW/m^2 heat fluxes. In a similar study, Lee and Diehl (105) investigated combustion of dry (density 0.738 g/cm^3) and wet oak (density 1.0 g/cm^3)at a heat flux of 83.7 kW/m^2. The samples were cylinders with a diameter of 19 mm and length of 127 mm. They also found that the mass loss varies linearly with time, after an initial non-linear period.

Blackshear and Murty Kanury (22) investigated radially flame heated cylinders, pressed from filter paper clippings of α-cellulose, in air. The density of the samples was 0.64 g/cm^3. They found that the burning rate is constant for the period following ignition up to one third of the entire burning time of the sample. The density distribution is reminiscent of the 31.8 kW/m^2 heat flux, parallel grain orientation from the Lee, Chaiken and Singer's paper. This is not surprising since a similar heat flux of about 40 kW/m^2 was involved.

In another paper Murty Kanury and Blackshear (83) have performed a pyrolysis of the

same type of samples (cylinders, pressed from filter paper clippings of α-cellulose, with a density of 0.605 g/cm^3). They concluded that a constant mass loss kinetic regime exists such that:

$$\frac{d\rho}{dt}\frac{1}{(\rho - \rho_{char})} \approx \text{Constant} = 0.2 \text{ per second}$$

Their explanation for the occurrence of the constant mass loss regime is that migrant condensates are reevaporating in the range of temperature between 300 and 400°C, where the plateau occurs.

It was also observed that for cellulose cylinders burning in free convection (81) a plot of fractional mass loss vs time can be normalized by a factor of diameter to the n-th power, to give linear behavior for at least the first half of the normalized burning time. These results suggested that the mass loss rate was constant for the first part.

In a series of papers, Phillips and Becker (14, 15, 16, 138) reported investigations of pyrolysis and burning of white pine sticks (diameters 9-50 mm, length 300 mm) in an air flow environment (wind tunnel with velocities of 3-18 m/s and temperatures of 357-857°C). Early in the process they observed a linear mass loss with time. It seems from their data (14) that the linearity extends over larger periods of time when the temperature is higher, although this was not discussed in the paper. They took the linear change of mass with time as an empirical generalization for their range of operating conditions.

Bennini et al. (17) studied the effect of an intense thermal flux on pyrolysis of pellets

pressed from ground poplar wood. The pellet diameter was 12 mm and there were four thicknesses used, from 1 mm to 4 mm. The density of a pellet was 0.884 g/cm^3. It is reported that the samples were heated by means of a lamp, with power from 2 to 6 kW. The heat flux used was not reported, but they use a value of 4000 kW/m^2 for mathematical modeling. They observed a linear variation of mass loss with time all the way up to 80% of mass loss. Their explanation for such a behavior was that the global reaction kinetics of a solid-gas reaction are limited by the kinetics of the chemical reaction. Further, they argue that in their case, the reaction kinetics are limited by the kinetics of two chemical reactions. It is not clear from the paper what the solid-gas reaction is, nor what are the two limiting chemical reactions. Their reasoning is a result of comparison to a shrinking core model.

It appears rather peculiar that none of the above studies addressed the question of mass loss linearity with time, except Bennini et al. (17). This phenomenon seems to be quite important in terms of fire behavior. The linearity of the mass loss with time means that the mass is being lost at a highest possible rate, through a significant part of pyrolysis. What can cause the mass loss rate to be constant? The pyrolysis proceeds, at a given constant heating rate, within fairly narrow temperature range, with an activation energy of probably no less than 125 kJ/mole, as will be seen later. With that activation energy, the kinetics determine the mass loss to behave as if it were "turned on" at a temperature that corresponds to the pyrolysis onset. Higher heat fluxes, or higher heating rates, in a bulk solid make temperature gradients steeper, and the pyrolysis is conducted in a thinner layer of the material and at a higher rate. That is true up to a certain amount of mass loss. Towards the completion of pyrolysis, the heat conduction through the built up char layer can no longer sustain the process of thermal wave penetration, the kinetics are not "turned on" over a thin zone, but rather proceeds at a low decomposition rate. This results in a deviation from a straight line. The same situation obtains for low severity pyrolysis conditions, where the thermal wave penetration is not fast enough, and the kinetics is not

"turned on".

What does all this mean for a fire engineer? The information that a solid can be decomposed at a constant rate is important for fire dynamics. The products of solid decomposition supply the fuel to the flame, which supplies a heat to the pyrolyzing solid. Towards the completion of pyrolysis, there are not enough tars being generated to sustain flaming combustion and the char becomes involved in smoldering combustion. Therefore, the rate at which the solid can decompose represents a valuable piece of information for a fire engineer.

During the pyrolysis of bulk cellulosic samples there is a temperature profile present, a sample is never isothermal. Of course, this could have been intuitively predicted, but the reason that it is important is because of the chemical kinetics of pyrolysis. The existence of a temperature profile means that the heating rates of different parts of a sample are different and, as it will be shown later, that fact can have a significant impact on pyrolysis kinetics and on different pyrolysis routes. Another feature of sample temperature profiles is the existence of inflection points. Some researchers report an inflection point for temporal temperature change, measured at various depths in a sample, apparently associated with the pyrolytic endotherm (16, 105), due to sample dehydration and/or drying (17, 103, 105) and in some studies both are noticed (22, 85, 91). The most important reasons for the appearance of an inflection point in time-temperature curves might be the endothermic heat effect of pyrolysis and sample dehydration and/or drying, but there might be other factors, maybe not as obvious as the endothermic heat effects. At the onset of pyrolysis there are several events occurring simultaneously. The material is being decomposed and its physical properties are being changed, density decreases, thermal conductivity decreases and emissivity might change. All those changes can significantly change the rate and

mechanism of heat transfer and they should not be neglected. As far as the inflection point due to sample dehydration and/or drying is concerned it is possible that it might be partly due to the reevaporation of condensed pyrolytic water that might have diffused deeper into the sample, further from the heated surface.

In papers by Lee's group (105, 106) and Tinney (183) the authors report pressure measurements inside a pyrolyzing sample. In (106) the pressure was shown to reach as high as 0.3 atmospheres inside the pyrolyzing cylinder of maple wood, in (105) 0.014 atmospheres inside the pyrolyzing cylinder of oak and in (183) 0.14 atmospheres inside the pyrolyzing white fir dowels. An interesting observation in those works was that the pressure due to the moisture reaches its maximum after 100°C, but the pressure due, presumably, to the volatiles release reaches its maximum before the apparent inflection point in the time-temperature curve (at about 320°C in Tinney's work and at about 300°C in Lee's work). In both papers the pressure starts to increase at about 200°C. In both works at about 200°C the pressure due to the moisture evaporation has already returned to zero, which means that this process is not responsible. Is it possible that gases can cause cracking of the structure and fissures formation prior to the main decomposition? According to McCarter (117), it is. He measured the sample temperature as well as the amount of total combustible gases and he found that, in small samples, the gases start to evolve prior to the main pyrolytic endotherm.

There was no evidence found in the literature that mass transport can limit the pyrolysis process. Even in the case where a significant pressure was developed (183), the temporal mass loss change is a smooth curve. The mass transport is important in terms of product composition, but it does not seem to be important as a limiting factor in overall kinetics of pyrolysis of bulk samples.

2.2.4 KINETICS OF CELLULOSE PYROLYSIS

A considerable amount of work has been done on the kinetics of cellulose pyrolysis under different conditions. It is an important subject, in terms of predicting and understanding fire behavior, since the evolution of combustible volatiles depends on the rate of pyrolysis and, therefore, the fire dynamics depend, at least partly, on the kinetics of thermal decomposition. Although it seems obvious that cellulose does not decompose by a single route, there were attempts made by various researchers to fit the experimental data with one set of kinetic parameters. The reason for doing so is not a desire to explain the pyrolysis process by a single mechanistic expression, which is very likely impossible, but to predict the mass loss rate, or the rate of combustible volatiles generation, with a single set of kinetic parameters. If this were possible it would enable fire modelers to focus on other aspects of modeling, other than chemical kinetics.

In a classical review of kinetic data of pyrolysis of wood and related substances Roberts (144) points out that there are two main groups of kinetic parameters. He concluded that the pyrolysis of carefully purified cellulose can proceed with an activation energy of about 235 kJ/mole, while traces of impurities can cause the process to proceed with the activation energy of about 125 kJ/mole. It is proposed that the former route involves a depolymerization and the latter, catalyst-sensitive decomposition. Roberts also notes that the lower value is the only one observed in large samples. This makes clear the fact that there are confusing reports of kinetics, because some may involve catalytic pathways, whereas other similar parameters can come from transport limited experiments.

Data of Lipska and Parker (110) and Lipska and Wodley (111) indicate that isothermal pyrolysis of cellulose is a process that can be described by a single activation energy of 176

kJ/mole in temperature range of 250°C to 360°C. It should be noted that the samples used by Lipska et al. were single disks 20 mm in diameter, 0.76 mm in thickness and had a density of about 0.75 g/cm^3. Their data are somewhat questionable since it was noted here that there might exist significant heat transfer limitations during the pyrolysis of large cellulose samples. However, since their study was isothermal, it is possible that the heat transfer limitations do not play a very significant role due to the length of experiments, of the order of several hours. They found that the initial period of pyrolysis follows zero-order reaction and later, depending on temperature (transition at 50% mass loss for 288°C) shifts to first order reaction.

Shafizadeh et al. (157) obtained an activation energy of 113 kJ/mole for isothermal pyrolysis in nitrogen after rapid heating. They observed an "initiation period", after which the process is found to follow first order kinetics. The same group (26) proposed low-temperature, first order, initiation reaction (with activation energy of 243 kJ/mole) followed by two competitive, first order, reactions, one leading to volatiles (with activation energy of 198 kJ/mole) and the other leading to volatiles and char (with activation energy of 153 kJ/mole). Broido and Weinstein (27) reported the activation energy for first order pyrolysis of ammonia-swelled cellulose of 230 kJ/mole and the pre-exponential factor of 5.25×10^{17} s^{-1}. They used a dynamic TGA technique, with the constant heating rate of 4.5°C/min.

Murty and Blackshear (83), in their X-ray photographic study of cellulose pyrolysis, found that the activation energies for first order decomposition of large (35 mm in diameter) cellulose cylinders depend on the relative radial position and it varied from 57 kJ/mole (pre-exponential 1.96×10^4 s^{-1}) to 95 kJ/mole (pre-exponential 4.42×10^6 s^{-1}). While it is tempting to dismiss these kinetics as artifacts of a transport limited system, we believe that there may, in fact, be a true shift in kinetic parameters in large bulk samples. Lower values are reported by Gulett and Smith (64) for the pyrolysis of pressed cellulose cylinders in

nitrogen of 7.85 mm in diameter and about 1g/cm^3 density in an isothermal furnace. They found that the activation energy of a first order pyrolysis reaction changes with the extent from 8.8 kJ/mole to 33.5 kJ/mole. Clearly these are purely empirical, transport limited values.

Rapid pyrolysis of cellulose (heating rates of 400 °C/s to 10,000 °C/s) under different pressures (vacuum to atmospheric) was reported by Lewellen et al.(108). The activation energy of first order cellulose filter paper decomposition was 140 kJ/mole. The pre-exponential factor was 6.79×10^9 s^{-1}. In a similar study Hajaligol et al. (68) (heating rate of 1000 °C/s) found the activation energy of the total mass loss during cellulose pyrolysis (the same material used by Lewellen et al.) to be 133 kJ/mole and the pre-exponential factor of 2×10^8 s^{-1}. Suuberg and Dalal (171) used the Lewellen et al. parameters to fit the data obtained from cellulose powder pyrolysis at heating rates of 5 °C/min, 100 °C/min and 1000 °C/min. They found good correlation for two higher heating rates but that those parameters do not fit the data very well for 5 °C/min.

Samolada and Vasalos (149) have done a pyrolysis study on fir wood in a fluidized bed reactor. They have obtained two different activation energies, both for first order reaction, 56.48 kJ/mole (pre-exponential factor of 136 s^{-1}) and 94.49 kJ/mole (pre-exponential factor of 23833 s^{-1}) for total volatiles and gases respectively. The samples they used had a mass of 2 g and the particle size was not reported. The fluidization medium was nitrogen and the estimated mean heating rate was 1000 °C/min. Again, it is unlikely that these kinetic parameters are representative of the true chemical kinetics. Antal and coworkers report the activation energy of rapid pyrolysis of cellulose powder (greater than 2°C/s) to be 100.5 kJ/mole with a pre-exponential factor of 1.2×10^6 s^{-1} (175). The reaction order was "nearly first" (0.9 ± 0.05). For lower heating rates of 10°/min and 80°/min the activation energies for

the first order decomposition they obtained were 234 kJ/mole (pre-exponential factor of 4.4×10^7 s^{-1}) and 205 kJ/mole (pre-exponential factor of 3.6×10^6 s^{-1}), respectively (187). In a recent paper Kashiwagi and Nambu (87) obtained an activation energy of 220 kJ/mole for pyrolysis in nitrogen of office supply black paper at heating rates of 0.5 °C/min, 1 °C/min, 1.5 °C/min, 3 °C/min and 5 °C/min. They found the order of pyrolysis reaction to be 1.8 and the pre-exponential factor of 2×10^{17} s^{-1}.

Tang and Neill (177) studied the effect of flame retardants on pyrolysis and combustion of cellulose at 3°C/min in vacuum. They found two different activation energies: for the initial stage, that changes from zero to first order, it was about 143 kJ/mole and for the final, first order, stage it was about 228 kJ/mole. That result is similar to Arseneau's (8) who used filter paper and obtained an activation energy of 152 kJ/mole for the first 5% of the mass loss and 190 kJ/mole for the mass loss up to 60%. The conditions that he used were: heating rate of 1.5°C/min and the atmosphere was flowing nitrogen.

McCarter (117) found that pyrolysis of a pure cellulose sample heated at 60°C/min differs from the quasi first order decomposition and observed initial reaction "indicating an activation energy as implausibly high as 754 kJ/mole". Upon pre-treatment, by heating for several seconds above 350°C, where the mass loss was no more than 30%, he found an activation energy of a single first order reaction of 170 kJ/mole.

Basch and Lewin (12) investigated the effect of crystallinity on the activation energy and found that for various cellulosic materials it ranges from 181 kJ/mole to 230 kJ/mole. They concluded that the activation energy is a function of crystallinity and the extrapolation to zero crystallinity yielded a value of 124 kJ/mole, whereas the extrapolation to total crystallinity yielded a value of 256 kJ/mole. Broido and Weinstein (28), however, saw the

effect of crystallinity only in early stages of pyrolysis, and found an activation energy of 230 kJ/mole for ammonia-decrystallized cellulose decomposition.

Overall, it does not seem that much has been changed since Roberts (144) reviewed the kinetic data. Reliable values of activation energy cluster about two numbers, one higher (about 210 kJ/mole) and one lower (about 150 kJ/mole). The values outside this range probably reflect some type of transport limitations in the experiment. It can be seen that if the kinetic parameters are deduced from large sample data they tend in general to be lower. That is probably due to the existence of temperature gradient within a sample. The higher the activation energy, the more temperature sensitive the process is, and if the temperature is not well known the less reliable the deduced kinetic parameters.

The source of the two different values for cellulose pyrolysis activation energy does not seem entirely obvious. Roberts (144) cannot be correct that the higher value is depolymerization activation energy and the lower is the activation energy for catalyst-sensitive decomposition because both values are seen in the same relatively pure material pyrolyzed under different condition. As noted above, there are a few studies on carefully prepared samples, with no impurities, where the low value is observed. Kashiwagi and Nambu (87) used office supply of paper for their study and yet obtained higher value. There is no conclusive proof that impurities can be the source of difference. It is more likely that the differences in conditions are the reason for the different observed kinetic parameters. The higher heating rates seem to favor the lower value and the lower heating rates seem to favor the higher value. This is inconsistent with Shafizadeh's group (26) who propose a lower value for char formation (favored by low heating rates) and higher value for volatiles formation (favored by high heating rates). Therefore, even though there are many studies on kinetics of cellulose pyrolysis, the question about cellulose pyrolysis kinetics parameters is still not completely answered. It will be addressed further in this

work.

2.3 CHEMICAL MODELS OF CELLULOSE PYROLYSIS

Cellulose decomposes upon pyrolysis to char, tars and gases. There are several chemical models proposed to describe a general course of pyrolysis. Such models are useful in analyses of kinetics of pyrolysis, as they can serve in identification of potential paths that the material is taking during the pyrolysis. It is entirely possible that a very simplified model could help in distinguishing the routes of pyrolysis and, consequently, help in showing the reason for the two different values for activation energy of pyrolysis, described above. A chemical model also describes the chemical processes that are involved during pyrolysis and, as such, can suggest a step that could be modified by the action of a fire retardant.

Agrawal et al. (2) divided all the available models into four categories, redrawn in Figure 2.16. Models 3 and 4 are simplifications used for mathematical modeling of pyrolysis in the context of a larger combustion model. Also, model 4 is made for wood, whose pyrolysis has been modeled as a sum of independent pyrolyses of separate constituents, each first order in unreacted substrate and each giving rise to a separate set of final products.

Kilzer and Broido (95) propose a model by which is cellulose decomposed endothermically to dehydrocellulose, with the evolution of water, at a temperature range from 200°C to 280°C, followed by an exothermic decomposition char and gases. Another route, at temperatures from 280°C to 340°C is from cellulose to tar (primarily levoglucosan), by endothermic decomposition. Bradbury et al. (26) propose a similar model, with cellulose activation, followed by competitive reactions to give volatiles, by one route, and char and

gases, by another. Mok and Antal (122) combined the models proposed by Kilzer and Broido (95) and Bradbury et al. (26). Their model is shown in Figure 2.17a. It can be seen that cellulose is first activated and then decomposed via competitive reactions to anhydrocellulose (by dehydration) and levoglucosan (by depolymerization). Levoglucosan evaporates to give volatiles and decomposes to give char, whereas anhydrocellulose is pyrolyzed to give char and gases. They extended anhydrocellulose pyrolysis (Figure 2.17b) to two competitive reactions to form volatile intermediate (by endothermic reaction) and residual char and gases (by exothermic reaction). Strong exothermic decomposition further yields gases and other volatiles from the volatile intermediate. Lewellen's model (108) includes an intermediate ("tentatively identified as levoglucosan") which can be transported out of the solid matrix to give tar or undergo different reactions to give gases, organic volatiles, free radicals and char. Pyrolysis autocatalysis and/or char inhibition by some of the organic volatiles and free radicals is included in the model.

Shafizadeh (156) points out that cellulose pyrolysis is highly influenced by conditions. The possible degradation mechanism may include three competitive reactions (Figure 2.18) to form gases and char (Reaction 1), levoglucosan (Reaction 2) and combustible volatiles (Reaction 3). By means of secondary reactions, levoglucosan can decompose to combustible volatiles (Reaction 4) and gases and char (Reaction 5). Of course the distinction between levoglucosan and "combustible volatiles" is purely arbitrary, since levoglucosan itself is combustible. Combustible volatiles can be decomposed to gases and char (Reaction 6) and, also, gases and char, according to Shafizadeh's model, can be involved in secondary reactions with combustible volatiles (Reaction 7). A similar model is proposed by Hajaligol (65). The only difference between Hajaligol's and Shafizadeh's model is in involvement of gases and char in secondary reactions with combustible volatiles (Reaction 7, Figure 2.18), which does not exist in (65). Kojima et al. (98) analyzed their

data according to Shafizadeh's model, without reactions 6 and 7.

Radlein et al. (142) proposed a model that takes into account temperature, heating rate and inorganic ion content (Figure 2.19). This model is slightly different from the others because it goes a step further and proposes a pathway by which certain compounds are formed. Radlein's model was found to agree with the experimental observations by Julien et al. (79).

In summary, the literature contains a wide variety of pseudo-mechanistic models for describing cellulose pyrolysis. Some features appear in many of these models e.g. the notion of an activation step, or the idea that tarry volatiles can be cracked to char and light gases. Beyond this, there is, however, still no general agreement on the mechanism of pyrolysis. It is little wonder that in light of the lack of agreement on mechanism, there have not yet been definitive measurements of cellulose pyrolysis kinetics.

2.4 MATHEMATICAL MODELING OF BULK MATERIAL PYROLYSIS

In general, there are two different types of bulk material pyrolysis models: those for non charring materials (materials that completely vaporize during pyrolysis, e.g. PMMA) and others for charring materials (materials that tend to leave carbonaceous residue after pyrolysis). Since this work is mainly concerned with understanding the behavior of a charring material the literature reviewed here is focused mainly on models for charring materials. Several models for non charring materials are however included for comparison.

Table 2.11 summarizes the assumptions, the typically included terms, and boundary conditions for the key model equations, i.e. the energy equation, mass transport equation and rate equation. All models are for a one dimensional solid material. The pyrolysis

process is, in general, modeled as endothermic except in references 3, 86, and 194, where it was taken to be thermo-neutral, 145 and 183, where it was taken as exothermic and 135, where both endothermic and exothermic processes were considered. The condensation and re-evaporation of volatiles are not taken into account in any of the models. In reference 16 these effects were included in the specific enthalpy of pyrolysis, but the separate effects were not examined.

In all models the mass flux is determined by chemical decomposition rate, except in reference 118, where existence of volatiles is ignored. In reference 135, there are three volatile species considered, in reference 70 a multicomponent mixture is considered and in reference 47 two volatile species are considered. In the rest of the models, only one volatile species is considered.

All the models include an Arrhenius-type rate equation with the order of reaction either zero or one, except reference 99 where n-order reaction can be used. In references 37, 47 and 70 gas-solid reactions are included, while the others do not include such secondary reaction processes. The following subsections give more details about the different key model equations. Table 2.12 summarizes the properties used in models. The questions of properties was recently raised at a panel discussion during the Fire Modeling Session at the Annual Conference on Fire Research (Rockville, MD, October 1993). The conclusion was that the sources of property values for many modeling works are various handbooks and textbooks. It was also concluded that, apparently, many models predict incorrect behavior in a fire situation, due to the unavailability of the correct properties. It is also important to note that a failure of a model to correctly predict behavior can be inappropriately blamed upon inaccurate property data, if relevant data cannot be found. For that reason it was decided that thermal properties of cellulose, related to this study should be measured.

2.4.1 ENERGY EQUATION

What is here called the "energy equation" actually represents a composite equation which was compiled from different models. None of the models include all the terms that are listed in this composite energy equation. There are actually two energy equations considered. The first one is for modeling pyrolysis of a material with temperature gradients present within the solid. This situation corresponds to pyrolysis of a solid particle large enough that an internal heat conduction limitation plays a significant role. The second one is for modeling pyrolysis of a material with no temperature gradients present within the solid. This situation corresponds to a pyrolysis of an isothermal solid particle, as might apply for small particles.

2.4.1.1 GENERALIZED ENERGY EQUATION - ANALYSIS WITH TEMPERATURE GRADIENTS WITHIN THE SOLID

The assumption is made that the problem is one-dimensional in nature (x is distance into the solid). The cases of cylindrical or spherical geometry are not explicitly presented, but follow easily. The energy equation is:

$$\underbrace{\frac{\partial}{\partial t}\left[\varepsilon_p \rho_g h_g + (1-\varepsilon_p)\rho_s h_s\right]}_{1} \underbrace{- \frac{\partial}{\partial x}\left[k^* \frac{\partial T}{\partial x}\right]}_{2} \underbrace{+ \frac{\partial}{\partial x}\left[\rho_g u h_g\right]}_{3} \underbrace{- \frac{\partial}{\partial t}\left(\varepsilon_p p\right)}_{4} \underbrace{+ h_R \frac{\partial}{\partial t}\left[(1-\varepsilon_p)\rho_s\right]}_{5} \underbrace{- \frac{dI_S}{dx}}_{6} \underbrace{= 0}_{7}$$

$$\underbrace{\rho_s h_s}_{2} = \underbrace{\rho_v h_v}_{2a} + \underbrace{\rho_c h_c}_{2b}$$

where the terms have the following significance:

1 - changes in the enthalpy of the gas (i.e. net accumulation or loss of enthalpy in the gas contained within the solid

ε_p - porosity

ρ_g - gas density

h_g - gas enthalpy

2 - the enthalpy of the solid (net accumulation or loss)

ρ_s - solid density

h_s - solid enthalpy

2a - the enthalpy of the virgin material (in a situation in which the virgin material coexists with char at some point x)

ρ_v - virgin material density

h_v - virgin material enthalpy

2b - the enthalpy of the char (in a situation in which the char coexists with char at some point x)

ρ_c - char density

h_c - char enthalpy

3 - net heat conduction through the solid matrix and the gas in the voids ($k^* = (1 - \varepsilon_p)\, k_s + \varepsilon_p\, k_g$)

k^* - total conductivity

k_s - solid conductivity

k_g - gas conductivity

4 - convective thermal transport of gas through the porous solid

u - superficial gas velocity

5 - the work done by the gas

p - pressure

6 - heat sink (source in some models) due to the pyrolysis

h_R - heat of pyrolysis per unit mass

7 - radiation absorbed by the solid (in depth)

I_S - radiative heat flux

2.4.1.2 GENERALIZED ENERGY EQUATION - ANALYSIS WITH NO TEMPERATURE GRADIENTS WITHIN THE SOLID

The energy equation is:

$$V_p (\rho_v C_{pv} + \rho_c C_{pc}) \frac{dT}{dt} = V_p h_R (-w_s) + A_p \alpha F I + A_p h (T_f - T) + A_p \varepsilon \sigma (T_w^4 - T^4)$$

8a **8b** **9** **10** **11** **12**

where:

8 - change of the enthalpy of the virgin material (**8a**) and the char (**8b**)

V_p - particle volume

C_{pv} - virgin material heat capacity

C_{pc} - char heat capacity

9 - heat sink due to the pyrolysis

w_s - reaction rate (mass pyrolyzed per unit time and volume)

10 - heat flux to the surface by radiation

A_p - surface area of the particle

α - surface absorptivity

F - view factor

I - wavelength integrated intensity of incident radiation

11 - heat transfer from the surface due to the convection

h - gas to solid surface heat convection coefficient

T_f - free stream temperature

12 - heat transfer from the surface due to radiation

ε - surface emissivity

σ - Stefan - Boltzmann constant

T_w - reactor wall temperature

Note that terms 10 and 12 may apparently "double count" radiation from different sources. There is no ambiguity in the particular cases reviewed in Table 2.11; the attempt to show the full range of terms in a single generic equation is responsible for the apparent ambiguity at this stage.

2.4.1.3 BOUNDARY AND INITIAL CONDITIONS FOR THE ENERGY EQUATION

The boundary conditions for the case of the one dimensional energy equation are as follows:

Surface Energy Balance:

$$-k_f \frac{\partial T_f}{\partial x} = -k_S \frac{\partial T_S}{\partial x} + k_g \frac{\partial T_g}{\partial x} - \alpha F I - h (T_f - T_S) - \varepsilon \sigma (T_f^4 - T_S^4) - \rho_S u h_R$$

(1) (2) (3) (4) (5) (6) (7)

(1) = (2) + (3) refers to a simple conduction boundary condition. Addition of the term (4) considers a case of a defined incident flux of radiation. Inclusion of (5) and leaving out (1) constitutes the case of a convective heat transfer process at the surface. Addition of (6) to

any of the above cases considers radiative exchange involving another hot zone or wall. Addition of (7) involves considering an evaporative sink at the surface of the material. Again, not all terms will be present in any real case - this "equation" indicates the different types of terms used by all the different authors, and Table 2.11 shows what was actually used in any particular model.

In addition, the following are used in addition or in lieu of the above, in some cases:

$T = T_0$ for all x at t = 0 (general uniform solid initial condition, applied virtually everywhere)

$\frac{\partial T}{\partial x} = 0$ **(8)** (centerline symmetry condition, if infinite slab geometry)

$\frac{\partial C}{\partial x} = 0$ **(9)** (centerline symmetry condition, if infinite slab geometry)

$N = K (C - C_\infty)$ **(10)** (convective mass transport at the surface)

$T = T_0 @ x \rightarrow \infty$ **(11)** (case of semi-infinite solid)

$\rho = \rho_0 @ x \rightarrow \infty$ **(12)** (case of semi-infinite solid)

$\rho = \rho_{char}$ **(13)** (density behind pyrolysis front)

$T = T_S = const$ **(14)** (surface temperature of solid assumed constant)

$T = T_0 (1 + \eta t)$ **(15)** (surface temperature of solid assumed to rise

linearly with time)

$\dot{m}_S = \rho_g u_S$ **(16)** (mass flux balance at the surface)

Conditions listed under (9), (10) and (16) are not boundary conditions for the energy equation, but are sometimes used in lieu of explicit consideration of transport limitations.

2.4.2 GENERALIZED MASS TRANSPORT EQUATION

The mass transport equation is (for the case in which volatiles are treated as a single pseudo species):

$$\underbrace{\frac{\partial}{\partial t}(\varepsilon_p C W)}_{13} - \underbrace{\frac{\partial}{\partial x}\left(p W \frac{B_0}{\mu} \frac{\partial C}{\partial x}\right)}_{14} = \underbrace{b w_s}_{15}$$

where:

13 - rate of accumulation of volatiles in the solid

C - molar concentration of volatiles

W - average molecular weight of volatiles

14 - flux of volatiles

B_0 - permeability

μ - viscosity

15 - chemical decomposition rate

b - stoichiometric coefficient

2.4.2.1 BOUNDARY AND INITIAL CONDITIONS FOR THE MASS TRANSPORT EQUATION

$$\frac{\partial C}{\partial x} = 0 \qquad \textbf{(9)}$$ (centerline symmetry condition, if infinite slab geometry)

$$N = K (C - C_{\infty}) \qquad \textbf{(10)}$$ (convective mass transport at the surface)

$$\dot{m}_S = \rho_g u_S \qquad \textbf{(16)}$$ (mass flux balance at the surface)

2.4.3 GENERALIZED CHEMICAL RATE EQUATION FOR PYROLYSIS

The pyrolysis rate equation is:

$$w_s = -\frac{\partial \rho_a}{\partial t} = \rho_a^n A \exp\left(-\frac{E}{RT}\right)$$

where:

ρ_a - active (as yet unpyrolyzed) material density

n - reaction order

A - Arrhenius' preexponential factor

E - activation energy

R - gas constant

This equation has been discussed at length already.

2.4.4 RESULTS FROM DIFFERENT MODELS

It is not possible to directly compare the results from all models, for the simple reason that many different types of materials and conditions were employed in their development. Since the main point of this literature survey was to establish to what were the available models that can be used in modeling the results of the present study, it was decided to examine some models that give results that are representative of experimental findings in this work. The results that are given in the figures are replotted from the original papers, without any changes; that is, the models were not rerun to fit our conditions, but key results of the original studies that seem to explain certain aspects of results in this study are considered. Modeling specific to our situation will be presented in Chapter 7.

Figure 2.20 shows the fractional mass loss with time from a 100 μm diameter particle of cellulose, pyrolyzed in a freestream at a temperature of 800°C with a heat flux 16,000 kW/m^2 (99). It can be seen that the fractional mass loss shows a similar type of behavior as observed in some experimental works noted in Chapter 2.2 (mass loss is linear in time). The reason is probably that the process is limited by conduction, as will be discussed below. Unfortunately, no data are reported for pyrolysis after 6.75 ms, not much is known about the ultimate char yield. The char yield will however be below 10%, the last point on the plot.

Figure 2.21 shows a comparison of the measured and predicted surface temperature for a 5 mm thick particle of wood heated at 167 kW/m^2 (37). It can be seen that the predicted temperature is higher than the measured temperature. The authors believe that this is due to a higher heat flux being used for calculations than the heat flux which really reaches the surface of the sample. This is one of the key issues in modeling - correct account must be

taken of actual surface emissivity and reflectivity. Another interesting point, not discussed by the authors, is that the surface temperature trace shows clear change in slope at about 700°C. A similar change in slope is observed in other experimental works and it is probably due to the combination of several factors. These will be discussed in connection with the results of this study, in Chapters 4 and 5.

Figure 2.22 shows a comparison of the measured and predicted non-condensable (excluding tar and water) mass flux for the above case, replotted from Reference 37. The period during which the predicted temperature is higher than measured coincides with the period of higher predicted mass flux rate than measured. Thus there is a significant shortcoming in prediction of both temperature and mass loss rate, showing the importance of getting surface temperature correct.

Figure 2.23 shows a comparison of predicted and measured mass loss for a 10 mm wooden dowel heated in 500°C air, replotted from Reference 183. It can be seen that the predicted mass loss profile is sharper than the measured profile. It should be noted that for this model there was a "breakpoint" introduced for a change of parameters at a mass loss of about 73%. The authors have measured and predicted the linear mass loss with time at a middle stage of pyrolysis. They did not explain the reasons for the discrepancy between predicted and measured mass loss.

Figure 2.24 shows a calculated fraction of unreacted mass as a function of dimensionless time, replotted from Reference 135. The material used for simulation was cellulose in a slab geometry with a convective surface condition. Again, the temporal mass loss is approximately linear over some part of the process. This is important, in that it shows that a radiative boundary condition is not necessary in order to obtain such profiles.

Figure 2.25 depicts the predicted unreacted fractional mass as a function of time for 0.2 mm cellulose particle with a surface heat flux of 200 kW/m^2, replotted from Reference 47. The crudely linear temporal mass loss is also obvious in this case.

Figure 2.26 shows a comparison of the measured and predicted temperature profiles for a 5 cm thick slab of maple after 5 min exposure to 22.2 kW/m^2, replotted from Reference 80. It can be seen that the agreement between measured and predicted profiles is good. Such profiles, as shown in Figure 2.26, are often seen in the literature. Fitting the temperature profile in Reference 80 did require many adjustable parameters, however, and the prediction of mass loss did not compare well with experiment. This illustrates clearly that fitting of one feature alone does not assure success in the modeling effort.

Figure 2.27 shows the predicted surface and interior temperatures of wood as a function of time for a heat fluxes of 22.2 kW/m^2 and 83.7 kW/m^2, replotted from Reference 80. The surface temperature change as calculated from the model does not predict any inflection point in the zone of active pyrolysis, but the interior profile does. This may be because the authors model the pyrolysis to be endothermic (418 J/g). Again, the reason for inflection in temperature profiles will be further examined in Chapter 5.

Figure 2.28 depicts the mass loss rate as a function of time for a heat flux 22.2 kW/m^2, replotted from Reference 80. The "damped oscillations" were explained as due to the competition of two processes, heat conduction to the solid, which accelerates pyrolysis and heat convection by volatiles, which decelerates the pyrolysis process. There is no evidence of such oscillations in the literature and there is a distinct possibility that they are a numerical artifact.

Figure 2.29 shows predicted surface temperature and net heat flux as a function of time for 10 mm thick cellulose slab with an applied heat flux of 50 kW/m^2, replotted from Reference 165. This result was obtained by Professor Sibulkin's group at this University. The assumption that they made was that, at zero time, a sample absorbs all of the applied radiative flux. That assumption might have been true in their experiments because they started with an artificially blackened surface, but it is clearly not valid for non-blackened sample surface (89, 155). It will be shown here that the net heat flux follows a different, more complicated, pattern than the one shown in Figure 2.29. The processes that are involved as the surface is completely pyrolyzed (blackened) include absorption of part of the applied heat flux to the surface, reflection from the surface due to the non unity emissivity, heat convection from the surface, heat convection by the evolving volatiles, heat conduction into the sample (net heat flux) and radiation from the sample surface. Of course, all of these fluxes are functions of sample surface temperature and thus time, except the applied heat flux. Since the question of how much heat the sample really absorbs is very important, it will be addressed experimentally here.

In summary, it may be said that an enormous variety of models has been studied, though they have all really basically involved application of the conduction equation, with various boundary conditions. It is fair to say that qualitative success has been achieved in numerous occasions. Detailed success has never been achieved, particularly when adjustable parameters have not been available. There have been nagging doubts as to thermal properties and even as to the importance of certain terms (e.g. the heat of reaction). From a distance, the field seems well-worked, and yet, there is an unsettling feeling that given a new set of conditions, there would not be great confidence in applying any existing model to prediction behavior under those conditions. The goal here is to experimentally push us toward a better understanding of the modeling.

Table 2.1: **Molecular Weights and Degrees of Polymerization of Various Celluloses and Cellulose Derivatives (from 71)**

Cellulosic Material	Molecular Weight	Degree of Polymerisation
Native cellulose	570,000	3500
Purified cotton linters	150,000–500,000	1000–3000
Wood pulps	90,000–150,000	600–1000
Commercial regenerated cellulose	30,000–90,000	200–600
Farr and Eckerson's cellulose particles	40,000	250
Beta-cellulose	3,000–15,000	15–90
Gamma-cellulose	3,000	15
Dynamite nitrocellulose	750,000–875,000	4600–5400
Plastics nitrocellulose	125,000–150,000	800–930
One-half secondary nitrocellulose	45,000	275
Commercial cellulose acetates	45,000–100,000	275–620

Table 2.2a: **Mean Results of Pyrolyses (in vacuum unless stated otherwise) (from 75)**

Cotton cloth	Temp., °C	Time, min.	No. of expt.	% Yield (w/w of dry cloth) V_{-196}	V_{-80}	V_{rt}	Tar	Char	Dec. tar†	Total
Poplin	418	15	4	0·9	3·2	13·2	76·3	5·2	0·0	98·8
Winceyette 1	418	15	4	1·0	2·2	7·8	77·3	4·0	2·0	94·3
Winceyette 1	318	130	2	$1·0_5$	2·1	$16·1_5$	64·5	13·2	0·0	97·0
Winceyette 1	318	960	2	$2·7_5$	$4·2_5$	13·6	$65·2_5$	10·2	0·0	$96·0_5$
Winceyette 1	418*	15	4	—	$1·5_5$	24·0	26·3	$12·7_5$	18·0	$82·6_5$
Winceyette 2	418	15	3	4·0	2·5	12·6	54·6	11·5	—	85·2
I treated with Pn1	418	285	4	3·6	3·1	30·3	20·5	38·3	3·4	99·2
I treated with Pn2	418	260	4	4·4	5·4	27·6	18·2	$37·6_5$	3·2	$96·4_5$
I treated with B/BA (8·3% w/w)	418	160	2	$6·6_5$	1·8	21·3	4·1	$59·2_5$	0·0	93·1
I treated with B/BA (8·3% w/w)	418*	160	5	—	2·0	41·1	2·7	46·4	5·3	97·5
I treated with $NaVO_3$ (2·8% w/w)	418	30	1	3·5	—	—	18·3	24·3	0·0	—
I treated with $NaVO_3$ (6·8% w/w)	418	30	1	4·0	—	—	3·2	38·6	0·0	—
Oxycellulose	418	45	4	3·2	23·3	17·4	30·1	23·6	0·7	98·3

* In dry air at atmospheric pressure

† 'Decomposed tar' is the material, insoluble in methanol, formed by the thermal decomposition of some of the tar remaining in the vicinity of the furnace

Table 2.2b: **Summary of Analytical Results for Tars from Pyrolyses at 418°C (from 75)**

Tar from	Elementary analysis[a] C	H	Mean mol. wt.	$[\alpha]_D$ (c 0·2–0·4 in water[b])	Bromine no.[c]	% Laevoglucosan w/w Tar	w/w Cotton	% Carbonyl compounds assuming average mol. wt. of 100 w/w Tar	w/w Cotton	% Acids assuming average mol. wt. of 100 w/w Tar	w/w Cotton	Acids, equiv. mole of tar
	%	%										
Winceyette 1 in vacuum	46·0	6·1	185	—32°	23·2	81·4 ± 2·5	62·9	13·2	10·2	7·2	5·6	0·133
1 in air	44·2	6·3	161	—9°	39·5	61·8 ± 1·3	16·3	28·3	7·4	19·8	5·2	0·318
1 treated with Pn2, in vacuum	52·2	6·0	183	—19°	54·8	53·9 ± 0·5	9·8	23·7	4·3	14·4	2·6	0·264

[a] Laevoglucosan, $C_6H_{10}O_5$, requires C, 44·4; H, 6·2%; mol. wt. 162

[b] Measured at room temperature

[c] Number of g. of bromine absorbed by 100 g. of tar

Table 2.3: **Analytical Results of the Pyrolysis of Cellulose Exposed to Low Thermal Irradiance (18.4 kW/m^2) (from 116)**

	Run												
	41	37	44	6	27	30	31	11	42	36	43	12	32
Exposure duration (sec)	2.50	2.52	3.03	3.3	3.31	3.32	3.33	3.80	3.99	4.78	6.00	7.04	8.02
Radiant exposure (cal cm^{-2})	10.5	10.6	12.7	13.9	13.9	13.9	14.0	15.9	16.8	20.1	25.2	29.5	33.7
Exposure weight loss (mg)	3.9	4.3	15.4	23.7	26.2	26.6	22.5	35.4	37.3	50.8	64.5	81.4	94.0
Total weight loss (mg)	7.1	6.7	16.1	45.3	31.7	29.3	—	—	53.3	61.8	71.3	106.7	133.5
Cellulose decomposed (mg)	13	14	35	45	75	32	—	—	68	73	105	99	150
Gas products (mg)													
H_2	—	—	0.0011	0.0022	0.0032	0.0013	0.0023	0.0051	0.0069	0.0085	0.022	0.067	0.110
CO	0.116	0.132	0.36	0.537	0.807	0.55	0.70	0.0	1.15	2.08	4.2	7.8	10.9
CO_2	0.35	0.41	0.88	1.16	1.70	1.25	1.6	2.0	2.4	4.2	8.8	11.8	13.8
CH_4	0.0006	0.0005	0.0028	0.0053	0.0091	0.0054	0.0088	0.0147	0.0166	0.035	0.092	0.302	0.50
C_2H_4	—	—	0.003	0.006	0.012	0.009	0.012	0.018	0.020	0.026	0.089	0.29	0.48
C_2H_6	—	—	—	—	0.0027	0.002	0.0022	0.0055	0.0036	—	0.035	0.130	0.20
Total	0.47	0.54	1.25	1.71	2.53	1.82	2.33	3.04	3.60	6.35	13.2	20.4	26.0
Liquid products (mg)													
CH_2CHO	0.0164	0.0158	0.044	0.073	0.091	0.085	0.090	0.164	0.198	0.43	0.76	1.4	1.9
C_2H_3CHO	0.0051	0.0055	0.0059	—	0.011	0.011	0.013	0.020	0.026	0.051	0.1	0.22	0.44
n-C_3H_7CHO	0.001	—	0.003	0.006	0.008	0.009	0.009	0.011	0.011	—	0.26	0.062	0.062
CH_2:CHCHO	0.0042	0.0044	0.013	0.026	0.026	0.023	0.024	0.055	0.064	0.096	0.21	0.41	0.4
CH_2CH:CHCHO	—	—	0.007	0.0099	0.013	0.0104	0.0113	0.021	0.025	—	0.071	0.087	0.102
CH:CHCH:CHO	0.0045	0.0050	0.0089	0.012	0.016	0.021	0.019	0.033	0.039	0.064	0.115	0.14	0.17
CH_3COCH_3	0.0038	0.003	0.0096	0.017	0.017	0.014	0.016	0.031	0.033	0.054	0.14	0.28	0.3
$CH_3COCOCH_3$	—	—	0.033	0.03	0.092	0.071	0.063	0.11	0.15	—	0.32	0.41	0.424
CH_3OH	0.008	—	0.013	0.017	0.019	0.014	0.014	0.029	0.037	—	0.105	0.18	0.22
H_2O	1.0	0.80	2.5	3.8	5.0	3.9	3.0	5.9	6.6	10.6	16	20.9	22.6
Total	1.06	0.84	2.9	4.2	5.4	4.3	3.4	6.9	7.5	~12	18.8	26.2	29.8
Tar (mg)	2.37	2.92	11.2	17.8	18.3	20.5	16.8	25.5	26.2	32	32.5	34.8	38.2

Table 2.4: Analysis of the Pyrolysis Products of Cellulose (from 158)

Product	*Atmospheric Pressure*	*1.5 mm Hg*	*1.5 mm Hg, 5% $SbCl_3$*
Char	34.2	17.8	25.8
Tar	19.1	55.8	32.5
levoglucosan	3.57	28.1	6.68
1,6-anhydro-β-D-glucofuranose	0.38	5.6	0.91
D-glucose	trace	trace	2.68
hydrolyzable materials	6.08	20.9	11.8

NOTE: Values (in percent) are for pyrolysis at 300 °C under N_2 and the percentages are based on the original amount of cellulose.

Table 2.5a: Effect of Temperature on the Products from Pyrolysis of Cellulose Powder in Vacuum (from 162)

Oven temperature °C	Pyrolysis time, min	Percent yield from cellulose				
		Char	Tar[b]	Levoglucosan	1,6-Anhydro-β-D-glucofuranose	Reducing sugar[c]
300	180	21	60	34	4	47
325	60	10	70	36	—	54
350	30	8	70	38	4	52
375	10	6	70	38	—	59
400	5	5	77	39	4	60
425	4	4	78	40	4	59
450	3	4	78	39	4	57
475	3	3	80	38	4	58
500	3	3	81	38	4	57

[a] Whatman CF 11 powder, Lot A.
[b] Method A, see Experimental section.
[c] Increase in reducing sugar after tar hydrolysis.

Table 2.5b: Effect of Temperature on the Products from Pyrolysis of Cellulose Powder at Atmospheric Pressure under Nitrogen (from 162)

Oven temperature, °C	Pyrolysis time, min	Percent yield from cellulose				
		Char	Tar[b]	Levoglucosan	1,6-Anhydro-β-D-glucofuranose	Total reducing sugar[c]
350	25	20	54	17	4	34
400	7	14	59	17	1	38
450	5	11	60	20	2	40
500	4	8	58	20	2	39

[a] Whatman CF 11, Lot A.
[b] Method A.
[c] After hydrolysis.

Table 2.5c: **Products from Pyrolysis of Celluloses at 400°C under Vacuum** (from 162)

Substrate	Percent yield from cellulose					Levoglucosan concentration in tar, %
	Char	Tar[a]	Levoglucosan	1,6-Anhydro-β-D-glucofuranose	D-Glucose after (hydrolysis)	
Cotton hydrocellulose	2	85	58	6	77	68
Baker microcrystalline	3	83	51	5	—	61
Avicel microcrystalline	3	84	49	5	—	58
Whatman CF 11, Lot A	5	69	39	4	49	57
Whatman No. 41 filter paper	5	69	38	4	—	55
Cotton linters	5	64	30	3	—	47
Whatman CF 11, Lot B	7	56	29	3	—	50
Cotton fabric	9	46	14	1	—	30

Table 2.6: **Products from Pyrolysis of Cellulose in Air** (from 13)

	Sample	Accessibility a	Pyrolysis at 251°C				Levoglucosan in tar (high-temp pyrolysis), %
			Rate × 10^4, min^{-1}	After 75 min			
				Cryst. ratio	DP	% Residue	
1	Cotton, Deltapine	0.20	7.3	0.711	198	94.0	25
2	Deltapine, hydrolyzed	0.20	7.3	0.764	166	94.5	30
3	Cotton, Pima	0.20	6.1	0.763	190	96.0	22
4	Pima, mercerized	0.20	4.4	0.677	139	97.1	28
5	Ramie	0.20	6.1	0.710	254	95.0	25
6	Ramie, hydrolyzed	0.20	6.1	0.713	197	96.0	35
7	Tire yarn	0.68	20.0	0.524	20	87.6	15
8	High modulus yarn	0.41	16.0	0.644	40	88.9	25
9	Vincel 64	0.47	12.4	0.541	—	90.6	15
10	Vincel 28	0.56	11.9	0.698	—	91.4	17
11	Textile rayon	0.57	26.5	0.416	18	82.0	13
12	Evlan	0.47	17.6	0.514	—	89.0	17

Table 2.7: Carbon, Hydrogen, Oxygen and Total Mass Balances for Cellulose Pyrolysis (from 68)

products	peak temp, 500 °C				holding temp,* 400 °C				peak temp, 750 °C				peak temp, 1000 °C			
	total	C	H	O	total	C	H	O	total	C	H	O	total	C	H	O
CO	0.99	0.42	-	0.57	0.25	0.11	-	0.14	16.82	6.78	-	9.04	22.67	9.67	-	12.9
CO_2	0.2	0.06	-	0.22	1.46	0.40	-	1.06	2.36	0.65	-	1.73	3.36	0.92	-	2.44
H_2O	8.55	-	0.39	8.16	6.49	0.0	0.72	5.77	8.72	-	0.97	7.75	9.22	-	1.03	8.19
CH_4	0.0	0.0	0.0	-	0.0	0.0	0.0	-	1.11	0.83	0.28	-	2.62	1.96	0.66	-
C_2H_4	0.0	0.0	0.0	-	0.0	0.0	0.0	-	1.05	0.9	0.15	-	2.18	1.87	0.31	-
C_2H_6	0.0	0.0	0.0	-	0.0	0.0	0.0	-	0.17	0.14	0.03	-	0.28	0.22	0.06	-
C_3H_6	0.0	0.0	0.0	-	0.0	-	0.0	-	0.70	0.6	0.1	-	0.80	0.69	0.11	-
H_2	0.0	-	0.0	-	0.0	0.0	0.0	-	0.86	-	0.86	-	1.18	-	1.18	-
CH_3OH	0.25	0.09	0.02	0.14	0.21	0.08	0.03	0.1	1.03	0.39	0.13	0.51	0.98	0.37	0.12	0.49
CH_3CHO	0.01	0.01	0.0	0.0	0.05	0.03	0.0	0.02	1.58	0.86	0.14	0.58	1.7	0.93	0.15	0.62
C_n + ethanol	0.00	0.0	0.0	0.0	0.0	0.0	0.0	0.0	0.29	0.15	0.04	0.10	0.38	0.2	0.05	0.13
AC + FU	0.07	0.04	0.01	0.02	0.16	0.1	0.02	0.04	1.00	0.62	0.10	0.28	0.82	0.51	0.08	0.23
CHO(CH,COOH)	0.12	0.05	0.01	0.06	0.0	0.0	0.0	0.0	0.85	0.84	0.06	0.45	0.58	0.23	0.04	0.31
tar	16.37	7.5	0.97	7.9	83.35	36.28	4.95	40.32	59.92	27.77	3.63	28.63	49.12	22.89	2.98	23.25
char	83.63	36.13	5.84	40.16	6.17	4.94	0.24	0.99	3.32	2.65	0.1	0.57	3.91	3.46	0.13	0.32
total	105.25	46.32	6.74	52.23	98.36	43.96	5.96	48.43	98.8	42.66	6.59	49.53	99.86	43.92	6.9	48.88
closure	105%	105%	108%	106%	98%	100%	96%	97%	99%	97%	106%	99%	100%	100%	111%	98%

* Holding time = 30 s.

Table 2.8: Effect of Temperature on the Formation of Gaseous Products at 100 ml/min (a) and 200 ml/min (b) Helium Flowrate (from 45)

	473K (mol $dm^{-3} \times 10^7$)	523K (mol $dm^{-3} \times 10^7$)	573K (mol $dm^{-3} \times 10^7$)	623K (mol $dm^{-3} \times 10^7$)	673K (mol $dm^{-3} \times 10^7$)	723K (mol $dm^{-3} \times 10^7$)	773K (mol $dm^{-3} \times 10^7$)	823K (mol $dm^{-3} \times 10^7$)
H_2	0.0	0.0	0.0	10	609	739	743	605
CH_4	0.0	1.83	3.35	20.7	434	4110	4600	3980
CO	0.0	0.0	0.0	50	8000	9700	8900	7100
C_2H_4	0.0	0.48	1.41	9.5	310	1390	1690	1510
C_2H_6	0.0	0.07	0.14	1.2	17.5	139	181	144
C_3H_6	0.0	0.002	0.05	3.0	107.7	359	361	223
CO_2	0.0	0.0	517	1400	4320	2400	1800	1400
C_3H_4	0.0	0.0	0.0	0.02	20.5	46	35	20
but-1-ene	0.0	0.0	0.00	0.01	0.1	8	7	2
C_4H_{10}	0.0	0.001	0.02	0.2	31.7	8.8	8.8	9

	473K (mol $dm^{-3} \times 10^7$)	523K (mol $dm^{-3} \times 10^7$)	573K (mol $dm^{-3} \times 10^7$)	623K (mol $dm^{-3} \times 10^7$)	673K (mol $dm^{-3} \times 10^7$)	723K (mol $dm^{-3} \times 10^7$)	773K (mol $dm^{-3} \times 10^7$)	823K (mol $dm^{-3} \times 10^7$)
H_2	0.0	0.0	7.0	146	352	460	344	275
CH_4	0.0	0.62	1.6	8.1	54	426	730	557
CO	0.0	25	48	279	1350	6600	3900	1100
C_2H_4	0.0	0.32	0.5	5.2	38.9	154	233	187
C_2H_6	0.0	0.0	0.08	0.4	1.8	23.6	24.0	12.6
C_3H_6	0.0	0.0	0.19	1.0	18.0	43.6	38.0	18.5
CO_2	0.0	60	110	759	1560	1680	1210	517
C_3H_4	0.0	0.0	0.0	0.06	2.0	7.6	0.07	0.02
but-1-ene	0.0	0.0	0.0	0.0	0.0	0.0	0.0	0.0
C_4H_{10}	0.0	0.0	0.01	0.04	2.4	2.0	3.1	0.3

Table 2.9: Major Ions in Mass Spectra of Wood and Compounds Reported in Primary Oils and Gases (from 55)

ion, m/z	formula	structure	likely product	major ion[a]	in product at >0.1%[a]	ref to show anal. of oils
16	CH_4	MeH	methane	×	×	f
18	H_2O	HOH	water	×	×	e, f
28	CO	CO	carbon monoxide	×	×	f
	C_2H_4	$CH_2{=}CH_2$	ethene	×	×	f
32	CH_4O	MeOH	methanol	×	×	a, b, d, e
44	CO_2	OCO	carbon dioxide	×	×	f
	C_2H_4O	OCHMe	acetaldehyde	×	×	b, e
46	CH_2O_2	HCOOH	formic acid	×	×	b, e
58	C_3H_6O	MeCOMe	2-propanone (acetone)	×	×	e
60	$C_2H_4O_2$	HO_2CMe	acetic acid	×	×	e, f
	$C_2H_4O_2$	$HOCH_2CHO$	hydroxyacetaldehyde (glycolaldehyde)	×	×	e, f
	$C_2H_4O_2$	MeOCHO	methyl formate	×	×	e
68	C_4H_4O	I	furan	×	×	a, e
72	C_3H_6O	EtCOMe	2-butanone		×	a, c, e
	$C_3H_4O_2$	$CH_2{=}CHCOOH$	acrylic acid		×	e
74	$C_3H_6O_2$	$HOCH_2COMe$	1-hydroxy-2-propanone (acetol)		×	e, f
	$C_3H_6O_2$	HO_2CEt	propanoic acid		×	a, c, e
	$C_3H_6O_2$	$HOCH_2CH_2CHO$	hydroxypropanal		×	a, b
	$C_3H_6O_2$	CH_3COOCH_3	methyl acetate		×	e
76	$C_2H_4O_3$	$HOCH_2COOH$	glycolic acid		×	d
82	C_5H_6O	II	2-methylfuran		×	a, b
		III	cyclopentenone		×	c
84	C_5H_8O	IV	cyclopentanone		×	b
	$C_4H_4O_2$	V	2(5*H*)-furanone	×	×	a, b, e
86	$C_4H_6O_2$	MeCOCOMe	2,3-butanedione		×	e
	$C_4H_6O_2$	$MeCH{=}CHCOOH$	crotonic acid		×	e
	$C_4H_6O_2$	VI	butyrolactone		×	c, e
88	$C_4H_8O_2$	HO_2CEtMe	butanoic acid		×	e
	$C_4H_8O_2$	$MeCH_2COCH_2OH$	1-hydroxy-2-butanone		×	a, d
94	C_6H_6O	PhOH	phenol		×	a, d
	C_7H_{10}	VII	dimethylcyclopentene		×	a
96	$C_5H_4O_2$	VIII	furfural	×	×	c, e, f
	C_5H_6O	IX	2-methyl-2-cyclopentene-1-one	×	×	d, e
98	$C_5H_6O_2$	X	furfuryl alcohol	×	×	d, e
	C_5H_6O	XI	5-methyl-2(3*H*)-furanone (*α*-angelicalactone)	×	×	a, e
		XII	3-methyl-2(3*H*)-furanone	×	×	a
100	$C_5H_8O_2$	XIII	valerolactone		×	d, e
	$C_5H_8O_2$	MeCOCOEt	2,3-pentanedione		×	c
102	$C_5H_{10}O_2$	$CH_3(CH_2)_3COOH$	pentanoic acid (valeric/isovaleric)		×	a, c
108	C_7H_8O	$CH_3C_6H_4OH$	*o*-cresol		×	a, d
			m/*p*-cresol		×	a
110	$C_5H_4O_2$	XIV	5-methylfurfural	×	×	c, d, f
	$C_6H_6O_2$	$C_6H_4(OH)_2$	dihydroxybenzenes (catechol, hydroquinone, resorcinol)	×	×	c, d
112	$C_6H_8O_2$	XV	2-hydroxy-3-methyl-2-cyclopentene-1-one		×	b, c, e
	$C_7H_{12}O$	XVI	dimethylcyclopentanone		×	a
114	$C_5H_6O_3$	XVII	3-hydroxy-2-penteno-1,5-lactone	×		f
116	$C_6H_{12}O_2$	$CH_3(CH_2)_4CO_2H$	hexanoic acid		×	c, d
	$C_5H_8O_3$	$CH_3CO_2CH_2(CO)CH_3$	1-acetyloxy-2-propanone		×	a
120	C_8H_8O	XVIII	vinylphenol	×		f
122	$C_8H_{10}O$	$C_6H_3(CH_3)_2OH$	dimethylphenols		×	c, d
	$C_8H_{10}O$	$C_6H_4(CH_2CH_3)OH$	ethylphenol		×	d
	$C_7H_6O_2$	$C_6H_4CO_2H$	benzoic acid		×	a
124	$C_7H_8O_2$	XIX	2-methoxyphenol (guaiacol)	×	×	a, c
	$C_9H_{16}O$	XLIV	trimethylcyclopentenone		×	a
126	$C_6H_6O_3$	XX	5-(hydroxymethyl)-2-furfural	×		f
	$C_6H_8O_3$	XXI	2-methyl-3-hydroxy-4-pyrone	×	×	d
132	$C_5H_8O_4$	$MeCOOCH_2(CO)CH_2OH$	1-hydroxy-2-propanone acetate		×	e
138	$C_9H_{10}O_2$	XXII	4-methylguaiacol	×	×	a, b, e
146	$C_6H_{10}O_4$	$MeCOO(CH_2)_2(CO)CH_2OH$	1-hydroxy-2-butanone acetate		×	c
150	$C_9H_{10}O_2$	XXIV	*p*-vinylguaiacol	×		f
	$C_9H_{10}O_2$	XXV	coumaryl alcohol	×		f
152	$C_9H_{12}O_2$	XXVI	4-ethylguaiacol		×	a
	$C_8H_8O_3$	XXVII	vanillin	×		f
154	$C_8H_{10}O_3$	XXVIII	2,6-dimethoxyphenol (syringol)	×	×	a, b, d, e
162	$C_6H_{10}O_5$	XXIX	levoglucosan		×	c, d, f
164	$C_{10}H_{12}O_2$	XXX	isoeugenol	×		f
			eugenol	×	×	d
166	$C_9H_{10}O_3$	XXXI	1-(4-hydroxy-3-methoxyphenyl)ethanone			a
168	$C_9H_{12}O_3$	XXXII	4-methyl-2,6-dimethoxyphenol		×	a, e
178	$C_{10}H_{10}O_3$	XXXIII	coniferyl aldehyde		×	a
180	$C_{10}H_{12}O_3$	XXXIV	coniferyl alcohol	×		f
	$C_{11}H_{12}O_3$	XXXV	vinylsyringol	×		f
	$C_6H_{12}O_6$	XLV	*α*-D-glucose	×	×	d
182	$C_9H_{10}O_4$	XXXVI	syringaldehyde		×	a, d
	$C_{11}H_{14}O_3$	XXXVII	4-ethylsyringol		×	a
194	$C_{12}H_{14}O_3$	XXXVIII	4-propenylsyringol	×		f
	$C_{10}H_{10}O_4$	XXXIX	ferulic acid	×		f
208	$C_{10}H_{12}O_4$	XL	(4-hydroxy-3,5-dimethoxyphenyl)ethanone		×	a
208	$C_{12}H_{16}O_3$	XLI	sinapyl aldehyde	×		f
210	$C_{12}H_{18}O_3$	XLII	sinapyl alcohol	×		f
272	$C_{20}H_{40}O_2$	XLIII				

Table 2.10: **Yields and Composition of the Charred Residue Obtained by Pyrolysis of Cellulose at the Final Temperatures Noted (Heating Rate 10°C/Min) (from 79)**

Cellulose Sigma	Untreated	Pretreated	Limits of error%
Temperature (°C)	525	525	
Heating rate (°C/min)	10	10	5.00
Cellulose (g)	40.1	40.2	0.25
Cellulose (m.a.f. basis) (g)	39.48	39.58	0.25
Moisture (% wt./wt.)	6.16	1.52	1.00
Ash (% wt./wt.)	0.20	0.02	5.00
DP	1100	500	1.00
% H_2SO_4 (% wt./wt.)	0.00	1.00	
Yields, % of m.a.f. feed			
Levoglucosan	3.73	33.09	1.15
Hydroxyacetaldehyde	11.13	0.00	1.05
Glucose	0.25	2.03	2.05
Acetic acid	11.84	6.94	1.50
Hydroxymethylfurfural	0.65	0.20	2.15
Formic acid	1.63	0.80	1.95
Levulinic acid	4.40	2.44	1.45
Propionic acid	3.09	4.04	1.30
Others (tar)	17.57	23.10	1.35
Total organic liquid	54.29	72.64	0.25
Water	21.89	14.50	0.50
Total liquid	76.18	87.14	0.75
Char	10.13	8.56	0.35
Gas	13.69	4.30	0.40
Total	100.00	100.00	1.50

Table 2.11: A Summary of the Models

Ref. No.	Energy Equation	Mass Transport Equation(s)	Rate Equation
49	• non char forming material • slab geometry • thermal radiation absorbed in depth according to Beer's law • constant solid properties (C_p, ρ, k) • endothermic heat of pyrolysis (77 J/g) • surface regression taken into account • included terms: 2a(ε=0); 3; 4; 6; 7 • BC's: x = 0: (1); (2)	• mass flux determined by chemical decomposition rate • single volatile species • BC: x = 0: (16)	• n = 0 • E = 134 kJ/mole A = 2.8×10^9 s^{-1}
99	• char forming material • spherical geometry For "small" particles: • negligible internal resistance to heat transfer • kinetic energy and rate of change of vapor phase enthalpy neglected • included terms: 8a; 8b; 9; 10; 11; 12 • time invariant properties • IC: T = T_0 at t = 0 For "large" particles: • temperature gradients within the solid • included terms: 2a; 2b(ε=0); 3; 4; 6 • BC's: r = 0: (8) r = R: (1); (4); (5); (6)	For "small" particles: • viscous flow dominated • single volatile species • ideal gas law • included terms: 13; 14; 15 • BC's: r = 0: (9); r = R: (10) For "large" particles: • negligible resistance to mass transfer • mass flux determined by chemical decomposition rate • single volatile species	• n-th order • no gas - solid reactions • E = 153 kJ/mole

Table 2.11 - continued

194	• char forming material • slab geometry (semi - infinite) • transient conduction model • conductivity proportional to density of unpyrolyzed material • condensation and regasification ignored • negligible heat of pyrolysis • no well defined pyrolysis front • dry material assumed • included terms: 2(ε=0); 3 • BC's: x = 0: (1); (4); (5); (6); (11)	• mass flux determined by chemical decomposition rate • single volatile species	• n = 1 • no gas - solid reactions • E = 100 kJ/mole $A = 0.178 \times 10^{11}\ s^{-1}$ (estimated)
16	• char forming material • infinite cylinder geometry • properties locally volume averaged • heat capacity and thermal conductivity of the solid are functions of temperature and extent of reaction • constant heat capacity of volatiles • enthalpy of pyrolysis reaction is a function of local temperature • condensation and vaporization included in specific enthalpy of the overall pyrolysis • included terms: 2a(ε=0); 3; 4; 6 • BC's: r = R: (1); (5), with h combined for convection and radiation	• mass flux determined by chemical decomposition rate • single volatile species	• n = 1 • no gas - solid reactions • different frequency factor and activation energy for two different stages of pyrolysis • $E_1 = 116$ kJ/mole $A_1 = 1.5 \times 10^{8}\ s^{-1}$ $E_2 = 135$ kJ/mole $A_2 = 1.9 \times 10^{9}\ s^{-1}$
37	• char forming material • slab geometry	• mass flux determined by chemical decomposition rate	• pyrolysis subdivided into five reactions • secondary reactions included

Table 2.11 - continued

	• volatiles have the properties of a mixture of CO and water • volatiles in local thermal equilibrium with the solid • (ρC_p) is constant for both gas and solid • latent heat of water is taken as one "heat of reaction" • included terms: 1; 2a; 3; 4; 6 • BC's: x = 0: (1); (4); (5); (6); x = L: (1); (5); (6)	• single volatile species	• for all reactions n = 1 • <u>Primary pyrolysis:</u> 1: solid → primary gas E_1 = 140 kJ/mole $A_1 = 1.3 \times 10^8\ s^{-1}$ 2: solid → primary tar E_2 = 133 kJ/mole $A_2 = 2 \times 10^8\ s^{-1}$ 3: solid → char E_3 = 121 kJ/mole $A_3 = 1.08 \times 10^7\ s^{-1}$ 4: moisture → vapor (+dehydration) E_4 = 88 kJ/mole $A_4 = 5.13 \times 10^6\ s^{-1}$ • <u>Tar cracking:</u> 5: tar → secondary gas + secondary tar E_5 = 144 kJ/mole $A_5 = 1.48 \times 10^6\ s^{-1}$
183	• char forming material • cylindrical geometry • exothermic heat of pyrolysis (4.8 to 7.2 J/g before the "breakpoint") (48 to 131 J/g after the "breakpoint") • solid is a nonshrinking matrix with constant heat transfer properties • "breakpoint" for changing the parameters	• mass flux determined by chemical decomposition rate • single volatile species	• n = 1 • no gas - solid reactions • <u>Before the "breakpoint"</u> E_1 = 126 kJ/mole $A_1 = 6 \times 10^7$ to $7.5 \times 10^8\ s^{-1}$ • <u>After the "breakpoint"</u> E_2 = 152 to 179 kJ/mole $A_2 = 4 \times 10^8$ to $2 \times 10^9\ s^{-1}$

Table 2.11 - continued

	(h_p, E, A) determined by density • included terms: 2a(ε=0); 3; 6 • BC's: r = 0: (8) r ≤ R: (1); (5) with h combined for convection and radiation		
86	• char forming material • transient conduction model • general equation for slab, cylinder and sphere • internal convection by volatiles and convection on the surface neglected • heat of pyrolysis neglected • char and virgin material separated by a front where the temperature is the pyrolysis temperature (Tp ≈ 325°C) • constant properties (C_p, ρ, k) • included terms: 2(ε=0); 3 • BC's: for different BC's at x = L solutions are available in literature	• details of pyrolysis neglected • volatiles instantaneously formed at the front where the temperature is the pyrolysis temperature	• actual pyrolysis reaction neglected • n=1 (not included, others' equations discussed) • no gas - solid reactions
135	• char forming material • slab geometry (infinite, thickness L) • constant density of the solid matrix excluding pores (allowed to grow) • constant conductivity of the solid matrix excluding pores (allowed to grow) • porosity fine and uniformly distributed • internal convection by volatiles neglected	• mass flux determined by chemical decomposition rate • three volatile species allowed (gas_1, gas_2, gas_3) • BC: x = L: (9)	• pyrolysis subdivided in three reactions • no gas - solid reactions • for all reactions n = 1 • <u>Primary pyrolysis:</u> 1: solid → secondary solid + gas_1 E_1 = 100 kJ/mole $A_1 = 1.78 \times 10^8\ s^{-1}$ (estimated) 2: solid → gas_2

Table 2.11 - continued

	• examined endothermic and exothermic heat of pyrolysis • included terms: 2(ε=0); 3; 6 • BC's: x = 0: (1); (5) or (6) x = L: (8)		E_2 = 130 kJ/mole $A_2 = 1.78 \times 10^{10}$ s^{-1} (estimated) • Secondary pyrolysis: 3: secondary solid → char + gas_3 E_2 = 151 kJ/mole $A_2 = 1.78 \times 10^{11}$ s^{-1} (estimated)
101	• char forming material • slab geometry • no inward moisture migration • thermal equilibrium between the volatiles and the solid • linear interpolation between wood and char properties used for heat capacity and thermal conductivity • no geometry change of the solid matrix • included terms: 2a; 2b(ε=0); 3; 4; 6 • BC's: x = 0: (1); (4); (5); (6) x = L: (8)	• mass flux determined by chemical decomposition rate • single volatile species • no inward moisture migration • BC: x = L: (9)	• n = 1 • no gas - solid reactions • E = 126 kJ/mole $A = 5.25 \times 10^7$ s^{-1}
102	• char forming material • slab geometry • both faces of the slab are heated • thermal equilibrium between volatiles and solid matrix • linear interpolation between wood and char properties used for heat capacity and thermal conductivity • included terms: 2(ε=0); 3; 4; 6 • BC's: x = 0 and x = L: (1); (4); (5); (6)	• mass flux determined by chemical decomposition rate • single volatile species • BC: x = L/2: (9)	• n = 1 • no gas - solid reactions • E = 126 kJ/mole $A = 2 \times 10^7$ s^{-1}

Table 2.11 - continued

	x = L/2: (8)		
80	• char forming material • slab geometry • physical properties (ρ, C_p, k) linear functions of local char or fuel concentration • no thermal swelling or shrinkage • local thermal equilibrium between solid and volatiles • included terms: 1; 2; 3; 4; 5; 6 • BC's: x = 0: (1); (4); (5); (6) x = L: (1); (5); (6)	• mass flux determined by chemical decomposition rate • single volatile species • ideal gas law • Darcy flow • physical properties (ε, κ) linear functions of local char or fuel concentration • BC: x = L: (9)	• n = 1 • no gas - solid reactions • E = 75 kJ/mole A = 2.5×10^4 s^{-1}
145	• char forming material • semi - infinite slab • exothermic heat of pyrolysis (0 or 210 J/g or 420 J/g) • two equations discussed: with and without convection between gas and solid • constant thermal diffusivity • heat of pyrolysis examined for effect on pyrolysis wave speed calculation • included terms (with convection): 2(ε=0); 3; 4 • included terms (without convection): 2(ε=0); 3 • BC's: x = 0: (13); (14) x = ∞: (10); (12);	• mass flux determined by chemical decomposition rate • single volatile species	• n = 0 • no gas - solid reactions • E = 126 kJ/mole A = 7×10^7 s^{-1}
165	• char forming material • semi - infinite slab	• mass flux determined by chemical decomposition rate	• n = 1 • no gas - solid reactions

Table 2.11 - continued

	• dried material assumed • thermally thick material • no change in geometry during pyrolysis • semi - infinite slab • included terms: 2a; 2b(ε=0); 3; 4; 6 • BC: integration from zero to infinity	• single volatile species	• E = 151 kJ/mole A = 10^{10} s^{-1}
81	• char forming material • slab geometry • solid matrix is inert while an entrained active part is pyrolyzed • local thermal equilibrium between solid and volatiles • specific heat is constant equal to that of the solid • included terms: 2a(ε=0); 3; 4; 6 • no IC's nor BC's reported	• mass flux determined by chemical decomposition rate • single volatile species	• n = 1 • no gas - solid reactions • E = 63 kJ/mole A = $15x10^{6}$ s^{-1}
60	• char forming material • slab geometry • insulated back face of the slab • solid density changes very little during the preignition heating • constant thermal conductivity of the solid • included terms: 2(ε=0); 3; 4; 6 • BC's: x = 0: (2); (3); (4); (6) x = L: (8)	• mass flux determined by chemical decomposition rate • single volatile species	• n = 1 • no gas - solid reactions • E = 126 kJ/mole A = $7x10^{7}$ s^{-1}
88	• non char forming material • semi - infinite solid	• mass flux determined by chemical decomposition rate	• n = 0 • two different activation energies

Table 2.11 - continued

	• incident radiation absorbed in depth according to the Beer's law • constant thermal properties of the solid (C_p and k) • neglected reradiation from the solid • examined endothermic and exothermic heat of pyrolysis • included terms: 2a(ε=0); 3; 4; 6; 7 • BC's: x = 0: (1); (2); (7) x = ∞: (11)	• single volatile species	167 kJ/mole and 226 kJ/mole $A = 5.5 \times 10^8$ cm s^{-1}
96	• non char forming material • semi - infinite solid • in depth absorption • constant density, heat capacity and thermal conductivity of the solid • constant heat capacity and the factor (ρλ) for the gas phase • included terms: 2a(ε=0); 3; 4; 7 • BC's: x = 0: (1); (3); (7) x = ∞: (11)	• mass flux determined by chemical decomposition rate • single volatile species	• n = 0 • two different activation energies 167 kJ/mole and 84 kJ/mole, frequency factor was a parameter
100	• char forming material • cylindrical geometry • close thermal contact between solid and volatiles as they flow out • linear interpolation between wood and char properties used for heat capacity and thermal conductivity	• mass flux determined by chemical decomposition rate • single volatile species • moisture migration toward the center of the solid ignored • BC: r = 0: (9)	• n = 1 • no gas - solid reactions • E = 63 kJ/mole $A = 1983$ s^{-1}

Table 2.11 - continued

	• energy accumulation of the gaseous species within the solid ignored • included terms: 2(ε=0); 3; 4; 6 • BC's: r = 0: (7) r = R: (1); (4); (5); (6)		
118	• char forming material • semi - infinite slab • heterogeneous model (with respect to the fiber structure) • existence of the volatiles ignored • inert solid matrix left after pyrolysis • constant thermal properties (C_p and k) • regression rate independent of time • constant temperature in pyrolysis zone • included terms: 2(ε=0); 3; 6 • BC's: x = 0: (13); (14) x = ∞: (11); (12);	• no mass flux equation • existence of the volatiles ignored	• n = 1 • no gas - solid reactions • E = 109 kJ/mole A = 1.7×10^6 s^{-1}
70	• char forming material • cylindrical geometry • conductivity and specific heat functions of temperature and conversion • an infinite gaseous medium for the radiative heat transfer considerations • constant porosity of the solid • solid maintains the original shape, but the size allowed to change • included terms: 2(ε=0); 3; 4; 6	• conservation equations for tars and gases are given • mass transfer resistance • multicomponent gas mixture • tar/gas flux at the fiber surface determined by rate of tar/gas formation and consumption	• pyrolysis subdivided in three reactions (both reaction and desorption step in intrinsic rate) • n not reported • secondary reactions included • <u>Primary pyrolysis:</u> 1: solid → tar E_1 = 155 kJ/mole $A_1 = 3.28 \times 10^{19}$ mol m^{-2} s^{-1} 3: solid → char

Table 2.11 - continued

	• BC's: r = 0: (8) r = R: (1); (6); (7)		E_3 = 155 kJ/mole $A_3 = 1.39 \times 10^{10}$ mol m^{-2} s^{-1} • Tar cracking: 2: tar → gas E_2 = 109 kJ/mole $A_2 = 4.28 \times 10^{6}$ s^{-1}
47	• char forming material • slab geometry • char retains the original shape • constant specific heat for solid • constant conductivities for solid and gas phases • local thermal equilibrium between solid and volatiles • molar average specific heat for gas • radiation within the particle included as a part of conduction term • included terms: 2; 3; 4; 6 • BC's: x = L/2: (8) x = 0 and x = L: (15)	• two volatile species: gas and tar • conservation equations for tars and gases are given • pseudo steady state for gas component fluxes • tar/gas flux determined by rate of tar/gas formation and consumption • BC: x=L/2: (9)	• pyrolysis subdivided in four reactions • n = 1 for all four reactions • secondary reactions included • Primary pyrolysis: 1: cellulose → active cellulose E_1 = 243 kJ/mole $A_1 = 2.83 \times 10^{19}$ s^{-1} 2: active cellulose → tars E_2 = 198 kJ/mole $A_2 = 3.17 \times 10^{14}$ s^{-1} 3: active cellulose → 0.65 gases + 0.35 char E_3 = 153 kJ/mole $A_3 = 1.32 \times 10^{10}$ s^{-1} • Tar cracking: 4: tars → gases E_4 = 153 kJ/mole $A_4 = 3.18 \times 10^{16}$ s^{-1}
39	• char forming material • semi - infinite slab geometry • thermal conductivities of cellulose and char linear functions of temperature	• mass flux determined by chemical decomposition rate • single volatile species	• n = 1 • no gas - solid reactions • E = 151 kJ/mole A = 10^{10} s^{-1}

Table 2.11 - continued

	• included terms: 2b(ε=0); 3; 4; 6 • BC: integration from zero to infinity		
178	• model for drying marinite and gypsum • slab geometry • specific heat and thermal conductivity linear functions of local density and temperature • included terms: 2b(ε=0); 3; 4; 6 • BC: measured temperatures at the front and back faces	• mass flux determined by chemical decomposition rate • single volatile species • laminar flow of volatiles • accumulation of volatiles neglected	• n = 1 • no gas - solid reactions • E = 40 kJ/mole $A_1 = 10\ s^{-1}$ (marinite) $A_2 = 100\ s^{-1}$ (gypsum)
136	• char forming material • slab geometry • local thermal equilibrium between solid and volatiles • no solid cooling by volatiles or water vapor • thermal properties functions of temperature and mass retention • included terms: 2(ε=0); 3; 4; 6 • BC's: x = 0: (1): (4); (5); (6) x = L: (5); (6)	• back surface impervious for mass flow • mass flux determined by chemical decomposition rate • no flow of volatiles to the cooler region	• n = 0 • no gas - solid reactions
77	• char forming material • slab geometry • properties linear function between wood and char density • local thermal equilibrium between solid and volatiles	• mass flux determined by chemical decomposition rate • single volatile species	• n = 1 • no gas - solid reactions • E = 126 kJ/mole (base case) $A = 5.25 \times 10^7\ s^{-1}$ (base case) $E_1 = 75$ kJ/mole (examined) $A_1 = 1.72 \times 10^4\ s^{-1}$ (examined)

Table 2.11 - continued

	• char remains intact (no fissuring or mechanical cracking) • included terms: 2b(ε=0); 3; 4; 6 • BC's: : (2); 4; (5) or (6)		E_2 = 176 kJ/mole (examined) $A_2 = 1.52 \times 10^{11}$ s^{-1} (examined)
84	• char forming material • slab geometry • three phases of pyrolysis (preheat, early charring, late charring) • no solid cooling by volatiles or water vapor • abrupt endothermical conversion from solid to char at pyrolysis temperature • thermal properties functions of density • linear spatial temperature distribution in regions of the slab • included terms: 2b(ε=0); 3; 6 • BC's: linear temperature distribution in three phases no flow of heat through the back face	• mass flux determined by chemical decomposition rate • single volatile species	• instantaneous conversion at pyrolysis temperature • no gas - solid reactions
191	• char forming material • slab geometry • model is fuel in inert solid matrix • matrix properties independent of fuel content • surfaces heating and cooling by uniform thermal convection with constant coefficient • included terms: 2b(ε=0); 3; 6 • BC's: (2); (5)	• mass flux determined by chemical decomposition rate • single volatile species	• n = 1 • no gas - solid reactions • E = 139 kJ/mole $A = 5.3 \times 10^8$ s^{-1}

Table 2.11 - continued

17	• the same model as in reference 84 with different properties		
9	• char forming material • slab geometry (semi - infinite) • no thermal interactions between gases and solid matrix • thermal properties independent of temperature • no heat of pyrolysis • included terms: 2b(ε=0); 3 • BC's: (2); (4); (5); (6)	• mass flux determined by chemical decomposition rate • single volatile species	• n = 1 • no gas - solid reactions • E = 123 kJ/mole
90	• char forming material and non - charring material • slab geometry • model only for surface temperature • transmittance function of time • surface regression accounted for • constant properties (ρ, C_p, k) • included terms: 2b(ε=0); 3 • BC's: (2); (4); (5); (6); (7)		

Table 2.12: A Summary of Properties[1]

Ref. No.	C_s [J/g-K]	α_s [mm^2/s]	$(\rho C_p)_s$ [J/m^3-K]	C_c [J/g-K]	$(\rho C_p)_g$ [J/m^3-K]	$C_{p,g}$ [J/g-K]	k_s [W/m-K]	k_c [W/m-K]	ρ_s [g/cm^3]	ρ_c [g/cm^3]	E [kJ/mole]	A [s^{-1}]	h_p [J/g]
49									1.19		134	2.8×10^9	77.4
99											153		
194											100		0
16		0.178					0.142				116	1.5×10^8	f(T)
											135	1.9×10^9	
37			10^5		10^3		0.1				140	10^8	
183		0.16 to 0.17					0.096	before the breakpoint			126	6×10^7 to	84[2]
												7.5×10^8	to 126
								after the breakpoint			152	4×10^8	837
											to 179	to 2×10^9	to 2303
86	No properties reported except h_p												0
135	The properties in non-dimensional form reported										100		exo and endo
101	2.51			2.51		1	0.126		0.5	0.125	126	5.25×10^7	
102	2.3			1.01		1.11	0.113	0.188	0.58		126	2×10^7	754

[1] h_p is taken positive for endothermic pyrolysis and negative for exothermic pyrolysis

[2] Denotes heat of combustion

Table 2.12: Continued

80	2.3		0.71	1.09	0.159	0.05	0.58	0.2	75	2.5×10^4	419
145	1.4				0.13		0.6		126	7×10^7	0, -210 or -420
165	1.5		1	1.7	0.2	0.08	0.5	0.15	151	10^{10}	500
81	f(T)	f(r)	f(conversion)		f(ρ,M)	f(conversion)			63	15×10^6	
60	2.7				0.12		0.6		126	7×10^7	360
88					0.126		1.18			5.5×10^8	1256
96	1.88			1.03	0.126				167		
100	1.38		0.67	1.11	0.147	0.041	0.6		63	1983	203
118	1.38				0.109		0.45	0.12	109	1.7×10^6	1256
70	f(T, conversion)				f(T, conversion)				155	3.28×10^{19} mol/m^2 s	
									109	4.28×10^6	
									155	1.39×10^{10} mol/m^2 s	
47	1.34			f(T)	0.243		1.4				
				cellulose → active cellulose					243	2.83×10^{19}	0
				active cellulose → tars					198	3.17×10^{14}	-1465
				active cellulose → 0.65 gases + 0.35 char					153	1.32×10^{10}	301
				tars → gases					153	3.18×10^{16}	-33

Table 2.12: Continued

39	1.3		0.9	1.7	0.1	0.027	0.55	0.055	150	10^{10}	230
178	f(T)		f(T)	f(T)	f(T)	f(T)	1.03	1	40	10	2440
	1.13		2.09	f(T)	0.242	0.125	0.8	0.713	40	100	2440
136	No properties reported										
77	2.09		1.05	1.05	0.188	k_s/k_c=1	0.6	0.125	126	5.25×10^{7}	418.7
					0.335	or 0.5			or 75	1.72×10^{4}	or 837.4
					0.0837	or 0.25			or 176	1.52×10^{11}	
84	2.5	0.113	2.0		0.17	0.03	0.6	0.2	$\rightarrow\infty$		300
191	2.3		2.3		0.113	0.113	0.6	0.225	139	5.3×10^{8}	360
17	2.0		1.8		0.2	0.113	0.9	0.09	$\rightarrow\infty$		600
9	1.38				0.126		0.47	0.118	123		0
90	1.5 (PMMA)				0.19		1.2				
	1.4 (Red Oak)				0.15		0.7				

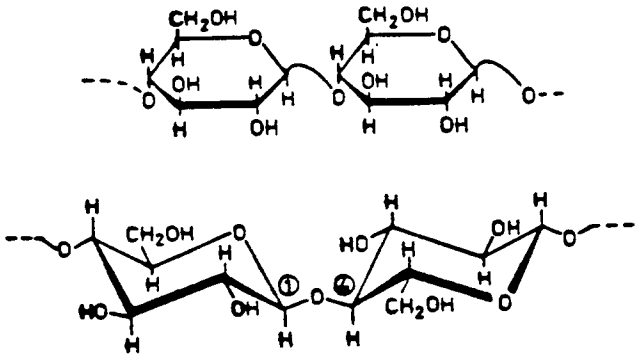

Figure 2.1 Cellulose, upper in Haworth formula and lower in the conformation formula (from 181)

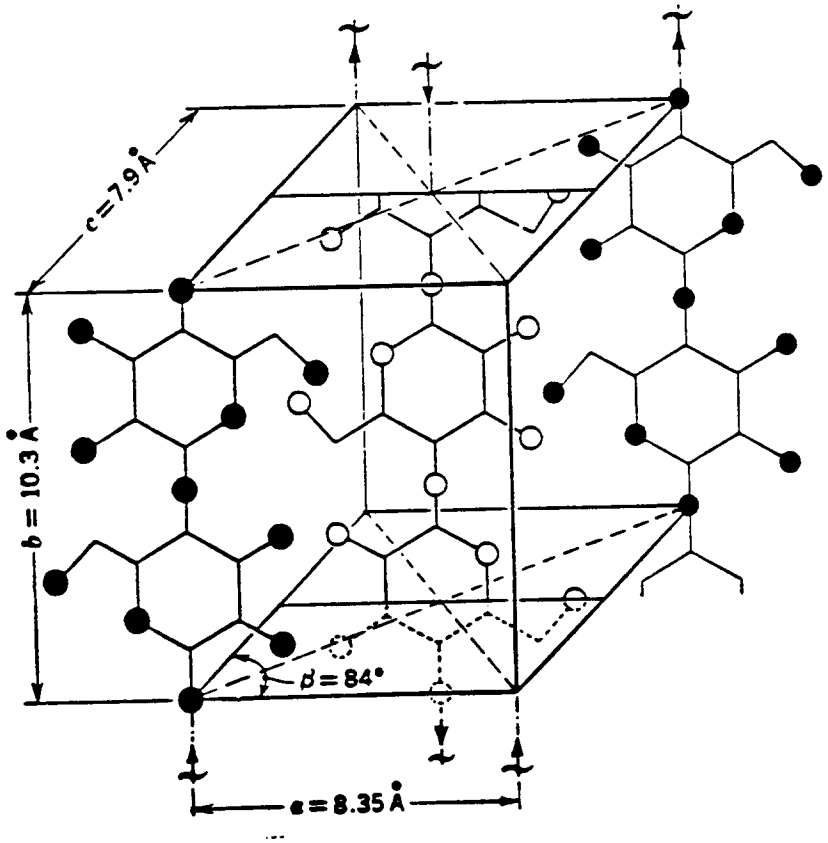

Figure 2.2 Diagrammatic sketch of the unit cell of cellulose and positions of component glucose anhydride units (from 169)

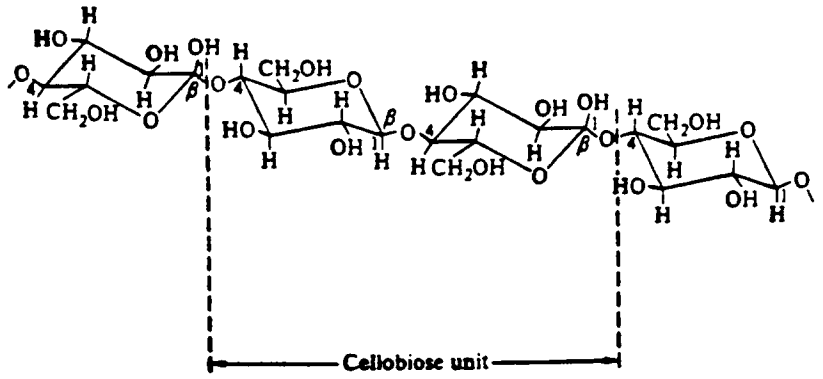

Figure 2.3 Structure of cellulose (from 44)

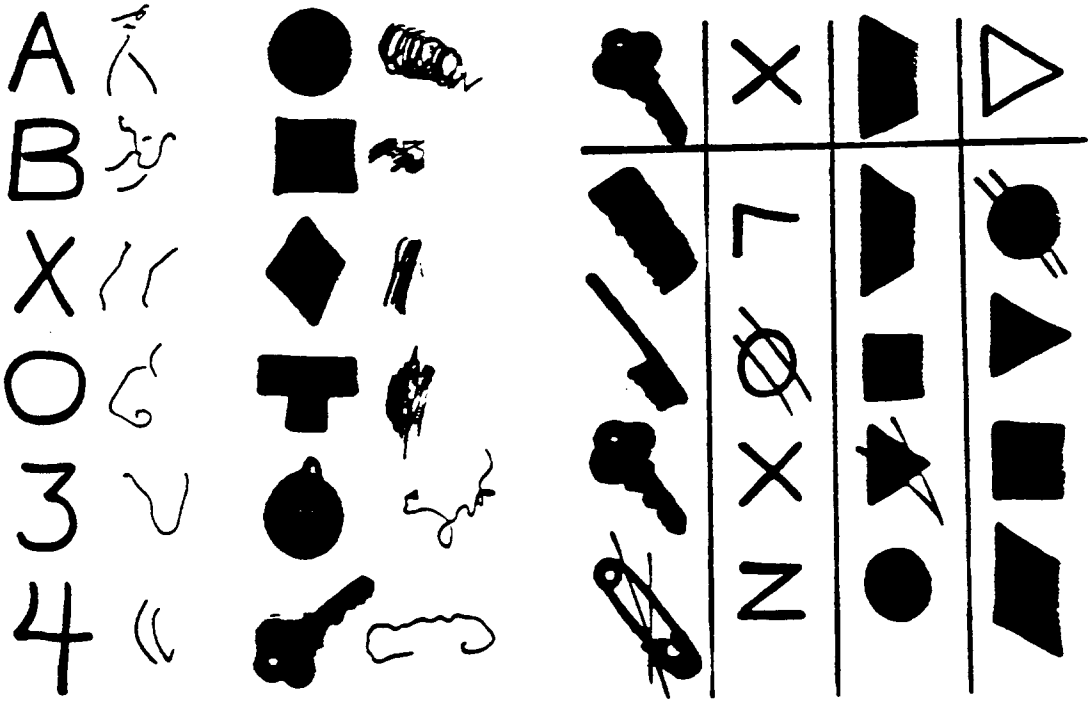

Figure 2.4 Examples of CO poisoned patient writings, drawings and figure matching (from 18)

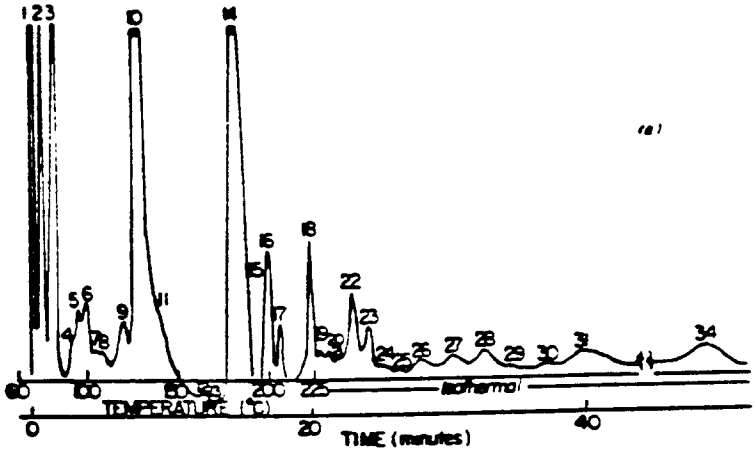

Identification of Cellulose Pyrolysis Products

Column 9 (Octoil-S)		Column 13 (Silicone oil-550)		Column 14 (Carbowax-20M)	
Peak no.	Compound	Peak no.	Compound	Peak no.	Compound
1	Fixed gases	1	Fixed gases	1	Fixed gases
2	Formaldehyde	2	Water/Formaldehyde	2	Formaldehyde
3	Acetaldehyde	3	Acetaldehyde	3	Acetaldehyde
4	Water	4	Propionaldehyde/ Acrolein/Acetone	4	Propionaldehyde
5	Propionaldehyde/ Acrolein/Acetone	6	Acetic acid	5	Acetone
6	Carbonyl containing	7	Methyl Ethyl Ketone/n-Butyraldehyde	6	Acrolein
7	Methyl Ethyl Ketone/n-Butyraldehyde	8	Glyoxal	7	n-Butyraldehyde/ Methanol
9	Glyoxal	10	Unidentified carbonyl compound	8	Methyl Ethyl Ketone
10	Formic acid	17	Furfural	10	Water
11	Acetic acid	31	5-Hydroxymethyl Furfural	14	Glyoxal
13	Carbonyl containing			15	Acetic acid
15	Furfural			16	Formic acid/ Furfural
23	Lactic acid			18	Carbonyl containing
				20	Lactic acid
				34	5-Hydroxymethyl Furfural

Figure 2.5a Gas chromatograms of cellulose pyrolysis products from pyrolysis on a hot wire in a carrier gas stream, (Carbowax-20M column) (from 151)

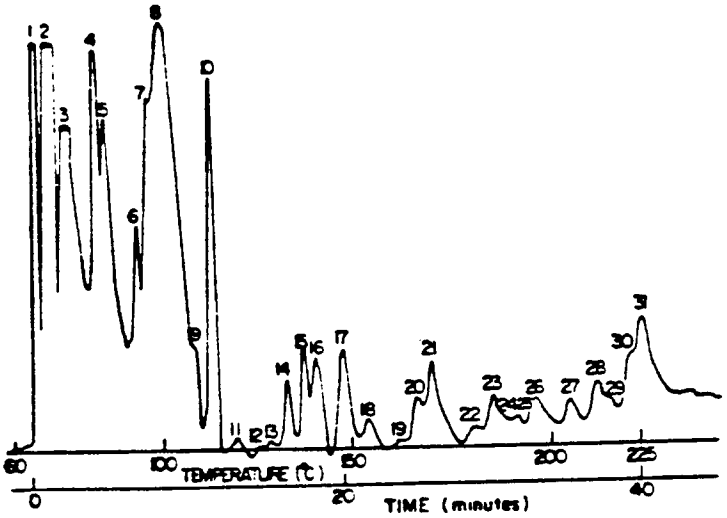

Figure 2.5b Gas chromatograms of cellulose pyrolysis products from pyrolysis on a hot wire in a carrier gas stream, (13 silicone oil-550 column) (from 151)

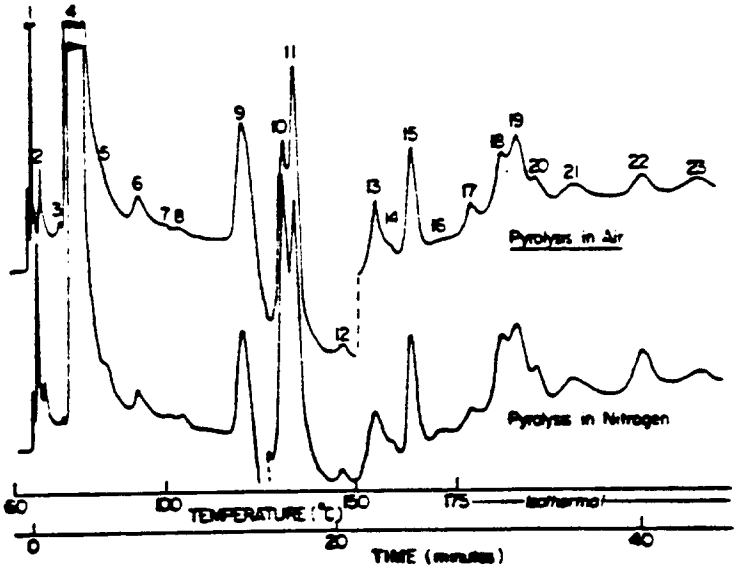

Figure 2.5c Gas chromatograms of cellulose pyrolysis products from pyrolysis on a hot wire in a carrier gas stream, (Octoil-S column) (from 151)

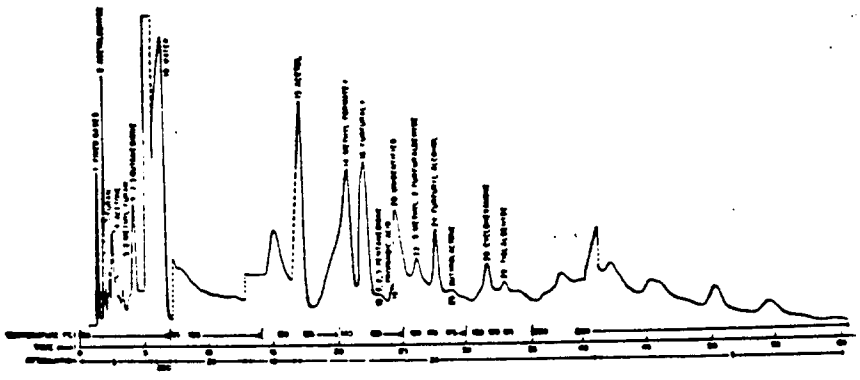

Figure 2.6 **Linear region chromatogram of the degradation products of untreated** cellulose pyrolyzed at 315°C (from 111)

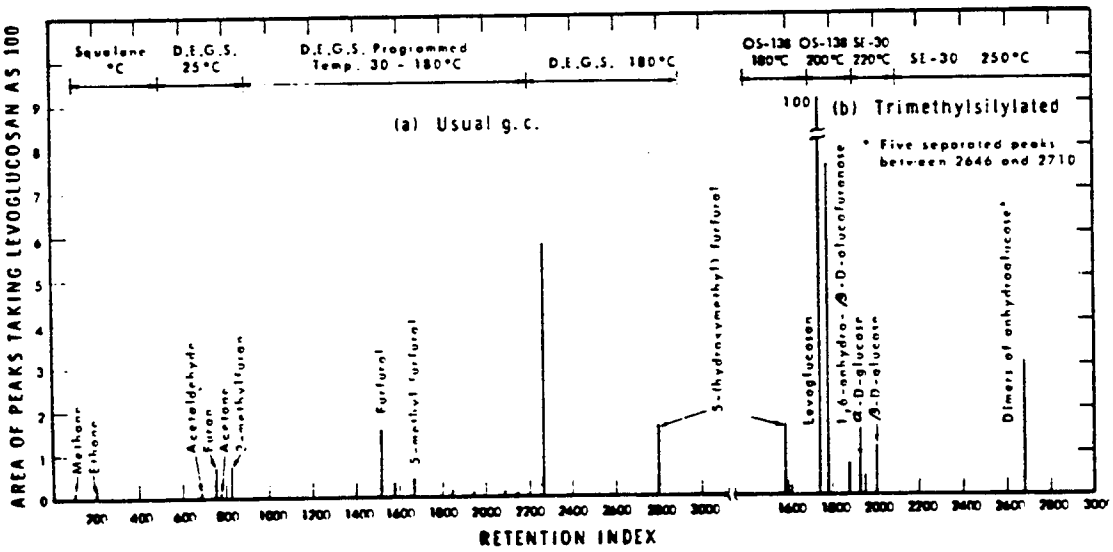

Figure 2.7 **Gas chromatographic analysis of the thermal decomposition products of** cellulose (from 185)

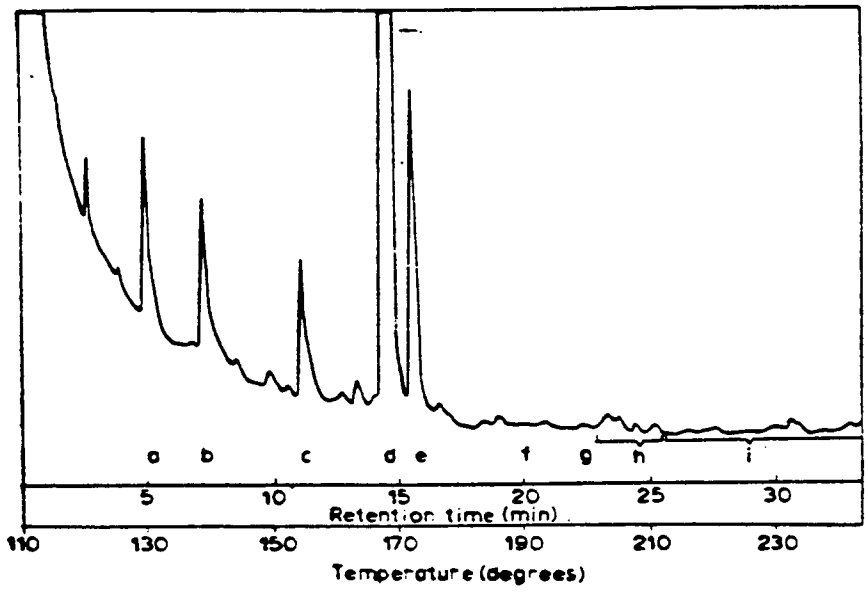

Figure 2.8 Chromatogram of cellulose pyrolysis tar (from 158)

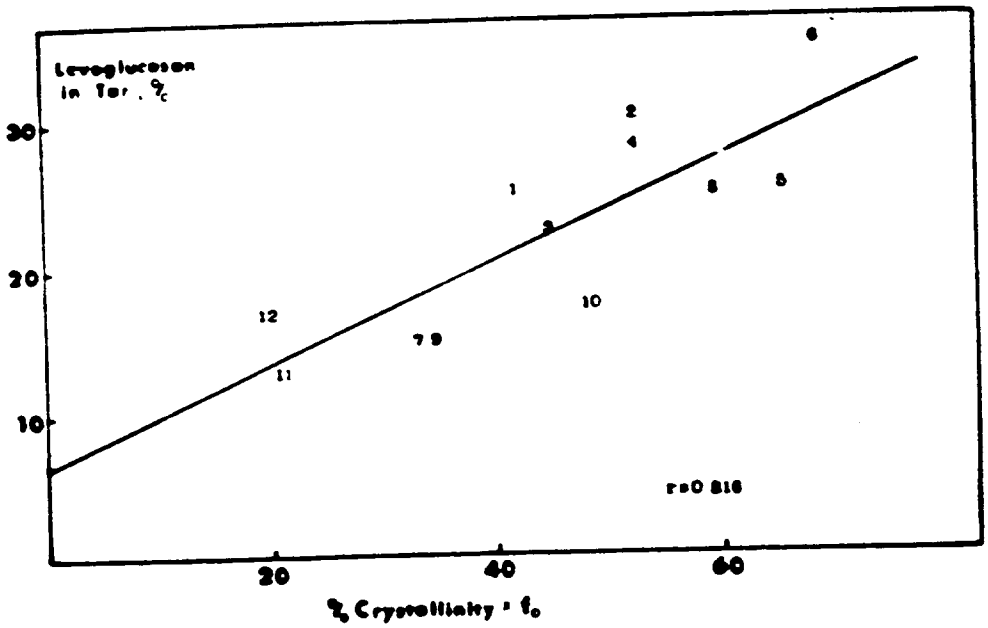

Figure 2.9 Levoglucosan content in tar formed during high temperature pyrolysis in air as a function of crystallinity (from 13)

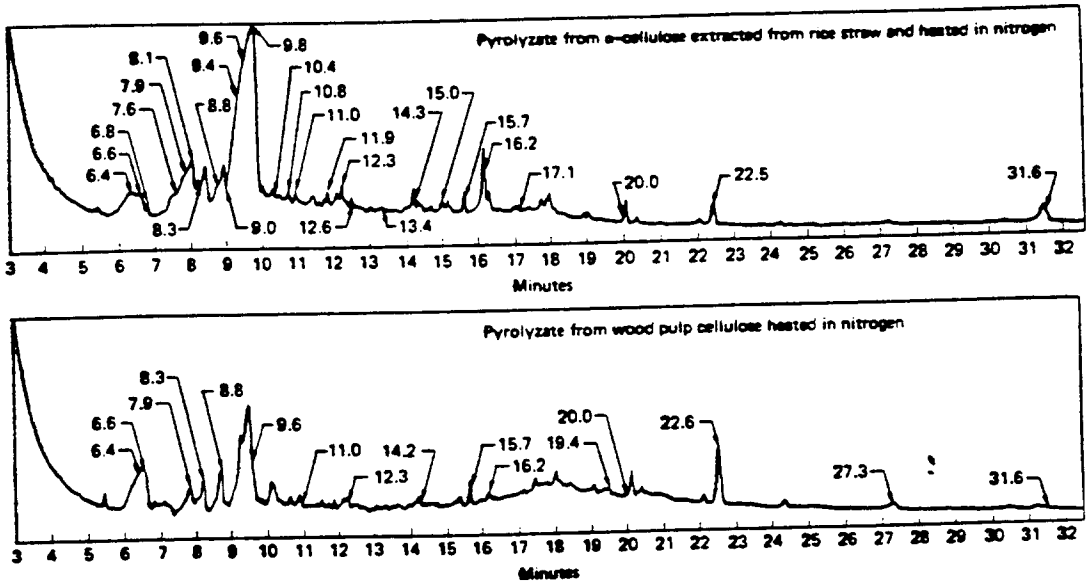

PEAK ASSIGNMENT

6·4	cyclohexanone
6·6	2,2-dimethyl-1-hexanol
6·8	3-buten-2-ol
7·9	decylaldehyde
8·1	4,5-dimethylnonane
8·3	vinyl isopropyl ether
8·8	3-ethyl-1-pentene
9·0	3-methyl-cis-2-hexene
9·4	2,3-dimethyl-1-butene
9·6	4-methyl-cis-pent-2-ene
9·8	4-cyclohexylbutan-2-one
10·4	alpha-humulene
10·8	3-(2,6,6-trimethyl-1-cyclohexene-1-yl)2-propen-1-ol
11·0	1,4-dimethylnaphthalene
11·9	hydroxybenzaldehyde
12·3	6-benzo-8,9-dimethylbicyclo(3,2,2)-non-6,9-diene
12·6	hexacosanol
13·4	2-phenyl-2,3-dihydroindene
14·3	n-butylacetoacetate
15·0	glucitol-1,2,3,4,5,6-hexaacetate
15·7	di-N-butyl-phthalate
16·2	palmitic acid
17·1	3-ethyl-5-(2-ethylbutyloctadecane)
19·5	unidentified
20·0	unidentified
22·5	unidentified
27·3	unidentified
31·5	farnesol

Figure 2.10 Comparison of thermal degradation products generated in nitrogen from pyrolyzing cellulose extracted from rice straw and wood pulp (from 112)

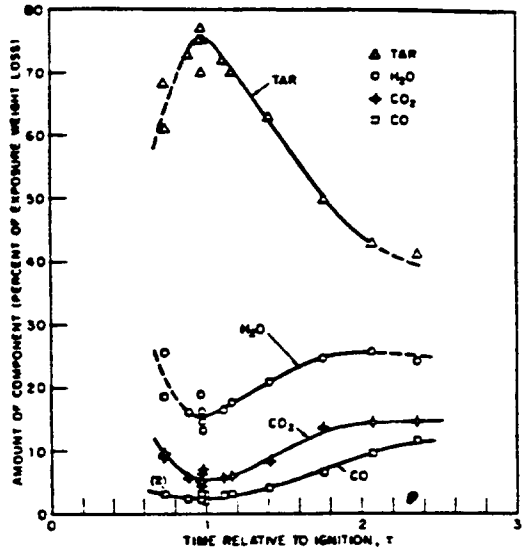

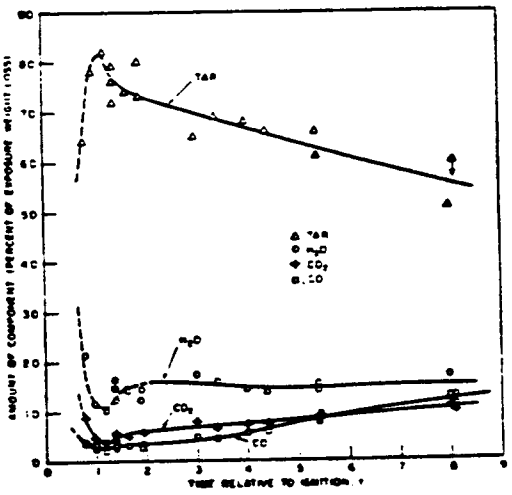

Figure 2.11 Major volatile pyrolysis products of cellulose irradiated with 176 kW/m^2 (a) and 460 kW/m^2 (b) (from 116)

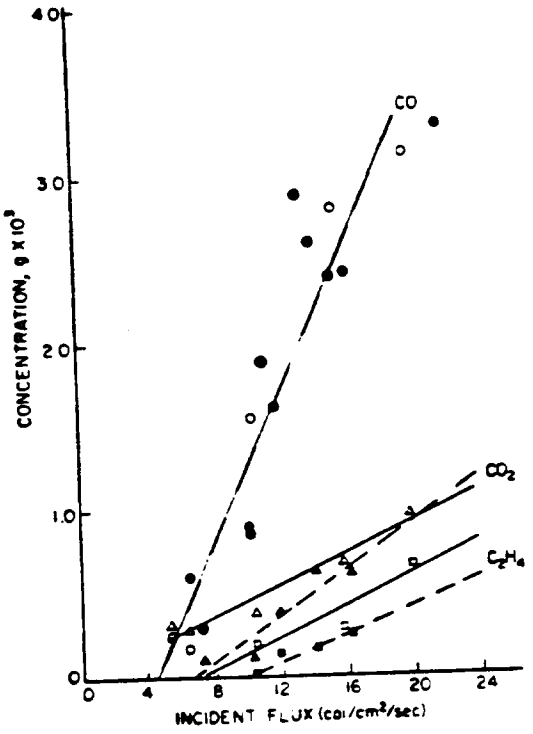

Figure 2.12a Components of fractions condensed at -90°C and -180°C (from 19)

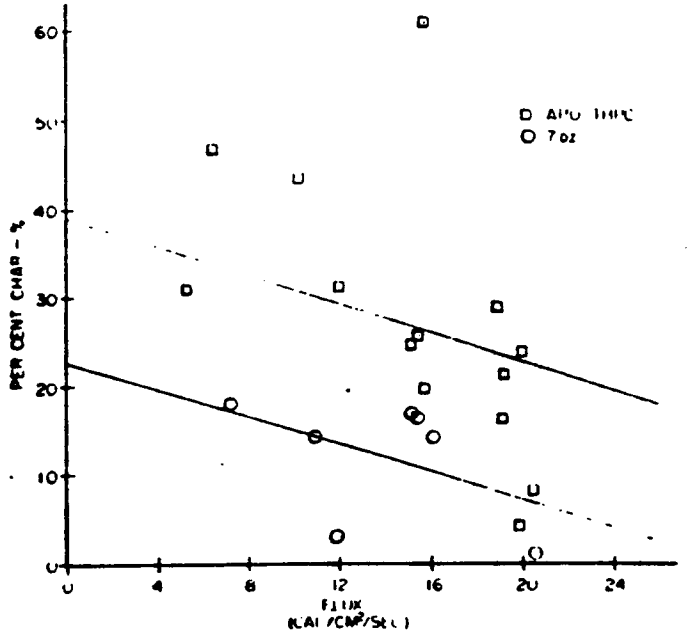

Figure 2.12b Char yield from treated and untreated cotton (from 19)

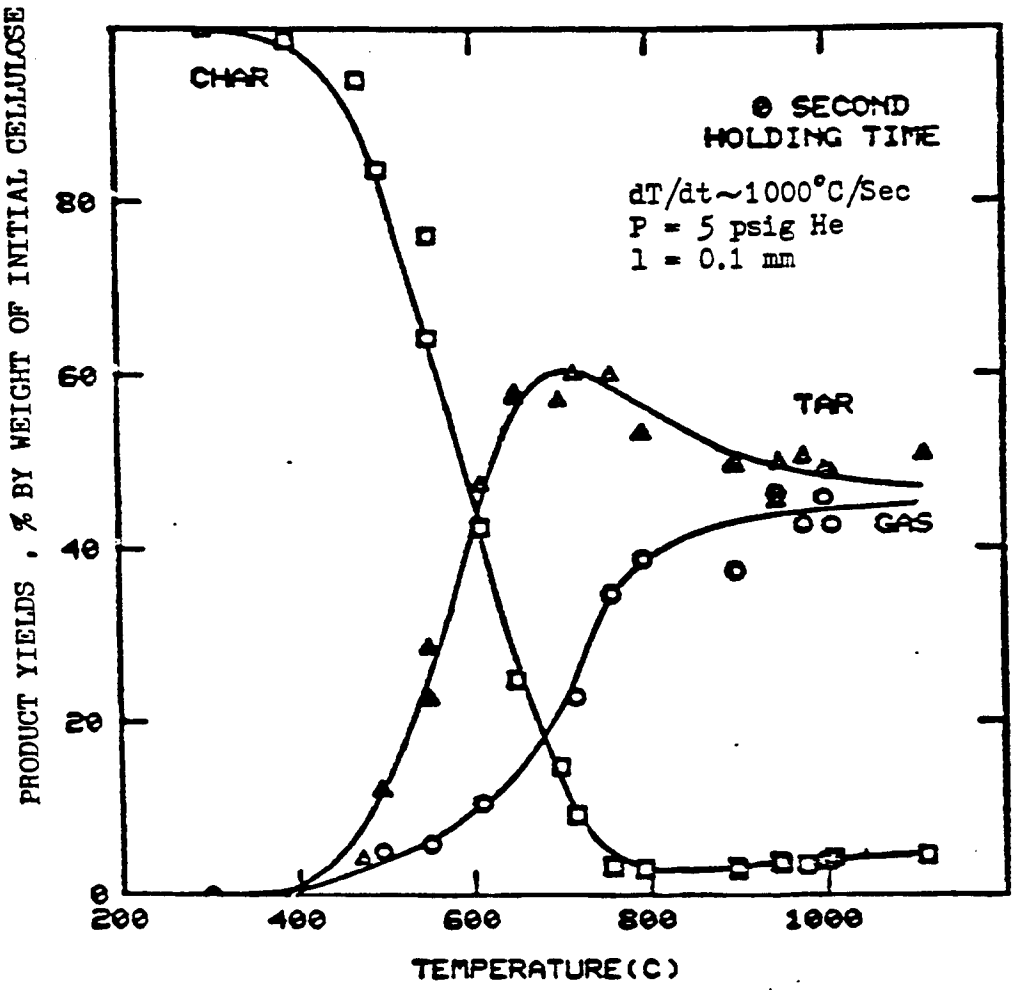

Figure 2.13 Effect of peak temperature on yield of char, tar and total gases from pyrolysis of cellulose filter paper (from 65)

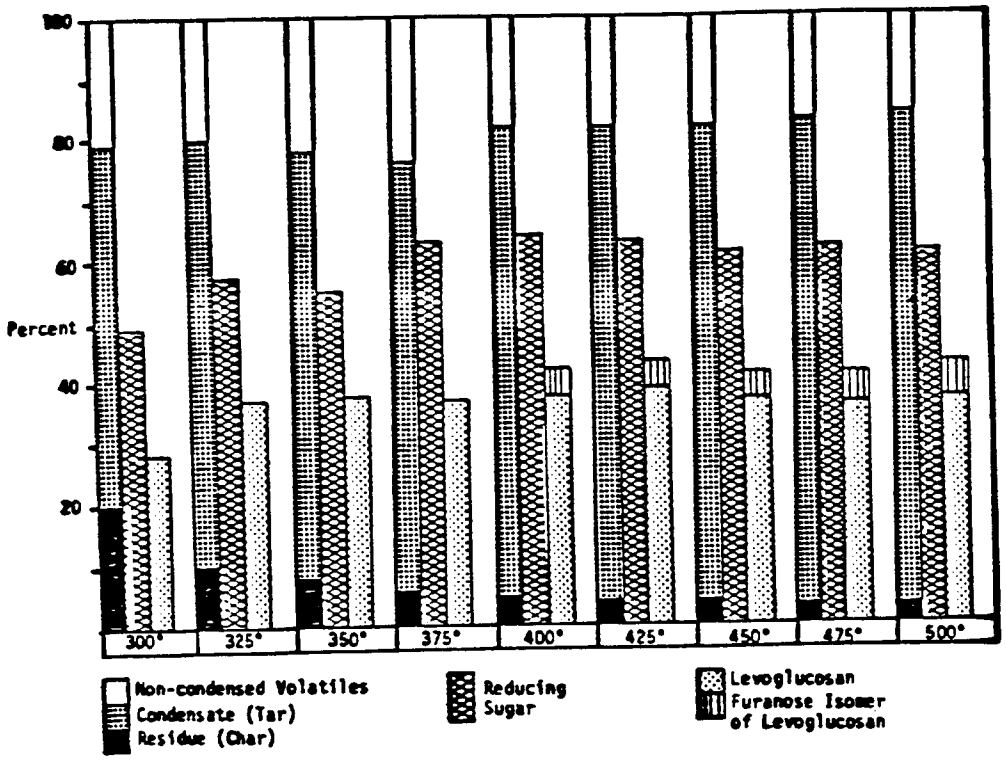

Figure 2.14 Products from pyrolysis of cellulose powder under vacuum (from 160)

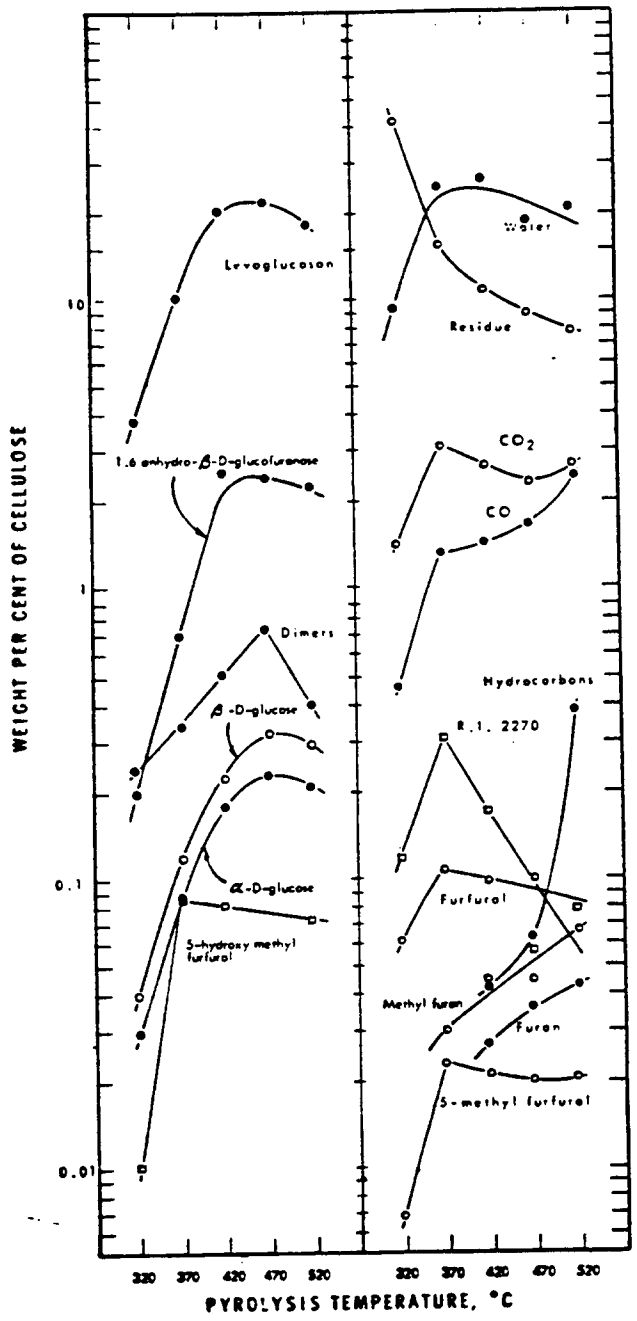

Figure 2.15 Decomposition products of cellulose at various temperatures (from 185)

Cellulose → levoglucosan → tars + gases / chars — Model I

Cellulose → anhydrocellulose → chars + gases / tars — Model II

Cellulose → tars + gases / chars — Model III

Substrate → gases / tars / chars — Model IV

Figure 2.16 Summary of the mechanistic models for cellulose pyrolysis (from 2)

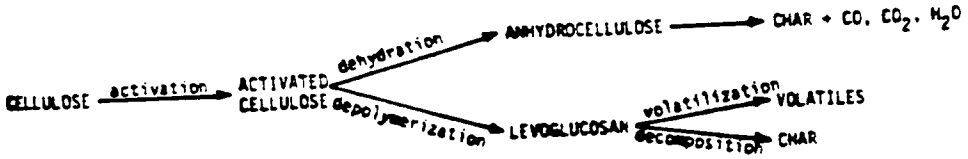

Figure 2.17a Mechanism for cellulose pyrolysis (from 122)

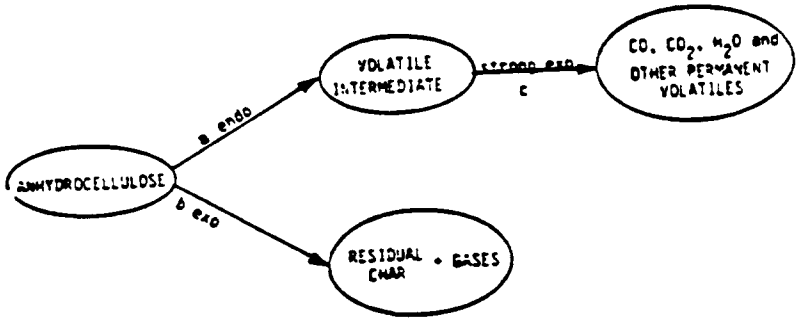

Figure 2.17b Mechanism for anhydrocellulose pyrolysis (from 122)

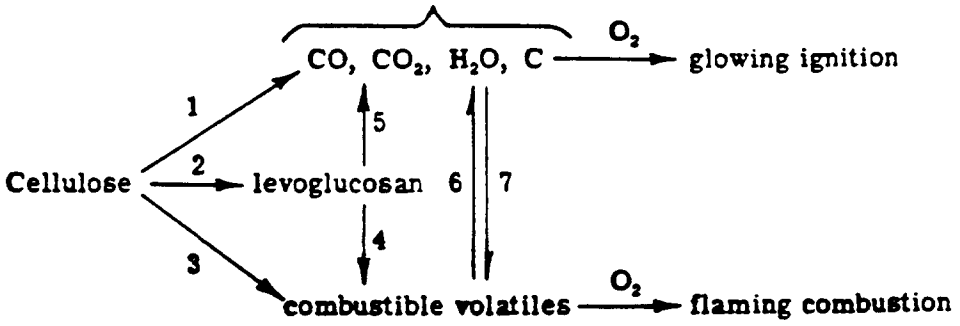

Figure 2.18 The general reactions involved in pyrolysis and combustion of cellulose (from 156)

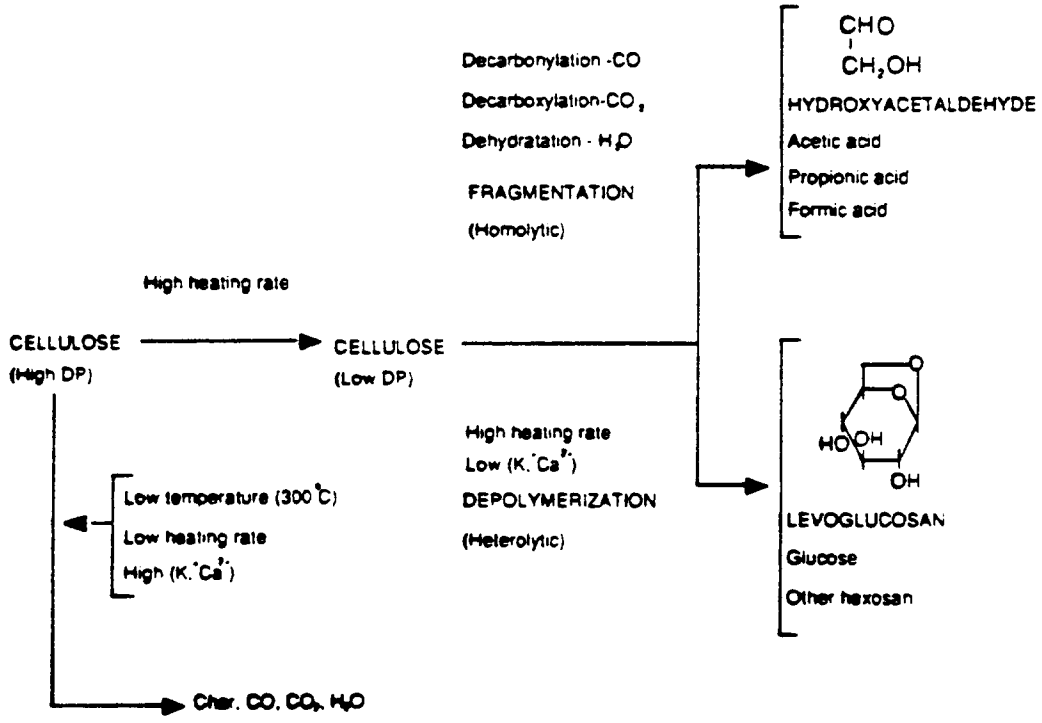

Figure 2.19 Mechanism for the pyrolysis of cellulose under different conditions (temperature, heating rate and inorganic ion content) (from 79)

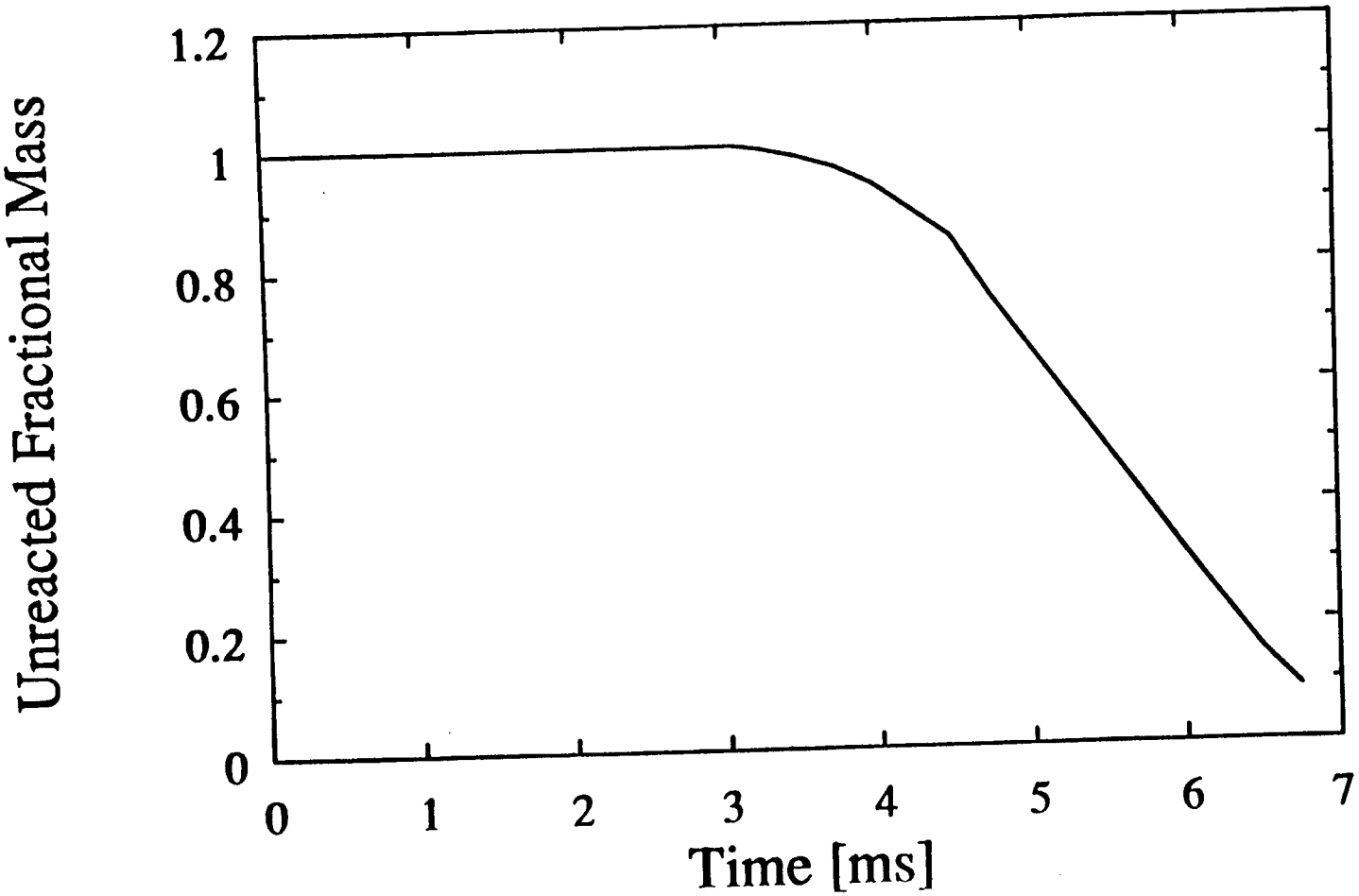

Figure 2.20 Fractional mass loss as a function of time (100 μm particle, 16000 kW/m^2) (from 99)

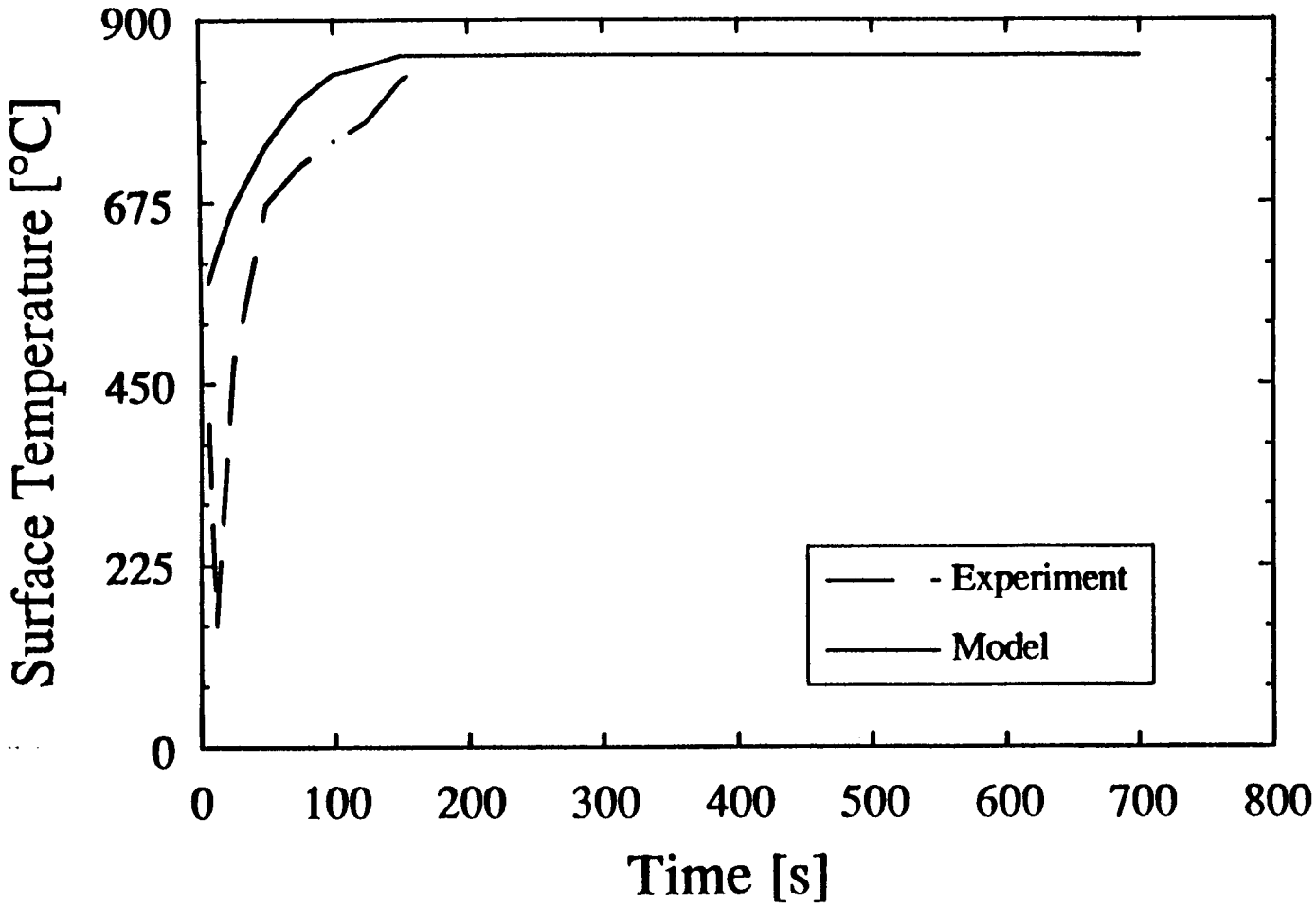

Figure 2.21 Comparison of measured surface temperature with temperature predicted by the model (5 mm thick particle, heated with 167 kW/m^2) (from 37)

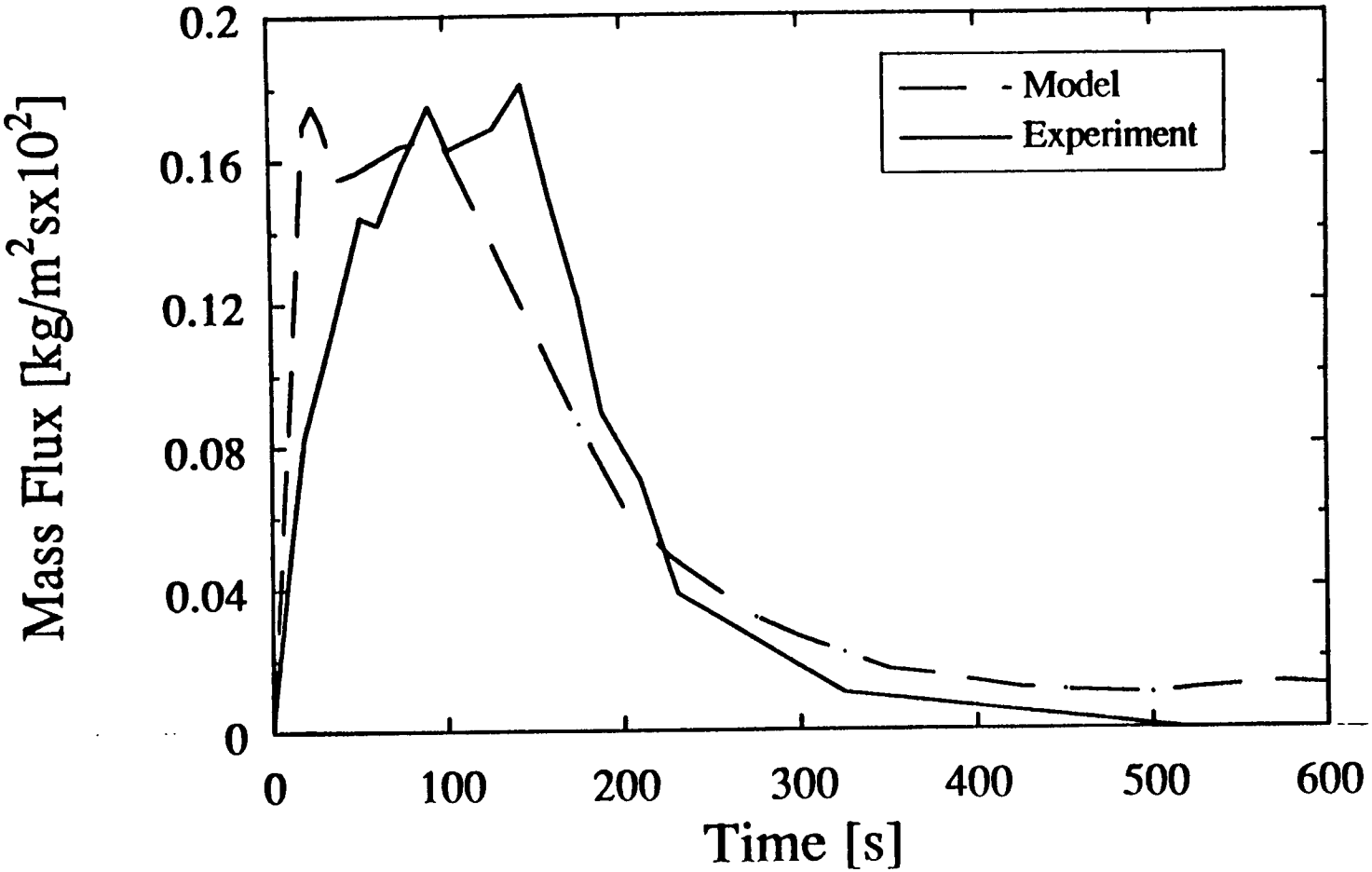

Figure 2.22 Comparison of measured and predicted non-condensable gas flux from particle surface (5 mm thick particle, heated with 167 kW/m^2) (from 37)

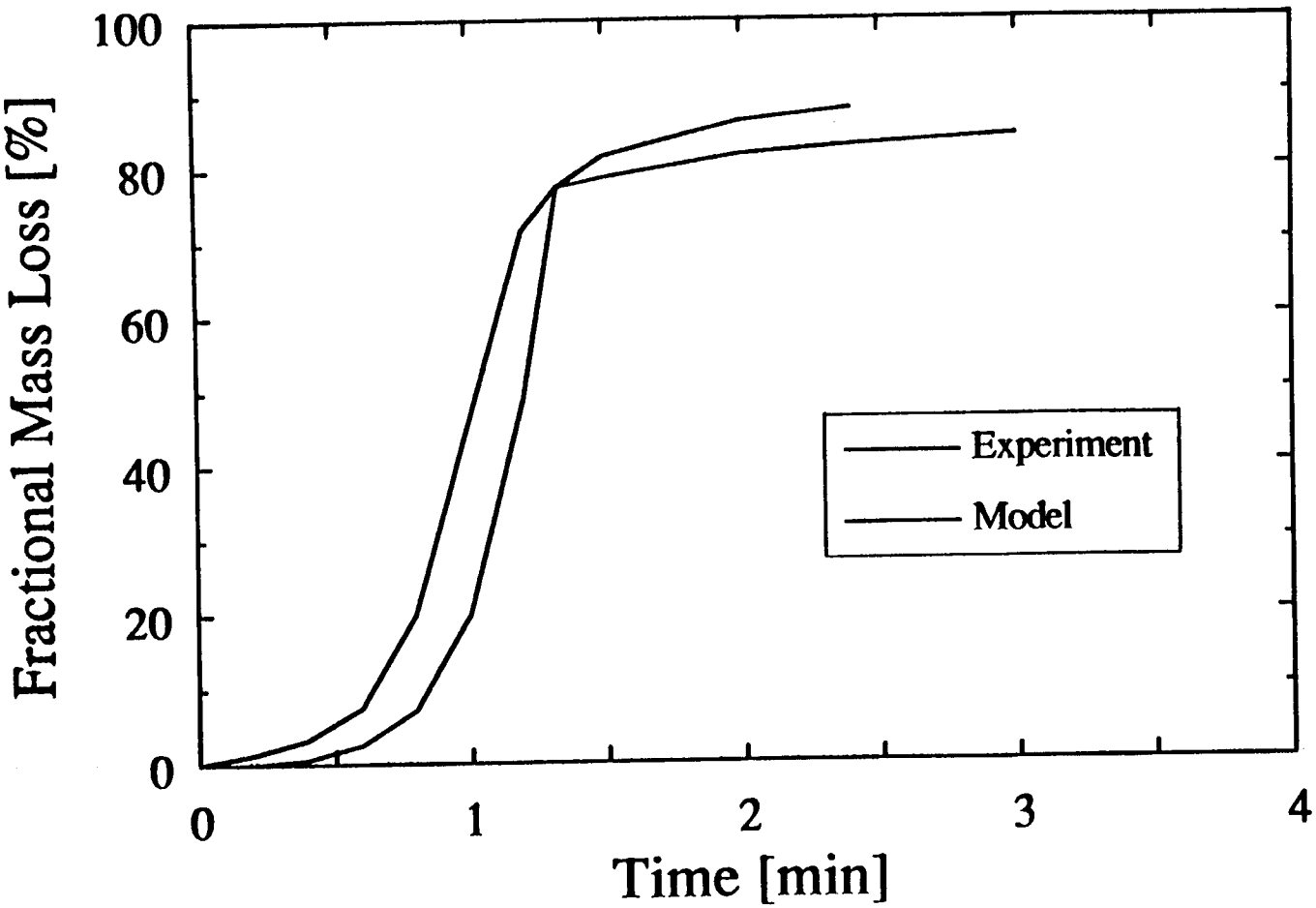

Figure 2.23 Comparison of experimental and predicted fractional mass losses (10 mm dowels, furnace temperature 500°C) (from 183)

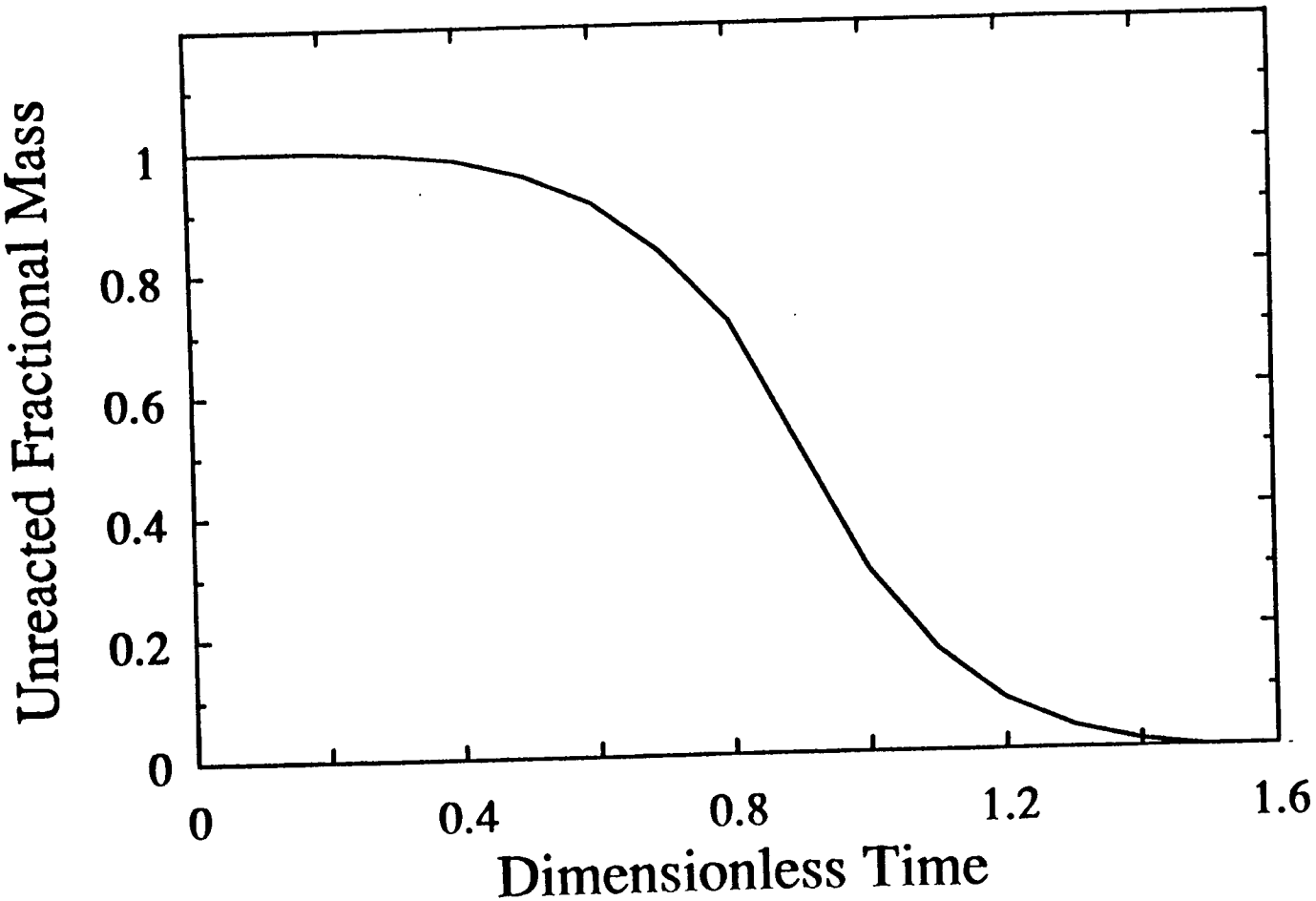

Figure 2.24 Unreacted fractional mass predicted by the model as a function of dimensionless time (from 135)

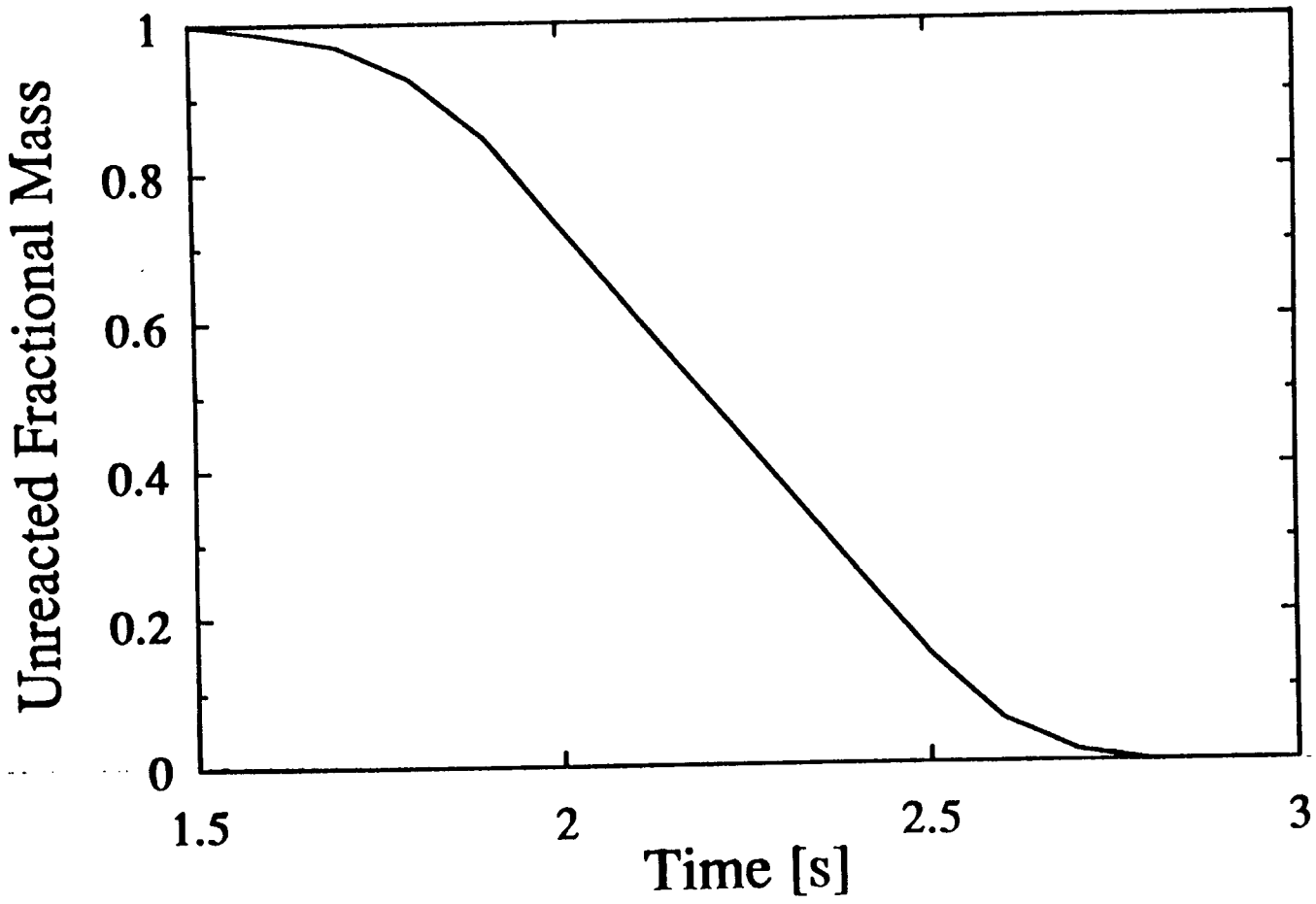

Figure 2.25 Unreacted fractional mass as a function of time (from 47)

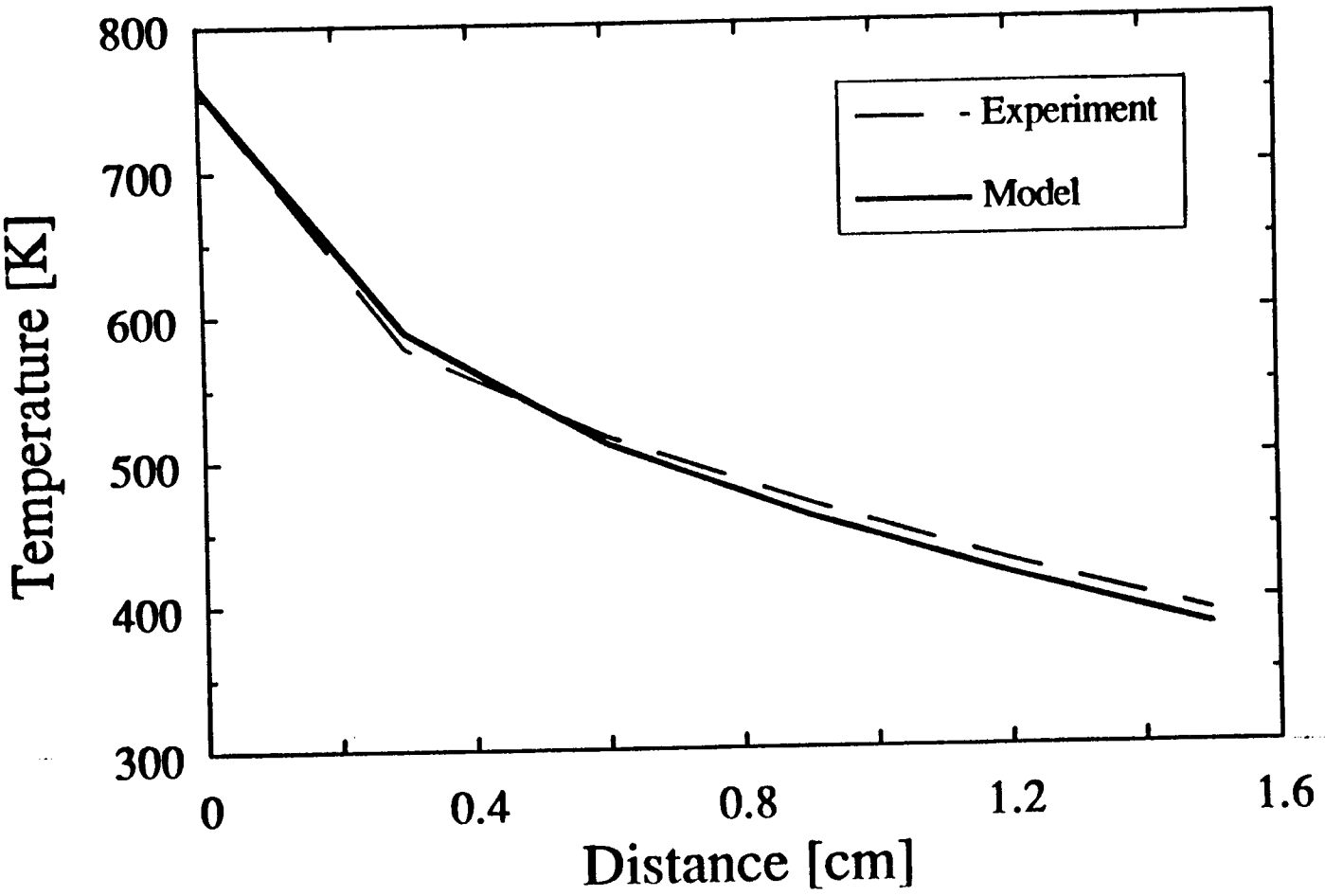

Figure 2.26 Comparison of predicted and measured temperature profiles (5 cm thick slab, D = 19 mm, after 5 min exposure to 22.2 kW/m^2) (from 80)

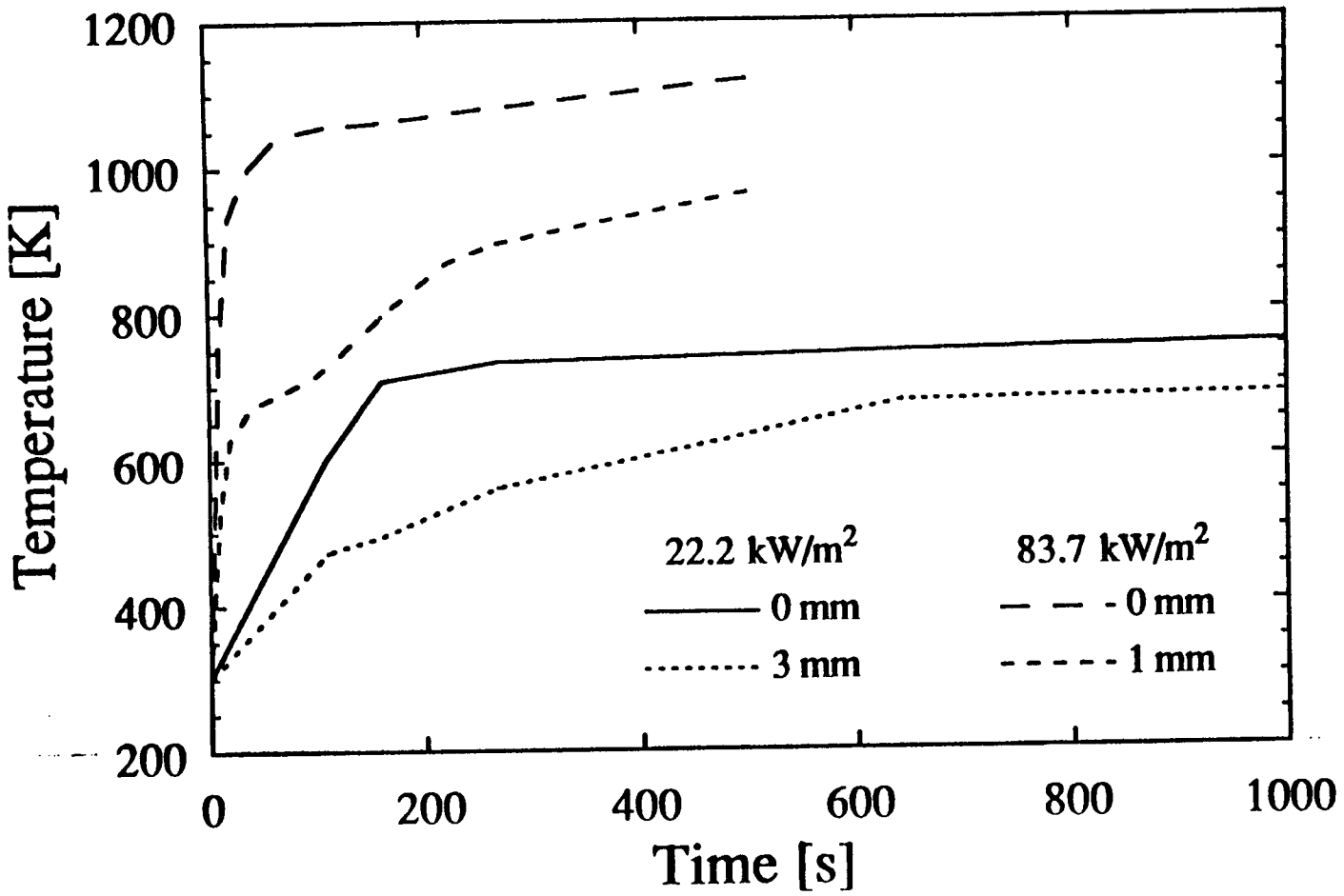

Figure 2.27 Temperature as a function of time at different distances from the surface and for different applied heat fluxes (from 80)

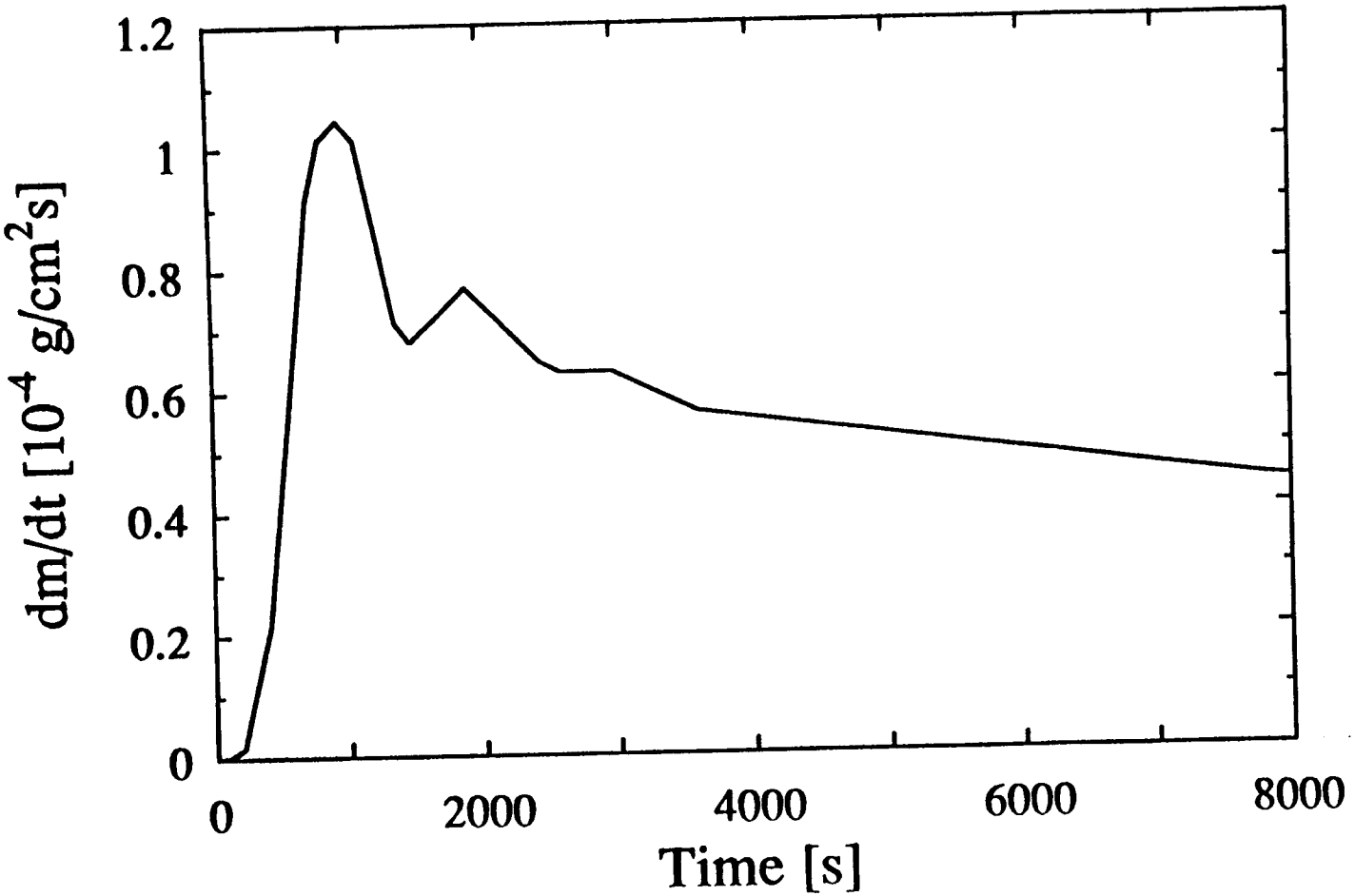

Figure 2.28 Predicted mass loss rate as a function of time (heat flux 22.2 kW/m^2) (from 80)

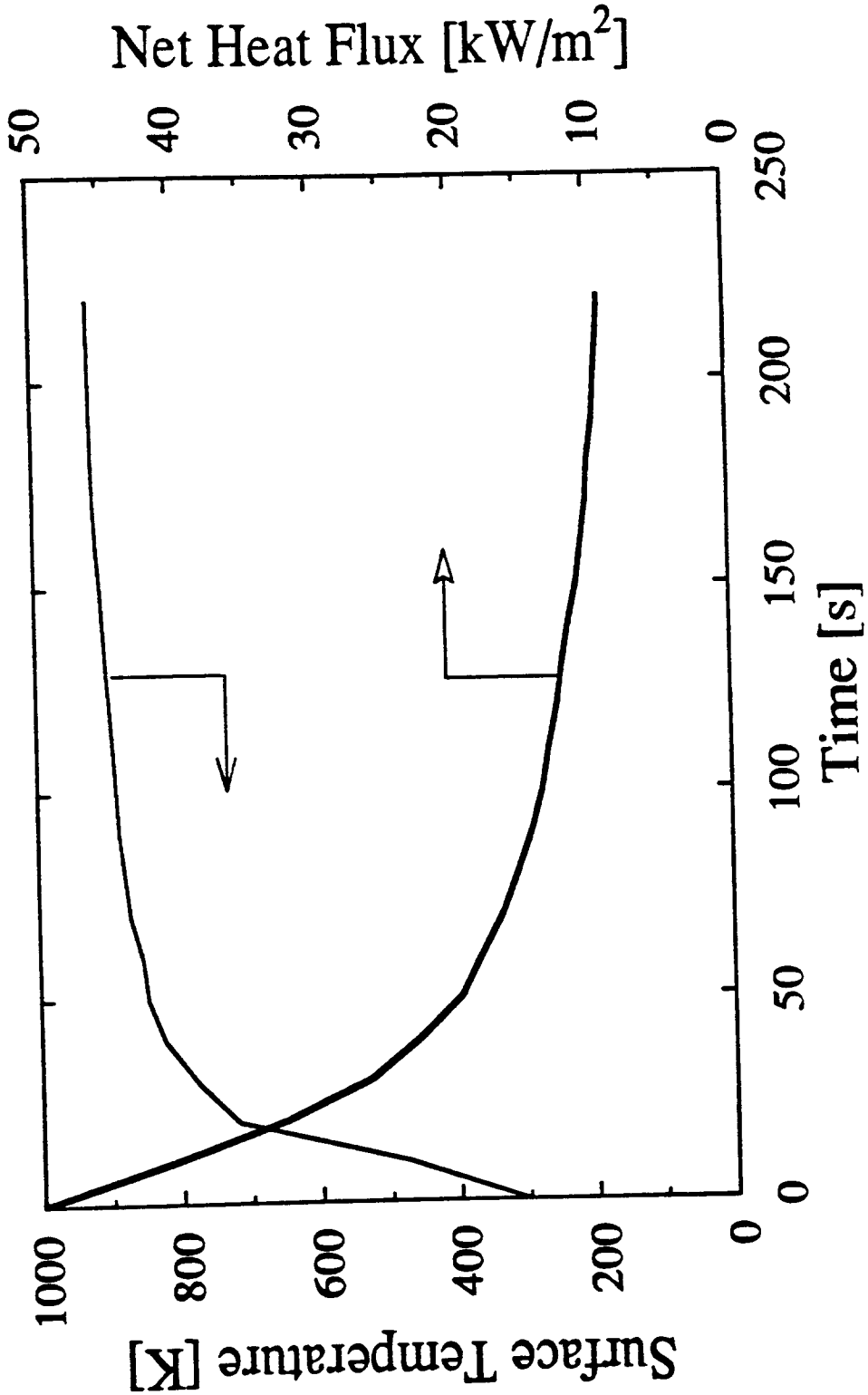

Figure 2.29 Predicted surface temperature and net heat flux as a function of time (10 mm slab, applied heat flux 50kW/m^2) (from (165)

3. EXPERIMENTAL

3.1 MATERIALS

The material used in this study was purified cellulose, prepared from high purity cotton of 99% alpha cellulose content. It was Whatman CF-11 Fibrous Cellulose Powder (advanced ion exchange cellulose for biopolymers). The molecular weight of this material is in the range of 36,000 to 45,000 Daltons, which corresponds to degree of polymerization between 220 and 280. The length of the fibers is between 50 and 250 μm, with a mean fiber length of 200 μm. The fiber diameter is in the range between 12 μm and 15 μm and in the swollen state 25 μm. The ash content is 0.009% and the water content, on an as-received basis, 7.68%. The iron content is 1.32 ppm of dry weight and copper content is 0.09 ppm of dry weight. The fiber density is in the range from 1.3 g/cm^3 to 1.6 g/cm^3 and the bulk density is 0.370 g/cm^3.

Some additional tests were done with wood (pine and oak) and with phenol-formaldehyde resin. The pine was received from NIST (kiln dried, standard material) in blocks of 41x41x51 mm, with a density of 0.377 g/cm^3. Oak was obtained commercially. The blocks had a thickness of about 20 mm and a density of 0.734 g/cm^3. Phenol-formaldehyde resin was molding powder black bakelite, obtained from Fisher Scientific Company.

3.2 SIMULATED FIRE APPARATUS

3.2.1 SAMPLES

Samples used for the simulated fire apparatus were pressed from the cellulose powder without any additives. It was learned that the original moisture content was high enough so that the pressed samples had sufficient structural integrity. Most of the samples used in this study were pressed in a direction collinear with the axis of incident radiative flux. For that purpose a die, was made that had an internal diameter of 38 mm. There is evidence of a planar structure, being formed during the pressing, which can be thought of as analogous to grains in wood. The possible significance of a grain structure will be discussed in connection with the results of the study. Most of the samples were cylinders with a diameter of 38 mm and a height of about 10 mm.

The samples were pressed to three different densities. The lowest density was determined by the poor structural strength of samples, and the highest density by the capabilities of the press. It turned out that samples obtained by this technique have densities close to that of wood. The densities used were: 0.965 ± 0.041 g/cm^3 (pressed continuously to 39.3 MPa and released afterwards), 0.691 ± 0.035 g/cm^3 (pressed to 19.6 MPa) and 0.458 ± 0.026 g/cm^3 (pressed to 2.4 MPa). Since the above three densities were the only ones studied they will be referred to as "high", "middle" and "low" density samples.

In order to avoid possible variability in pressing, batches of samples were made on the same day, usually containing 40 samples of each density. The density variation within the same batch was found to be smaller than the values noted above, e.g. in the case of high density samples the standard deviation over all batches is 0.041 g/cm^3, or 4.2%. For two

different batches the deviations are 2.2% and 2.0%, respectively. Nevertheless, the density standard deviation calculated for the entire set of samples is more representative, since the results are often compared without regarding to what batch a sample was from.

The density standard deviation changes with the density, for high density it is 4.2%, for middle density it is 5.1% and for low density it is 5.7%. The reason for the variation is that the higher pressing force shows greater level of repeatability.

The samples made for determining the effect of "grain" orientation were made in the same fashion, except that the die was larger (63 mm ID). Large cylindrical samples (63 mm in diameter and about 60 mm in height) were pressed and the usual size sample was cut from the large one, with a diameter of 38 mm, by cutting perpendicular to the pressing axis. Using this procedure, a sample was made that had a "grain" orientation parallel to the axis of incident radiative flux.

Pine samples were made from blocks by cutting them to the same dimensions that cellulose samples were pressed to a diameter of 38 mm and thickness of about 10 mm. The initial size of a pine block made it possible to acquire samples with parallel and perpendicular orientation, with respect to the axis of incident heat flux. Oak samples could be made from blocks with only one grain orientation with respect to the axis of incident heat flux, and that turned out to be tangential. Phenol-formaldehyde resin samples were pressed in the same way as cellulose samples (38 mm in diameter and about 10 mm in thickness), at a pressure of 39.3 MPa, without addition of binders. That was the only pressure high enough to provide sufficient structural integrity. There were only three samples pressed with densities of 1.094 g/cm^3, 1.077 g/cm^3, and 1.082 g/cm^3, respectively.

3.2.2 EQUIPMENT

There is a need to tie the impressive progress that has been made in measuring and predicting char yields from pyrolyzing organic solids under laboratory conditions to predicting the yield under actual fire conditions. The particular approach employed here involves the use of equipment that has been specifically developed to simulate the environment of real wall fires.

The equipment allows bulk samples of several centimeters in diameter and length to be held in an insulating ceramic holder atop an electronic balance. The sample holder, balance, and heater assembly are held in a controlled gas environment, which was nitrogen purged at a flowrate of 15 l/min, for the most of this work. The environment can then simulate a diffusion flame environment, in which little or no oxygen reaches the surface of the sample. Heating of the sample is accomplished by use of radiant heaters, which can provide a flux of up to about 100 kW/m^2, which covers the range of relevance in fire situations (somewhere around 40 kW/m^2 is a "standard" condition). During this work three different incident heat fluxes were used: 20, 40 and 60 kW/m^2. The design of the device is shown schematically in Figures 3.1, 3.2 and the arrangement of the entire system is displayed in Figure 3.3. The names and specifications for various pieces of equipment are given in Appendix A.

Figure 3.1 shows a schematic side view of the pyrolysis chamber. The chamber is made of ordinary glass (a modified aquarium), 600 mm wide, 400 mm tall and 300 mm deep (inside dimensions), which gives a total volume of 72 liters. A cylindrical sample is insulated with a previously cured ceramic cup and both are placed in the sample holder that was positioned directly on the load cell assembly of the balance. The balance itself is covered by a water cooled aluminum plate that was introduced as a protection of the balance mechanism from

high heat fluxes during the operation. As noted above, the entire experimental chamber was nitrogen purged. There are no purge gas lines represented in Figure 3.1. The main portion of the gas stream was introduced at the cooling fins at the back of the balance mechanism, for two reasons: the first reason was to provide balance cooling at the factory installed fins, in addition to the water cooling system, and the second reason was to provide the starting point of the purge gas, right in the vicinity of the balance, so that the products of pyrolysis could be swept in the vertical direction to the exhaust system.

The other part of the gas stream was introduced into the "optical connection tube" between the optical pyrometer and the sample. The function of the tube was to avoid possible interference from reflected radiation from various pieces of equipment. For that purpose the tube was painted inside with black enamel. The tube is also purged so that the pyrolysis products did not interpose between the pyrometer and the sample.

The sides of the chamber that could receive significant radiation were covered from the inside with marinite insulating blocks. An insulation plate behind the sample was positioned at an angle in order to avoid reflection back to the pyrometer and that is the only insulating block that is represented in Figure 3.1. A top view of the system, including the radiative heaters and aperture plates is shown schematically in Figure 3.2a. The chamber was closed at the top with two abutting aluminum plates, shown in Figure 3.2b, where the positions of the various feed-through holes and the exhaust hole can be seen. The aluminum plates were placed on the top of the chamber onto plastic seat, where silicon sealant was previously applied to improve sealing. The sealant was also applied between the two aluminum plates. After drying, the sealant was cut and tight resealing was assured by applying a compressive force between the plates and by virtue of the mass of the plates themselves.

Two radiant heaters, with the water cooled shielding (water cooling lines are omitted from figures), were focused at the vertical centerline of the sample surface and positioned in such a way to provide concentrated power. The tungsten filament of the heaters essentially delivers blackbody radiation. The desired incident heat flux control is accomplished by regulating voltage that is applied to the heaters. As a result, the filament is being heated to various temperatures, depending on the desired intensity of the heat flux. By varying the filament temperature, in order to prescribe the heat flux, the spectral distribution of the delivered radiation is changing. Figure 3.4 represents a radiation spectrum obtained from the manufacturers specification for this type of heater, for the maximum power and three different voltages that result in heat flux at the center of the sample surface of 20, 40 and 60 kW/m^2. As can be seen the majority of the radiation is delivered at about 1.52 μm, 1.30 μm and 1.22 μm for heat fluxes of 20, 40 and 60 kW/m^2 respectively. The wavelength range of the delivered radiation had a significant impact on some measured quantities, which will be discussed below.

The aperture plates in front of the heaters were introduced to minimize the radiative loss to other surfaces in the system and they enhance the uniformity of the heat flux at the sample surface. It should be pointed out that the heat flux measurements, which will be described in more detail below, were performed with the focusing plates in place. The heat flux distribution at the sample surface is shown in Figure 3.5, where the effect of the vertical arrangement of the radiative heaters becomes obvious. Viewing from the sample direction, the left half of the sample is exposed mostly to the incident heat flux in the range of 96% to 104% of the prescribed heat flux. The major portion of the right half of the sample is exposed to the incident heat flux in the range of 113% to 122% of the prescribed heat flux.

The data collection was done by Macintosh microcomputer at a sampling frequency of 1 Hz. This frequency was unnecessarily high for mass recording, but for simplicity of data collection it was kept as such for all recorded variables. The computer program that was used for data collection is listed in Appendix B. It can be seen from the code that the original idea was to collect data from four channels, data from the balance, from the digital thermometer, from the optical pyrometer and from a gas analyzer. The fourth channel was inactive, because a gas chromatograph was used for the gas analyses, instead of the originally selected infrared CO/CO_2 analyzer, which lacked the necessary sensitivity. However, the fourth channel was kept and it served as an auxiliary channel for various types of measurements, the most important of which was the flux measurement. The arrangement of the entire system is represented in Figure 3.3. All components, used for measurements, had to be followed by some kind of signal conditioners, in order to be fed to an AD/DA converter, that accepts an input voltage of ±10V. Each signal conditioner will be separately described in the appropriate chapter. The resolution of the AD/DA converter was 4.882 mV.

3.2.3 MASS MEASUREMENT

The sample mass was monitored continuously. The factory installed balance output was digital. In the present work it was necessary to obtain an analog signal in the range of ±10 V, for simplicity in data collecting. The analog signal was acquired directly from the load cell, amplified 20 times, tared, filtered and fed to the AD/DA converter and, subsequently, to a Macintosh microcomputer.

Unfortunately, by taking the signal from the load cell, the existing ambient temperature compensation was made unusable. It was established that the temperature close to the load cell changes by several degrees during the course of a run, even with the water and gas

cooling systems operating. Since the load cell is very sensitive to temperature variation, the baseline drifted in time. The drift, due to the load cell temperature increase, was found to be very reproducible and a function of the incident heat flux used, flowrates of cooling water and gas and, to some extent, on the total mass placed on the load cell. It was determined that the actual sample mass loss during the pyrolysis experiment does not contribute to the overall drift of the baseline, since it represented only a minute fraction of the total mass located at the load cell. In order to overcome the problems with the drift, the baseline was recorded for a particular set of conditions, prior to an experiment.

With the taring capabilities incorporated into the amplifier, the mass recording system was used for registering the relative sample mass, with an arbitrary starting point, in voltage units. After an experiment, the baseline was subtracted from the original mass recording, that included a baseline drift. Thus the real mass change, still in voltage units, was obtained. A typical baseline, recorded mass and the mass corrected for the baseline drift are displayed in Figure 3.6. The correct mass was determined by weighing a sample before and after each experiment on another balance with a sensitivity of ± 0.1 mg. In such a way, a calibration is determined for each run. The balance output varies linearly with the mass on the load cell and that fact was applied in ascertaining a real mass change with time, by converting voltage units to mass units.

The reproducibility of the mass measurement was found to be very good. Figures 3.7a, 3.7b and 3.7c show several different mass recordings for high, middle and low density, respectively. The reproducibility is the worst for low density samples due to weak structural integrity. It was observed on several occasions that pyrolyzed pieces fell off from the surface of a lower density sample, and such experiments had to be disregarded. Another reason for the lowest level of reproducibility in mass recordings for the low

density samples can be seen from the sample density reproducibility. As noted above the pressure employed during the pressing low density samples was very small and, therefore, difficult to reproduce exactly.

3.2.4 TEMPERATURE MEASUREMENT

Temperature measurement was performed at sample surfaces (front and back) and at four more points in the sample interior using 0.5 mm chromel-alumel thermocouples. The installation of thermocouples was rather tedious, especially in lower density samples. In order to avoid any contamination of a sample with adhesives, thermocouples were held at a place purely by physical contact. Naturally, the most important (and the most difficult to install) thermocouple was that for measuring the front surface temperature. A difficulty in its installation was associated with recession of the front surface. Cellulose, under the conditions used in this study, shrinks during pyrolysis; the actual amount of shrinkage depending on the severity of heating. Since heating is applied to the front surface, the entire decrease in sample size is manifested through its recession. Therefore, the thermocouple to be used for measuring the front surface temperature had to have a capability to follow it while moving. For that purpose, the thermocouple was installed in such a way so as to make use of a spring effect. The probe itself was fixed onto the sample holder and bent to exert some tension on the part of the probe that was close to the sample surface. One half of the bead, which had the same diameter as the probe - 0.5 mm, was buried into the sample. With that technique, used for all three density samples, a thermocouple was able to follow the receding surface and to measure the temperature of a slice, not more than 0.25 mm in thickness.

The thermocouples in the sample interior were positioned in pre-drilled holes of 0.5 mm in

diameter. During the installation special care was taken such that thermocouples would be located at the centerline of a sample. Unfortunately, the holes could be drilled only in high density samples, due to problems of structural integrity. Attempts to drill holes in the medium and low density samples resulted in disintegration of the samples. Therefore, a different interior thermocouple fixing technique was used. A ceramic cup was prepared, with thermocouple probes cast into it. After curing, a sample was carefully pushed towards the cup, with front and back surfaces (bases of the cylinder) parallel to the probes, so that the thermocouples slowly penetrated the sample. It should be noted that, even with this, relatively simple technique, only one out of five installations was successful.

Thermocouple positions were determined using a caliper with a resolution of 0.01 mm. The distances from the front surface, at which temperatures were measured, were determined with an error of 0.25 mm, which represented half the thermocouple hole diameter. With a typical distance from hole to hole of about 2 mm, that meant that the uncertainty in position determination was no better than 12.5%.

Another difficulty in measuring the interior temperature profile in a sample was due to sample shrinkage. Hence, the position of a thermocouple, once pyrolysis started, continuously changed. The corrections for position were done by measuring the distances after the pyrolysis was finished. The first layer, close to the front, heated, surface, that experienced the most severe pyrolysis conditions shrinks to about 75%, 46% and 29% of initial dimensions, for 20, 40 and 60 kW/m^2, respectively. That means that the, above noted, uncertainty of 0.25 mm in distance measurement represents about 17%, 27% and 43% uncertainty in final thermocouple position, for 20, 40 and 60 kW/m^2, respectively. Even though there were relatively fine gauge thermocouple probes employed, the uncertainty in position determination for temperature measurements in the char is shown to

be extremely high, especially in cases of higher incident heat flux experiments.

Sometimes, a surface thermocouple would change its position, if it was under large tension and, in that case, it would break the char layer between itself and the front surface. Normally, an anomaly of this type was easily detectable during the experiment, and any such measurements were disregarded.

The thermocouples were connected to a six channel digital thermometer whose output was calibrated to be zero volts and 10 V at 0°C and 1000°C, respectively, with linear variation of voltage between those two temperatures. With an output so conveniently chosen, the digital thermometer served as an amplifier as well. It was connected to an AD/DA converter which was in turn connected to Macintosh microcomputer (see Figure 3.3). Even though it was a six channel digital thermometer, it was not capable of simultaneous reading of six channels and, hence, it had only one output. Since the temperature data was collected on one channel only, it was necessary to manually select the readout and therefore the digital thermometer output, so that all six channels, or temperatures, could be recorded. The data were collected at a 1 Hz sampling frequency and there were actually six different temperatures recorded on one channel. A typical temperature recording is shown in Figure 3.8.

3.2.5 OPTICAL PYROMETRY

Originally there was a hope that an optical pyrometer could be used for surface temperature measurements. The advantages of such a measurement were obvious: optical measurement of the surface temperature, requiring no mechanical contact. However, it turned out that the particular pyrometer used has a fairly narrow wavelength sensitivity range; in fact the wrong range to be conveniently applied in this work. Nevertheless, the pyrometer provided some useful qualitative information. A typical pyrometer signal for a typical experiment is

shown in Figure 3.9. It can be seen that, upon inducing a thermal radiation, the pyrometer signal abruptly changes to a higher value, apparently due to the significant reflection of the radiation from the sample surface, due to the non-unity emissivity of the smooth, white sample surface. It should be noted that thermocouple measurements of surface temperature did not indicate this sudden change in temperature. Further, when the surface begins to pyrolyze, the pyrometer signal starts to decrease, probably indicating a surface emissivity change. After passing through a minimum, the signal starts to increase again, in this case indicating significant thermal radiation from the hot char layer at the sample surface.

Although it seemed obvious that the surface temperature could not be conveniently measured by means of optical pyrometry, the pyrometer signal was continuously recorded and, as noted, the data was used qualitatively.

3.2.6 GAS ANALYSES

Gas analyses were performed by gas chromatography, using a thermal conductivity detector. There were two columns used, Porapak Q and Molecular Sieve, connected either in series or parallel. The carrier gas was helium, at a flowrate of 27 ml/min. The gas chromatograph used here did not have a temperature programming capability, so the oven temperature was kept constant at 50°C. The oven houses the sample injection loop, hence the sample loop was also kept at 50°C. The gas chromatograph was connected to an integrator, so the data was available in the form of chromatograms, with printout of calculated peak areas.

Gaseous products of pyrolysis were analyzed for carbon dioxide, ethylene, ethane, water, methane and carbon monoxide. It was assumed that these gases represent the majority of

the gaseous products of pyrolysis, according to the literature (Chapter 2). The total analysis time per sample was 30 minutes. The actual column selection was performed by timer controlled valves. Upon sample injection, the columns are connected in series for 1.5 minutes, then the Molecular Sieve column is bypassed, and the Porapak Q column is purged for 11 minutes. During that time interval carbon dioxide, ethylene, ethane and water are desorbed from the column. The next event is reconnection of both columns in series when oxygen, nitrogen, methane and carbon monoxide are desorbed from Molecular Sieve column.

Initially there was a problem with the product gas concentration being too low to conveniently measure, given the large nitrogen purge through the system. In order to increase the concentration of volatile products from the sample surface, a small chamber was constructed with a free volume of 20 ml in front of the sample, with a quartz window on the front and with an aluminum foil seal on the back (see Figure 3.10). This chamber was continuously purged by a flow induced by attaching the outlet of the small chamber to a small vacuum pump. This resulted in a flowrate of 10 ml/min. The source of the purging gas was the simulated fire apparatus, which itself was purged by the usual flowrate of 15 l/min of nitrogen.

The gas was sampled by suddenly opening the small chamber to a previously evacuated 20 ml sample volume. The gas first passed through a tar trap. The tar trap was made from a 20 ml test tube, densely packed with, particle free, quartz wool. It was kept in a water-ice bath during an experiment. At the time of sampling, the sample flowrate through the chamber and sampling line was 200 ml/min. Such a high flow rate at the time of tube filling provided a representative sample of gas released at the surface of a pyrolyzing sample. Seven test tubes were filled with gas at different times during a run. When all seven tubes

were filled, the gases were analyzed by gas chromatography. An obvious disadvantage of this technique is that the data from the analyses are relative rather than absolute concentrations at a certain time during a run. The reason for that is the high flowrate through the chamber at the time of tube filling. That means that the gas withdrawn from the chamber was not just gas released by the pyrolyzing sample, but a mixture of pyrolysis gases and nitrogen that was pulled from the chamber surroundings.

A typical chromatogram is represented in Figure 3.11. Unfortunately, as can be seen from the chromatogram, methane desorption often started before the desorption of nitrogen was over. This was due to the enormously high concentration of nitrogen, the purging gas. Attempts were made to overcome this problem. The helium carrier gas in the gas chromatograph was replaced by nitrogen. The idea was to eliminate the nitrogen peak from the chromatograms. Of course, this occurred, except that all the other peaks disappeared as well due to the large decrease in sensitivity. Finally, helium could have been used as a purge gas in the simulated fire apparatus, but that would have changed the convective losses from the sample surface, due to the higher thermal conductivity of helium, and that situation would not be as representative of actual fire behavior. For all these reasons, the gas analyses were performed as noted above with the deficiency that the amounts of methane could not be precisely determined. However, the data are useful from the point of view of comparison methane concentrations. It is also noted that methane was not a major product in any case.

Reproducibility of gas analyses was checked in a similar way as temperature measurement reproducibility -- by duplication of experiments. Gas analyses were performed in different experiments, but the sampling times were shifted, so the resulting analyses, given here are a result of, usually, four different experiments, performed with four different samples of the same density and thickness. It was found that the water analyses were completely

unreproducible, probably due to the variable efficiency of the tar trap with respect to water. Tar, due to the high content of hydroxyl groups, has a high affinity towards water and it is possible that, during the same experiment, tar was adsorbing and desorbing water in an unpredictable fashion.

3.2.7 MASS BALANCE

An attempt was made to close the mass balance. This involved use of another tar and gas collection system (separate from that just described). For this purpose, a new tar trap was designed. The trap was made in such a way as to provide as efficient as possible tar trapping at a flowrate of about 2 l/min. It consisted of a cotton gauze placed in a cooled (0°C) part of the trap, followed by a filter at room temperature, placed at the exit of the trap, inside of an Ultratorr™ fitting (5 mm in diameter and 8 mm long). The efficiency of the trap was judged based on the visual appearance of the room temperature filter. If the filter retained its original color for more than a half of its length, trapping was considered sufficient. After passing through the tar trap, the gases in this series of experiments were collected in an initially evacuated large vessel of about 120 l in volume. The actual duration of the collection was the same as the duration of heating by the radiative heaters. The tar trap was weighed before and after collection, and the gases from the large collection vessel were analyzed by gas chromatography. This technique provided absolute amounts of the tars and gases collected, since all products were collected. In fact, however, only a fraction of the total purge gas flow could be sampled, so even this technique did not give a truly "absolute" collection. The amounts of volatile products collected were scaled, since the volatile products represent the mass of the original material less the char produced. The results are presented in section 5.7.

3.2.8 HEAT FLUX MEASUREMENT

The incident heat flux was measured by positioning a factory calibrated, water cooled, fluxmeter in place of a sample. These measurements were done at several settings of a variable transformer that controls the voltage applied to the radiative heaters.

It was noted that the gaseous pyrolysis products might intercept a portion of the radiation from the radiative heaters. The variation in the net heat flux as a function of purge gas flow rate was first addressed qualitatively; namely, by comparison of the pyrometer signals for different flow rates of purge gas. In addition to this qualitative approach, an attempt was made to quantify the differences by direct measurement of the heat flux reaching the surface by positioning the fluxmeter in the center of a large (63 mm in diameter) sample. Results are given below.

3.3 HEATED WIRE MESH, TGA AND DSC STUDIES

Studies performed in the simulated fire apparatus (Chapter 3.2) are characterized by the existence of temperature gradients in the sample. There was a need to examine the possible differences between pyrolytic behavior of cellulose in the simulated fire apparatus and in laboratory equipment with better temperature control. The usual laboratory equipment used here involved a heated wire mesh reactor, a thermogravimetric analyzer (TGA) and a differential scanning calorimeter (DSC). The advantage of the usual laboratory equipment is well prescribed heating rate, without temperature gradients within a sample. However, it is questionable how representative the data from such measurements is of an actual fire situation. It was this concern that motivated the work in the first place. Thus such measurements were always referenced to conditions defined in the simulated fire apparatus.

3.4.1 SAMPLES

In general, it can be said that the samples used in devices with the better controlled temperature environments were at least an order of magnitude smaller than those used in the simulated fire apparatus.

Cellulose samples used in a heated wire mesh reactor were pressed in a "standard" procedure, described in Chapter 3.2.1, but to a thickness of about 2 mm. The density of two thin cellulose pellets were 0.902 g/cm^3 and 0.960 g/cm^3, respectively. Those samples were than cut to strips of 20 mm length and different widths, from 1 mm to 23 mm; which means that two sample dimensions were fixed to 2 mm and 20 mm, respectively.

Cellulose samples used in a TGA and in a DSC were of two different kinds. Some samples were cut out of "standard" cellulose samples in such a manner as to preserve the bulk nature of the sample, with the original pressing density. For a TGA they were cut to cubes of 3x3x3 mm and for a DSC to 3x3x1 mm. These samples served a purpose of deliberately introducing a transport limitation. The other type of samples consisted of powdered cellulose samples (as received CF-11 powder, described in Chapter 3.1); a form normally used in thermal analyses.

Tar samples used for evaporation studies were obtained by washing the top plates of the simulated fire apparatus, followed by solvent evaporation. It can be argued that those tar samples represent averaged tar samples, with questionable temperature history, but they were representative of real tar products.

3.3.2 HEATED WIRE MESH REACTOR

The details of this particular apparatus are given elsewhere (92) and, since it did not represent the major focus of this work it will only be briefly described here. Samples are heated in a folded stainless steel wire gauze, stretched between two massive brass electrodes. The wire gauze temperature is monitored by a fine gauge thermocouple, embedded between the folds. The environment around the mesh is essentially at room temperature, which provides quick quenching of escaping volatiles from a pyrolyzing sample. The atmosphere used here was helium and the heating rate was 60°C/min. Gas analyses were not performed.

3.3.3 THERMOGRAVIMETRIC ANALYSIS (TGA)

The instrument used here was a standard TGA apparatus. Since it is well known that temperature measurement can represent a problem in a TGA the temperature profile was first checked in the vicinity of the sample pan. It was found that, in the temperature range of interest here, the furnace (controlling) temperature does not deviate more than ±3°C from setpoint, which was considered to be satisfactory. Although the mass calibration was done using a calibrated mass, it was not sufficient, since the balance mechanism had to be checked at elevated temperatures of interest. For that purpose, another check was made with the known mass loss of calcium oxalate, when scanned at a prescribed heating rate and with prescribed flowrate of inert gas through the sample tube. Overall mass loss was within ±5% from the theoretical, which was considered sufficiently accurate.

Cellulose pyrolysis under prescribed pyrolysis conditions, proceeds within a fairly narrow temperature range. Typically the majority of the mass loss occurs over a temperature range on the order of 50°C. Pyrolysis is a process with a heat effect. That means that the actual

sample temperature might be different from the furnace (and recorded) temperature. In order to record the proper sample temperature in this work there were, at least, two different experiments done for each sample. The first one was for actual mass recording and the other one for temperature calibration. A sample temperature was recorded by actually inserting another thermocouple into a sample, while maintaining the same control as in the mass recording. The extra thermocouple unambiguously recorded sample temperature. The two results were combined and these are represented here.

Three different sets of experiment were done in the TGA. The first was a determination of initial sample density effect, with 3x3x3 mm and 5x5x5 mm cubes used as samples. These experiments were not temperature corrected. The other two sets were done with cellulose powder, one in an open sample pan, with diameter of 10 mm and sample height of 1 mm, and the other in a standard DSC aluminum pan, for comparison on the same basis with DSC data.

The system was purged with nitrogen at a flowrate of 50 ml/min. The heating rates employed were 0.1, 1, 6, 15 and 60°C/min. The latter three heating rates were chosen to mimic the situation at the back face, middle of the sample and front surface of a high density sample undergoing pyrolysis in the simulated fire apparatus, under an incident heat flux of 40 kW/m^2.

3.3.4 DIFFERENTIAL SCANNING CALORIMETRY

Heat effects of cellulose pyrolysis were determined in a standard Differential Scanning Calorimeter (DSC). The DSC cell was calibrated at three different, well defined, melting point temperatures of indium, zinc (standard materials) and water. The melting point temperatures of these three materials cover the temperature range of interest.

The sample holders used were standard covered aluminum DSC pans, with a diameter of 6 mm and sample height of 1 mm. A typical sample had a mass of about 5 mg. To allow for the escape of volatile products of pyrolysis, a sample pan was closed, but not crimped on, and two or more pinholes were added on the top cover.

Similar to the TGA experiments, the DSC cell was continuously purged with nitrogen at a flowrate of 50 ml/min. The heating rates used were 1, 6, 15 and 60°C/min.

3.4 THERMAL PROPERTIES MEASUREMENTS

It was observed early in the study that the mathematical model of pyrolysis did not give results which were in good agreement with the experimental findings. Therefore it was necessary to make measurements of the thermal properties to be used in the modeling work to establish whether the failure was due to poor property values or incorrect representation of the physics. Previously, the thermal properties were taken from property tables for materials similar to the pressed cellulose used in this work.

3.4.1 SAMPLES

Originally, there was an attempt to use the char generated in the simulated fire apparatus for property measurements. However, the problem with this approach was that the char from the cellulose sample pyrolyzed in the simulated fire apparatus had a high density gradient along the axis parallel to the incident radiative flux. Indeed, the first results from the measurements performed on the char from the cellulose sample pyrolyzed in the simulated fire apparatus gave very scattered data. In order to avoid measurements with poorly characterized char samples, two different char samples, with different uniform extents of pyrolysis, were prepared from the same initial material. For the measurement of the surface emissivity, the char generated in the simulated fire apparatus was used, since it is more representative of the actual material, insofar as the emissivity is concerned. In addition, since emissivity is a surface property, the density gradient would make no difference.

All of the samples used for measurements of radiative thermal properties were "standard" cellulose samples (as described in Chapter 3.2.1), with a pressing direction parallel to the incident radiative flux. Only high and middle density cellulose samples were used for these measurements. The low density sample could not be used due to the structural weakness.

The char samples for other thermal property measurements were generated by pyrolysis of the "standard" cellulose samples in a tube furnace under a helium purge. All the samples were 38 mm in diameter and around 20 mm in thickness. After the initial density of the cellulose samples was measured, they were cut to approximately 20x20x35 mm, since the inside diameter of the tube used for the furnace was 30 mm. The parameters for all pyrolysis treatments were the same: helium purge gas at a flowrate of 0.7 l/min and a heating rate of 15°/min (furnace limitation). The holding time at the final temperature was 2

hours. The final temperature was either 300°C or 600°C. These two different temperatures were chosen in attempt to have one final temperature below the starting point of the endotherm observed by differential scanning calorimetry (DSC), and one final temperature well above the end of the endotherm. Thermal decomposition certainly takes place at 300°C but at a significantly lower rate than at 600°C. The lower final temperature of pyrolysis results in incomplete pyrolysis of a cellulose sample, and with that, a higher char density and higher char yield.

3.4.2 SURFACE EMISSIVITY

The surface emissivity is of considerable importance for determination of the net heat flux available for conduction from the surface deeper into the sample. If it is less than unity, meaning non-zero reflectivity, the surface absorbs just a fraction of the incident radiation, but the re-radiation losses are also smaller. It was discovered in this work, with the help of mathematical modeling, that the surface emissivities had to differ from unity. Therefore, there was a need to characterize sample surface emissivity of both cellulose and char.

Two different approaches were used. The first was direct measurement by fluxmeter of the reflected heat flux from the sample surface, from which emissivity was deduced. The second was calculation of the surface emissivity from the measured temporal change of surface temperature and from the temperature profiles, by applying the heat conduction equation. The second approach is straightforward prior to pyrolysis, as long as care is exercised to perform calculations when heat effects on the surface (e.g., water evaporation or pyrolysis) are negligible. However, when the front part of the sample is completely pyrolyzed, the second approach is not that straightforward. A cellulose sample shrinks during pyrolysis, with the actual amount of shrinkage depending on the extent of pyrolysis,

as noted above. For this reason, the positions of the thermocouples within the sample are uncertain and, therefore, the calculation becomes problematic. Thus the calculations were performed for the pre-pyrolysis period only.

3.4.3 THERMAL DIFFUSIVITY

Thermal diffusivity can be viewed as a material property that determines how fast a thermal wave can penetrate into the material. It can be determined by imposing a quasiequilibrium perturbation at a point in the material and measuring the time lag as the perturbation propagates in the material. The idea applied here was to make use of, one might say, poor surface temperature control of a standard laboratory hot plate. The hot plate control works on an ON/OFF basis and, therefore, results in a periodic surface temperature. This periodic temperature is imposed on the surface of a sample whose thermal diffusivity is to be measured. The disadvantage of this technique is that the period of the oscillations is quite long, which makes the technique rather time consuming, unless the hot plate is controlled with a separate controller.

The thermal diffusivity measurements of cellulose and char samples were performed at three different temperatures in order to deduce the temperature dependence of thermal diffusivity. The actual range of temperatures was a function of the sample itself. In other words, for cellulose samples the temperature had to be low enough to avoid possible pyrolysis of the material at the surface which is in contact with the hot plate. Usually the surface of the hot plate was kept under 240°C. The pyrolysis problem was not an issue for the char samples. However, in some of the early experiments a "runaway" combustion condition was achieved due to the high reactivity of char, and exothermic reaction in the sample interior. After that, all of the char samples were covered by a glass bell which was

purged by a nitrogen stream in order to avoid possible interference from reactions with oxygen.

The actual sample was composed of two similar samples placed on the top of each other in order to increase the total sample thickness. Temperatures were measured with six thermocouples, two of which had a diameter of 0.25 mm and were placed between the sample and the hot place surface and between the two similar samples, respectively. The other four thermocouples, which had a diameter of 0.5 mm, were positioned in the sample interior at different distances from the heated surface. The actual distance from the heated surface varied, but care was taken that the thermocouples be equidistantly positioned from each other. This provided a good measurement of the sample temperature profile. The data were collected by the same data acquisition system used for the simulated fire apparatus (Chapter 3.2.4).

3.4.4 HEAT CAPACITY

Heat capacity was determined in a DSC. In addition to temperature calibration, described above, the cell calibration was done by scanning a sapphire standard sample from room temperature to 580°C, at a heating rate of 10°C/min under a nitrogen purge.

The samples used for DSC were taken from the same samples that were used for the thermal diffusivity determination. The samples were cut out from the large char samples and pulverized. All samples were handled in air so there was a possibility of moisture and/or gas adsorption on the surface of the samples. All samples were run under identical conditions in the DSC. These conditions were: equilibration at 30°C for 5 minutes; heating at 15°/min (the same heating rate as for pyrolysis) to 580°C for samples pyrolyzed at 600°C, and 320°C for samples pyrolyzed at 300°C; cooling to room temperature; and repeating the

procedure for another scan, from which the heat capacities were calculated. The DSC cell was continuously purged with nitrogen and the cell exterior was cooled by a flow of air.

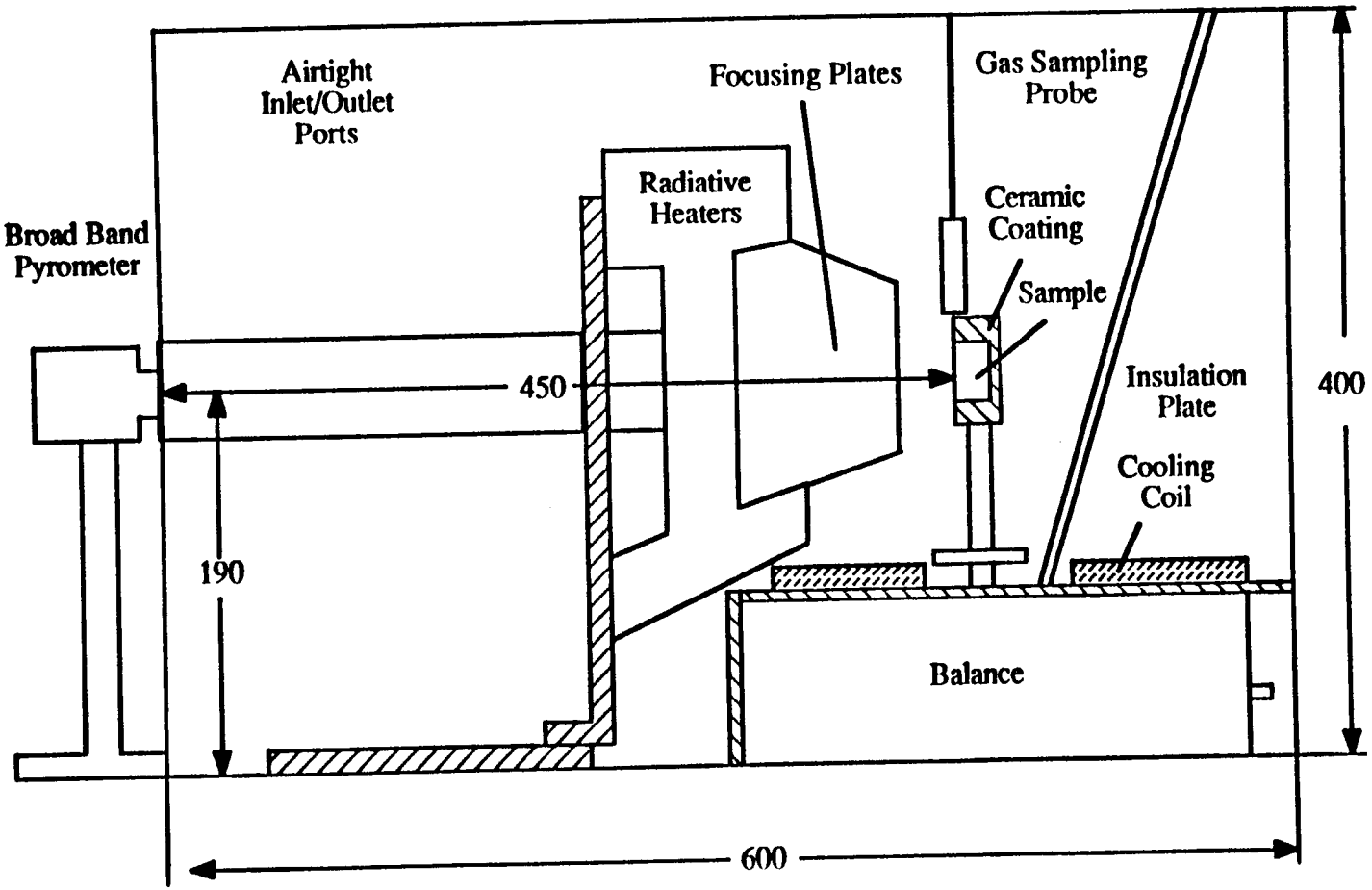

Figure 3.1 Simulated fire apparatus (all dimensions in millimeters)

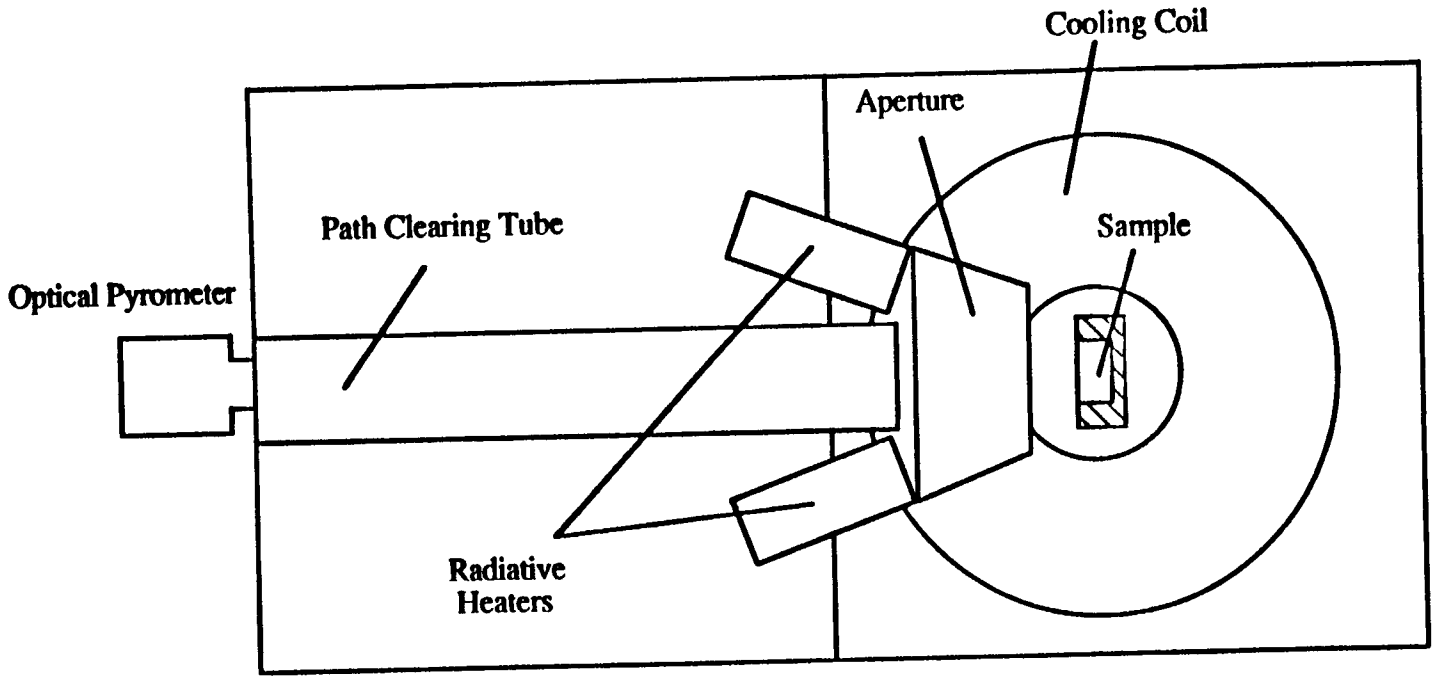

Figure 3.2a Top view of simulated fire apparatus (all dimensions in millimeters)

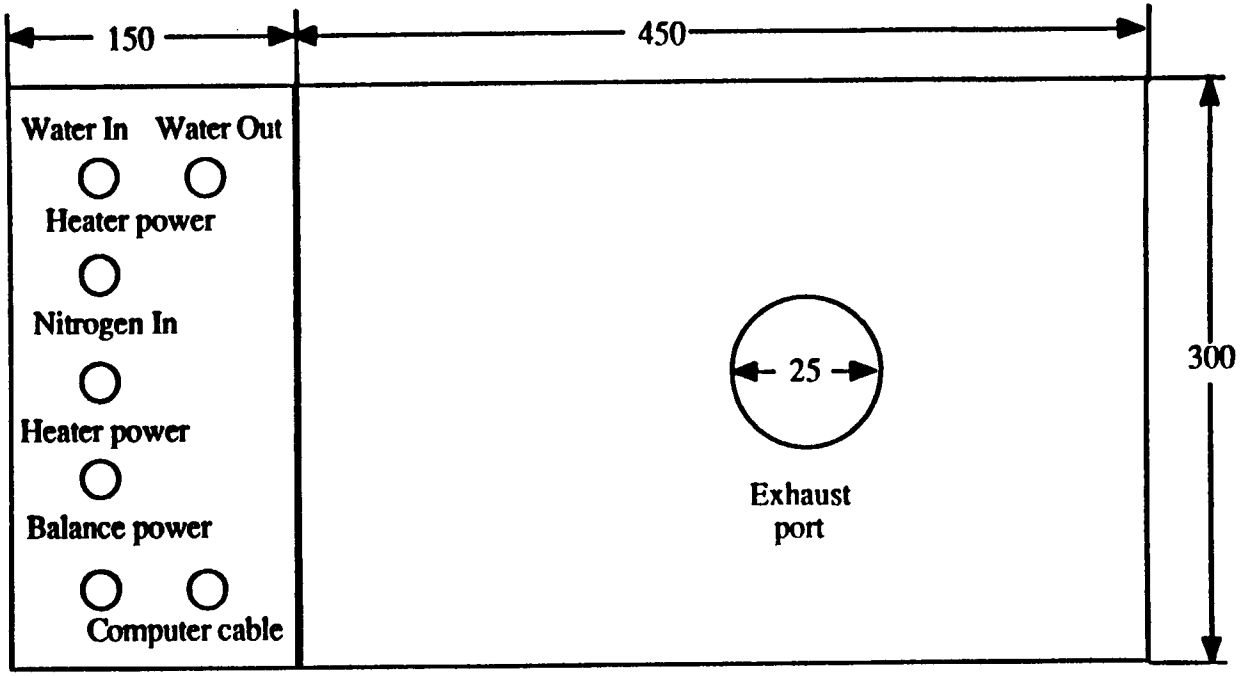

Figure 3.2b Cover plates for simulated fire apparatus (all dimensions in millimeters)

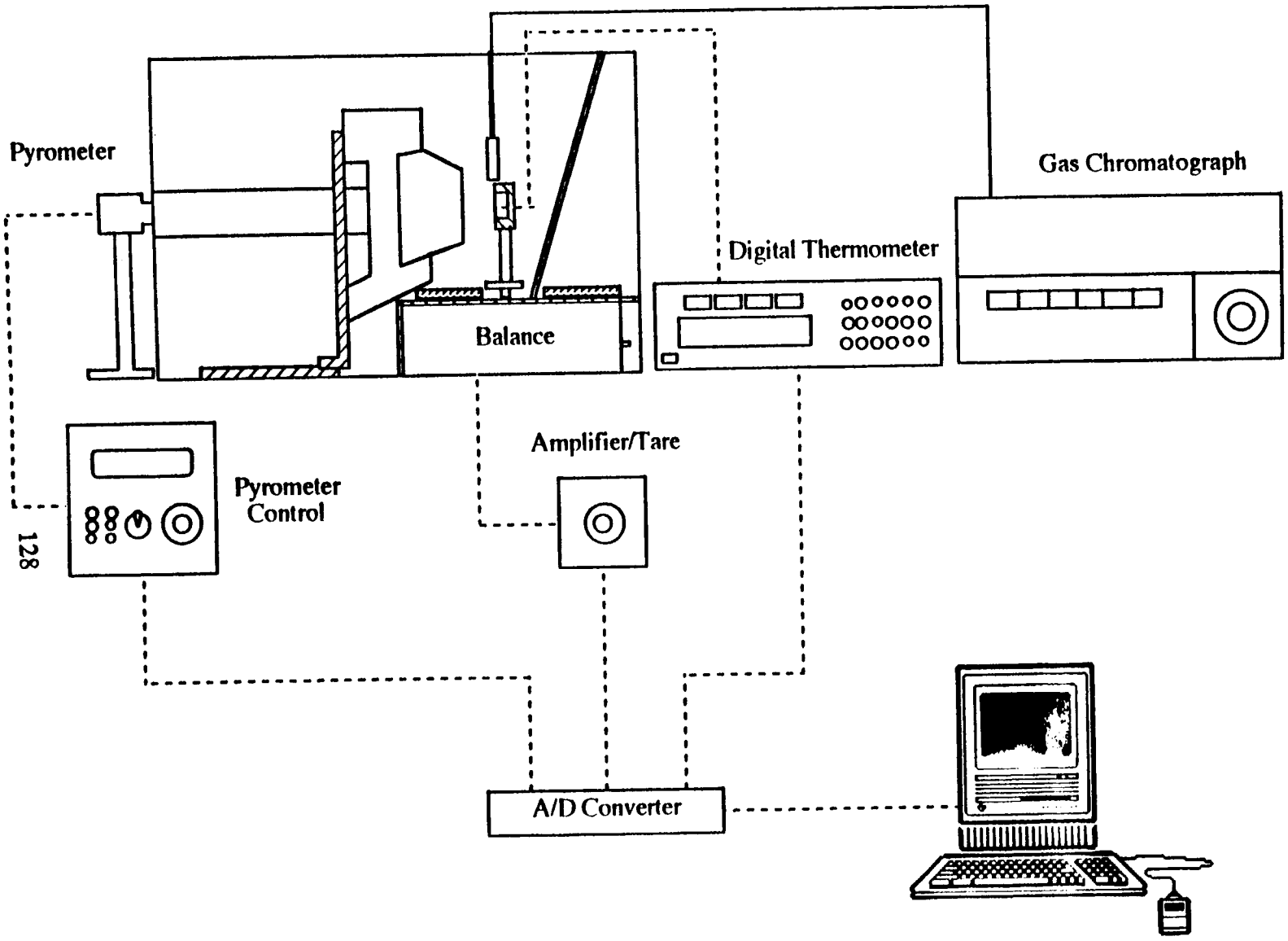

Figure 3.3 Arrangement of the simulated fire apparatus with control and measurement system

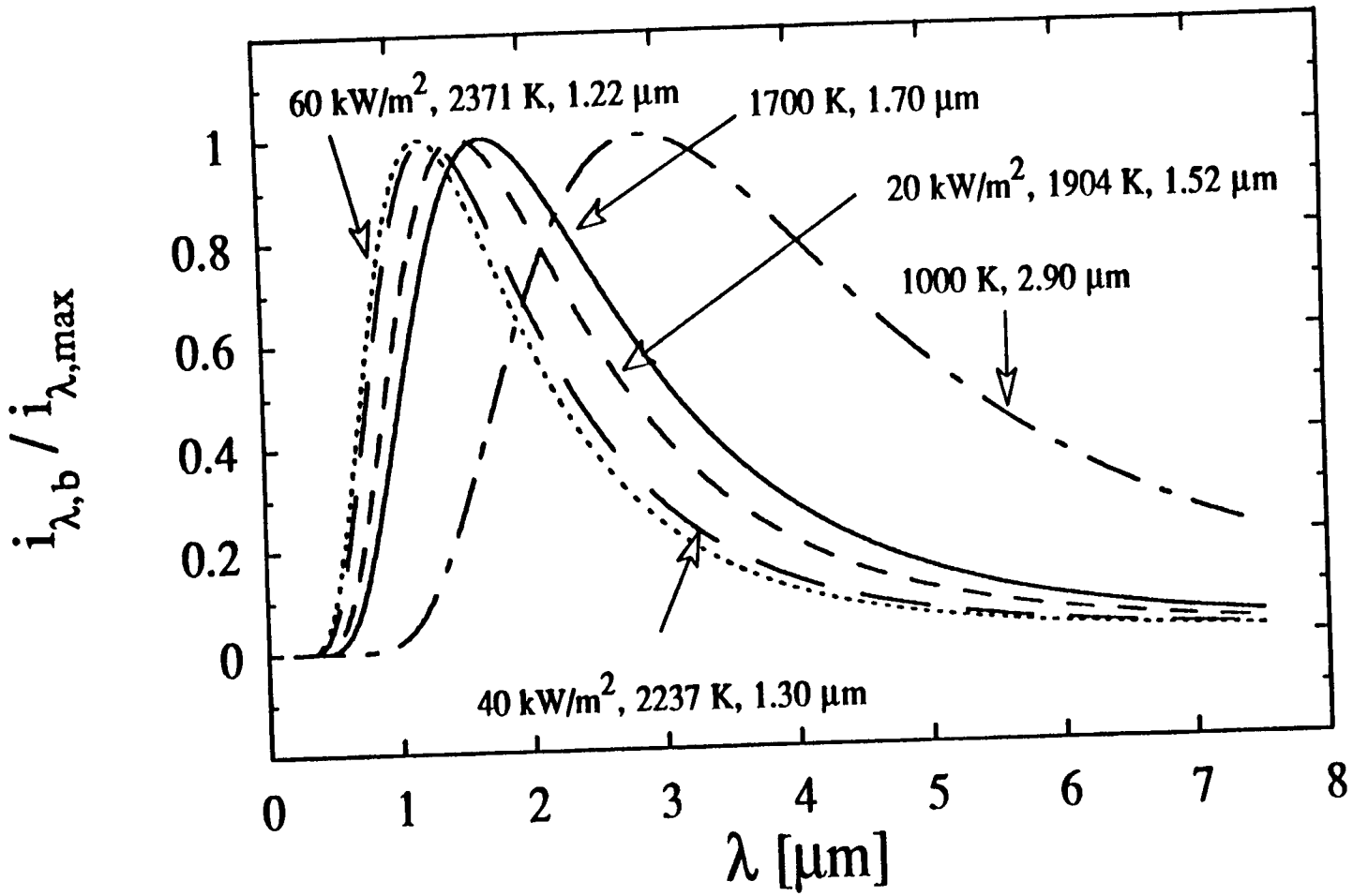

Figure 3.4 Radiation spectra and filament temperature at three heat fluxes and the wavelength at maximum intensity of radiation. Also shown are spectra for blackbody radiation of a flame (1700 K) and a body with temperature of 1000 K

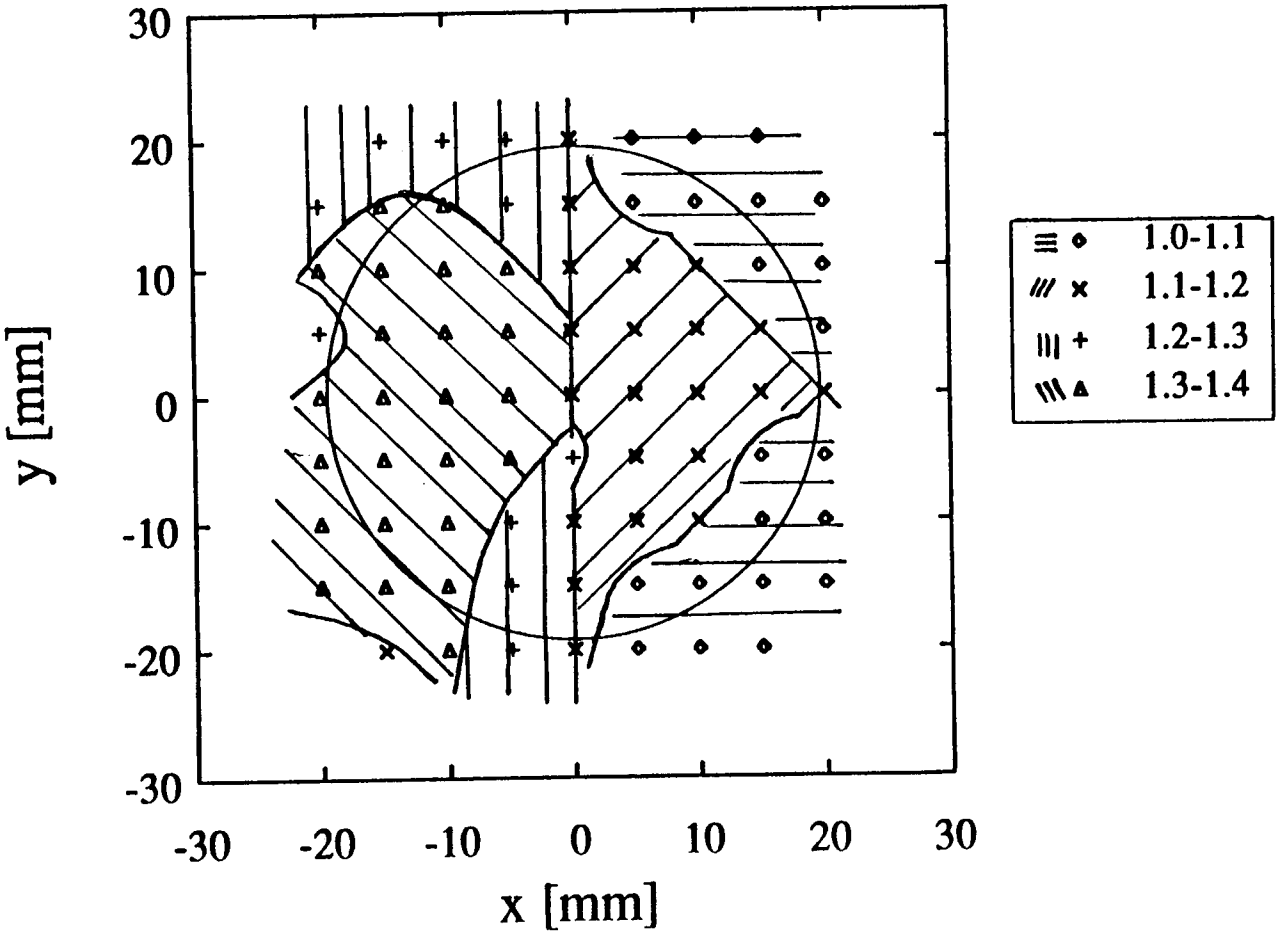

Figure 3.5 Relative incident heat flux (1 represents a 100% of nominal heat flux) at different points of the 38 mm sample (circle)

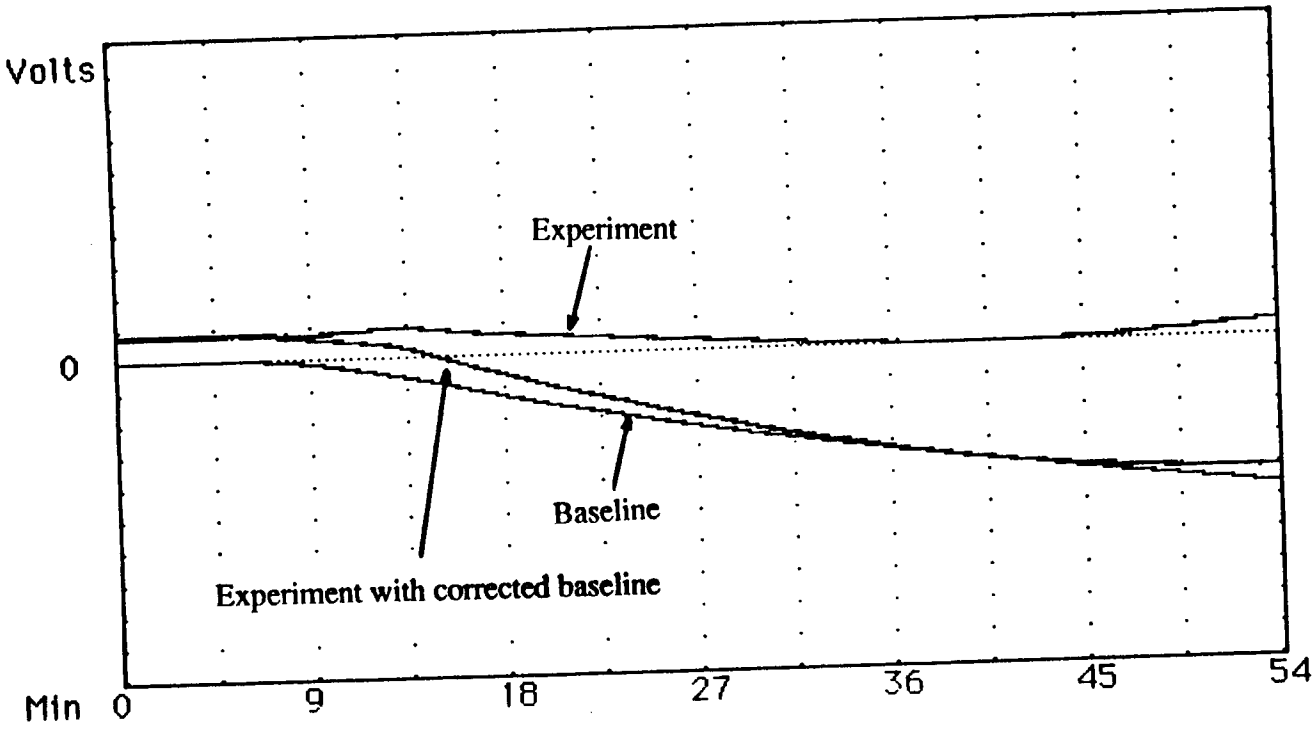

Figure 3.6 Raw mass data (arbitrary zero) as a function of time. Also shown are baseline drift and corrected mass data for the baseline drift (baseline subtracted from the raw data)

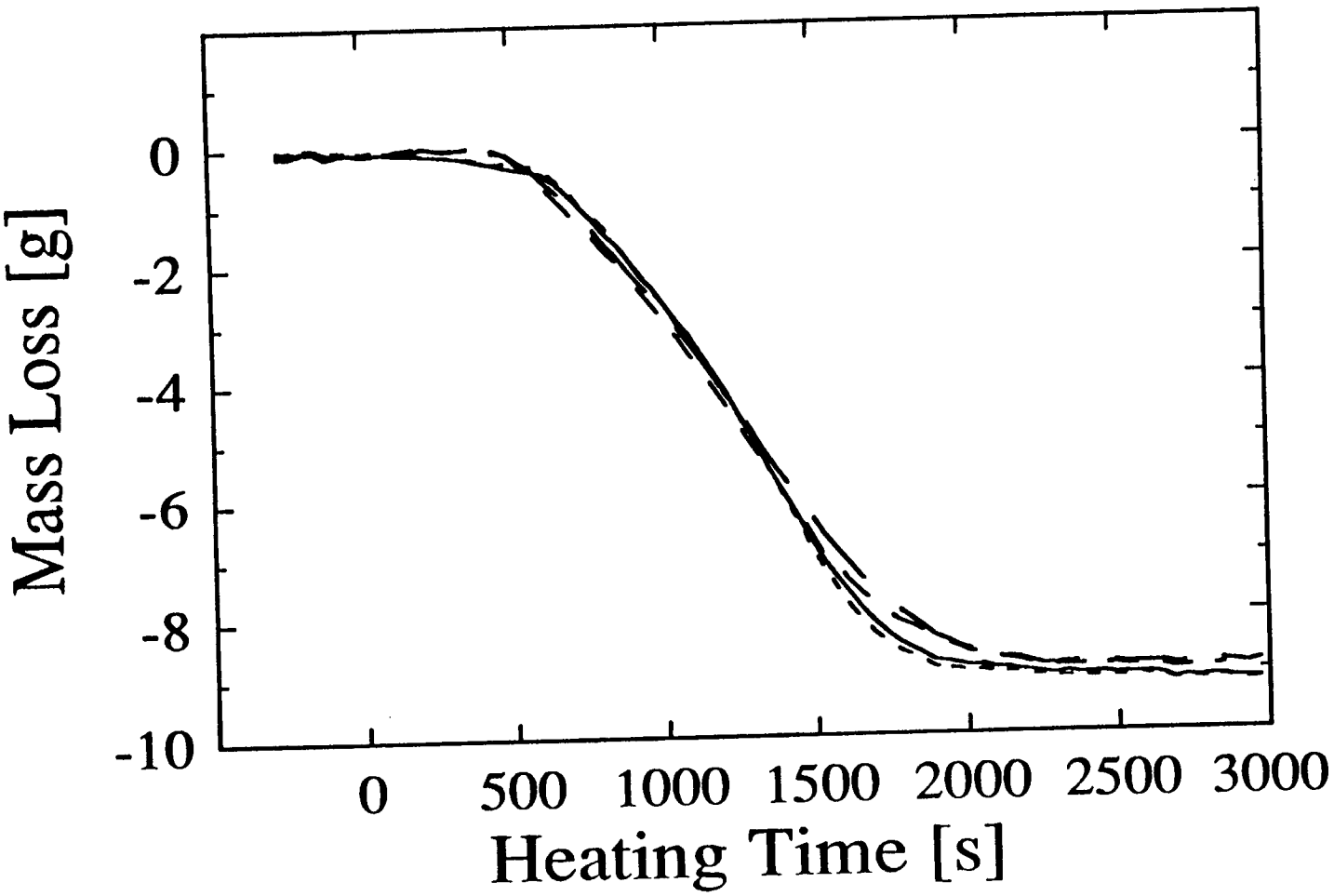

Figure 3.7a Mass loss as a function of time for four high density (0.965 g/cm^3) samples. The imposed heat flux was 40 kW/m^2

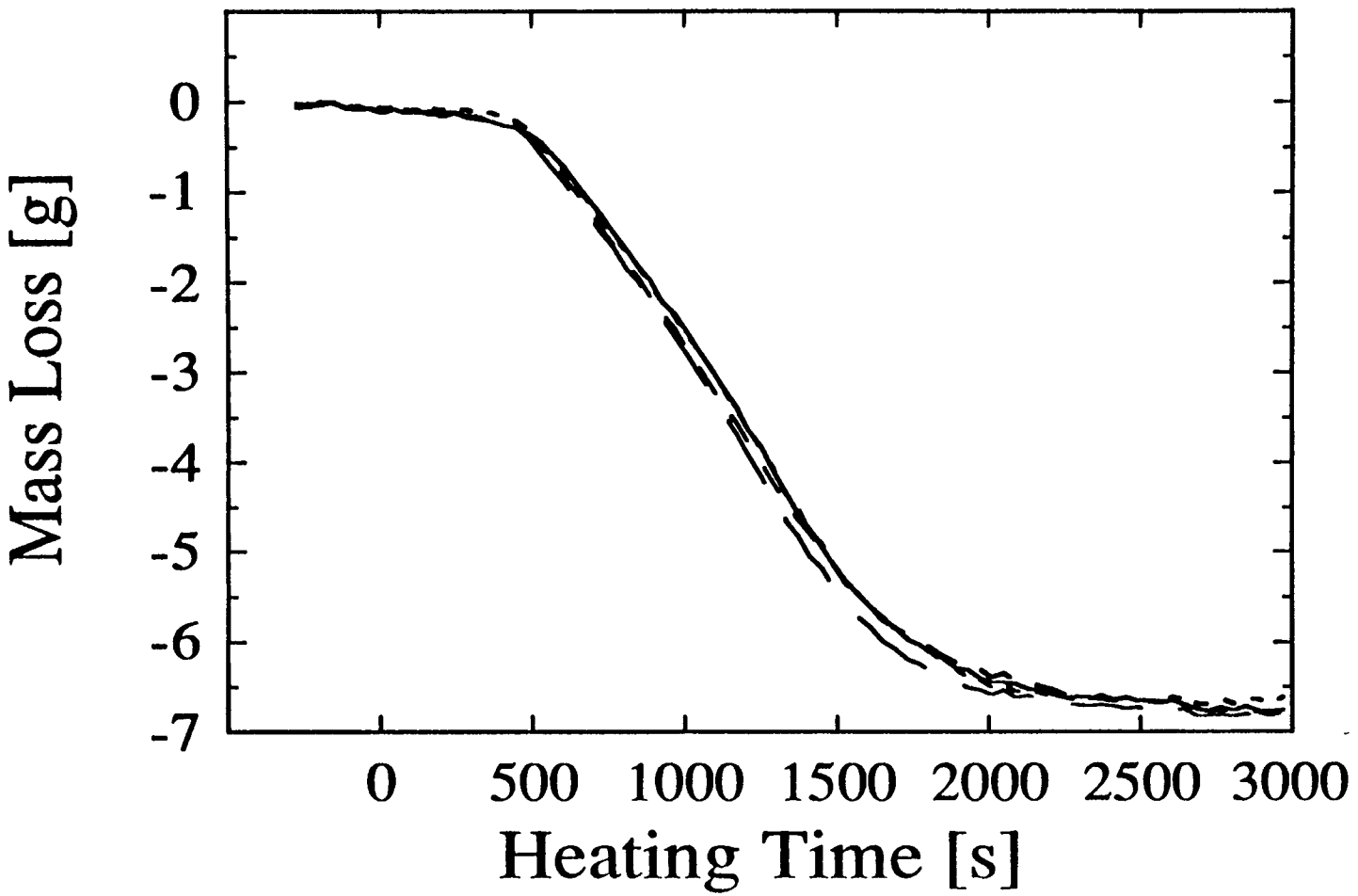

Figure 3.7b Mass loss as a function of time for four medium density (0.691 g/cm^3) samples. The imposed heat flux was 40 kW/m^2

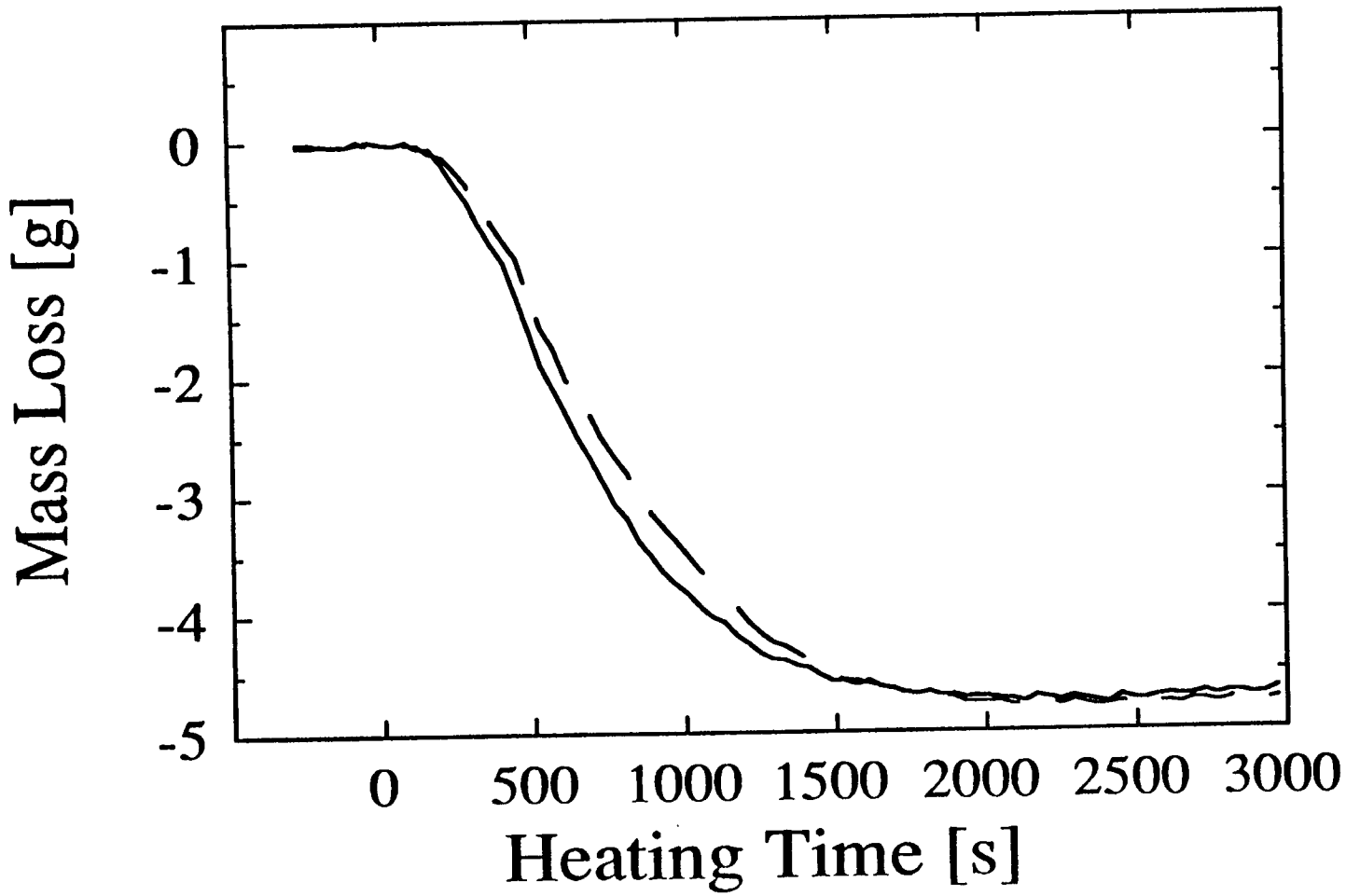

Figure 3.7c Mass loss as a function of time for two low density (0.458 g/cm^3) samples. The imposed heat flux was 40 kW/m^2

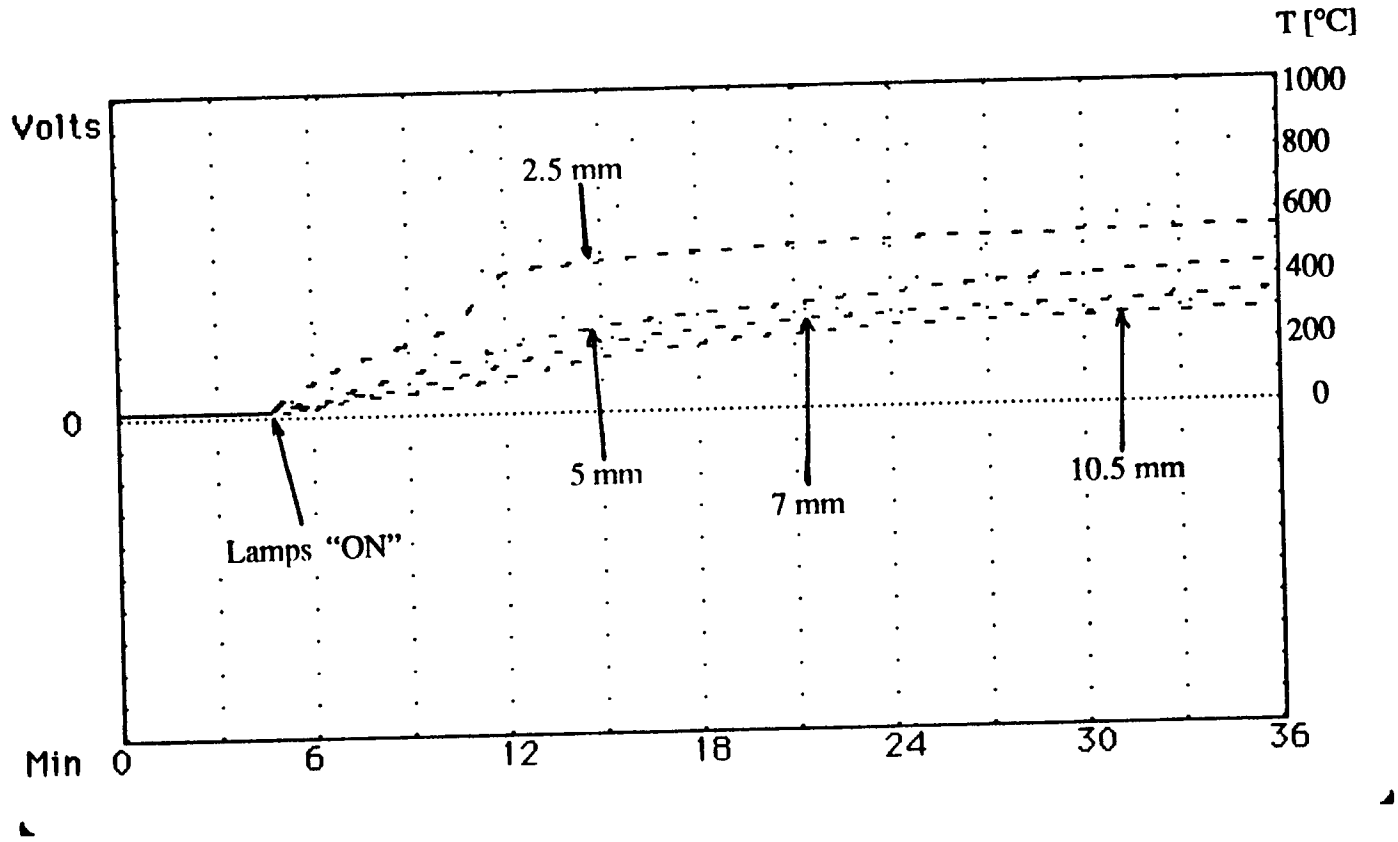

Figure 3.8 Raw temperature data as a function of time and different distances from the front surface

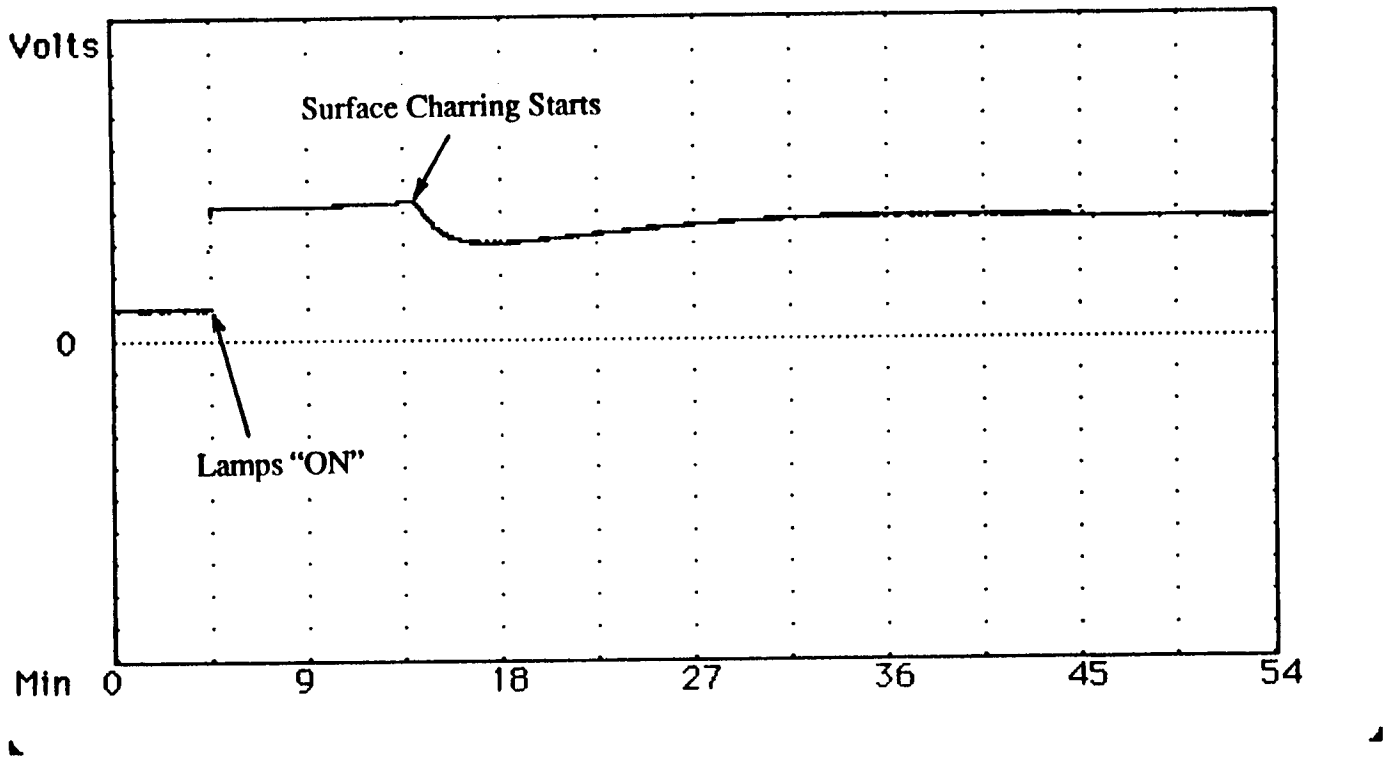

Figure 3.9 Raw optical pyrometer signal as a function of time

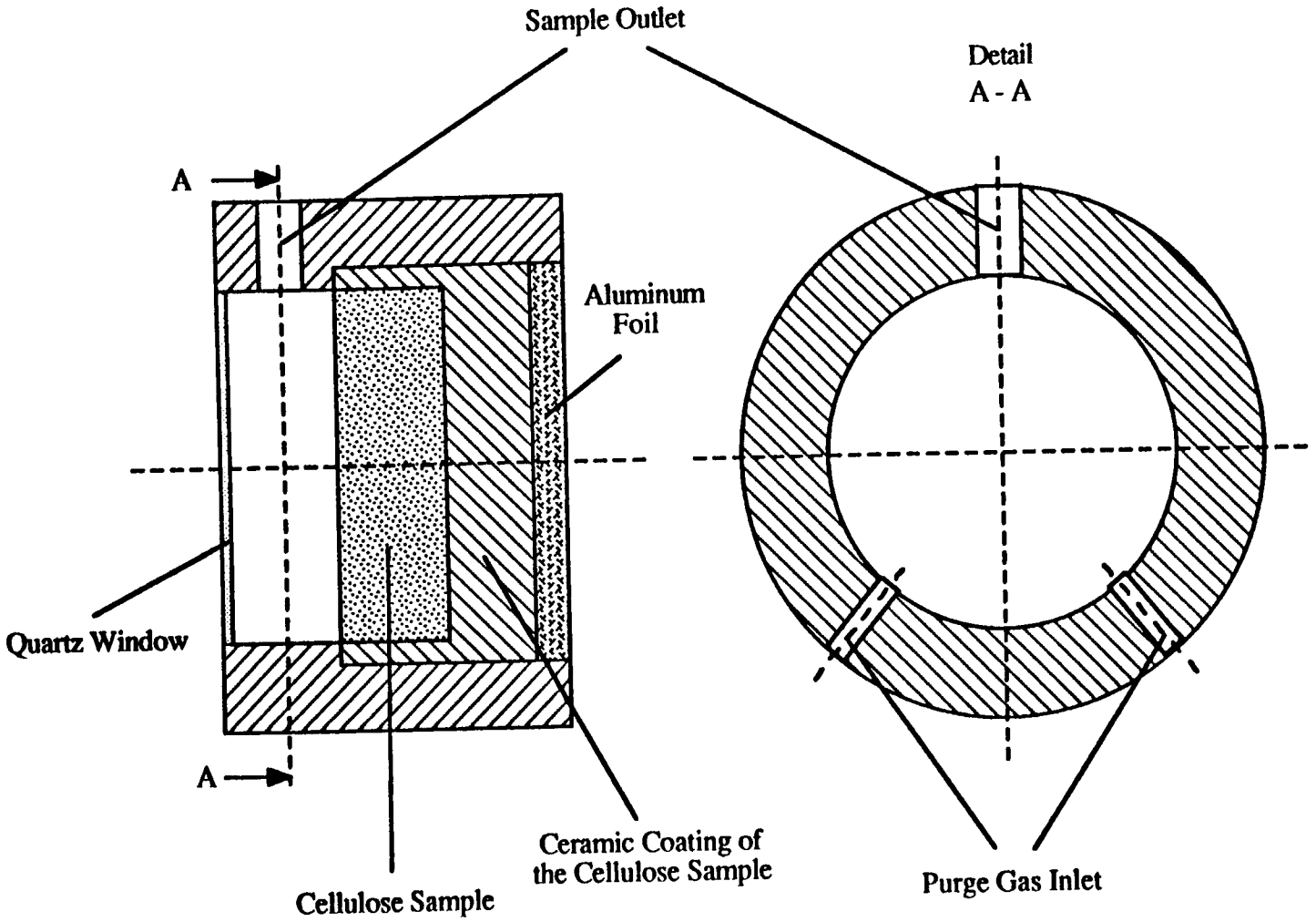

Figure 3.10 Small chamber, used for gas analyses

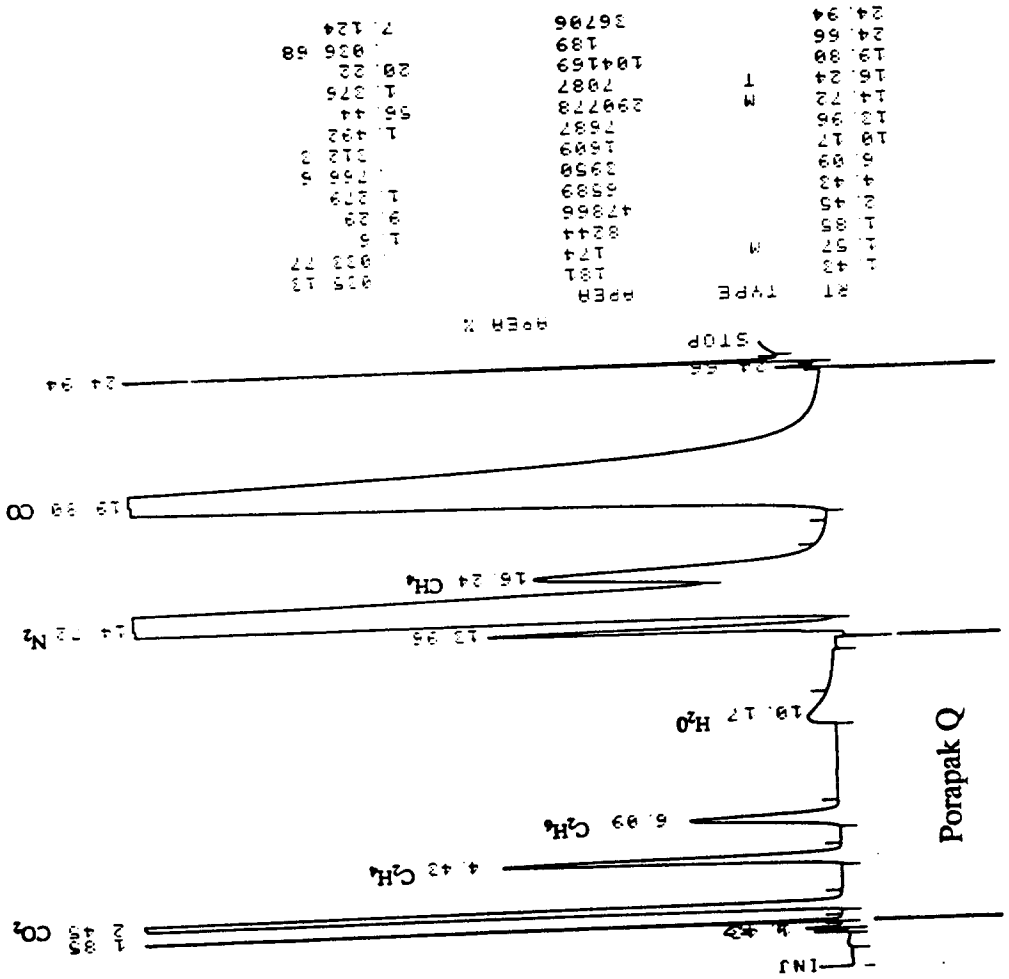

Figure 3.11 Sample chromatogram from analysis of dry tar-free products of pyrolysis (attenuation x16). Note that the methane peak is on the trailing part of the nitrogen peak

4. THERMAL PROPERTIES

Thermal properties represent an important part of this work. Analyses to be presented in subsequent chapters largely depend on the knowledge of thermal properties. That is the reason that this chapter precedes all other chapters in which actual pyrolysis data are discussed.

The thermal properties that were measured, for both cellulose and char, were the heat capacity, the thermal diffusivity and the surface emissivity. The thermal conductivity was calculated from the thermal diffusivity and heat capacity data, using also density measured in a usual manner (by dividing a sample mass by its volume). Hence, the thermal conductivity was determined by an indirect method, while the rest of the properties were measured.

4.1 HEAT CAPACITY

The definition of the heat capacity is:

$$C_p = \left(\frac{\partial H}{\partial T}\right)_p \tag{4.1}$$

Under constant pressure experimental conditions, the enthalpy change is equal to the heat addition to a system. Thus the heat capacity can be expressed in terms of measured DSC quantities as:

$$C_p = \frac{1}{m}\frac{\dot{q}}{\beta} \tag{4.2}$$

where:

C_p - heat capacity [J/g-K]

m - sample mass at a temperature at which the heat capacity is to be determined [mg]. If there is no mass loss during the determination of the heat capacity, it is the initial sample mass in a DSC pan.

$\dot{q}$ - the heat flow into the DSC pan that includes a sample [mW]

β - heating rate [K/s]

The heat capacity of the empty sample holder itself is subtracted from the actual measured value. The heat capacity is represented by the instantaneous slope of the DSC curve. Figure 4.1 depicts a typical DSC curve for cellulose with the contribution of the sample pan subtracted. The temperature range of interest for determining cellulose heat capacity is from about 185°C, where the endotherm due to water evaporation ends, up to the onset of pyrolysis, which is, from Figure 4.1, about 330°C. Outside this range, enthalpy change with temperature is dominated by latent heat and reaction enthalpy changes. Cellulose samples were scanned only once. Of course, a second scan could have been used for heat capacity determinations between 50°C and 185°C, since the sample would then have been moisture free. The reason that such a procedure was not followed is because there is enough evidence in the literature that cellulose begins to decompose at very low temperatures, and that cellulose can be changed by exposure to an elevated temperature, even as low as 100°C. Thus the most useful part of a DSC curve is between 185°C and 330°C. This portion of the curve can be linearized; the resultant regression equation is presented in Figure 4.1. The expression represents raw cellulose heat capacity, valid over the temperature range of 185°C to 330°C. There was little incentive to develop an equation for a lower temperature range, since, again, the enthalpy change in that region will depend more upon the moisture content of the raw sample.

Figures 4.2a, 4.2b, 4.2c and 4.2d show DSC traces for cellulose chars, that were used for determination of the char heat capacities. All of the data presented in Figures 4.2 were taken from the second scans of what were chars prepared in a different apparatus. Thus the first scan involved loss of sorbed species, created by handling in air. As noted earlier, two chars were studied -- one prepared at 300°C, and the other at 600°C. After the second scan was completed, the samples were weighed and that final mass was used for determination of heat capacities. The raw data in Figures 4.2 are shown in absolute units; i.e. the data were not normalized with respect to the initial sample mass in order to avoid incorrect normalization due to the different initial water and adsorbed gas contents of the samples. The data were fit with an expression of a similar form to that used for graphite heat capacity, taken from Perry's Chemical Engineers' Handbook (137). The reasoning was that the two materials, cellulose char and graphite, roughly belong to the same family of materials. Cellulose char can be converted to graphite, upon heating to very high temperatures, in excess of 2000°C. The "best fit" equations are presented in Figures 4.2. These expressions are valid over the temperature range between 50°C and 300°C, for the chars pyrolyzed at 300°C, and between 50°C and 550°C, for the chars pyrolyzed at 600°C.

The temperature dependencies of heat capacities of cellulose and the chars prepared at different pyrolysis temperatures are summarized in Figure 4.3. Also shown in Figure 4.3 are data taken from Perry's Handbook for cellulose, wood charcoal and graphite. Although the values for cellulose heat capacity from the measurements reported here and from Perry's appear to be in a similar range, there is a significant discrepancy (about 30%) between the two. It should be noted that the temperature range of validity is not stated in Perry's and it was assumed here that the value is given for 20°C. The discrepancy between Perry's value for wood charcoal (again assumed to be given for 20°C) and cellulose chars

heat capacities is smaller, about 13%.

Heat capacity is an intensive property and thus one would expect that it should not depend on density (at least when the total heat capacity of included gases is not significant in comparison to the heat capacity of the solid). Nevertheless, it can be seen from Figure 4.3 that the char heat capacities do not show a clear trend with heat treatment temperature, nor with the initial cellulose sample density. It can be seen that the agreement among different chars is quite good, and the char heat capacity can be viewed as independent of heat treatment temperature or initial sample density. The results of the best regression through all data points, irrespective of char, is also shown in Figure 4.3. The equation for that regression is presented in Table 4.1, which is a summary of all thermal properties measured in this work.

4.2 THERMAL DIFFUSIVITY

The experiments used for determining thermal diffusivity were described in section 3. Again, the experiment involved imposing a periodic temperature at the surface of a sample and measuring propagation of the thermal wave in the sample. Figures 4.4a and 4.4b show temperature traces for a raw cellulose sample of density 0.691 g/cm^3 and a char produced from a cellulose sample of initial density 0.691 g/cm^3, respectively. The char was pyrolyzed at 300°C, and had a char density of 0.33 g/cm^3. It should be noted that the data from Figure 4.4a or Figure 4.4b were used for obtaining just one value of thermal diffusivity at an average temperature. The data for all the other samples look similar.

The mathematical expression used for analyzing the data shown in Figures 4.4a and 4.4b is given by Carslaw and Jaeger (34). The expression is for the temperature profile as a function of time within the solid bounded by two planes where one plane is subjected to

periodic temperature and the other is fixed at "zero" temperature (i.e., a constant reference temperature). If the periodic variation of a plane temperature is of the form:

$$\sum_{m=1}^{\infty} a_m \sin (m \omega t + \varepsilon_m) \tag{4.3}$$

(in this case the first summation term, for m=1, describes the oscillatory part; the second summation term, for m=2, was used impose a step change from zero at time zero to the baseline temperature during the oscillations, during the "off" cycle. This means that here a_2=const, $\sin (2 \omega t + \varepsilon_2) = 1$ and a_i=0 for i=3,4,...). The solution to the heat conduction equation takes the following form:

$$\theta = \sum_{m=1}^{\infty} a_m A_m \sin (m \omega t + \varepsilon_m + \phi_m) + 2 \pi \kappa \sum_{n=1}^{\infty} \frac{n (-1)^n (\kappa n^2 \pi^2 \sin \varepsilon - \omega l^2 \cos \varepsilon)}{\kappa^2 n^4 \pi^4 + \omega^2 l^4} \sin \frac{n \pi x}{l} \exp\left(- \frac{\kappa n^2 \pi^2 t}{l^2} \right) \tag{4.4}$$

where:

$$A_m = \left| \frac{\sinh \omega'_m x (1 + i)}{\sinh \omega'_m l (1 + i)} \right| = \left\{ \frac{\cosh 2 \omega'_m x - \cos 2 \omega'_m x}{\cosh 2 \omega'_m l - \cos 2 \omega'_m l} \right\}^{1/2} \tag{4.5}$$

$$\phi_m = \arg \left\{ \frac{\sinh \omega'_m x (1 + i)}{\sinh \omega'_m l (1 + i)} \right\} \tag{4.6}$$

$$\omega_m' = \left(\frac{m \omega}{2 \kappa} \right)^{1/2} \tag{4.7}$$

t - time

ε_m - initial phase shift

k - thermal diffusivity

x - position where the temperature is θ

l - slab thickness

This equation is valid for an infinite slab, which is clearly not the case in the experiments

reported here. Gradients parallel to the surface of the hot plate were, however, negligible, in comparison to those through the middle of the sample. The thermocouples in the interior were 0.5 mm in diameter and the shortest dimension of a sample was never less than 20 mm. Thus, near the middle the infinite slab approximation appears valid. Another assumption, the validity of which is more questionable, is that the plane at x=l is kept at zero (reference) temperature. In this case, this would mean that this reference temperature should have been the same as the value of θ at t=0, and for convenience, a_2 would also have been the same temperature.

In fact, at t=0, the temperature of the sample was nearly ambient 25°C. From Figures 4.4a and 4.4b, the hot plate in the "off" part of the cycle generates a surface temperature of between 210°C and 250°C. The back face of the sample is observed to oscillate between 100 and 150°C. Application of the expression for θ thus requires some care. It is seen that behavior approximating infinite time is already achieved in the experiments of Figures 4.4a and 4.4b. Thus the term involving the exponential term can be neglected. The constant temperature boundary condition at x=l is not realized in practice, as the data show. Thus an approach could have been attempted based upon application of a convective boundary condition at the back face. This is not necessary in practice because it is really only the information from near the front face that was used for the determination of thermal diffusivity. A virtual slab of greater thickness is defined, and the near - front temperature profile examined using this approach. In this experiment, the idea was to use thick enough samples so that a temperature profile is formed, and information on a virtual "slab thickness" can be calculated from the profile itself. The calculated value of slab thickness was later used in the calculations. In the above equations, the only unknown is thermal diffusivity and it can be calculated from the temperature profiles whose examples are shown in Figures 4.4a and 4.4b. To perform that task, first, a correlation expression for

the actual data was developed. There was some difficulty associated with this approach simply because the phase shifts were quite small and the best correlation for the data actually introduced unnecessary errors in the phase shift. Eventually, the phase shifts were determined "by hand"; i.e., as a time lag between the two maximum values of temperatures. The period of the oscillations was also determined by similar methods. The value of the phase shift was found by dividing an average value of the time lags by the period of oscillation and 2π. The thermal diffusivity was determined from the parameter ϕ, which represents the phase shift.

The thermal diffusivities for the raw cellulose samples were found to be constant in the range of temperatures investigated, between 116°C and 289°C. The data was quite scattered, and the mean value for cellulose thermal diffusivity was 0.0806 mm^2/s, but the standard deviation was ± 0.0174 mm^2/s, or $\pm 22\%$. The reason for this large scatter cannot be explained by the experimental technique, since the data for chars, obtained in exactly the same way, as will be shown below, do not exhibit nearly as much scatter. The differences among the samples are certainly not a reason for scatter, since the samples used were from the same batch and, as shown in Chapter 3.2.1, the reproducibility in preparing samples is quite high. Therefore, the only logical reason would be that samples were thermally degrading. Indeed, a visual examination of post-experiment samples revealed that the surface, which was in the contact with the hot plate, was yellow in color, similar to old paper. Bearing in mind that cellulose can be degraded, by prolonged exposure to temperatures even only slightly higher than room temperature, and that the experiments reported here were several hours in duration, this explanation seems fairly plausible.

Obviously, the temperature range is quite narrow and thus it is not surprising that the thermal diffusivity is relatively constant with temperature. A wider temperature range was not investigated because of problems with low temperature pyrolysis. There is a danger that

the measured properties are not representative for the entire range of temperatures between room temperature and 330°C defined by Figure 4.1 to be the onset of pyrolysis. The temperature range examined covers most of the range of interest, however. These values are certainly better representative of the situation in the simulated fire apparatus than the values from the literature, even given the relatively large data scatter.

Figure 4.5 presents the summary of the data for different chars and Table 4.1 depicts their respective temperature dependencies. It can be seen that, even over this small temperature range, some trends exist. All chars exhibit an increase of thermal diffusivity with temperature. Apparently there is curvature in the data, indicating that the thermal diffusivity of char varies as a nonlinear function of temperature. The chars that were made out of two different density cellulose samples and pyrolyzed at 600°C appear to have very similar thermal diffusivities. This means that the thermal diffusivity of a completely pyrolyzed cellulose sample does not depend on the density of a sample. There are no such similarities for the raw cellulose samples or the chars made out of two different density cellulose samples and pyrolyzed at 300°C. The char derived at 300°C from a lower density cellulose sample has higher thermal diffusivity whereas the char derived at 300°C from a higher density cellulose sample has lower thermal diffusivity than both density cellulose samples chars derived at 600°C.

If the trend with final char density, irrespective of the preparation temperature, is examined in Figure 4.5 it can be seen that the lower the density, the higher its thermal diffusivity for all chars except for one prepared from lower density cellulose sample at 600°C. If the trend with density actually exists, as the data of Figure 4.5 suggests, this might indicate that the thermal diffusivity for char prepared from lower density cellulose sample at 600°C is not correct. This question will be further addressed below.

The data can be examined in terms of the parameters that determine the thermal diffusivity; i. e., heat conductivity, density and heat capacity. It is clear from the preceding that cellulose thermal conductivity scales linearly with the density, since the heat capacity does not depend on density. The heat capacity does not seem to be a very sensitive function of char preparation conditions (Figure 4.3). Upon pyrolysis, density decreases, as does the heat capacity. It is obvious that the density does not decrease as rapidly as the heat capacity does. In other words, the low temperature (300°C) char heat capacity already achieved its final state, while density is just a bit more than halfway there. Therefore, it appears possible that the low temperature chars exhibit some properties of high temperature chars (heat capacity) and some properties of cellulose (thermal conductivity). This hypothesis explains the phenomena evident in Figure 4.5; i.e., the low density, low temperature char has a higher thermal diffusivity than high temperature chars or cellulose.

4.3 THERMAL CONDUCTIVITY

Thermal conductivity was not measured, *per se*. Values were determined from the density, heat capacity and thermal diffusivity data. The values obtained for two cellulose samples of different densities and their respective chars, prepared at 300°C and 600°C, are shown in Table 4.1. Also shown are the values for the thermal conductivities of the lowest density cellulose samples, written in italics, to highlight that the actual diffusivity for that density was not measured, but derived assuming that the constancy of thermal diffusivity with density pertains in that region as well.

The properties represented thus far -- heat capacity and thermal diffusivity -- are similar to the values that appear in the literature and thus are reasonable on this basis. A summary of

the calculated thermal conductivities is shown in Figure 4.6, for the valid temperature range shown in Table 4.1. This figure shows the variation of thermal conductivities for cellulose samples of three different densities, their chars and nitrogen. The thermal conductivity of nitrogen was obtained from property tables (53). The values for thermal conductivity of char prepared from lower density cellulose sample at 600°C are not shown in Figure 4.6. The reason is that those values were lower than the values for nitrogen, which is impossible. This suggests that there was an error in measurement of thermal diffusivity, which is also the reason that these values do not follow the trend with final density shown in Figure 4.5. It is noted that the thermal diffusivity measurements were performed by positioning several thermocouples within the sample and, bearing in mind very low final density of the "problematic" char (0.18 g/cm^3), the possibility of thermocouple positioning error, due to the breakage of the structurally weak sample, cannot be ruled out. Disregarding the thermal conductivity values for the char of 0.18 g/cm^3 final density, the values for thermal conductivities of chars can be compared to the values of cellulose samples. It is evident from Figure 4.6 that the low (0.458 g/cm^3) density cellulose sample thermal conductivity compares well with the values for chars. That means that the thermal conductivity of a char is lower mainly due to the porosity of a sample, rather than to the difference in material. This is consistent with the approach for determining thermal conductivity from the porosity (81):

$$k_c = k_{carbon}(1-\varepsilon) + k_{gas}\varepsilon \qquad (4.8)$$

where k is the thermal conductivity, ε is the void fraction and subscripts "c", "carbon" and "gas" refer to char, carbon in the structure and gas in the voids.

Therefore, it can be concluded that, the thermal conductivity scales with sample density for both cellulose and char samples, despite the fact that the materials are different, the reason

being that the decrease in thermal conductivity is due to the increased presence of gas (nitrogen in the case studied here), with lower thermal conductivity in the voids.

4.4 SURFACE EMISSIVITY

In radiative heat transfer surface emissivity represents a crucial thermal property of a material. It is common to make an analogy between surface emissivity and the color of a surface, although the two properties are fundamentally different. The color of a surface is determined by the ability of a surface to absorb, or reflect, the radiation of certain wavelength range better than the other ranges, but only in the visible region of the radiation spectrum (from 400 μm to 700 μm). Infrared waves have much a broader wavelength range -- from 700 μm to about 10^5 μm. Although surface emissivity can be defined for a wavelength range, it is obvious that the human eye is not a good sensor for it. An example is frost. It is bright white, which means that it reflects mixed wavelength radiation in the visible region of the radiation spectrum, yet it has an emissivity very close to unity. Therefore, caution must be exercised when judging the surface emissivity from color. In general, it is safer to judge the emissivity by the roughness of a surface. Smooth surfaces tend to have a higher emissivity than rough ones. However, since emissivity is not something that the human eye is sensitive to, it must be measured.

Surface reflectances were measured in a standard FTIR and the surface emissivities were calculated from reflectances as a complement to unity, since transmittance is equal to zero for the samples used here. Measurements were performed in the wavelength range from 2.5 μm to 25 μm. Samples were prepared at different extents of pyrolysis in the simulated fire apparatus from "standard" samples of high density, and at an incident heat flux of 40 kW/m^2. The extents of pyrolysis were judged based on data from the optical pyrometer

(Figure 3.9). The data obtained is shown in Figures 4.7a through 4.7f (analysis of FTIR spectra is presented below). In each of the figures a small inset sketch indicates the stage of the pyrolysis process during which the sample was taken out of the apparatus.

Reflectances were averaged over the entire FTIR wavelength range. They are shown as a function of heating time in Figure 4.8. It can be seen that the reflectance is about 0.105 (or an emissivity of 0.895) for the cellulose sample, than it passes through a minimum at about 0.03 (or maximum emissivity of 0.97) and increases again to about 0.05 (or emissivity of 0.95) at the end of a run. Interestingly enough, if the data from Figure 4.8 are compared to the output of the optical pyrometer, operating at a wavelength range 2.2 μm to 2.4 μm (from Figure 3.9), it can be seen that they appear very similar in shape. Hence it can be concluded, based on this comparison, that the optical pyrometer signal yields a qualitative measure of reflectance.

The data from Figure 4.8 is similar to values from other studies in the literature (39). However, despite the fact that it gives a reliable measurement of surface emissivities, the FTIR reflectance measurements are of limited value in modeling the results from this work, simply because they are not for the corresponding wavelength range. As shown in Figure 3.4 the radiative heaters deliver most of the radiation well below 2.5 μm, the lowest wavelength in the FTIR measurements. There is evidence in the literature that the emissivities of virgin material and chars can be very different than those calculated from the data shown in Figure 4.8. Kansa et al.(80) found with a mathematical model of pyrolysis that the "best fit" emissivity for virgin material is 0.64 and for char 0.94. Bennini et al. (17) used a wood emissivity of 0.35 in their modeling work, and 0.93 for char. For red oak Kashiwagi (89, 90) found experimentally an emissivity of about 0.40 at 2 μm and about 0.95 for wavelengths greater than 6 μm. Serio et al. (155) determined a polyurethane

surface emissivity of about 0.85 and about 0.67 for its char, averaged over the wavelength range 1.5 μm to 20 μm.

Indeed, the preliminary mathematical modeling of the simulated fire apparatus results performed in this work indicated that the surface emissivities cannot be as high as measured by FTIR. The front surface boundary condition is:

$$\dot{q}_r'' - (1-\varepsilon)\,\dot{q}_r'' - \left(-k\,\frac{\partial T_s}{\partial x}\right) - \sigma\,\varepsilon\,T_s^4 - h\,(T_s - T_\infty) = 0 \qquad (4.9)$$

where the terms from left to right represent: incident heat flux from the radiative heaters, the fraction of the incident heat flux reflected due to the non - unity emissivity, the loss from the surface due to conduction into the sample, the radiative heat loss from the surface (T_s^4 » T_∞^4) and the convective heat loss from the surface. All the terms in this expression are known or measured, except for the emissivity, ε, and the heat transfer coefficient, h. If the values for these are estimated to be 0.95 (as measured by FTIR) and 10 W/m^{2}K (for natural convection, see section 4.5) respectively, it is determined that for all surface temperatures the heat flux available for conduction ($-k\partial T_s/\partial x$) is much greater than that measured (using heat conduction coefficients determined as described above, and $\partial T_s/\partial x$ calculated from temperature profiles, to be presented below).

Since clearly there was a problem in closing the surface energy balance, it was decided that emissivity should be checked *in situ*. In an attempt to determine the surface emissivity, valid over the range of the wavelengths used here, two different approaches were taken. The first involved a calculation and the second a direct measurement of the reflected flux. For calculations, care must be taken to operate under conditions satisfying the boundary condition, which is represented by equation (4.9). This means that the calculations should

be performed in the absence of other heat effects (water evaporation and pyrolysis) at the solid surface except those included in the boundary condition. For this reason, calculations of the cellulose surface emissivity were performed for surface temperatures between 180°C and 300°C. The calculations were not performed for char. The reason is that the temperature profile was not completely defined. The temperature profile was measured, but since the sample shrinks after it has been pyrolyzed, the distance from the front surface to where the temperature was measured becomes undefined. Direct measurements could be performed on the char, however.

For the purposes of checking the indirect measurement method, the thermal conductivity was first determined from the heat conduction equation ($\partial T_s/\partial \tau = \kappa \, \partial^2 T_s/\partial x^2$, for $x = 0$). The conductivity determined in this manner was no more than 10% different from the thermal conductivity measured previously. Following this check of thermal conductivity, calculations of surface emissivity were performed. These calculations were done for all three density samples and for several different surface temperatures, depending on the value of incident heat flux used, but over the range from 180°C to 330°C. The calculated surface emissivities are shown in Table 4.2a. Calculations were also done for three different values of heat convection coefficient (0, 10 and 20 W/m^2K) to establish the sensitivity of the surface emissivity value to errors in estimation of the heat transfer coefficient. These values are shown in Table 4.2a.

Direct measurements of reflected heat flux from both cellulose and char surfaces, were performed using a fluxmeter. The fluxmeter was first positioned in place of a sample, with its surface at an angle of approximately 45° from the radiative heater beam. Only one radiative heater was used for this measurement in order to have a better defined beam geometry. The flux was measured and then the fluxmeter was replaced by a sample. The

fluxmeter was trained on the sample surface and thus measured the reflected radiation. The measurements of reflected flux were done as quickly as possible in order to avoid surface heating and the contribution of the radiative loss from the sample surface to the reflected radiation. The ratio of reflected heat flux to the radiative heat flux is surface reflectivity, which is unity minus the surface emissivity.

Before measurements of surface reflectivity by fluxmeter there was a need to determine the geometric relations (shape factor) between the radiative heaters and the fluxmeter or sample. That was done by coating a ceramic cylinder surface with aluminum foil, with a reflectivity of 0.95. The fluxmeter was positioned where the sample was positioned afterwards. The flux was measured and the sample, coated with the aluminum foil was set at the place. The fluxmeter was directed at the sample surface, as close as possible, but in such a way as not to block any incoming radiation from the radiative heater. It was shown that the flux was greater when the fluxmeter was directed towards the sample surface than when it was pointed towards the radiative heater. The reason for this was that the shape factor was smaller than unity when the fluxmeter was pointed towards the radiative heater, since there was a significant viewfactor of cold objects. When the fluxmeter was pointed towards the sample surface, it resulted in a configuration for which the shape factor became very close to unity, if not actually unity. The experiment performed with the aluminum foil provided a combined shape factor for these two arrangements. From the ratio of reflected to measured radiation, the combined shape factor was calculated to be 0.85. With the known shape factor, measurements of reflectivities of cellulose and char could be performed. These measurements had to be done rapidly in order to avoid significant contributions from sample surface radiation. The calculated emissivities for the cellulose and char are shown in Table 4.2b. There are two columns for char emissivities. It was observed that the surface of a cellulose sample, after it was pyrolyzed at 20 kW/m^2 incident flux, appeared different

than the surface of a sample pyrolyzed at higher incident heat fluxes. For that reason, the emissivity of that char was also measured, and it was shown that it had slightly higher surface emissivity.

It can be seen, by comparing the values in Tables 4.2, that there are slight differences between measured values and those calculated from the boundary condition, but no trend in differences is obvious. It should be noted, however, that the values calculated from the boundary condition rely heavily on the value of the temperature gradient at the surface, which means that the reason for the differences is probably the uncertainty in surface temperature gradient. Usually the temperature profile was measured with thermocouples about 2 mm apart from each other, which is enough for a temperature profile, but might not be sufficient to determine the surface temperature gradient. Again, the value of the char emissivities could not be checked due to the inability to reliably measure a temperature gradient at the surface.

Values for the surface emissivities of cellulose and chars are lower than expected. It must be pointed out that the values for emissivities were judged from the literature, most often from various textbooks and handbooks (53, 74, 137), which do not specify the wavelengths at which the measurements were performed. The other source of the values for emissivities was the FTIR measurements. It was tacitly assumed that the emissivity in the wavelength range given by the radiative heaters is close to that measured by FTIR, although it is known that the emissivity can be a very strong and often, unpredictable function of the wavelength. Although the data shown here is representative of the situation for cellulose pyrolysis in the simulated fire apparatus used in this work, it is obvious that it might not be representative for a different wavelength range and, certainly not representative for other charring materials.

4.5 HEAT TRANSFER COEFFICIENT

The heat transfer coefficient was determined from relationships available in the literature for averaged Nusselt numbers. The assumptions that were used for calculations of heat transfer coefficients were vertical wall geometry and that natural convection dominated. The assumption that a sample pyrolyzed in the simulated fire apparatus can be approximated by a vertical wall geometry is well justified by the actual experimental geometry. No attempts were made to analyze the flow at the sample surface. The assumption that the heat transfer is by natural convection has to be proven. The total flowrate through the experimental chamber is 15 l/min. The chamber has an inside area, in the flow direction, of 18 dm^2 (Chapter 3.2.2). This gives a velocity in the flow direction, over the sample surface, of about 1.4 mm/s, which means that for practical purposes the fluid is quiescent, such that the natural convection would be expected to dominate.

Two correlations were examined. One was obtained from Eckert and Drake (53), and the other from Perry's Handbook (137). They are, respectively:

$$Nu = \frac{0.508\ Pr^{0.25}}{(0.952 + Pr)^{0.25}} (Gr\ Pr)^{0.25} \tag{4.10}$$

$$Nu = \frac{0.683\ Pr^{0.25}}{(0.861 + Pr)^{0.25}} (Gr\ Pr)^{0.25} \tag{4.11}$$

In equations 4.10 and 4.11, Nu is an average Nusselt number ($Nu=hx/k$), Pr is the Prandtl number ($Pr=C_p\mu/k$) and Gr is Grashof number ($Gr=g\beta(T_s-T_\infty)x^3/v^2$). All calculations were performed for nitrogen, and the properties were taken from Eckert and Drake (53).

The heat transfer coefficients were calculated from equations 4.10 and 4.11 using the sample diameter as the characteristic dimension x. Results are presented in Figure 4.9 for the temperature range of interest here. It can be seen that the two correlations yield slightly different heat transfer coefficients. However, both are in the range used for calculations of surface emissivities, shown in Table 4.2a. Emissivity is not a strong function of the value of h.

It is debatable whether nitrogen properties are representative of the situation in the simulated fire apparatus when a sample undergoes pyrolysis. During pyrolysis, the majority of the gases flowing around the surface are volatile products of pyrolysis that have very different properties (viscosity, thermal diffusivity and thermal conductivity) than those of pure nitrogen. On the other hand, comparison of the results shown in Table 4.2a suggest that the heat transfer coefficient might well be between 0 and 10 W/m^2K. In order for the heat loss due to convection to be significant, the sample surface temperatures must be greater than 300°C. The data from Figure 4.9 imply that a significant error will not be introduced if a value used for heat transfer coefficient is approximated by a constant of about 10 W/m^2K.

Table 4.1: Summary of thermal properties. [The temperature range indicates the validity of an equation; eg. the temperature range for the validity of thermal conductivity is the smallest range of validity of both thermal diffusivity and heat capacity.].

• Cellulose[1]

- $\rho = 0.928$ g/cm^3	
κ [mm^2/s] = const. = 0.0806±0.0174	389K - 562K
C_p [J/g-K] = -0.297 + 4.19x10^{-3} T	459K - 607K
k [W/m-K] = *-0.0222 + 3.13x10^{-4} T*	*459K - 562K*
- $\rho = 0.678$ g/cm^3	
κ [mm^2/s] = const. = 0.0806±0.0174	389K - 562K
C_p [J/g-K] = -0.297 + 4.19x10^{-3} T	459K - 607K
k [W/m-K] = *-0.0162 + 2.29x10^{-4} T*	*459K - 562K*
- $\rho = 0.458$ g/cm^3	
κ [mm^2/s] = *const. = 0.0806±0.0174*	*389K - 562K*
C_p [J/g-K] = -0.297 + 4.19x10^{-3} T	459K - 607K
k [W/m-K] = *-0.0110 + 1.55x10^{-4} T*	*459K - 562K*

[1] Temperatures in degrees Kelvin

Table 4.1: Continued

• Chars[2]

- Pyrolysis Temperature 600°C; Initial Density 0.944 g/cm^3; Final Density 0.41 g/cm^3	
κ [mm^2/s] = -0.157 + 7.95x10^{-4} T - 5.97x10^{-7} T^2	447K - 533K
C_p [J/g-K] = 0.960 + 2.02x10^{-3} T - 33505/T^2	423K - 823K
k [W/m-K] = *-0.0993 + 4.29x10^{-4} T - 1.89x10^{-7} T^2*	*447K - 533K*
- Pyrolysis Temperature 300°C; Initial Density 0.934 g/cm^3; Final Density 0.52 g/cm^3	
κ [mm^2/s] = -0.151 + 7.50x10^{-4} T - 5.99x10^{-7} T^2	422K - 530K
C_p [J/g-K] = 0.922 + 2.04x10^{-3} T - 40036/T^2	398K - 548K
k [W/m-K] = *-0.117 + 5.03x10^{-4} T - 2.65x10^{-7} T^2*	*422K- 530K*
- Pyrolysis Temperature 600°C; Initial Density 0.682 g/cm^3; Final Density 0.18 g/cm^3	
κ [mm^2/s] = -0.227 + 1.09x10^{-3} T - 9.21x10^{-7} T^2	410K - 522K
C_p [J/g-K] = 1.19 + 1.49x10^{-3} T - 49626/T^2	423K - 823K
k [W/m-K] = *-0.0612 + 2.67x10^{-4} T - 1.80x10^{-7} T^2*	*423K - 522K*
- Pyrolysis Temperature 300°C; Initial Density 0.701 g/cm^3; Final Density 0.33 g/cm^3	
κ [mm^2/s] = -0.447 + 2.02x10^{-3} T - 1.68x10^{-6} T^2	403K - 580K
C_p [J/g-K] = 2.08 - 1.11x10^{-4} T - 77136/T^2	423K - 548K
k [W/m-K] = *-0.235 + 1.02x10^{-3} T - 7.77x10^{-7} T^2*	*423K - 548K*

[2] Temperatures in degrees Kelvin

Table 4.2a: Summary of surface emissivities calculated from the fron surface boundary condition (equation 4.9).

		EMISSIVITY			
		DENSITY [g/cm^3]			
Flux [kW/m^2]	h [W/m^{2}K]	Low	Middle	High	Average
20	0	0.35	0.73	0.73	0.60
	10	0.51	0.85	0.83	0.73
	20	0.67	0.96	0.93	0.85
40	0	0.25	0.25	0.45	0.32
	10	0.32	0.30	0.51	0.38
	20	0.38	0.35	0.56	0.43
60	0	0.36	0.60	0.52	0.49
	10	0.42	0.65	0.57	0.55
	20	0.48	0.71	0.61	0.60

Table 4.2b: Summary of surface emissivities calculated from measured reflectivities.

	EMISSIVITY		
Flux [kW/m2]	Cellulose	Char[1]	Char[2]
20	0.57	0.82	0.85
40	0.48	0.72	0.81
60	0.53	0.68	0.75

[1] Char from cellulose pyrolyzed under an incident heat flux of 40 kW/m^2 or 60 kW/m^2.

[2] Char from cellulose pyrolyzed under an incident heat flux of 20 kW/m^2.

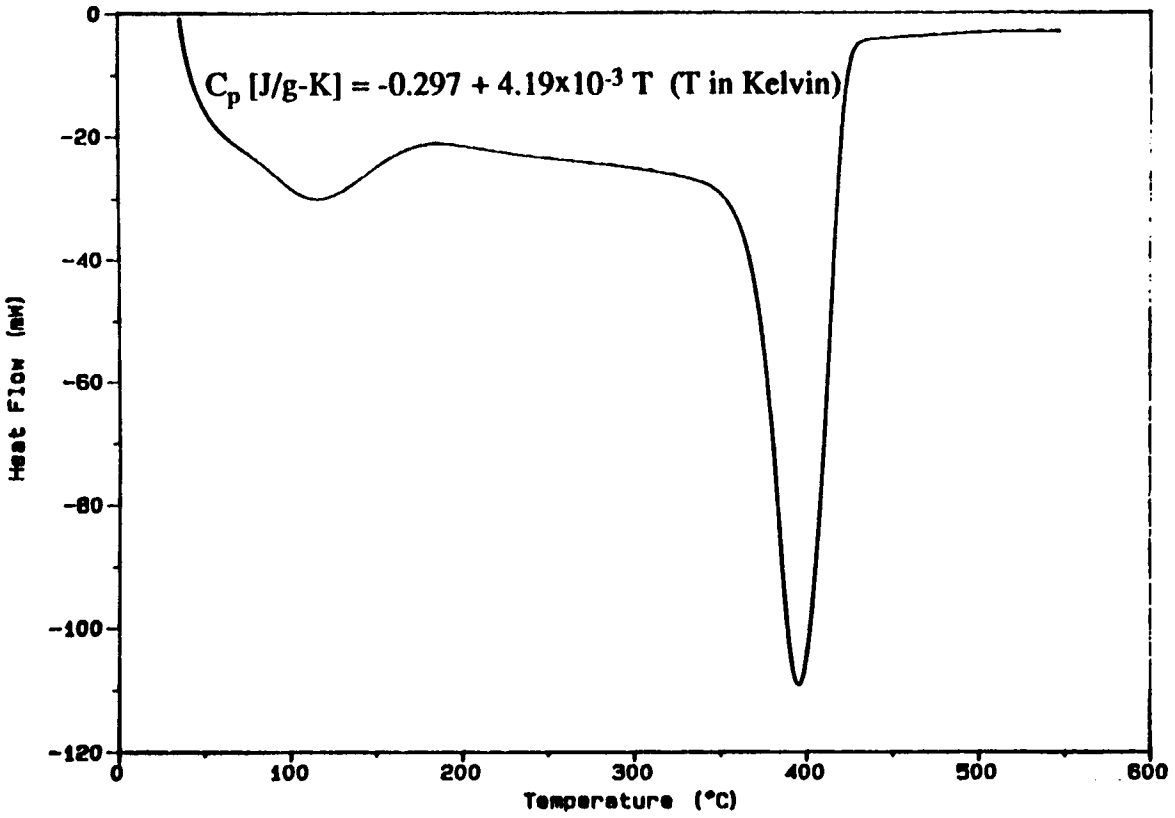

Figure 4.1 DSC of raw cellulose showing the heat capacity equation relevant to pre-pyrolysis zone, and showing the pyrolysis endotherm

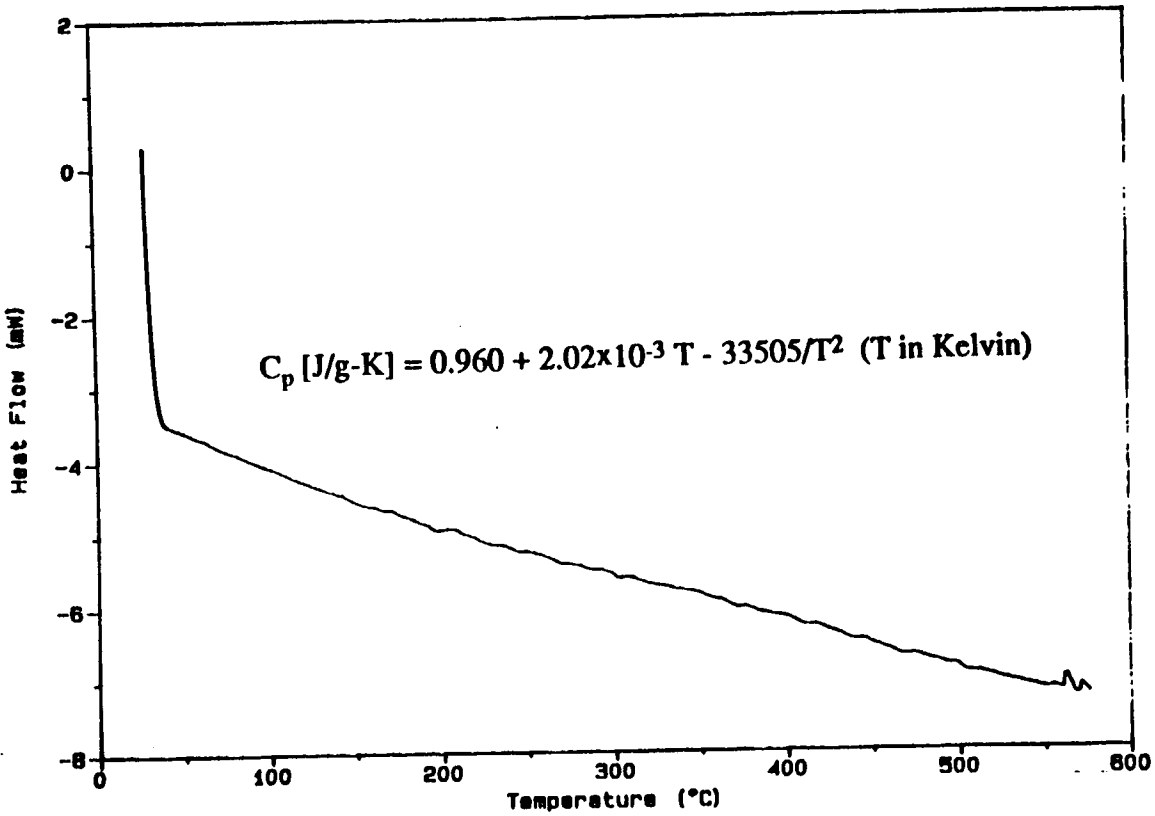

Figure 4.2a DSC of a 600°C char sample made from high density (0.965 g/cm^3) cellulose sample, showing the heat capacity equation

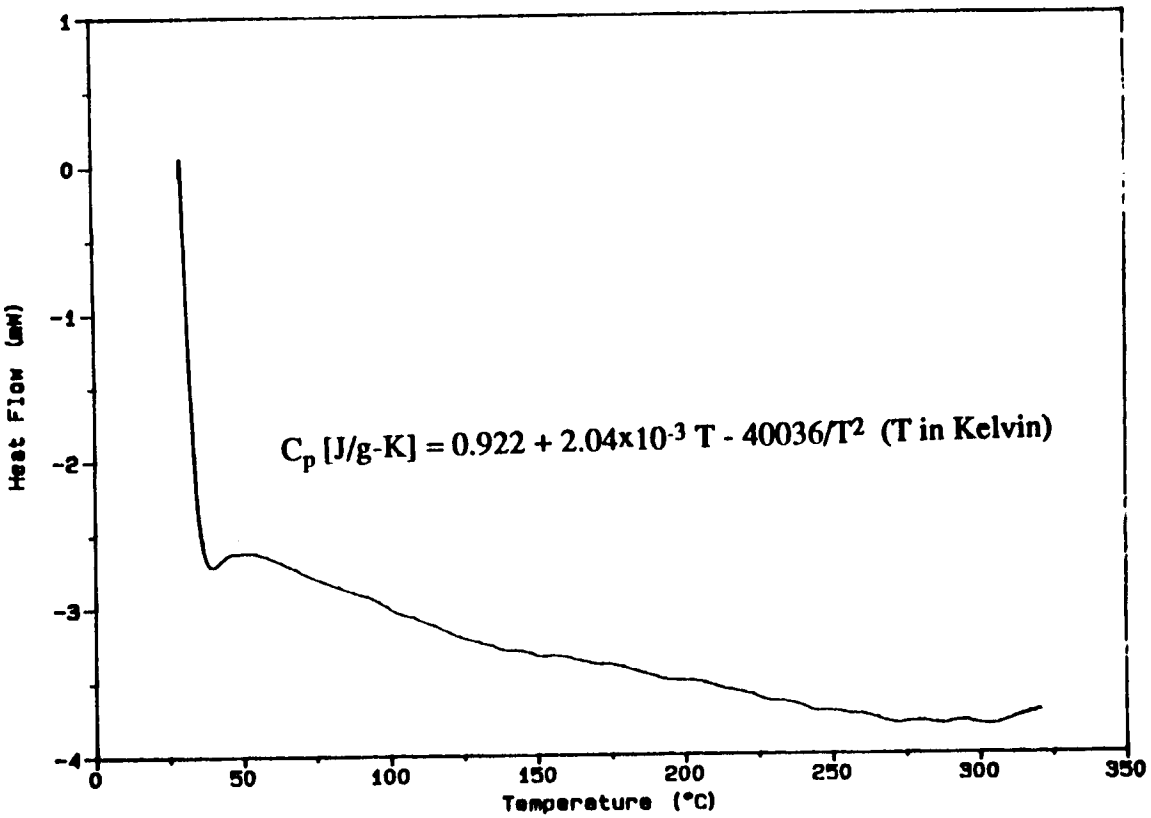

Figure 4.2b DSC of a 300°C char sample made from high density (0.965 g/cm^3) cellulose sample, showing the heat capacity equation

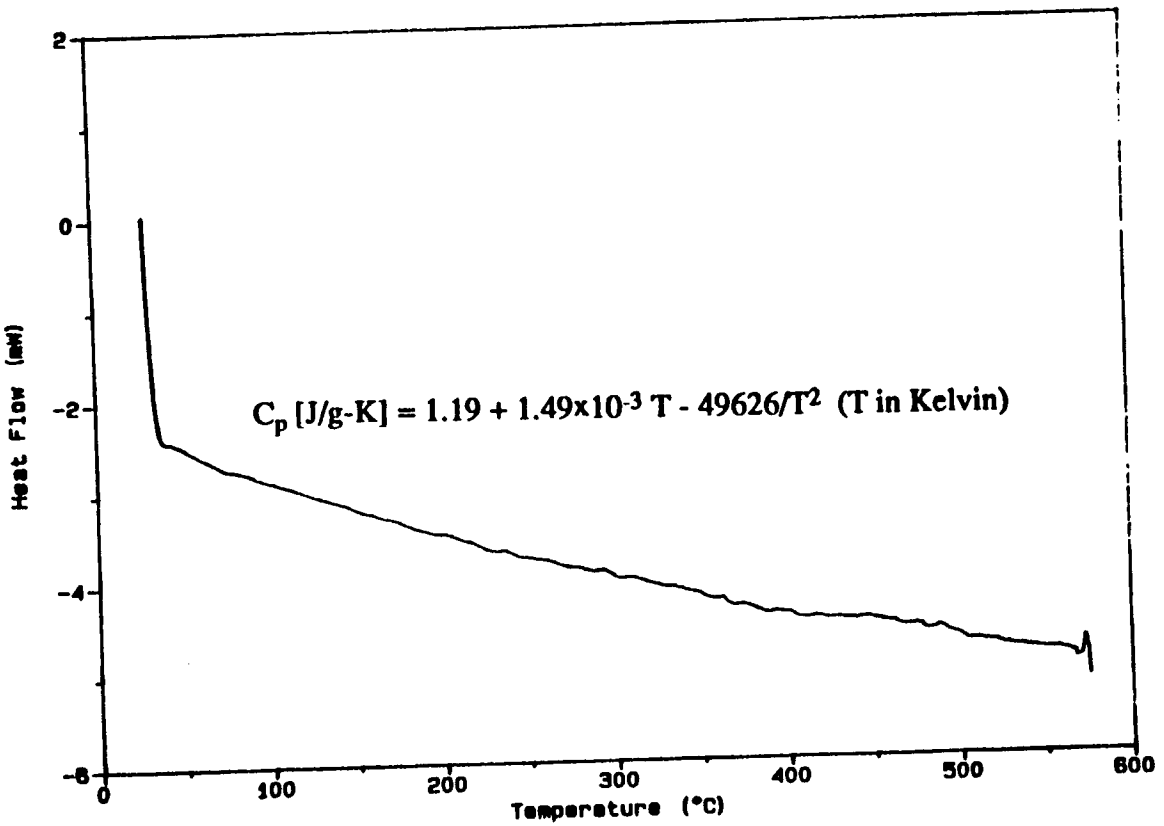

Figure 4.2c DSC of a 600°C char sample made from medium density (0.691 g/cm^3) cellulose sample, showing the heat capacity equation

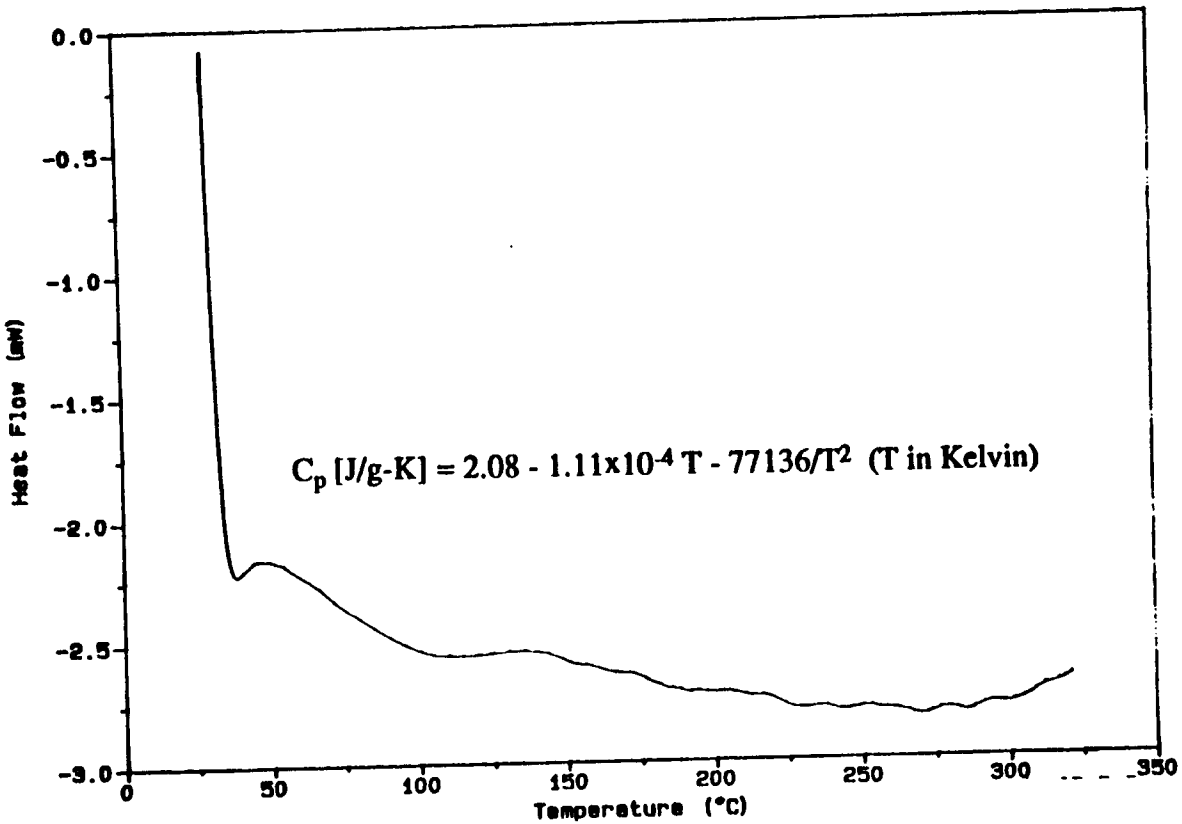

Figure 4.2d DSC of a 300°C char sample made from medium density (0.691 g/cm^3) cellulose sample, showing the heat capacity equation

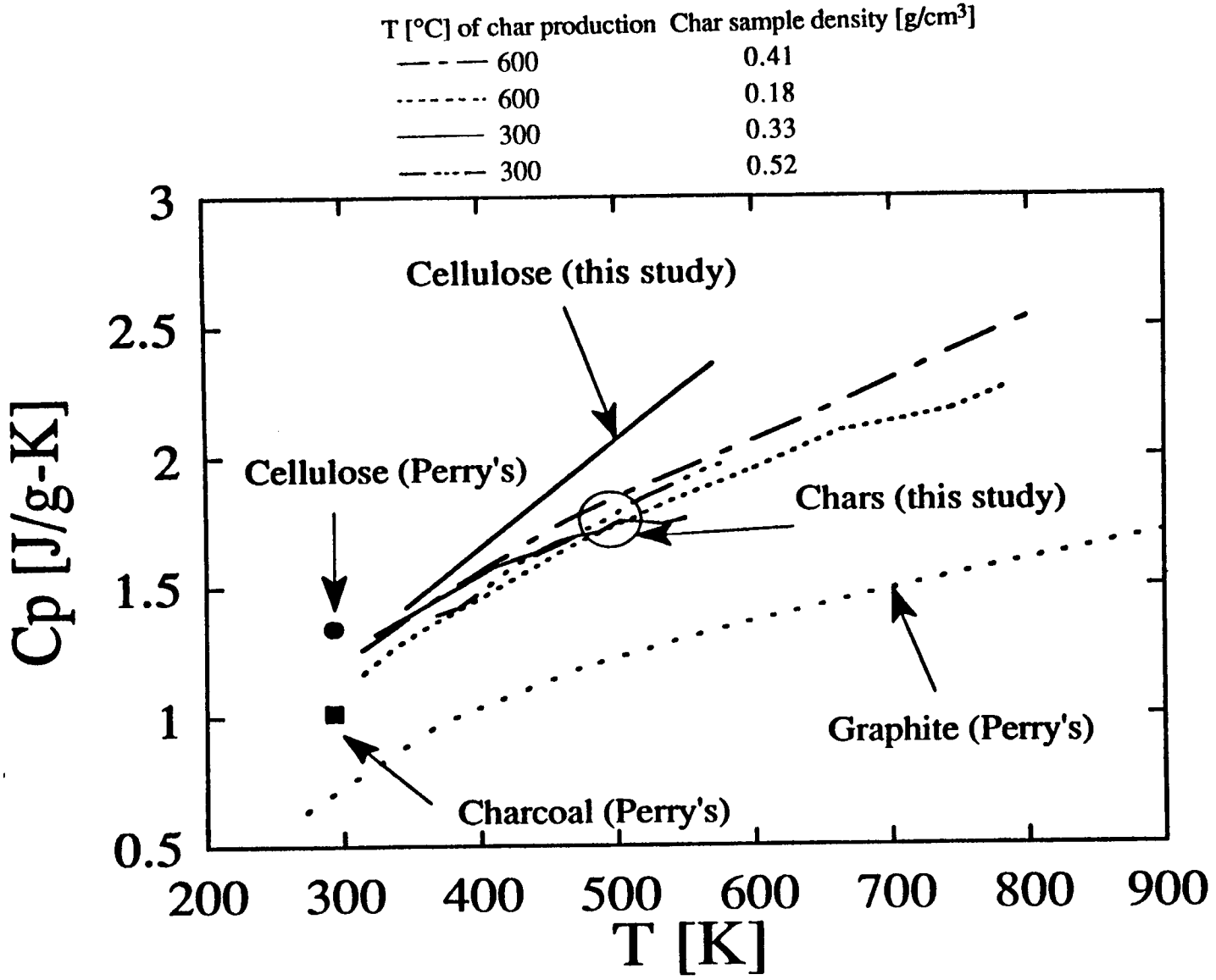

Figure 4.3 Heat capacities of raw cellulose and char samples. Also shown are the values for cellulose, charcoal and graphite from Perry's Handbook (137)

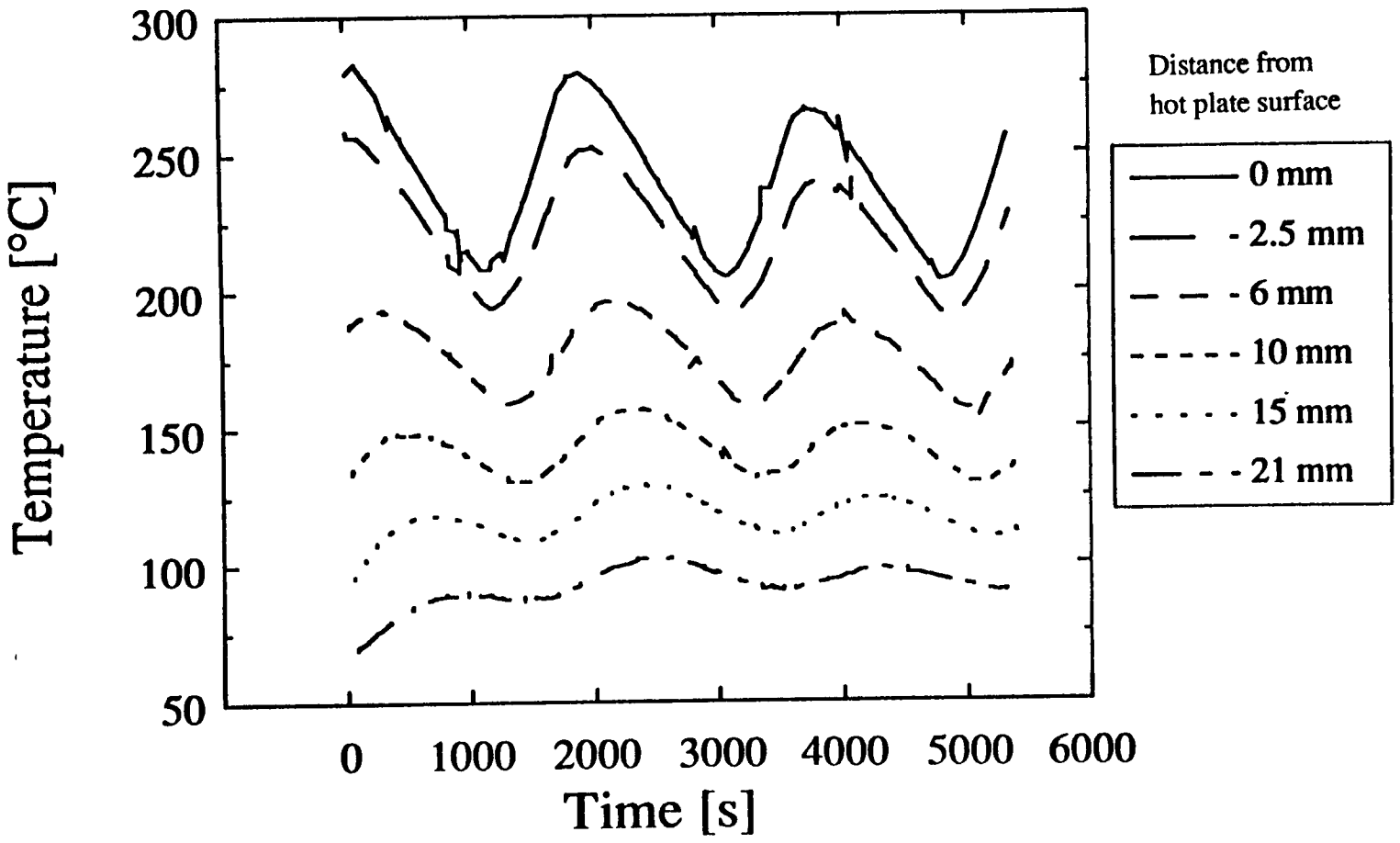

Figure 4.4a Temperature traces in raw cellulose sample of density 0.691 g/cm^3, at different distances from the surface of the hot plate (hot plate at x=0)

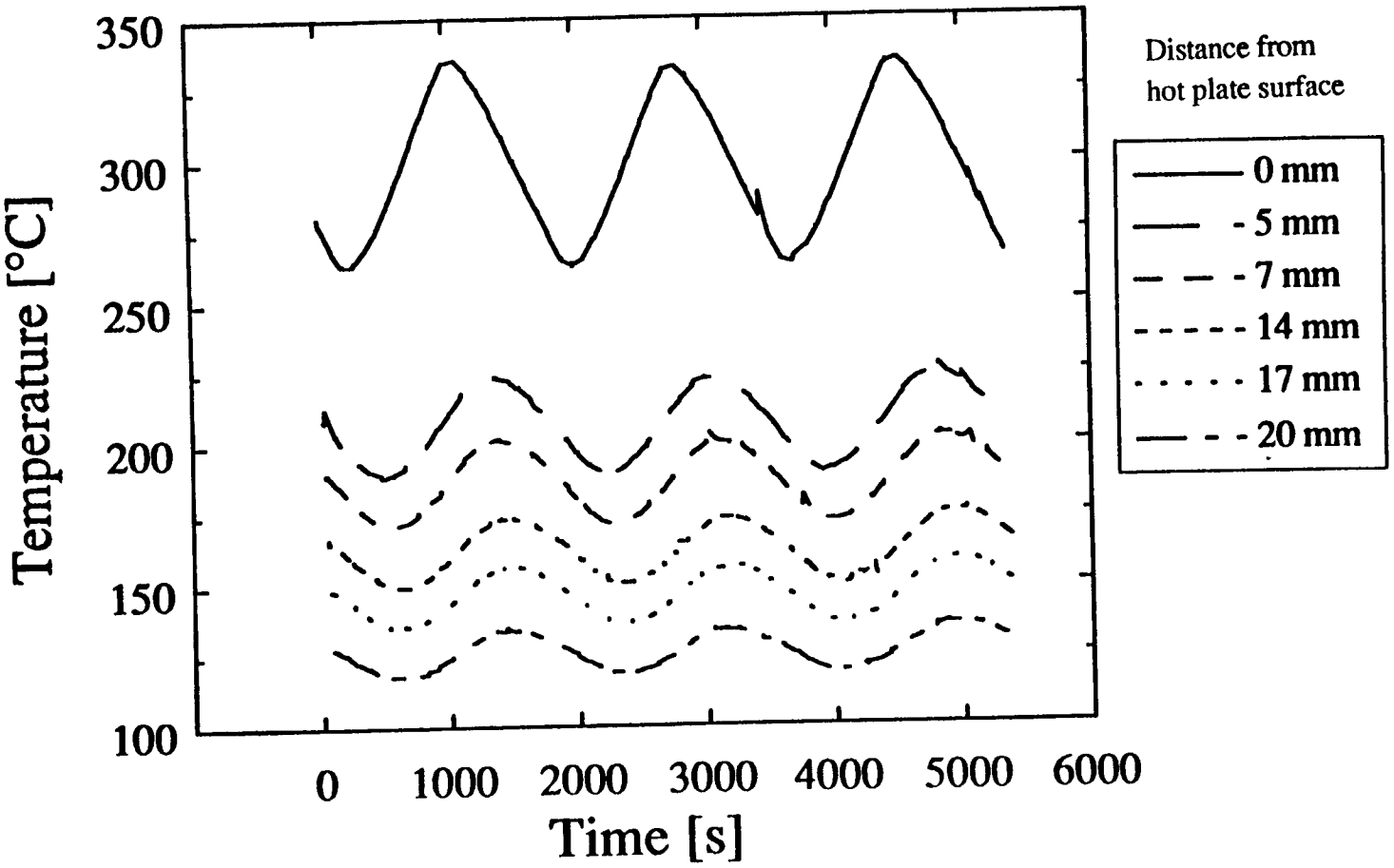

Figure 4.4b Temperature traces in a 300°C char sample made from a cellulose sample of density 0.691 g/cm^3, at different distances from the surface of the hot plate (hot plate at x=0)

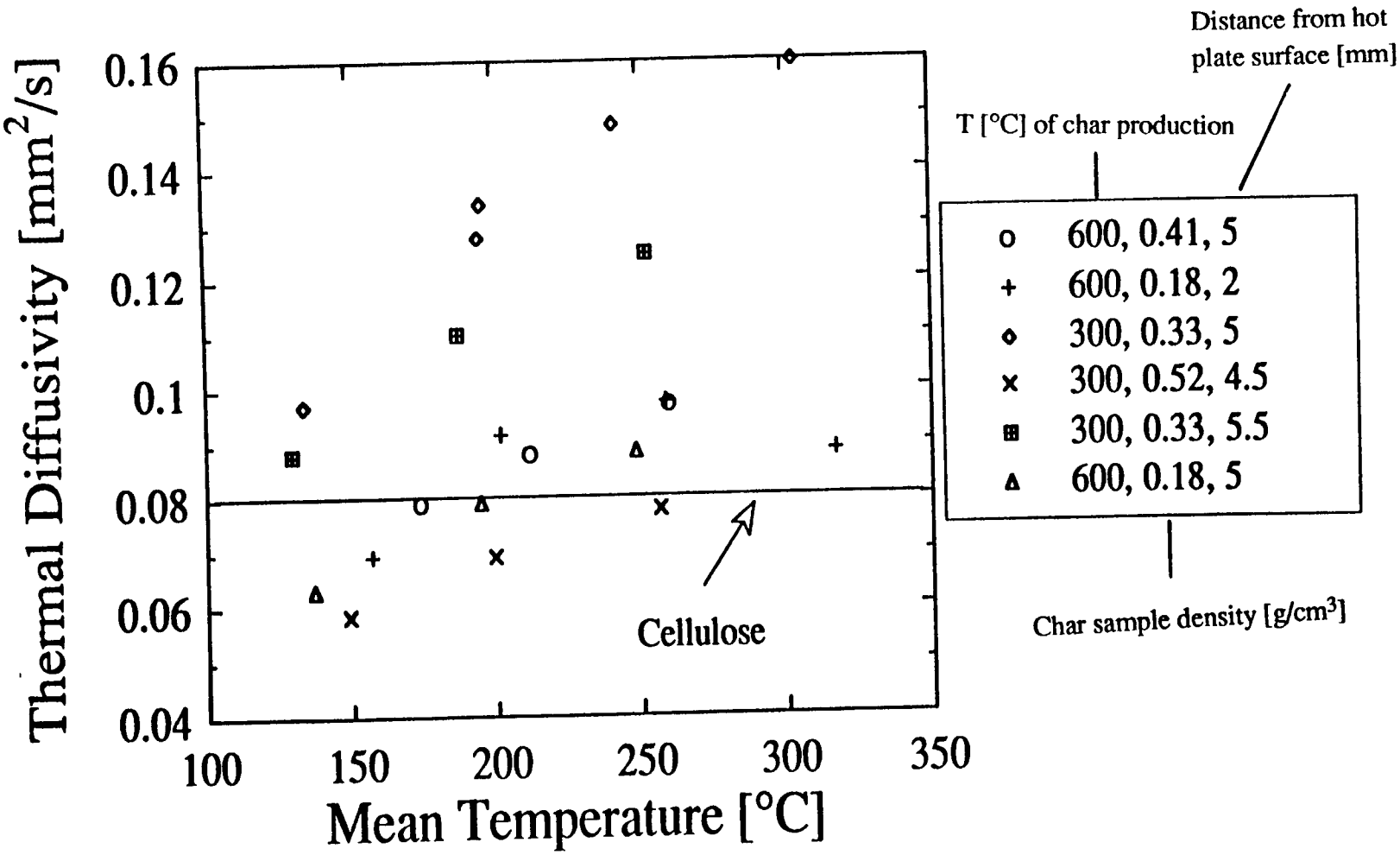

Figure 4.5 Thermal diffusivities of cellulose and different cellulose chars as a function of temperature

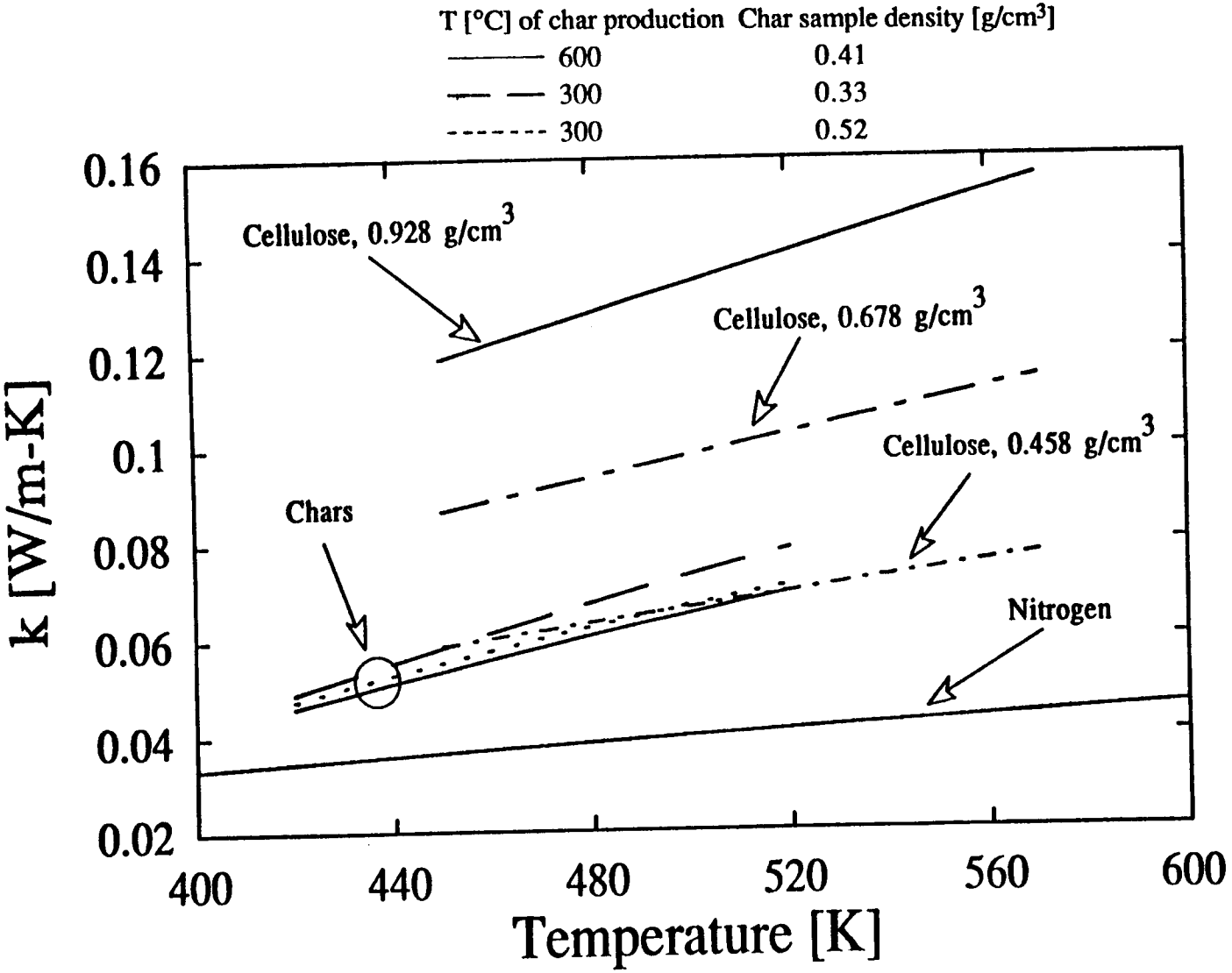

Figure 4.6 Thermal conductivities of raw cellulose and char samples calculated from their thermal diffusivities and heat capacities

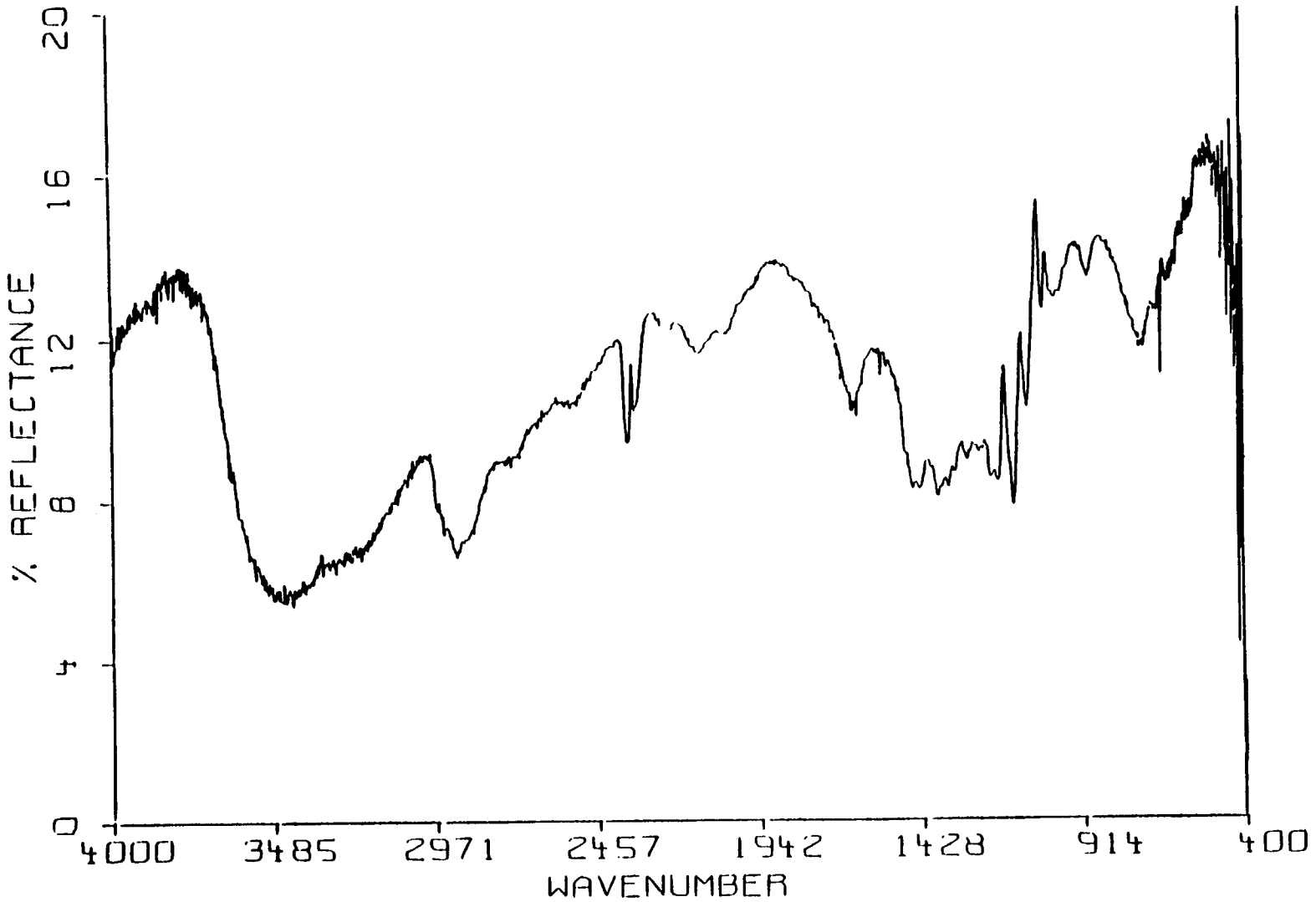

Figure 4.7a FTIR scan of the raw cellulose sample (white, temperature 25°C)

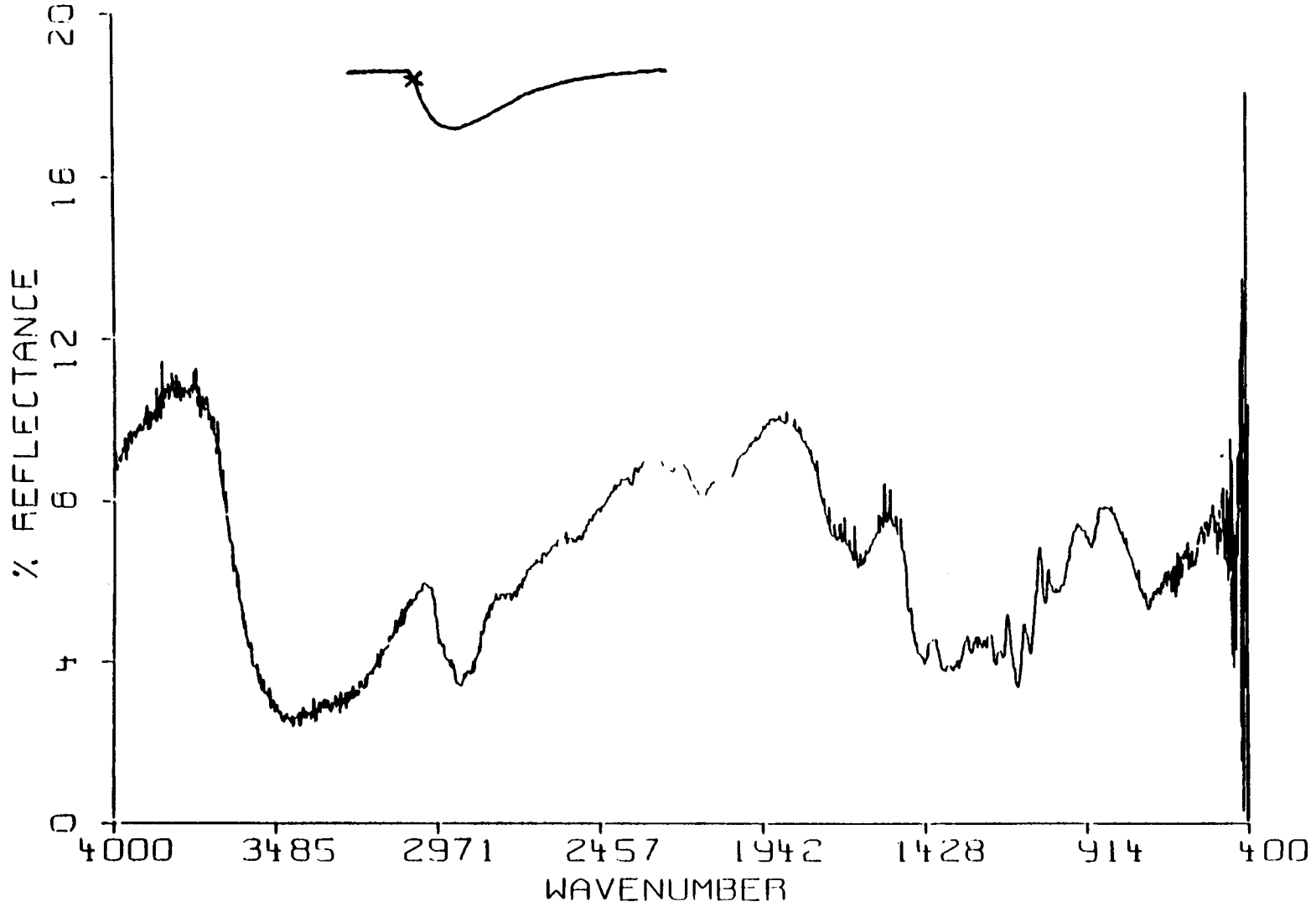

Figure 4.7b FTIR scan of the first char (brown, temperature 380°C)

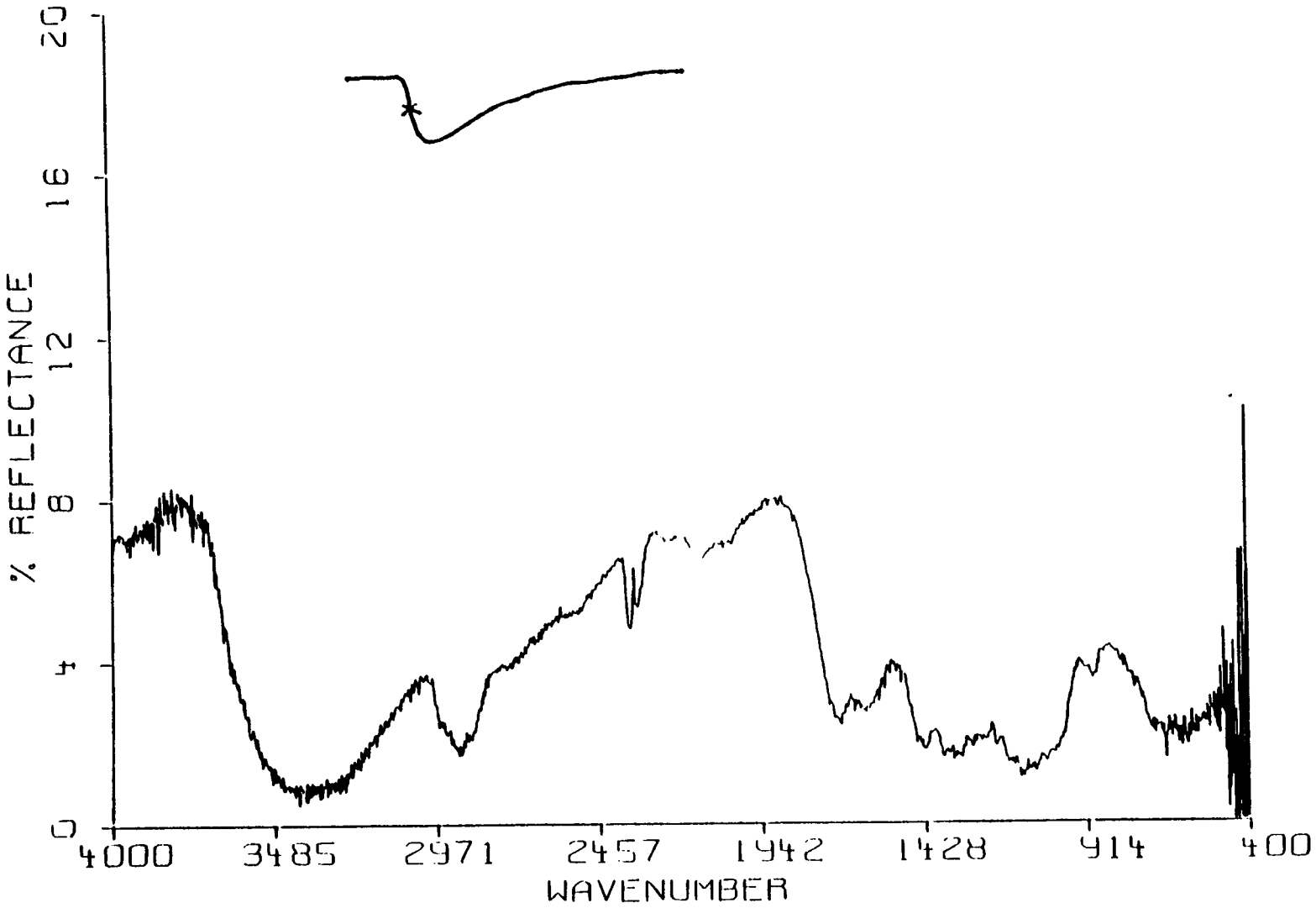

Figure 4.7c FTIR scan of the second char (dark brown, temperature 405°C)

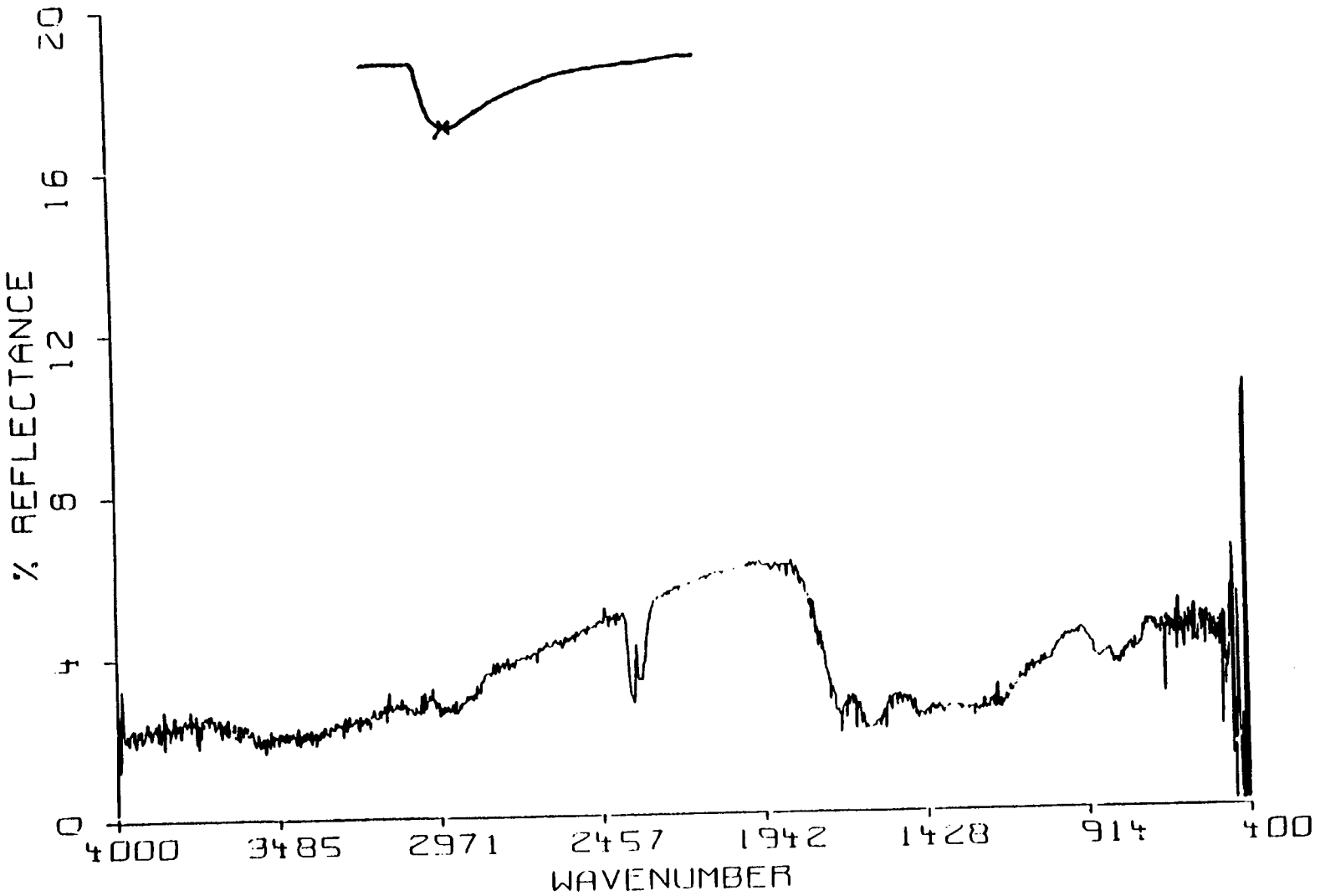

Figure 4.7d FTIR scan of the third char (black, temperature 430°C)

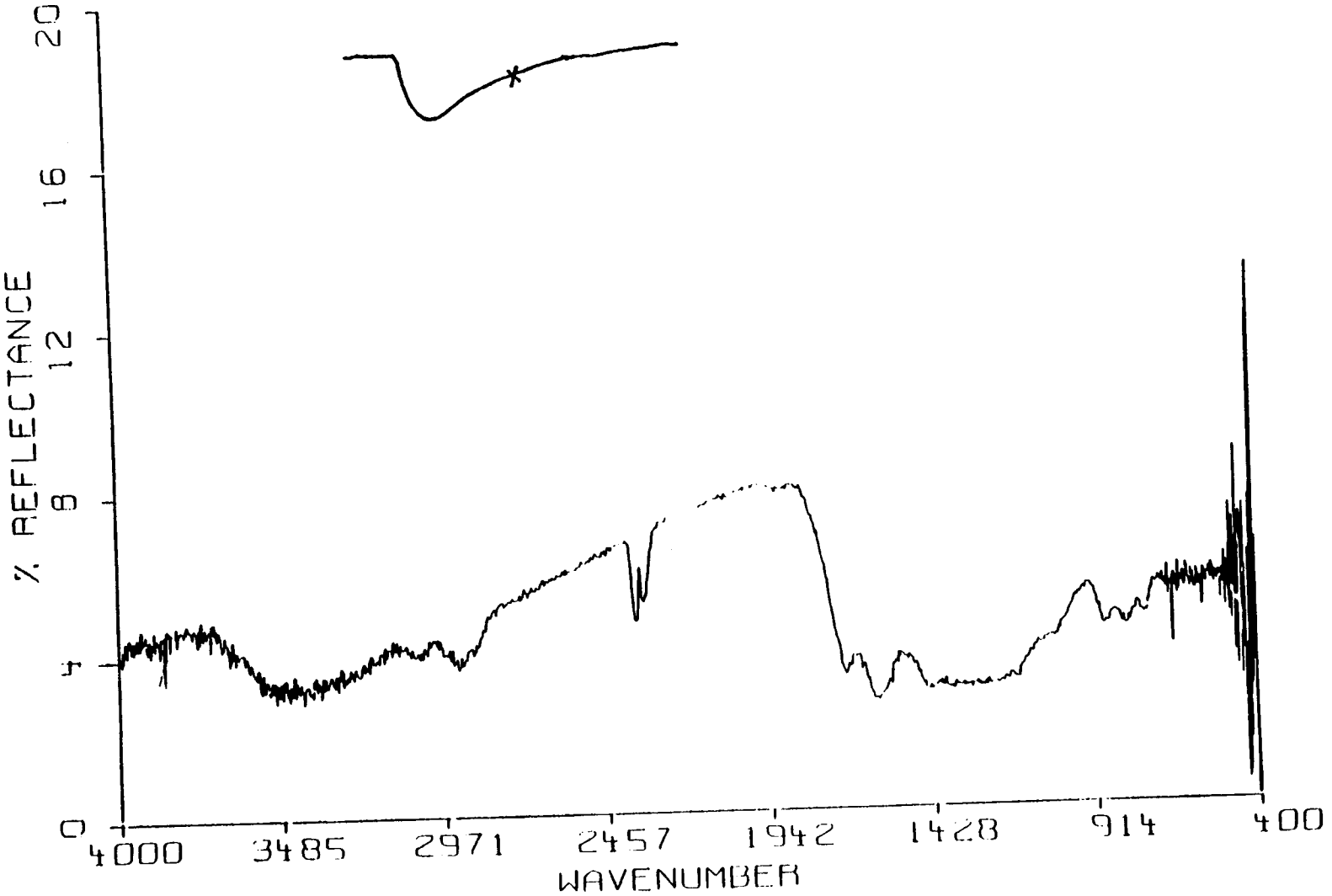

Figure 4.7e FTIR scan of the fourth char (black, temperature 520°C)

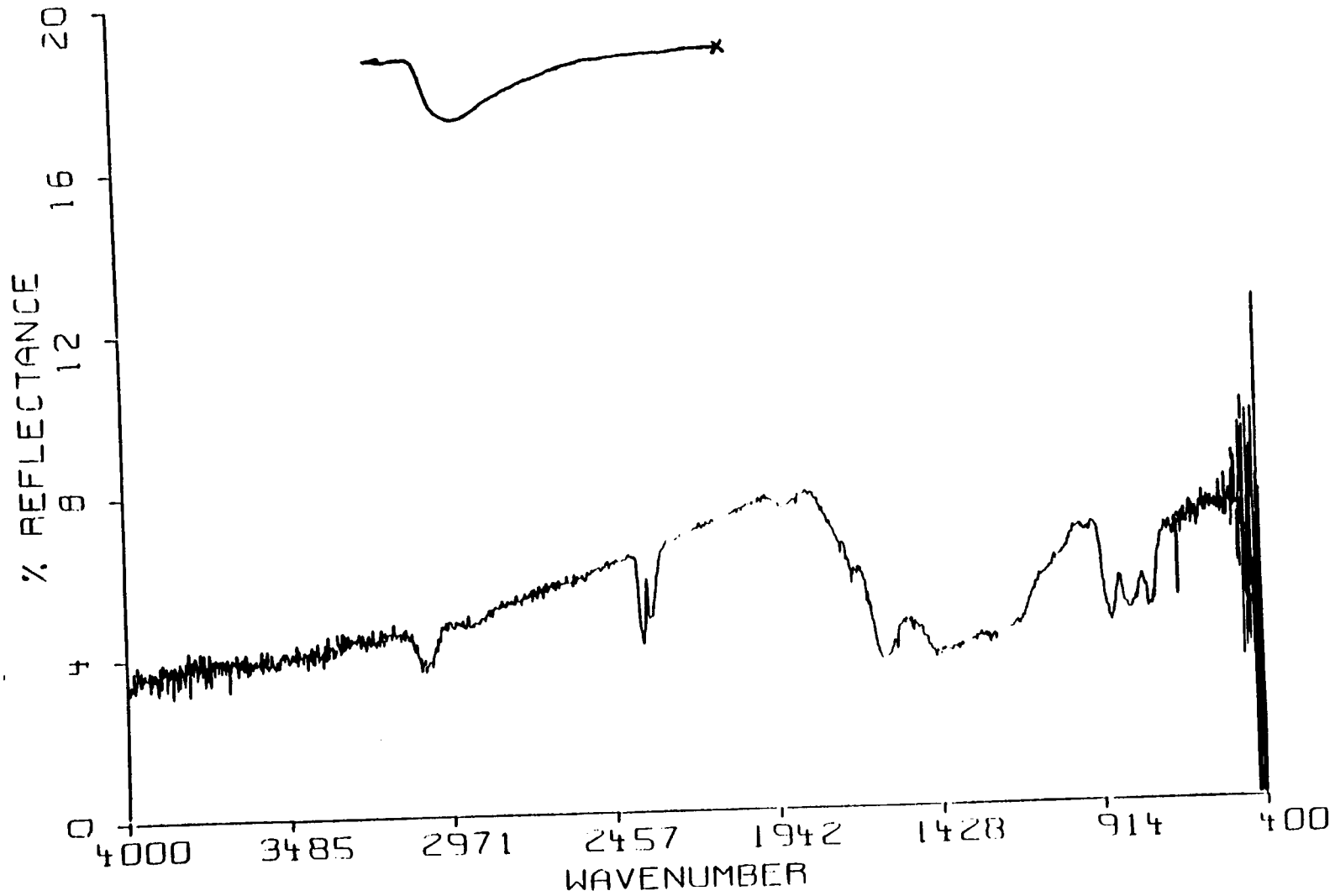

Figure 4.7f FTIR scan of the fifth char (black, temperature 550°C)

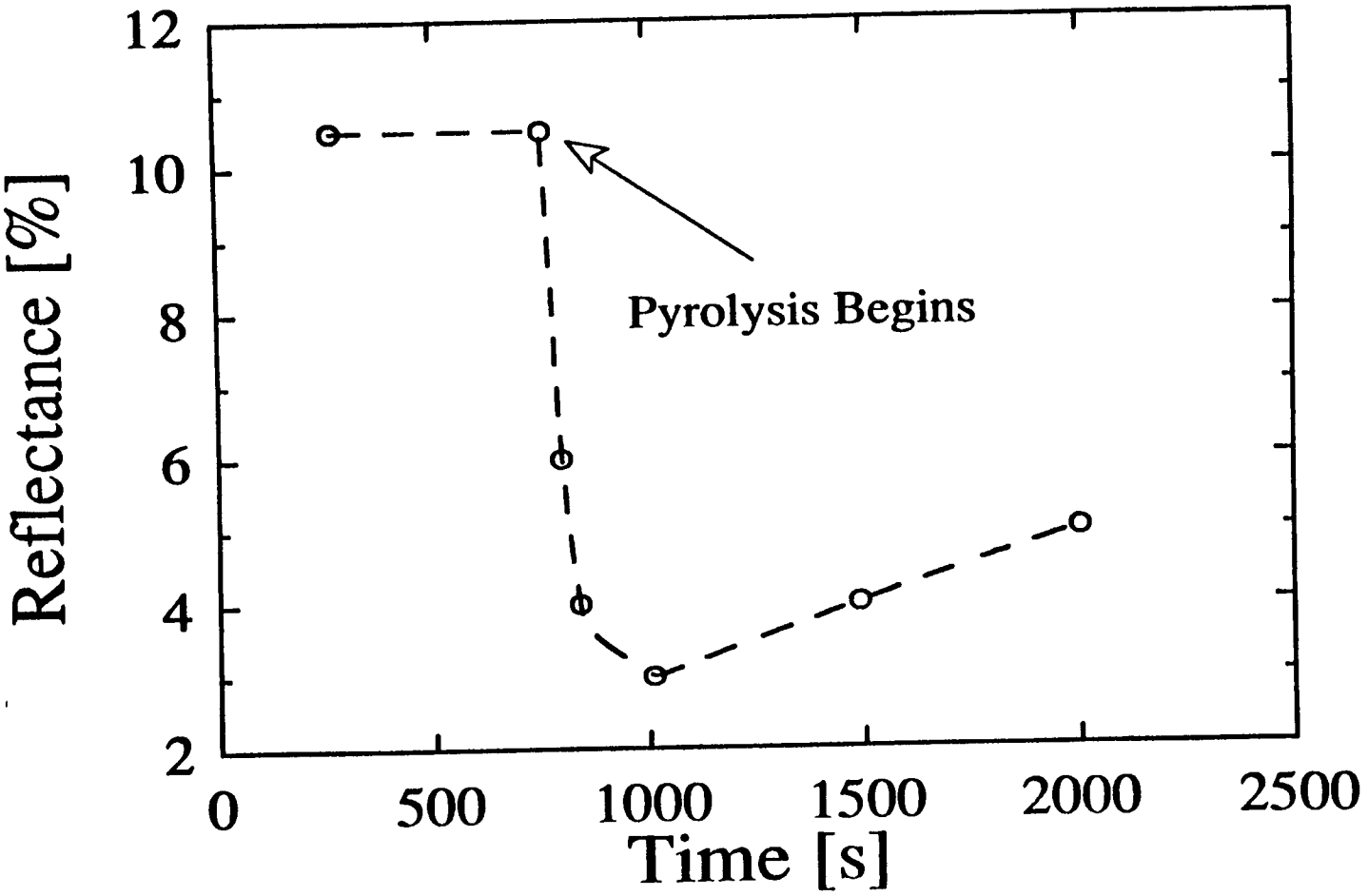

Figure 4.8 Surface reflectance as measured by FTIR as a function of time at which the cellulose char samples were taken

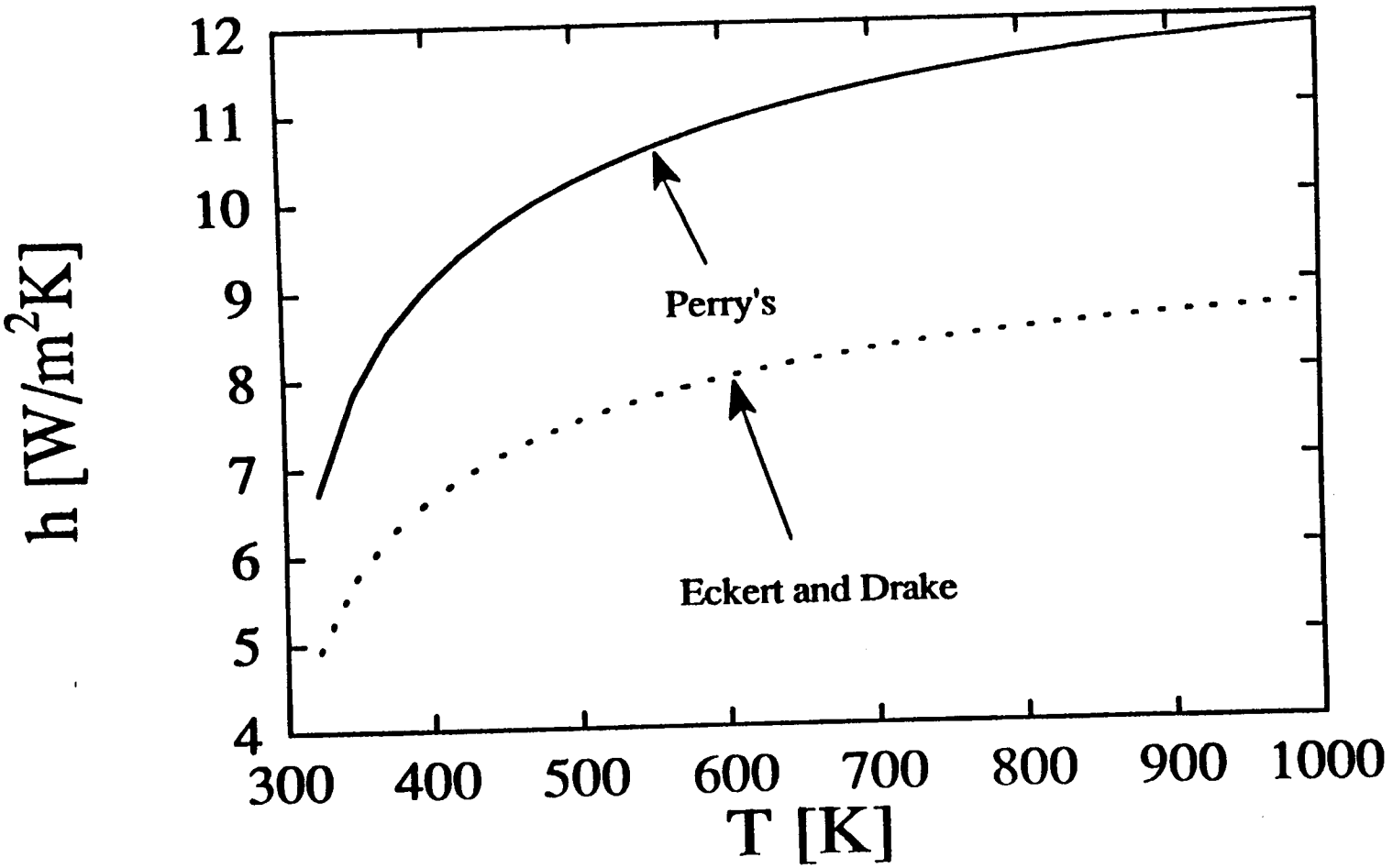

Figure 4.9 Heat transfer coefficient, calculated from correlations in Perry's Handbook (137) (Eq. 4.10) and from Eckert and Drake (53) (Eq. 4.10)

5. BEHAVIOR OF CELLULOSE IN A SIMULATED FIRE ENVIRONMENT

In this chapter the results obtained from experiments in the simulated fire apparatus are presented. It was noted previously that there are differences observed in cellulose pyrolysis under controlled conditions and under heat and/or mass transport limited conditions.

Several effects were explored here. The principal ones were the effect of the initial sample density and the incident radiative heat flux. The goal was to establish the differences in cellulose pyrolysis behavior under different heat and mass transfer conditions. The effects of other variables were also explored, including the effects of initial sample thickness, grain orientation and purge gas.

Sample face cracking or "alligatoring", commonly observed in the pyrolysis of wood and related materials, was not observed here in most samples. Cracking was observed only in samples that were not allowed to shrink radially. These were the samples that were embedded in ceramic in order to form a tight seal between sample and insulation. Although the situation that promotes sample face cracking is more representative of real fire behavior, the approach of embedding in ceramic was not followed here due to the continuation of ceramic curing at higher temperatures which influenced the mass loss measurement. In this work, the samples were positioned in pre-cured sample holders without any adhesives so that they were free to shrink during pyrolysis.

5.1 THE EFFECT OF INITIAL SAMPLE DENSITY

Three different cellulose sample densities were studied: 0.965±0.041 g/cm^3, 0.691±0.035 g/cm^3 and 0.458±0.026 g/cm^3. Samples were also made from oak blocks, with a density of 0.734 g/cm^3, and from pine blocks, with a density of 0.377 g/cm^3. These were used for comparison of mass loss behavior only; i.e., temperature profiles were not determined and gas analyses were not performed.

5.1.1 MASS LOSS BEHAVIOR

The sample mass was monitored continuously up to the time where no additional mass loss was observed under incident heat fluxes of 40 and 60 kW/m^2. Since it was difficult to reach this endpoint at lower heat flux levels, experiments were stopped 90 minutes into the experiments with an incident heat flux of 20 kW/m^2.

During this study, the "base case" incident radiative heat flux was 40 kW/m^2. For this reason, the data are generally presented for this case first. Figures 5.1, 5.2 and 5.3 show mass loss (5.1a, 5.2a and 5.3a) and fractional remaining mass (5.1b, 5.2b and 5.3b) as functions of time for all three density cellulose samples and for incident heat fluxes of 40, 60 and 20 kW/m^2, respectively. The purge gas flowrate was 15 l/min. After initiation of sample irradiation an initial heating period of several minutes in duration can be seen during which little mass loss takes place. Actually, some small amount of mass loss was always observed, even without heating (in Figures 5.1, 5.2 and 5.3 for heating times less than zero) due to the sample drying in the stream of dry nitrogen purging the chamber. The samples were handled in air and their equilibrium moisture content was a function of relative humidity on the day of the experiment. However, the moisture content was only on

the order of few weight percent, and thus it was not considered crucial to characterize it more precisely. Since the samples did dry in nitrogen during purging of the experimental chamber, and subsequently during initial heating, for practical purposes the samples were pyrolyzed in a dry state. Following the initial heating period, pyrolysis begins, as indicated by the rapid loss of sample mass. For the heat fluxes of 40 and 60 kW/m^2, the duration of rapid pyrolysis was about 30 min and 20 min respectively, while for the heat flux of 20 kW/m^2 the process required more than the 90 minutes allowed for an experiment.

Some observations can be made from Figures 5.1 and 5.2, for cases of pyrolysis under incident heat fluxes of 40 and 60 kW/m^2. First, the mass loss is approximately a linear function of time during the middle portion of pyrolysis. This implies that heat is being transferred inside the sample to a pyrolysis front with a constant propagation velocity. Theory (34) predicts that the propagation velocity of a thermal wave varies with the square root of time for constant temperature at the surface from which the heat propagates. The only variable that is kept constant here is the incident heat flux. As a result of the constant incident heat flux, the net heat flux and the temperature at the front surface vary continuously. When the material pyrolyzes, all of its properties also vary continuously. The data suggest that, under the conditions of interest here, heat is deposited at the front surface faster than it can be conducted away, so that the surface temperature rises continuously during the period of active pyrolysis. Thus even though heat must be conducted deeper into the sample as the pyrolysis wave moves in, the temperature difference increases at the same time, keeping the net gradient roughly constant. Therefore, the mass loss rate, which is determined by the rate of conduction, is roughly constant.

The time of pyrolysis onset depends on sample density. It can be seen from Figures 5.1a and 5.2a, and more clearly from Figures 5.1b and 5.2b, that the earlier pyrolysis starts, the

lower the sample density. It was shown in Chapter 4 that thermal diffusivity does not depend on density, but that thermal conductivity does. That is the reason for earlier pyrolysis onset in lower density samples. The lower density sample behaves as a better "insulator". Its front surface temperature rises faster, which results in an earlier onset of pyrolysis. This reasoning will be confirmed by front surface temperature measurements shown below.

The onset and, especially, the endpoint of pyrolysis can be more easily discerned by comparing the derivatives of the measured mass loss data from Figures 5.1b and 5.2b. These derivatives are shown in Figures 5.4 and 5.5 (5.4a; 5.5a - as functions of time and 5.4b; 5.5b - as functions of fractional remaining mass) for incident fluxes of 40 and 60 kW/m^2, respectively. The derivatives represent an instantaneous mass flux of volatiles from the solid matrix. It is clear from Figures 5.4a and 5.5a that pyrolysis begins earlier for the lower density sample. Another point, that is not as clear in Figures 5.1 and 5.2 is that the pyrolysis ends more quickly in the higher density sample. Since the thermal conductivity increases with sample density, the back part of a higher density sample is subjected to higher temperatures than the back part of a lower density sample under the identical conditions at the front surface.

It can be recalled that a constant pyrolysis wave propagation rate would seemingly require that the value of $[d(M/M_0)/dt]$ be constant, throughout active pyrolysis. The extent to which this is violated is seen in Figures 5.4 and 5.5. The maximum rate is always seen earlier in samples of lower density. This is because the low density samples have lower thermal conductivity. The lowest density samples are unable to supply heat to a propagating front, because of their lower thermal conductivity. The final back face temperature never gets as high as in higher density samples. This is why the lowest density samples do not pyrolyze

as quickly or completely as higher density samples. This explanation is supported by the actual temperature profiles, presented subsequently.

Figure 5.6a compares temporal changes of mass loss and its time derivative for a high density sample at an incident heat flux of 40 kW/m^2. It can be seen that at about 1000 seconds after initiation of heating, the mass loss curve appears to change slope, which corresponds to an inflection point in the mass loss time derivative. Figure 5.6b presents data similar to that in Figure 5.6a, but for a low density sample. As can be seen, there is no strong evidence of any change in slope; the curves are rather smooth.

The preceding results are important from a practical point of view. They indicate that the maximum mass loss rate, or maximum volatiles flux out of the solid matrix, depends on density and the incident heat flux, and that it can occur at the later stages of pyrolysis. For the middle density sample, the maximum mass loss rate is observed when 45% of the initial mass is already lost, and for the high density sample it is observed when 50% of the initial mass is already lost. The maximum mass loss rate occurs at similar conversions for incident heat fluxes of 40 and 60 kW/m^2, for the same density samples. For low density samples and an incident heat flux of 40 kW/m^2, a maximum loss rate could not be determined, and it occurred at about 15% of the initial mass loss for an incident heat flux of 60 kW/m^2.

The char yield is operationally defined here as the fractional mass left after the mass loss ceases under given conditions. Char yield can be very high in cases in which the pyrolysis was terminated by heat losses before the reactions go to completion. In particular, high char yields were observed in the case of pyrolysis under an incident heat flux of 20 kW/m^2. Table 5.1 summarizes all char yields determined in this work. It can be seen from Table 5.1 and from Figures 5.7 that the char yield is not a very strong function of initial sample

density. As a matter of fact, it can be seen in Figure 5.7a that it almost does not vary with initial sample density for the case of incident heat flux of 40 kW/m^2. In the case of higher incident heat flux (60 kW/m^2) shown in Figure 5.7b, the trend is more obvious; the char yield increases with the initial sample density. However, although the trend is obvious, the variation is not very large; the difference in char yields between low and high density is about 2%, similar to the case of 40 kW/m^2. The variation of char yield with density is more pronounced for the lowest incident heat flux (20 kW/m^2) shown in Figure 5.7c, where the difference in char yields between low and high density is about 10%. Nevertheless, it is clear from Figures 5.3 that the samples are far from completely pyrolyzed and that fact is reflected in the data from Figure 5.7c, which show much higher "char yields" than do the other cases. The above comment highlights the importance of carefully defining what is meant by "char yields". In the low flux case, the "char" actually contains quite a bit of material with significant volatile matter content, which can be released by longer heating or heating to higher temperatures.

The fact that density has a small influence on char yields could arise from a number of causes. It has already been pointed out that lower density chars are better insulators, and thus do not get as hot in their interiors as do higher density chars. This would mean that pyrolysis would be able to go to completion sooner in higher density samples, all else being equal. Since char yield actually seems to <u>increase</u> with density, this explanation cannot be responsible for the observed trends in Figure 5.7.

A more plausible explanation for the increase in char yield with density has to do with mass transfer limitations. When tars are released from the cellulose solid, they do not immediately enter the vapor phase. Rather, they must be transported through a hot char layer to the sample surface. A slight increase in char yield with initial sample density might

be due to tar decomposition as they pass over the hot char layer. As a result of tar decomposition, gases are formed and more char is deposited in the char layer. The higher the sample density, the more tars are formed per unit volume in the zone of active pyrolysis. Additionally, the higher the sample density, the more surface is available per unit volume for promoting what are likely heterogeneous cracking-type reactions. The char matrix between the pyrolysis zone and the front surface, can be viewed as a fixed bed reactor. That means that the amount of tars cracked during the contact with the char layer is proportional to the tar concentration and the residence time spent in contact with the char layer. In the higher density samples the residence time of tars in the char layer must be smaller, but the concentration of tars is higher. There are apparently more tars decomposed the higher the sample density, and that results in the higher ultimate char yields. The char yield dependency on initial sample density under controlled conditions will be addressed in more detail in Chapter 6.

Comparisons of mass loss profiles for different density cellulose samples, and also pine and oak samples, are shown in Figures 5.8. The results of Figure 5.8a are for experiments in which the grain orientation of the sample was perpendicular to the direction of the incident radiative flux and Figure 5.8b for the grain orientation parallel to the direction of the incident radiative flux. The data shown in Figures 5.8 are for an incident heat flux of 40 kW/m^2 and a nitrogen flow of 35 l/min. It should be noted that these data are different from the data represented in Figure 5.1a due to the effect of a different nitrogen flowrate. This difference is discussed below. The point that can be made here is that the mass loss profiles of wood samples are similar to those of cellulose samples. Again the effect of density on the time of pyrolysis onset can be seen here. From these data it seems that pressed cellulose samples can be used as a reasonable model material for the investigation of wood-like behavior in a simulated fire, at least insofar as mass loss behavior is concerned.

5.1.2 TEMPERATURE PROFILES

An attempt was made in the design of the experimental system to assure that the pyrolysis would be unidimensional. The lamps were arranged to try to illuminate the entire sample surface as uniformly as possible. The edges of the samples were insulated with ceramic to minimize heat losses. Still, the ideal of one-dimensional behavior could not be realized in practice. It was observed that pyrolysis always started in the middle of the upper half of the sample, about 10 mm from the center in the vertical direction, and centered in the horizontal direction. When this visual observation is compared to the flux profile presented in Figure 3.5 (the point in question is at x = 0 and y = 10 mm), it is noticed that pyrolysis does not begin in a zone of higher incident heat flux. The reason for the off-center start of pyrolysis at the point of highest local temperature is convective heat loss from the lower half of a sample. Heat losses to the ceramic holder must be present, otherwise pyrolysis would start at the very top of a sample if there were only convective losses. Figure 5.8 shows the radial temperature profiles in the vertical direction, taken at 4 mm from the front surface, at about 320°C and 525°C, respectively (y corresponds to the vertical coordinate, the same as shown in Figure 3.5; positive is in upward direction from the sample center). Indeed, it can be seen that the radial temperature profiles exhibit some rather interesting features. Before pyrolysis begins, for a surface temperature of 320°C, the inner part of the sample is at relatively constant temperature and the part of the sample closer to the edges is at a slightly lower temperature. It cannot be said that there are large heat losses to the upper side of the sample, judging from the temperature profile for a surface temperature of 320°C. For a surface temperature of 525°C (essentially a char radial profile), in the zone of higher heat flux the temperature is higher, and it drops fairly steeply closer to the edges, despite the fact that the lower edge is in the zone of higher incident heat flux. Likewise in the upper part of the sample, the temperature decreases as the edge is approached, but not as dramatically as

in the case of the lower edge.

The existence of a radial temperature profile means that the situation in the simulated fire apparatus does not truly represent a one-dimensional system. A visual inspection of the samples when pyrolysis was terminated revealed the existence of a meniscus - like pyrolysis front. A photograph of high density samples that were partially pyrolyzed at incident heat fluxes of 60, 40 and 20 kW/m^2 is shown in Figure 5.10. The pyrolysis was terminated when the thermocouple positioned at about midway along the sample reached 350°C. This means that the pyrolysis was conducted for different lengths of time for different incident heat fluxes. It can be seen that the meniscus is the most pronounced for the case of low incident heat flux, where a higher fraction of incident heat flux conducted into the sample is being lost to the sides. Although it was found that the present system does not fully represent a one dimensional heat transfer situation it will be shown more quantitatively later that the heat losses to the sides do not necessarily play an important role in determining the course of the process.

The more important temperature profiles for current purposes are the in-depth profiles. Except where noted otherwise, the profiles are measured near the centerline, where radial profiles were the smallest. Temperatures were measured at different distances from the front heated surface for all three sample densities at all three incident heat fluxes. These data are displayed in Figures 5.11, 5.12 and 5.13, respectively for high, medium and low density samples. Each of the figures is divided into three parts (a, b and c) which represent temperatures as functions of time in a sample heated with incident heat fluxes of 40, 60 and 20 kW/m^2, respectively. The general temperature profiles are very similar for all densities. The front heated surface temperature as a function of time curve always shows an inflection point at around the pyrolysis onset temperature. The obvious reason for this is that as

cellulose decomposes, the material properties (surface emissivity and thermal conductivity) change, and a reaction endotherm occurs. The question remains whether there is one particular property that is the most responsible for this behavior.

From Figures 5.11, 5.12 and 5.13, the portion of the temperature versus time curve in the vicinity of the inflection point looks similar for different densities and the same incident heat flux, but it looks different for constant density and different incident heat fluxes. The rate of temperature increase after the inflection point is higher, the lower the incident heat flux. The data suggest that the surface emissivity change might most influence the temperature profile around the inflection point. It should be recalled that the reflectivity of the surface drops sharply as it begins to pyrolyze, so the effective flux increases at that time. Figure 5.14a shows a comparison of the surface temperatures of three different density samples at a constant flux. Clearly the inflection point is associated with the same type of process in the sample, irrespective of density. The point at which the slope begins to increase sharply again corresponds well to the temperature of most active pyrolysis, as discussed below. It appears unlikely that the inflection point is associated with either a strong endotherm or a change in thermal transport properties, since the strongest evidence of the effect is seen only at the surface. It appears that the disturbance propagates into the sample, as would be expected, generally in much attenuated form, and appearing at a lower temperature than at the surface. This argues strongly against the inflection being associated with a reaction endotherm, although care must be exercised in drawing this conclusion because of the very complex thermal nature of the cellulose pyrolysis process (see below). It will be shown that the strength of the endotherm increases with heating rate. This means that, if the endotherm were the principal cause of the inflection point, one would expect that at higher heat fluxes (or higher surface heating rate) the inflection point would be more pronounced, which is not the case from the data shown in Figures 5.11, 5.12 and 5.13.

The argument for relatively constant mass loss rate with time can now be re-examined with the aid of temperature profiles from Figures 5.11, 5.12 and 5.13. Rapid pyrolysis can be assumed to begin at temperatures above 300°C, as indicated by the appearance of the inflection point in the surface temperature versus time curves. The thermal wave propagates with a relatively constant average velocity up to about 300°C, at least for the front part of a sample, as shown in Figure 5.11d. Since the mass loss rate is proportional to the absorbed heat flux ($=-k\partial T/\partial x$), and since k=constant, then $\partial T/\partial x$=const. During the period of nearly constant mass loss rate, the temperature gradient must be maintained. This happens as a result of an increase in surface temperature, the deeper the wave penetrates. If the surface temperature climbs to levels at which convective/radiative losses do not permit further increase, the constancy of $\partial T/\partial x$ cannot be maintained, and the mass loss rate decreases with time. This is what happens in the low density samples, which are the ones in which surface temperature climbs to the highest values.

Temperatures in the back half of a sample (i.e., more than 5 mm from the front surface) for an incident heat flux of 60 kW/m^2 exhibit interesting behavior, especially in the cases of high and medium density samples. Temperatures start to rise quickly above about 300°C, followed by a rather abrupt change in the rate of temperature increase. This does not involve the propagation of the surface disturbance into the sample, since as Figures 5.11b, 5.12b and 5.13b show, the strength of the inflection grows with depth. The temperature at which it occurs is again very near the pyrolysis temperature of cellulose. There are two possible explanations.

The first explanation for the in-depth temperature inflections is that as a result of severe pyrolysis conditions, the samples have a greater propensity to cracking. The cracks develop

in a direction perpendicular to the flux. If a crack develops immediately ahead of the pyrolysis front, then the effective thermal conductivity of the sample can be strongly influenced by radiative processes, within the sample. The same explanation would then apply in this case as applied in the case of the surface temperature inflection. As the cellulose ahead of the crack begins to pyrolyze, its emissivity increases, and the effective thermal conductivity increases.

There is, however, a second explanation for the in-depth inflections in the temperature profiles. Careful examination of Figures 5.11b and 5.12b shows a second inflection near 100°C. This inflection can only be associated with endothermic moisture loss, and thus gives another clue to the nature of the higher temperature inflection. When pyrolysis products are formed, they can diffuse out, towards the front of the sample or diffuse backwards towards the back. The latter process is not normally favored, but when mass evolution becomes very rapid, as at high heat fluxes, then the volatiles may have difficulty in escaping through the front face. Backward diffusion, into the cold, unpyrolyzed sample can occur, and the products can condense ahead of the pyrolysis front. When the temperature in the back part of the sample becomes high enough, the condensed pyrolysis products start to re-evaporate and/or decompose, with an endothermic heat effect, causing the temperature to rise slower at that point. As soon as the evaporation and/or decomposition is completed, the temperature rises quickly to the temperature that would have occurred if there were no endothermic disturbances. Since there is no particular reason to postulate two different mechanisms for the in-depth inflections, the conclusion is that the evaporation mechanism is responsible.

The effect of density on surface temperature can be seen from Figure 5.14a, for three different density samples heated at an incident heat flux of 40 kW/m^2. Figure 5.14b, shows the back surface temperatures of three different density samples heated at an incident heat

flux of 40 kW/m^2. Again, the difference in thermal conductivities among different density samples is responsible for the highest front surface temperature to be the highest for the lowest density sample, while its back surface temperature is the lowest. The lower density sample, again, represents a better insulator than the higher density sample.

Pre - pyrolysis temperature profiles for three different sample densities and the incident heat flux of 40 kW/m^2 (200 s of heating) are shown in Figure 5.15. The error bars for temperature are determined by the manufacturer's (Omega) limits of error specification for chromel - alumel, K - type, thermocouples, which is the greater of $\pm$2.2°C or $\pm$0.75%. The error bars for distance were determined by the inability to position a 0.5 mm thermocouple probe to better than $\pm$0.25 mm. Unfortunately, the actual position and hence the error limit, could have been judged only from the side of a sample from which the probes were inserted into the sample. Obviously, there might have been other positioning errors, not accounted for. However, it seems from the temperature profiles shown in Figure 5.15, that the unexplained errors are the largest for the lowest density sample. This is reasonable since the probability of a probe accidentally moving during insulation and positioning of the sample inside the experimental chamber is largest for the lowest density sample, due to its structural weakness.

Since the data set here is the same as shown in Figures 5.11, 5.12 and 5.13 the above noted difference in front and back surface temperatures, due to different thermal conductivities, can be also seen here. Overall, the profiles appear similar and the differences in temperatures are not very large. This means that the heat transfer processes are similar for different density samples, at least prior to the onset of pyrolysis.

Char temperature profiles are shown in Figure 5.16a for a heating time of 2500 s under an

incident heat flux of 40 kW/m^2 and three different sample densities. In addition to the thermocouple positioning uncertainty, in this case there are also errors introduced by sample shrinkage during pyrolysis and by thermocouple movement inside the char layer, due to the structural weakness of the char. Pyrolysis caused samples to shrink and the relative positions of thermocouples changed. Since the thermocouples were always relatively stationary due to the rigidity of the probes (0.5 mm in diameter), they could easily break the char structure and change their relative position. Unfortunately, the uncertainties introduced by thermocouple movement were always observed, but there was no way to estimate the ultimate position. The post - pyrolysis samples were extremely brittle, and removing the thermocouple probes usually resulted in destroying the sample without any possibility of determining where the thermocouples actually were at the end of pyrolysis. We did not have access to in-situ X-ray equipment, as has been used by others.

Estimates of the shrinkage were made by assuming uniform shrinkage of the entire sample from the front, and the original distances from the front surface were correspondingly decreased. The recession of the front surface was directly measurable from the measurement of the sample surface relative to the ceramic holder. A typical value of total surface recession was 4 to 5 mm, depending on the incident heat flux. The corrected distances were then calculated using the scaling factor:

(Original Sample Thickness - Recession)/(Original Sample Thickness)

The resulting correction is shown in Figure 5.16b, which represents the same data of Figure 5.16a with corrected distance from the front surface. The fundamental shape of the profiles is not significantly changed. Although the appropriateness of this correction is arguable, the general appearance of the profiles points to some differences due to density. The front and back surface temperatures are again consistent with the variation of conductivity with density. All the data support the proposition that thermal conductivity is

highest, and thus the temperature gradient lowest, in the high density sample.

An interesting comparison of behavior of different density samples can be made by plotting the temperature profiles at the same fractional mass loss. This comparison is shown in Figure 5.17 for three density samples and an incident heat flux of 40 kW/m^2. The profiles shown are for different real times, but for 20% mass loss in all cases. The data indicate that for the same fractional mass loss, the temperature in the low density sample is the highest. The difference is also illustrated using the data shown in Figure 5.18, which represent fractional mass loss as a function of front surface temperature. One would expect that the kinetics of decomposition do not depend on sample density, and, indeed, that is seen in Figure 5.18. Although the surface temperatures are different at different real times, the onset of pyrolysis occurs at approximately the same temperature for all three different density samples. Further mass loss follows a different pattern in the different density samples, not because the pyrolysis kinetics are different but because of different heat transfer within the sample. That in turn means that the reason for the different temperature profiles in Figure 5.17 at the same fractional mass, is not a difference in kinetics, but rather heat sink-related. This hypothesis is supported by Figure 5.19, which shows the same data presented in Figure 5.17, but normalized with the initial sample density. The term $x \rho_0$ (distance multiplied by sample density), in fact represents initial mass per unit area up to the distance x. Thus normalization brings the profiles closer together, which means that the reason for their initial discrepancy was somehow volumetric mass related. In other words, if one takes into account the mass per unit volume, the temperature profiles are scaled (except near the back face, where the heat losses cause difficulties). The fact that there is a scaling with mass is not surprising. Both the endothermic heat of pyrolysis and the heat capacity are proportional to mass, so it is apparent that a heat sink explanation is appropriate (the relative contribution of reaction enthalpy and specific heat is discussed below). Since Figure 5.19 shows profiles at a constant extent of mass loss, the profiles

would be expected to come together at a characteristic temperature of pyrolysis (somewhere between 300 and 350°C), at a pyrolysis front, here seen to be near $x\rho_0 \approx 2$ or 3 mm g/cm^3. The amount of sample pyrolyzed is proportional to $x_F\rho_0$, where x_F is the position of the pyrolysis front. The total mass of sample is $L\rho_0$, where L is the thickness. Then M/M_0=constant means (x_F/L)=constant, and this in turn means that the value of x_F is the same in all density samples, since L is the same for all. Since L≈10 mm for all, $x_F \approx 2$ to 3 mm for all these cases (since the sample does not completely volatilize, it is clear that $x_F > 2$ mm).The scaling is then effectively a scaling of the time it takes for a particular point in the solid to reach the pyrolysis temperature. The higher the density, the longer the time. This is a consequence of both the larger heat sink in the higher density material, as well as the higher thermal conductivity (the latter since higher conductivity implies a greater ability to conduct heat away into the colder interior). This analysis will be formalized in a later section.

5.1.3 GAS ANALYSES

Analyses of gases evolved during pyrolysis were performed by gas chromatography, as described in Section 3.2.6. A gas sample was collected into a tube of 20 ml volume, at a flowrate of 200 ml/min during sampling. The sampling line itself was purged between sample collections with a flowrate of 10 ml/min. Consecutive samples were taken at 200 second interval. The gases were collected after the tars were trapped, using the 20 ml chamber in front of the sample loop (Figure 3.10). Analyses were performed for pyrolysis products under incident heat fluxes of 40 and 60 kW/m^2. The analyses were not done for conditions of 20 kW/m^2 incident heat flux due to the very low rates of mass loss, and, therefore, very low gas production rate. The sensitivity of the gas chromatograph was not sufficient for analyses of evolved gas under these conditions.

Figures 5.20 to 5.24 show results from the gas analyses of the volatile products of pyrolysis under an incident heat flux of 40 kW/m^2. One data point represents a single analysis from a sample collected at the indicated time. The data points on each figure were obtained from at least four different experiments, and show the extent of reproducibility. The trend lines are obtained by least squares weighted smoothed curve fitting of the data. The data for carbon dioxide are presented in non-normalized form, whereas the rest of the data are presented in normalized form with respect to carbon dioxide concentration. Although the carbon dioxide concentration is presented in non - normalized form, it should be noted that it does not represent the absolute carbon dioxide concentration in the volatiles evolved from a sample, but rather the amount in the mixture of gases withdrawn from the 20 ml chamber. This also included nitrogen, i.e. the purge gas.

All the data are presented as a function of real time (zero corresponds to the initiation of radiative heating), or as a function of fractional unreacted mass of sample. The data were not corrected for the lag time that a sample needs to reach the sampling tube. The volume of the sampling line was estimated to be about 10 ml (2 m of 1/8" tubing and the tar trap of 20 ml, packed tightly with the quartz wool). This means that the transit time in the sampling line was about 3 seconds at a flowrate of 200 ml/min, which is about 0.1% of the total pyrolysis time under an incident heat flux of 40 kW/m^2, and about 0.15% of the total pyrolysis time for an incident heat flux of 60 kW/m^2. This means that, for all practical purposes, no correction for sampling time itself is required.

Figures 5.20a to 5.20d present carbon dioxide concentrations for three different density samples. It can be seen that the higher the density, the later the initiation of carbon dioxide evolution. This is consistent with both the mass loss data and the temperature

measurements. This clearly indicates that the time of pyrolysis inception is a function of heat transfer conditions. How fast the heat deposited at the surface (at the same rate for all different density samples) can be conducted into the sample depends on sample density. The higher the density of a sample, the higher its thermal conductivity, and the faster heat is conducted into the sample. Thus the surface temperature rises more slowly, which results in a slower onset of pyrolysis, and delayed evolution of carbon dioxide.

It should be recalled that the percentage of total gaseous product indicates a relative rate of release. Again, the sampling line was continuously purged with the gaseous pyrolysis products at a flowrate of 10 ml/min. At the time of sample collection, the flowrate of gas through the sampling line was 200 ml/min. The between - samples purge of 10 ml/min is not sufficient to allow the gas analysis to occur on a truly "instantaneous" basis. For example, the evolution rate of all volatiles is on the order 10^{-2} g/sec in the high density samples. This means that if the volatiles have an average molecular weight of order 100 Daltons, then 10^{-4} mol/sec are evolved, implying a volumetric rate of somewhere between 180 to 240 ml/min, depending on the temperature of the volatiles mixture. This is more than an order of magnitude greater than the externally applied purge rate (10 ml/min). On the other hand, based on the purge rate imposed by the gases themselves, the residence time of gases in the small sampling chamber is no more than of order 10 seconds, so from this perspective the sampling is "instantaneous", on the time scale of the pyrolysis experiment. Thus the percentage of CO_2 in the gas indicates its relative evolution rate.

From Figure 5.20d it can be seen that carbon dioxide concentration rises sharply during the initial stages of pyrolysis, indicating that carbon dioxide is a primary product of pyrolysis. An interesting phenomenon can be observed as the pyrolysis proceeds. The evolution rate of carbon dioxide from the low density sample seem to exhibit two peaks; one early in the

process (near 750 seconds) and the other midway through the process (near 1500 seconds). The evidence for the peaks is, however, not strong (see Figure 5.20a). The existence of the two peaks is arguable, but the fact that the rate goes through peaks earlier than in higher density samples seems clear. The observed peaks are consistent with the mass loss data. A comparison of mass loss rate data and the carbon dioxide concentration data are discussed below.

Figures 5.20e to 5.20h present the same data as in Figures 5.20a to 5.20d, except as a function of fractional sample mass remaining. Plotting the data in this manner, as opposed to the manner of Figure 5.20d, has the effect of scaling the results to a more comparable basis. Pyrolysis is completed more quickly in lower density samples because there is less mass to pyrolyze. The differences in temporal behavior evident in Figure 5.20d are partially removed in Figure 5.20h. The high degree of comparability in the early behavior of all three density samples, as visible in Figure 5.20h, gives some confidence to the hypothesis that the rate of the pyrolysis process is determined by heat transfer, as discussed above. It should be recalled that the measured CO_2 concentrations are for a mixed purge and volatiles stream. Since the purge rates were kept constant for all densities, a comparison of CO_2 concentration gives a rough indication of relative yields. There is an apparent sample density effect on CO_2 yields. The higher the density, the greater the volatiles flowrate relative to chamber purge rate, and thus the higher the CO_2 concentration. Additionally, there is a sample density effect on the cracking of primary volatiles to gaseous products, CO_2 included. This effect is explored in more detail in connection with the result of the TGA studies of pyrolysis, as shown in Figure 6.4. The effect of cracking processes is greatest in the highest density samples. There are thus two reasons for higher CO_2 yields with higher densities. The two possible explanations for the differences in CO_2 patterns can be investigated by examining evolution patterns for other gases as well.

If the hypothesis concerning dilution by purge gas is correct, then the molar ratios of other gases to CO_2 should not show "unusual" behavior, relative to the other lower density samples (the presumption being that a basic change in the pyrolysis process itself due to cracking would be reflected as a change in product gas ratios). It will be seen below that such shifts are not seen, and the effects of purge diluent are responsible for what is seen in Figure 5.20h.

Figures 5.21a to 5.21d present carbon monoxide concentrations to carbon dioxide ratios as functions of time for three different density samples. It appears that carbon monoxide begins to evolve at the same time as carbon dioxide. At early stages of pyrolysis, the CO/CO_2 ratio is less than unity. As the process proceeds, the ratio becomes greater than unity. There are two possible explanations for this pattern, which is evident for all three densities. Both have to do with the differences in routes of formation of these products. If both are primary products of pyrolysis, then the trend is attributable to the difference in kinetics of evolution of CO and CO_2. There is also the possibility that the later appearing product, CO, is a product of secondary reactions, as for example through:

$$C + CO_2 \rightarrow 2\,CO$$

in the char layer. It is doubtful that this reaction is fast enough at the temperatures of interest here to play much of a role; generally the rate of this reaction is not high below 600°C (196).

An interesting feature can be seen in Figures 5.21a - 5.21d at long pyrolysis times. The ratio of carbon monoxide to carbon dioxide decreases for the low density sample, remains unchanged for the middle density sample, and increases for the high density sample. Similar behavior was observed for the rest of the gases.

Figures 5.21e to 5.21h show the same data as in Figures 5.21a to 5.21d, but as functions of fractional sample mass remaining. It can be seen from Figure 5.21h that the ratio of carbon monoxide to carbon dioxide exhibits a moderate increase between fractional sample mass remaining of 0.8 and 0.4 in the low density sample, whereas the ratios for middle and high density samples remain relatively unchanged. The ratio for the middle and high density samples, during the middle portion of pyrolysis, stays relatively constant, which seems to suggest that the thickness and density of the char layer does not affect the proportion of carbon monoxide to carbon dioxide. Again, this argues against secondary reaction processes involving conversion of CO_2 to CO. In addition, the CO/CO_2 ratio for the high density sample is quite similar to that of the middle density sample. Thus, there is no evidence of a different pyrolysis pathway in the high density sample, and it is concluded that the apparently higher yields of CO_2 in the high density samples were due solely to higher evolution rates.

Figures 5.22a to 5.22d present ethane concentrations normalized with respect to carbon dioxide concentration for the three different density samples. It can be seen that ethane is not a major product; its amount relative to carbon dioxide is quite low, about few percent. The evolution of ethane starts slightly after the evolution of carbon dioxide begins. There are two primary possibilities for early ethane evolution. One would be that ethane represents one of the products of primary pyrolysis (or if it arises from secondary reactions, it does not need a very thick layer of char to be decomposed). The second possibility is that tars are actually decomposed in the gas phase in front of the sample surface, in the gap between the sample and the radiative heaters. This second possibility is discussed below.

From the comparison in Figure 5.22d, the densities of the samples have a significant

impact on the evolution of ethane. The data in Figures 5.22a to 5.22c show the differences to be attributable to more than just scatter. There is a possibility that ethane is a product of tar cracking and that those reactions are affected by the thickness and the density of the char layer.

The comparison of trend lines as functions of fractional mass remaining are presented in Figure 5.22h. It seems that while significant differences exist between the three samples, there is no clear trend with density. Ethane is a later, minor product in all three cases.

Figures 5.23a to 5.23h show the amount of ethylene normalized with respect to the amount of carbon dioxide. The general conclusions are the same as for ethane. Ethylene represents an even smaller fraction of the total gas composition than ethane.

Figures 5.24a to 5.24h display methane concentrations normalized with respect to carbon dioxide concentrations. These data should be viewed with caution, especially insofar as the numerical values are concerned. There was a problem in methane analyses in the setup of the gas chromatograph used. Methane starts to come off the column shortly after nitrogen, the major component of the gas mixture. That introduced a problem for peak integration, since the shape of methane peak also depended on the shape and size of nitrogen peak. Still, the scatter of the data in the cases of low and high density samples is no worse than for the other gases; only the middle density results were unusually scattered. It can be seen from Figures 5.24 that the methane-to-carbon dioxide ratio trends look somewhat similar to those for the other gases. As for other hydrocarbon gases, CH_4/CO_2 ratios increased sharply late in the pyrolysis of high density samples.

Figures 5.25 to 5.29 present results from the gas analyses of the volatile products of pyrolysis under an incident heat flux of 60 kW/m^2. Essentially, there is no new information

in these plots; the data appear similar to those shown in Figures 5.20 to 5.24. Some observations, however, can be used for clarification of hypotheses described above.

The existence of two peaks in carbon dioxide concentration and their shift in real time with density are also exhibited during pyrolysis under higher incident heat flux. This is consistent with the mass loss rate data, shown below. The completion of pyrolysis appears to be more sudden the higher the sample density. The data for higher incident heat flux suggests that there are no differences among the three density samples. The obvious difference is seen only in the concentration of carbon dioxide, and again this does not represent the effect of sample density, but the effect of the total sample mass. This is also confirmed by the molar ratios of carbon monoxide, ethane and ethylene to carbon dioxide. There is, it might be said, remarkable similarity among the molar ratios of the different density samples. The only gaseous product for which differences can be seen is methane. Again by virtue of the difficulty with peak integration, these results do not yield definitive conclusions, especially since the methane concentration represents the only "outlier" among the five gaseous pyrolysis products.

5.2 INCIDENT HEAT FLUX EFFECT

In this chapter the effects of different incident heat fluxes will be discussed.The same data will be used as in Section 5.1, but viewed from the perspective of incident heat flux. As before, three different incident heat fluxes were used: 20, 40 and 60 kW/m^2. It should be emphasized that the incident heat fluxes were chosen to simulate the feedback from a flame to the surface. For example, for sustained combustion of wood (fir) it was determined that the surface should receive a net heat flux of 25 kW/m^2 (113), which means that for surface emissivity of 0.5, the incident heat flux should be about 50 kW/m^2. The incident heat flux

of 20 kW/m^2 was chosen in order to examine this behavior, which is well below the sustained combustion threshold level.

5.2.1 MASS LOSS BEHAVIOR

Figures 5.30 through 5.32 show mass loss (a) and fractional mass loss (b) as functions of time for low, medium and high density samples, respectively. The results might already be anticipated. The higher the incident heat flux, the earlier pyrolysis starts and finishes. In the case of pyrolysis with an incident heat flux of 20 kW/m^2, at the time when the experiments were terminated, the observed mass loss was 3 to 4 times smaller than in the cases of pyrolysis with higher incident heat fluxes. Of course, this was because the lower the incident heat flux, the less heat is available for conduction into the sample interior. Thus its temperature rises more slowly, and the kinetics of decomposition are slower. It will be shown later in Chapter 6 that the range of temperatures over which cellulose "rapidly" decomposes on the time scale of these experiments, is fairly narrow; typically about 50°C, provided that there are no transport limitations. A large part of a sample, pyrolyzed at an incident heat flux of 20 kW/m^2, actually never reaches the temperature required for "rapid" pyrolysis to occur. This can be seen in Figure 5.33, which compares temperature profiles in the three different flux cases. Using the range of 300 to 350°C to indicate rapid pyrolysis conditions (i.e., conditions under which pyrolysis goes to "completion" in at most a few minutes), it is clear that only in the 20 kW/m^2 case are these values not attained in a significant fraction of the sample. This means that the time scale-defining factor in the case of pyrolysis under an incident heat flux of 20 kW/m^2 may actually be the kinetics of decomposition, simply because the externally applied heat flux is not high enough to provide the required temperatures for rapid pyrolysis. The process at 20 kW/m^2 is, however, still conduction limited, in part, because the front of the sample can achieve

sufficiently high temperatures to be in the rapid pyrolysis regime. As the thermal wave penetrates, the process passes from heat transfer-limited to kinetic rate-limited. If this hypothesis is correct, then the case of cellulose pyrolysis under an incident heat flux of 20 kW/m^2 will not fit into the same dimensionless pattern as the case of pyrolysis under the other two, higher, incident heat fluxes. The data are presented in dimensionless form in Section 5.3 where it is shown that the pyrolysis under an incident heat flux of 20 kW/m^2 indeed does not follow the pattern.

As noted above, the experiments with the 20 kW/m^2 surface flux were terminated before the samples were fully pyrolyzed. The mass loss rates at the time when the experiments were terminated were lowest for lowest density samples. This was also expected. This is again because the back face of the sample is coolest for the low density material.

The ultimate char yield decreases with increasing incident heat flux, as indicated in Table 5.1. This is consistent with findings in the literature that an increase in the severity of pyrolysis conditions results in a decrease of the ultimate char yield. It is also consistent with the observations in the present work, for pyrolysis under controlled conditions (to be discussed in Chapter 6).

Overall, pyrolysis proceeded in a relatively predictable pattern for different incident heat fluxes. From the data shown in Figures 5.30 through 5.32 it is confirmed that pyrolysis is governed by the ability of the thermal wave to penetrate into the sample, with the possibility that slower thermal wave penetration might not be the only reason for slower pyrolysis under incident heat flux of 20 kW/m^2.

5.2.2 TEMPERATURE PROFILES

Figures 5.34a, b and c show temperature profiles for the three different incident heat fluxes and for three different sample densities, at 200 seconds of heating. It can be seen that the higher the incident heat flux, the steeper the temperature gradients ($\partial T/\partial x$). This is reasonable, since the thermal conductivity is the same for constant sample density and the only difference is the heat flux available for conduction. The profiles resemble those that would be seen in any inert material heating under variable heat flux conditions. Although the temperature in the first few millimeters of a sample heated at an incident heat flux of 60 kW/m^2 is above the pyrolysis temperature, and a thin char layer is already present between the surface and unpyrolyzed material, there is no evidence of an abrupt change in the profile. This suggests that the char layer does not influence the temperature profile significantly, at least in the early stages of pyrolysis, apparently because there is no very abrupt change in thermal properties.

The surface temperature in samples pyrolyzed with an incident heat flux of 20 kW/m^2 is about 50°C lower than in samples pyrolyzed with an incident heat fluxes of 40 kW/m^2 and about 250°C lower than that pyrolyzed with a 60 kW/m^2 flux. It should be recalled that a 50°C difference in cellulose pyrolysis represents a major temperature difference, since the pyrolysis proceeds over a very narrow temperature range.

Steady-state temperature profiles are shown for three different incident heat fluxes and for three different densities, respectively, in Figures 5.33a, b and c. Again the reason for the very slow pyrolysis of a sample heated with an incident heat flux of 20 kW/m^2 is obvious. If rapid pyrolysis starts at temperatures between 300°C and 350°C it can be seen that approximately two thirds of a sample never gets to that temperature range. The pyrolysis

proceeds, but at a very low rate below this range of temperatures. It can be easily calculated, by integration of Arrhenius type (isothermal) kinetic expression for a first order reaction, that the time for mass decrease from an initial mass, M_0, to some other mass, M, is:

$$t = -\frac{\ln\left(\frac{M - M_f}{M_0 - M_f}\right)}{A \exp\left(-\frac{E_a}{RT}\right)} \qquad (5.1)$$

where:

t - time

M_f - final mass

M_0 - initial mass

A - pre-exponential factor

E_a - the activation energy

R - universal gas constant

T - temperature

Using an activation energy of E_a=212 kJ/mole (50.7 kcal/mole, a reasonable value, as will be shown later), a pre-exponential A = 5.59×10^{15} s^{-1} and an ultimate char yield M_f=20%, in order for material to lose 70% of its original mass at a constant pyrolysis temperature of 250°C, it can be calculated from expression (5.1) that it would take about 6 days and 15 hours. This is much longer than the time scales of experiments performed here. For 350°C, the time required is only on the order of one minute. Therefore, the pyrolysis under incident heat flux of 20 kW/m^2 appears different mainly due to the low externally applied heat flux, which causes temperatures to rise only to low levels.

With the temperature profiles shown in Figures 5.33 and 5.34 it is possible to roughly

estimate the radial heat losses from the sample. From the radial temperature profile at 4 mm from the front surface of a sample heated with an incident heat flux of 40 kW/m^2 (Figure 5.9), the temperature gradient in the radial direction ($\partial T/\partial r$) can be estimated. The estimate was made for the upper half of the sample ($y>0$), since the bottom half ($y<0$) is influenced by convection losses. The estimate involved averaging the gradient between y=0 and y=12 mm. The values are 0.6°C/mm and 3°C/mm for cellulose for a temperature of 175°C, and char at a temperature of about 400°C, respectively. Similar estimates were made from the data shown in Figures 5.33a and 5.34a. In those cases the axial temperature gradients ($\partial T/\partial x$) at about 4 mm from the front surface of a sample heated with an incident heat flux of 40 kW/m^2, were 34°C/mm and 35°C/mm for cellulose (temperature about 175°C) and char (temperature about 400°C), respectively. If the thermal conductivities are similar it means that the radial heat losses represent about 1.8% for cellulose and about 8.6% for char.

5.3 MASS AND TEMPERATURE NORMALIZATION

Several methods for scaling all of the data are suggested by the preceding analysis. An attempt was thus made to "put all results on the same plot". Apart from this objective there is utility in scaling the data from the simulated fire experiments, in that if the data can be scaled with a single set of parameters this gives more insight into the correct form of model needed to represent all the results.

All the mass loss data are presented in Figure 5.35. The mass scaling factor, the initial mass M_0, was already introduced before. Time is scaled by thermal diffusivity and thickness of sample, using the Fourier number determined using char properties, char thermal diffusivity and the final sample (char) thickness. The char thermal diffusivity was

shown to be a mild function of density and the ultimate sample (char) thickness turned out to be a function of the incident heat flux. Table 5.2 summarizes the properties used in the calculations of Fourier number.

From Figure 5.35, this normalization appears to be satisfactory for incident heat fluxes of 40 and 60 kW/m^2, but not for an incident heat flux of 20 kW/m^2. This confirms the hypothesis that the mass losses were governed by heat conduction limitations when higher incident heat fluxes were used, and by the kinetics of decomposition due to low temperatures in the case of the 20 kW/m^2 incident heat flux. Note, however, that even in this case, scaling appears to be somewhat successful early in the process, when the near-surface temperature exceeds the value needed for rapid pyrolysis. Although the data seems to be well scalable at higher, fire level, heat fluxes it does not seem that the scaling is necessarily very useful in terms of predicting the mass loss behavior under those heat fluxes. The reason for this is that the Fourier number includes an, a priori unknown, characteristic length - the ultimate thickness of pyrolyzed material. This question is addressed below.

The Fourier number calculated with the char properties appears to be a good factor for scaling time. It can be seen in Figure 5.36a that it can also scale surface temperature vs. time. Similar logic was followed in the case of front surface normalization as in the case of mass loss normalization. The surface temperatures were normalized with respect to the ultimate, steady-state, surface temperatures. This method of scaling the temperature introduces yet another difficulty. Even though the scaling is reasonable, it is unlikely that the final temperature can be predicted in a simple manner, without more complete mathematical modeling.

The surface temperature normalization for 20 kW/m^2 experimental conditions is as

satisfactory as for the others. This means that the surface temperature is, naturally, governed only by heat transfer. However, the successful surface temperature normalization does not mean that the temperatures inside the sample are high enough for rapid pyrolysis to occur. Hence, although the surface temperature of a sample heated at incident heat flux of 20 kW/m^2 can be reasonably scaled, the mass loss data cannot.

The same scaling, with respect to the maximum front surface temperature, for the back surface temperature data, is shown in Figure 5.36b. Clearly, this scaling does not work very well for back surface temperatures. It is unclear why the scaling fails as badly as it does, but the rear surface temperature is perhaps the most severe test, since that surface is subject to an ill-defined boundary condition. The mid-sample temperatures, shown in Figure 5.36c, scale better than those at the back surface, although not as well as the front surface temperatures.

5.4 INITIAL SAMPLE THICKNESS EFFECT

Figure 5.37 shows mass loss as a function of time for the samples of high density and different thicknesses, pyrolyzed with an incident heat flux of 40 kW/m^2. It appears that, as long as the sample thickness is 4.25 mm or greater, mass loss proceeds with a similar rate as the thermal wave propagates through it.

In order to better characterize the behavior of individual parts of a thick pyrolyzing cellulose slab, a "sample" was made by stacking five thin discs, each of thickness of about 2 mm. This sample was pyrolyzed under an incident heat flux of 40 kW/m^2. A comparison of mass loss behaviors for the composite sample and a one piece sample of similar thickness is shown in Figure 5.38. It is obvious that the composite sample pyrolysis proceeds more

slowly, due to the additional heat transfer resistance at the planes separating individual discs. When small gaps are introduced between the discs, the total thermal conductivity of a composite sample was lower than the thermal conductivity of a single sample and this is reflected in the earlier onset of pyrolysis for the composite sample.

Using the data of Figures 5.37 and 5.38 it was possible to explore a distribution of char yields, final densities and final volumes in a sample. A summary of the data is presented in Table 5.3. The first part of Table 5.3 is the average data for different thickness samples where char yields, final densities and final volumes refer to the entire sample. That data was used to obtain the average char yields, final densities and final volumes for "slices" in a sample. For example, the data for the third "slice" (4.25 to 10.88 mm) was calculated by subtracting the final values for 4.25 mm sample from the final values for 10.88 mm sample and dividing by the initial subtracted values. In this manner, the data, comparable to composite sample data, were obtained. These values are presented in the second part of Table 5.3. The composite sample was already divided into individual slices and the final values of single slices are presented in the third part of Table 5.3.

The data of Table 5.3 is presented in Figures 5.39 and 5.40. In both figures the calculated data for different thickness samples (second part of Table 5.3) was used. Figure 5.39 shows char yield variation with the mean distance, which is defined as a distance of a center plane of an individual slice from the front, heated, surface. The agreement between the two different approaches for char yield calculation is good, except for the fifth slice in the composite sample, that was the most influenced by the contact heat resistance between the slices. Again, it should be recalled that the "char" in this case does not refer to the material with very high carbon content, but rather to the ultimate mass of material which was normalized with respect to the initial mass to obtain "char yield".

Obviously, a char yield profile exists in a sample. This can be explained by the existence of temperature profile, such that material at a different depths is pyrolyzed at different temperatures. Table 5.3 presents the temperatures in the interior of the large bulk samples, under the 40 kW/m^2 conditions. We believe, on the basis of kinetics discussed below, that the 0-2.32 and 2.32 to 4.25 mm sections should have had enough "heat soak" time to be fully pyrolyzed, and yet there is a large difference in char yield. The 4.25 to 10.88 mm section should have had enough time at elevated temperatures to be almost fully pyrolyzed. Only the 10.88 to 25.51 mm section would be predicted to have not had enough exposure to be fully pyrolyzed.

To test this hypothesis, tests were performed on the chars sectioned from a sample pyrolyzed under an incident heat flux of 40 kW/m^2. These results are also shown in Table 5.3.

As a consequence of the temperature profile, there is also a heating rate profile present in a sample. It will be shown later that the heating rate has an effect on the ultimate char yield. Another possibility is that mass transport limitations influence the char yield. There is little argument that the secondary reactions are present, as shown by gas analyses and char yield variation with the initial sample density. It will be shown later that mass transport limitations have a large influence on the ultimate char yield, but only if coupled with the heating rate effect.

It is interesting to note that the regression line in Figure 5.39 does not pass through the origin, but has an intercept of about 8.5% char yield. This char yield value of about 8.5% will be recalled later.

Figure 5.40 presents final density variation with the char yield, with the initial condition (char yield 100% for $\rho_f/\rho_i=1$) included. The data of the fifth slice in the composite sample was out of correlation in Figure 5.39, but it seems that its final density correlates well with the char yield. This presumably means that it simply did not get as hot as did the back of a single, thick slab.

5.5 "GRAIN" ORIENTATION EFFECT

As noted above, a "grain" is defined in pressed cellulose samples as a planar structure formed during pressing. Perpendicular grain orientation, used in most of this work, is defined as when the planar structure is perpendicular to the axis of the incident heat flux, whereas the parallel grain orientation means that the planar structure is parallel to the axis of the incident heat flux. Samples with parallel grain orientation were made by cutting larger (63 mm in diameter) samples. Only two density, high and medium, parallel grain samples were made, due to the structural weakness of low density samples that precluded cutting.

Figures 5.41a and 5.41b show mass loss as a function of time for perpendicular and parallel grain orientation for high and medium density samples, respectively, for an incident heat flux of 40 kW/m^2 and a purge gas flowrate of 35 l/min. It can be seen that, apart from the sample thickness effects, discussed above, the grain orientation does not have much effect on the overall mass loss behavior. The data suggest that the thermal conductivities in the two grain directions are similar, which means that the pressed cellulose samples do not show much anisotropy in thermal properties. This does not seem unreasonable, since the nature of grains in pressed cellulose samples might be very different from the nature of grains in wood.

The ultimate char yield as a function of initial sample density, for perpendicular and parallel grain orientation, is shown in Figure 5.42 (the data is also included in Table 5.1). The char yield is slightly lower, by about 1%, for the parallel grain orientation. Despite the fact that the ultimate char yield appears lower for parallel grain orientation, no firm conclusions can be drawn, since the difference is smaller than the data scatter shown in Figure 5.7a. The question of the effect of grain orientation on char yield will be further addressed below.

5.6 THE PURGE GAS EFFECT

5.6.1 THE PURGE GAS FLOWRATE EFFECT

Figure 5.43 presents a comparison of mass loss under different flowrates of nitrogen purge gas. The exhaust port (Figure 3.2b) for most of the work was loosely closed in order to decrease the possibility of oxygen back diffusion. The mass loss recorded at a flowrate of 35 l/min of nitrogen was with the exhaust port completely open, and so is not directly comparable. As evident in Figure 5.43, it seems that the flowrate plays an important role. Convective heat losses cannot explain the observed behavior because the trend is in the opposite direction from what would be expected. If convective heat losses increase with increasing flowrate, as expected, then the higher flowrates should give lower mass loss rates, the opposite of what is observed. This raises concerns about the possibility that an aerosol of volatiles intercepts a significant fraction of the radiation above the surface. The effect of higher purge rate was to remove the "smoke" aerosol from between the lamps and sample surface, effectively increasing the flux. This would, again, have significant consequences for practical models of a real fire process. Furthermore, if the volatile aerosols can significantly intercept radiation, this suggests that there is a possibility for tars to decompose in the gas phase, in front of the sample surface. This possibility was

insinuated by the gas analysis.

Although the calculations show that the purging gas moves very slowly (at a flowrate of 15 l/min through a chamber of 72 liters volume, which gives an apparent linear velocity of the order of millimeters per second) there is an effect of the purge gas flowrate. The qualitative analysis of this phenomena is aided by the data shown in Figure 5.44, the signal recorded by optical pyrometer for three different flowrates of purging gas. All other parameters were the same. While it was indicated earlier that the information from the optical pyrometer should be used with caution, the data from Figure 5.44 are useful since they show how much radiation in a certain wavelength range reaches the pyrometer. Indeed, it is obvious from Figure 5.44, that the most radiation reaches the pyrometer when the purge gas flowrate is highest. This might indicate that the pyrolysis products are obstructing the radiation, at least in the range of wavelengths where the pyrometer is sensitive. These data indicated a need for another measurement, the heat flux as a function of purge gas flowrate, the result of which is presented in Figure 5.45. The measurement was made using a fluxmeter, which was positioned in the center of a large cellulose sample (63 mm in diameter). The sample served the purpose of generating pyrolysis gases. It can be seen from Figure 5.45 that the highest heat flux was observed for quiescent gas, without a sample around the fluxmeter. For different flowrates of purge gas, the measured heat flux is slightly lower (by 5 kW/m^2). However, it cannot be said that this experiment completely represents the situation in real experiments for two reasons. The first is that the exposed surface of the fluxmeter was 25 mm in diameter (although the active element is about 2 mm in diameter), thus covering 50% of the area where the incident radiative heat flux is taken to be uniform (38 mm in diameter, the size of "standard" sample). The second reason is that the jacket of the fluxmeter was water cooled and, therefore, it introduced a heat sink in the middle of the sample. The data from Figure 5.45 cannot be directly used for mathematical

modeling. However, it is still useful since it shows that the pyrolyzates do really obstruct the heat flux to the surface.

5.6.2 THE EFFECT OF THE PURGE GAS TYPE

The purge gas is involved in convective heat transfer around the sample surface. This effect was addressed by using three more purge gases, in addition to the commonly used nitrogen. Two obvious choices were the gases with lower and higher thermal conductivities, argon and helium, respectively. The third gas was a mixture of helium and argon. The mixture was made in such a ratio to obtain an average molecular weight of 28, the same as that of nitrogen (33% helium in argon). The results are shown in Figure 5.46. The mass loss rate in pure helium is lower than that in nitrogen, whereas the mass loss rate in pure argon is somewhat higher than in nitrogen. Also, the observed char yield in pure argon was lower than usually observed in nitrogen (the initial masses of the samples used in obtaining the data from Figure 5.46 were the same). The higher mass loss rate suggests more severe conditions; i.e., higher heating rate, surface temperature and net heat flux. The mass loss rate in the mixture of 33% helium and argon shows an insignificant difference from that in nitrogen.

The result that the mass loss in the mixture of 33% helium and argon is the same as in pure nitrogen was a little surprising. This result implies that the heat loss by convection from the front surface of a sample is similar in the two purge gases. If the thermal conductivities of the gases are compared, one would expect the mass loss in argon to be closer to that of nitrogen than the mass loss obtained when the mixture was used as a purge gas. For non-polar mixtures of gases several possible mixture rules give good results (to within 1 to 3%). The Wassiljewa equation (143) allows estimation of the mixture conductivity from:

$$k_m = \sum_{i=1}^{n} \frac{y_i k_i}{\sum_{j=1}^{m} y_j A_{ij}} \qquad (5.2)$$

where k_m is the mixture conductivity, k_i the pure component conductivity, y_i the mole fraction and A_{ij} is calculable by the Mason and Saxena method (143) from:

$$A_{ij} = \kappa \frac{\left[1 + \left(\frac{\eta_i M_j}{\eta_j M_i}\right)^{1/2} \left(\frac{M_i}{M_j}\right)^{1/4}\right]^2}{\left[8\left(1 + \frac{M_i}{M_j}\right)\right]^{1/2}} \qquad (5.3)$$

where

M_i - molecular weight of component i

κ - numerical constant close to unity (here $\kappa = 1$)

η_i - viscosity of component i

For helium M_{He}=4, η_{He}(800K)=3.817x10^{-5} kg/m-s, k_{He}(800K)=0.275 W/m-K. For argon M_{Ar}=39.9, η_{Ar}(800K)=4.224x10^{-5} kg/m-s, k_{Ar}(800K)=0.044 W/m-K (20, 74). These calculations give $A_{He/Ar}$=2.44, $A_{Ar/He}$=0.270 and a mixture thermal conductivity at 800 K of 0.0850 W/m-K. For the purpose of comparison, the thermal conductivities of nitrogen and argon at the same temperature are 0.0561 W/m-K and 0.044 W/m-K, respectively.

The data from Figure 5.46 are consistent with the trend of thermal conductivity change as a function of purge gas for all gases except for the mixture. The reason might be that a pure gas behaves differently from a mixture in a presence of large temperature gradients. It is well established that the composition of a mixture changes in an area where the large

temperature gradients are present, due to the phenomenon of thermal diffusion. The explanation for the data of Figure 5.46 can be that the actual mixture of helium and argon in the boundary layer, which is important for heat convection, is different from the "cold mixture". The difference in concentration of lighter component caused by difference in temperatures of regions 1 and 2 is:

$$\Delta C = K_T \ln \frac{T_1}{T_2} \Rightarrow C_1 = C_2 - K_T \ln \frac{T_1}{T_2} \tag{5.4}$$

where K_T represents the ratio of thermal diffusion and molecular diffusion coefficients. The ratio of diffusion coefficients K_T was estimated from Kestin et al. (94) to be 0.075. With surface temperature of 800 K and surrounding temperature of 300 K the difference in helium concentration is 7.4%, which predicts the mixture to be 25.6% helium and 74.4% argon at the surface of the sample.

In order to establish what the concentration of helium in the mixture would have to be for heat losses to convection to be the same as when nitrogen is used as a purge gas some calculations were done. The calculations were performed for 800K. The expression that was used for the calculations of the heat convection coefficient was:

$$h = \frac{k}{l} Nu = \frac{k}{l} \frac{0.638\ (Pr^2\ Gr)^{0.25}}{(0.861 + Pr)^{0.25}} \tag{5.5}$$

where h is the heat transfer coefficient, k the gas phase thermal conductivity, l the characteristic length of the sample, Pr the Prandtl number, Nu the Nusselt number and Gr the Grashof number.

The heat convection coefficients were set equal and after replacing the expressions for Prandtl and Grashof numbers with their respective definitions, the expression that assures

equality of heat loss in nitrogen and in the mixture is:

$$\frac{0.861\ k_2^2 + k_2\,\eta_2\,C_{p2}}{k_2^4\,C_{p2}^2\,\rho_2^2} = \frac{0.861\ k_1^2 + k_1\,\eta_1 C_{p1}}{k_1^4\,C_{p1}^2\,\rho_1^2} \qquad (5.6)$$

where subscript 1 refers to the mixture and subscript 2 refers to nitrogen.

All the variables on the left side are functions of composition and the right side is calculable from the properties for nitrogen at 800K. The calculated composition that gives the same heat convection coefficient of the mixture to that of nitrogen is 15.3% helium and 84.7% argon. The difference between calculated helium concentration at the surface due to thermal diffusion and calculated concentration which gives the same heat convection coefficient is significant, but due to the uncertainties in several aspects of the calculation, one cannot rule out these possibilities. One important thing to bear in mind is that the volatiles themselves change the composition of the gas near the surface, adding components more like argon than helium.

Moreover, it is possible by considering how the mass loss rate scales with thermal conductivity, to crudely estimate the heat loss to convection. Since at the surface the heat balance is:

$$\dot{q}_l - \dot{q}_\rho - \dot{q}_\varepsilon - \dot{q}_k - \dot{q}_h = 0 \qquad (5.7)$$

where the terms are, respectively: heat flux given by the radiative heaters, reflected heat flux, radiative heat loss from the surface, conduction into the sample and convective heat loss. Since the first two terms are constant and the third term depends just on the temperature of the sample surface, irrespective of the purge gas, they can be combined into one term, viz:

$$\dot{q}_l - \dot{q}_\rho - \dot{q}_\varepsilon = C\,(T_S)$$

or

$$\dot{q}_k + \dot{q}_h = C\,(T_S) \tag{5.8}$$

For equal surface temperatures the following expression holds:

$$\dot{q}_{k\,He} + \dot{q}_{h\,He} = \dot{q}_{k\,N_2} + \dot{q}_{h\,N_2} \tag{5.9}$$

Upon rearrangement, this expression becomes:

$$\frac{\dot{q}_{k\,N_2}}{\dot{q}_{h\,N_2}} = \frac{\dfrac{\dot{q}_{h\,He}}{\dot{q}_{h\,N_2}} - 1}{1 - \dfrac{\dot{q}_{k\,He}}{\dot{q}_{k\,N_2}}} = \frac{C(T_S) - \dot{q}_{h\,N_2}}{\dot{q}_{h\,N_2}} \tag{5.10}$$

Equation (5.10) can be solved for convective loss when nitrogen is used as a purge gas:

$$\dot{q}_{h\,N_2} = \frac{C(T_S)\left(1 - \dfrac{\dot{q}_{k\,He}}{\dot{q}_{k\,N_2}}\right)}{\dfrac{\dot{q}_{h\,He}}{\dot{q}_{h\,N_2}} - \dfrac{\dot{q}_{k\,He}}{\dot{q}_{k\,N_2}}} \tag{5.11}$$

Finally, the convective loss from the surface, when nitrogen is used as a purge gas, can be estimated (as a function of surface temperature):

$$\dot{q}_{h\,N_2} = \frac{C(T_S)\left[1 - \dfrac{(\partial M/\partial t)_{He}}{(\partial M/\partial t)_{N_2}}\right]}{\dfrac{(k\,Nu)_{He}}{(k\,Nu)_{N_2}} - \dfrac{(\partial M/\partial t)_{He}}{(\partial M/\partial t)_{N_2}}} \tag{5.12}$$

where $\partial M/\partial t$ are measured quantities and k Nu (product of thermal conductivity and Nusselt number) are calculated.

If the surface temperatures are not equal, the term $C(T_S)$ is not equal in both cases and the equation is slightly modified:

$$\dot{q}_{k\,He} + \dot{q}_{h\,He} + C(T_S)_{He} = \dot{q}_{k\,N_2} + \dot{q}_{h\,N_2} + C(T_S)_{N_2} \tag{5.13}$$

After rearranging and solving for convective heat loss from the surface when nitrogen is used as a purge gas:

$$\dot{q}_{h\,N_2} = \frac{C(T_S)_{N_2}\left(1 - \dfrac{\dot{q}_{k\,He}}{\dot{q}_{k\,N_2}}\right)}{\dfrac{\dot{q}_{h\,He}}{\dot{q}_{h\,N_2}} - \dfrac{\dot{q}_{k\,He}}{\dot{q}_{k\,N_2}}} + \frac{C(T_S)_{N_2} - C(T_S)_{He}}{\dfrac{\dot{q}_{h\,He}}{\dot{q}_{h\,N_2}} - \dfrac{\dot{q}_{k\,He}}{\dot{q}_{k\,N_2}}} \tag{5.14}$$

The above expression differs from the constant surface temperature expression in the correction term for different surface temperatures in nitrogen purge gas and helium purge gas.

When the ratios and difference in radiative heat losses from the surface are replaced, the expression for the convective heat loss from the sample surface becomes:

$$\dot{q}_{h\,N_2} = \frac{C(T_S)_{N_2}\left[1 - \dfrac{(\partial M/\partial t)_{He}}{(\partial M/\partial t)_{N_2}}\right]}{\dfrac{(k\,Nu)_{He}}{(k\,Nu)_{N_2}} - \dfrac{(\partial M/\partial t)_{He}}{(\partial M/\partial t)_{N_2}}} + \frac{\sigma \varepsilon T_{S\,N_2}^4\left[1 - \left(\dfrac{T_{S\,He}}{T_{S\,N_2}}\right)^4\right]}{\dfrac{(k\,Nu)_{He}}{(k\,Nu)_{N_2}} - \dfrac{(\partial M/\partial t)_{He}}{(\partial M/\partial t)_{N_2}}} \tag{5.15}$$

It should be noted that in expression (5.15) the ratio of conductive heat losses from the surface is replaced by the derivative with respect to time since the equation applies for a

particular instant of time, when the surface temperatures are different.

For the above analysis, the necessary data are surface temperatures and mass loss traces when helium and nitrogen are used as purge gases. Mass loss traces were shown in Figure 5.46 and the surface temperature traces are shown in Figure 5.47 for high density samples and an incident heat flux of 40 kW/m^2. Apparently, even though the mass loss traces look quite different, the surface temperatures for two purge gases are not very different - about 50°C around the pyrolysis temperature.

The calculations were performed for a surface temperature of 450°C, when nitrogen was used as a purge gas. At the same time the surface temperature of a sample, pyrolyzed in an atmosphere of helium was 417°C. The properties for helium and nitrogen were taken from (53) for their respective temperatures. The convective heat loss in nitrogen was estimated from (5.15) to be 7.1 kW/m^2. This value seems reasonable and it can be used for calculation of an average heat transfer coefficient when nitrogen is used as a purge gas. For a surface temperature of 450°C and a temperature of surrounding gas of 25°C, the calculated heat transfer coefficient is 16.7 W/m^{2}K. This value is about 59% higher than the value calculated from (5.5), which was 10.5 W/m^{2}K. There are two possibilities for this discrepancy. It could be that the calculation is very sensitive to the determination of time derivatives or that the expression (5.5) for some reason does not hold. The sensitivity was checked by simultaneously varying the both time derivatives in the opposite directions by 100% (time derivative, $\partial M/\partial t$, for nitrogen increased by 100% and for helium decreased by 100%) and the calculated convective heat loss was higher for about 90%. This means that the sensitivity is probably not the reason for the discrepancy in heat transfer coefficients. Of course, the accuracy of the estimate of $C(T_s)_{N_2}$, or the soundness of using pure gas values of k, are also open to question. If the value of 16.7 W/m^{2}K is used for iteration in equation

(5.15) the heat loss to convection increases, causing the heat transfer coefficient for nitrogen to diverge.The measurements of heat transfer coefficient were not performed and the real cause of the discrepancy remains unestablished. Nevertheless, as discussed in an earlier section, the value of h has been bounded in a narrow enough range so as to allow radiative properties to be calculated accurately.

5.7 MATERIAL BALANCE

An attempt was made to close the material balance during pyrolysis. The original concept was to measure the absolute amount of various products collected at a certain flowrate through the trapping system and to scale the amounts obtained in that way to the actual flowrate through the apparatus. This approach proved to have difficulties associated with the complexity of the apparatus and volatiles escape from the apparatus by routes other than via the exhaust, despite efforts to completely seal the system. An alternative approach was to allow purge gas and volatile products to first mix well, and then to take a representative mixture under constant flowrate, through the trapping system and eventually to the gas collecting vessel. The amount of condensable products collected was determined by weighing the tar trap before and after an experiment. Gas yields were determined by chromatography. The amounts obtained in this way were then scaled to add up to 100% together with the char. For the purpose of these tests the amounts of methane, ethane, ethylene and water vapor were not taken into account. Most water was condensed in the tar trap, operated at 0°C. Also, the other possible products of pyrolysis that normally constitute no more than a few percent by mass were not analyzed for by the chromatographic method. Confidence in the procedure is boosted by the fact that the actual product collection seemed to scale, at least crudely, with the amount of sample; a constant fraction of products was "missed". Reproducibility is seen to be poor in particular for condensables collection, but it

is noted that when condensables collection was poor, so too was gas product collection. This clearly shows that loss of a part of the entire product stream was responsible for low collection. Again, this had to do with how the system was set up - complete collection of all the gas was very difficult. These tests were done in order to determine the relative contributions of solid residue, condensables and the major gas contributors, carbon monoxide and carbon dioxide to the material balance. The results are shown in Table 5.4 for three different density samples and for two higher incident heat fluxes. The last four columns present the amounts of char, condensables, carbon dioxide and carbon monoxide as fractions of the original cellulose. It can be seen that the major category of decomposition products are condensables, which includes tars and water.

The data can be compared to that of Hajaligol et al. (68), shown in the last row in Table 5.4. Their data are for the rapid, isothermal, pyrolysis of cellulose sheets of 0.101 mm thickness, at various peak temperatures (from 400°C to 1000°C) and holding time at the peak temperature of 30 seconds, or without holding. Their main conclusion was, from the perspective of the findings in the present work, that the amount of tar formed decreases with increasing temperature and residence time. The amounts of gases produced increases with increasing temperature and residence time. Although the data from this study and the data from Hajaligol et al. are not directly comparable, since there are differences in conditions, there are some similarities. The relative amounts of products appear to be comparable. In this work the temperature is a function of location in the sample, but for the incident flux of 40 kW/m^2 the maximum front surface of the sample ranges from 523°C (high density sample) to 564°C (low density sample). The maximum back surface temperature of a sample ranges from 240°C (low density sample) to 320°C (high density sample). In other words the average maximum ("peak") temperature is very close to Hajaligol et al.'s 400°C.

The data of Table 5.4 indicate that the initial sample density affects the amount of products formed. The higher the sample density the higher the ultimate char yield and the total yields of CO and CO_2, and the lower the total amount of condensables. Again, if the char layer is viewed as a fixed bed reactor, where the decomposition (cracking) of tars takes place, the amount of tars cracked would depend on tar residence time and on tar concentration in the hot char layer matrix. The higher the sample density, the more tars are formed, and the velocity of tars and their concentration in the char layer are higher.

A similar effect of the incident heat flux, observed in the gas analyses, is seen here. It seems that the more important product at lower, 40 kW/m^2, incident heat flux is carbon dioxide, whereas at higher incident heat flux, 60 kW/m^2, the more important product is carbon monoxide. This is consistent with Hajaligol's data. However, their observation are due to different phenomena than play a role in this work. The system used in their work (68) was free of any transport limitations and the effect of severity of pyrolysis conditions is seen. In the system used here, transport limitations were shown to play an important role during the pyrolysis and the reason for a larger amount of carbon monoxide formed during the pyrolysis with higher incident heat flux is probably due to the reduction of carbon dioxide to carbon monoxide in the char layer. Again, the amounts are relatively close and the reason for a very small difference might be argued.

5.8 PRODUCTS CHARACTERIZATION

Char and tar obtained by pyrolysis under simulated fire conditions were subjected to several standard laboratory tests. The tests performed on the chars included determination of the residual amount of volatiles, determination of the activation energy of gasification in air, the measurement of total surface area (TSA), micrographic studies and FTIR analysis. The tests performed on tar included determination of average molecular weight by vapor pressure osmometry and tar pyrolysis.

5.8.1 CHAR CHARACTERIZATION

The char samples from a single sample pyrolyzed in the simulated fire apparatus were pulverized and placed in a quartz boat, heated in a tube furnace at a 40°C/min rate to 600°C and held for 10 minutes. The environment was helium, at a flowrate of 130 ml/min. The following table presents a summary of the results from these experiments. All the layers were 1.5 mm thick, except for the last one, which was 2.5 mm thick; 0 mm indicates the front surface.

Distance [mm]	0 - 1.5	1.5 - 3	3 - 4.5	4.5 - 7
Mass Loss [%]	8.8	13.6	18.5	18.1
Original Cellulose Basis [%]	0.88	2.04	3.70	5.43

As can be seen, the pyrolysis process is terminated at different extents of reaction at different distances from the front surface. It should be noted that the mass loss in the above table refers to the mass loss of char, which would be different from the mass loss based on the initial mass of cellulose. For example, if the char yield from pyrolysis of the first slice

(0-1.5 mm) was about 10% that means that the additional mass loss would be about 0.88% of the original material and the ultimate char yield after additional pyrolysis would be about 9.12%, as compared to 10%. Likewise, if the char yield for the last slice was about 30% the additional mass loss would be about 5.43%, giving the ultimate char yield of about 24.57%. Although the mass losses from the above table appear to be high at first glance, they are really not when put on the same basis as the usual char yield calculations. That means that the char yield is higher at the back part of the sample only partly due to the low temperature. The other reason, to be explored later, is the heating rate effect on the ultimate char yield.

There is another consideration in estimating residual volatile matter by the above method. Since the fresh char is highly reactive to oxygen, upon exposure to air, numerous surface oxides are formed. These will desorb with the volatile matter, and might represent a few percent of the mass loss. Thus the reported values probably slightly overestimate the residual volatile content, by perhaps 2 or 3%.

The total char surface areas were determined from the amount of nitrogen absorbed at 77K and calculated from BET equation. The char samples were from the composite sample and they were outgassed at 100°C for two hours in helium. Note that the usual outgassing procedure is at 300°C, was not followed here because of a concern about promoting additional pyrolysis. The results are presented in the following table:

Slice [mm]	Surface Area [m^2/g]
0 - 2.03	7.06
2.03 - 4.22	10.02
4.22 - 6.45	10.41
6.45 - 8.49	2.98
8.49 - 10.63	2.12

The surface areas are lower than the usual value for activated chars (of the orders of several hundreds of square meters per gram). The chars used in this work were not "burned off" and, therefore, not activated. It was somewhat surprising that the maximum surface area was observed for the middle portion of the sample. However, such behavior is not unknown. Christner and Walker (41) reported a maximum in surface area of cellulose chars (from filter paper and powder) when n-butane and iso-butane were used, for pyrolysis temperature of about 500°C. At higher and lower pyrolysis temperatures lower surface areas observed. Brunner and Roberts (31) have shown that decreasing the heating rate increased the specific micropore volume of the char accessible to CO_2 uptake at -78°C, thus caution should be exercised relative to using these values to represent chars produced under other heating conditions.

The kinetics of char gasification in air was determined in a standard thermogravimetric analyzer (TGA). The char sample was taken from the front surface, the char layer was 1.5 mm in thickness and it included the front surface. The activation energy for gasification was shown to be 126 kJ/mole. When this value is compared to the usual value for phenol formaldehyde resin chars earlier studied here (pyrolysis temperatures between 1000°C and 1400°C) of 142 kJ/mole (196) it can be seen that the kinetics of cellulose char (obtained by pyrolysis under simulated fire conditions) gasification in air is similar to other, very

different, chars.

A micrographic analysis was performed on the pyrolyzed high density cellulose samples. The optical magnification was 150. The results are shown in Figures 5.48. Figure 5.48a presents a micrograph of the front surface of a sample, Figure 5.48b shows a micrograph of the sample interior, perpendicular to the front surface and Figure 5.48c presents a micrograph of the back surface. None of the samples was extensively prepared for micrography in order to preserve the original appearance as much as possible. A comparison of front and back surfaces shows a much higher extent of pyrolysis for the front surface, which was expected. It can be seen from the figures that the fibrous structure looks larger in the case of the front surface. The reason for that might be that the tars are contributing some char after they are pyrolyzed on the fibers of front surface. Indeed, there were clearly observable small "drops" (some of the information is lost by taking a photograph and especially by photo reproducing the original photograph), which might indicate that tar aerosol was deposited on a fiber and decomposed. However, it was observed that char fibers look larger than the fibers of starting material (it should be noted that the micrographs were taken for the cellulose samples as well but, unfortunately, due to the nature of the surface much less can be seen on the photographs than under the microscope itself). This suggests that some tars are depositing on the surfaces of the fibers and pyrolyze there, leaving char residue. The back surface looks as it retained the appearance of the original material. The original material does not show any planar orientation, which might be expected due to pressing. A micrograph of the sample interior when it is pyrolyzed, Figure 5.48b, shows random orientation of char clusters. This was suggested by the data of Figures 5.41, where it was seen that turning the sample by 90° in order to study grain orientation effects did not exhibit much difference. It was concluded that thermal conductivity is similar in both directions. Figure 5.48b seems to support the

hypothesis that there should be no preferred direction. It is thus believed that the cracking of the sample in a direction perpendicular to the direction of applied flux is a consequence of the shrinkage resulting from one-dimensional propagation of the thermal wave into the sample.

The spectral information provided by the FTIR gives much more insight into the process of pyrolysis than merely what is happening to the reflectivity of the surface. Figures 4.8a through 4.8f showed the FTIR scans of surface chars when the pyrolysis was quenched at different extents, as indicated by a small sketch of pyrometer signal at the top of each figure. The significance of certain peaks is outlined here. The sharp peaks near 2400 cm^{-1} have no significance in those figures, since they are artifacts due to fluctuations in background CO_2 levels in the spectrometer.

Starting from the highest wavenumbers, the broad peaks from about 3000 -3600 cm^{-1} are quite obviously hydrogen-bonded hydroxyl groups. These peaks decrease sharply by the time the third char sample is taken. The approximate surface temperature by this point is 430°C. This indicates a significant loss of hydroxyl content from the char by this point. Care must be exercised in concluding when the native hydroxyls are totally eliminated, based upon such spectral data alone. This is because the samples were handled in air and thus some moisture adsorption was certainly possible. Such moisture would also give rise to signal in this wavelength range. Thus the apparent rise in hydroxyl content between the third and fourth char might be an artifact due to moisture pickup.

The next distinct feature is the C-H stretch near 2910 cm^{-1}, corresponding to aliphatic hydrogens. The magnitude of the peak relative to the neighboring spectral features does not change much until the third char sample. Then beginning with the fourth sample, there is a

shift of the peak towards 3030 cm^{-1}, which is interpreted in terms of an aliphatic to aromatic conversion of the remaining hydrogens. The aromatization of the char structure is supported by the three peaks centered near 800 cm^{-1}, which are clearly visible in the third fourth and fifth char samples. Also, there is in these samples a corresponding change in the shape of the baseline from 2000 to 4000 cm^{-1} wavenumbers, as it assumes a distinct slope characteristic of the extension of electronic absorptions into the mid-infrared, again characteristic of condensed aromatic structures. Finally, there is a peak near 1590 cm^{-1} in the fifth char, whose development began in the third char, and which can probably only be assigned to aromatic carbon-carbon structures.

Between the first and second chars, there is a distinct growth of a band near 1700 cm^{-1}. This band persists through the fourth char, and begins to disappear thereafter. This band almost surely represents the formation of carbonyl groups during the pyrolysis. Its loss during the aromatizing end stage of the pyrolysis is attributed to loss of oxygen. The broad, generally featureless peak in the fifth char sample, between 1700 and 1000 cm^{-1}, is difficult to assign. There could be a contribution of aromatic ethers or any of a number of other aromatic ring absorptions.

In summary, it is possible to track the course of pyrolysis of the sample surface through the use of FTIR spectroscopy. The expected course of aromatization is followed. What these data clearly show is that the process of pyrolysis continues, with attendant changes in surface properties, well past the time when the surface is "black" in appearance. It is the initial aromatic ordering of the surface that increases the reflectivity of the surface, after its initial sharp decrease early during pyrolysis.

5.8.2 TAR CHARACTERIZATION

Tars were collected by washing the surfaces of the experimental chamber with ethanol. The solvent was evaporated in vacuo at room temperature and the residue was used for tar samples. The number average molecular weight was determined by a standard vapor pressure osmometer. The solvent was the same as used in tar collection, i.e. methanol. Unfortunately, the choice of solvent proved to have difficulties associated with the calibration standard. There was no polymer standard soluble in methanol. For that reason glucose was used as a calibration standard. Glucose is also a good choice in terms of similarities to cellulose. The solubility of glucose is lower in methanol than in water and the solution was promoted with prolonged mixing. The number average molecular weight of tars was then determined to be 201 Daltons. For comparison purposes, the molecular weight of levoglucosan, a frequently cited tar component, is 162 Daltons. However, there were no attempts made here to identify the tar components, due to the complexity of the mixture of compounds called tar.

As is well known, it is difficult to "evaporate" sugars-most will decompose at a temperature lower than that needed to evaporate them. The question may then be raised as to how do the tars escape? It is clear that levoglucosan, whose structure is shown below,

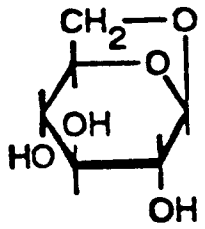

is quite similar to glucose in many respects. It is quite prone to strong hydrogen bonding interactions, and also to thermal decomposition, if attempts are made to evaporate it (122). In light of these concerns, it was of interest to see if the tars that evolved from the cellulose

could evaporate at a temperature below pyrolysis temperatures, or whether their escape required a new cycle of thermal decomposition.

Experiments were performed in which tars collected from the simulated fire apparatus, could be reheated in a mass-transfer limitation-free environment. The heated wire mesh reactor was chosen for this purpose, since in this reactor, tars are held on a fine wire gauze which can be electrically heated to the desired temperatures. The gauze offers little mass transfer resistance to gas flow. The tars were subjected to heating in a helium atmosphere, with a heating rate of 60K/min to a preselected final temperature. Tars were positioned in the folded wire mesh, which was weighed before and after an experiment to determine the mass loss. The variation of mass loss with the maximum wire mesh temperature is shown in Figure 5.49. It is evident that tars start to evaporate or decompose at a temperature of about 180°C. Again, for comparison, the boiling point of levoglucosan is 180°C. At temperatures above 350°C no more mass is lost, and the char yield from tar pyrolysis is about 30%. The fact that the tar decomposition temperature is so low is important from the point of view of results from the pressed cellulose sample. The data suggest that tar decomposition in the hot char matrix is very likely and that the decomposition might be the reason for the observed increase in char yield with sample density. As relates to the issue of tar evolution, it is quite clear that most of the tar evaporates well below the observed cellulose decomposition temperature. What this means is that the cellulose decomposition reaction effectively produces a gas phase tar product, rather than a mixture of high molecular weight tars in the condensed phase that must evaporate in order to escape. The behavior of cellulose thus appears to be rather unlike that in coal, in which a large amount of marginally vaporizable intermediate is formed during pyrolysis.

5.9 SUMMARY

The pyrolysis of pressed cellulose samples in a simulated fire environment, under incident radiative heat fluxes up to 60 kW/m^2, was demonstrated to be a heat transfer-limited problem. It was shown that the pyrolysis is governed by the sample's ability to conduct heat. Accordingly, the effects of sample density on the pyrolytic behavior were seen to be mainly due to different thermal conductivities and volumetric heat capacities. Small mass transport limitation effects, due to different sample densities, were observed in char yields and gas analyses. Generally, the observed char yields were about 20% for the two higher incident heat fluxes (40 and 60 kW/m^2), and much higher (never less than 64%) for an incident heat flux of 20 kW/m^2. Temperature profiles in the different samples confirmed their different thermal conductivities. The higher the sample density, the lower the front surface temperature and the higher the back surface temperature.

The incident heat flux had a predictable effect on pyrolysis. Pyrolysis proceeded faster higher the incident heat flux. With the lowest incident heat flux, 20 kW/m^2, heat transfer was shown not to be sufficient for "rapid" pyrolysis to take place, based on the experimental time scales employed here. It was only in this case, in which sample interior temperatures were quite low, that the chemical kinetics of pyrolysis became limiting. Other cases were all conduction-rate limited. It was seen that the mass loss and front surface temperatures can be scaled using a Fourier number, with respect to char properties, as a dimensionless time. On the other hand, this normalization was not successful for mass loss during the pyrolysis under the lowest incident heat flux, of 20 kW/m^2. This also suggests that pyrolysis under the lowest incident heat flux (20 kW/m^2) is not heat conduction limited.

The main products of pyrolysis are condensables, which included tar and water. Char, carbon dioxide and carbon monoxide were also key products. Carbon dioxide was a more abundant product at the very early stages of pyrolysis and carbon monoxide became more abundant subsequently. It was demonstrated that relatively less carbon dioxide and relatively more carbon monoxide were formed at higher incident heat fluxes (60 kW/m^2) than at lower incident heat fluxes (40 kW/m^2), probably due to a reduction reaction of carbon dioxide to carbon monoxide in the hot char layer.

The pyrolysis of samples of different thickness proceeded with similar rates of mass loss. Back face boundary effects, therefore, played no role on the overall mass loss, as long as the sample was thicker than few millimeters. A char yield profile was always observed in bulk samples. The reason for that is, as yet, not clear. It is attributable to the lower temperatures reached in the sample interior, which affects both the extent of pyrolysis, as well as the pathway of pyrolysis. The grain orientation of samples was established not to have much of an effect on the overall mass loss during the pyrolysis.

The purge gas flowrate was shown to have an effect as a result of cleaning the area between the radiative heaters and a sample from pyrolysis products. Thus the rate of pyrolysis was observed to be higher for higher flowrates of purge gas. The type of purge gas was important in convective heat transfer from the front surface. It was noted that the lower the gas thermal conductivity, the higher the mass loss rate during the pyrolysis. This was understood in terms of lowering of the front surface temperature in the presence of high thermal conductivity gas. It was also shown that a mixture of helium and argon can be used to simulate nitrogen, insofar as the apparatus used here and the mass loss are concerned.

The char obtained by pyrolysis under simulated fire conditions had a reactivity towards oxygen quite common for disordered chars. Total surface area (of unoxidized chars) was of

a similar order as total surface areas of unactivated chars prepared under different conditions. FTIR spectroscopy was shown to be a good tool for characterizing the functional groups in the char obtained under simulated fire conditions. It was noted that the changes in surface optical properties played an important role in determining surface heat transfer.

Tars were shown to have a number average molecular weight of 201 Daltons. The temperature where the evaporation and/or decomposition of tars first occurred was about 180°C. It was demonstrated that the tars were completely decomposed, with the char yield of about 30%, at temperatures higher than 350°C.

Table 5.1: Summary of char yields for different incident heat fluxes, flowrates, densities and grain orientations.

Flux [kW/m^2]	Flowrate [l/min]	Orientation	Density [g/cm^3]	Char Yield [%]
40	15	Perpendicular	0.455	22.6
			0.458	18.4
			0.462	22.3
			0.465	14.7
			0.469	14.5
40	15	Perpendicular	0.673	20.7
			0.678	21.7
			0.683	22.2
			0.684	19.9
			0.688	20.4
			0.698	20.0
			0.701	22.4
			0.704	20.1
			0.704	21.0
			0.711	20.2
			0.728	22.0
			0.733	21.3
			0.740	19.8
			0.744	21.2
			0.752	19.9
40	15	Perpendicular	0.922	21.6
			0.929	18.6
			0.937	22.1

Table 5.1 Continued

Flux [kW/m^2]	Flowrate [l/min]	Orientation	Density [g/cm^3]	Char Yield [%]
40	15	Perpendicular	0.940	20.7
			0.946	21.0
			0.947	21.5
			0.947	20.9
			0.948	20.2
			0.949	21.0
			0.950	19.3
			0.951	20.6
			0.952	19.2
			0.956	20.8
			0.956	20.6
			0.957	19.8
			0.957	20.2
			0.960	19.7
			0.961	21.2
			0.964	21.6
			0.965	20.6
			0.969	19.8
			0.969	20.8
			0.975	19.2
			0.975	21.5
			0.976	21.2
			0.980	21.5
			0.980	20.8
			0.984	20.0
			0.998	21.2

Table 5.1 Continued

Flux [kW/m^2]	Flowrate [l/min]	Orientation	Density [g/cm^3]	Char Yield [%]
60	15	Perpendicular	0.453	13.6
			0.471	14.5
			0.476	13.7
60	15	Perpendicular	0.658	16.4
			0.669	15.3
			0.696	15.8
60	15	Perpendicular	0.950	15.7
			0.956	17.4
			0.957	16.8
			0.970	15.6
20	15	Perpendicular	0.420	66.4
			0.447	64.2
			0.465	71.3
20	15	Perpendicular	0.656	73.9
			0.661	73.4
			0.673	86.2
20	15	Perpendicular	0.926	77.5
			0.931	82.4
			0.933	87.7

Table 5.1 Continued

Flux [kW/m^2]	Flowrate [l/min]	Orientation	Density [g/cm^3]	Char Yield [%]
20	15	Perpendicular	0.941	75.0
			0.945	78.5
			0.948	74.9
40	15	Parallel	0.723	18.4
40	15	Parallel	0.995	18.8
			0.995	20.8
40	55	Perpendicular	0.718	18.6
			0.749	18.2
40	35	Perpendicular	0.464	15.2
			0.472	15.3
40	35	Perpendicular	0.702	17.8
			0.727	17.5
40	35	Perpendicular	1.060	22.1
			1.065	20.8

Table 5.1 Continued

Flux [kW/m^2]	Flowrate [l/min]	Orientation	Density [g/cm^3]	Char Yield [%]
40	35	Parallel	0.493	21.3
40	35	Parallel	0.723	16.3
			0.723	17.7
40	35	Parallel	0.926	23.4
			0.926	18.8
			0.995	20.2
			0.995	19.2
40	15 (Helium)	Perpendicular	0.931	29.2
			0.948	29.7
40	15 (Argon)	Perpendicular	0.983	18.9
40	15 (Ar/He)	Perpendicular	0.928	20.9

Table 5.2: Properties used for Fourier number calculations.

α_{Char} = const. = 0.1 mm^2/s (at 320°C)

	SAMPLE DENSITY		
Flux [kW/m2]	High	Middle	Low
	L_{Char} - Measured Final Thickness [mm]		
60	5.18	5.22	5.12
40	6.86	7.02	6.57
20	10.57	11.40	11.05

Table 5.3: Char yields, final densities and final volumes for different sample thicknesses and a sample composed of five thin samples

a: Data from bulk samples of different sample thickness

Thickness [mm]	Char Yield [%]	ρ_f/ρ_i	V_f/V_i
2.32	9.0	0.154	0.585
4.25	15.2	0.285	0.533
10.88	24.4	0.348	0.702
25.51	49.1	0.634	0.774

b: Calculated propertes for individual "slices" of different thickness (see text)

"Slice" [mm]	Char Yield [%]	ρ_f/ρ_i	V_f/V_i	Residue Volatile Matter[1] [%]	Maximum Temperature Achieved[2] [°C]
0-2.32	9.0	0.154	0.585	0.8	520
2.32-4.25	20.2	0.429	0.471	2.7	515
4.25-10.88	31.7	0.391	0.811	5.9	450
10.88-25.51	65.8	0.795	0.828	26[3]	320

c: Composite sample data (five 2 mm samples)

Slice [mm]	Char Yield [%]	ρ_f/ρ_i	V_f/V_i
0-2.03	12.2	0.180	0.676
2.03-4.22	19.9	0.345	0.578
4.22-6.45	24.2	0.464	0.522
6.45-8.49	32.0	0.545	0.587
8.49-10.63	59.2	0.700	0.846

[1] relative to cellulose

[2] at the front boundary of a "slice"

[3] estimated (20 mm thick sample, heated at 300°C for 2 hours with a char yield of 40%)

Table 5.4: Material balances for three different density samples and two incident heat fluxes (amounts of methane, ethane, ethylene, water vapor and other undetectable products are not taken into account).

a: Incident heat flux of 40 kW/m^2

			COLLECTED[1]			CALCULATED[2]			
Initial Mass [g]	Density [g/cm^3]	Char [g]	Condensables [g]	CO_2 [g]	CO [g]	Char [%]	Condensables [%]	CO_2 [%]	CO [%]
11.3282	0.960	2.2299	0.68	0.0514	0.0177	19.7	72.9	5.5	1.9
11.2773	0.947	2.4219	0.69	0.0498	0.0305	21.5	70.3	5.1	3.1
11.3519	0.951	2.3355	0.45	0.0332	0.0214	20.6	70.8	5.2	3.4
11.2723	0.965	2.3251	0.50	0.0410	0.0318	20.6	69.3	5.7	4.4
11.2140	0.937	2.4782	0.39	0.0369	0.0163	22.1	68.5	6.5	2.9
8.4290	0.678	1.8291	0.62	0.0179	0.0190	21.7	73.9	2.1	2.3
8.3765	0.683	1.8593	0.52	0.0181	0.0179	22.2	72.8	2.5	2.5
5.6266	0.465	0.8245	0.26	0.0060	0.0012	14.7	83.0	1.9	0.4
5.5844	0.469	0.8118	0.25	0.0101	0.0092	14.5	79.4	3.2	2.9

[1]Collected means the actual amount collected during the run

[2]Calculated means extrapolated to 100%

Table 5.4: continued

b: Incident heat flux of 60 kW/m^2

Initial Mass [g]	Density [g/cm^3]	Char [g]	COLLECTED[3] Condensables [g]	COLLECTED[3] CO_2 [g]	COLLECTED[3] CO [g]	CALCULATED[4] Char [%]	CALCULATED[4] Condensables [%]	CALCULATED[4] CO_2 [%]	CALCULATED[4] CO [%]
11.3044	0.956	1.9700	0.87	0.0674	0.0639	17.4	71.7	5.6	5.3
11.4201	0.957	1.9191	0.66	0.0338	0.0430	16.8	74.5	3.8	4.9
8.5205	0.658	1.4015	0.33	0.0654	0.0794	16.4	80.1	1.6	1.9
8.4885	0.696	1.3449	0.69	0.0416	0.0643	15.8	73.0	4.4	6.8
5.6123	0.471	0.8127	0.54	0.0278	0.0369	14.5	76.4	3.9	5.2
5.6318	0.476	0.7733	0.56	0.0275	0.0448	13.7	76.4	3.8	6.1
Hajaligol et al[5], 400°C peak temperature, 30 s hold						6.17	89.84[6]	1.45	0.25
500°C peak temperature, no hold						83.63	19.92	0.30	0.99
750°C peak temperature, no hold						3.32	68.64	2.38	15.82
1000°C peak temperature, no hold						3.91	58.34	3.36	22.57

[3]Collected means the actual amount collected during the run

[4]Calculated means extrapolated to 100%

[5]Data for 0.101 mm thick cellulose sheets (rapid, isothermal pyrolysis)

[6]Water and tar

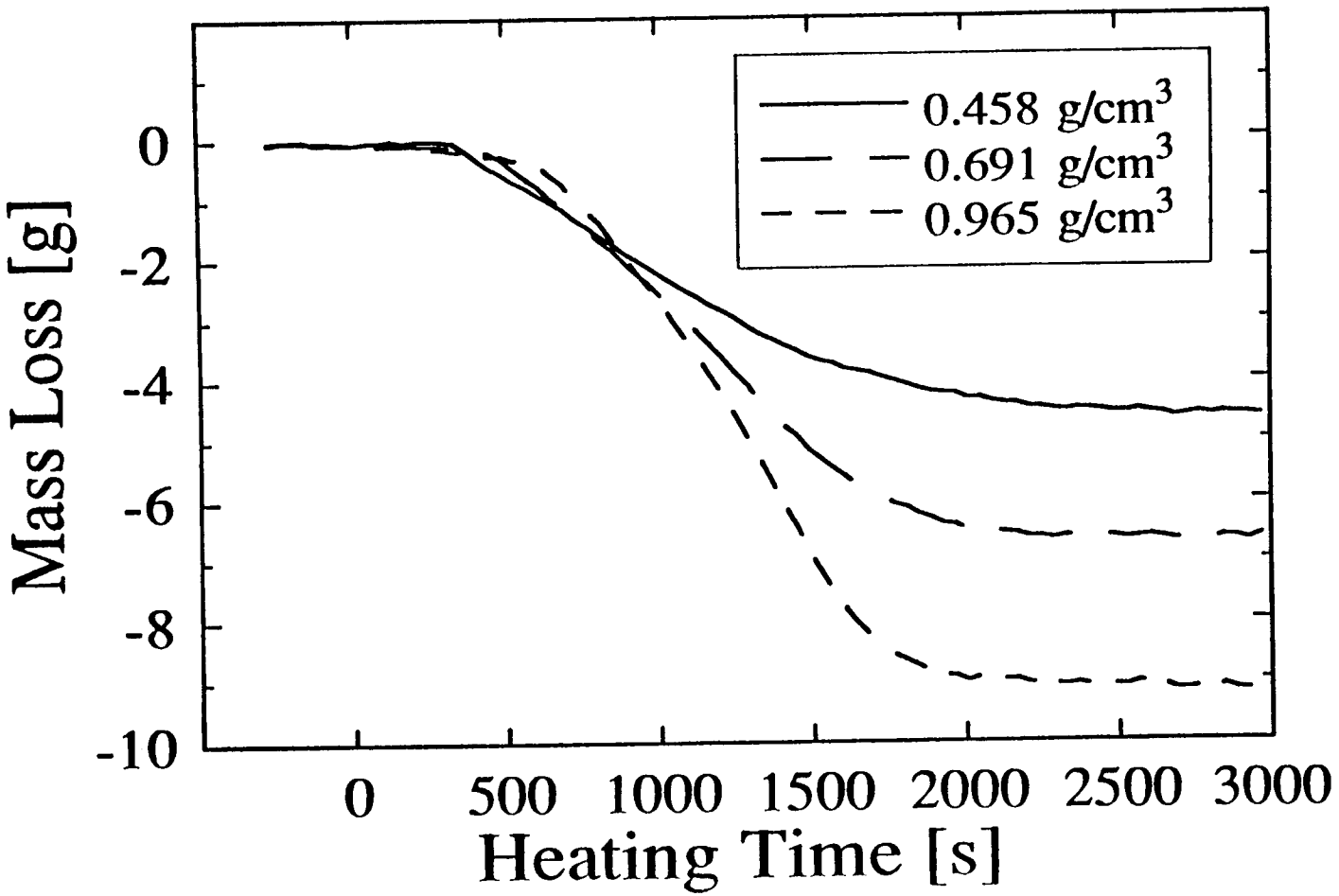

Figure 5.1a Mass loss as a function of time for three different density samples, pyrolyzed with an incident heat flux of 40 kW/m^2

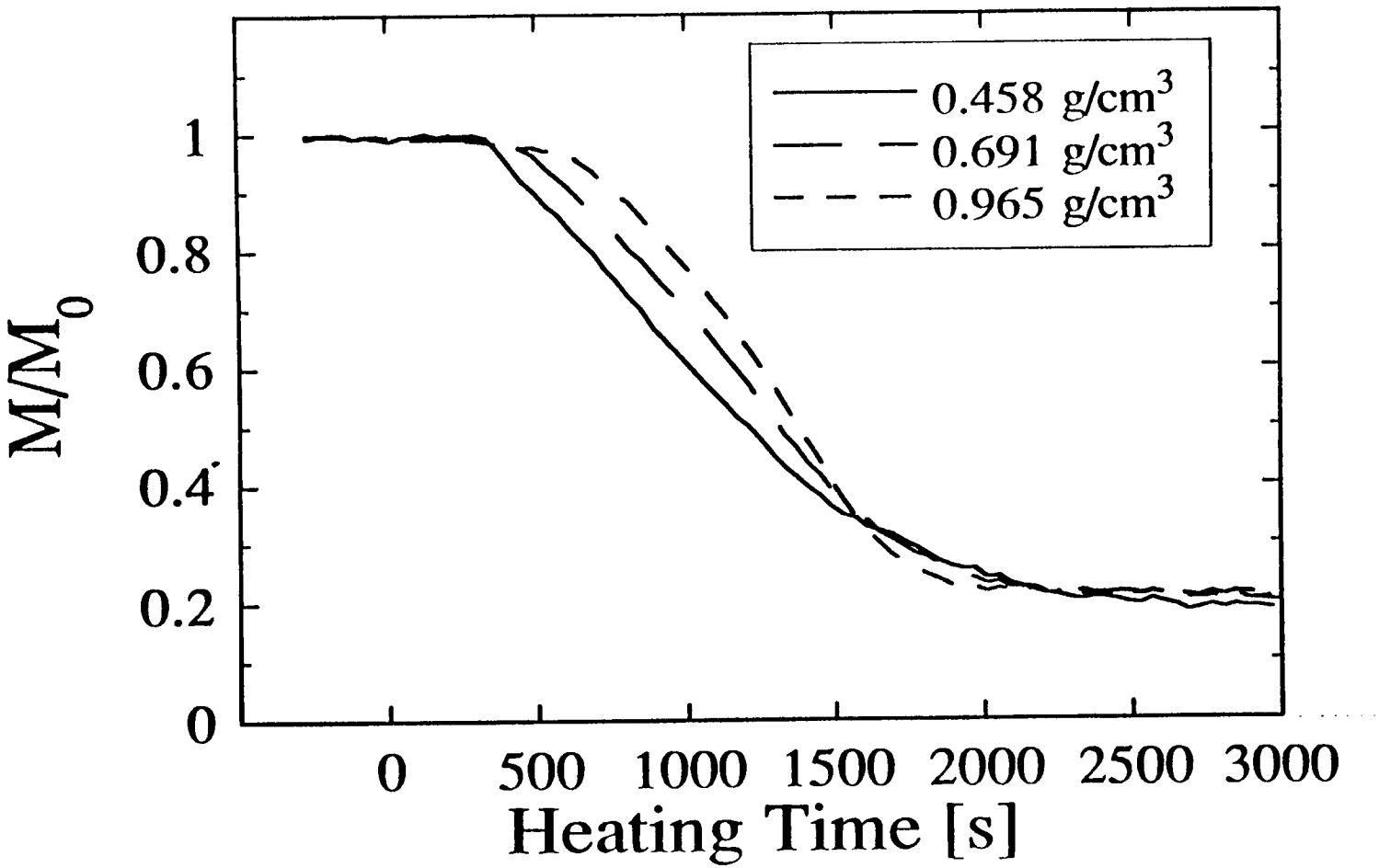

Figure 5.1b Fractional remaining mass as a function of time for three different density samples, pyrolyzed with an incident heat flux of 40 kW/m^2

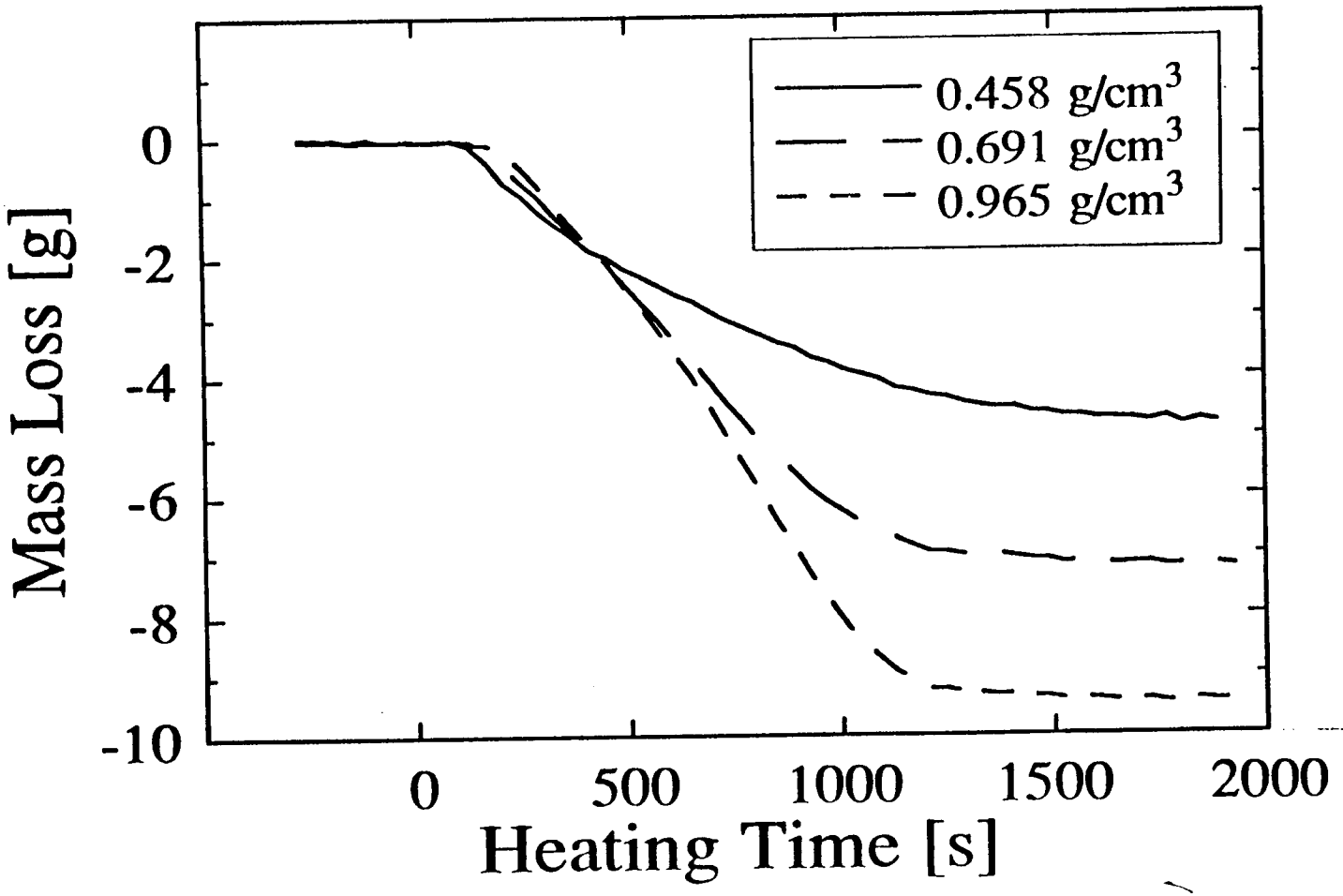

Figure 5.2a Mass loss as a function of time for three different density samples, pyrolyzed with an incident heat flux of 60 kW/m^2

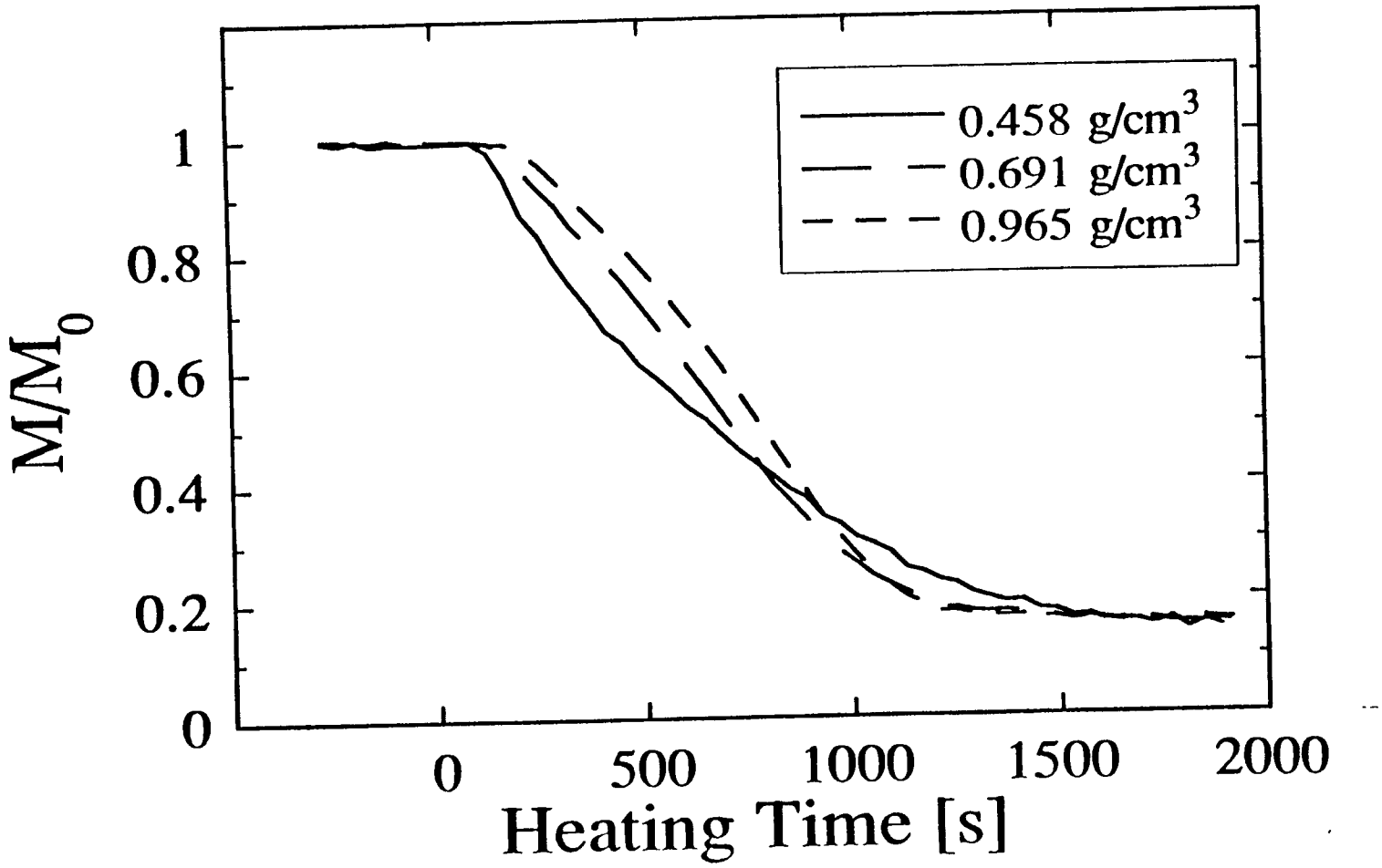

Figure 5.2b Fractional remaining mass as a function of time for three different density samples, pyrolyzed with an incident heat flux of 60 kW/m^2

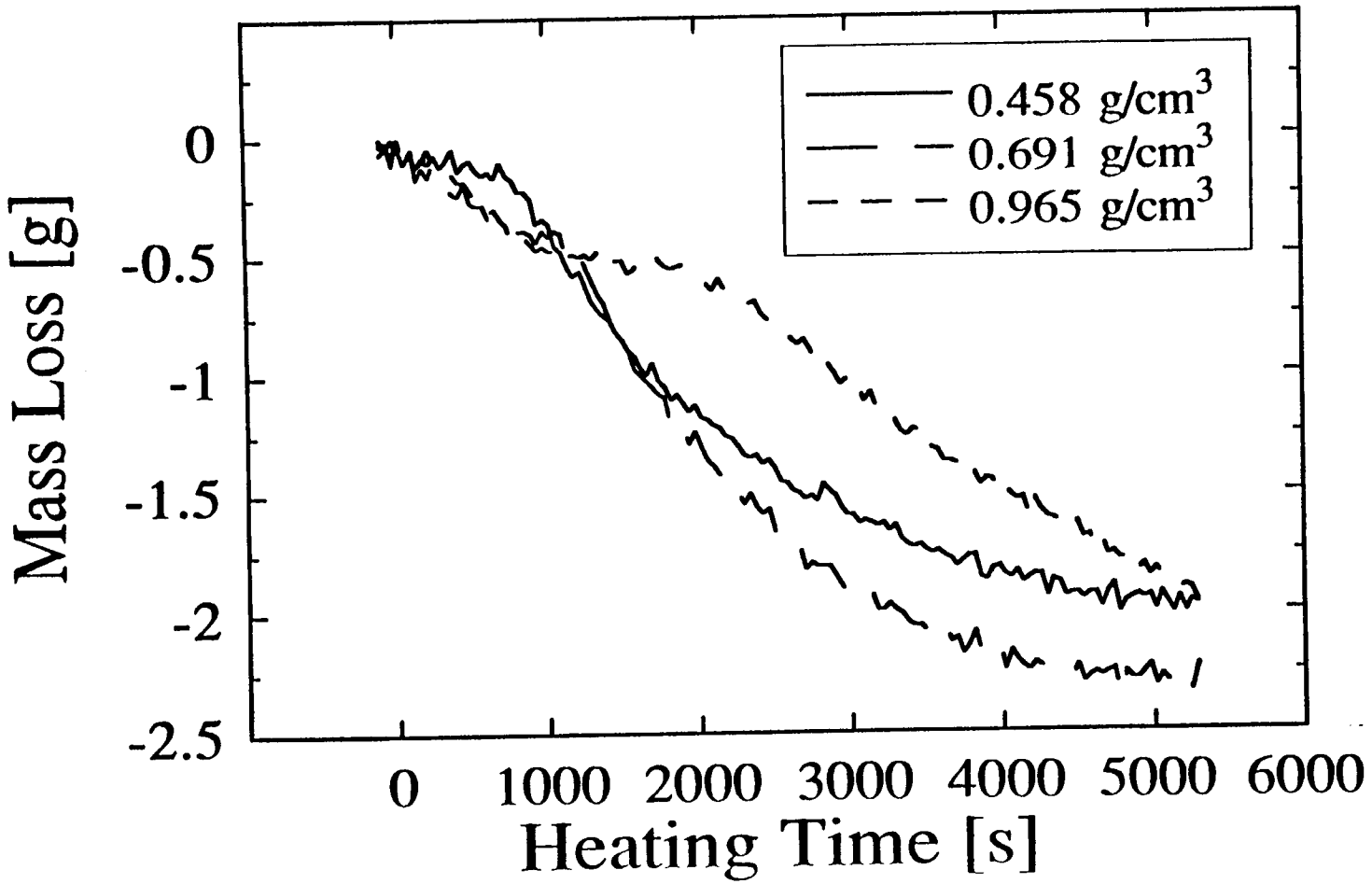

Figure 5.3a Mass loss as a function of time for three different density samples, pyrolyzed with an incident heat flux of 20 kW/m^2

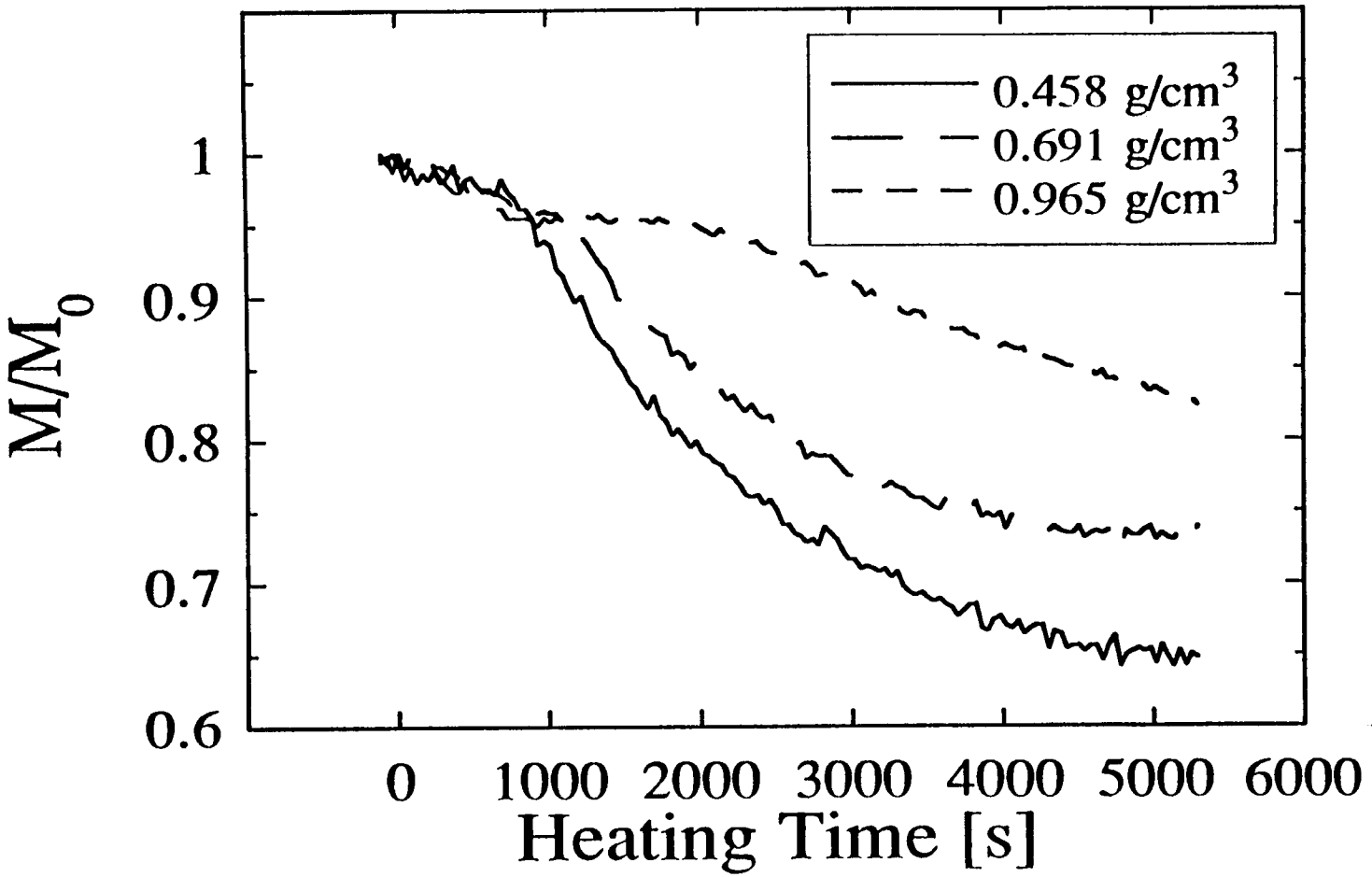

Figure 5.3b Fractional remaining mass as a function of time for three different density samples, pyrolyzed with an incident heat flux of 20 kW/m^2

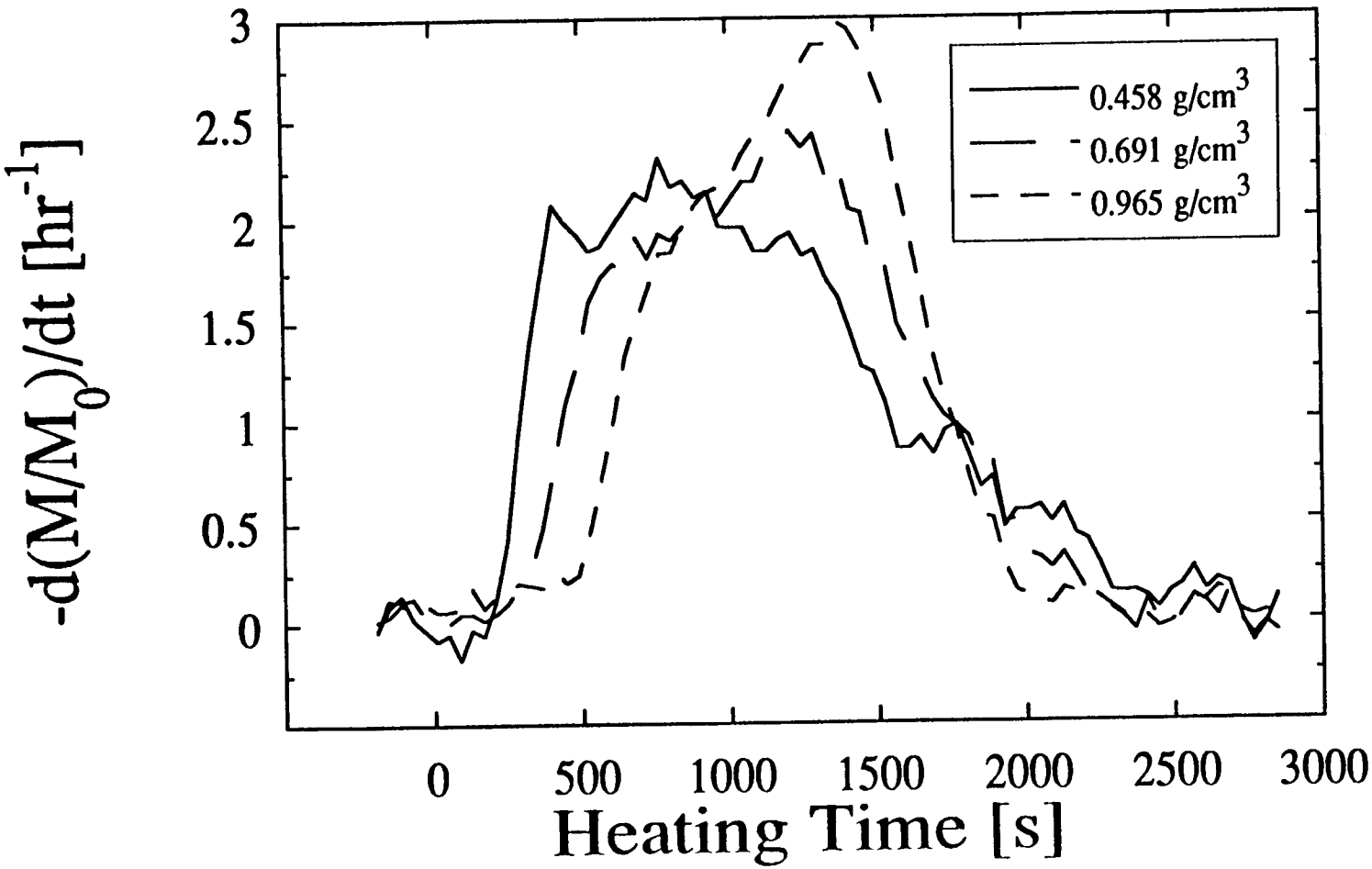

Figure 5.4a Mass loss rate as a function of time for three different density samples, pyrolyzed with an incident heat flux of 40 kW/m^2

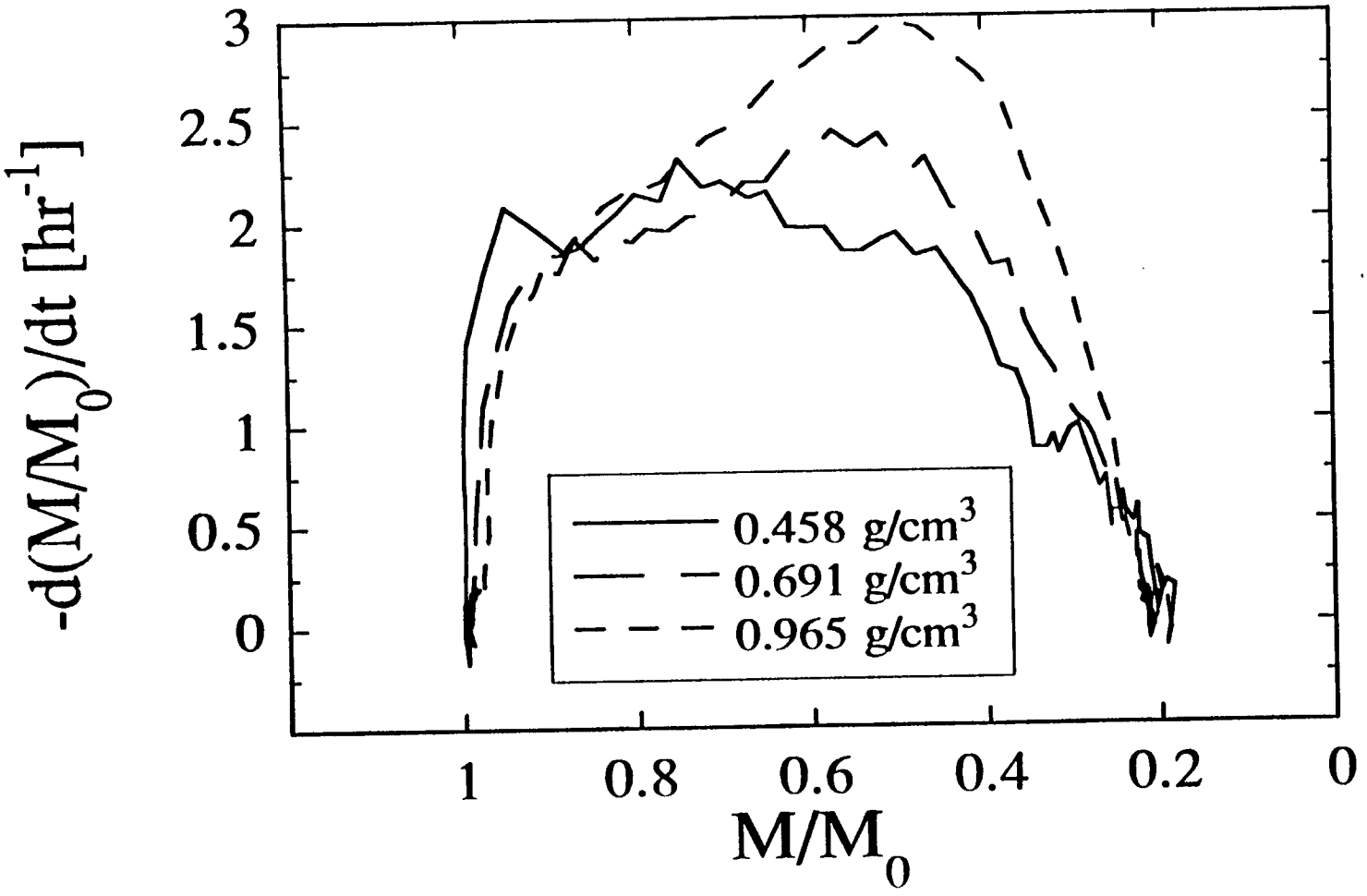

Figure 5.4b Mass loss rate as a function of fractional remaining mass for three different density samples, pyrolyzed with an incident heat flux of 40 kW/m^2

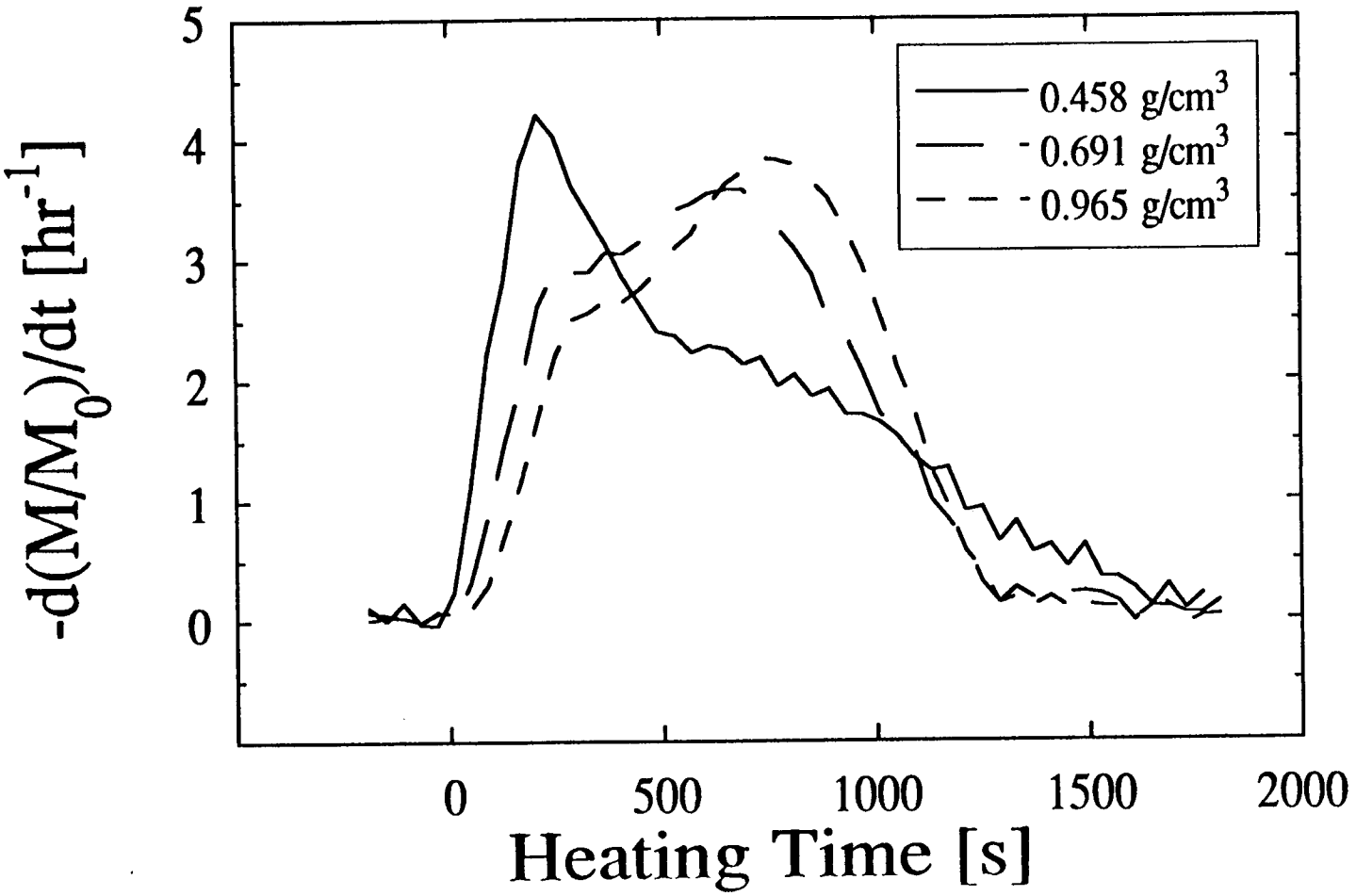

Figure 5.5a Mass loss rate as a function of time for three different density samples, pyrolyzed with an incident heat flux of 60 kW/m^2

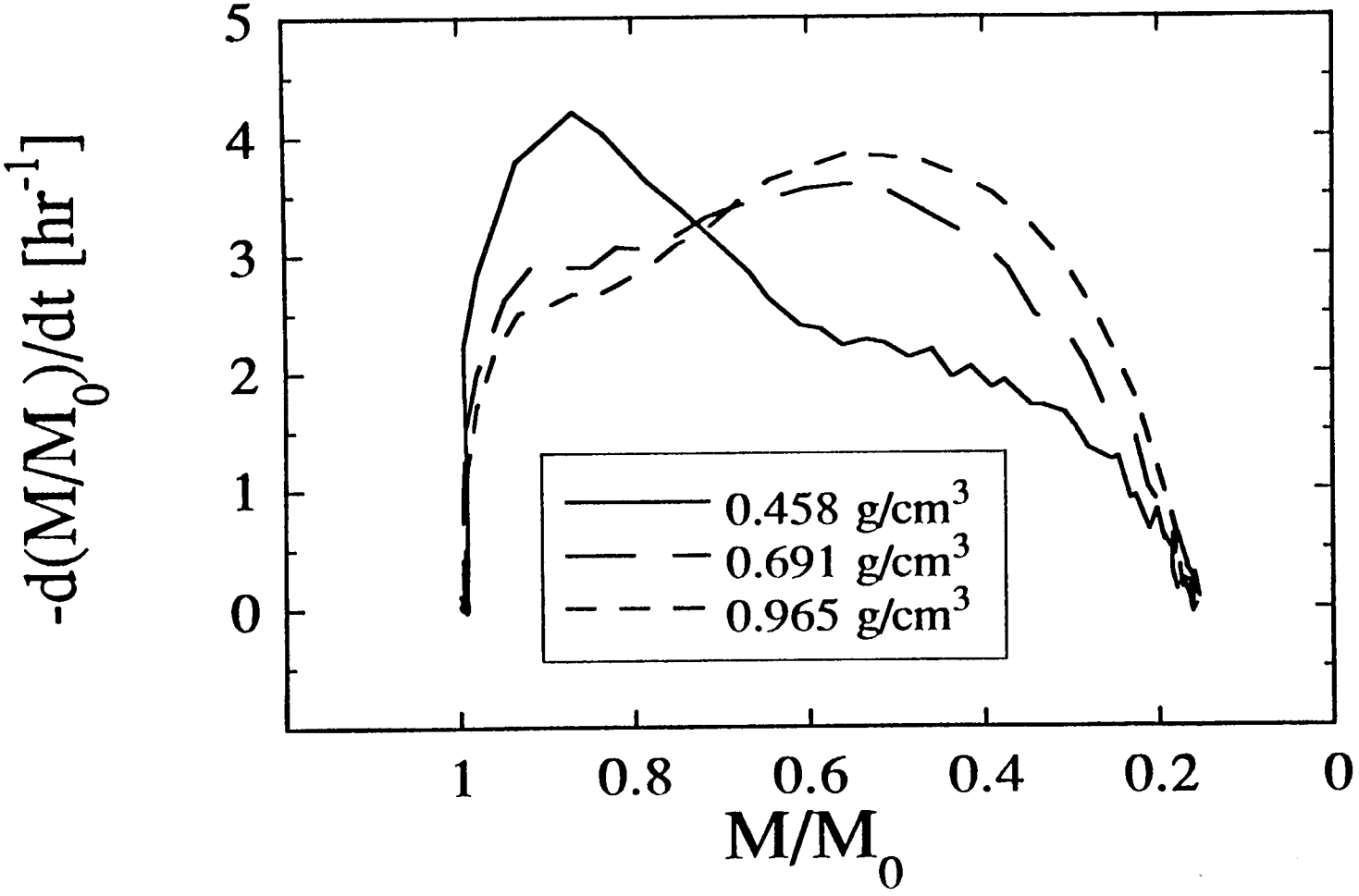

Figure 5.5b Mass loss rate as a function of fractional remaining mass for three different density samples, pyrolyzed with an incident heat flux of 60 kW/m^2

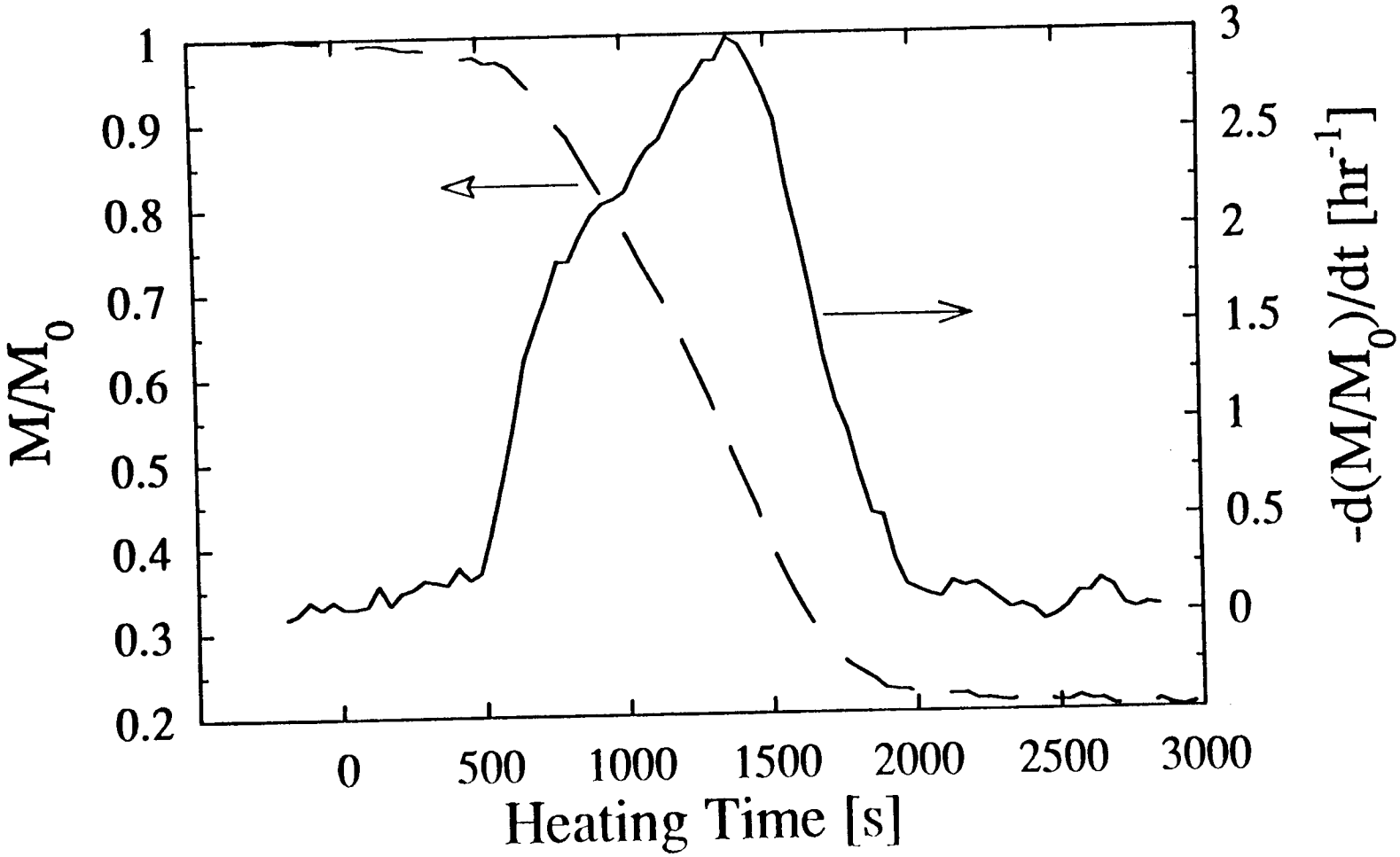

Figure 5.6a Fractional remaining mass and mass loss rate as functions of time for high density sample (0.965 g/cm^3), pyrolyzed with an incident heat flux of 40 kW/m^2

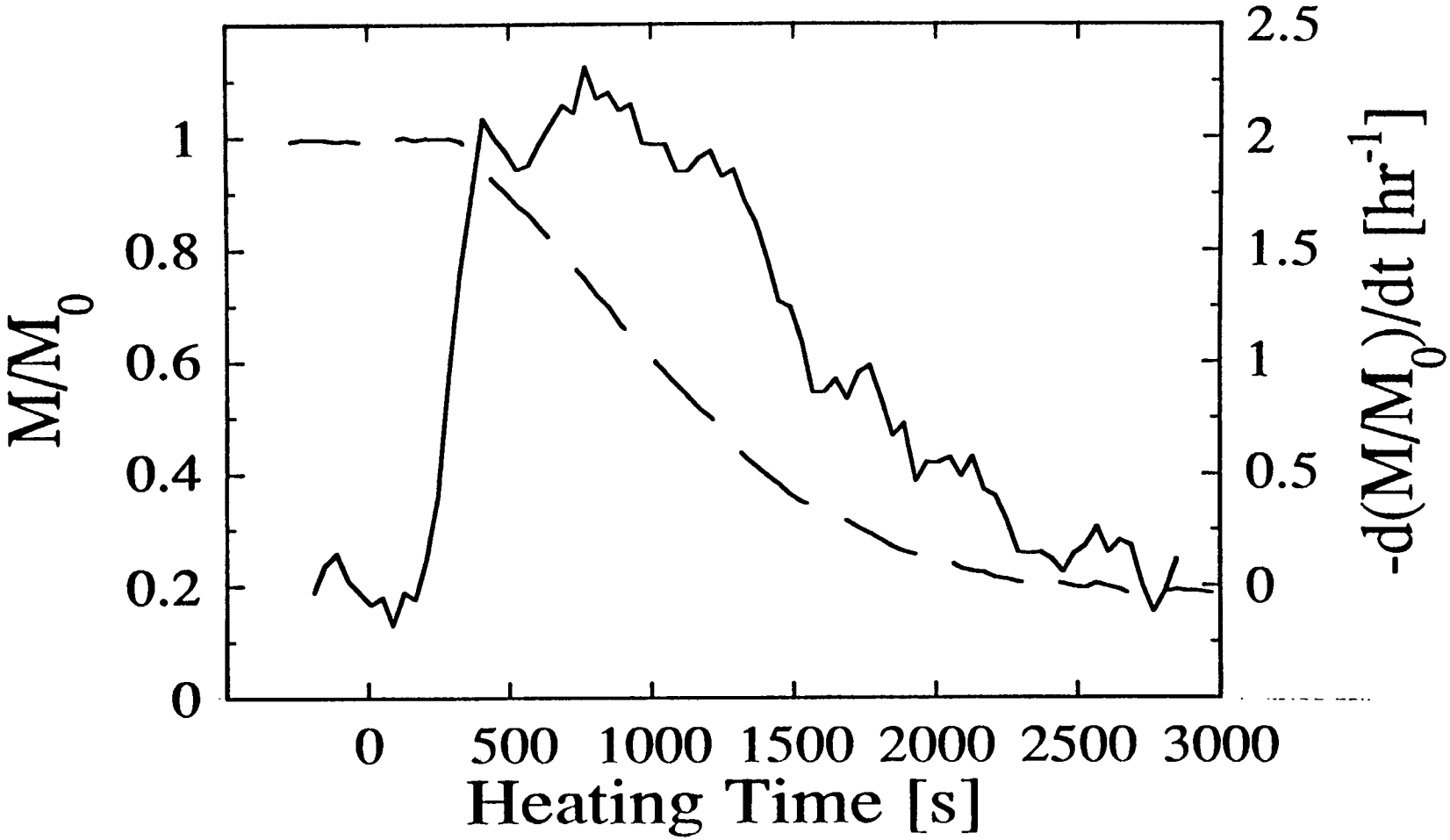

Figure 5.6b Fractional remaining mass and mass loss rate as functions of time for low density sample (0.458 g/cm^3), pyrolyzed with an incident heat flux of 40 kW/m^2

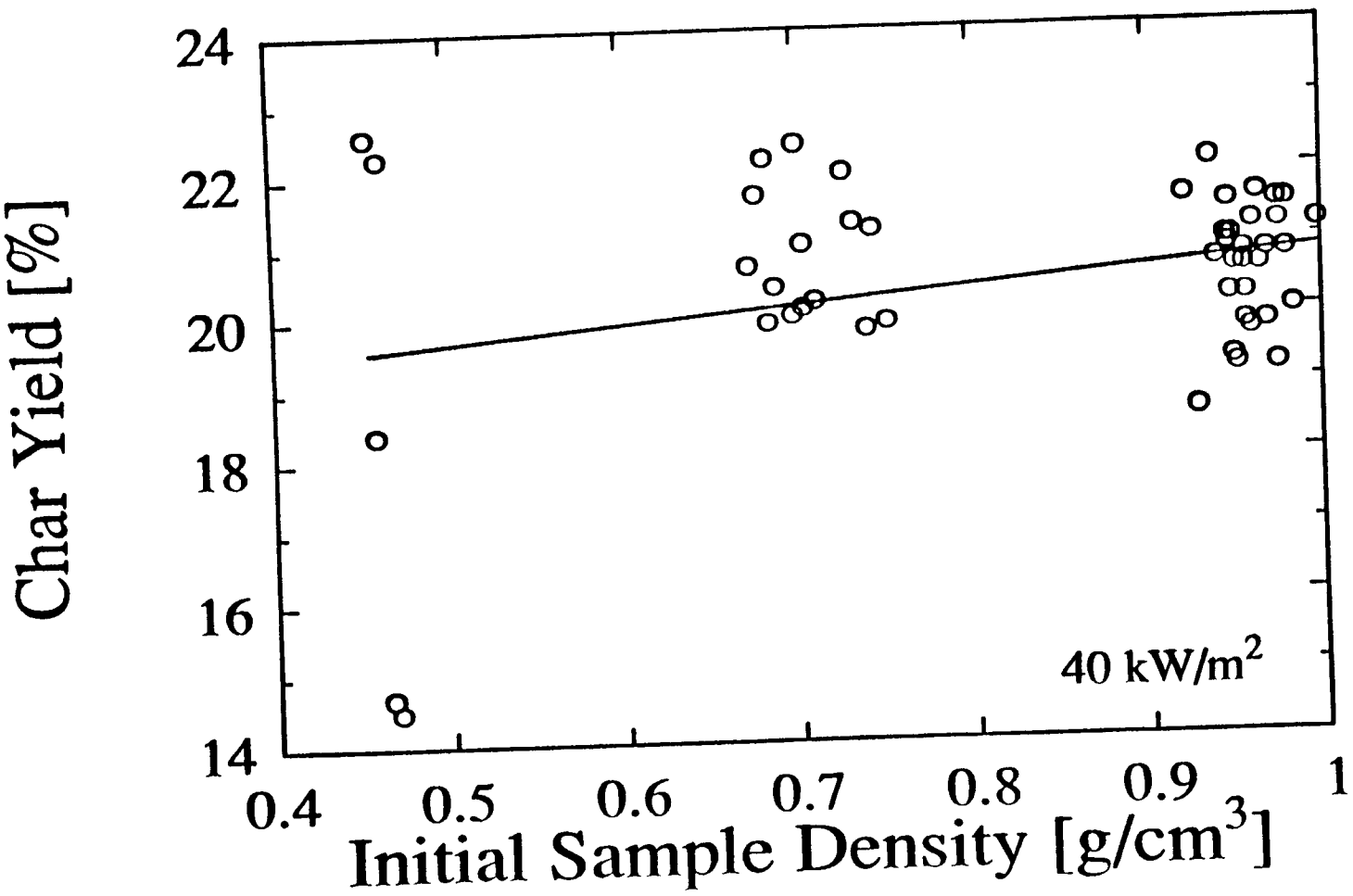

Figure 5.7a Ultimate char yield with an incident heat flux of 40 kW/m^2 as a function of initial sample density

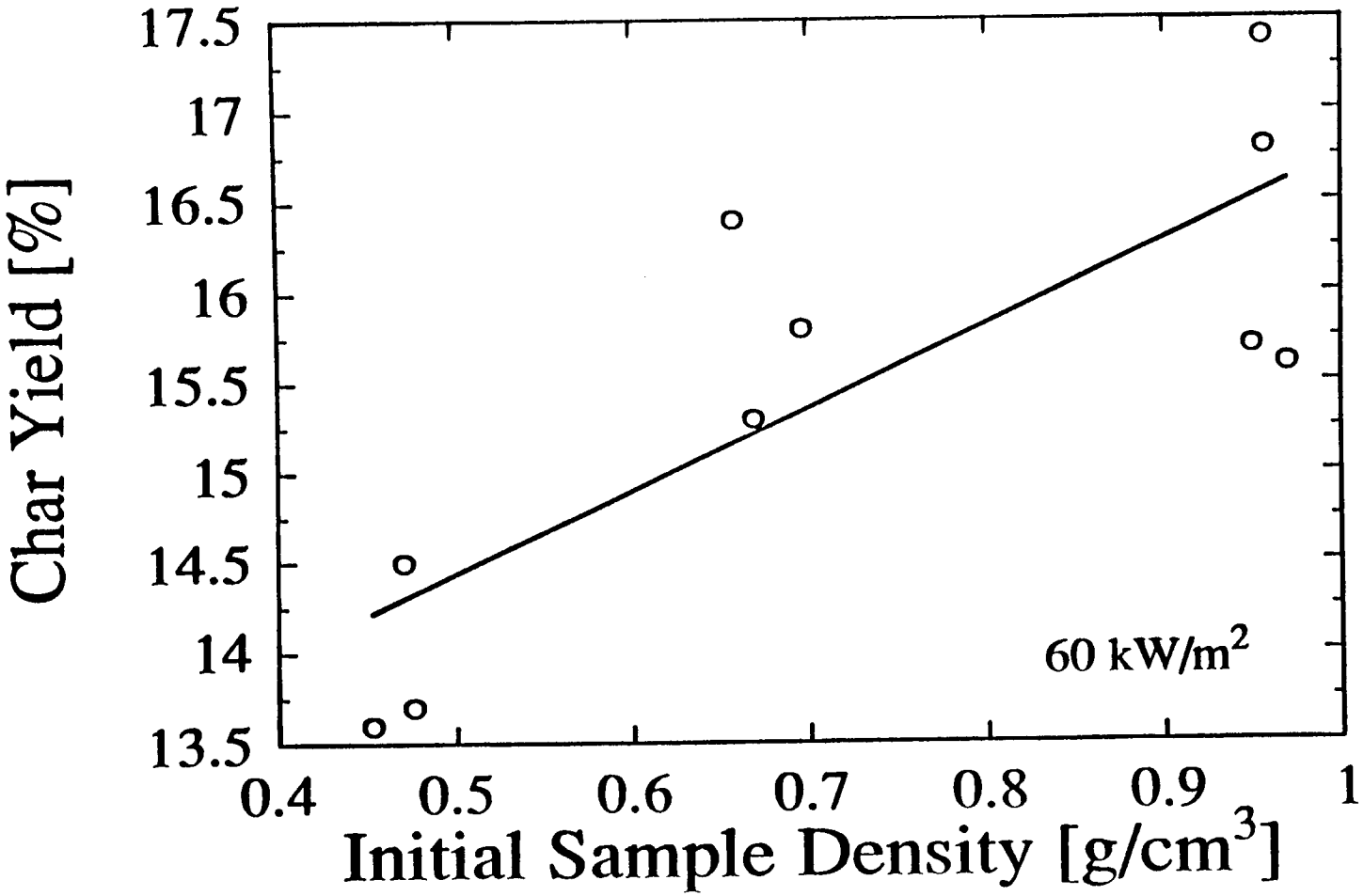

Figure 5.7b Ultimate char yield with an incident heat flux of 60 kW/m^2 as a function of initial sample density

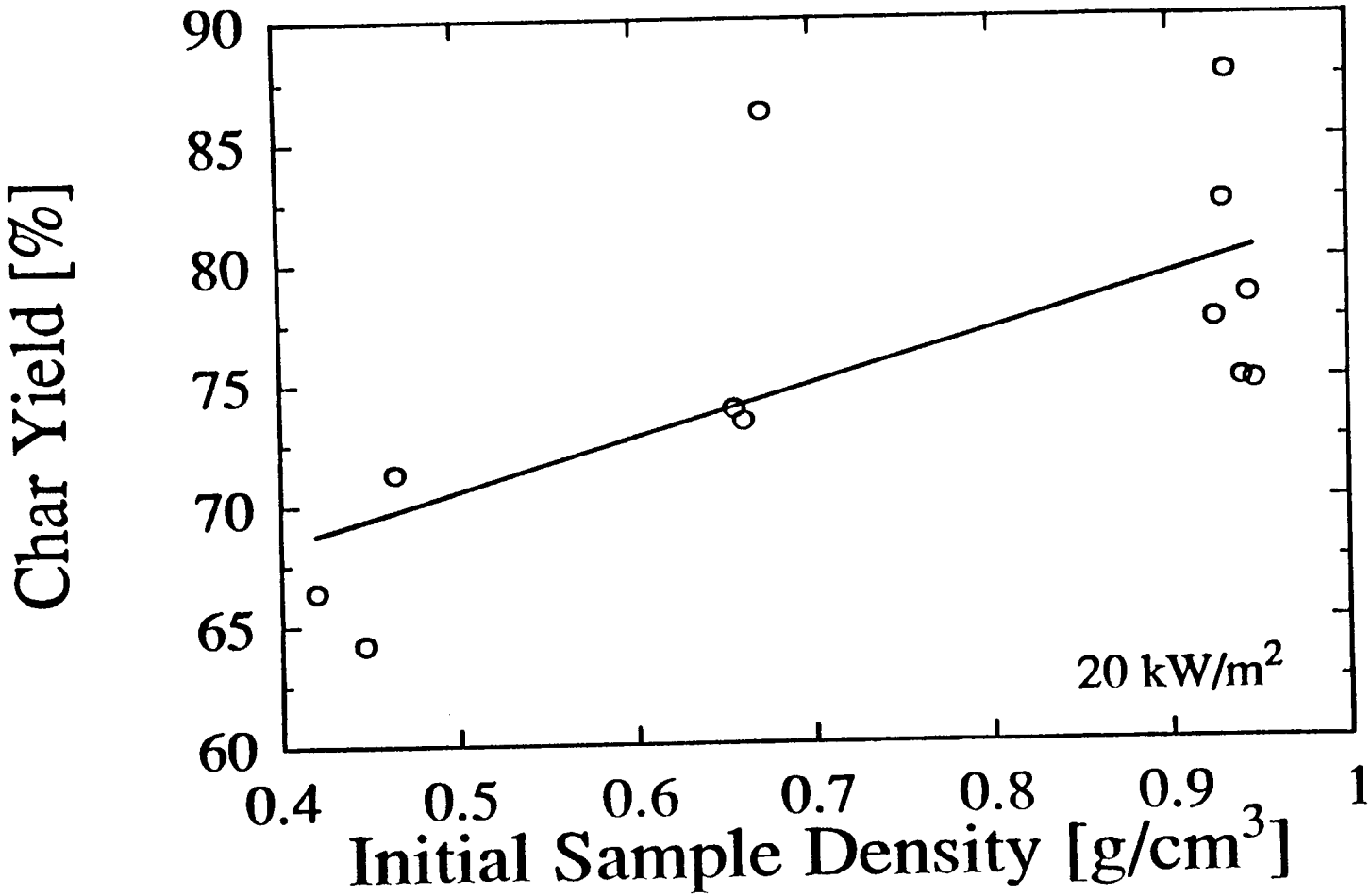

Figure 5.7c Ultimate char yield with an incident heat flux of 20 kW/m^2 as a function of initial sample density

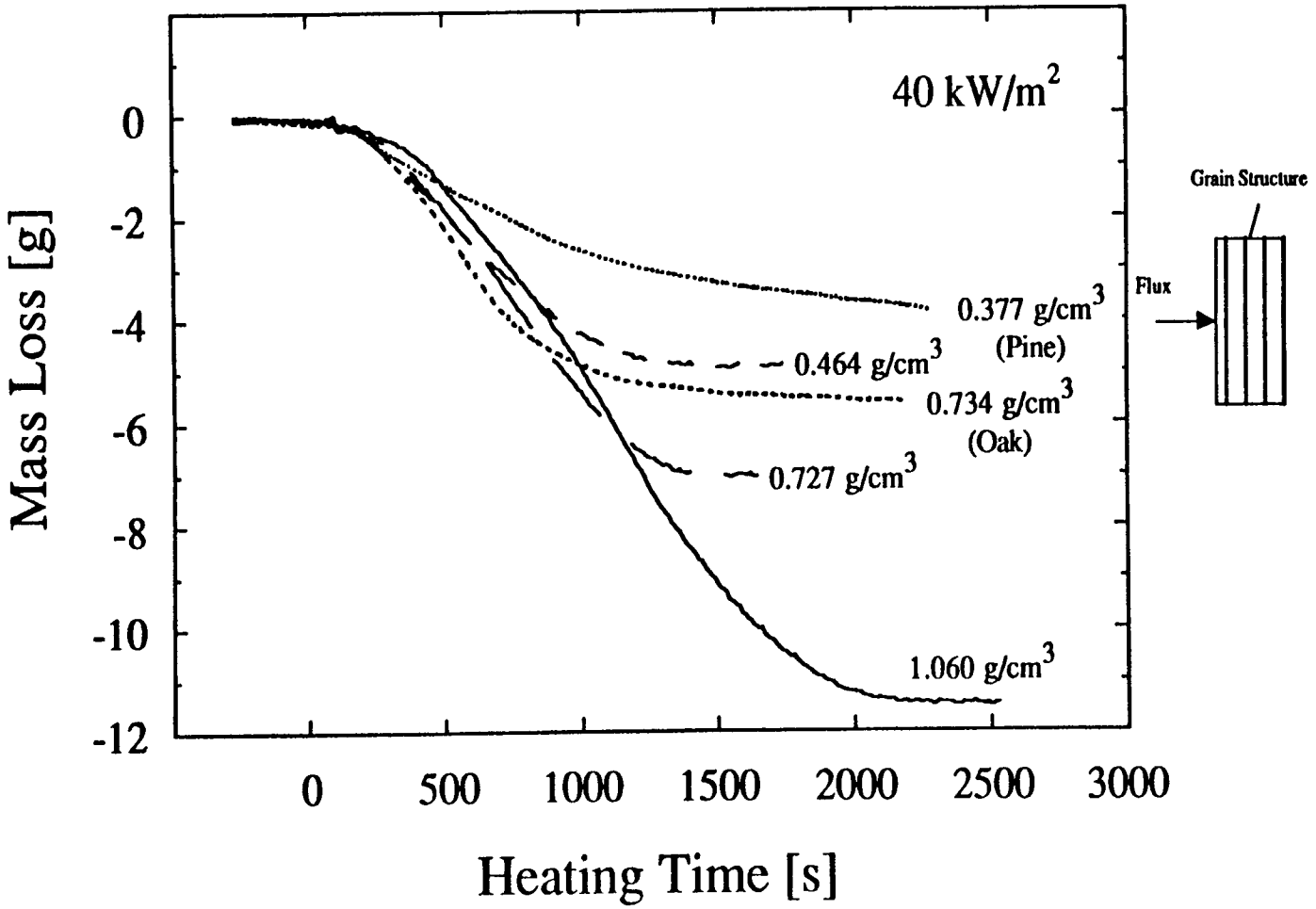

Figure 5.8a Mass loss as a function of time for three different cellulose samples, oak and pine, for perpendicular grain orientation and an incident heat flux of 40 kW/m^2

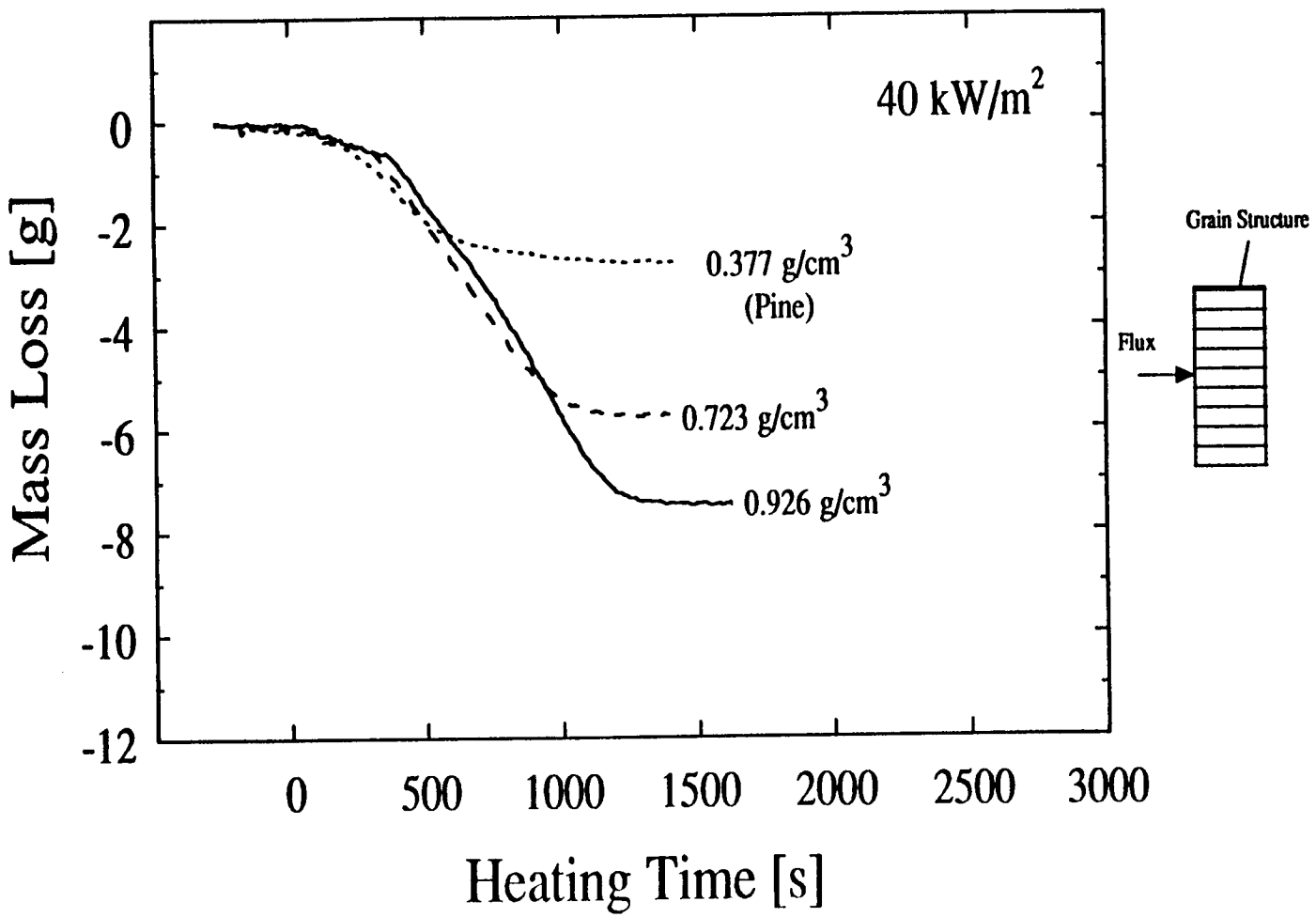

Figure 5.8b Mass loss as a function of time for three different cellulose samples and pine, for parallel grain orientation and an incident heat flux of 40 kW/m^2

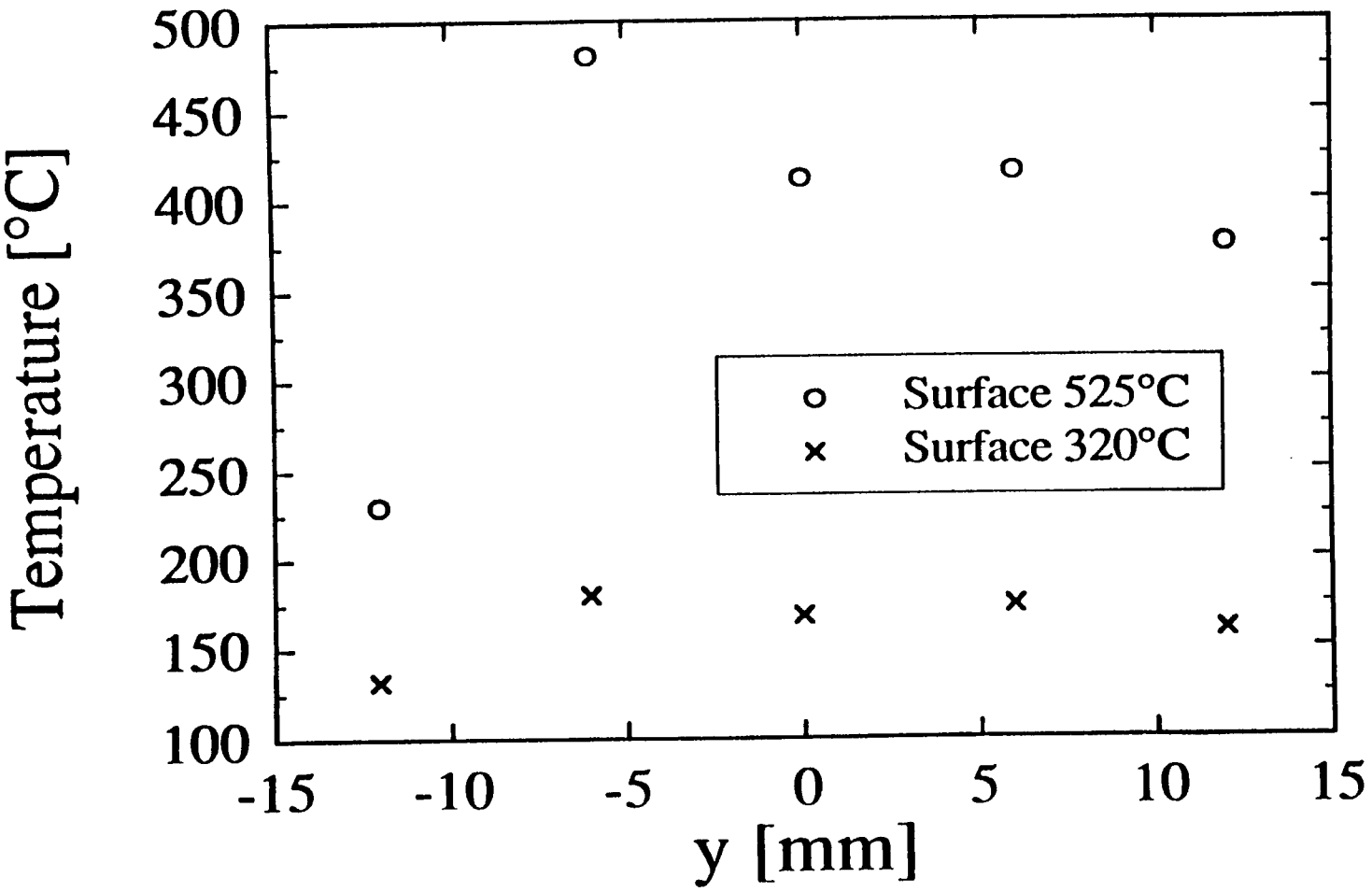

Figure 5.9 Radial temperature profile in a high density (0.965 g/cm^3) sample undergoing pyrolysis with an incident heat flux of 40 kW/m^2, for surface temperatures of 320°C and 525°C

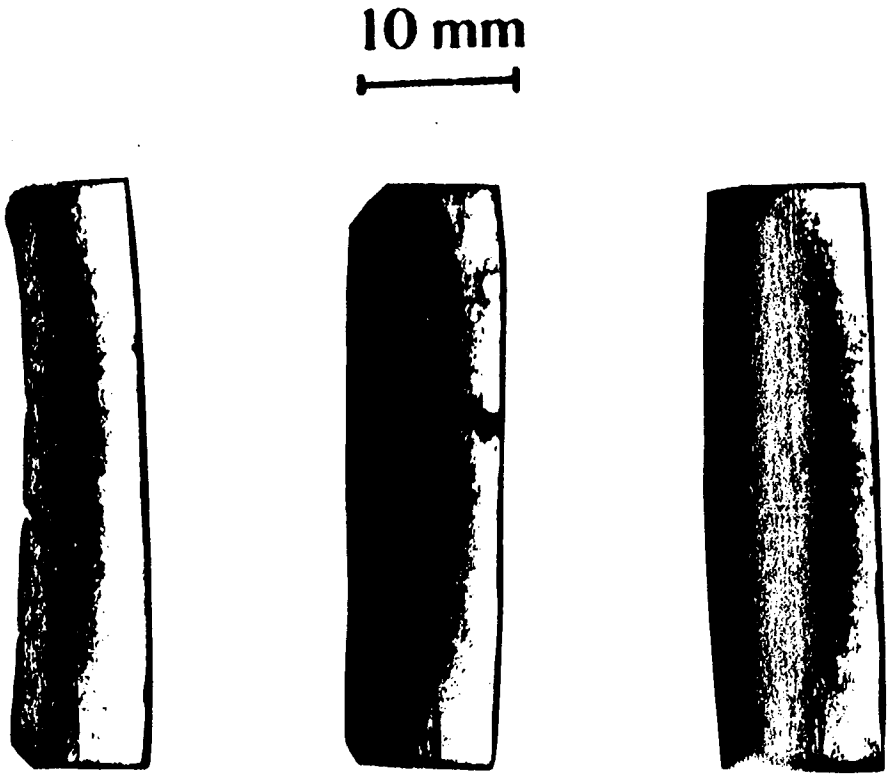

Figure 5.10 Pyrolysis front in high density (0.965 g/cm^3) samples of the same initial thickness of 10 mm (note different amount of shrinkage), with pyrolysis quenched at different times and for three different incident heat fluxes (from left to right: 60, 40 and 20 kW/m^2).

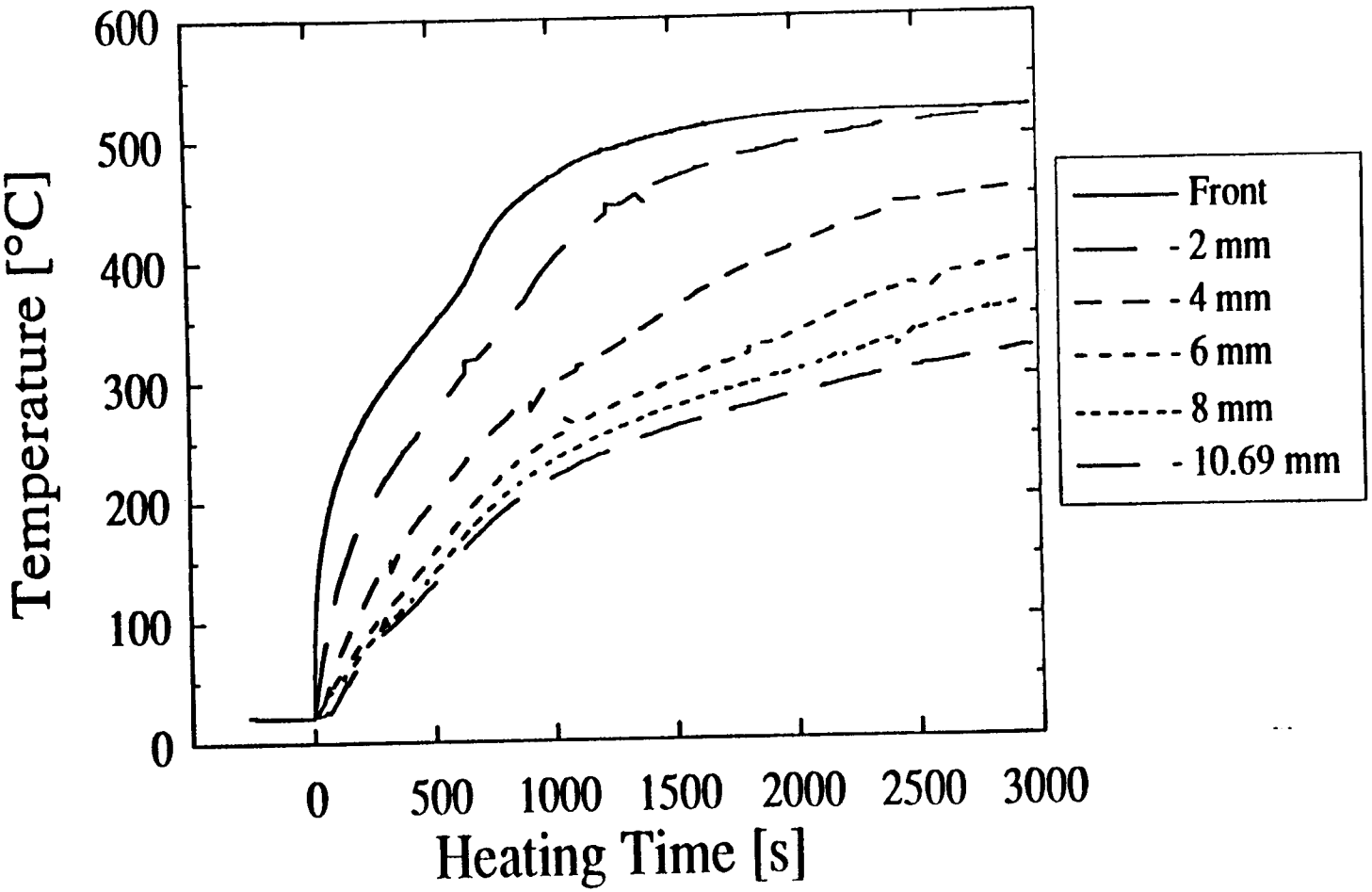

Figure 5.11a Temperatures as a function of distance from the front surface and time for a high density (0.965 g/cm^3) sample, pyrolyzed under incident heat flux of 40 kW/m^2

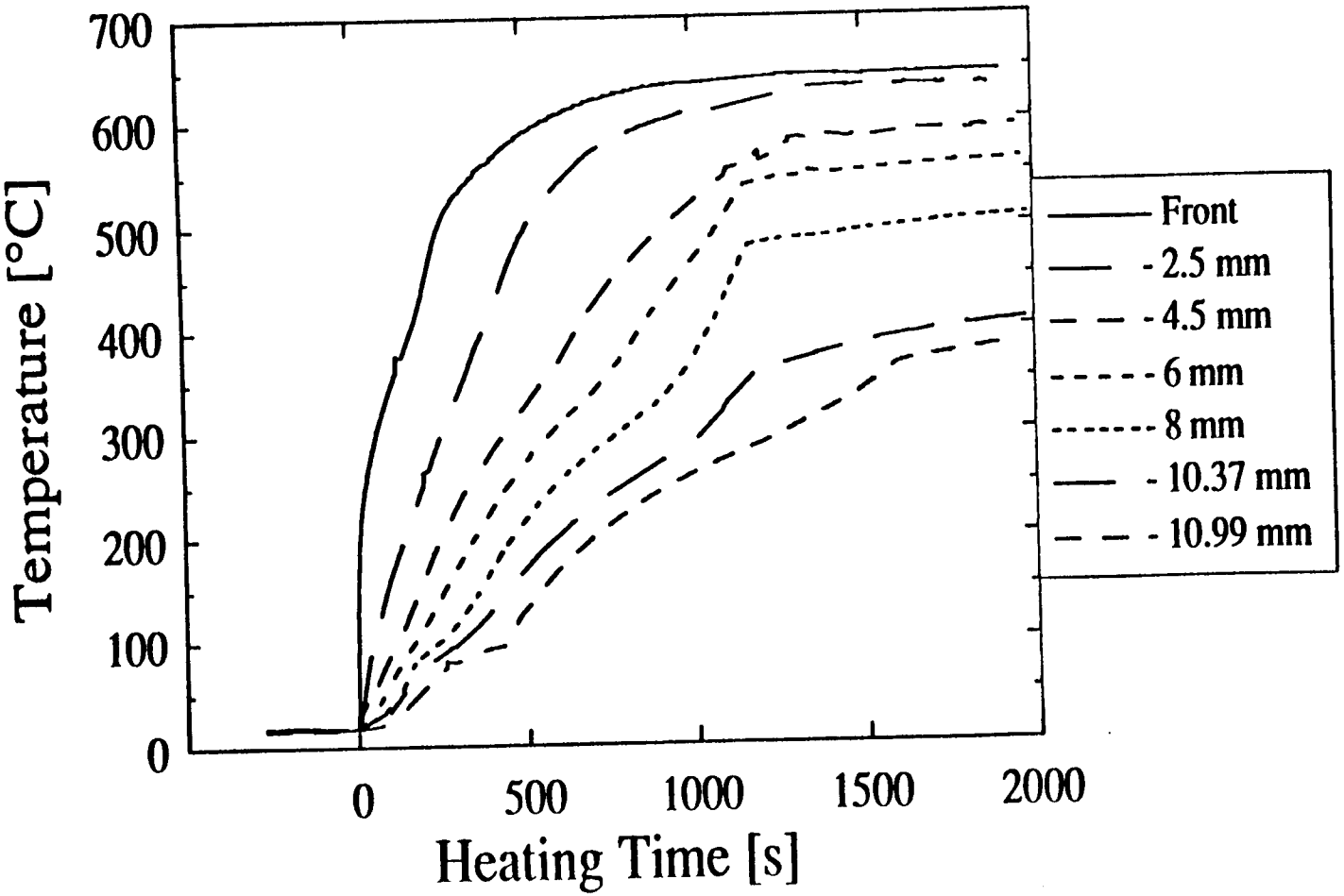

Figure 5.11b Temperatures as a function of distance from the front surface and time for a high density (0.965 g/cm^3) sample, pyrolyzed under incident heat flux of 60 kW/m^2

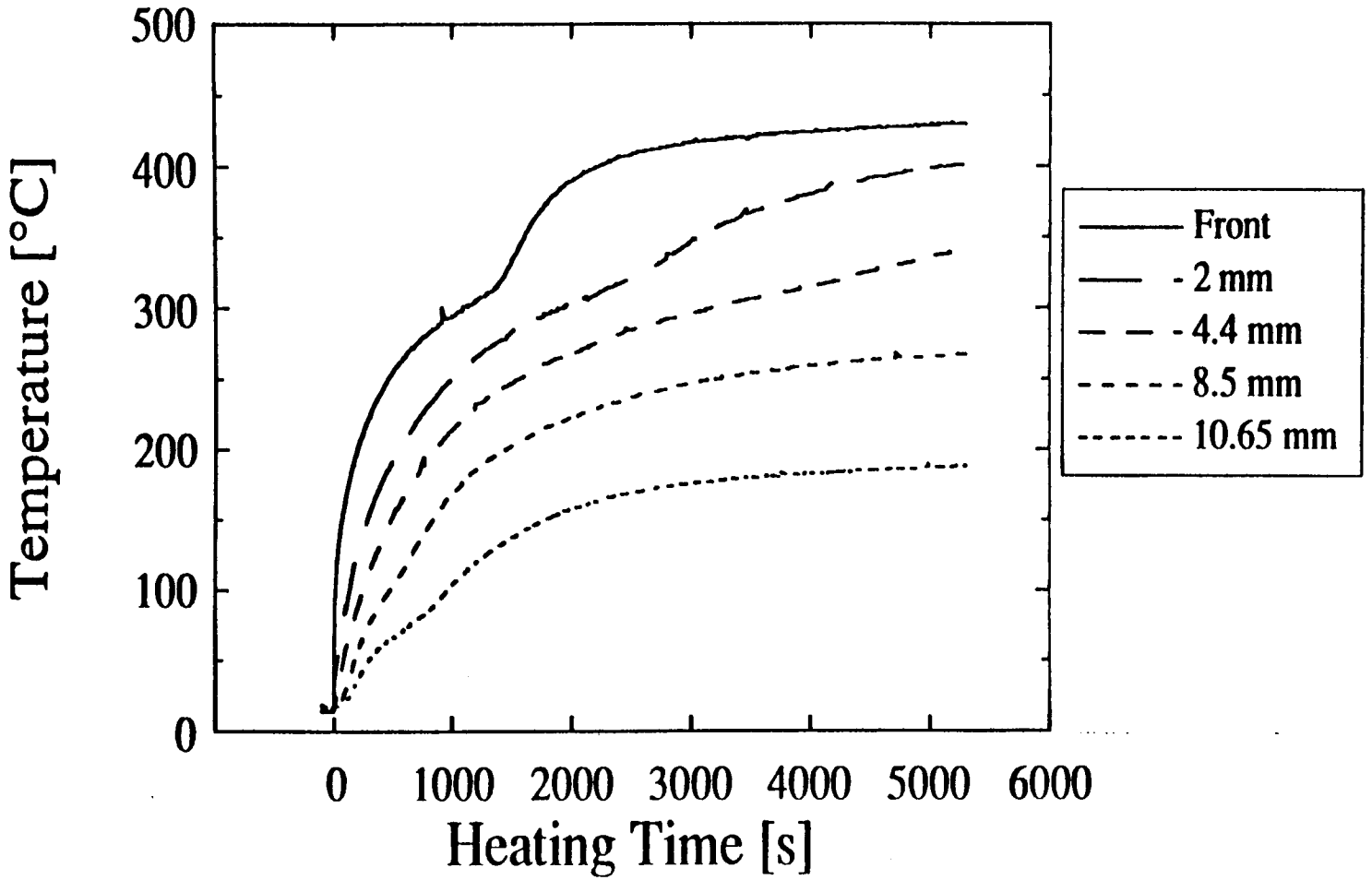

Figure 5.11c Temperatures as a function of distance from the front surface and time for a high density (0.965 g/cm^3) sample, pyrolyzed under incident heat flux of 20 kW/m^2

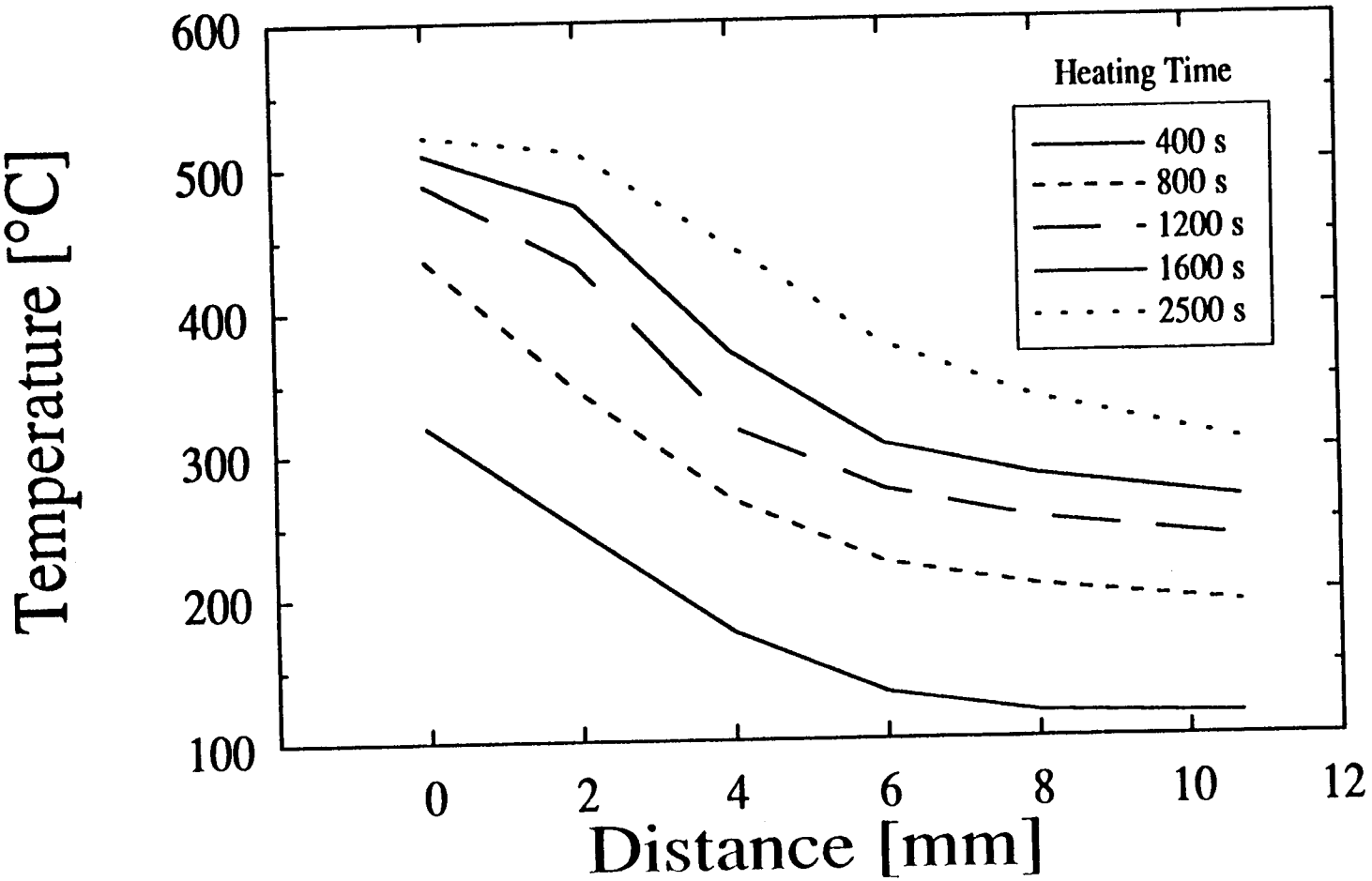

Figure 5.11d Axial temperature profiles in a high density (0.965 g/cm^3) sample, undergoing pyrolysis with an incident heat flux of 40 kW/m^2

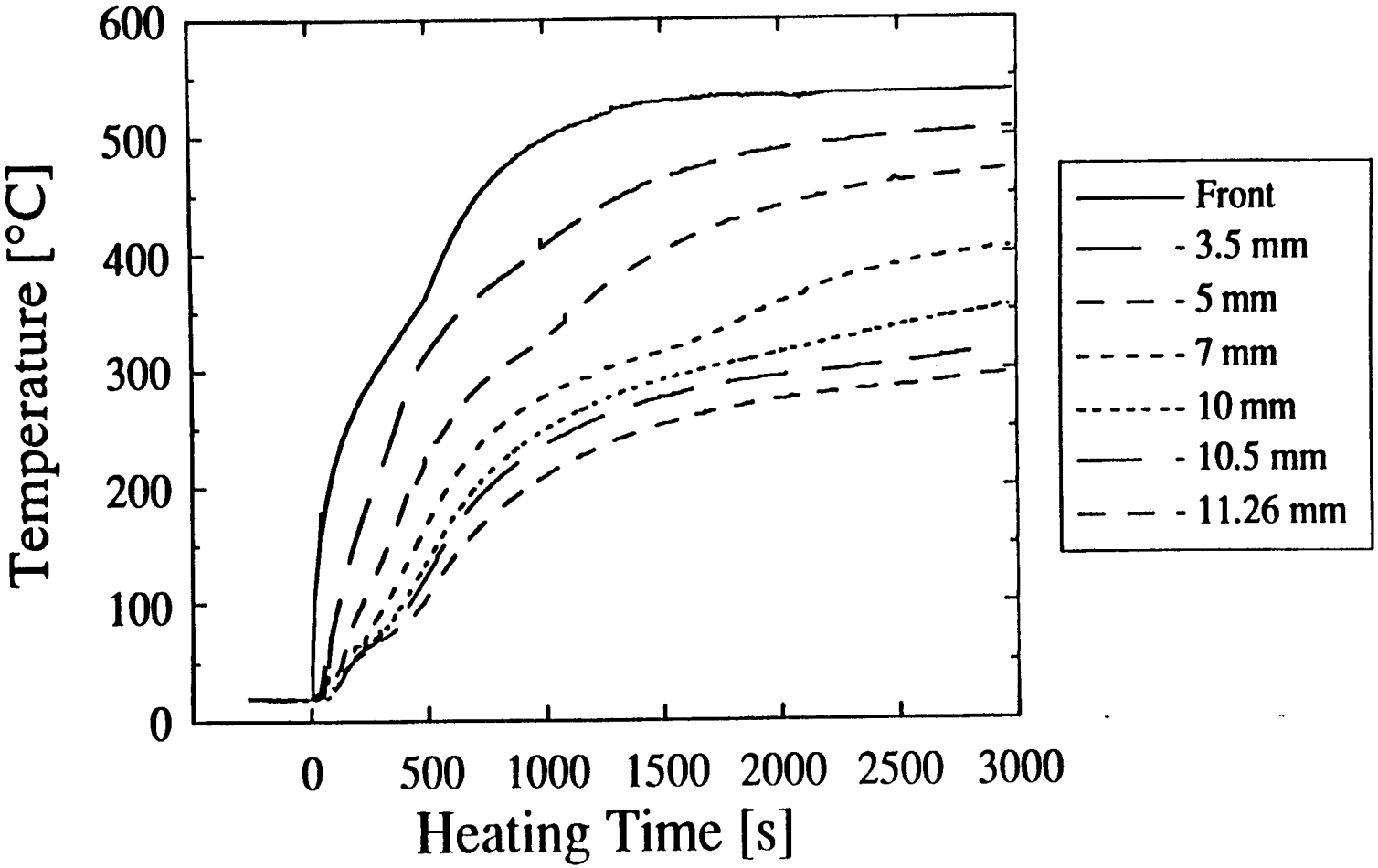

Figure 5.12a Temperatures as a function of distance from the front surface and time for a medium density (0.691 g/cm^3) sample, pyrolyzed under incident heat flux of 40 kW/m^2

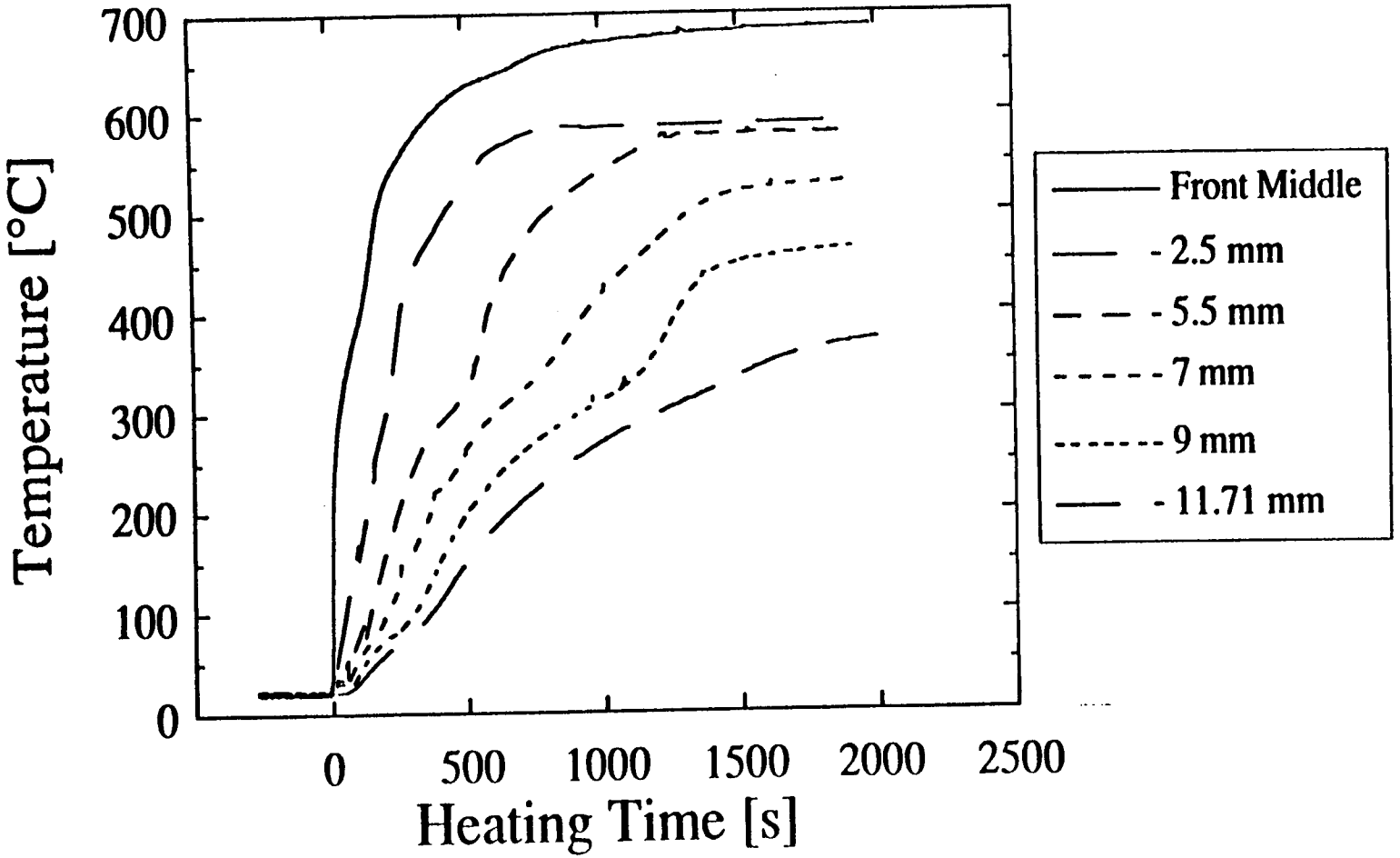

Figure 5.12b Temperatures as a function of distance from the front surface and time for a medium density (0.691 g/cm^3) sample, pyrolyzed under incident heat flux of 60 kW/m^2

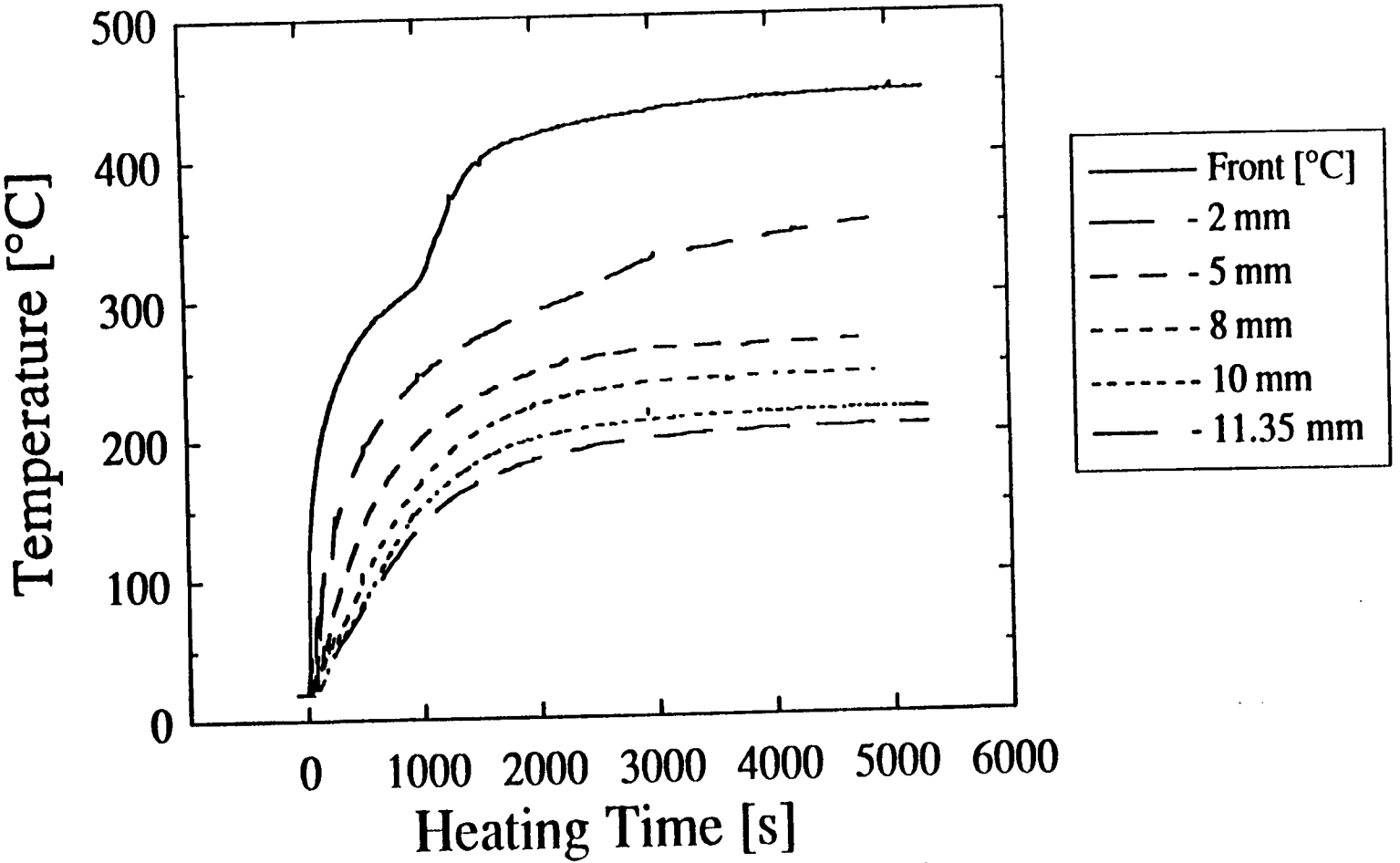

Figure 5.12c Temperatures as a function of distance from the front surface and time for a medium density (0.691 g/cm^3) sample, pyrolyzed under incident heat flux of 20 kW/m^2

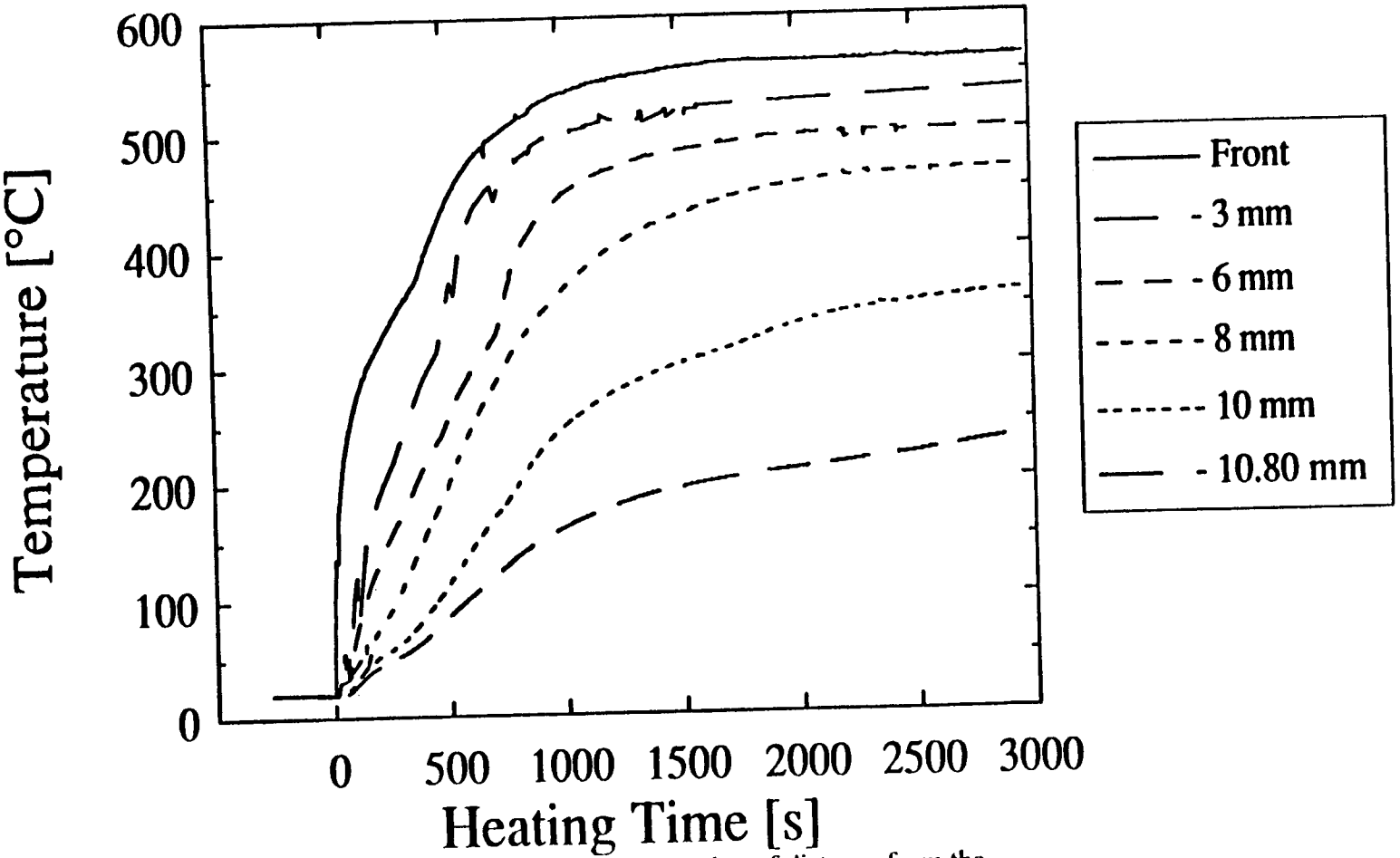

Figure 5.13a Temperatures as a function of distance from the front surface and time for a low density (0.458 g/cm^3) sample, pyrolyzed under incident heat flux of 40 kW/m^2

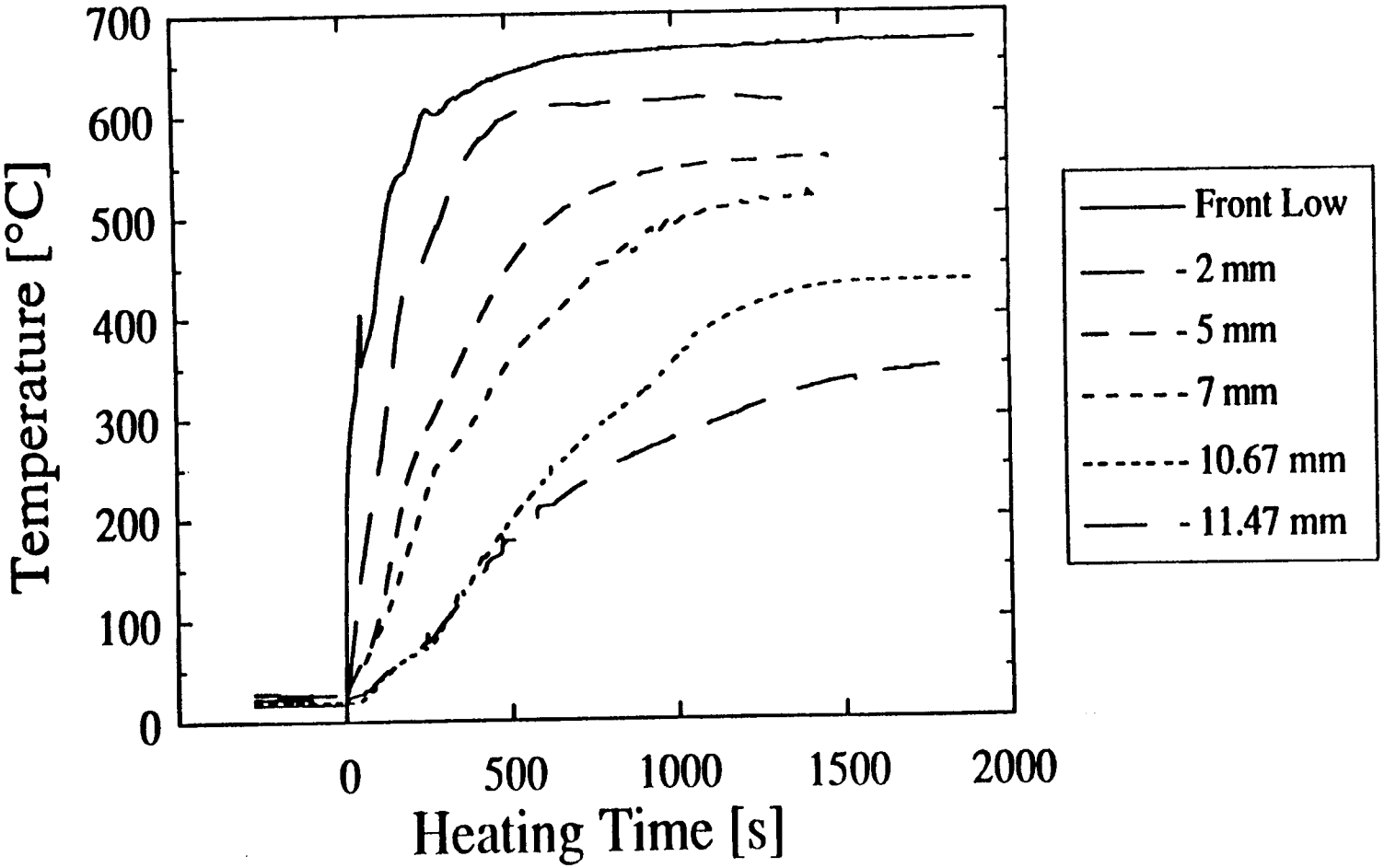

Figure 5.13b Temperatures as a function of distance from the front surface and time for a low density (0.458 g/cm^3) sample, pyrolyzed under incident heat flux of 60 kW/m^2

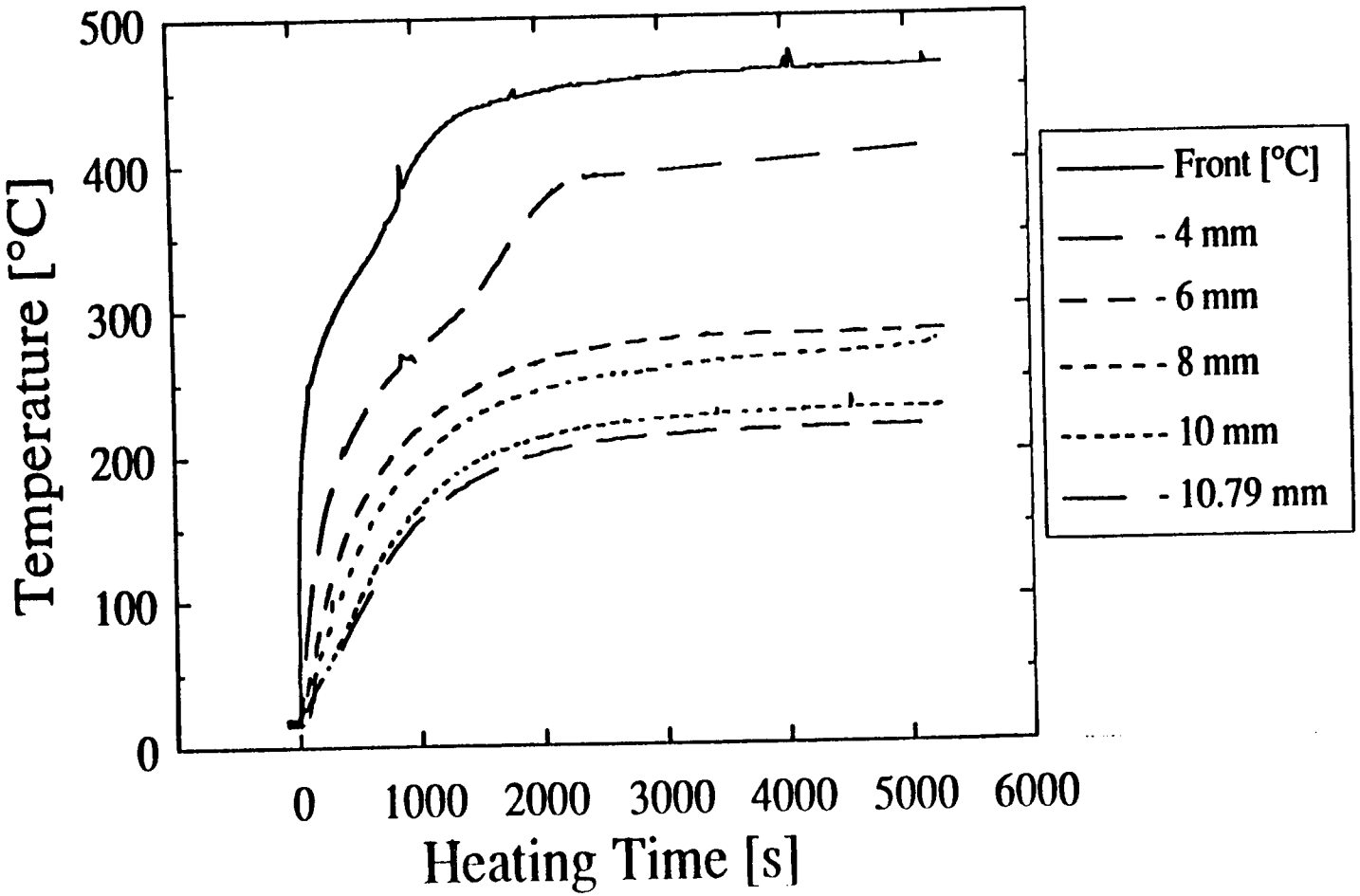

Figure 5.13c Temperatures as a function of distance from the front surface and time for a low density (0.458 g/cm^3) sample, pyrolyzed under incident heat flux of 20 kW/m^2

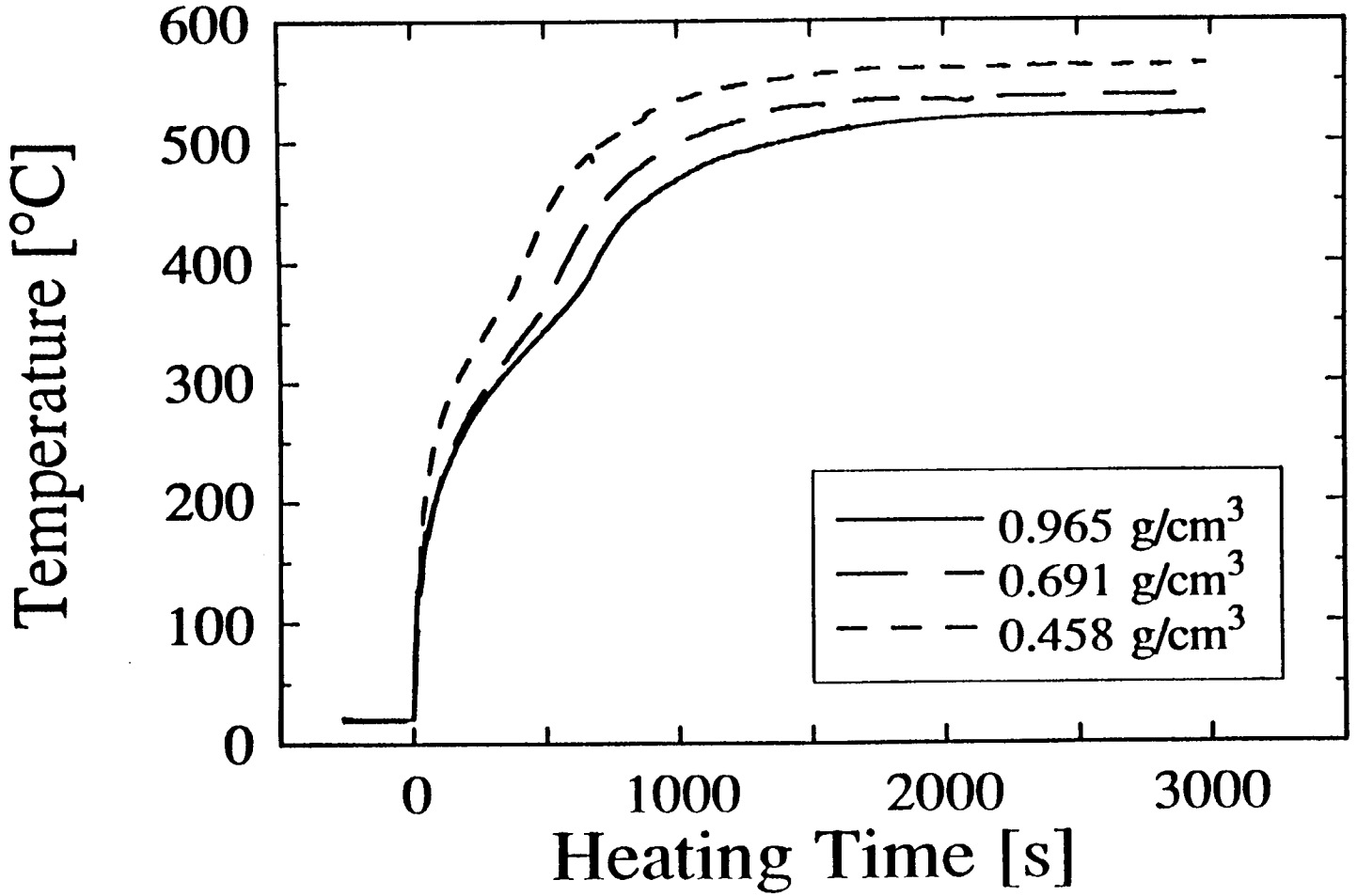

Figure 5.14a A comparison of front surface temperatures for three different density samples, undergoing pyrolysis with an incident heat flux of 40 kW/m^2

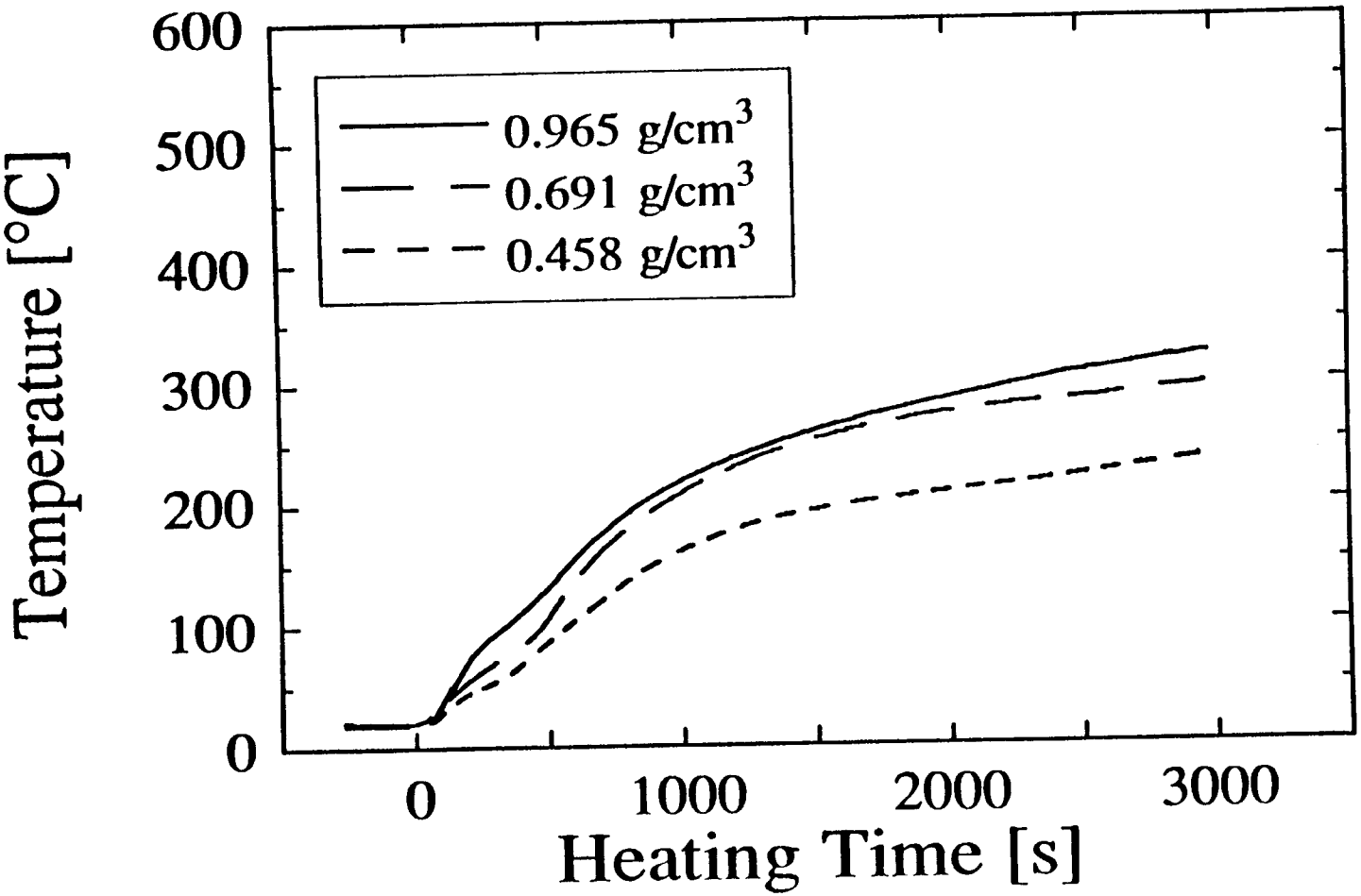

Figure 5.14b A comparison of back surface temperatures for three different density samples, undergoing pyrolysis with an incident heat flux of 40 kW/m^2

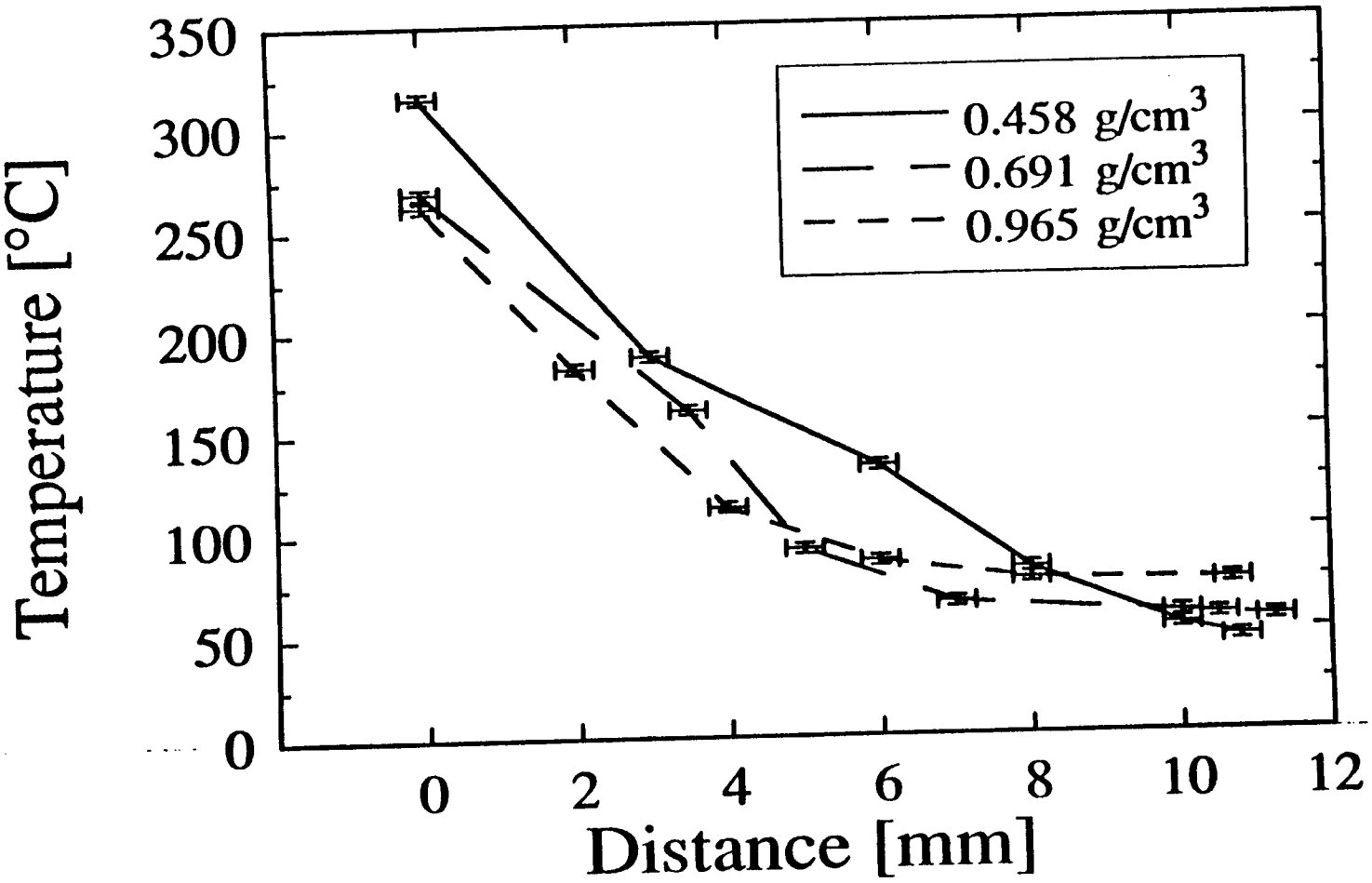

Figure 5.15 A comparison of temperature profiles in three different density samples, heated for 200 s (cellulose temperature profile) under incident heat flux of 40 kW/m^2

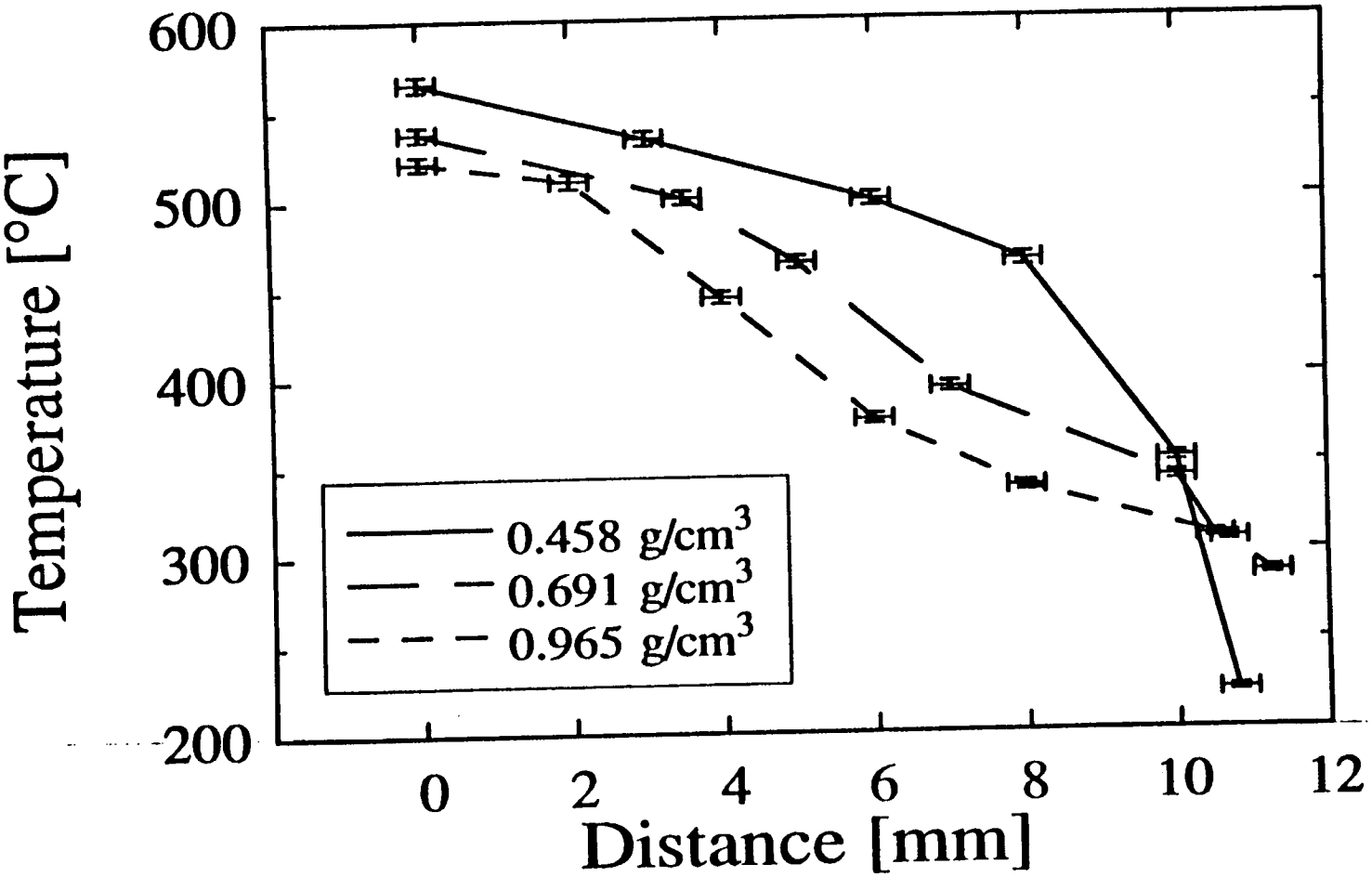

Figure 5.16a A comparison of temperature profiles in three different density samples, heated for 2500 s (char temperature profile) under incident heat flux of 40 kW/m^2

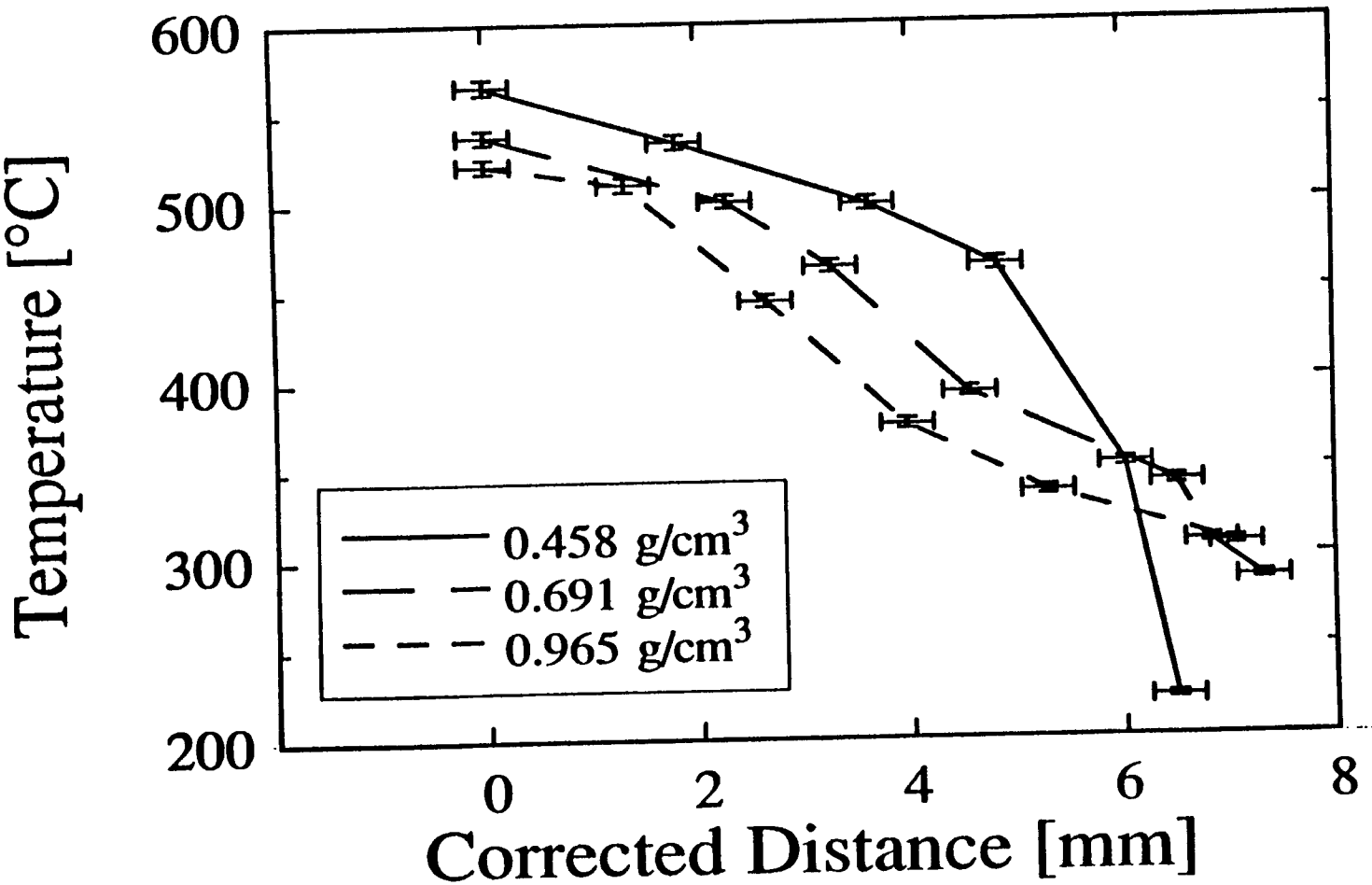

Figure 5.16b A comparison of temperature profiles in three different density samples, heated for 2500 s (char temperature profile) under incident heat flux of 40 kW/m^2, with sample shrinkage correction performed (the same data as in Figure 5.16a, with corrected distance)

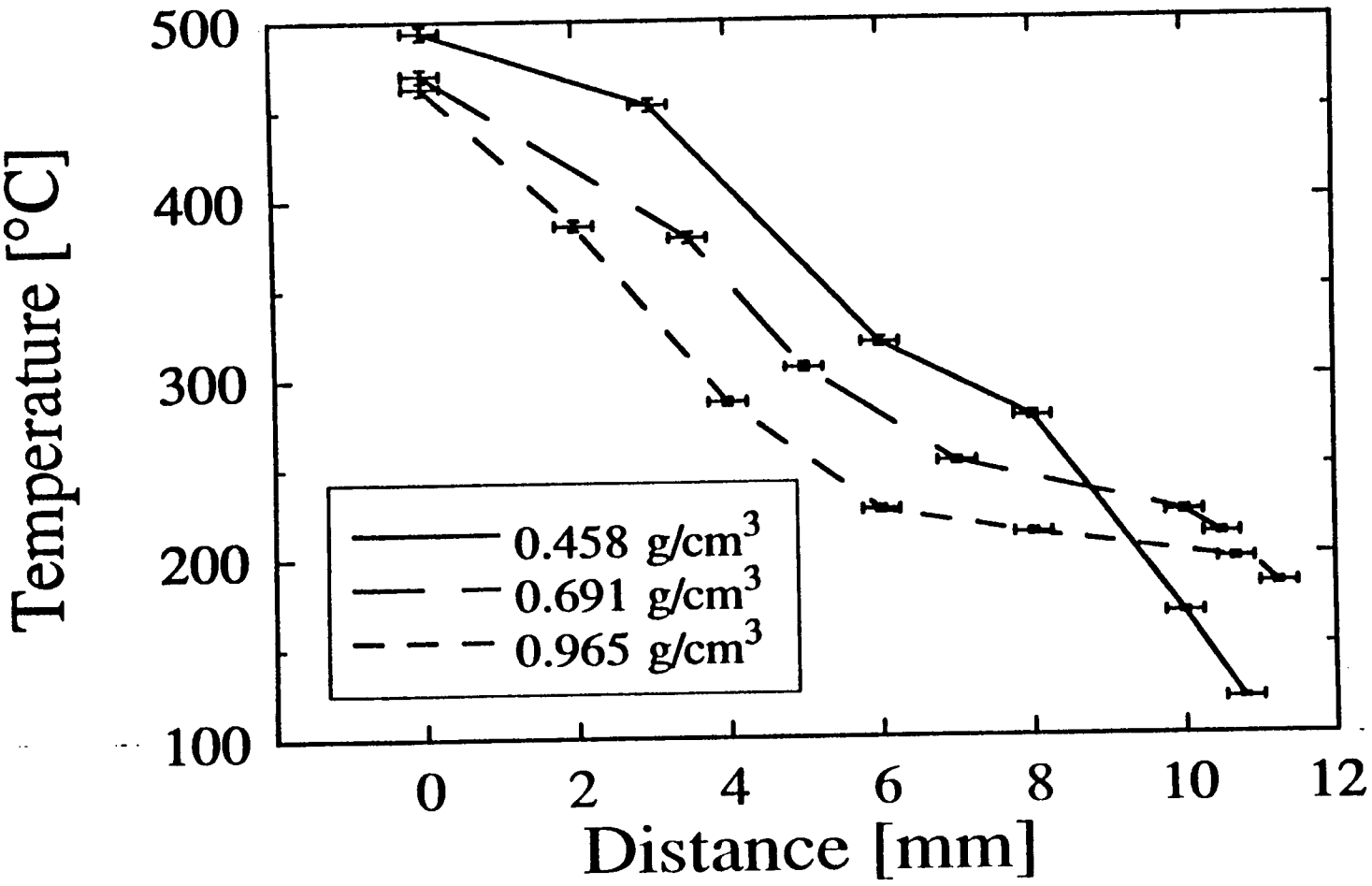

Figure 5.17 A comparison of temperature profiles in three different density samples, heated for different times, up to mass loss of 20%, under incident heat flux of 40 kW/m^2

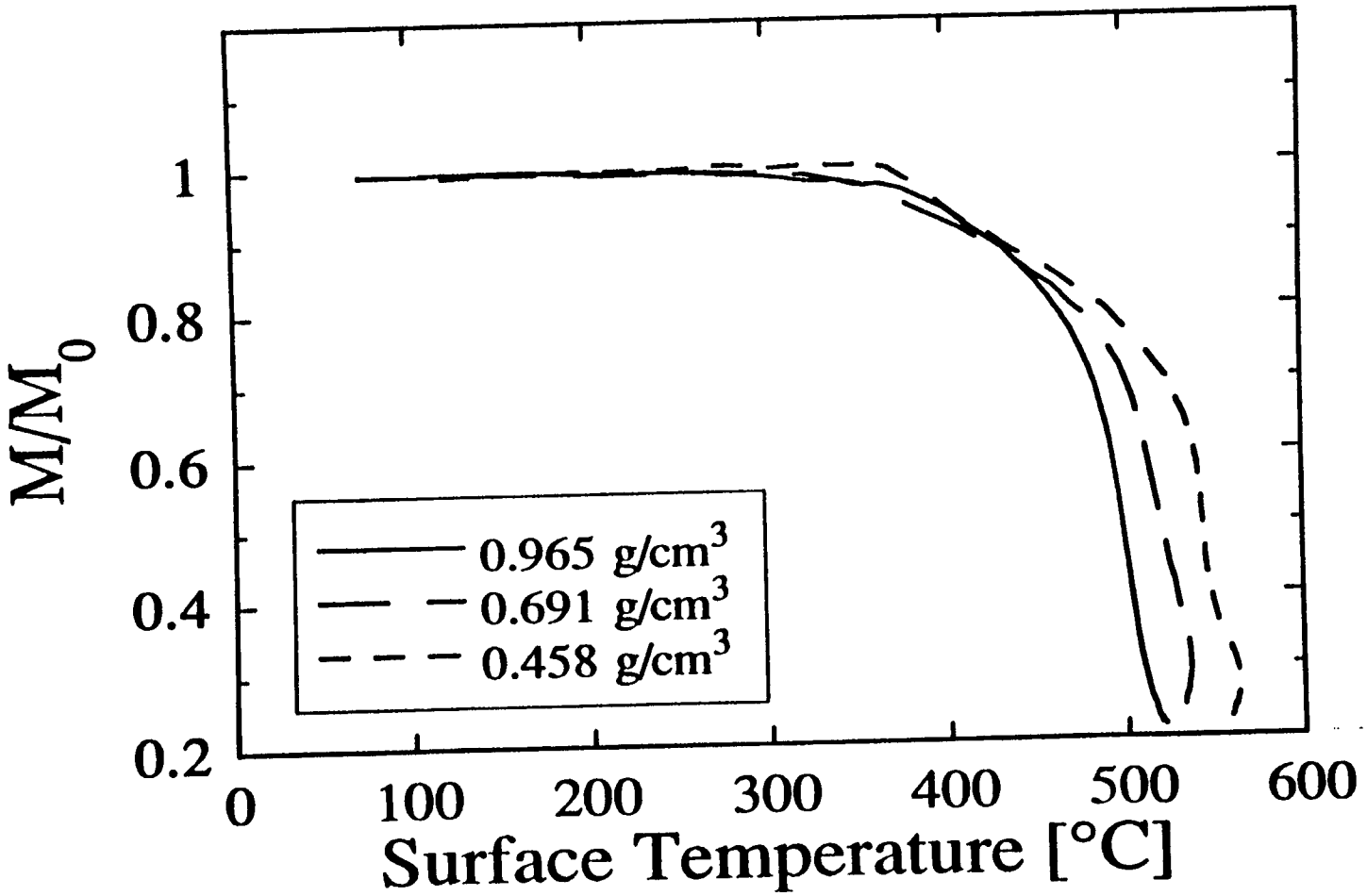

Figure 5.18 Fractional mass remaining as a function of front surface temperature for an incident heat flux of 40 kW/m^2

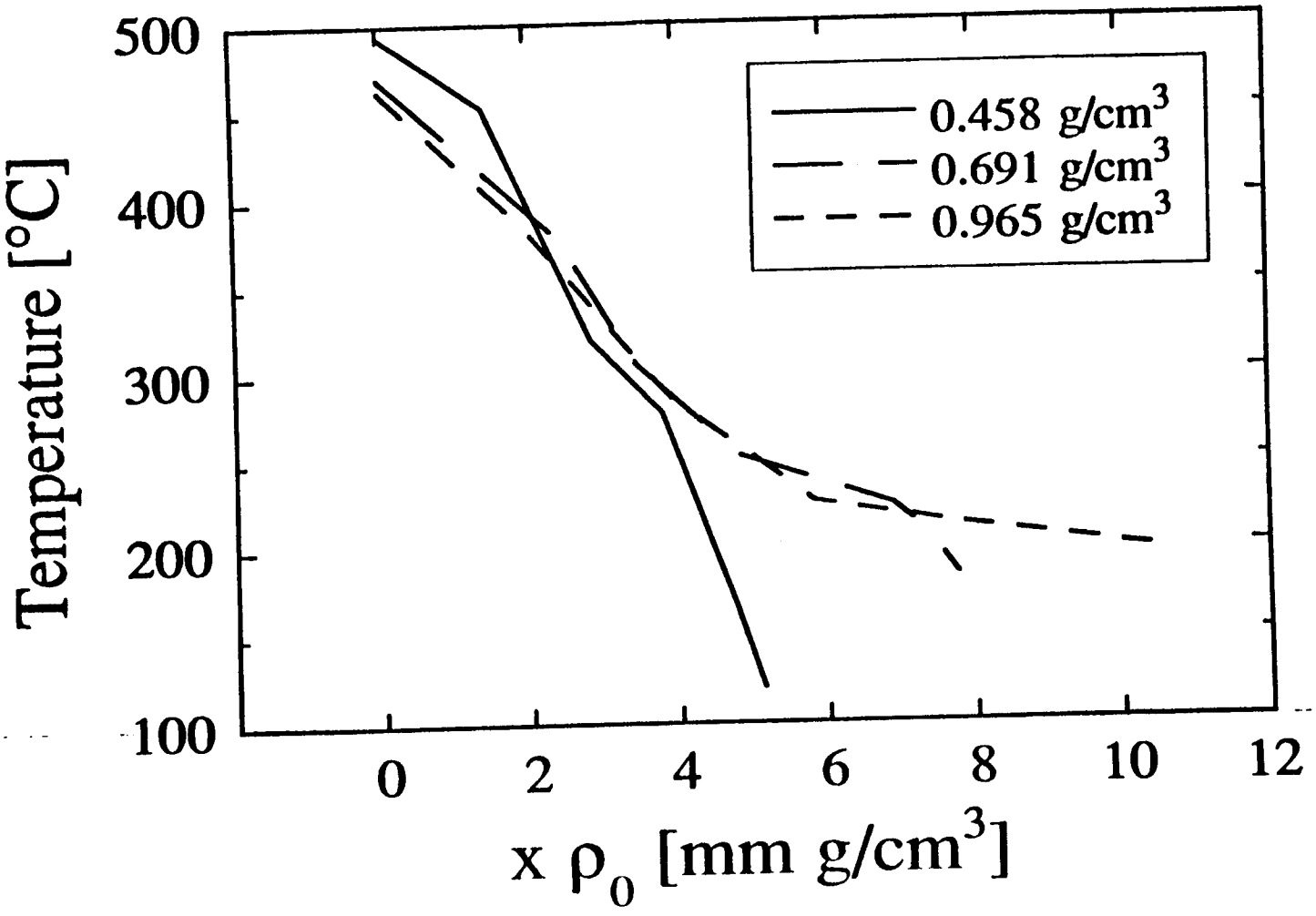

Figure 5.19 Temperature profiles in three different density samples as a function of mass per unit area of a sample (incident heat flux of 40 kW/m^2)

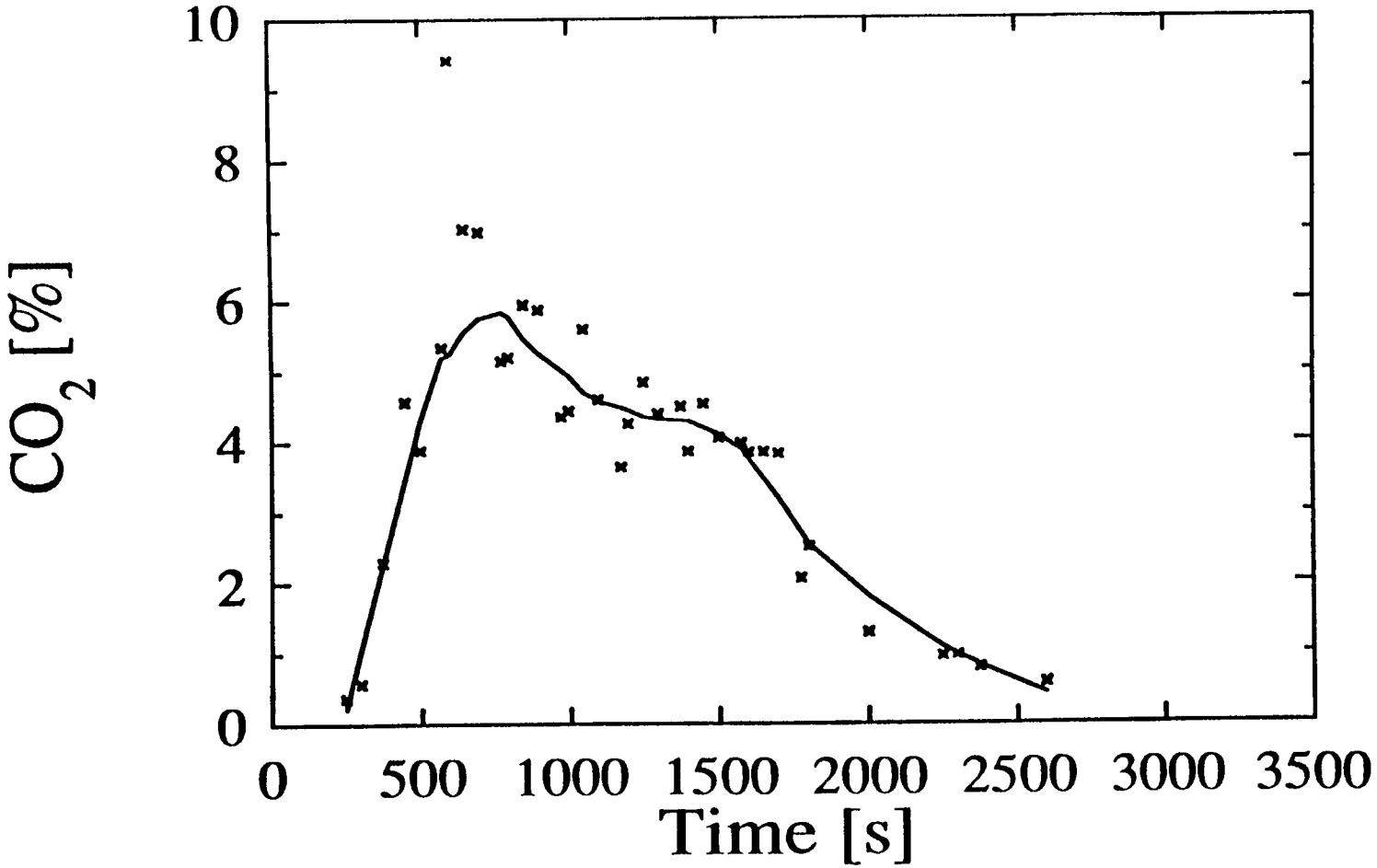

Figure 5.20a: Carbon dioxide content of dry, tar - free pyrolysis gases released from low density (0.458 g/cm^3) samples of cellulose, subject to a nominal heat flux of 40 kW/m^2

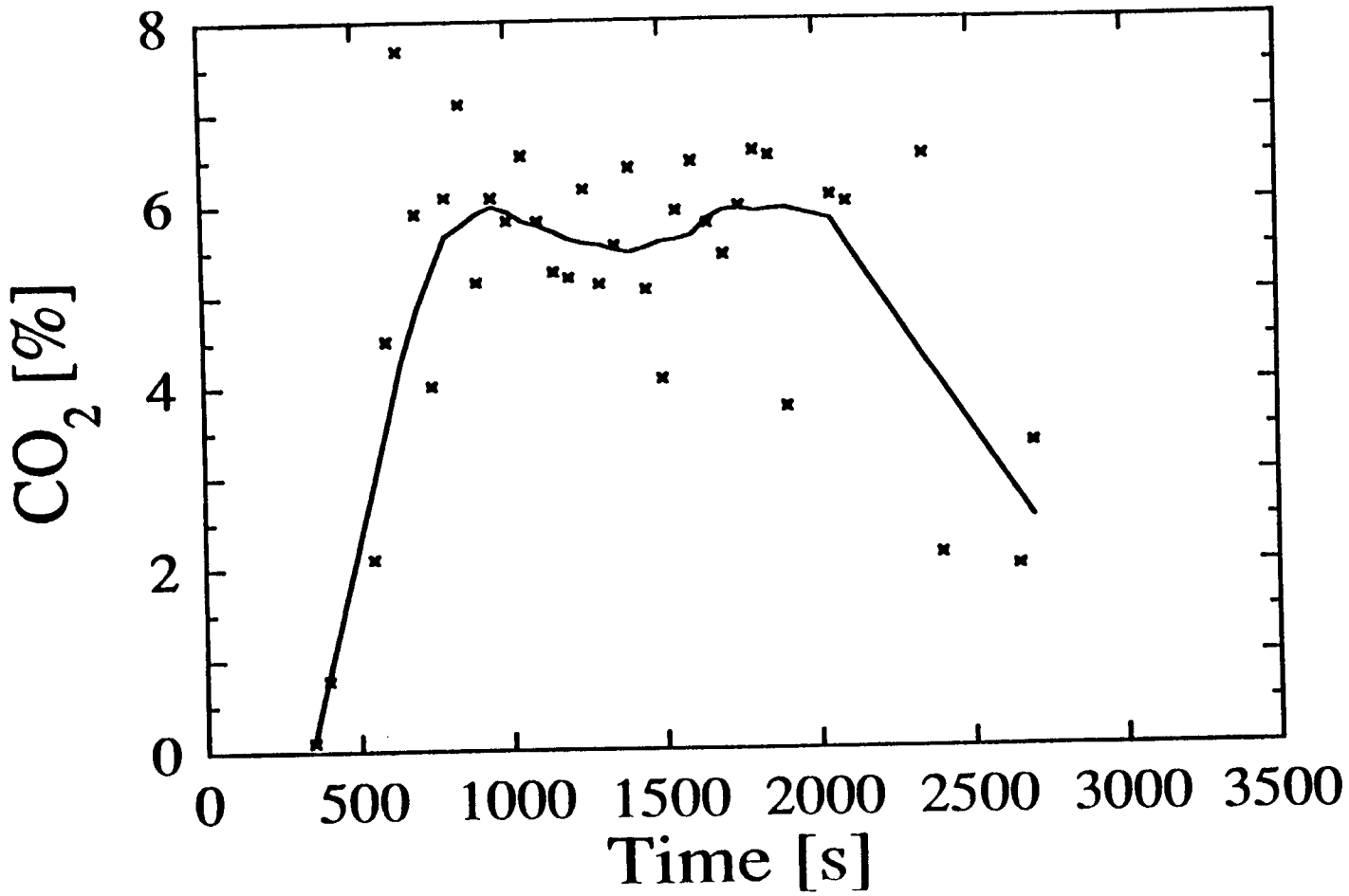

Figure 5.20b: Carbon dioxide content of dry, tar - free pyrolysis gases released from middle density (0.691 g/cm^3) samples of cellulose, subject to a nominal heat flux of 40 kW/m^2

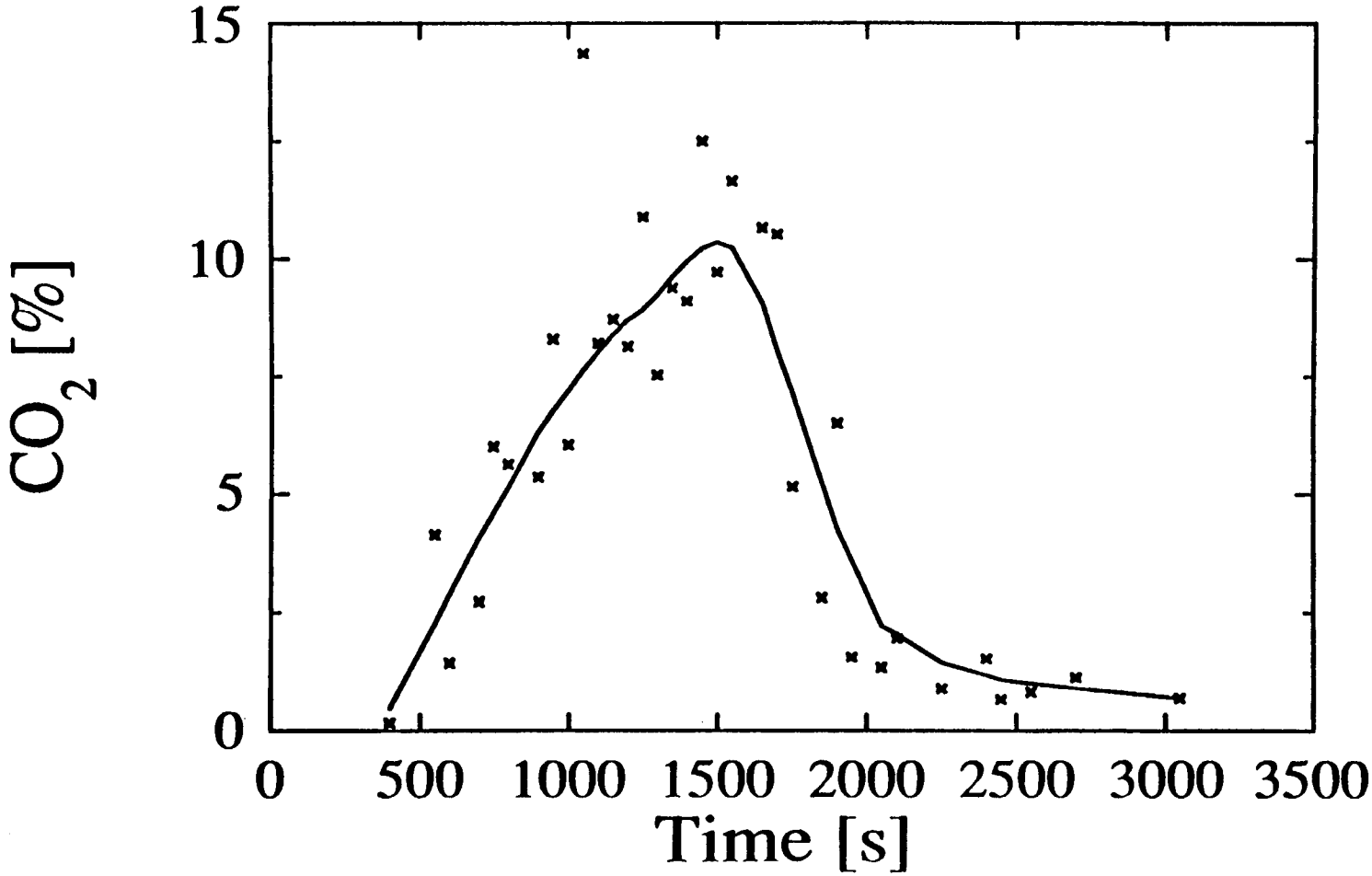

Figure 5.20c: Carbon dioxide content of dry, tar - free pyrolysis gases released from high density (0.965 g/cm^3) samples of cellulose, subject to a nominal heat flux of 40 kW/m^2

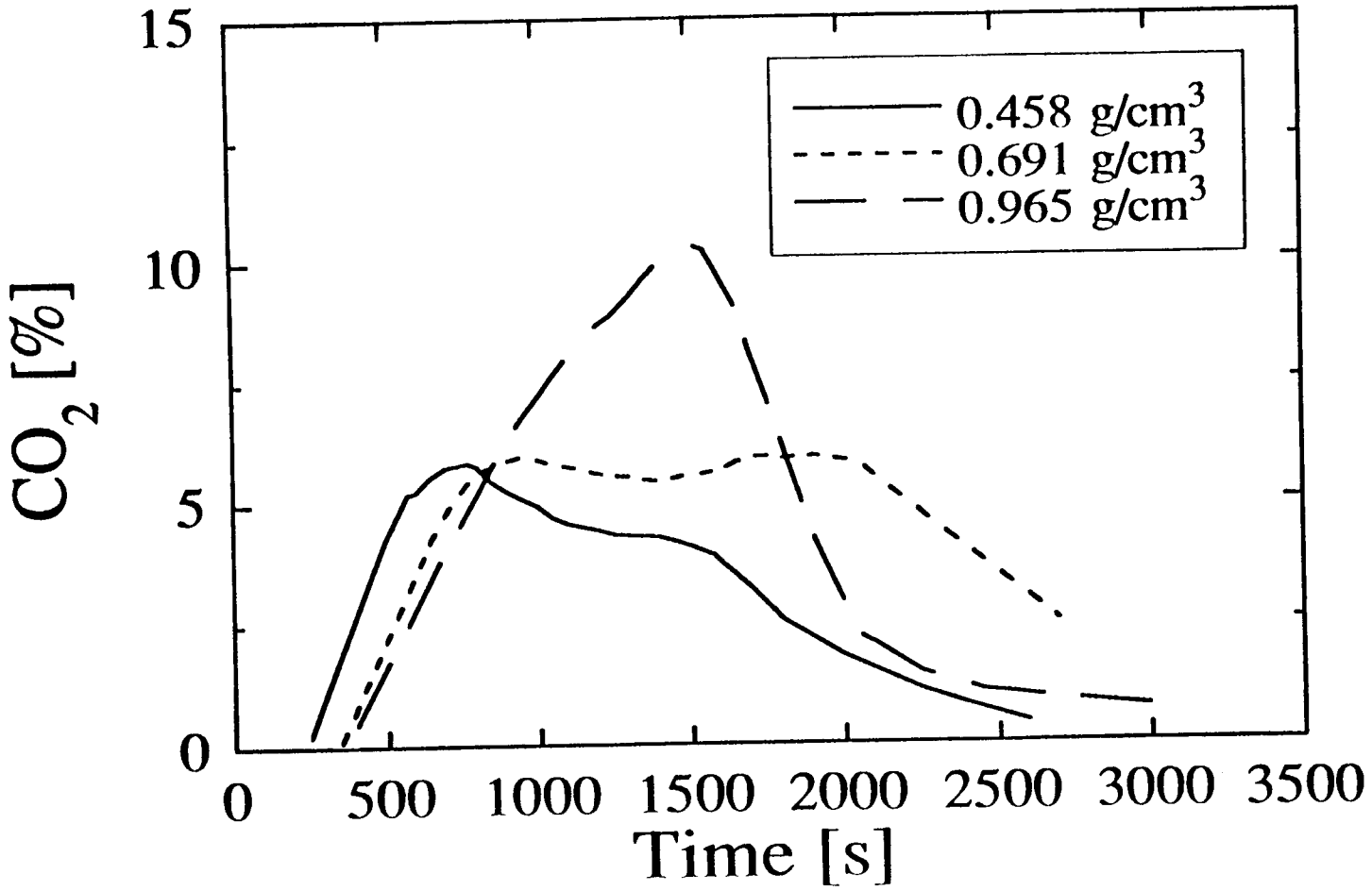

Figure 5.20d: Comparison of results for different density samples. Data are those shown in Figures 5.20a, 5.20b and 5.20c, with data points omitted for clarity

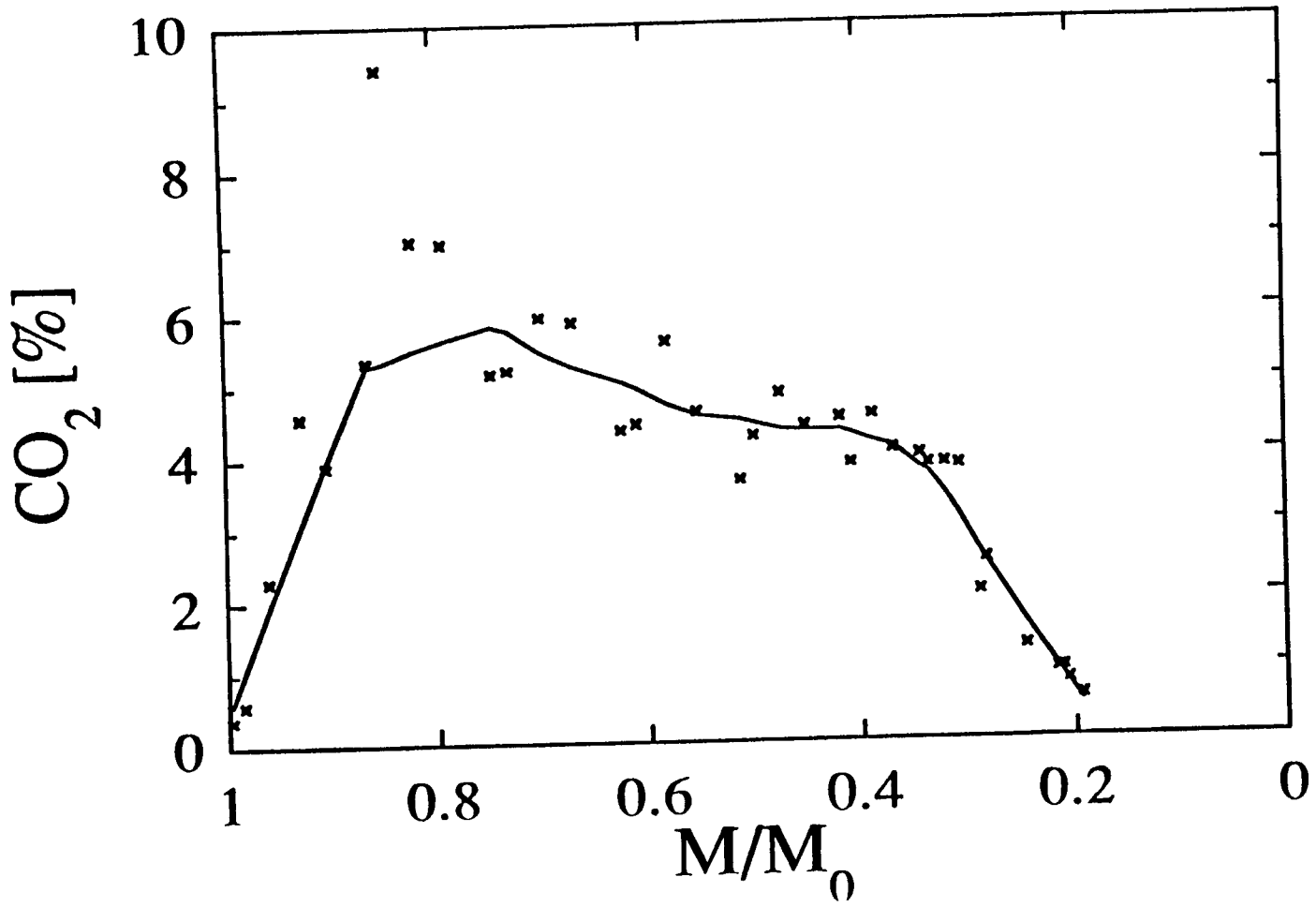

Figure 5.20e: Carbon dioxide content of dry, tar - free pyrolysis gases released from low density (0.458 g/cm^3) samples of cellulose, subject to a nominal heat flux of 40 kW/m^2. These are the data of Figure 5.20a, replotted against remaining sample mass

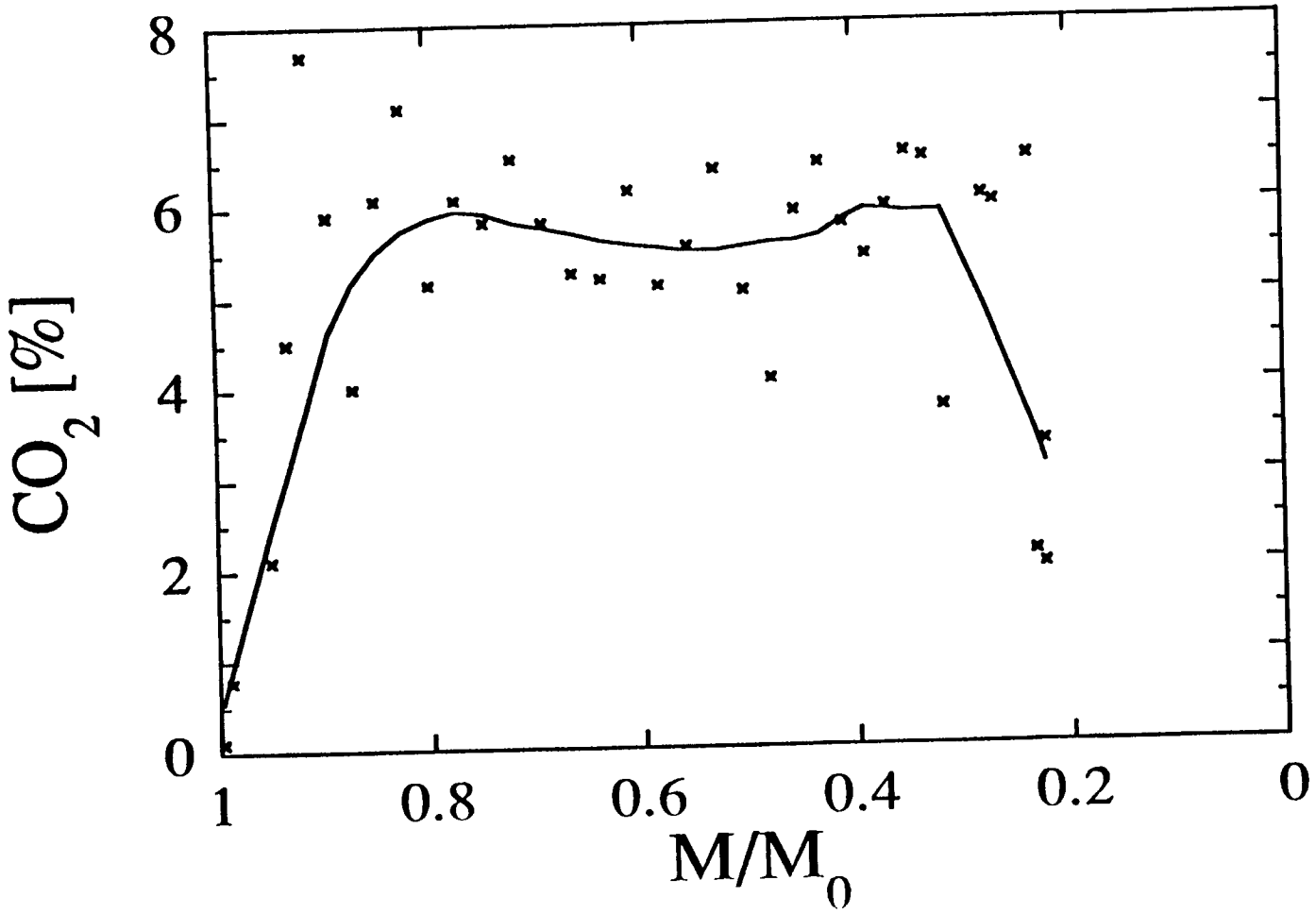

Figure 5.20f: Carbon dioxide content of dry, tar - free pyrolysis gases released from middle density (0.691 g/cm^3) samples of cellulose, subject to a nominal heat flux of 40 kW/m^2. These are the data of Figure 5.20b, replotted against remaining sample mass

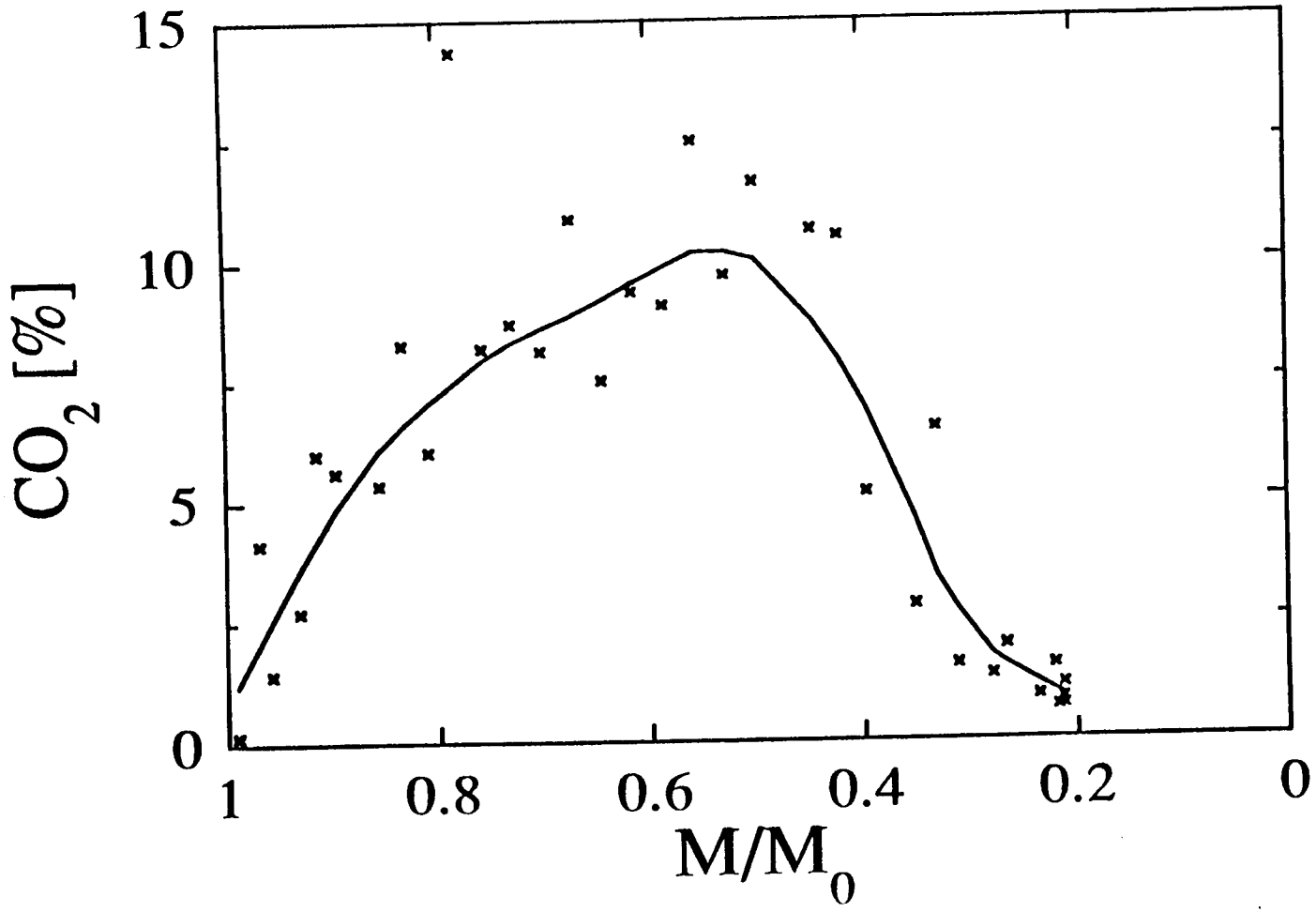

Figure 5.20g: Carbon dioxide content of dry, tar - free pyrolysis gases released from high density (0.965 g/cm^3) samples of cellulose, subject to a nominal heat flux of 40 kW/m^2. These are the data of Figure 5.20c, replotted against remaining sample mass

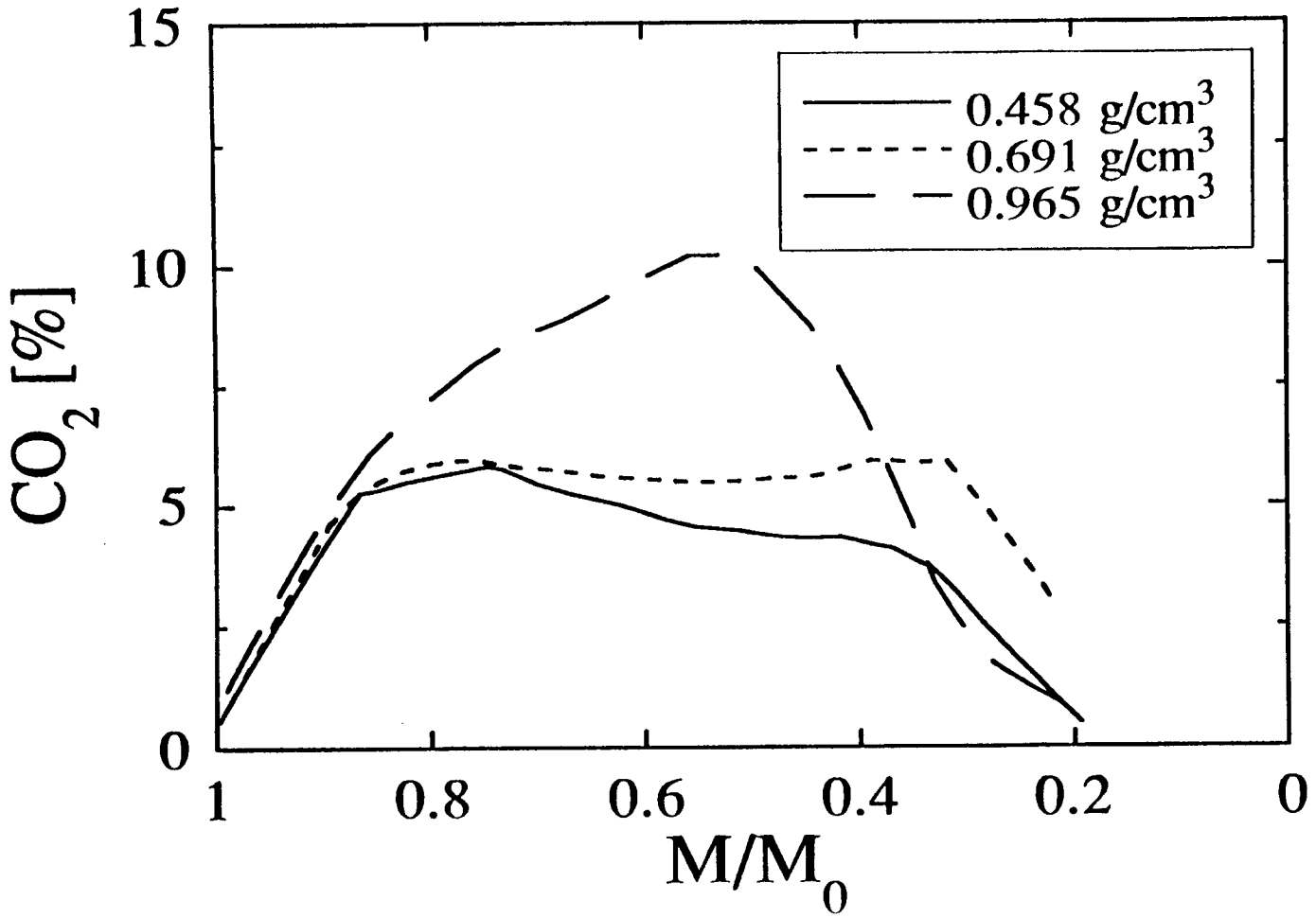

Figure 5.20h: Comparison of results for different density samples. Data are those shown in Figures 5.20e, 5.20f and 5.20g, with data points omitted for clarity. These are the data of Figure 5.20d, replotted against remaining sample mass

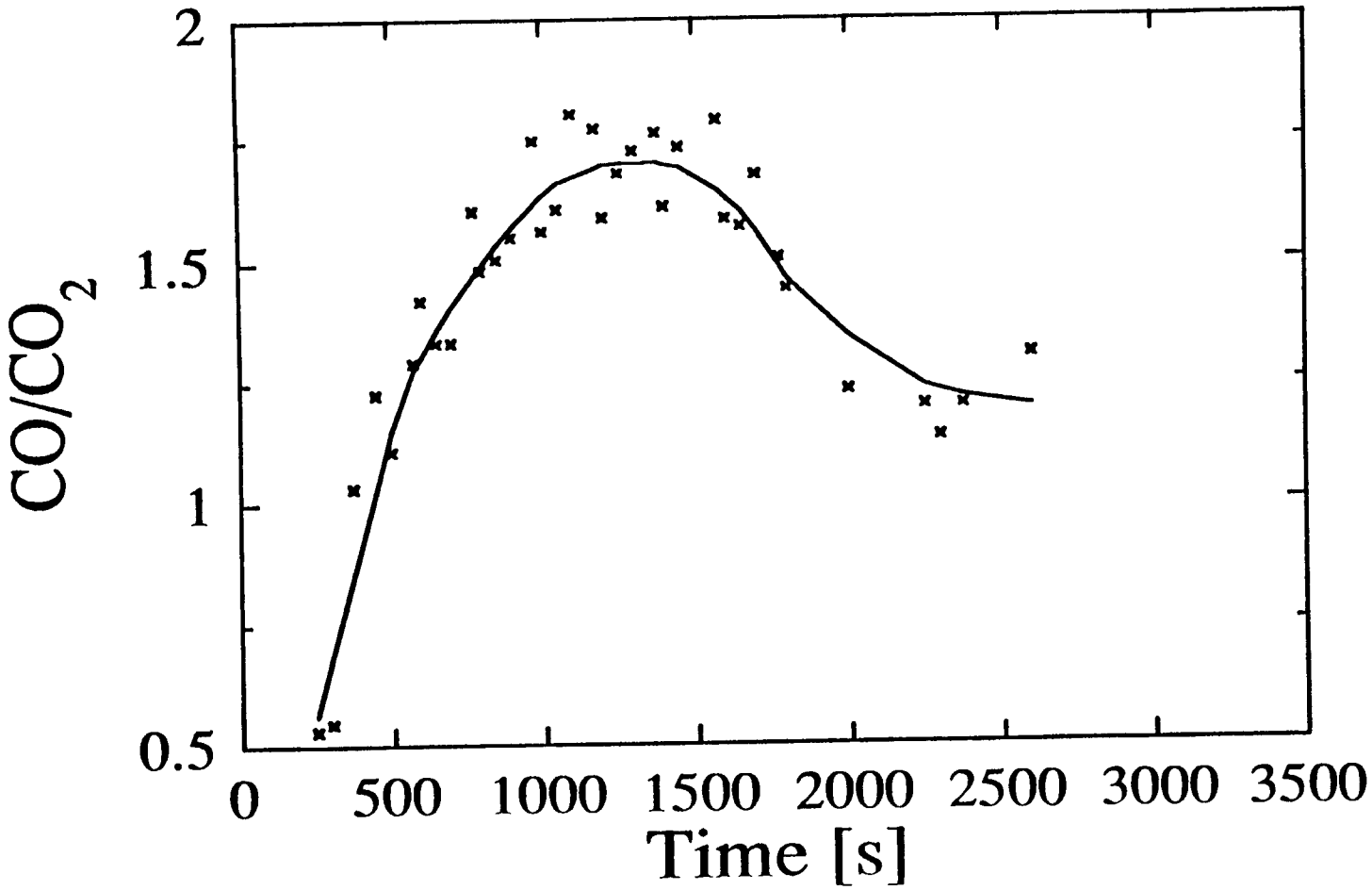

Figure 5.21a: Carbon monoxide to carbon dioxide molar ratio from low density (0.458 g/cm^3) samples of cellulose, subject to a nominal heat flux of 40 kW/m^2

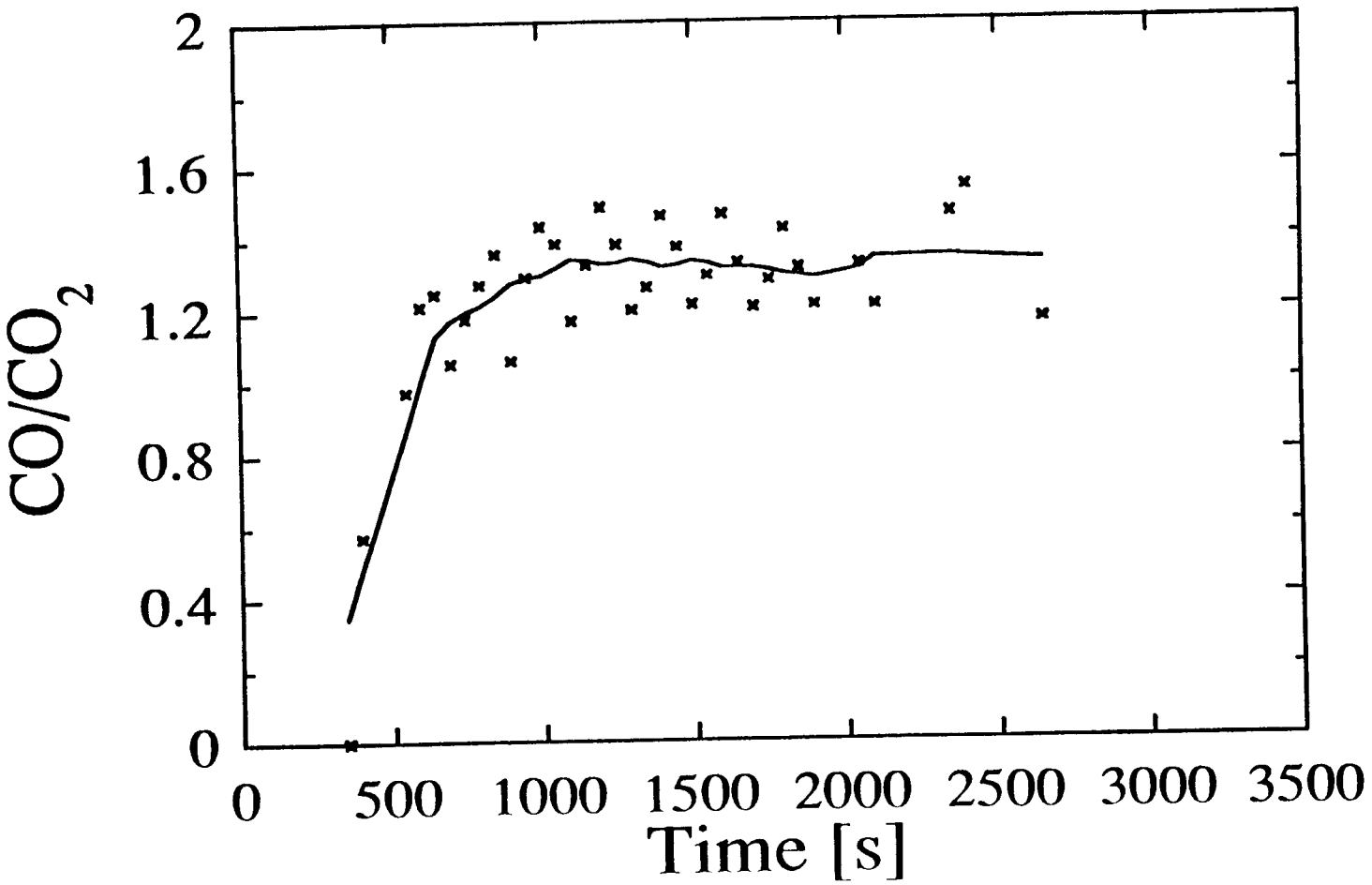

Figure 5.21b: Carbon monoxide to carbon dioxide molar ratio from middle density (0.691 g/cm^3) samples of cellulose, subject to a nominal heat flux of 40 kW/m^2

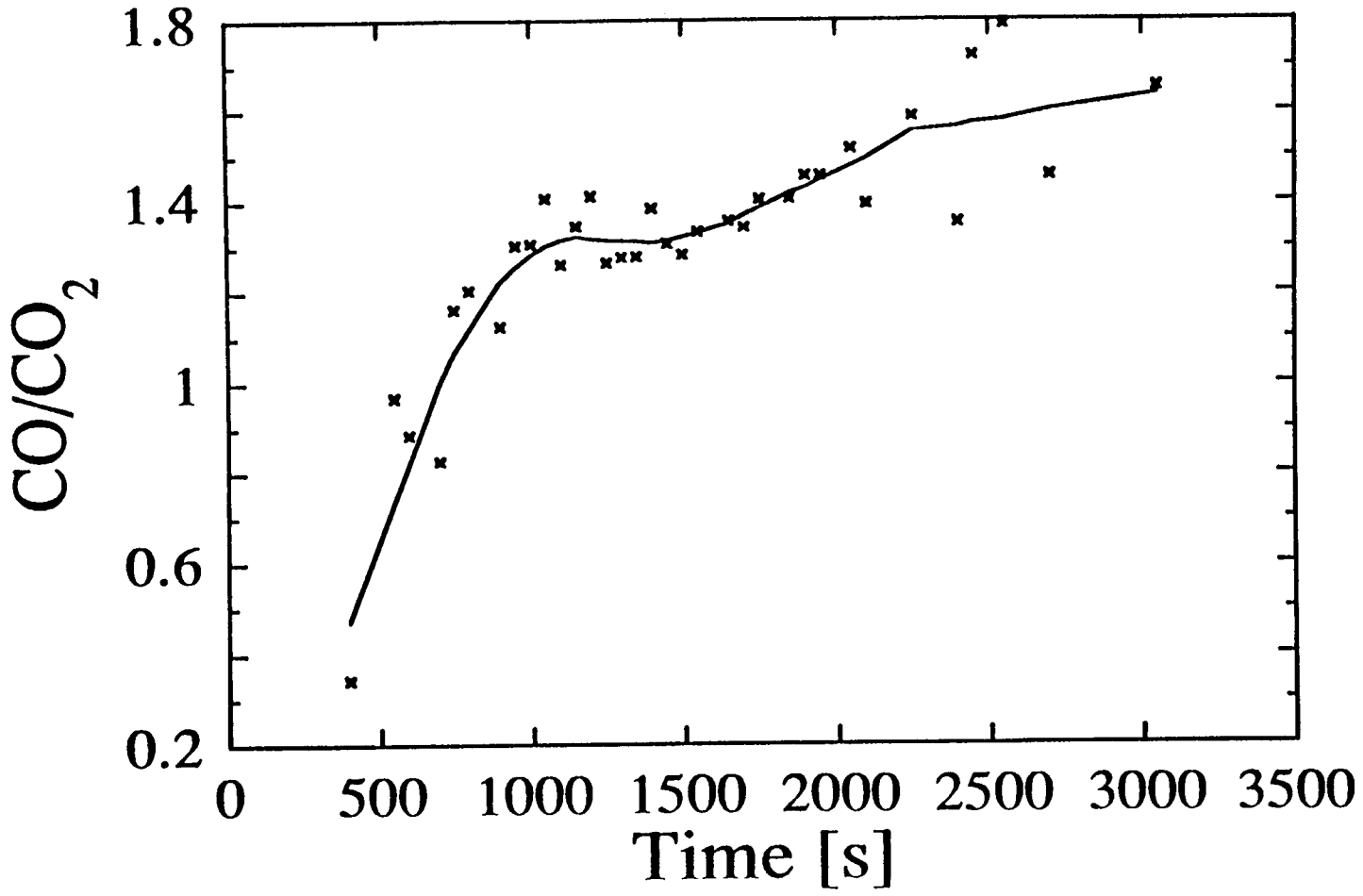

Figure 5.21c: Carbon monoxide to carbon dioxide molar ratio from high density (0.965 g/cm^3) samples of cellulose, subject to a nominal heat flux of 40 kW/m^2

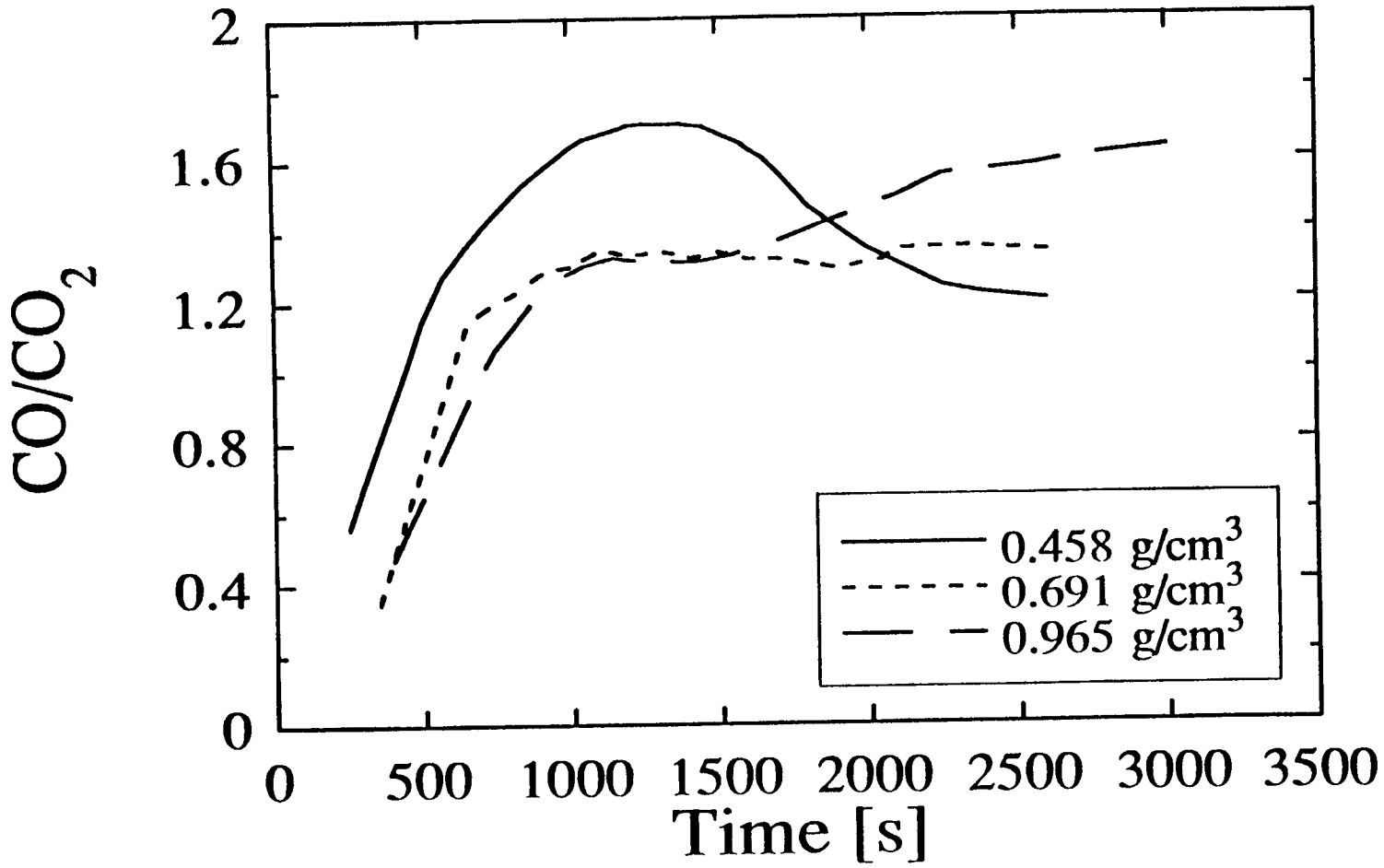

Figure 5.21d: Comparison of results for carbon monoxide to carbon dioxide molar ratio for different density samples. Data are those shown in Figures 5.21a, 5.21b and 5.21c, with data points omitted for clarity

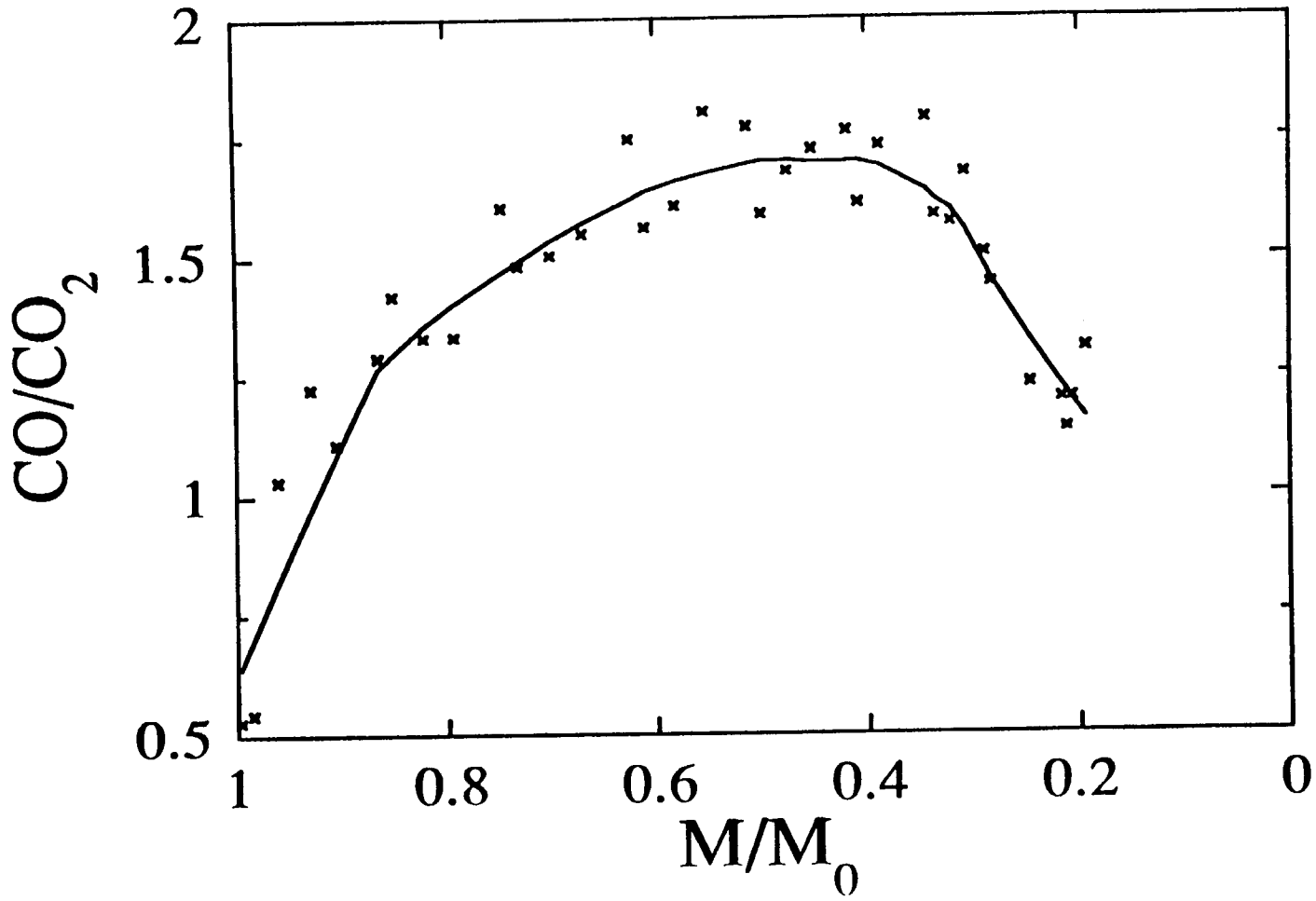

Figure 5.21e: Carbon monoxide to carbon dioxide molar ratio from low density (0.458 g/cm^3) samples of cellulose, subject to a nominal heat flux of 40 kW/m^2. These are the data of Figure 5.21a, replotted against remaining sample mass

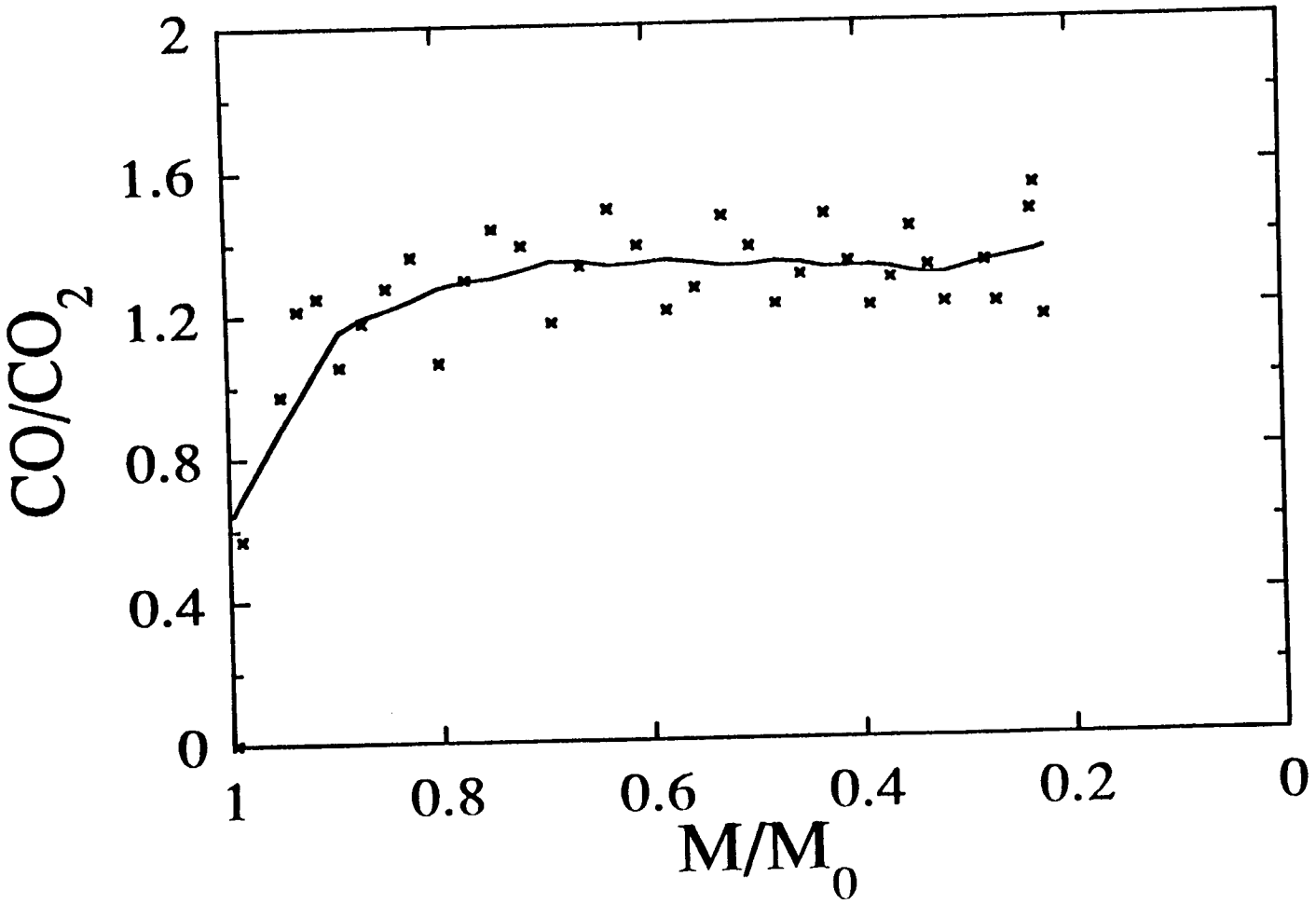

Figure 5.21f: Carbon monoxide to carbon dioxide molar ratio from middle density (0.691 g/cm^3) samples of cellulose, subject to a nominal heat flux of 40 kW/m^2. These are the data of Figure 5.21b, replotted against remaining sample mass

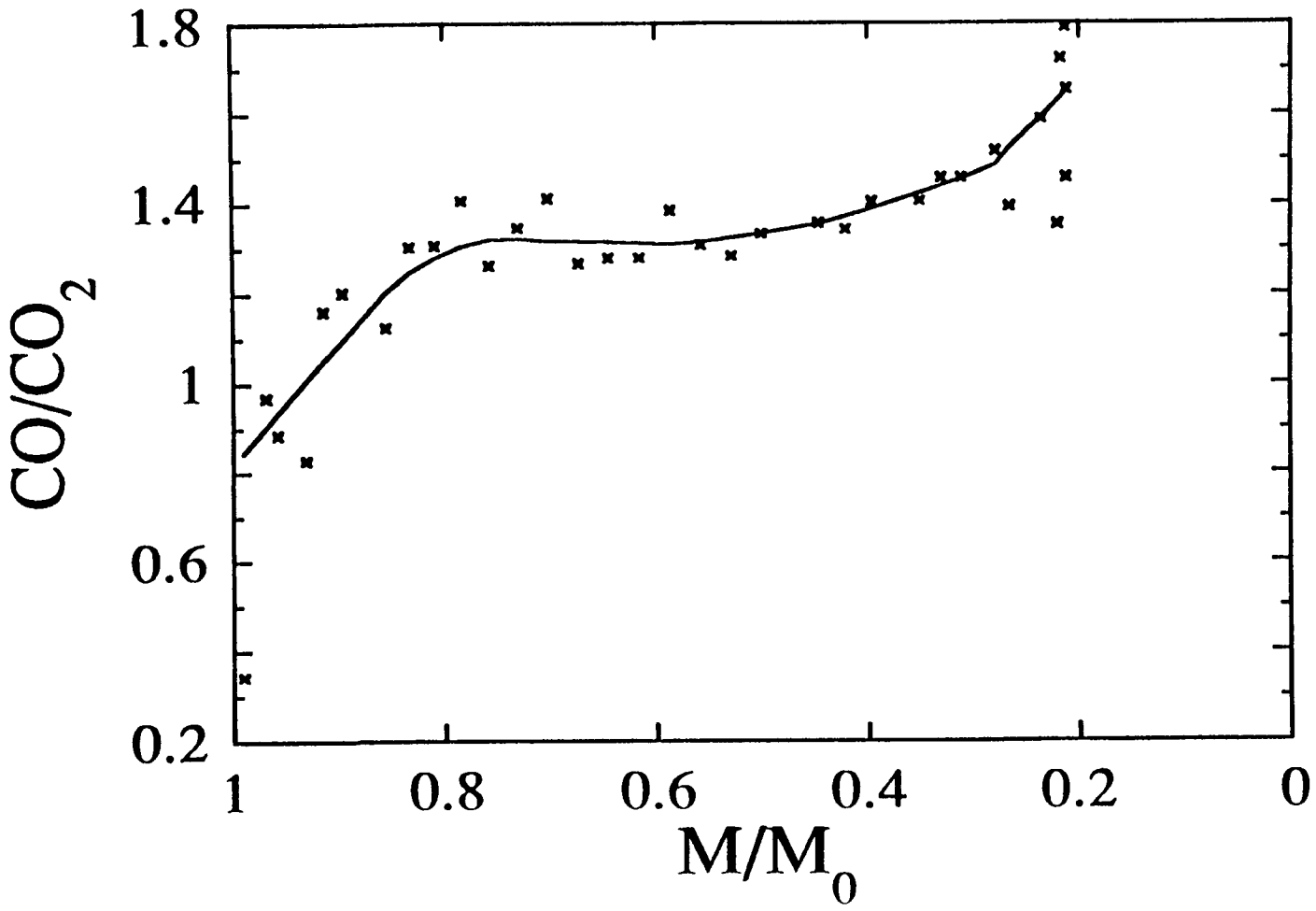

Figure 5.21g:Carbon monoxide to carbon dioxide molar ratio from high density (0.965 g/cm^3) samples of cellulose, subject to a nominal heat flux of 40 kW/m^2. These are the data of Figure 5.21c, replotted against remaining sample mass

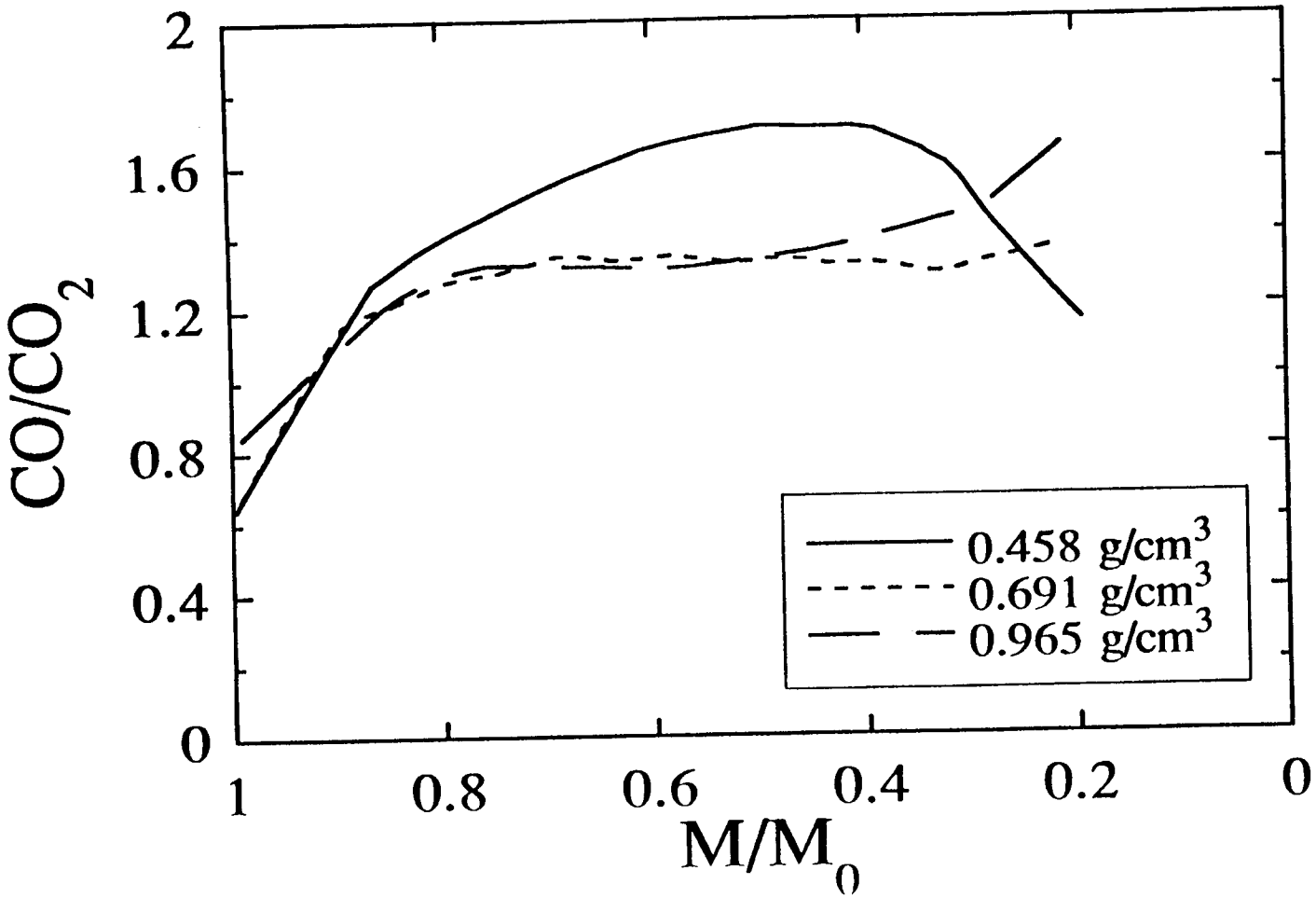

Figure 5.21h: Comparison of results for carbon monoxide to carbon dioxide molar ratio for different density samples. Data are those shown in Figures 5.21e, 5.21f and 5.21g, with data points omitted for clarity. These are the data of Figure 5.21d, replotted against remaining sample mass

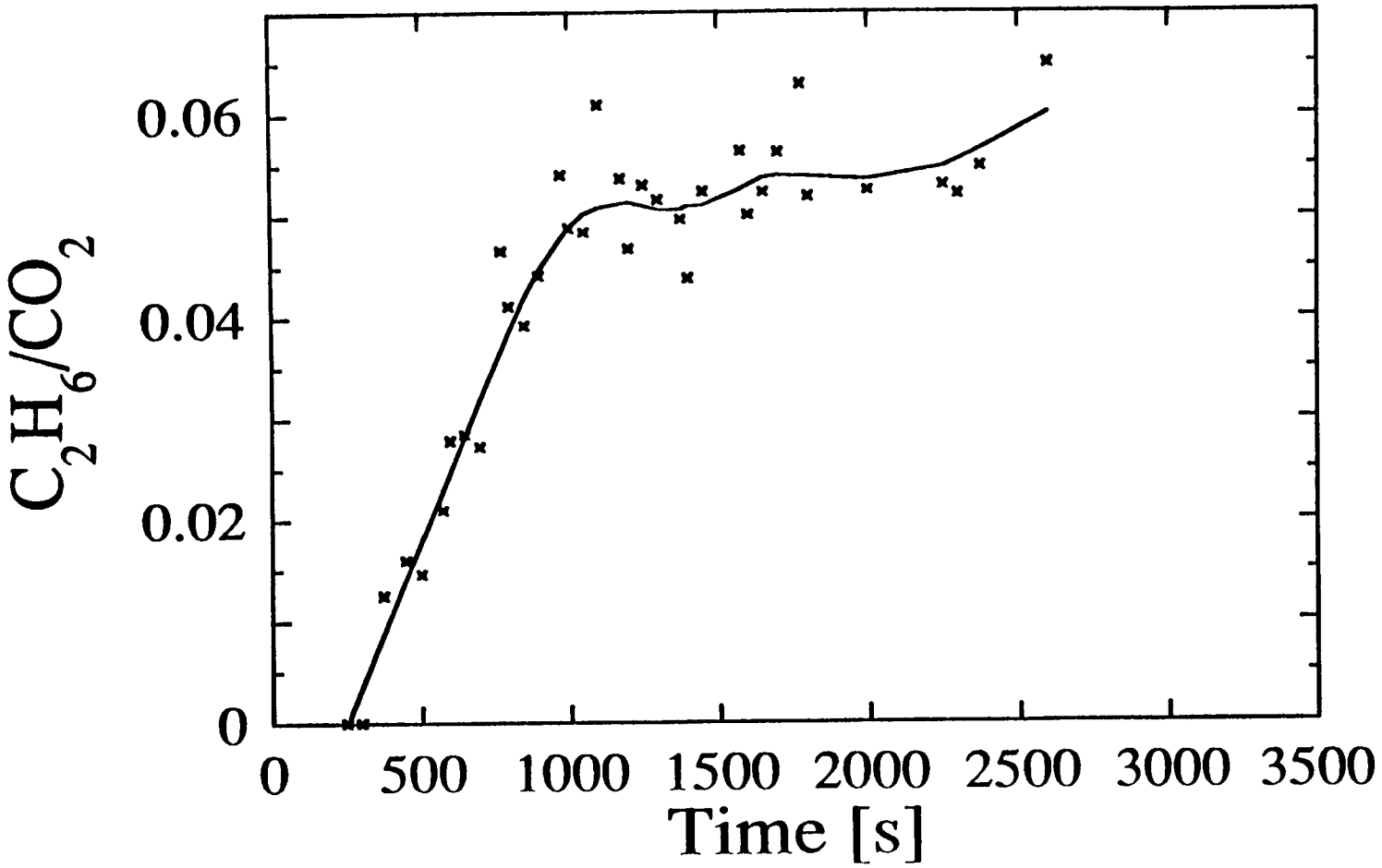

Figure 5.22a: Ethane to carbon dioxide molar ratio from low density (0.458 g/cm^3) samples of cellulose, subject to a nominal heat flux of 40 kW/m^2

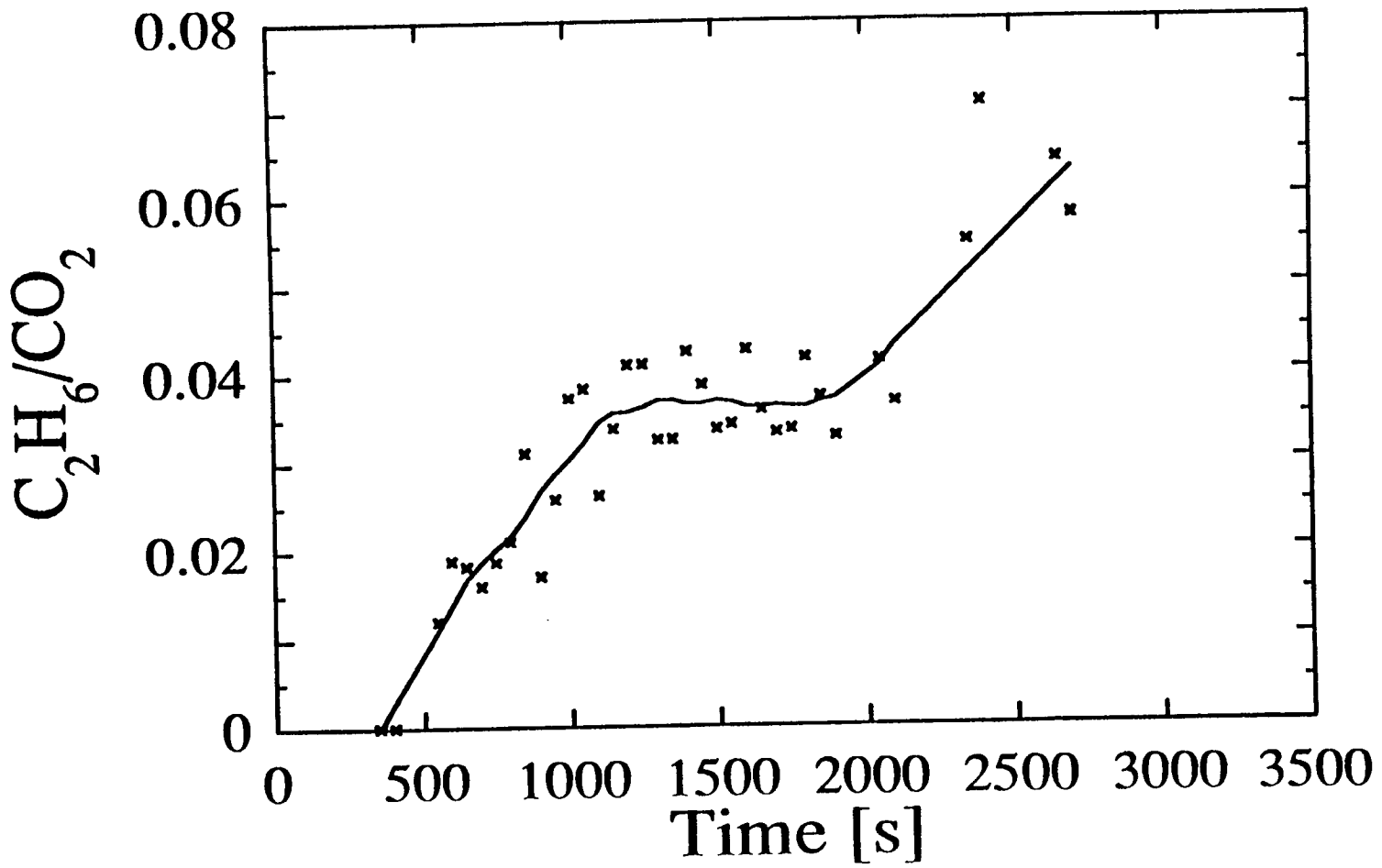

Figure 5.22b: Ethane to carbon dioxide molar ratio from middle density (0.691 g/cm^3) samples of cellulose, subject to a nominal heat flux of 40 kW/m^2

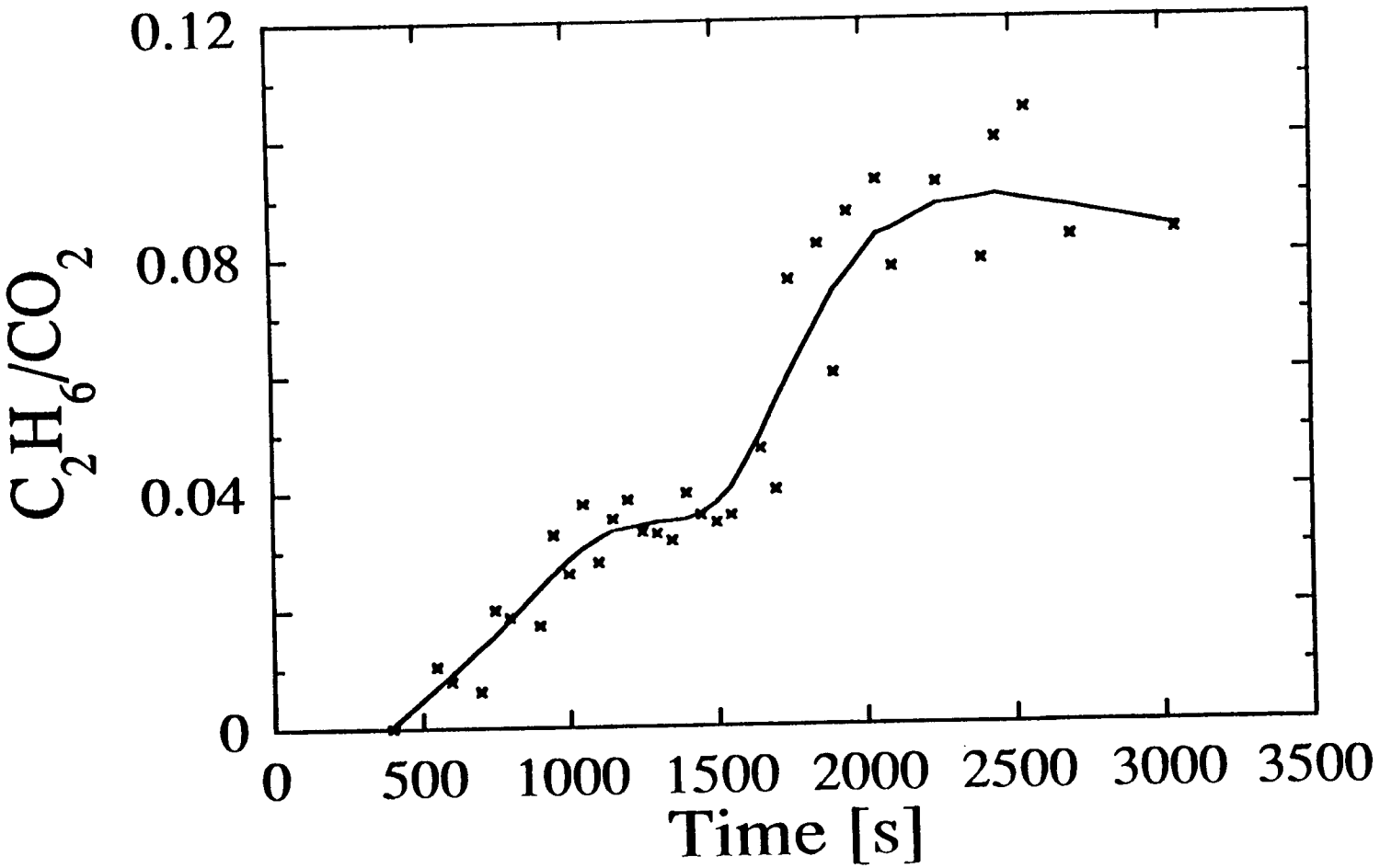

Figure 5.22c: Ethane to carbon dioxide molar ratio from high density (0.965 g/cm^3) samples of cellulose, subject to a nominal heat flux of 40 kW/m^2

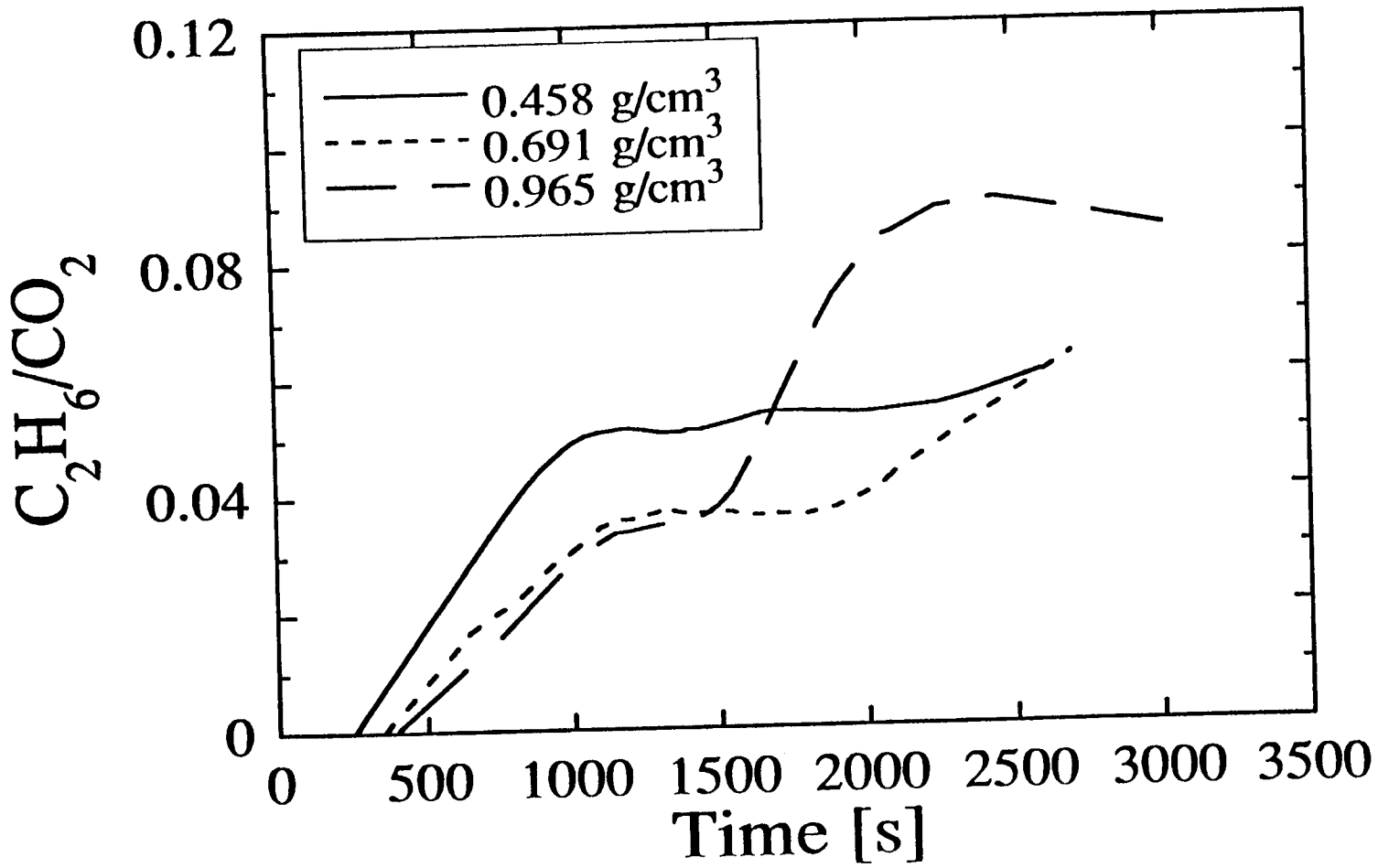

Figure 5.22d: Comparison of results for ethane to carbon dioxide molar ratio for different density samples. Data are those shown in Figures 5.22a, 5.22b and 5.22c, with data points omitted for clarity

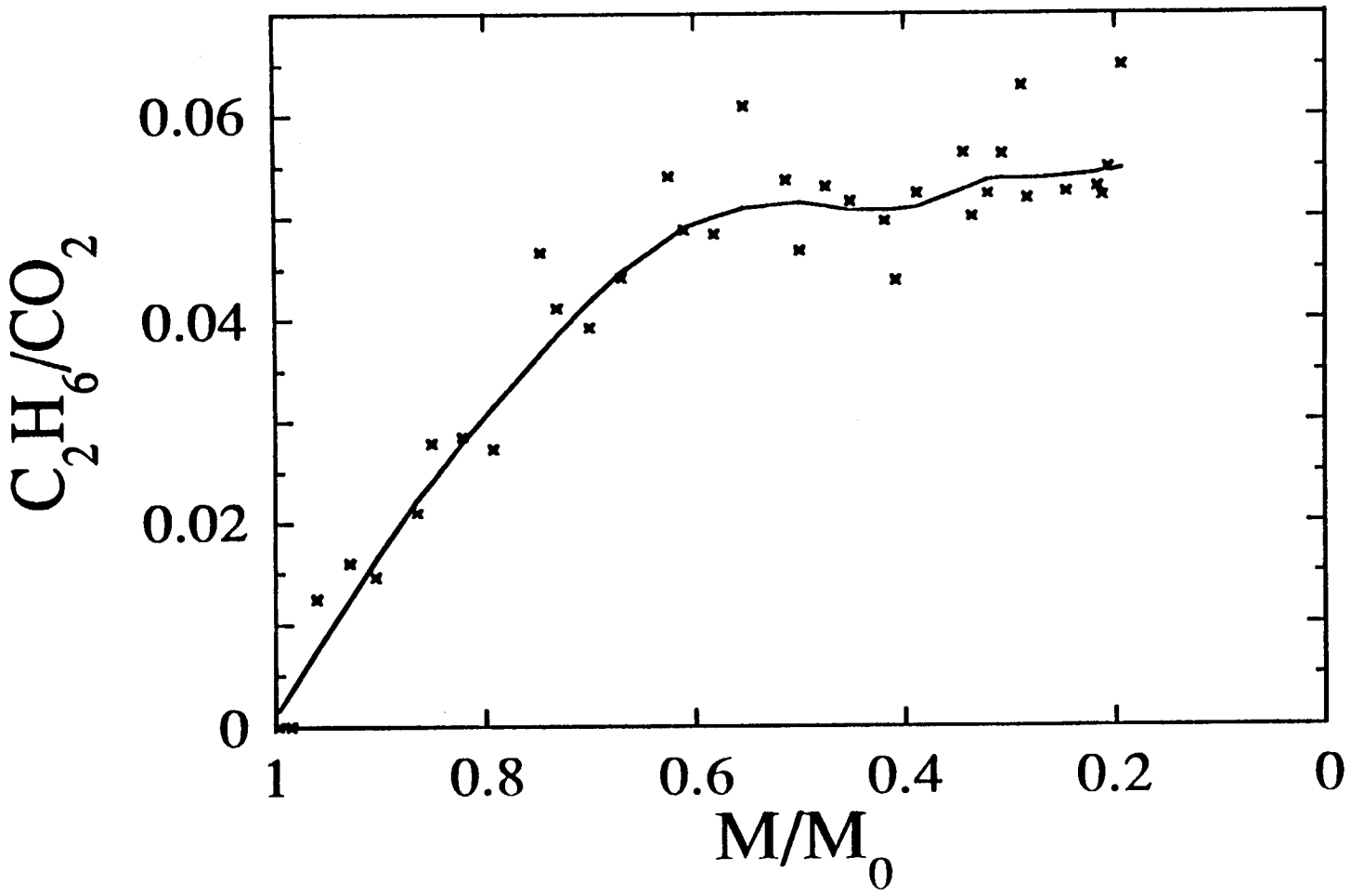

Figure 5.22e: Ethane to carbon dioxide molar ratio from low density (0.458 g/cm^3) samples of cellulose, subject to a nominal heat flux of 40 kW/m^2. These are the data of Figure 5.22a, replotted against remaining sample mass

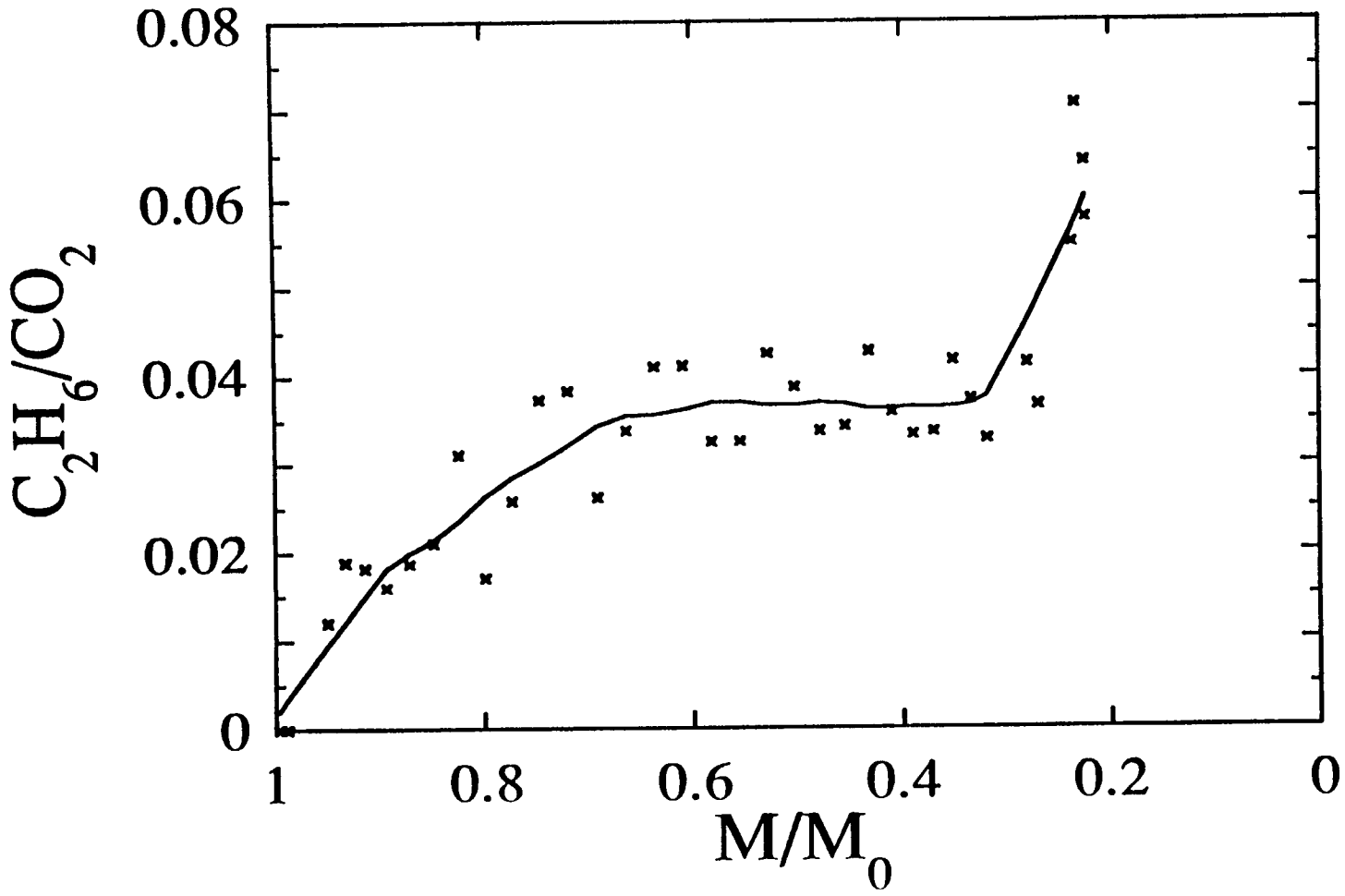

Figure 5.22f: Ethane to carbon dioxide molar ratio from middle density (0.691 g/cm^3) samples of cellulose, subject to a nominal heat flux of 40 kW/m^2. These are the data of Figure 5.22b, replotted against remaining sample mass

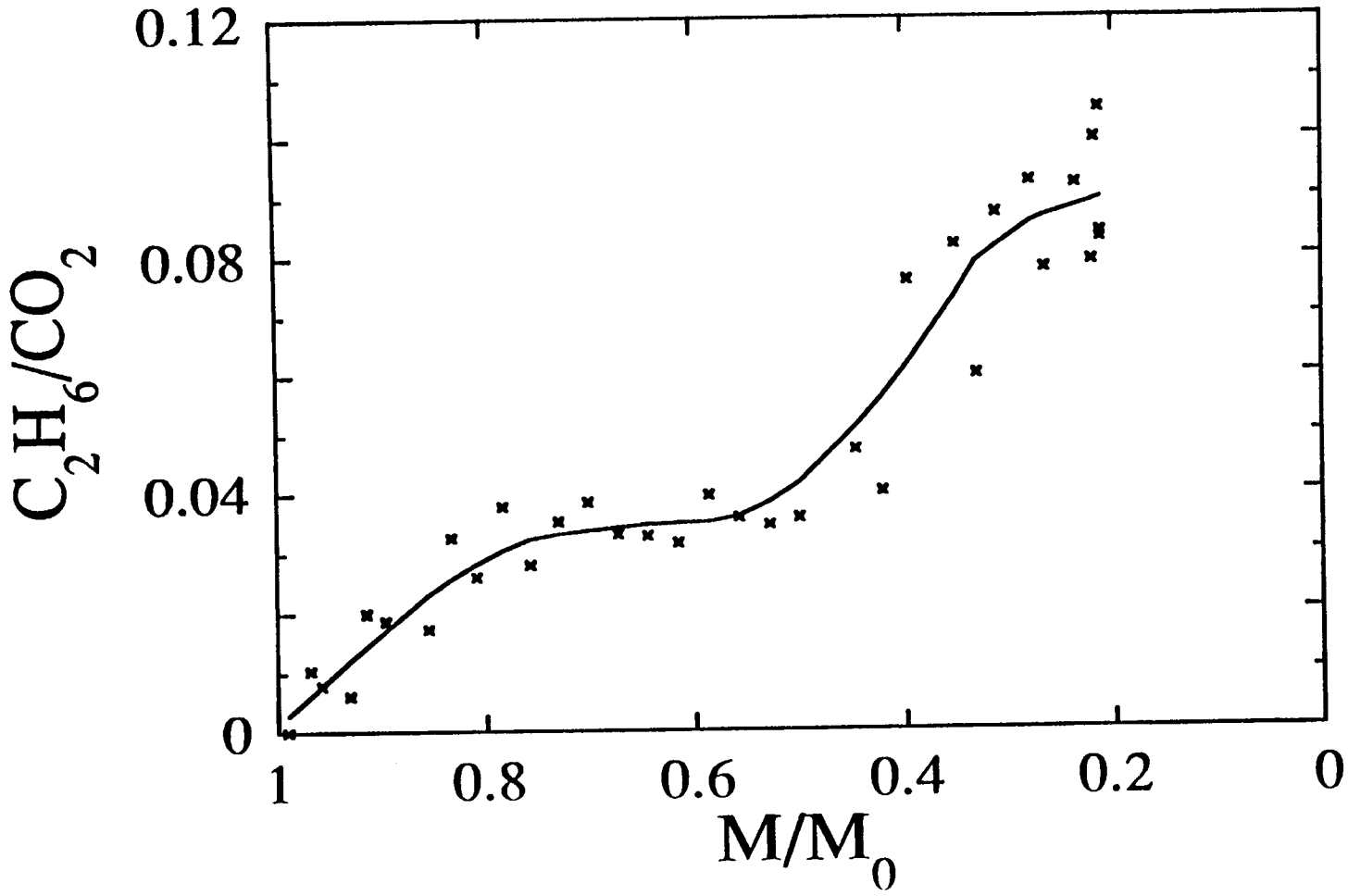

Figure 5.22g: Ethane to carbon dioxide molar ratio from high density (0.965 g/cm^3) samples of cellulose, subject to a nominal heat flux of 40 kW/m^2. These are the data of Figure 5.22c, replotted against remaining sample mass

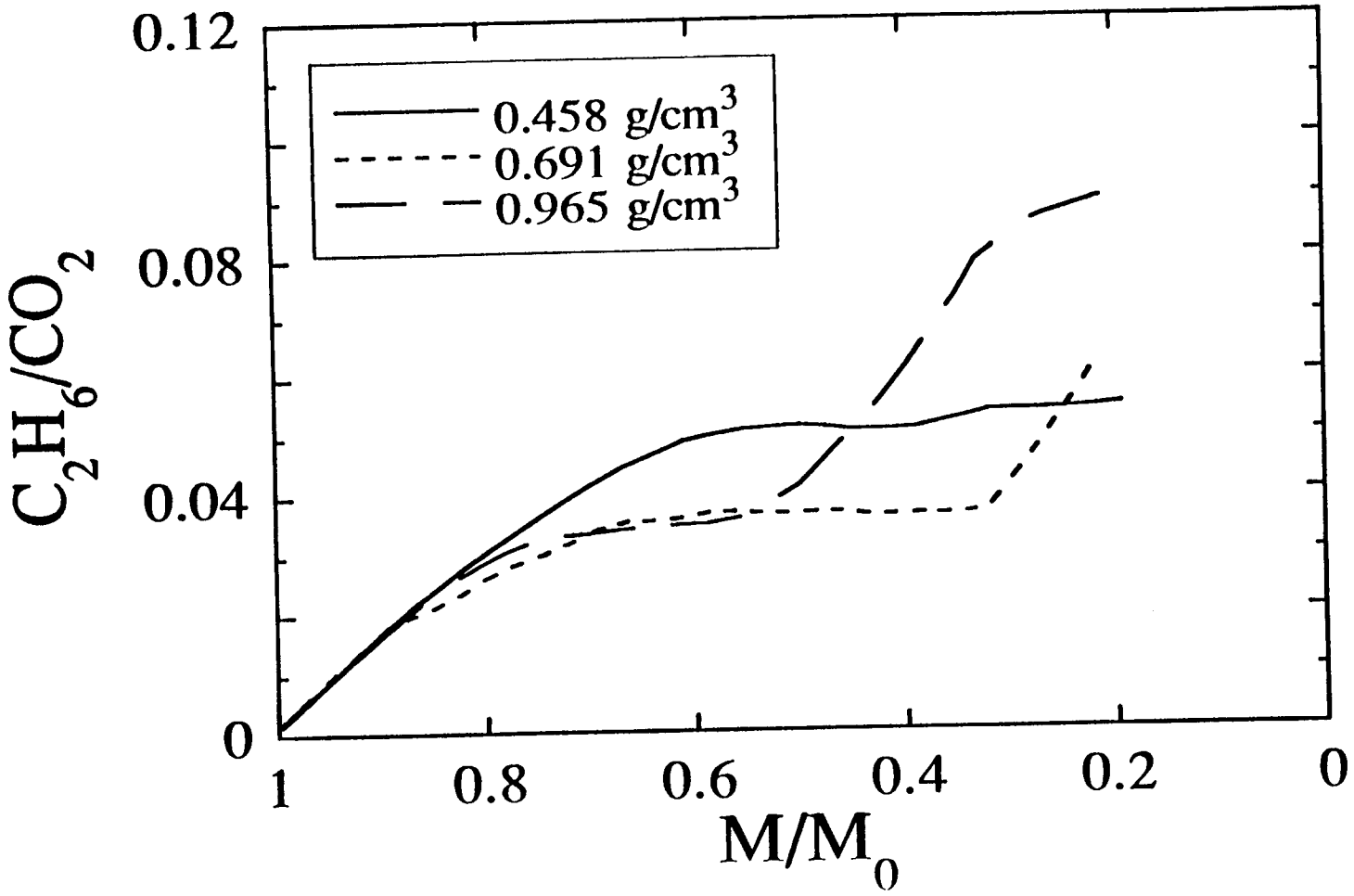

Figure 5.22h: Comparison of results for Ethane to carbon dioxide molar ratio for different density samples. Data are those shown in Figures 5.22e, 5.22f and 5.22g, with data points omitted for clarity. These are the data of Figure 5.22d, replotted against remaining sample mass

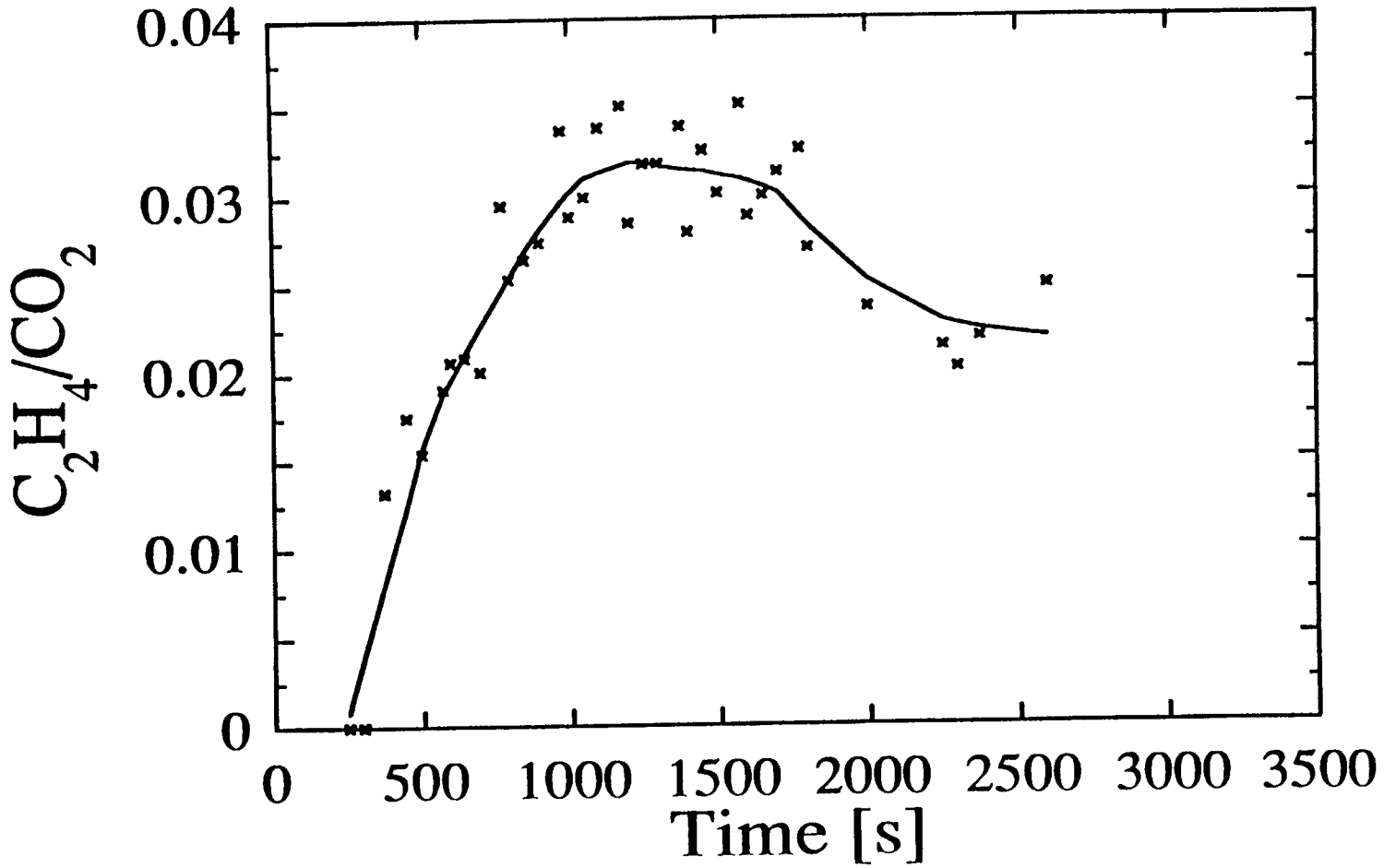

Figure 5.23a: Ethylene to carbon dioxide molar ratio from low density (0.458 g/cm^3) samples of cellulose, subject to a nominal heat flux of 40 kW/m^2

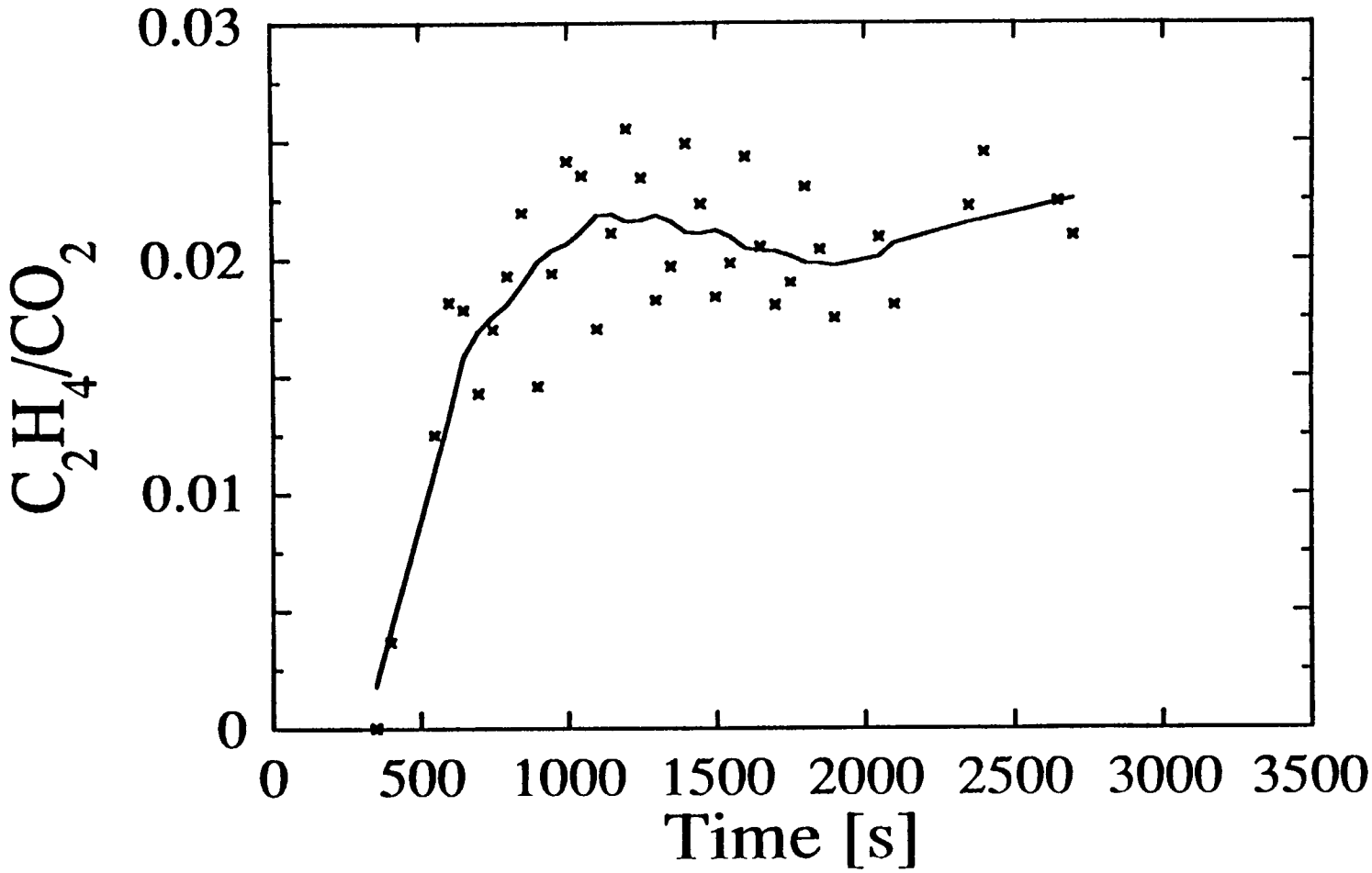

Figure 5.23b: Ethylene to carbon dioxide molar ratio from middle density (0.691 g/cm^3) samples of cellulose, subject to a nominal heat flux of 40 kW/m^2

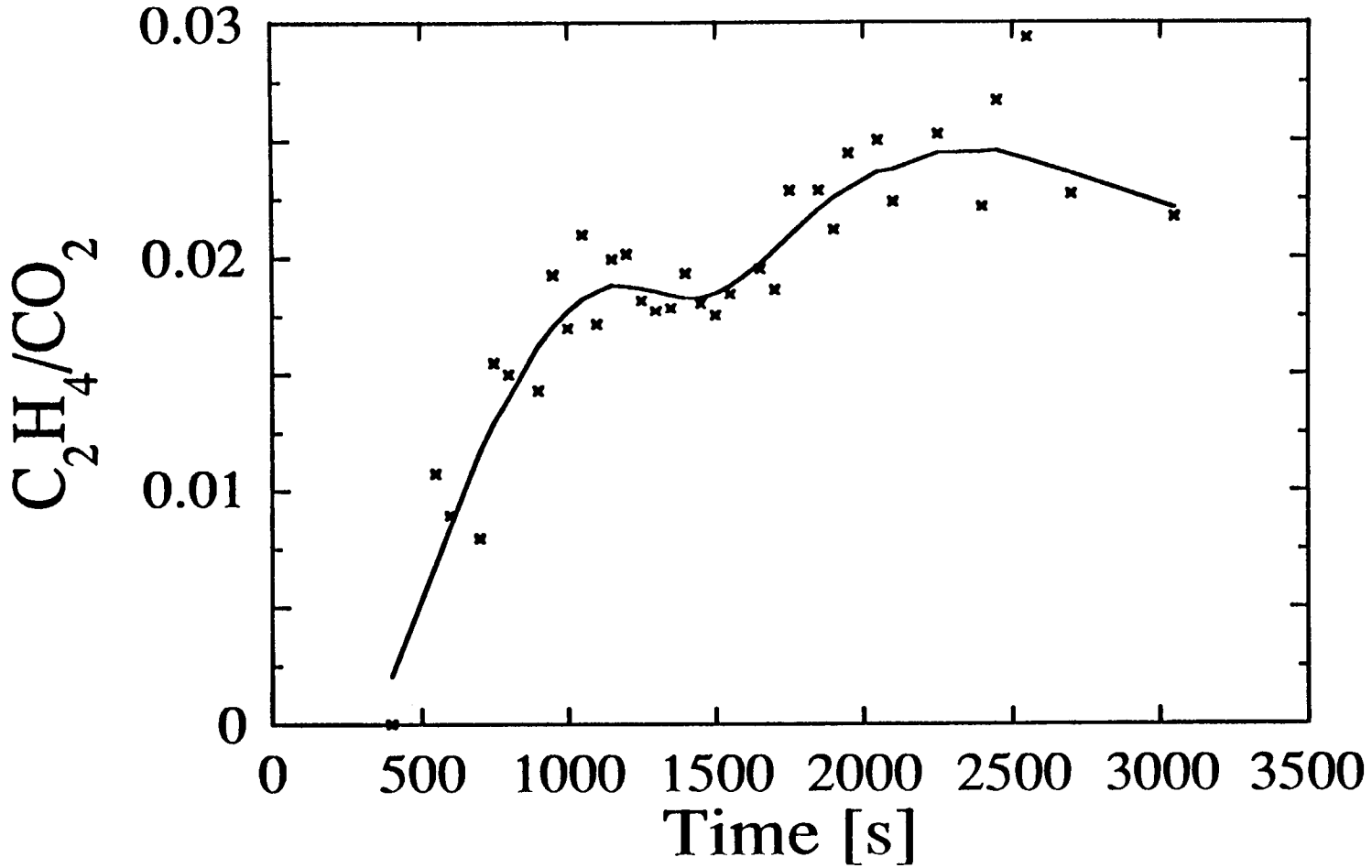

Figure 5.23c: Ethylene to carbon dioxide molar ratio from high density (0.965 g/cm^3) samples of cellulose, subject to a nominal heat flux of 40 kW/m^2

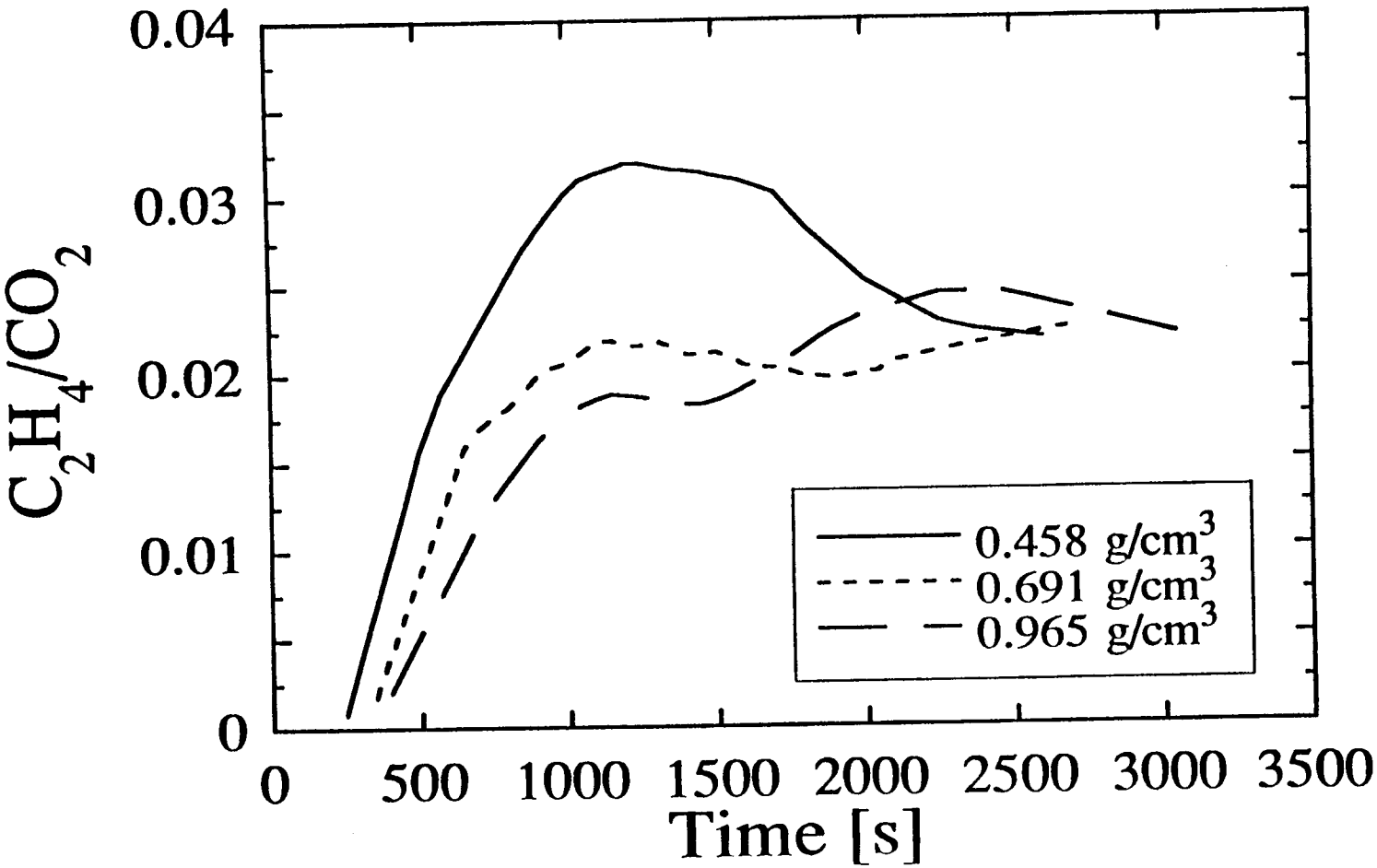

Figure 5.23d: Comparison of results for ethylene to carbon dioxide molar ratio for different density samples. Data are those shown in Figures 5.23a, 5.23b and 5.23c, with data points omitted for clarity

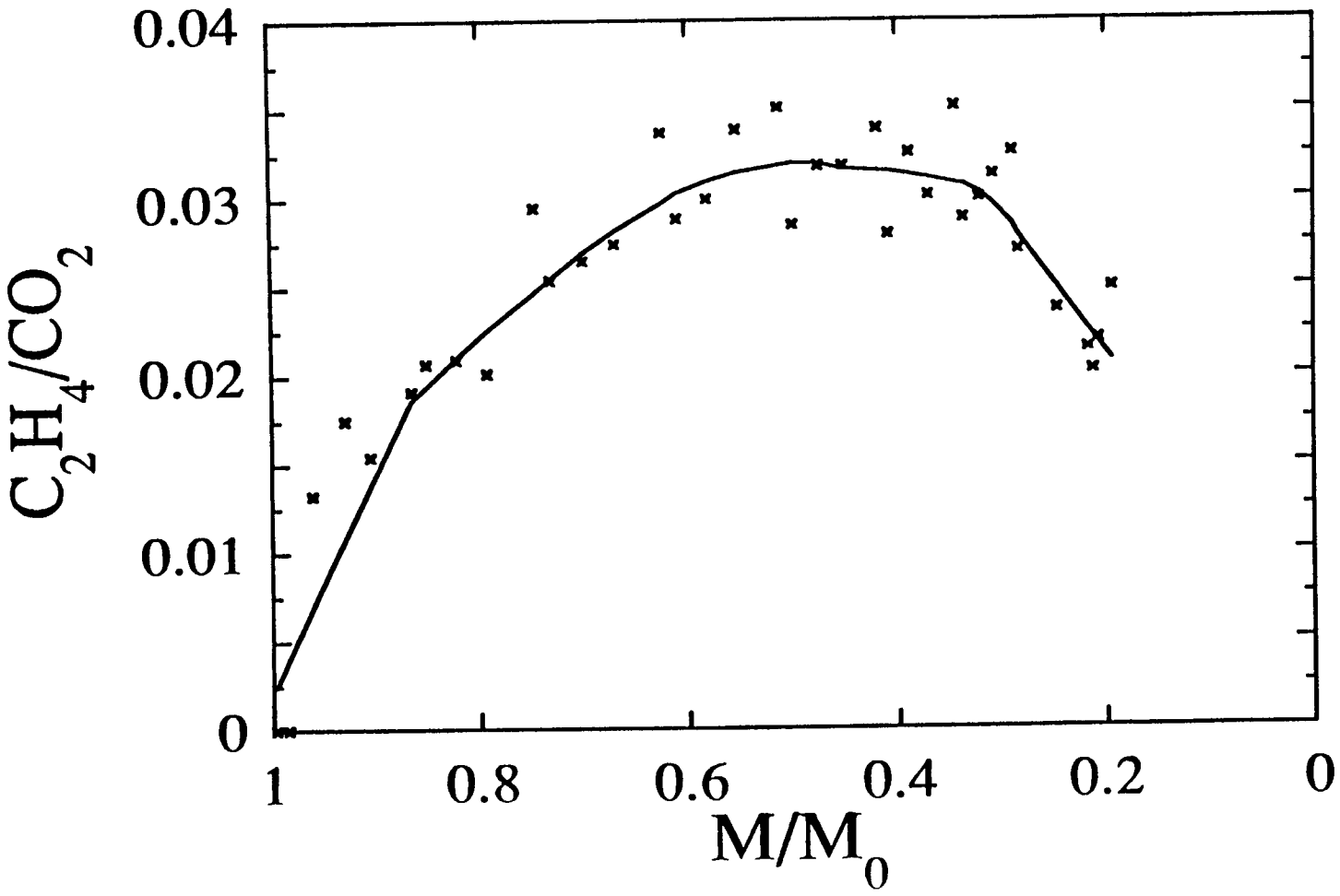

Figure 5.23e: Ethylene to carbon dioxide molar ratio from low density (0.458 g/cm^3) samples of cellulose, subject to a nominal heat flux of 40 kW/m^2. These are the data of Figure 5.23a, replotted against remaining sample mass

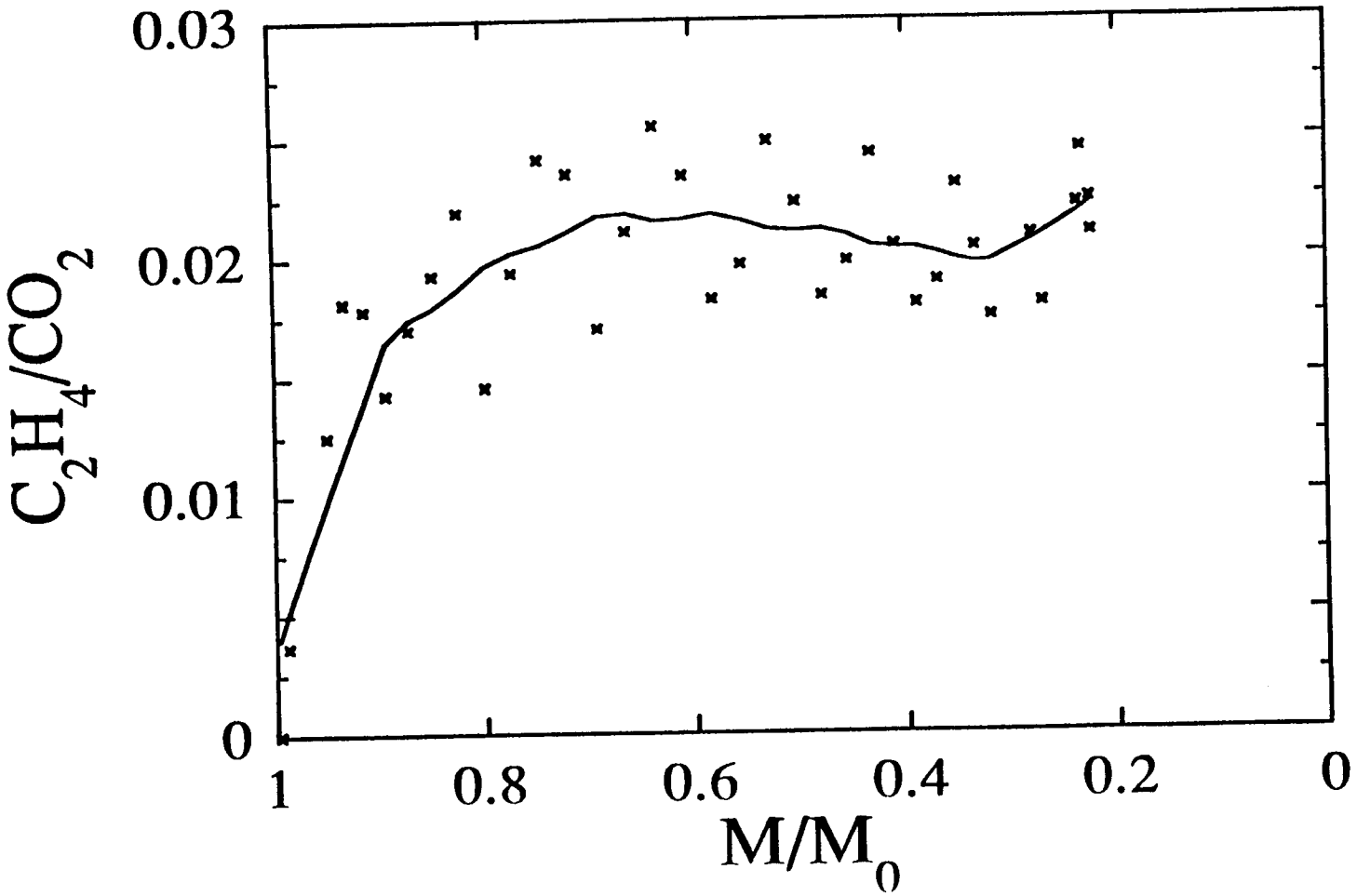

Figure 5.23f: Ethylene to carbon dioxide molar ratio from middle density (0.691 g/cm^3) samples of cellulose, subject to a nominal heat flux of 40 kW/m^2. These are the data of Figure 5.23b, replotted against remaining sample mass

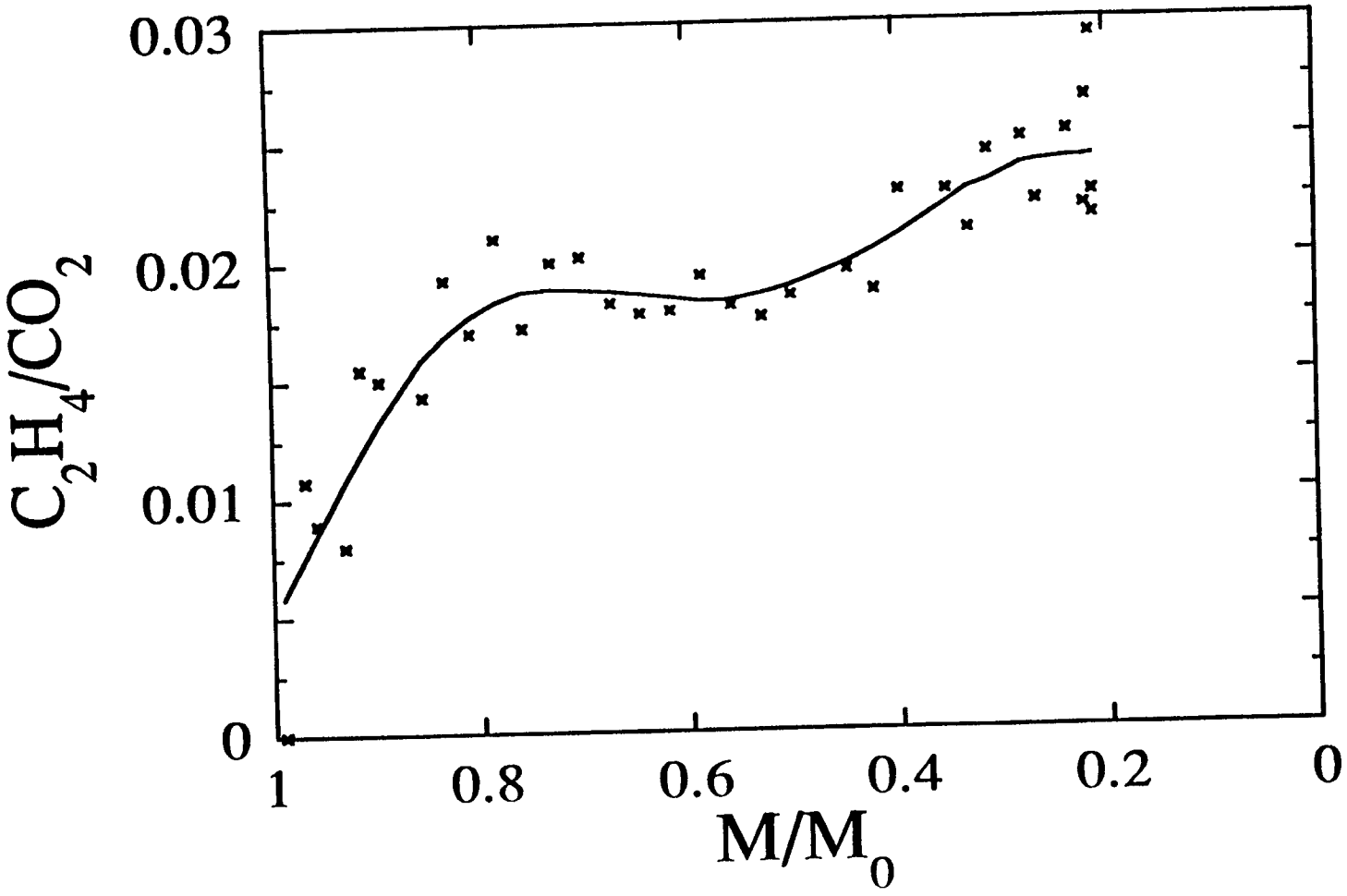

Figure 5.23g: Ethylene to carbon dioxide molar ratio from high density (0.965 g/cm^3) samples of cellulose, subject to a nominal heat flux of 40 kW/m^2. These are the data of Figure 5.23c, replotted against remaining sample mass

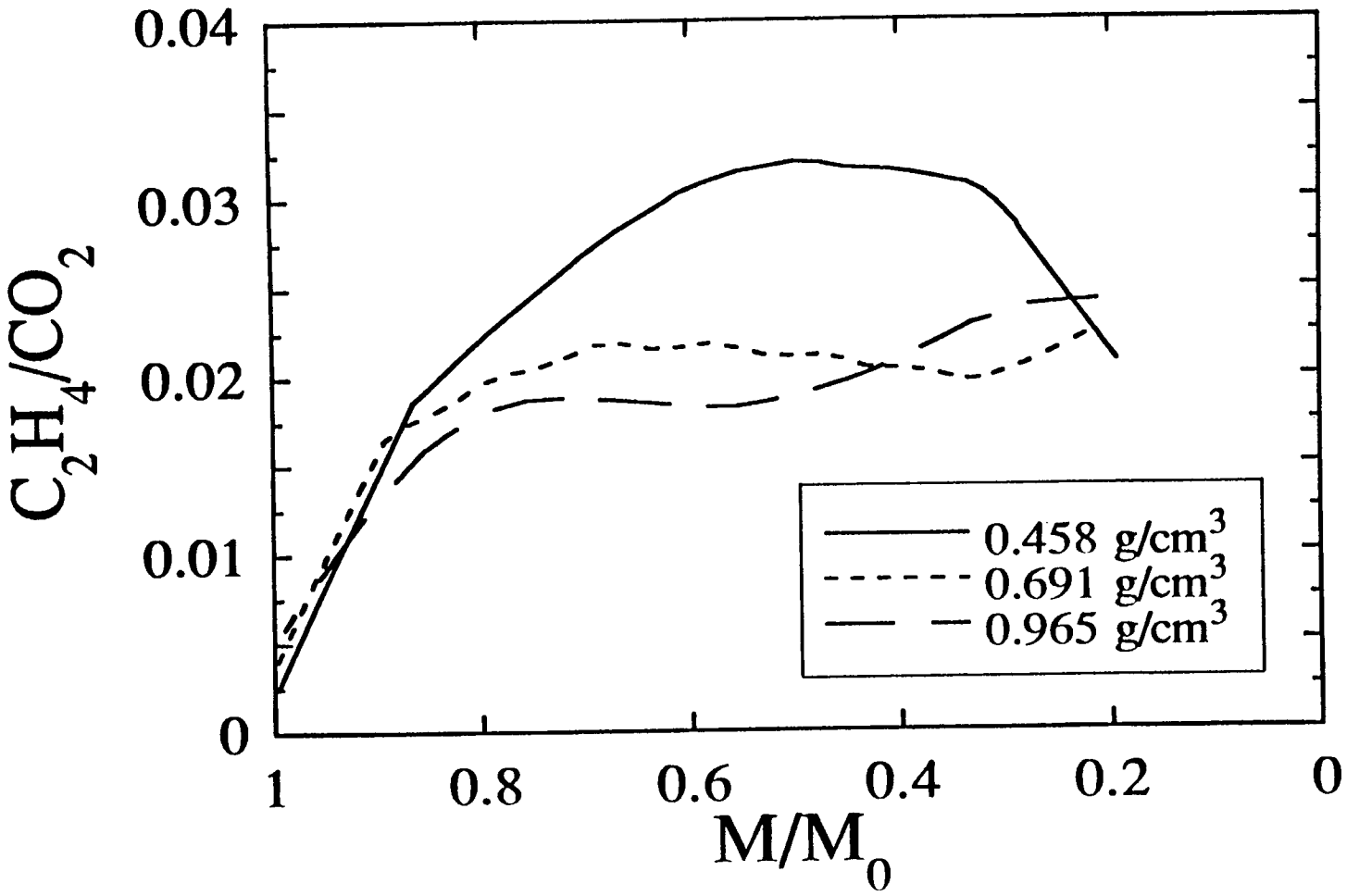

Figure 5.23h: Comparison of results for ethylene to carbon dioxide molar ratio for different density samples. Data are those shown in Figures 5.23e, 5.23f and 5.23g, with data points omitted for clarity. These are the data of Figure 5.23d, replotted against remaining sample mass

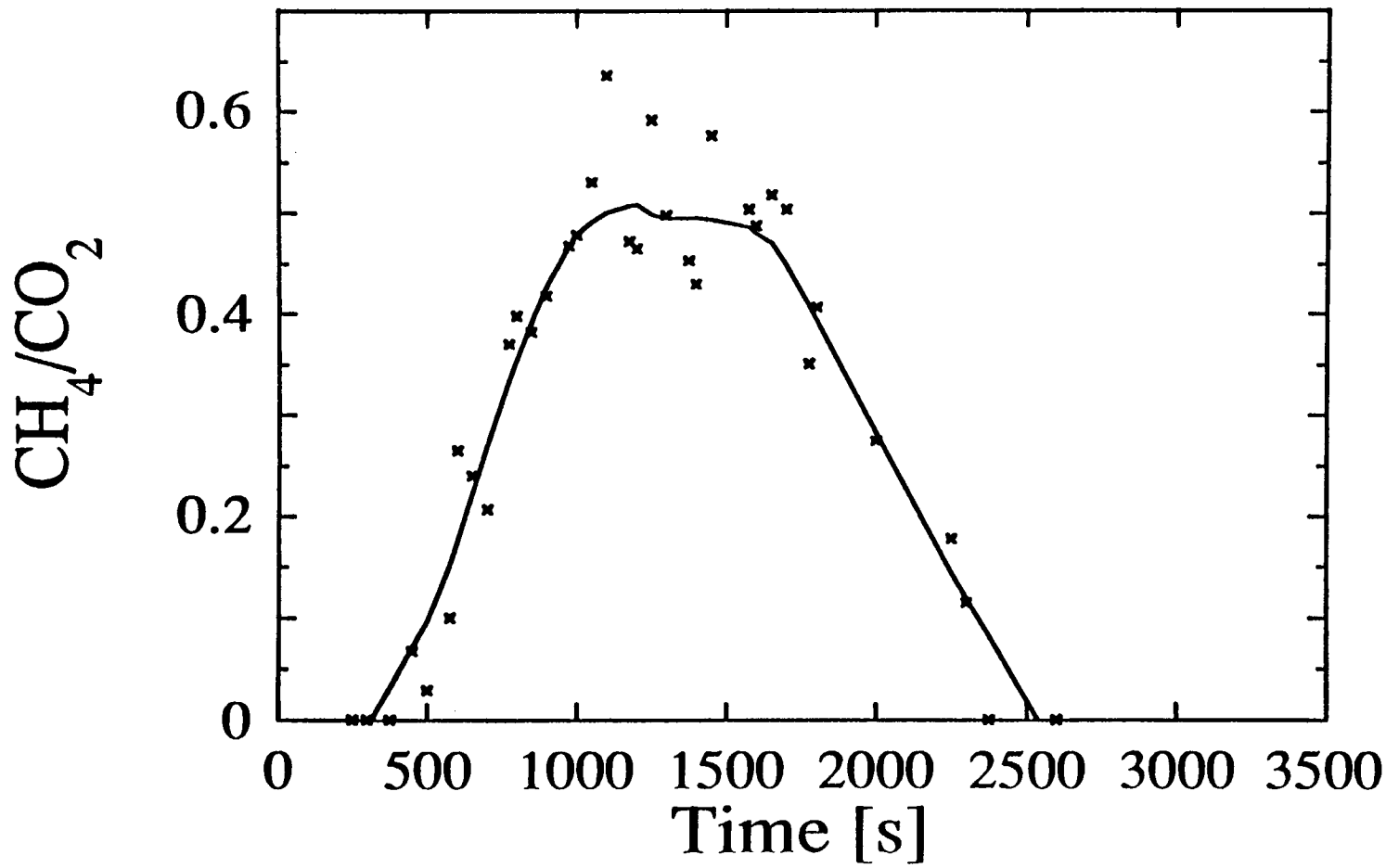

Figure 5.24a: Methane to carbon dioxide molar ratio from low density (0.458 g/cm^3) samples of cellulose, subject to a nominal heat flux of 40 kW/m^2

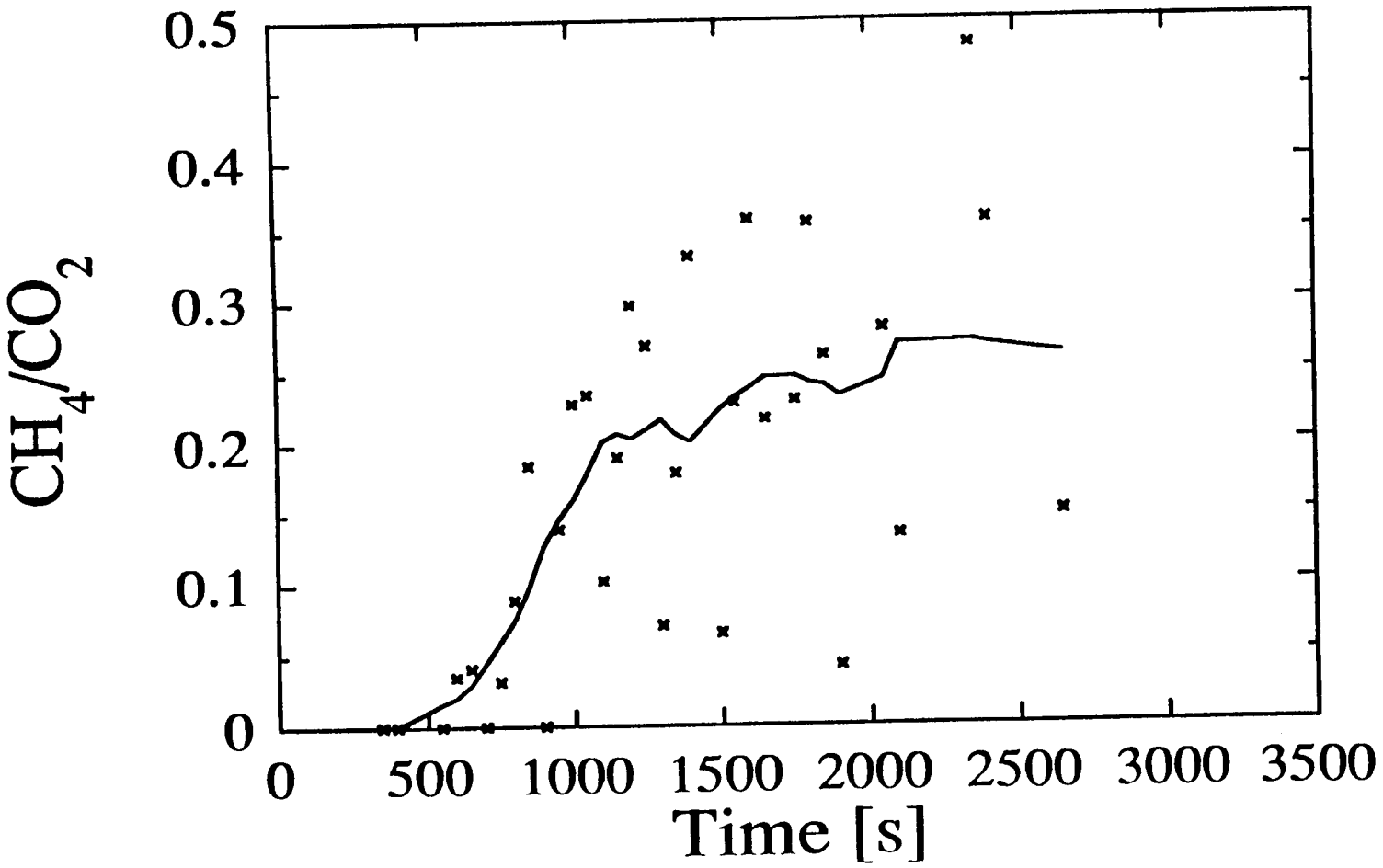

Figure 5.24b: Methane to carbon dioxide molar ratio from middle density (0.691 g/cm^3) samples of cellulose, subject to a nominal heat flux of 40 kW/m^2

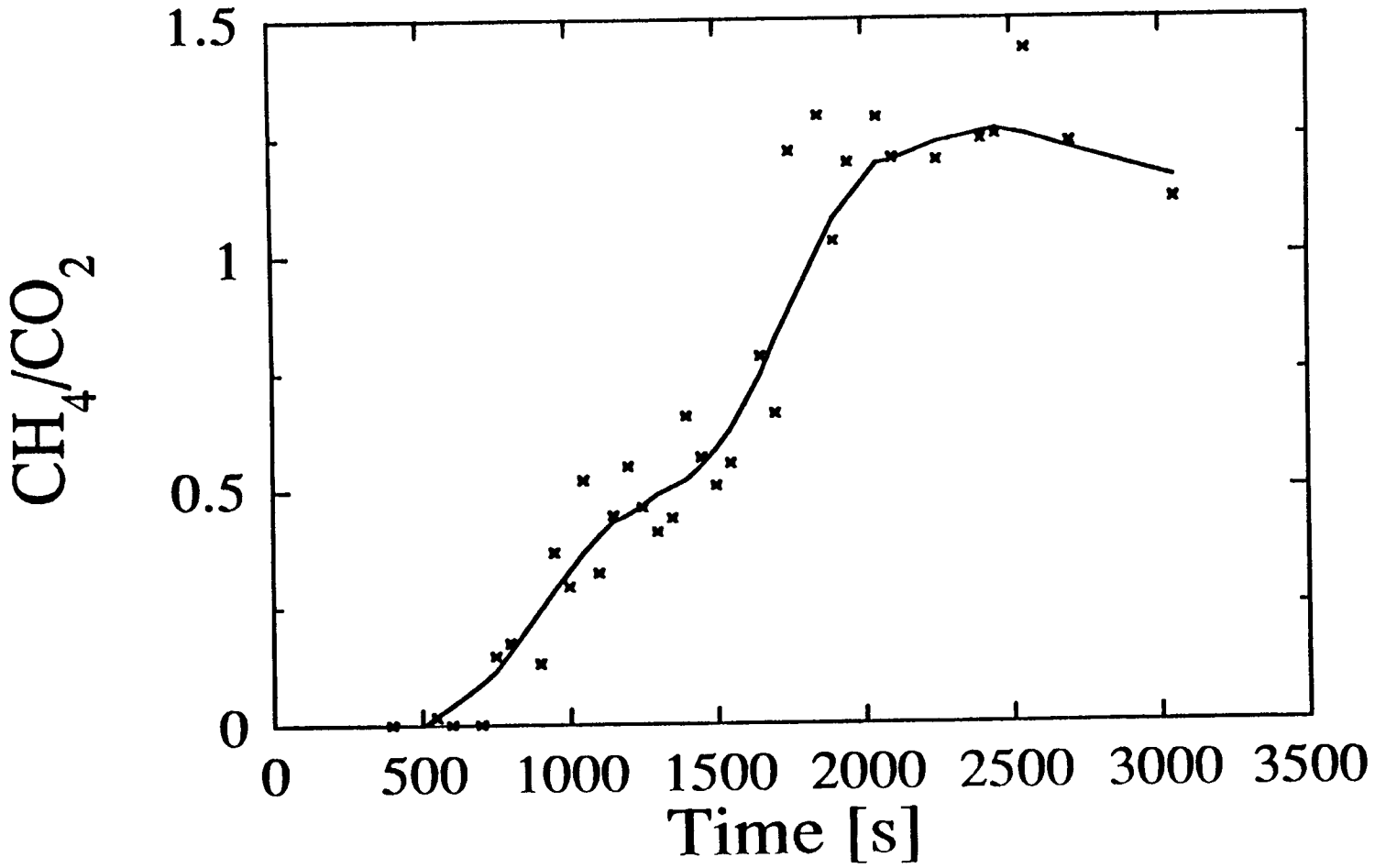

Figure 5.24c: Methane to carbon dioxide molar ratio from high density (0.965 g/cm^3) samples of cellulose, subject to a nominal heat flux of 40 kW/m^2

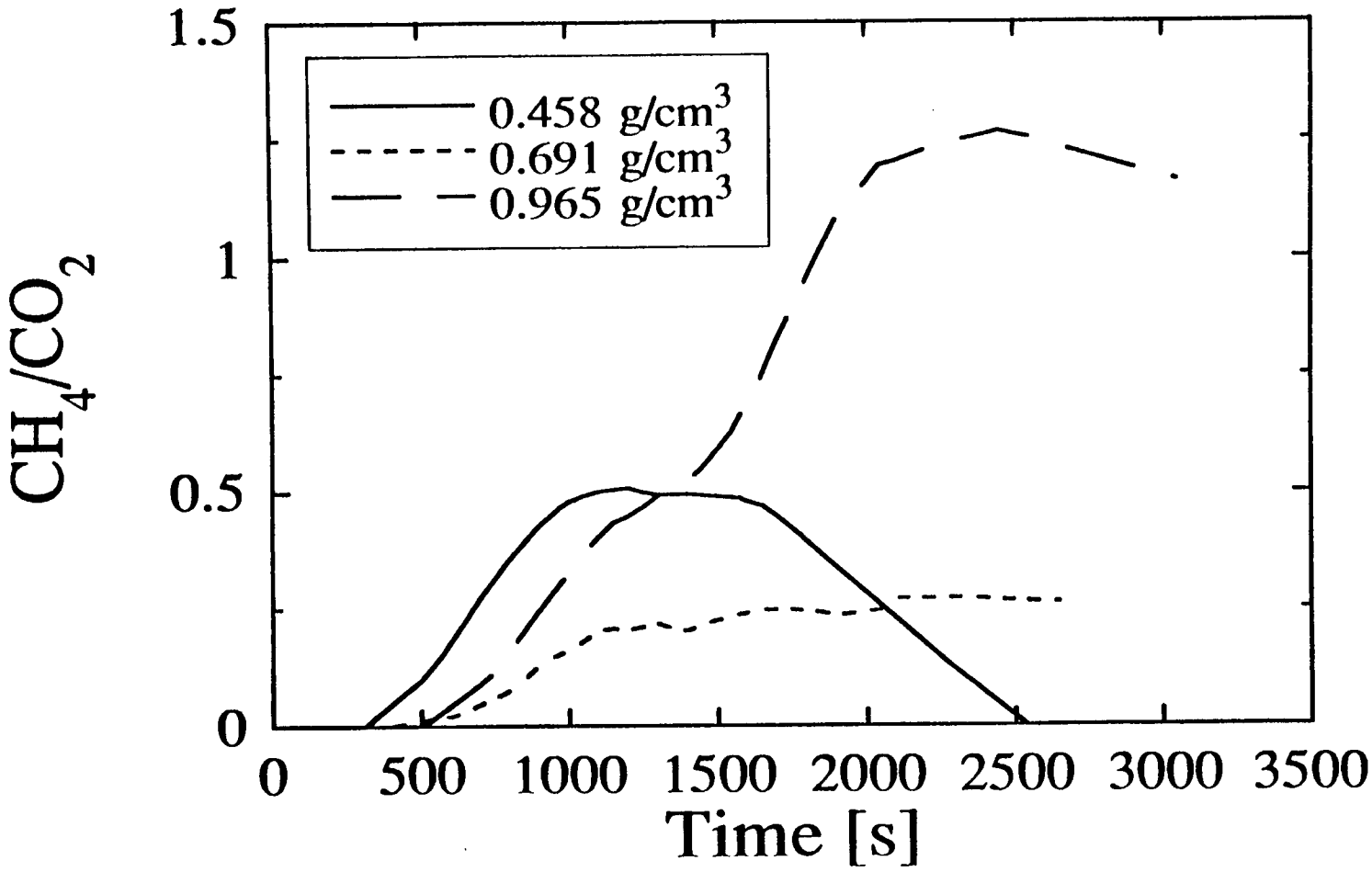

Figure 5.24d: Comparison of results for methane to carbon dioxide molar ratio for different density samples. Data are those shown in Figures 5.24a, 5.24b and 5.24c, with data points omitted for clarity

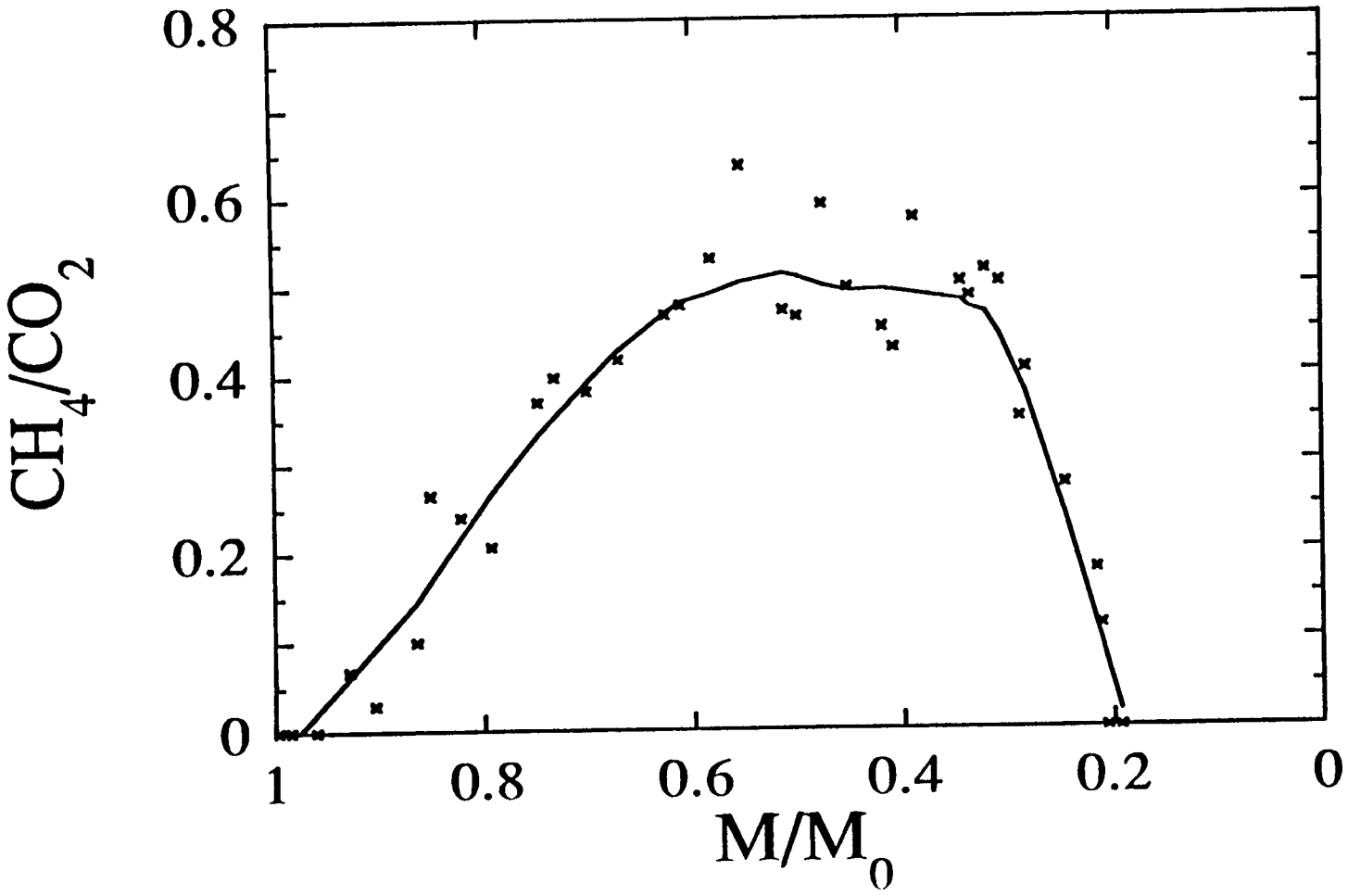

Figure 5.24e: Methane to carbon dioxide molar ratio from low density (0.458 g/cm^3) samples of cellulose, subject to a nominal heat flux of 40 kW/m^2. These are the data of Figure 5.24a, replotted against remaining sample mass

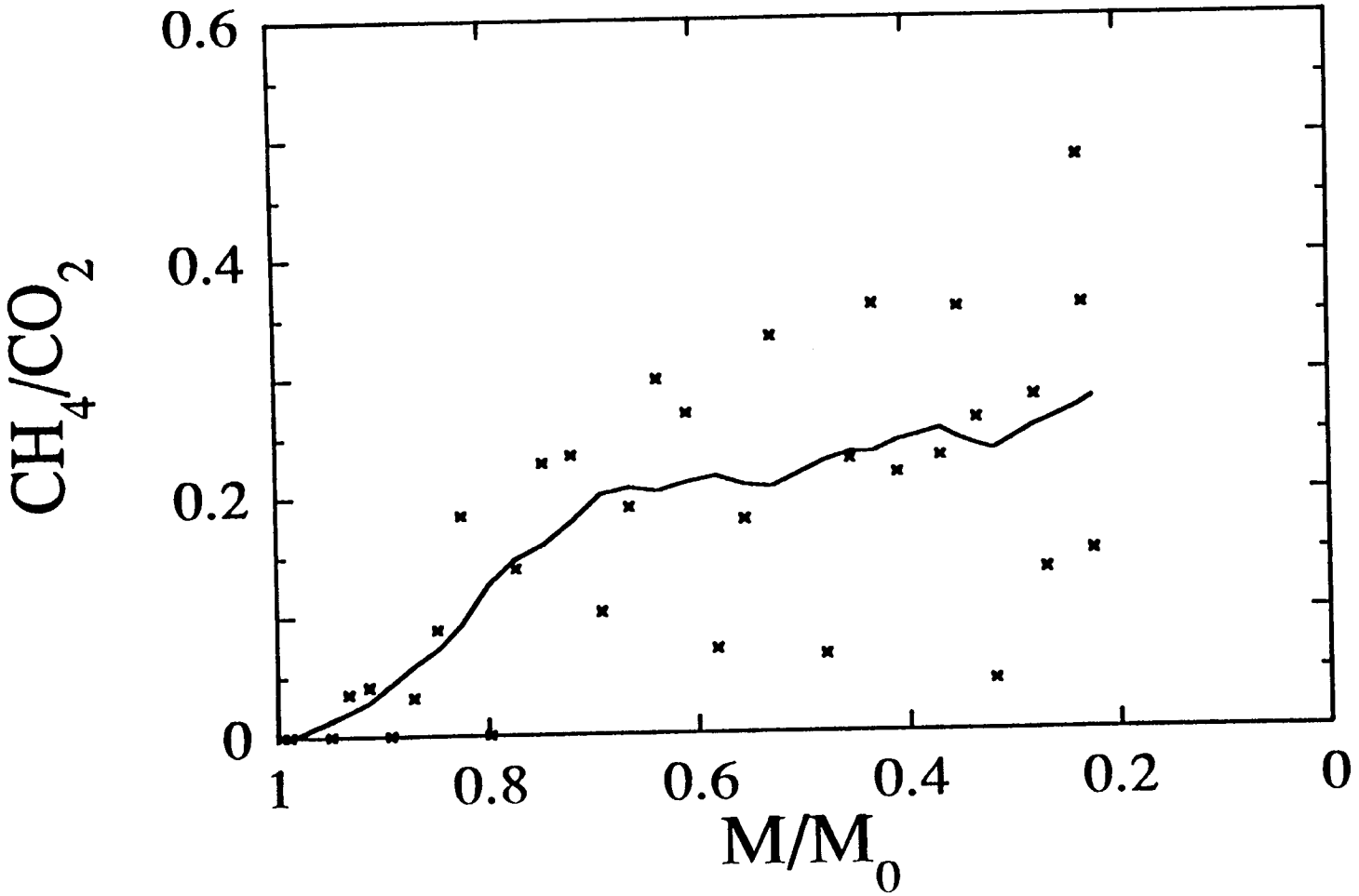

Figure 5.24f: Methane to carbon dioxide molar ratio from middle density (0.691 g/cm^3) samples of cellulose, subject to a nominal heat flux of 40 kW/m^2. These are the data of Figure 5.24b, replotted against remaining sample mass

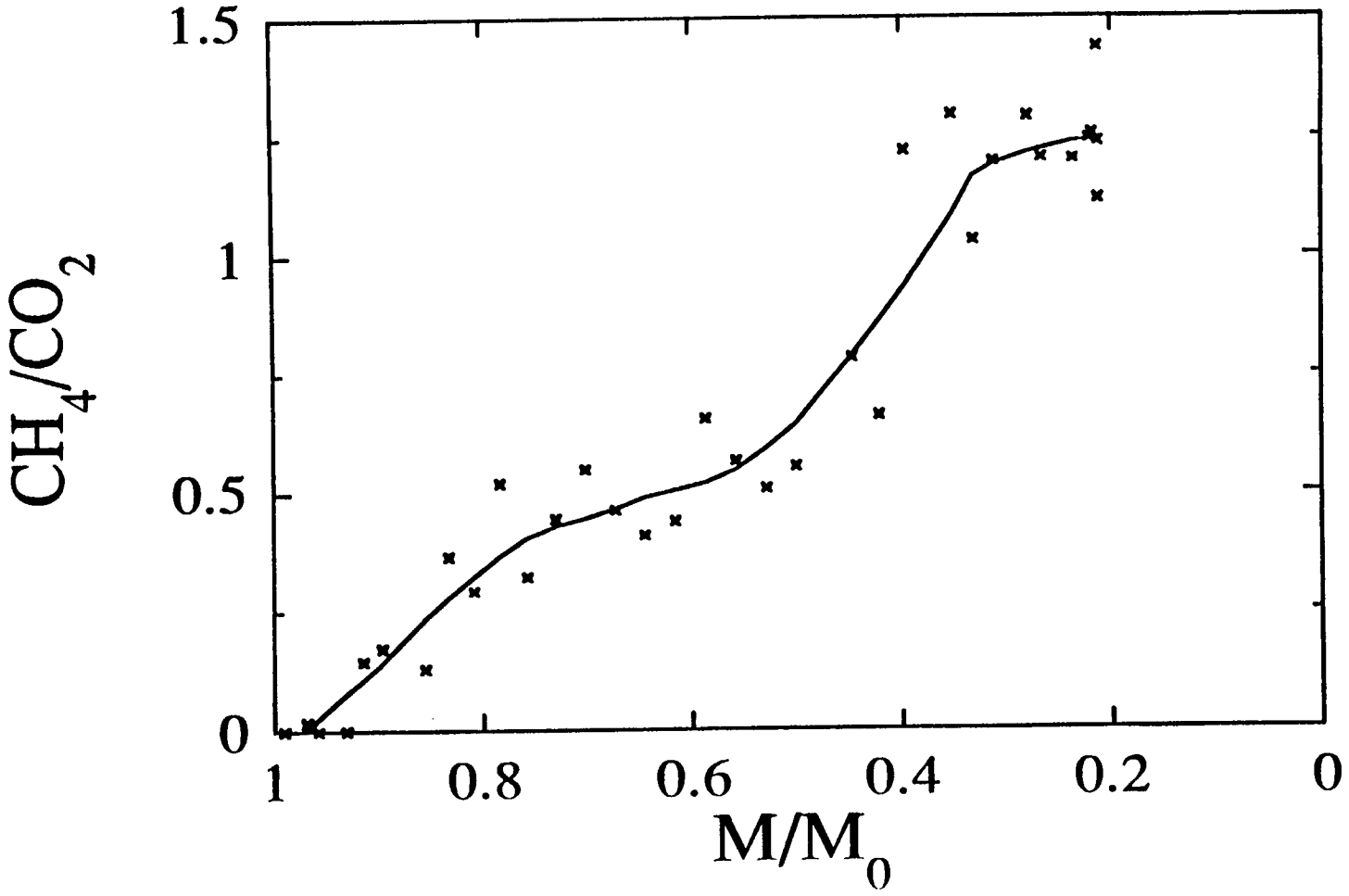

Figure 5.24g: Methane to carbon dioxide molar ratio from high density (0.965 g/cm^3) samples of cellulose, subject to a nominal heat flux of 40 kW/m^2. These are the data of Figure 5.24c, replotted against remaining sample mass

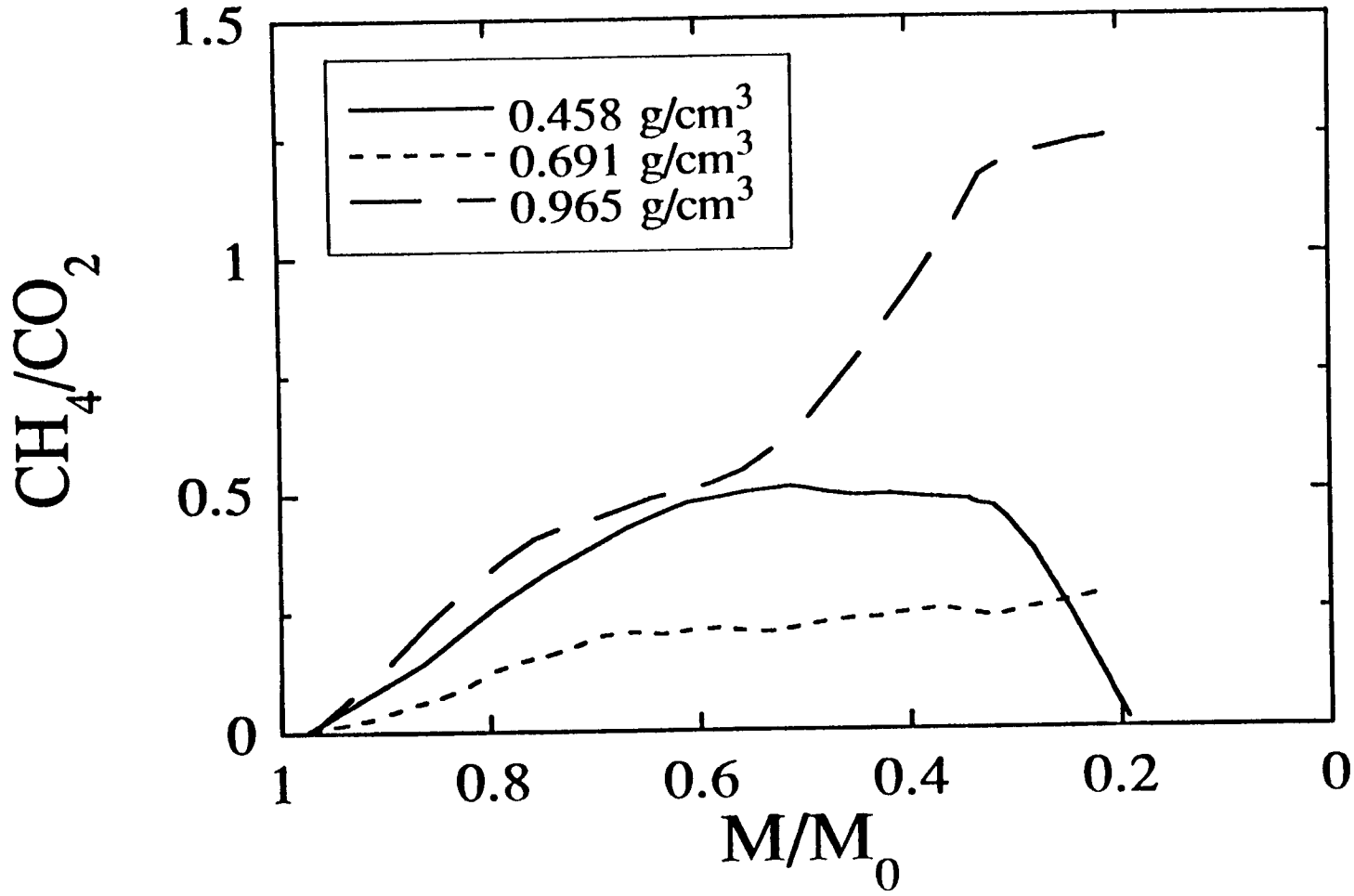

Figure 5.24h: Comparison of results for methane to carbon dioxide molar ratio for different density samples. Data are those shown in Figures 5.24e, 5.24f and 5.24g, with data points omitted for clarity. These are the data of Figure 5.24d, replotted against remaining sample mass

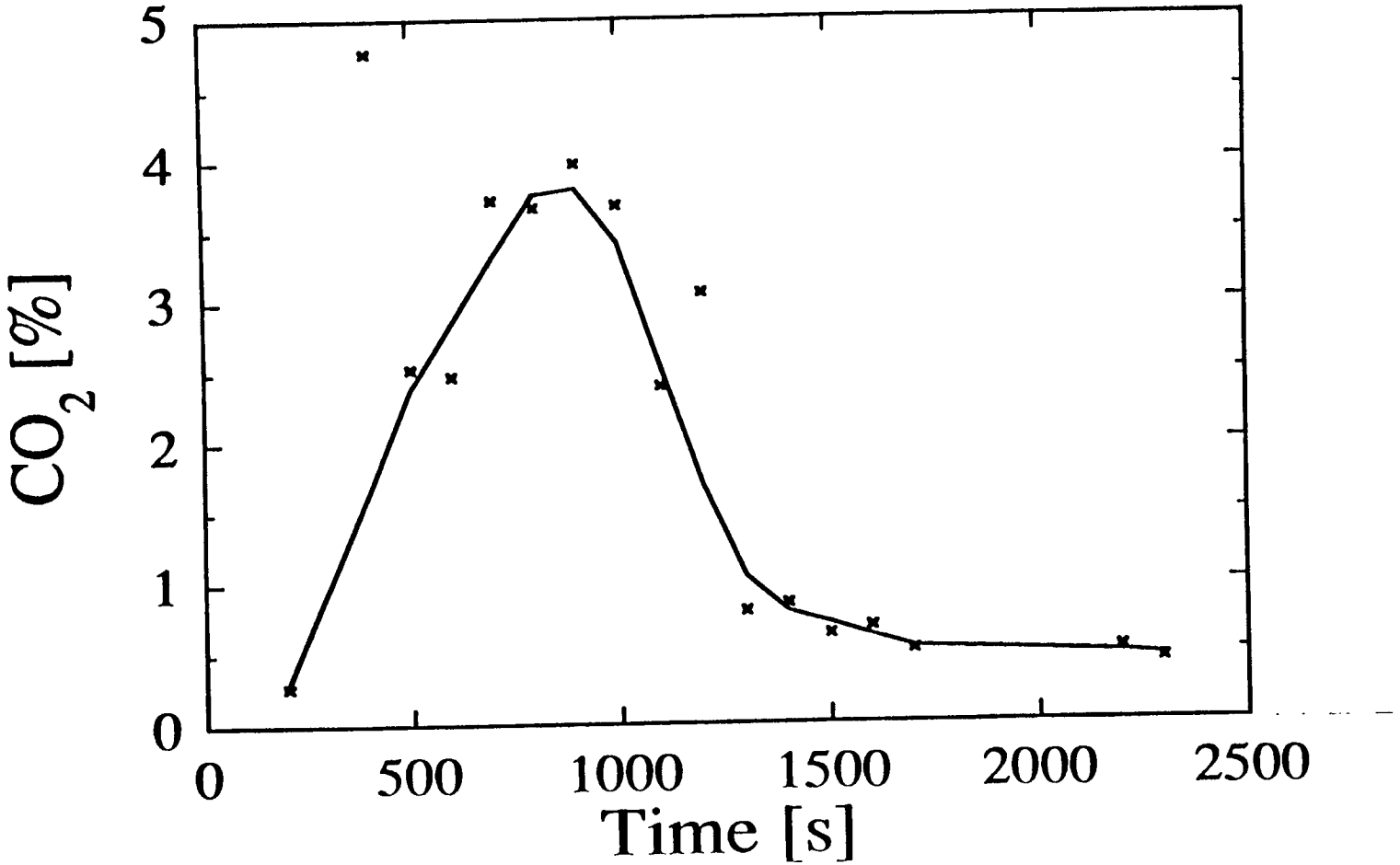

Figure 5.25a: Carbon dioxide content of dry, tar - free pyrolysis pyrolysis gases released from low density (0.458 g/cm^3) samples of cellulose, subject to a nominal heat flux of 60 kW/m^2

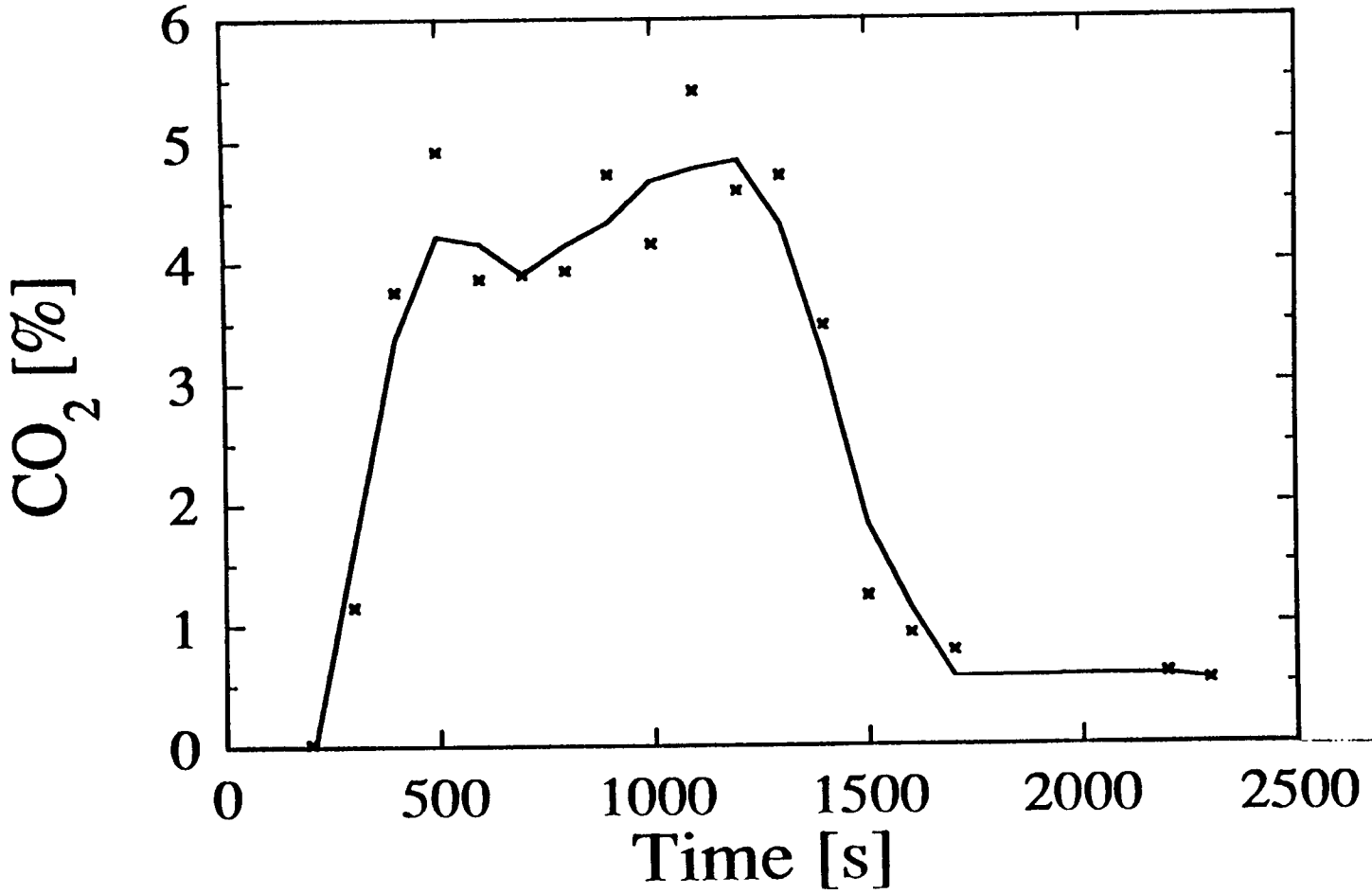

Figure 5.25b: Carbon dioxide content of dry, tar - free pyrolysis gases released from middle density (0.691 g/cm^3) samples of cellulose, subject to a nominal heat flux of 60 kW/m^2

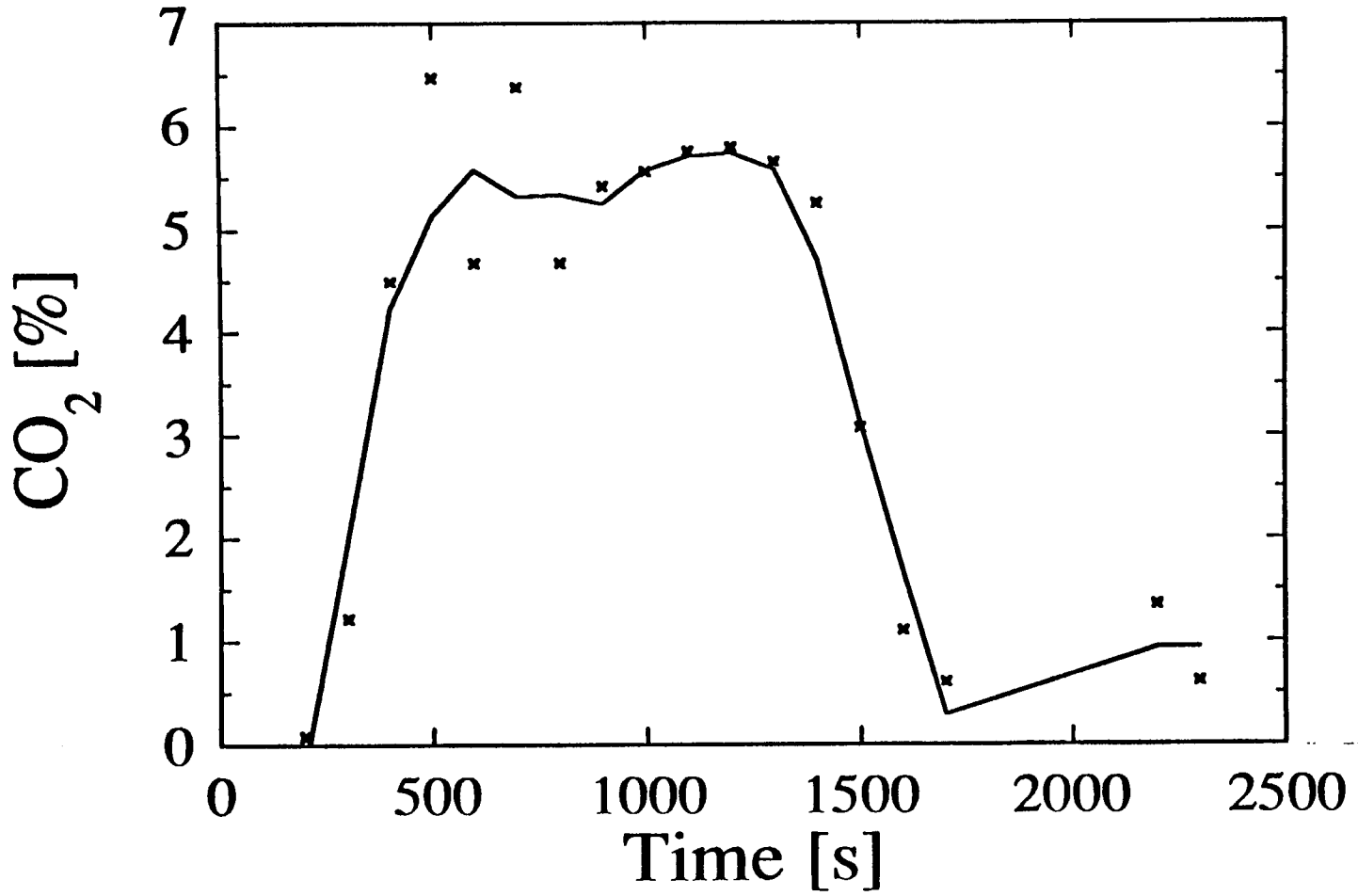

Figure 5.25c: Carbon dioxide content of dry, tar - free pyrolysis gases released from high density (0.965 g/cm^3) samples of cellulose, subject to a nominal heat flux of 60 kW/m^2

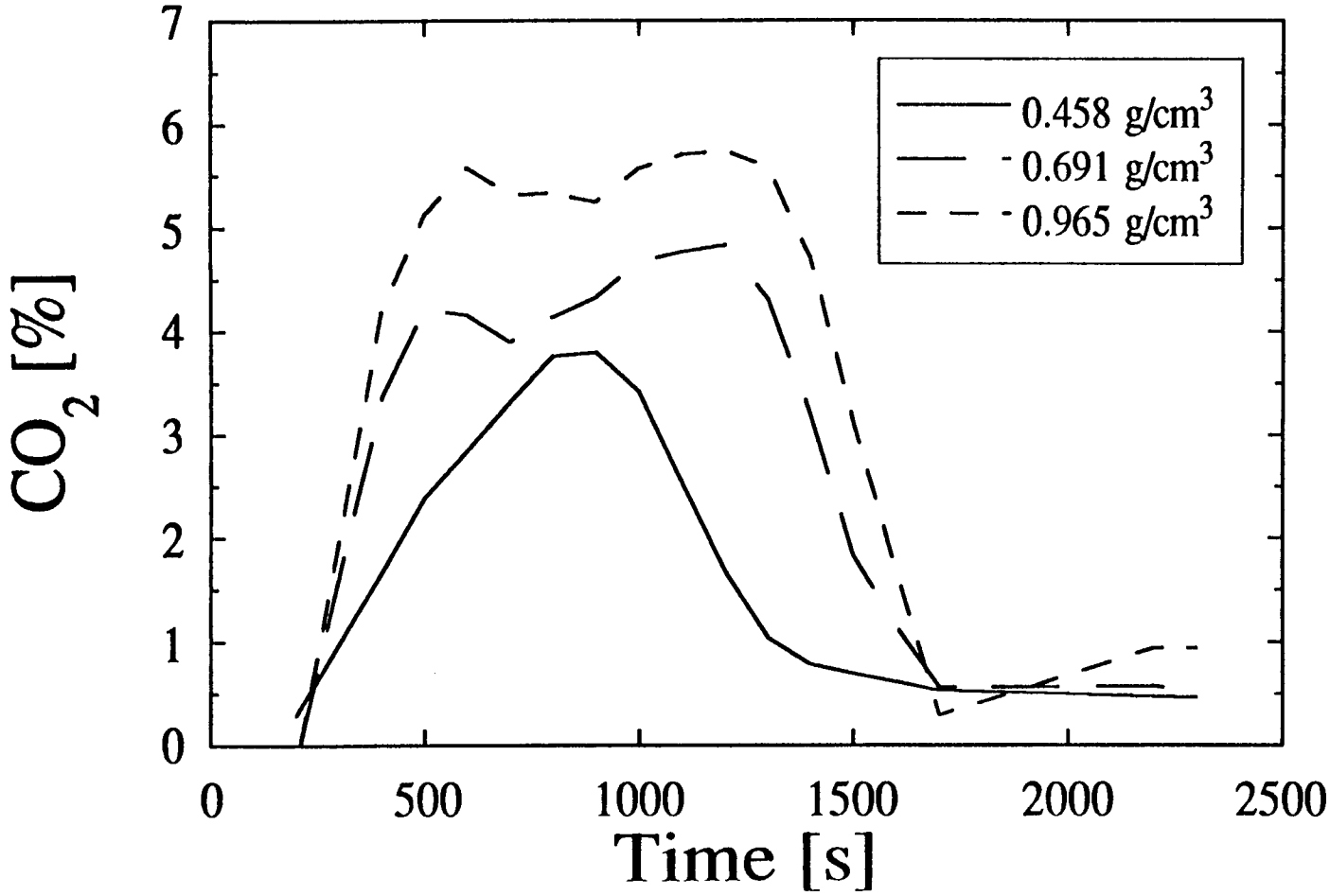

Figure 5.25d: Comparison of results for different density samples. Data are those shown in Figures 5.25a, 5.25b and 5.25c, with data points omitted for clarity

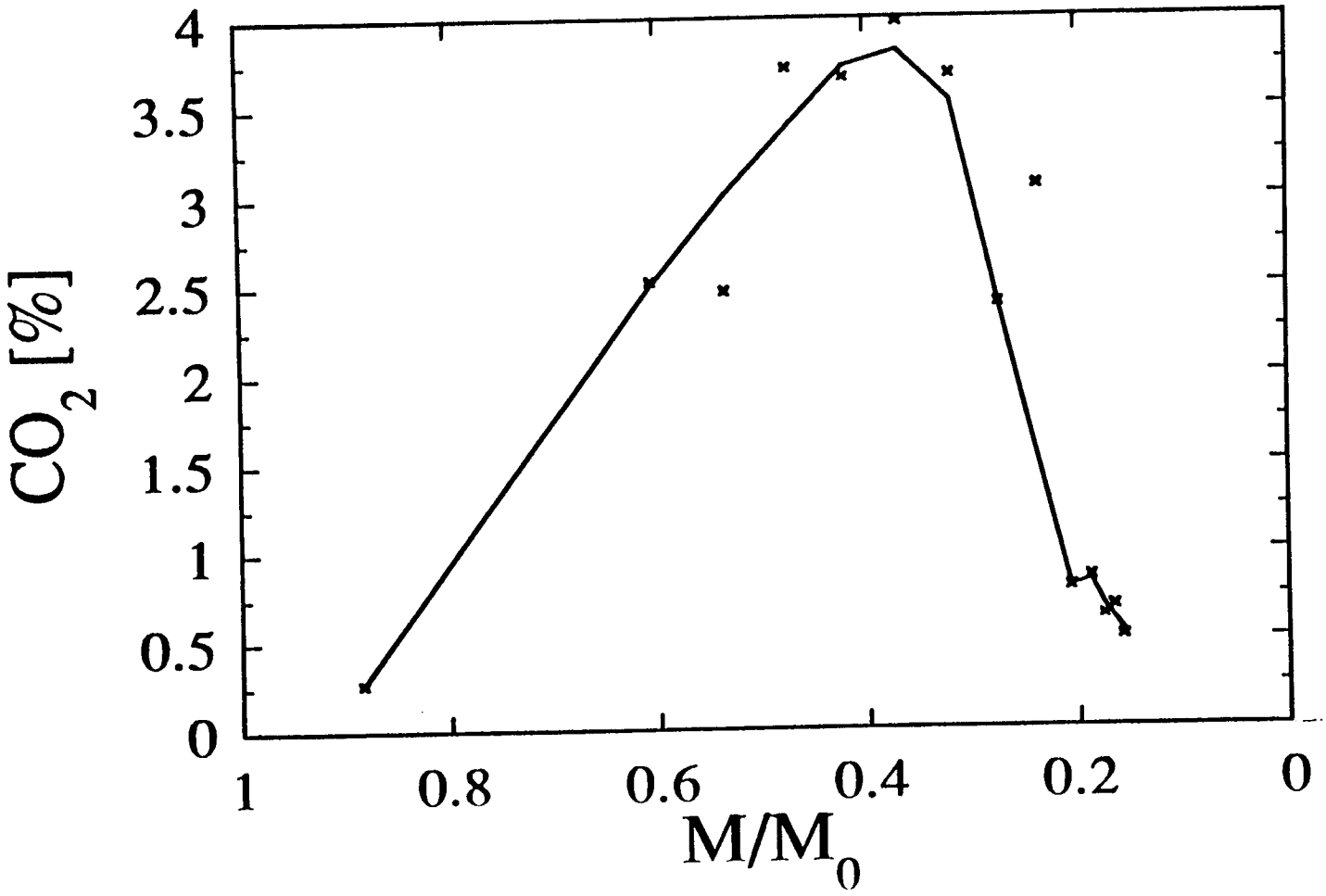

Figure 5.25e: Carbon dioxide content of dry, tar - free pyrolysis gases released from low density (0.458 g/cm^3) samples of cellulose, subject to a nominal heat flux of 60 kW/m^2. These are the data of Figure 5.25a, replotted against remaining sample mass

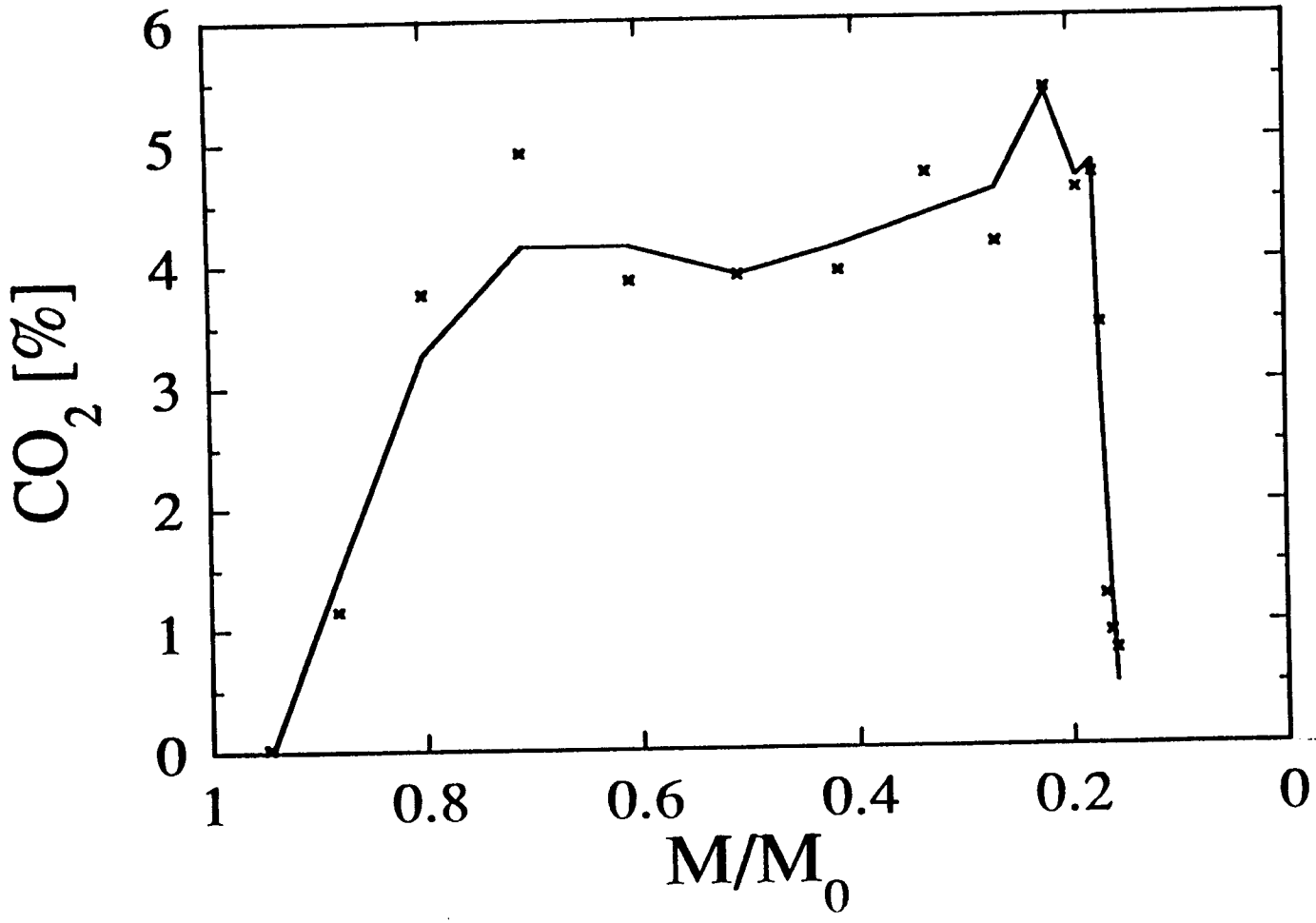

Figure 5.25f: Carbon dioxide content of dry, tar - free pyrolysis gases released from middle density (0.691 g/cm^3) samples of cellulose, subject to a nominal heat flux of 60 kW/m^2. These are the data of Figure 5.25b, replotted against remaining sample mass

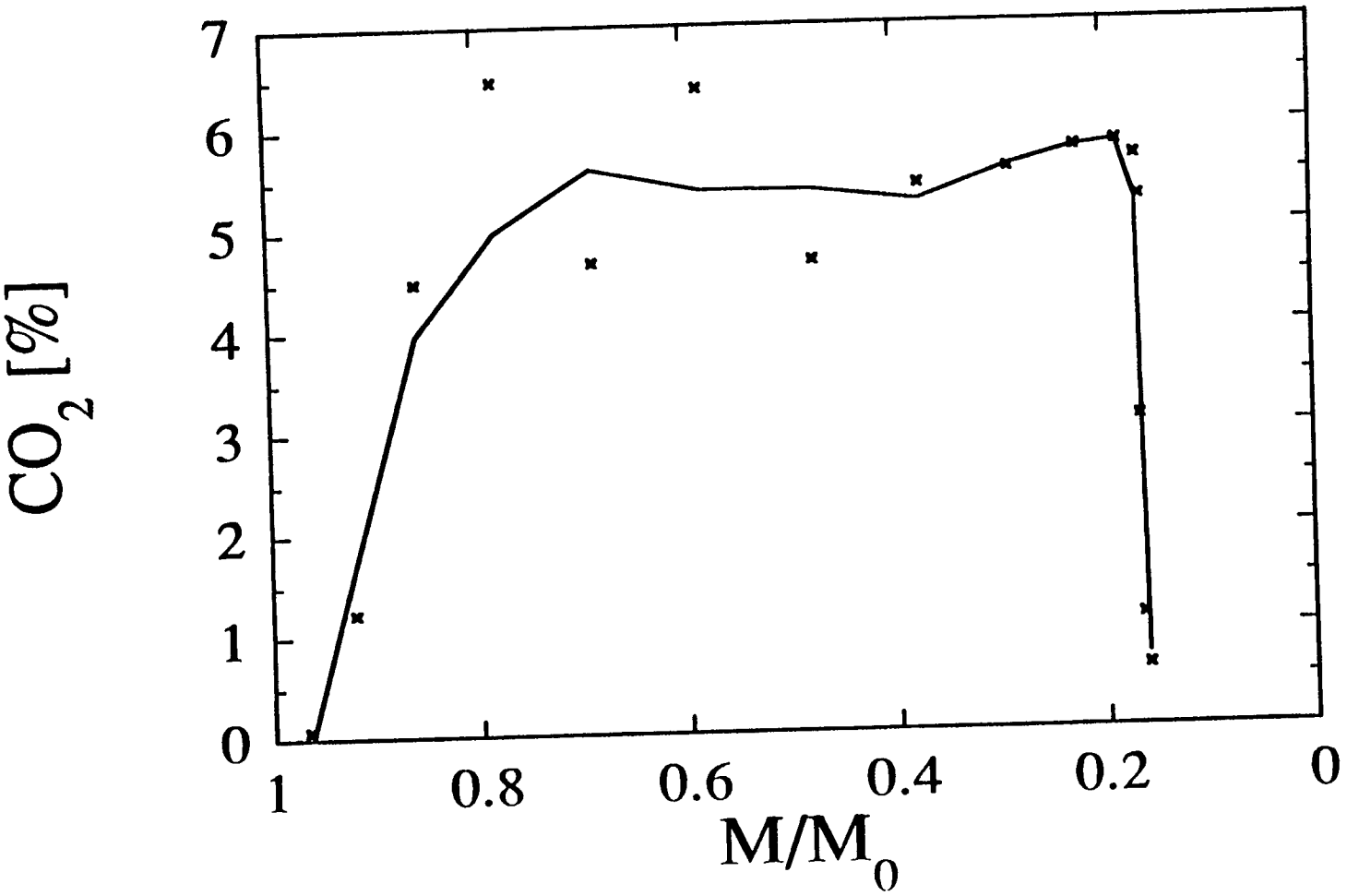

Figure 5.25g: Carbon dioxide content of dry, tar - free pyrolysis gases released from high density (0.965 g/cm^3) samples of cellulose, subject to a nominal heat flux of 60 kW/m^2. These are the data of Figure 5.25c, replotted against remaining sample mass

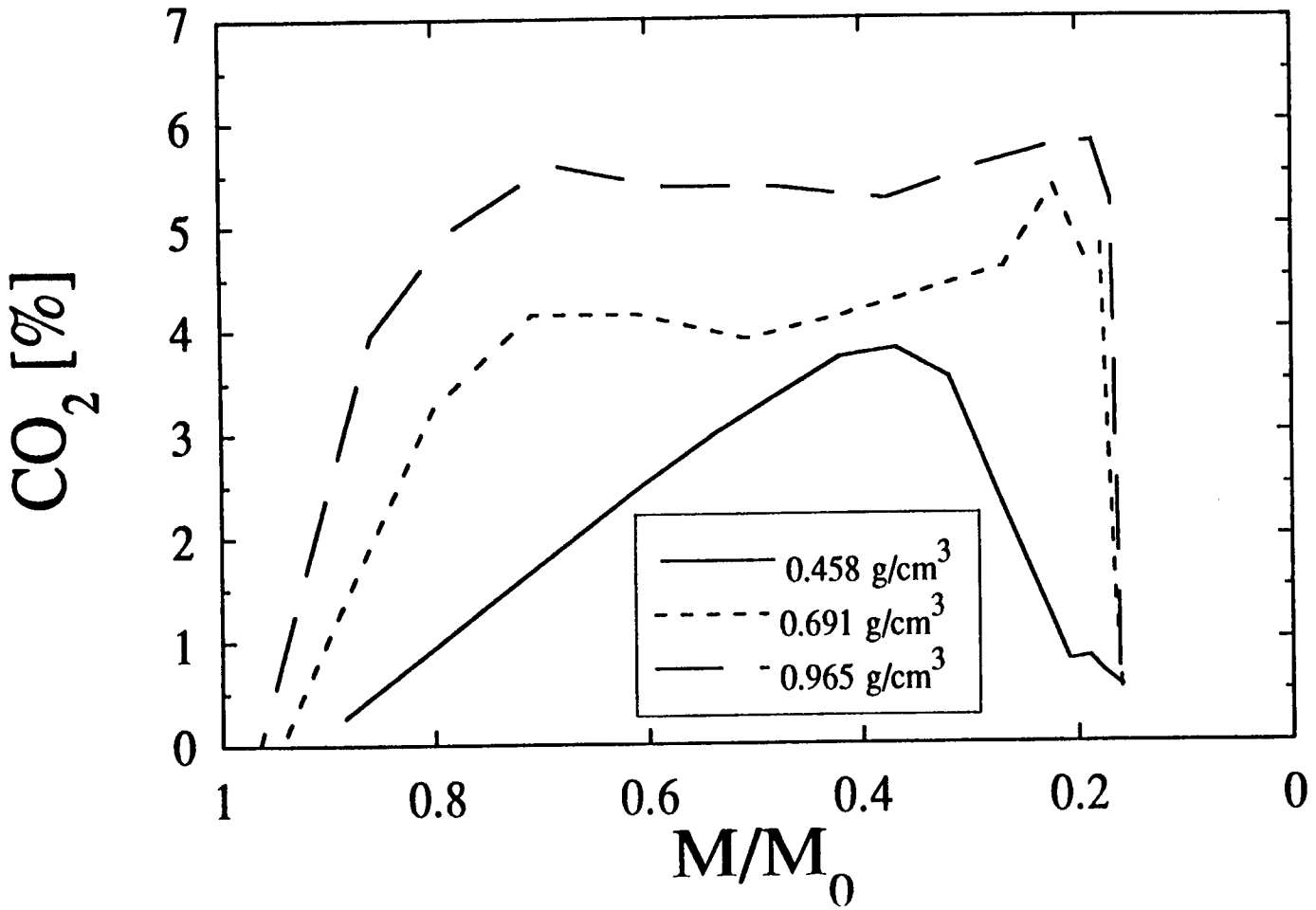

Figure 5.25h: Comparison of results for different density samples. Data are those shown in Figures 5.25e, 5.25f and 5.25g, with data points omitted for clarity. These are the data of Figure 5.25d, replotted against remaining sample mass

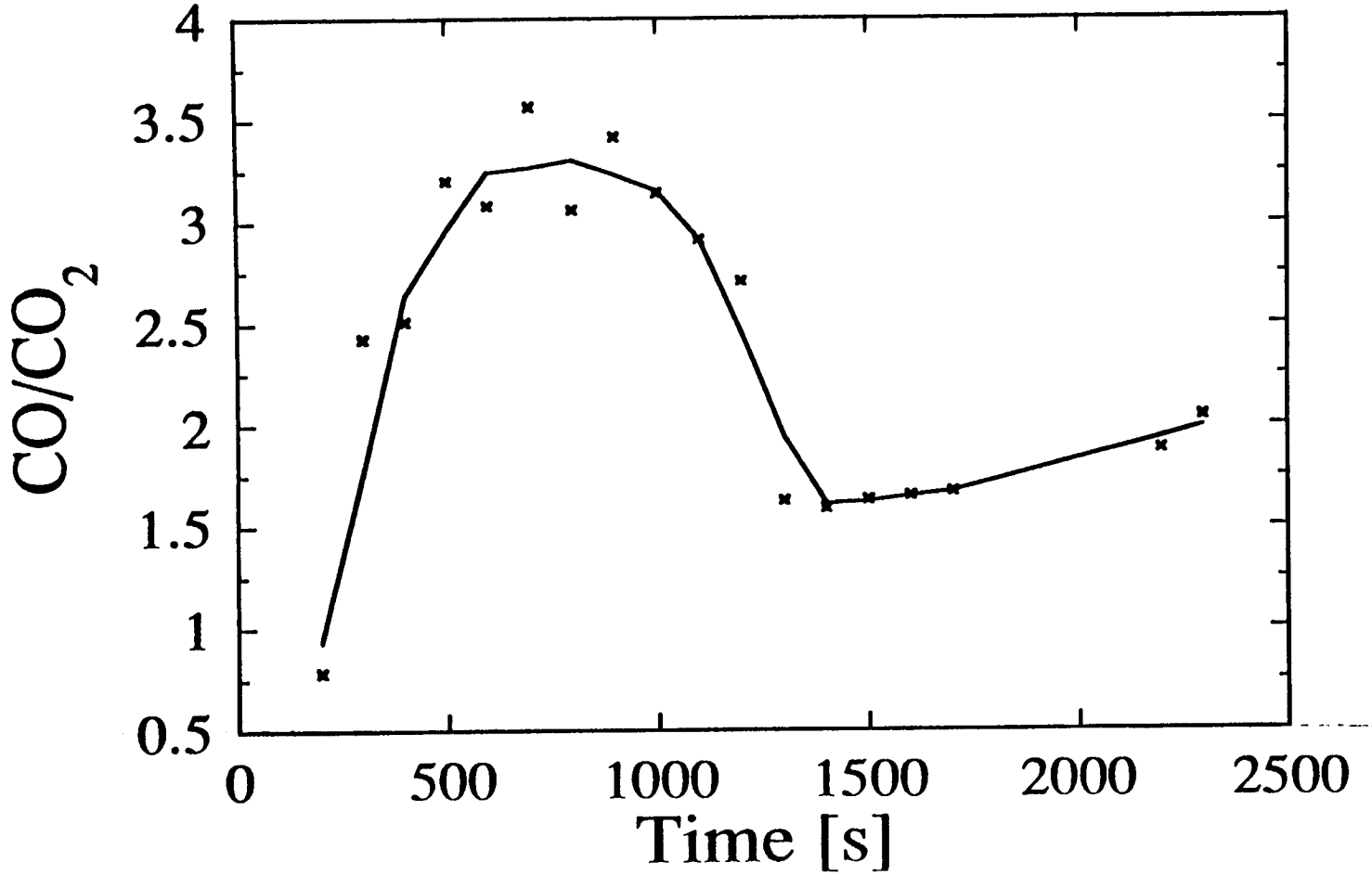

Figure 5.26a: Carbon monoxide to carbon dioxide molar ratio from low density (0.458 g/cm^3) samples of cellulose, subject to a nominal heat flux of 60 kW/m^2

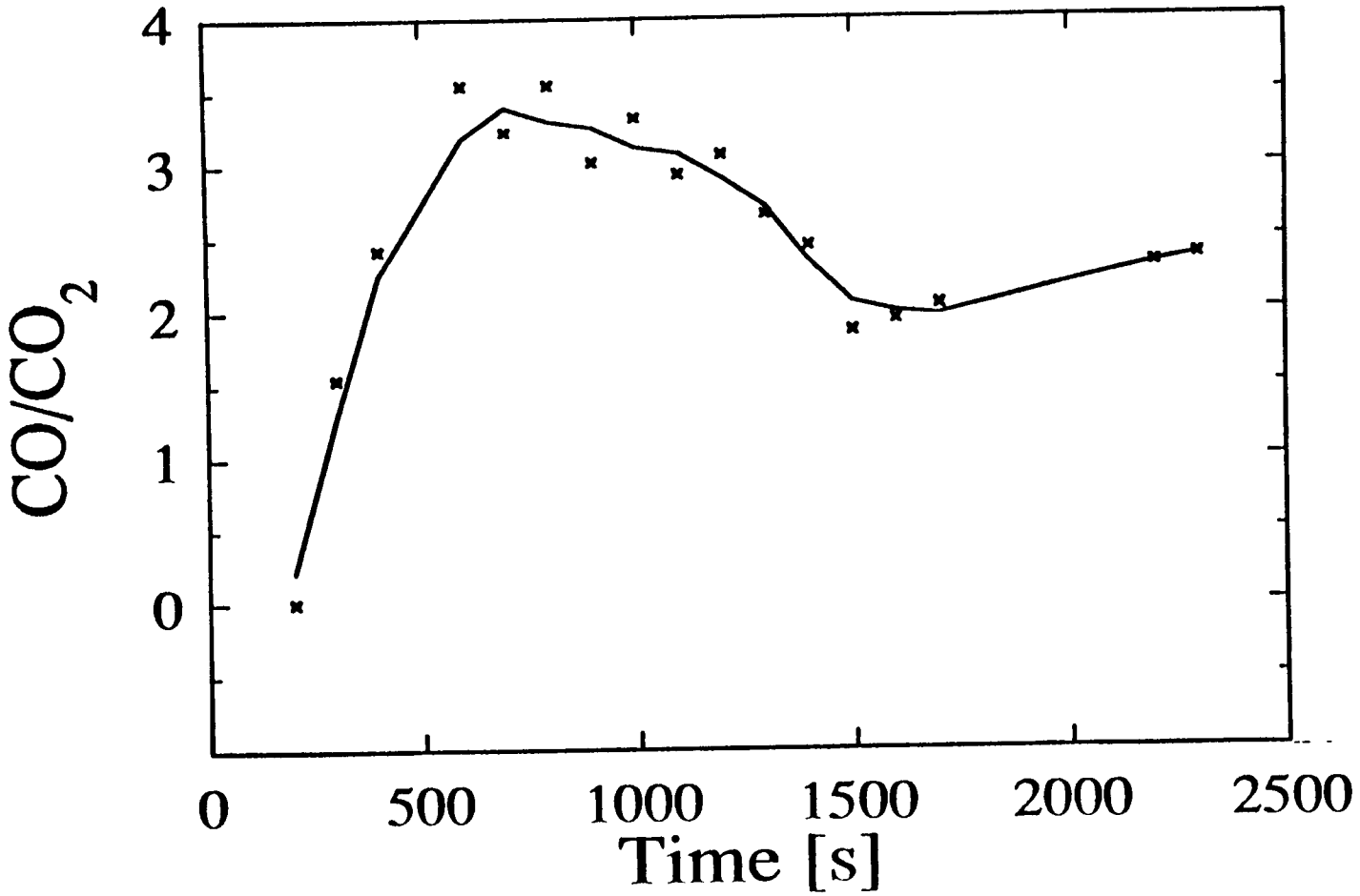

Figure 5.26b: Carbon monoxide to carbon dioxide molar ratio from middle density (0.691 g/cm^3) samples of cellulose, subject to a nominal heat flux of 60 kW/m^2

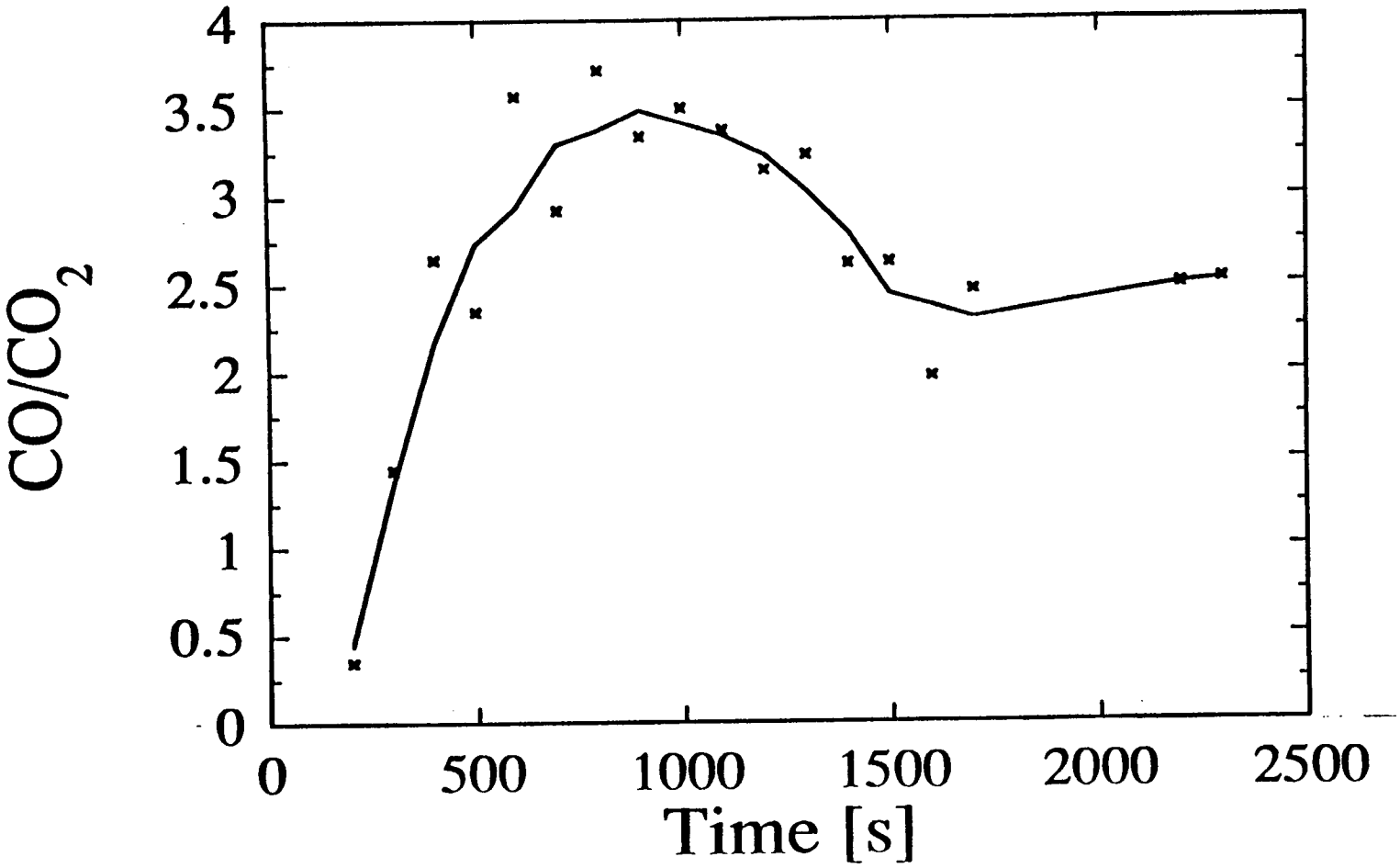

Figure 5.26c: Carbon monoxide to carbon dioxide molar ratio from high density (0.965 g/cm^3) samples of cellulose, subject to a nominal heat flux of 60 kW/m^2

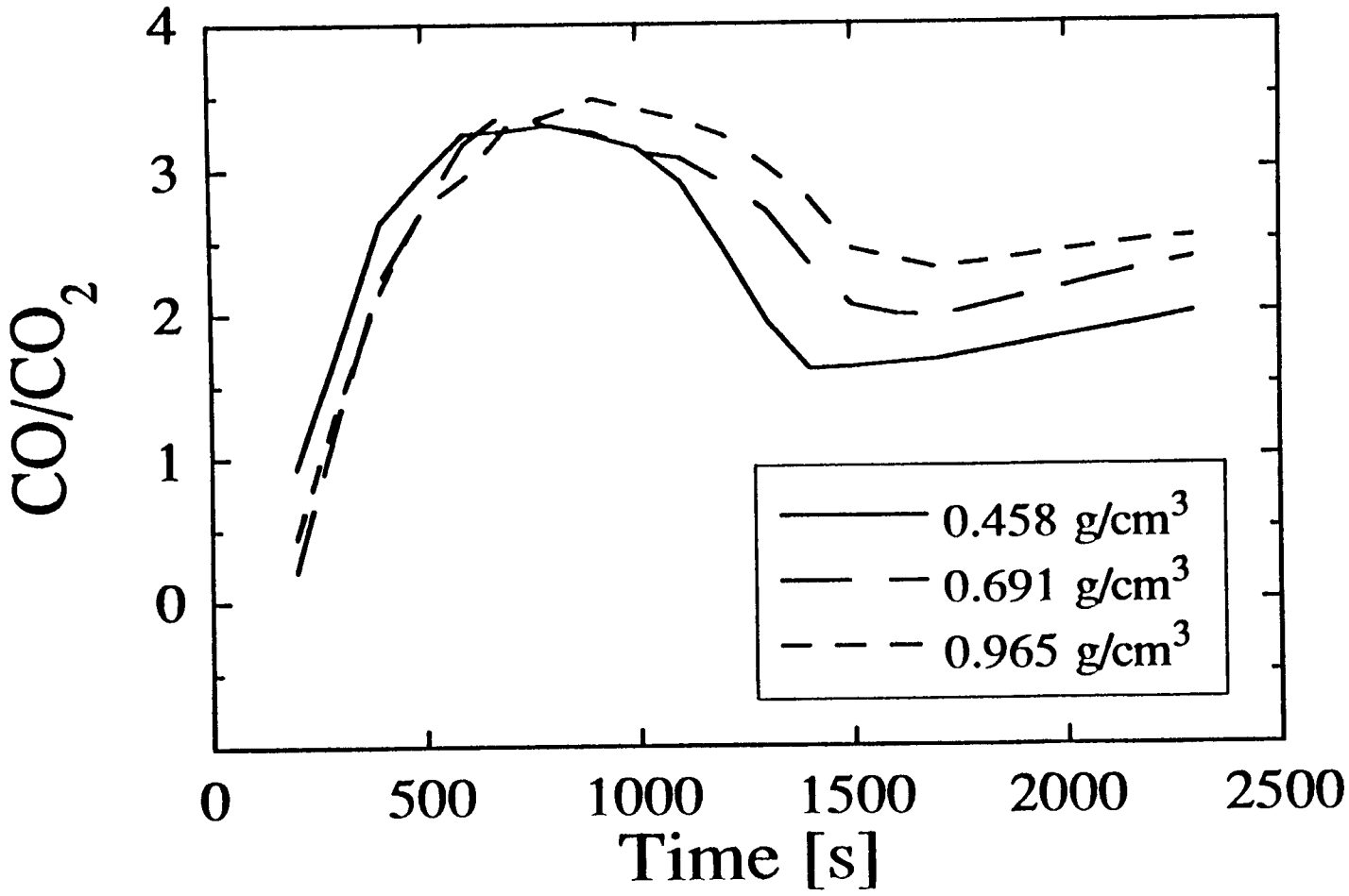

Figure 5.26d: Comparison of results for carbon monoxide to carbon dioxide molar ratio for different density samples. Data are those shown in Figures 5.26a, 5.26b and 5.26c, with data points omitted for clarity

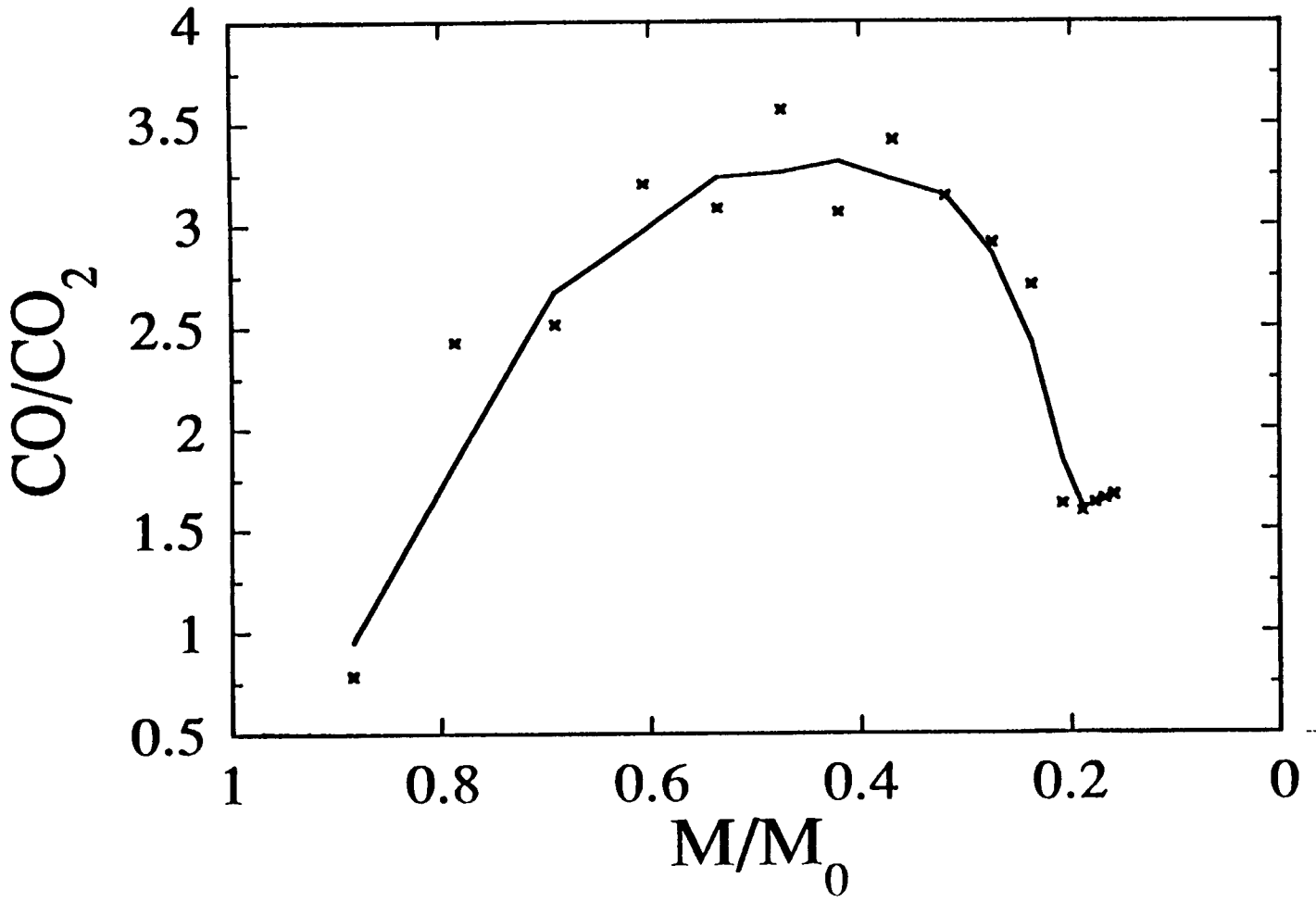

Figure 5.26e: Carbon monoxide to carbon dioxide molar ratio from low density (0.458 g/cm^3) samples of cellulose, subject to a nominal heat flux of 60 kW/m^2. These are the data of Figure 5.26a, replotted against remaining sample mass

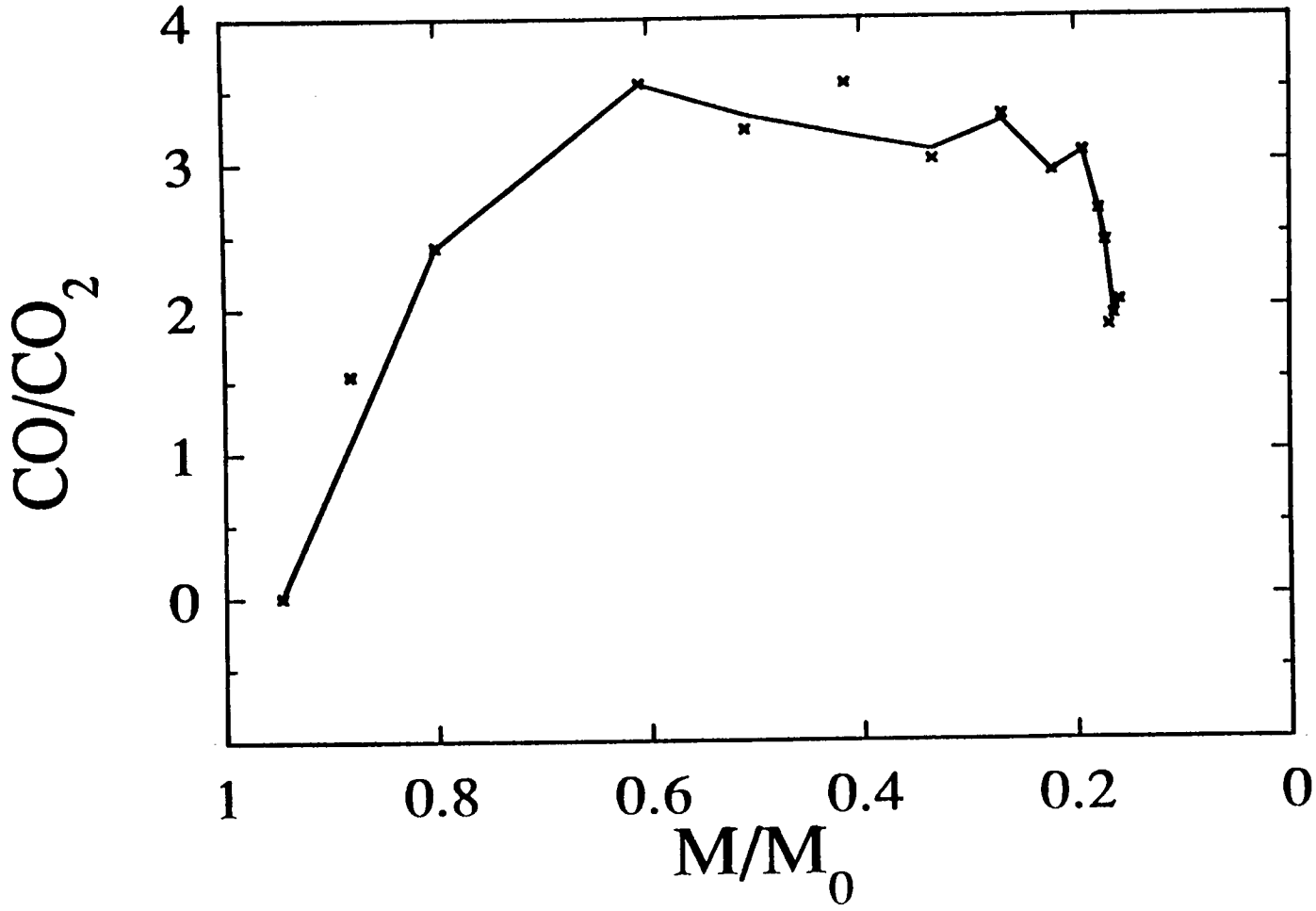

Figure 5.26f: Carbon monoxide to carbon dioxide molar ratio from middle density (0.691 g/cm^3) samples of cellulose, subject to a nominal heat flux of 60 kW/m^2. These are the data of Figure 5.26b, replotted against remaining sample mass

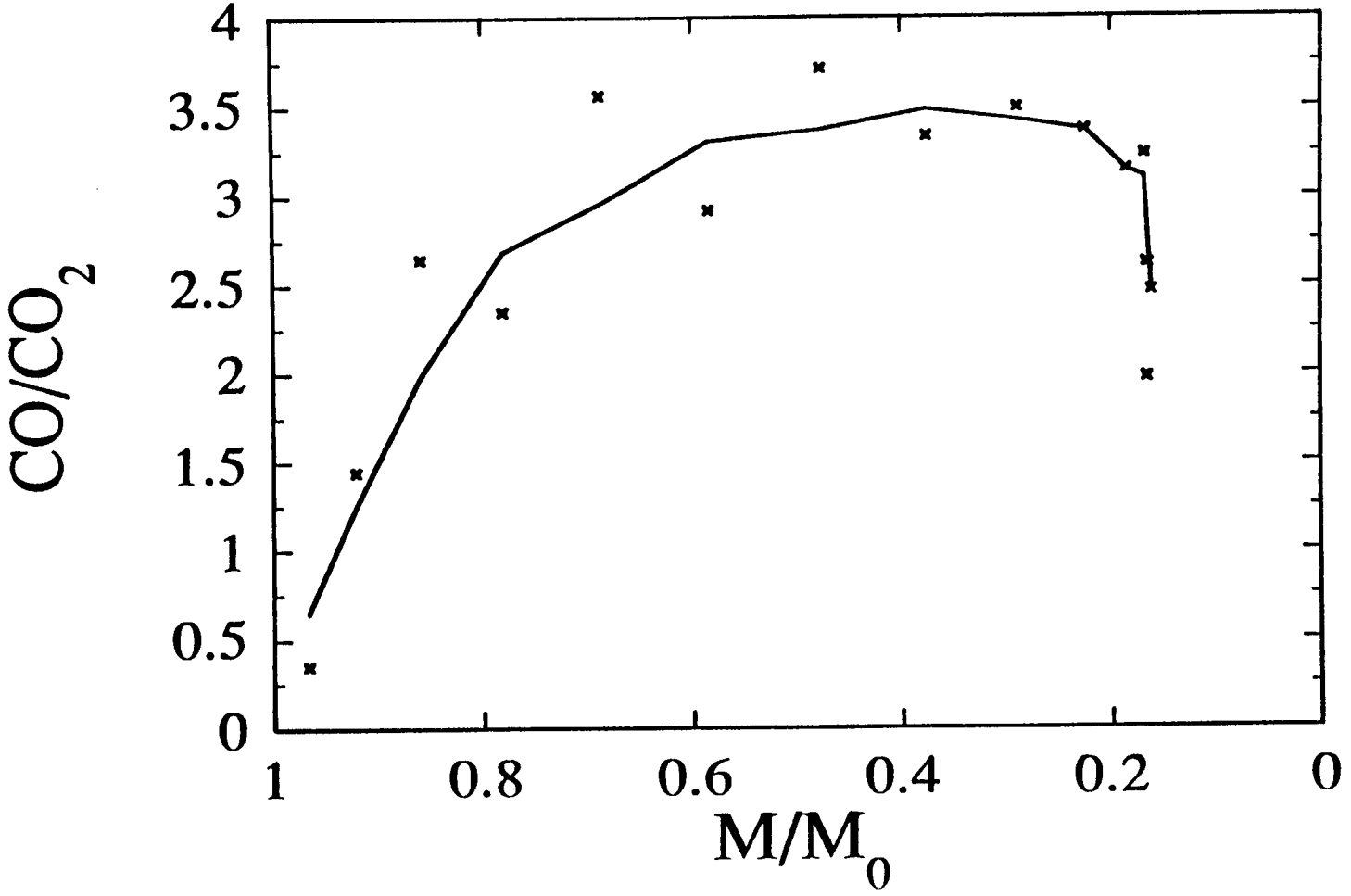

Figure 5.26g:Carbon monoxide to carbon dioxide molar ratio from high density (0.965 g/cm^3) samples of cellulose, subject to a nominal heat flux of 60 kW/m^2. These are the data of Figure 5.26c, replotted against remaining sample mass

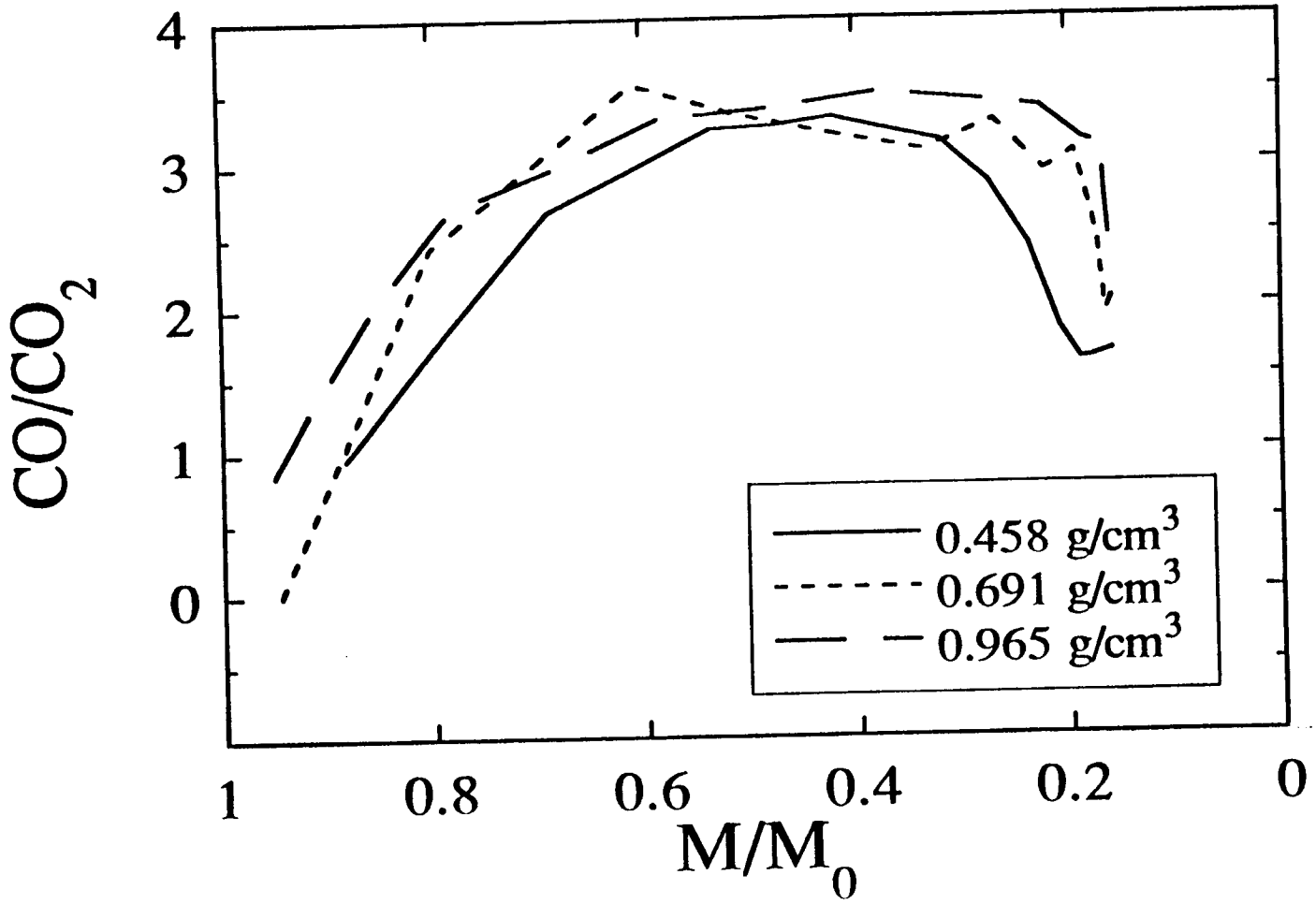

Figure 5.26h: Comparison of results for carbon monoxide to carbon dioxide molar ratio for different density samples. Data are those shown in Figures 5.26e, 5.26f and 5.26g, with data points omitted for clarity. These are the data of Figure 5.26d, replotted against remaining sample mass

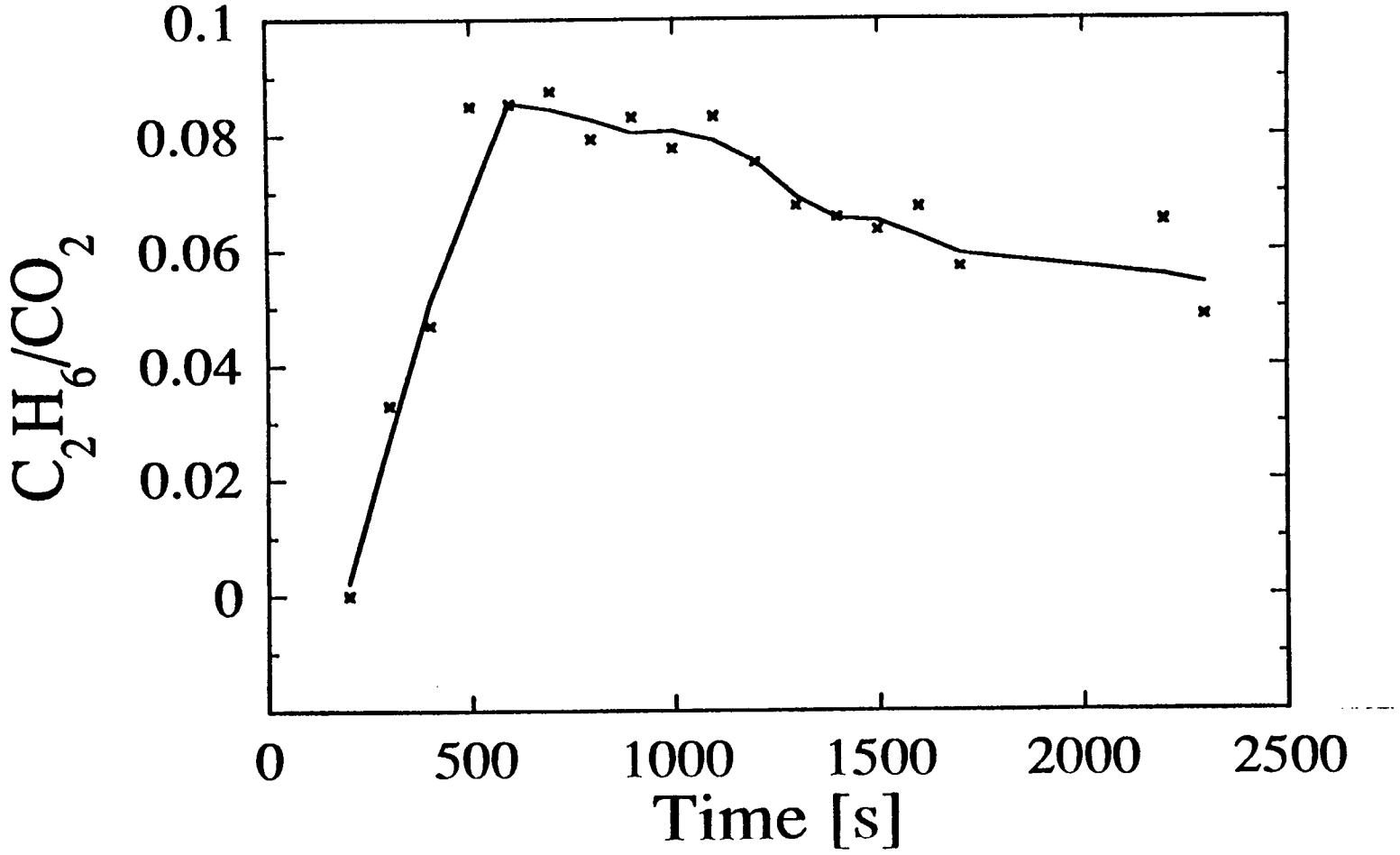

Figure 5.27a: Ethane to carbon dioxide molar ratio from low density (0.458 g/cm^3) samples of cellulose, subject to a nominal heat flux of 60 kW/m^2

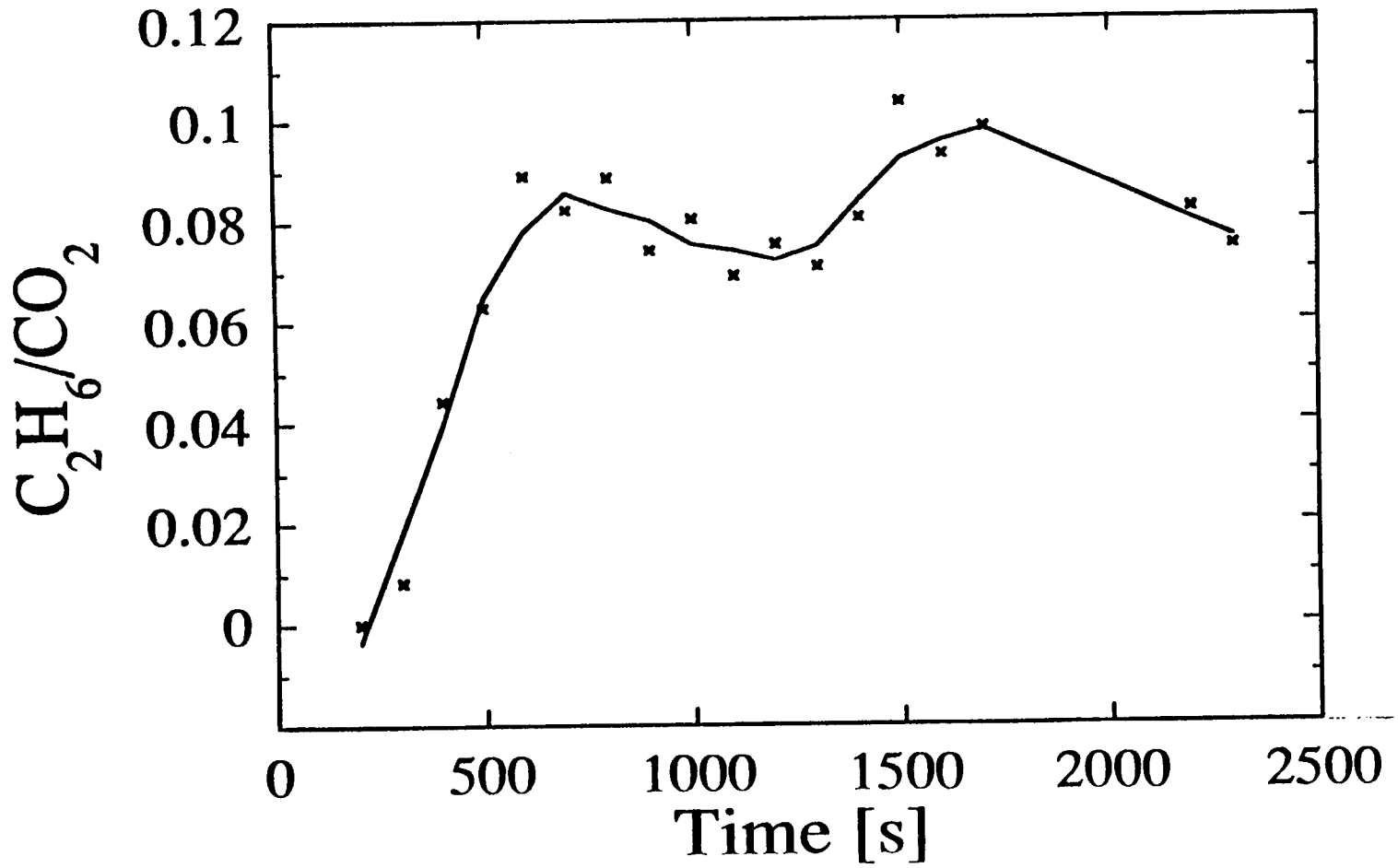

Figure 5.27b: Ethane to carbon dioxide molar ratio from middle density (0.691 g/cm^3) samples of cellulose, subject to a nominal heat flux of 60 kW/m^2

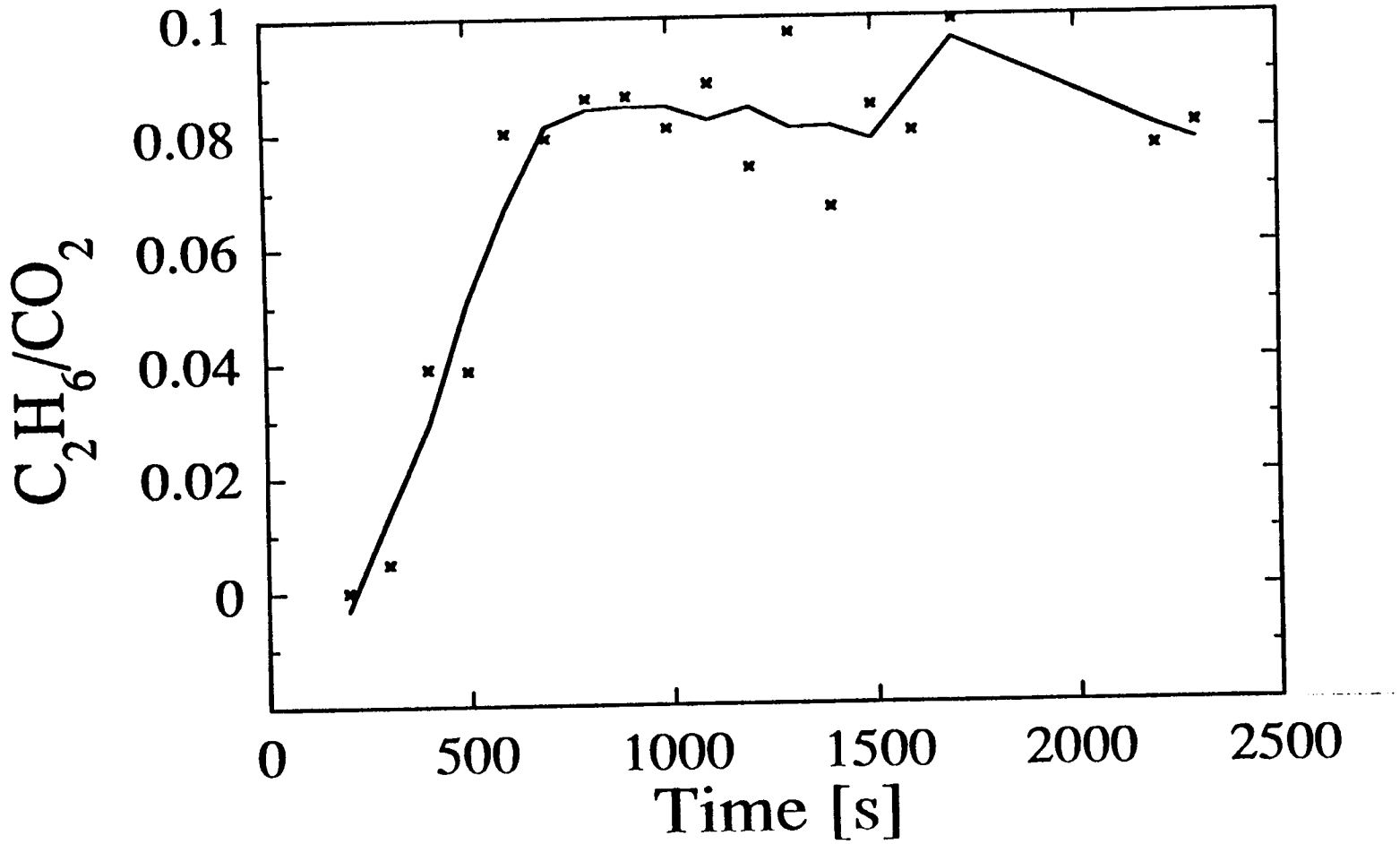

Figure 5.27c: Ethane to carbon dioxide molar ratio from high density (0.965 g/cm^3) samples of cellulose, subject to a nominal heat flux of 60 kW/m^2

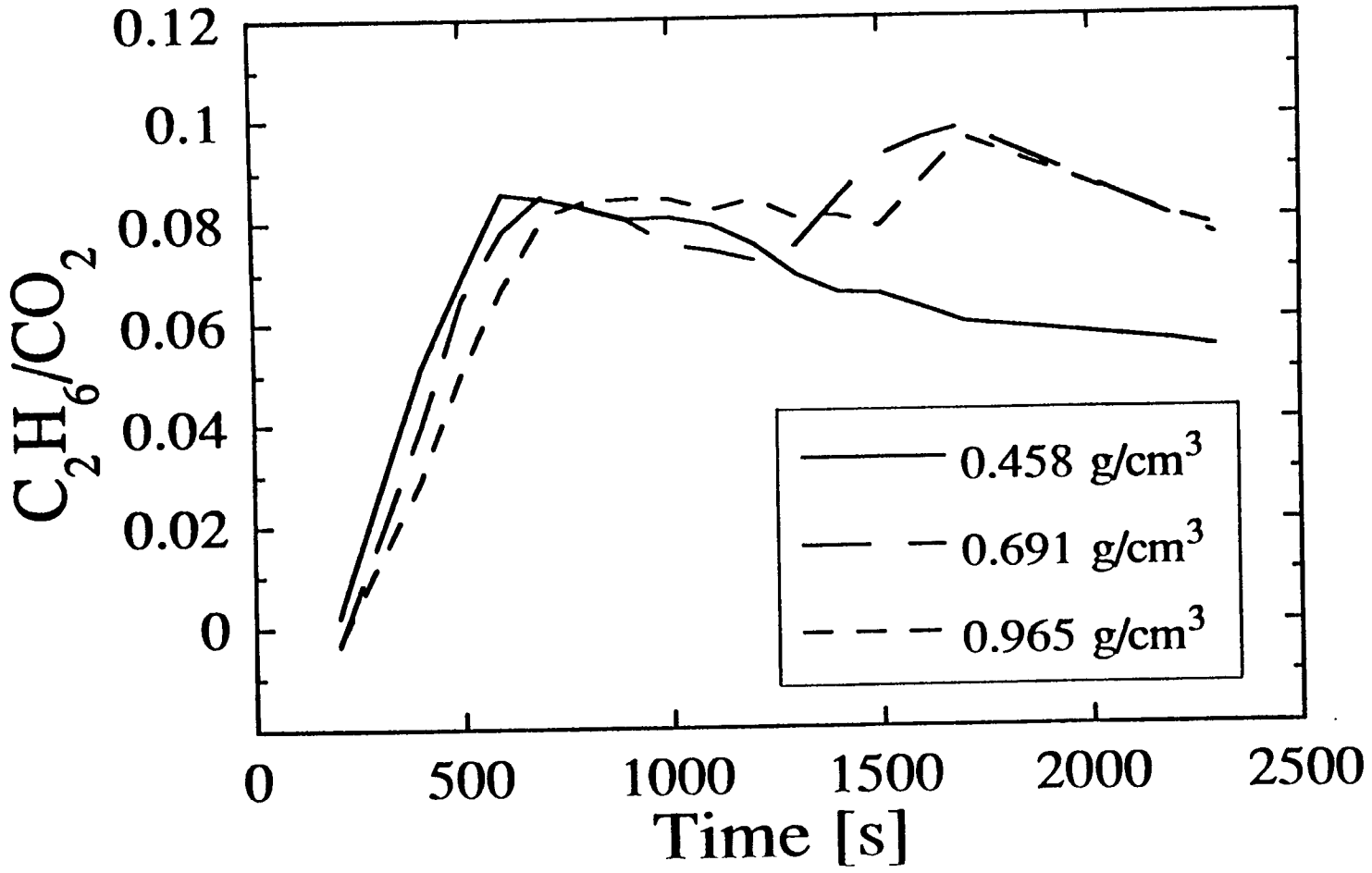

Figure 5.27d: Comparison of results for ethane to carbon dioxide molar ratio for different density samples. Data are those shown in Figures 5.27a, 5.27b and 5.27c, with data points omitted for clarity

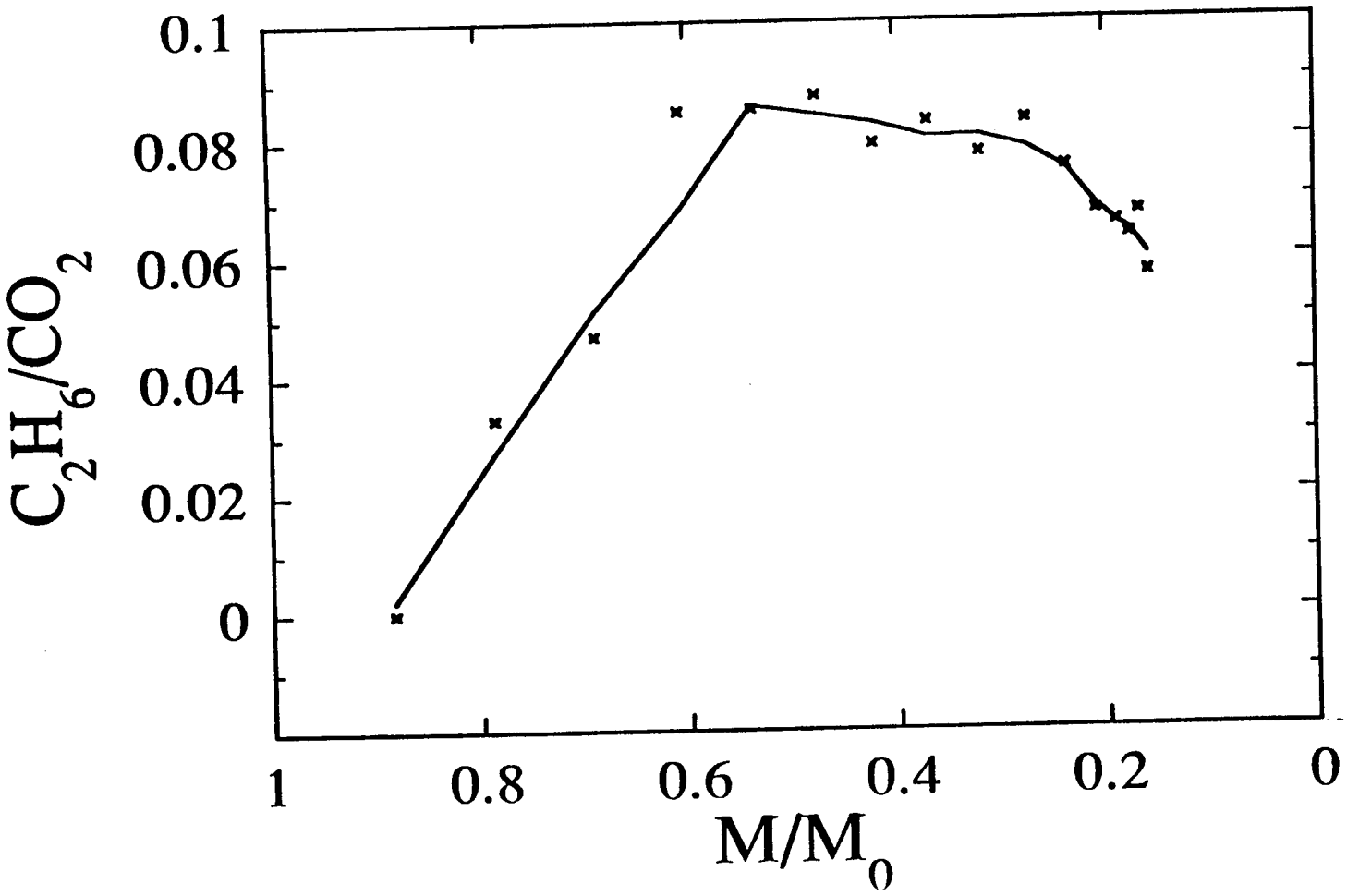

Figure 5.27e: Ethane to carbon dioxide molar ratio from low density (0.458 g/cm^3) samples of cellulose, subject to a nominal heat flux of 60 kW/m^2. These are the data of Figure 5.27a, replotted against remaining sample mass

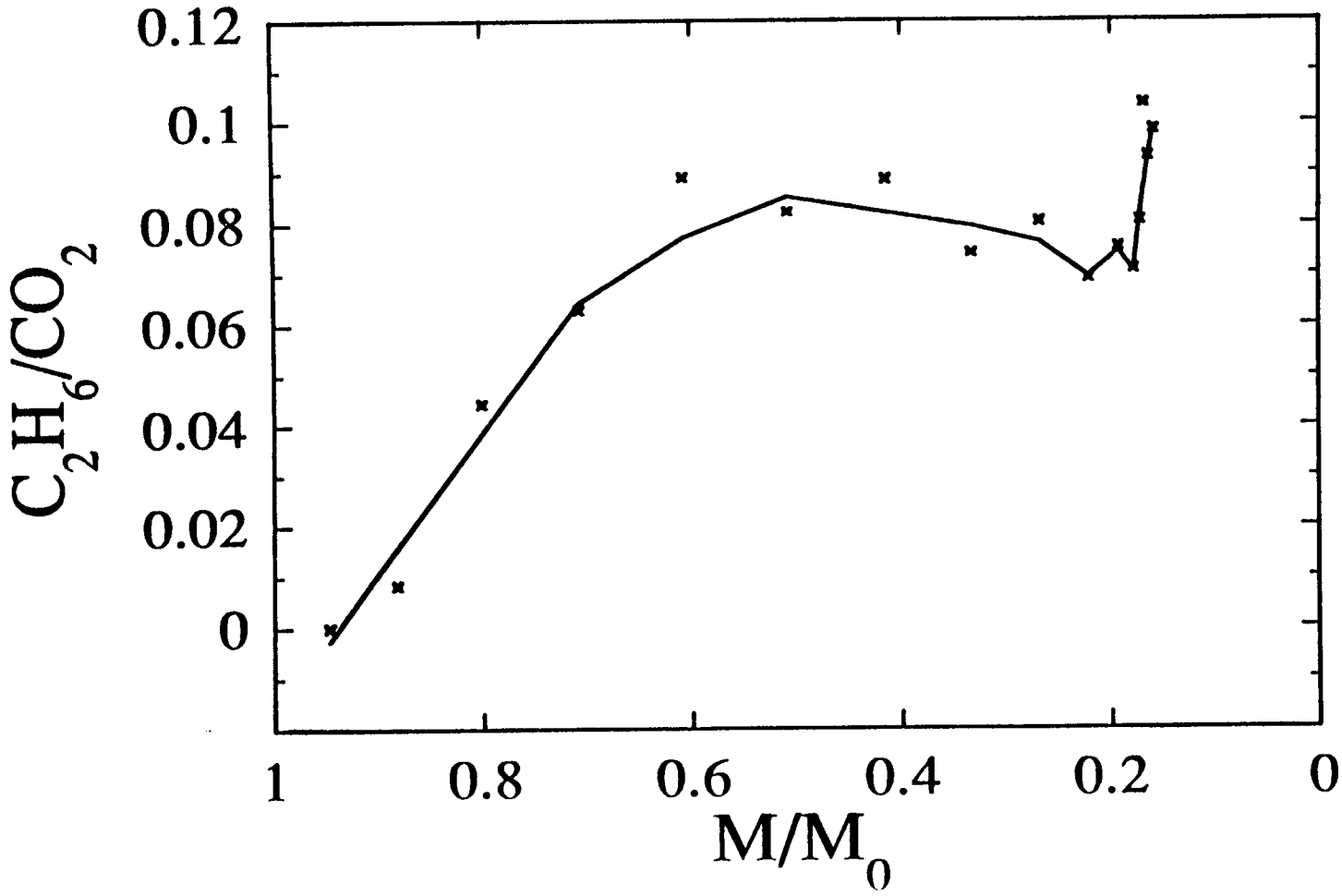

Figure 5.27f: Ethane to carbon dioxide molar ratio from middle density (0.691 g/cm^3) samples of cellulose, subject to a nominal heat flux of 60 kW/m^2. These are the data of Figure 5.27b, replotted against remaining sample mass

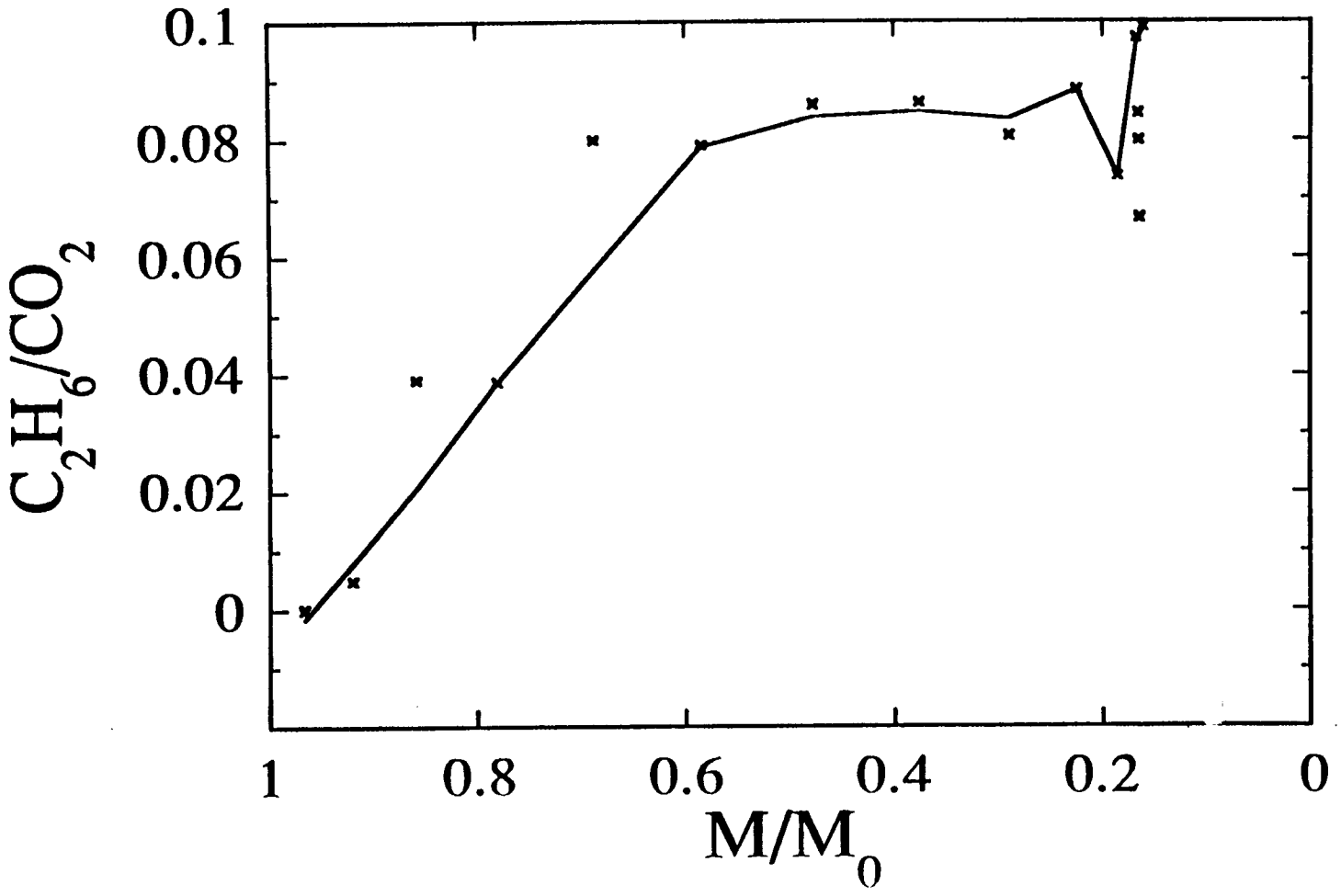

Figure 5.27g: Ethane to carbon dioxide molar ratio from high density (0.965 g/cm^3) samples of cellulose, subject to a nominal heat flux of 60 kW/m^2. These are the data of Figure 5.27c, replotted against remaining sample mass

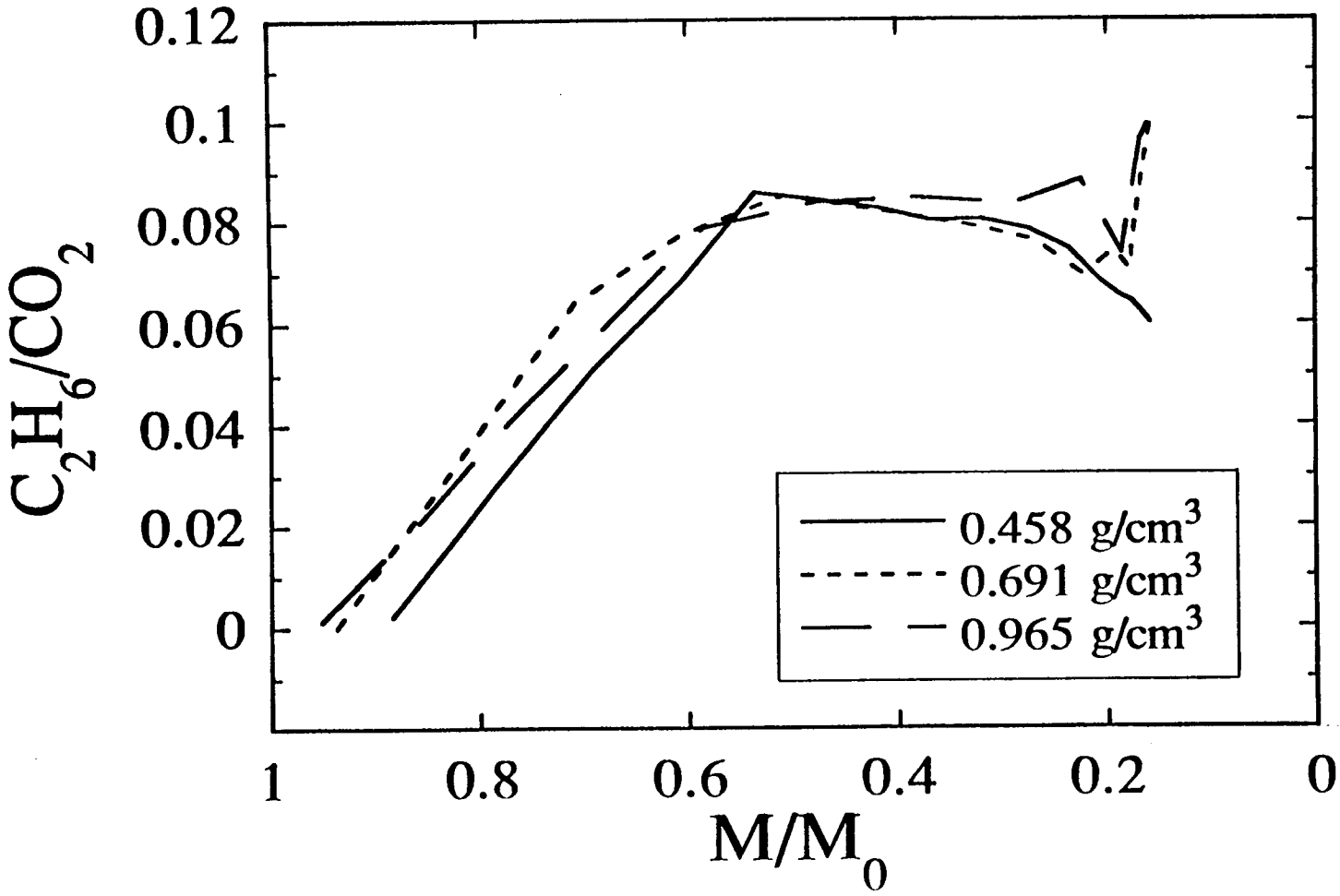

Figure 5.27h: Comparison of results for Ethane to carbon dioxide molar ratio for different density samples. Data are those shown in Figures 5.27e, 5.27f and 5.27g, with data points omitted for clarity. These are the data of Figure 5.27d, replotted against remaining sample mass

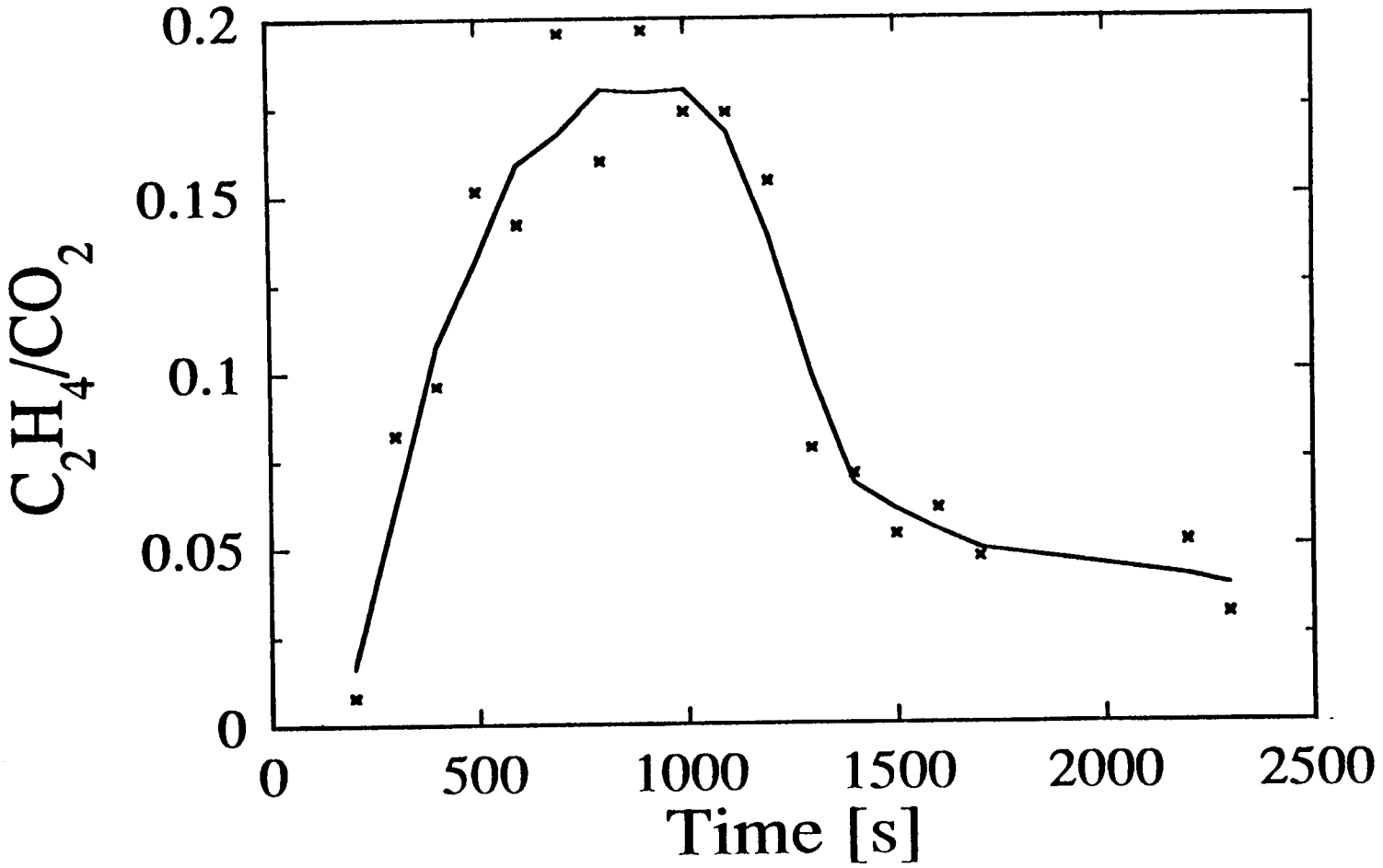

Figure 5.28a: Ethylene to carbon dioxide molar ratio from low density (0.458 g/cm^3) samples of cellulose, subject to a nominal heat flux of 60 kW/m^2

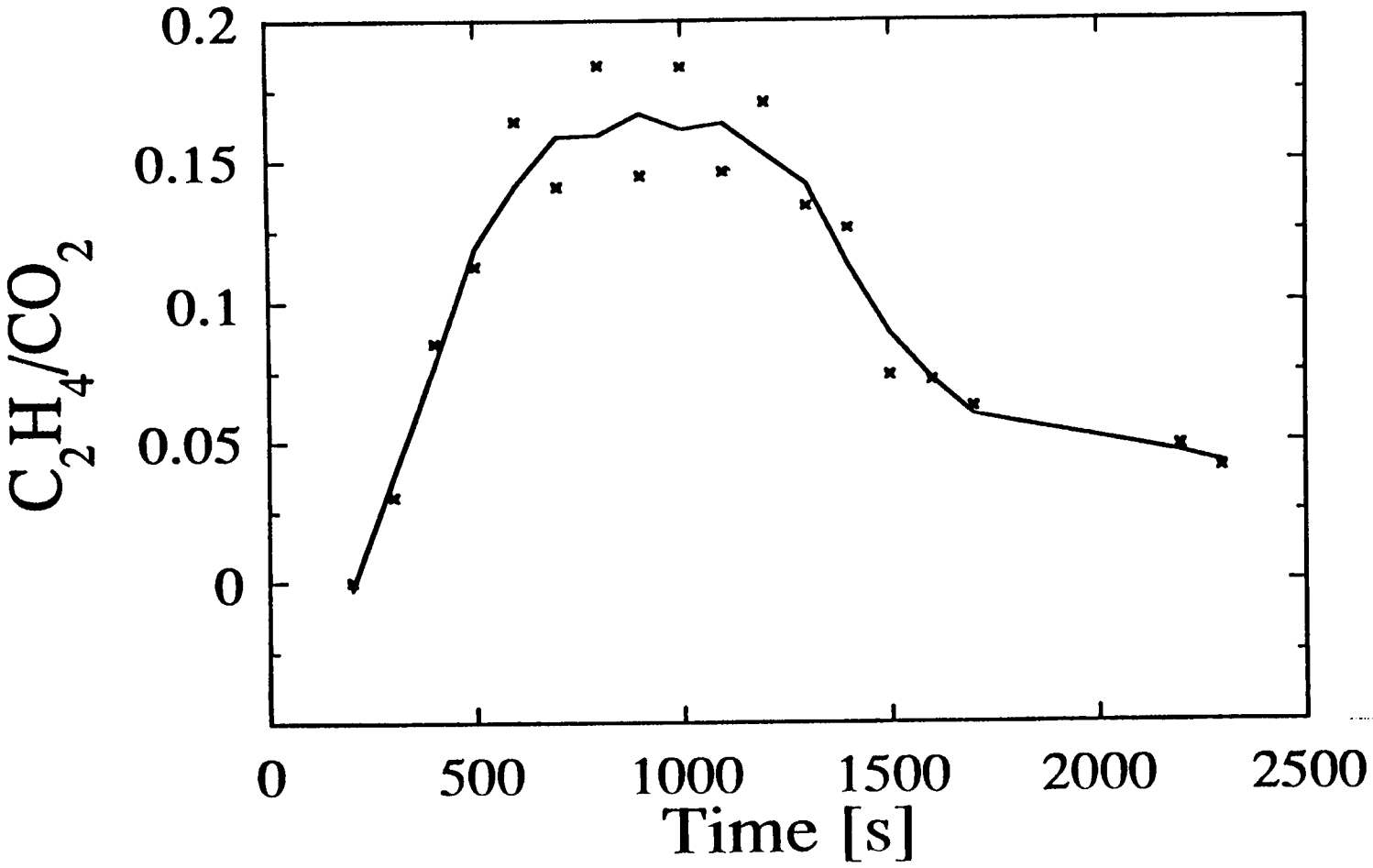

Figure 5.28b: Ethylene to carbon dioxide molar ratio from middle density (0.691 g/cm^3) samples of cellulose, subject to a nominal heat flux of 60 kW/m^2

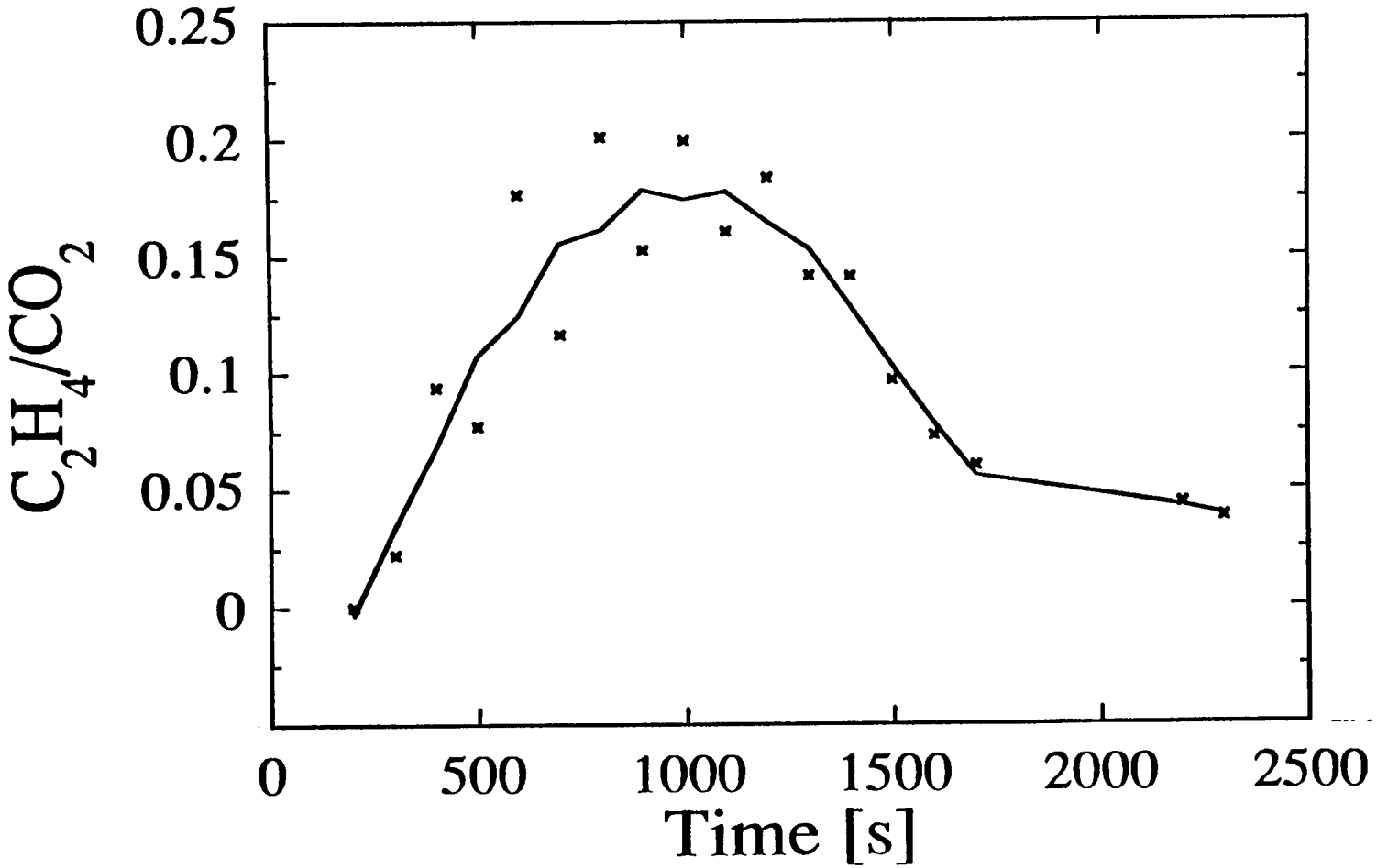

Figure 5.28c: Ethylene to carbon dioxide molar ratio from high density (0.965 g/cm^3) samples of cellulose, subject to a nominal heat flux of 60 kW/m^2

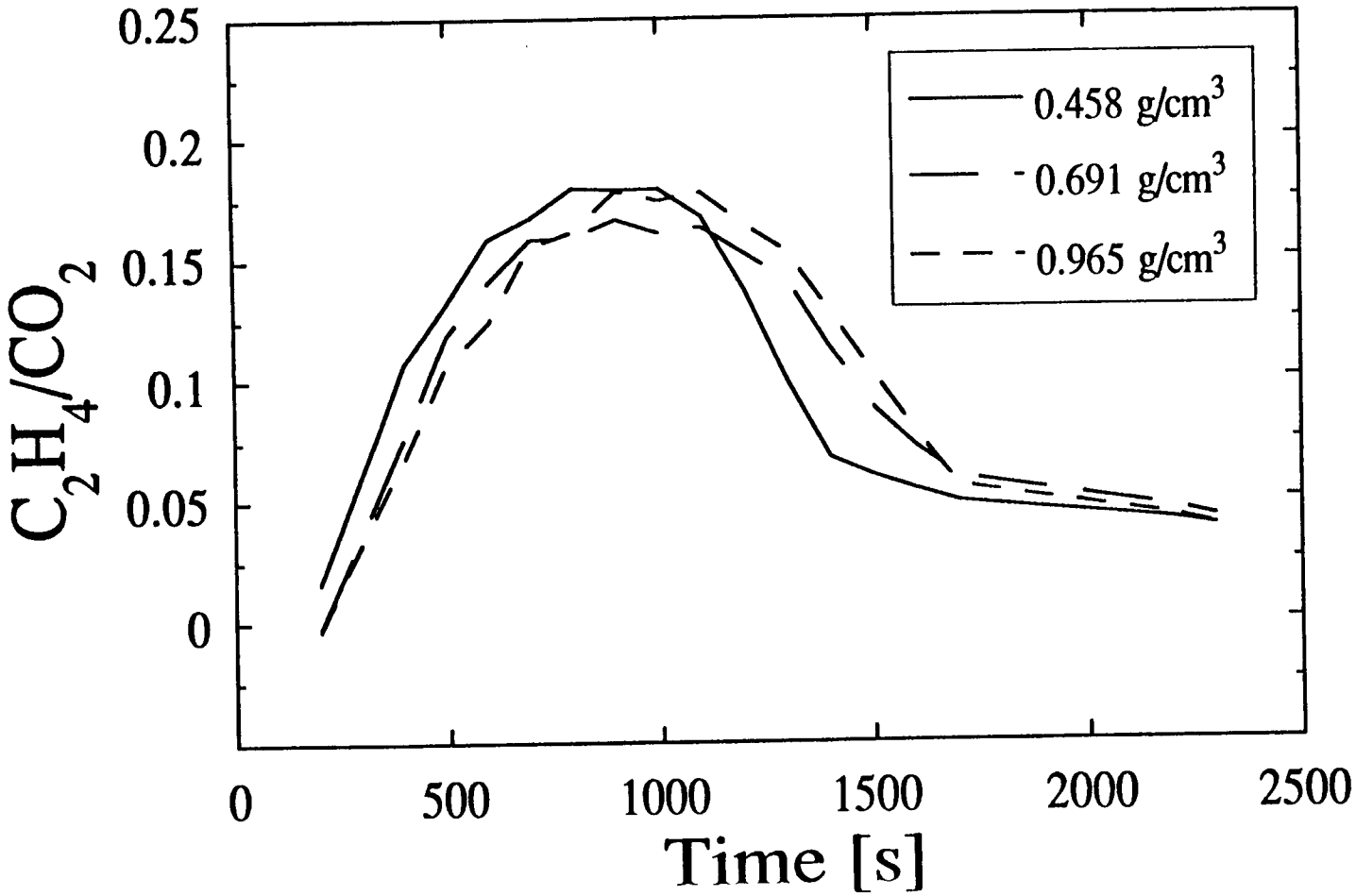

Figure 5.28d: Comparison of results for ethylene to carbon dioxide molar ratio for different density samples. Data are those shown in Figures 5.28a, 5.28b and 5.28c, with data points omitted for clarity

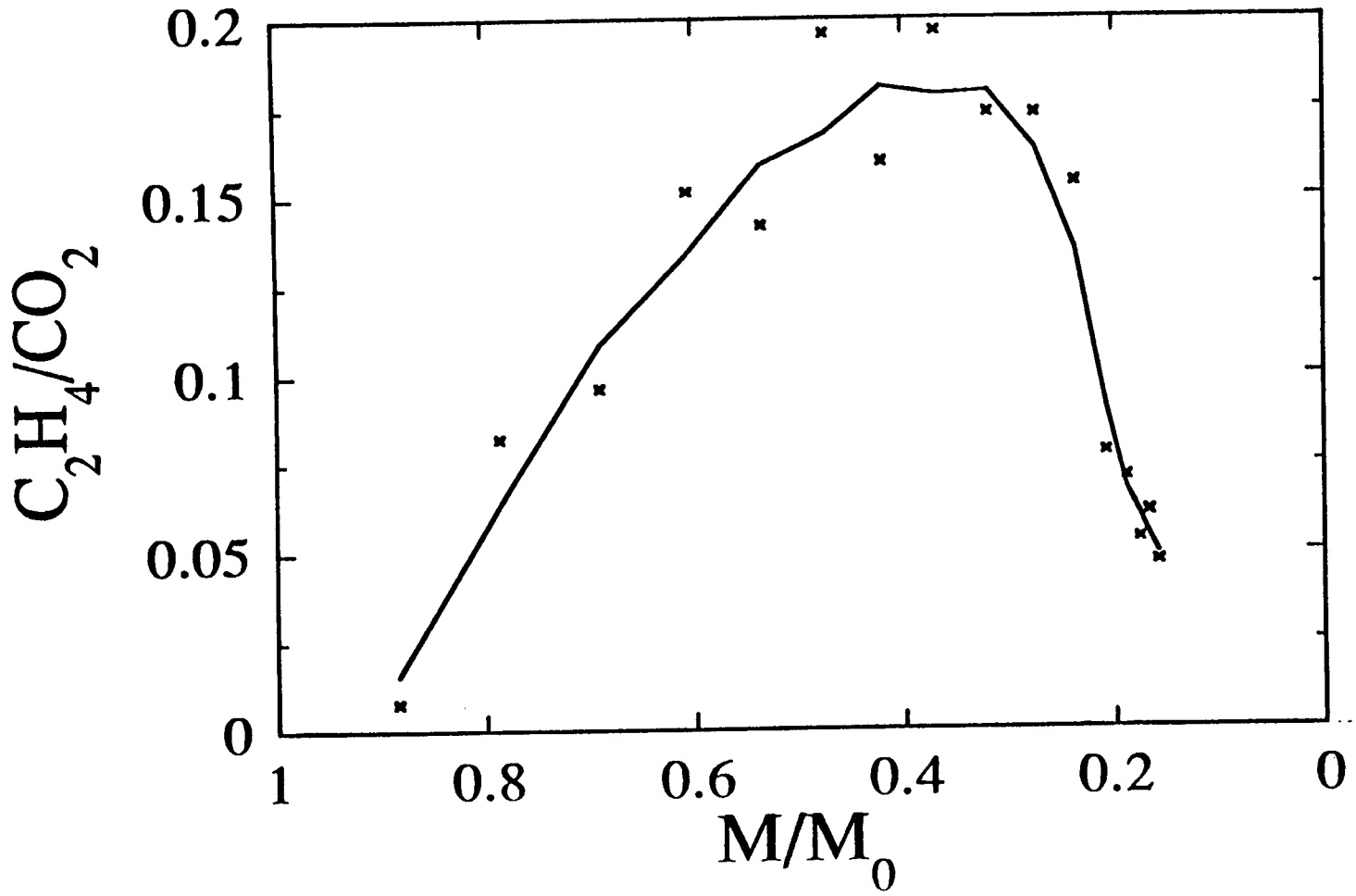

Figure 5.28e: Ethylene to carbon dioxide molar ratio from low density (0.458 g/cm^3) samples of cellulose, subject to a nominal heat flux of 60 kW/m^2. These are the data of Figure 5.28a, replotted against remaining sample mass

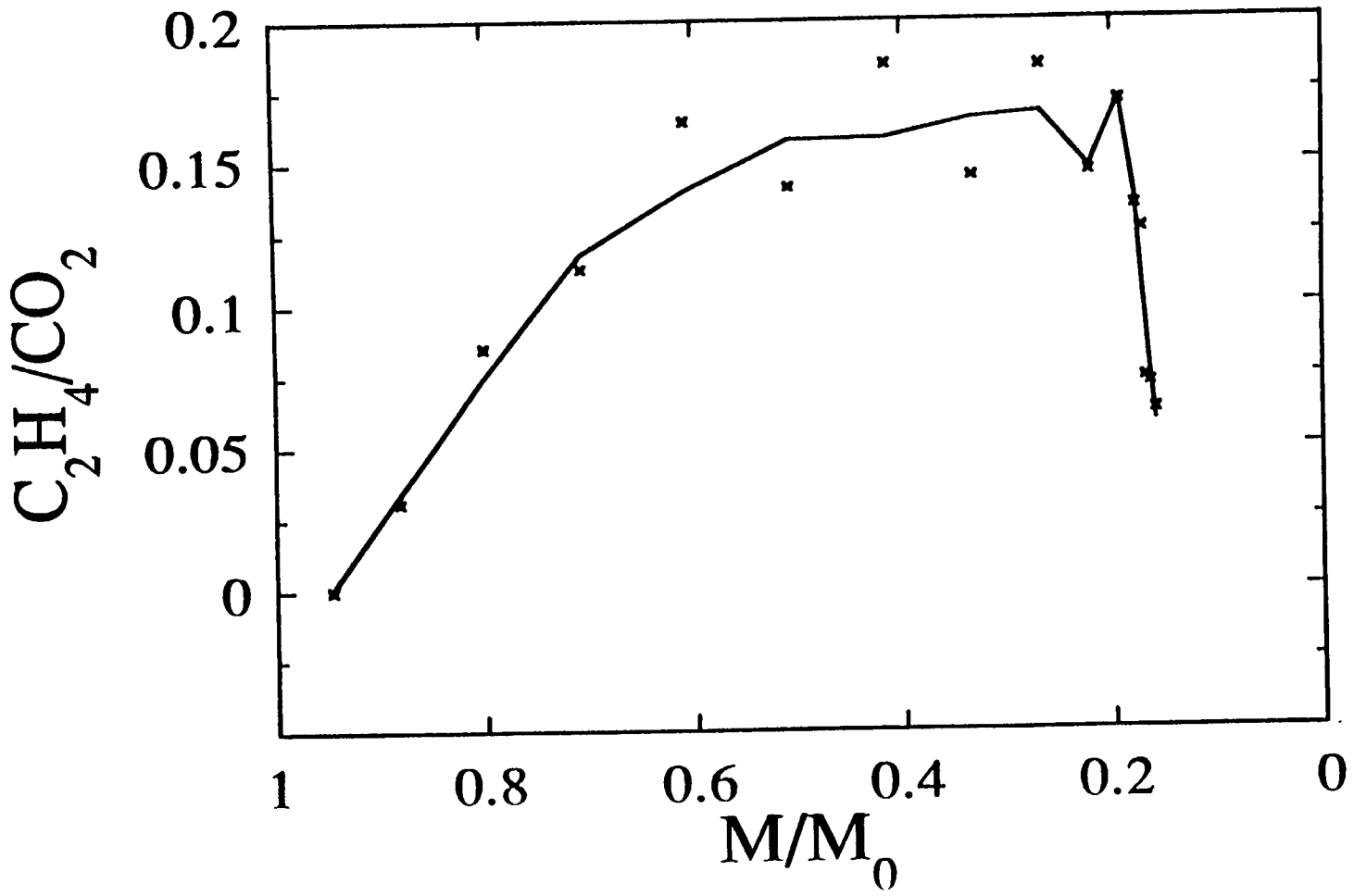

Figure 5.28f: Ethylene to carbon dioxide molar ratio from middle density (0.691 g/cm^3) samples of cellulose, subject to a nominal heat flux of 60 kW/m^2. These are the data of Figure 5.28b, replotted against remaining sample mass

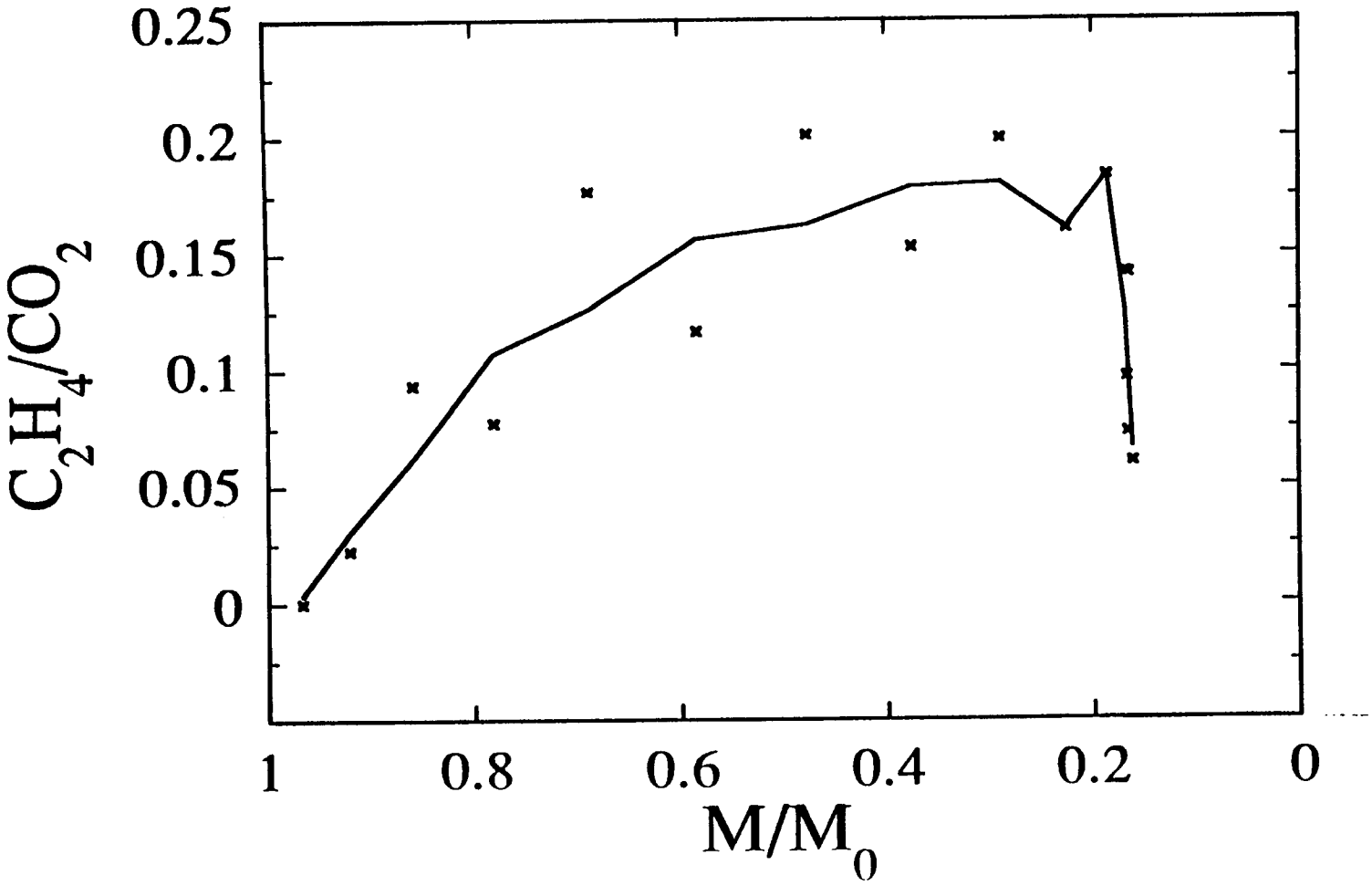

Figure 5.28g: Ethylene to carbon dioxide molar ratio from high density (0.965 g/cm^3) samples of cellulose, subject to a nominal heat flux of 60 kW/m^2. These are the data of Figure 5.28c, replotted against remaining sample mass

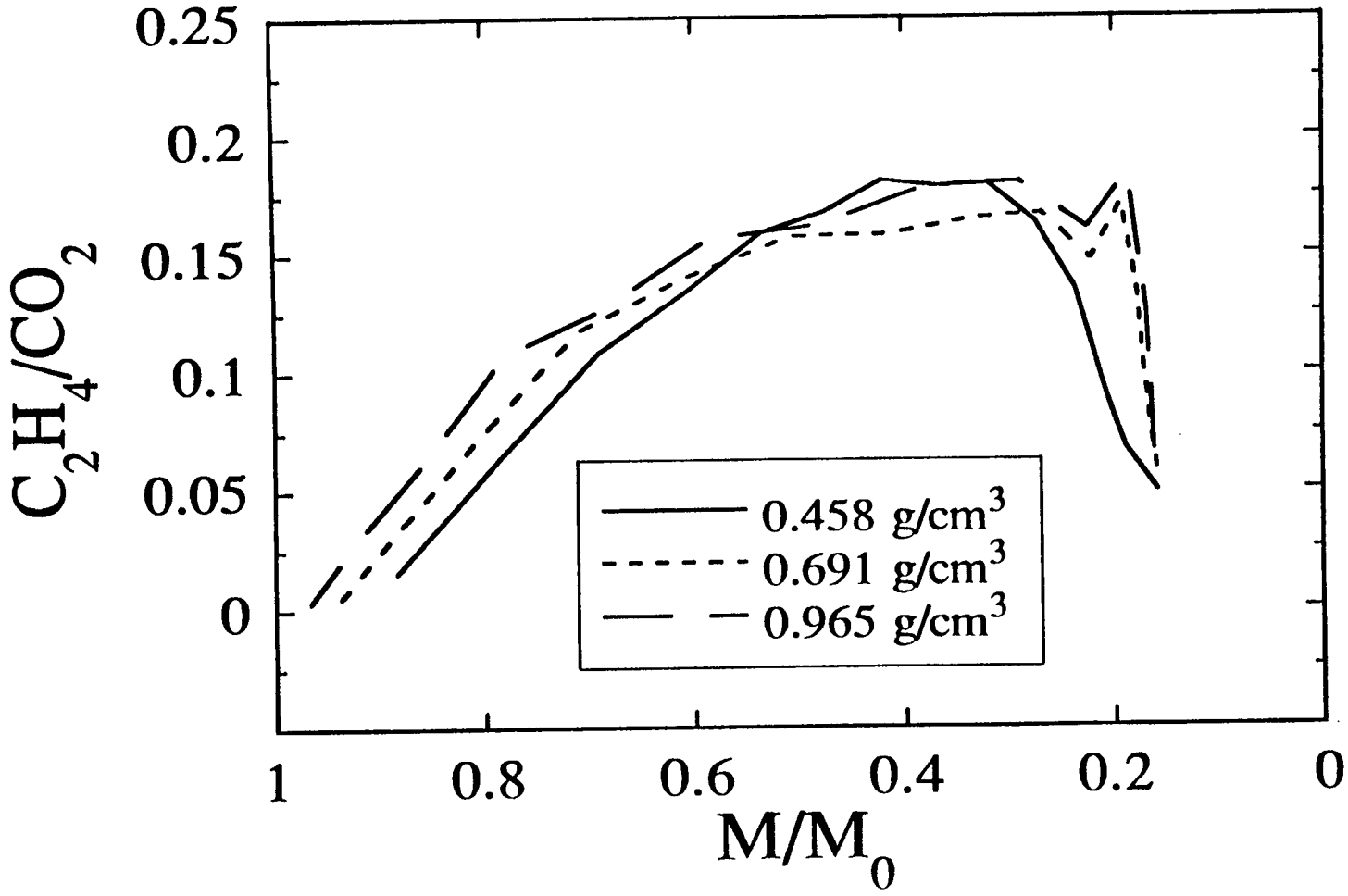

Figure 5.28h: Comparison of results for ethylene to carbon dioxide molar ratio for different density samples. Data are those shown in Figures 5.28e, 5.28f and 5.28g, with data points omitted for clarity. These are the data of Figure 5.28d, replotted against remaining sample mass

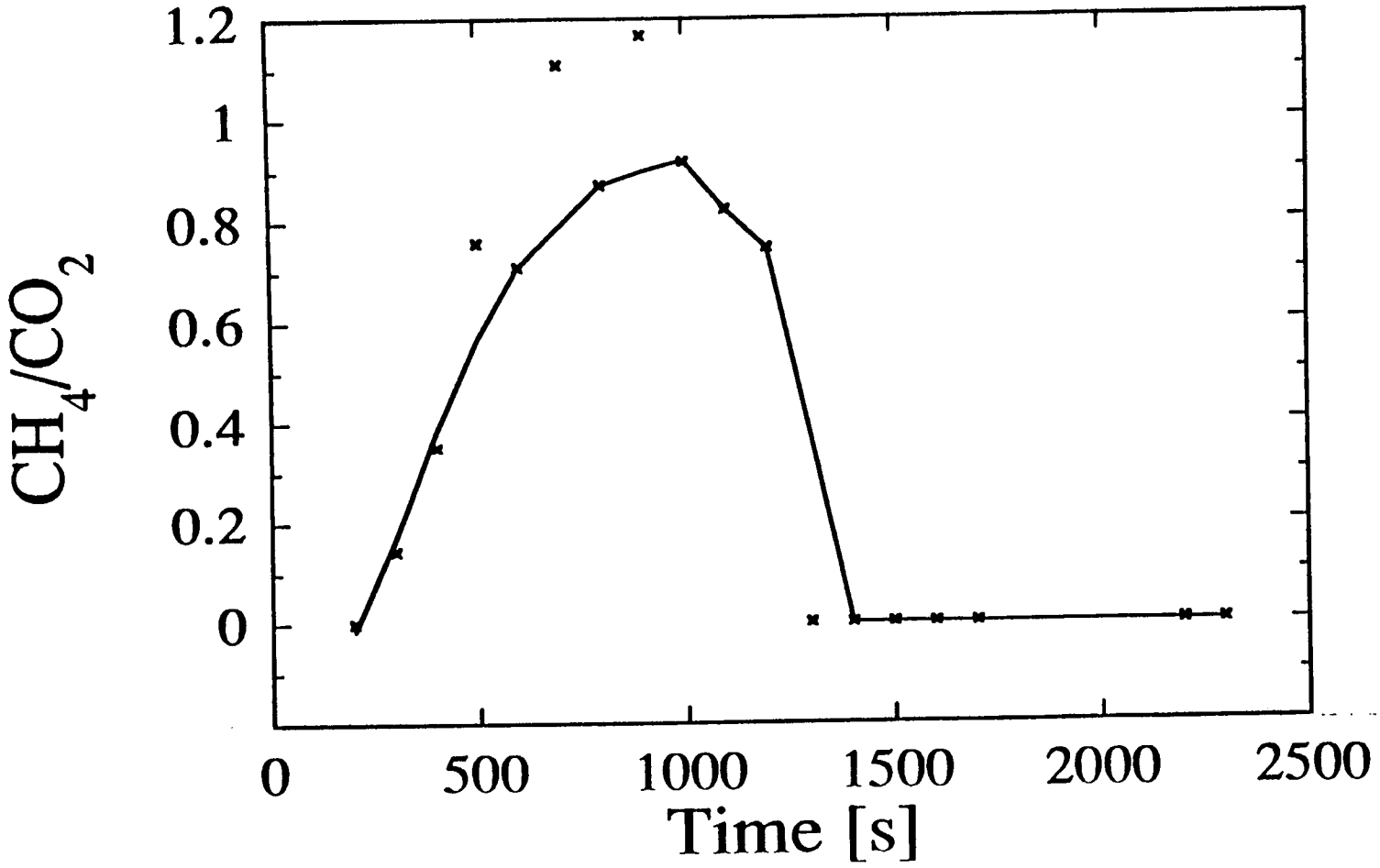

Figure 5.29a: Methane to carbon dioxide molar ratio from low density (0.458 g/cm^3) samples of cellulose, subject to a nominal heat flux of 60 kW/m^2

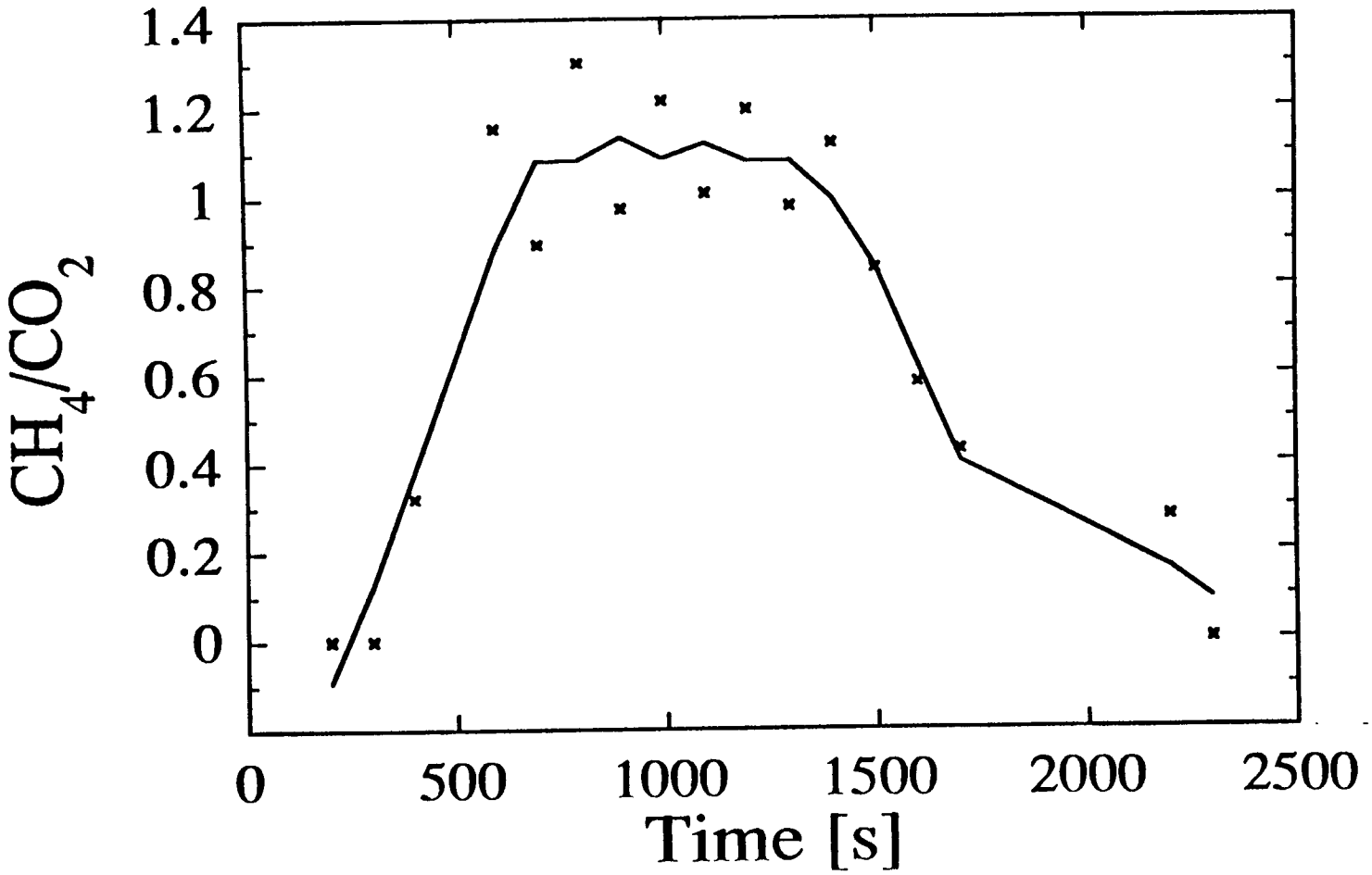

Figure 5.29b: Methane to carbon dioxide molar ratio from middle density (0.691 g/cm^3) samples of cellulose, subject to a nominal heat flux of 60 kW/m^2

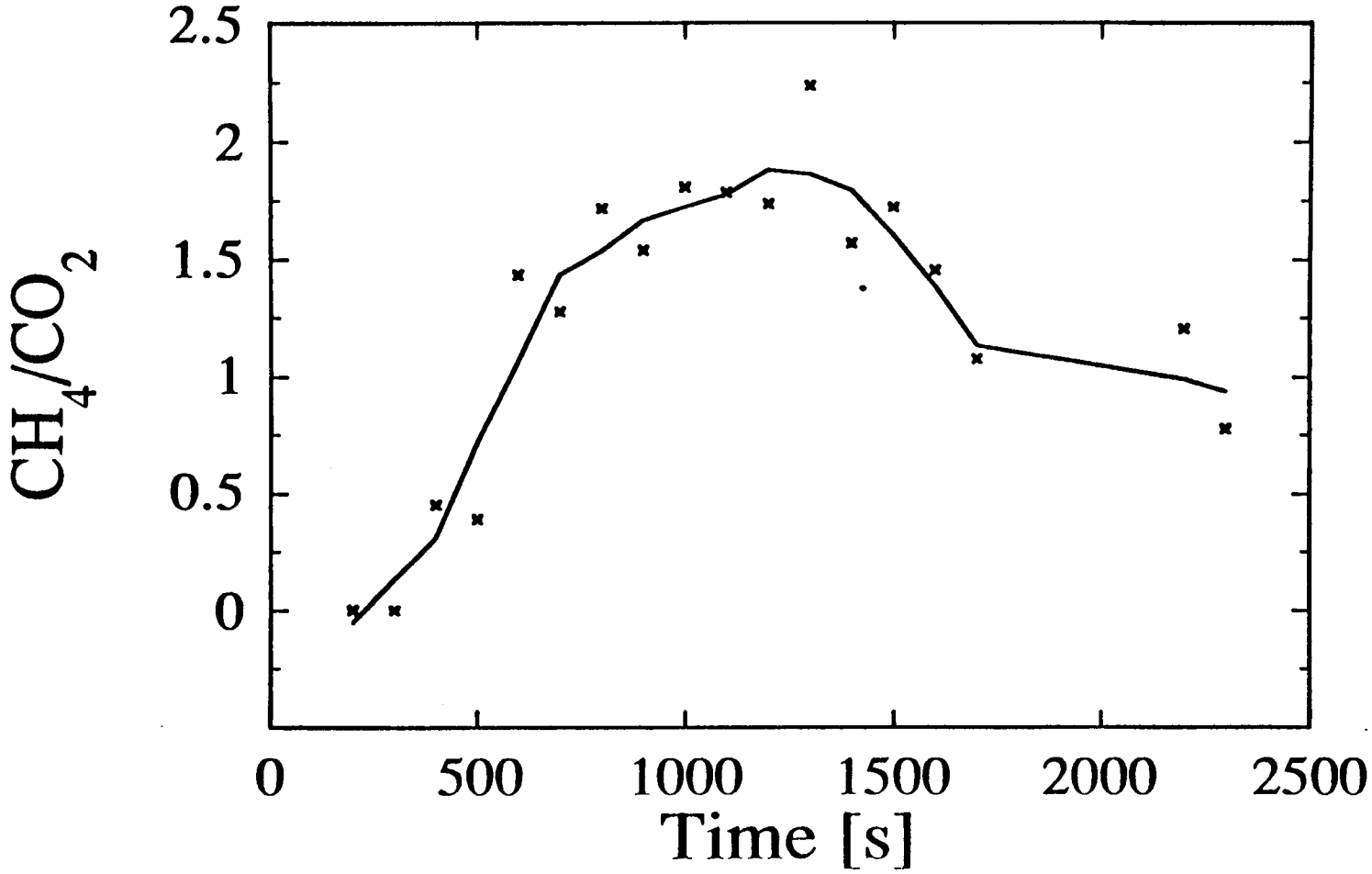

Figure 5.29c: Methane to carbon dioxide molar ratio from high density (0.965 g/cm^3) samples of cellulose, subject to a nominal heat flux of 60 kW/m^2

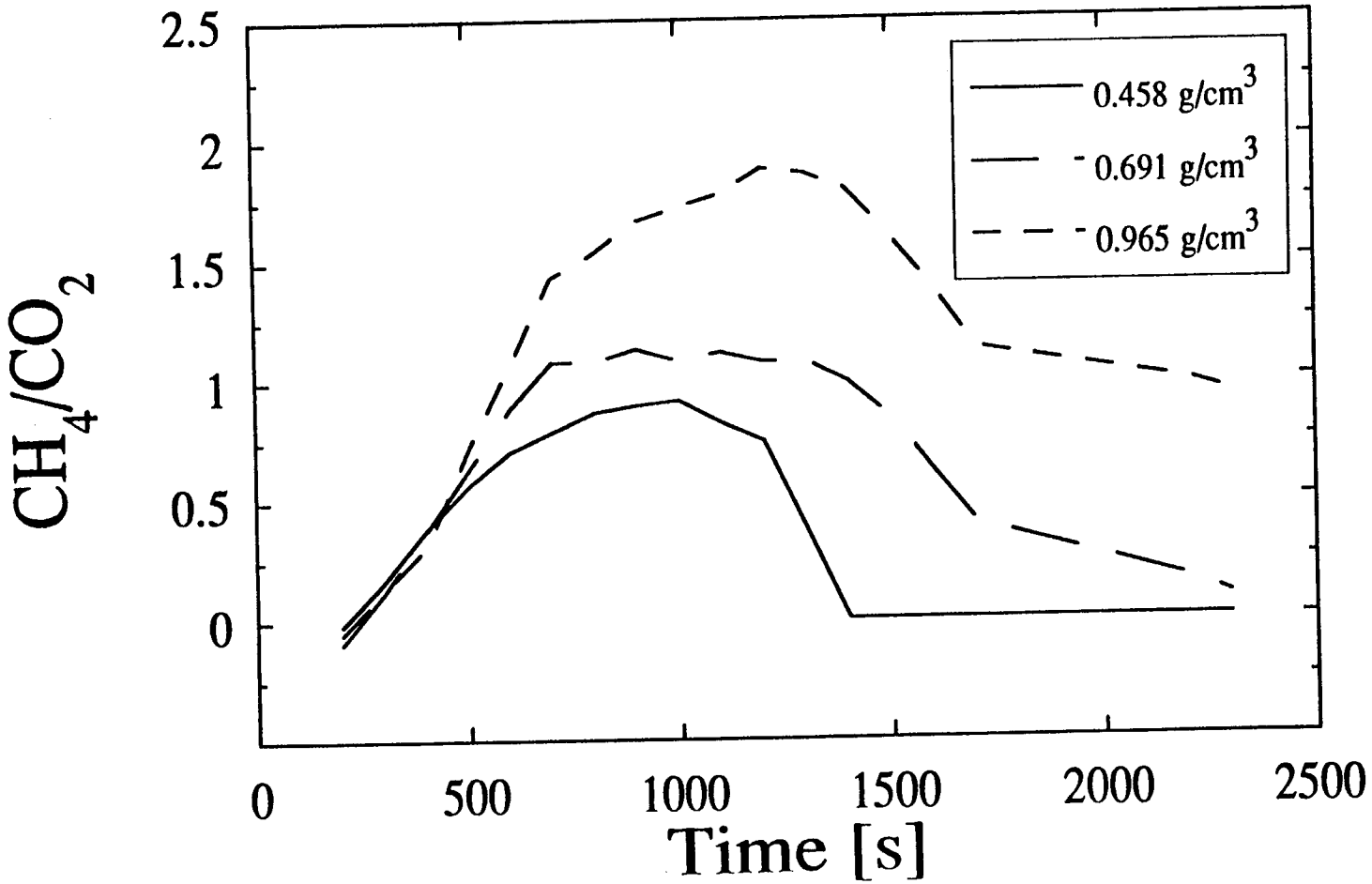

Figure 5.29d: Comparison of results for methane to carbon dioxide molar ratio for different density samples. Data are those shown in Figures 5.29a, 5.29b and 5.29c, with data points omitted for clarity

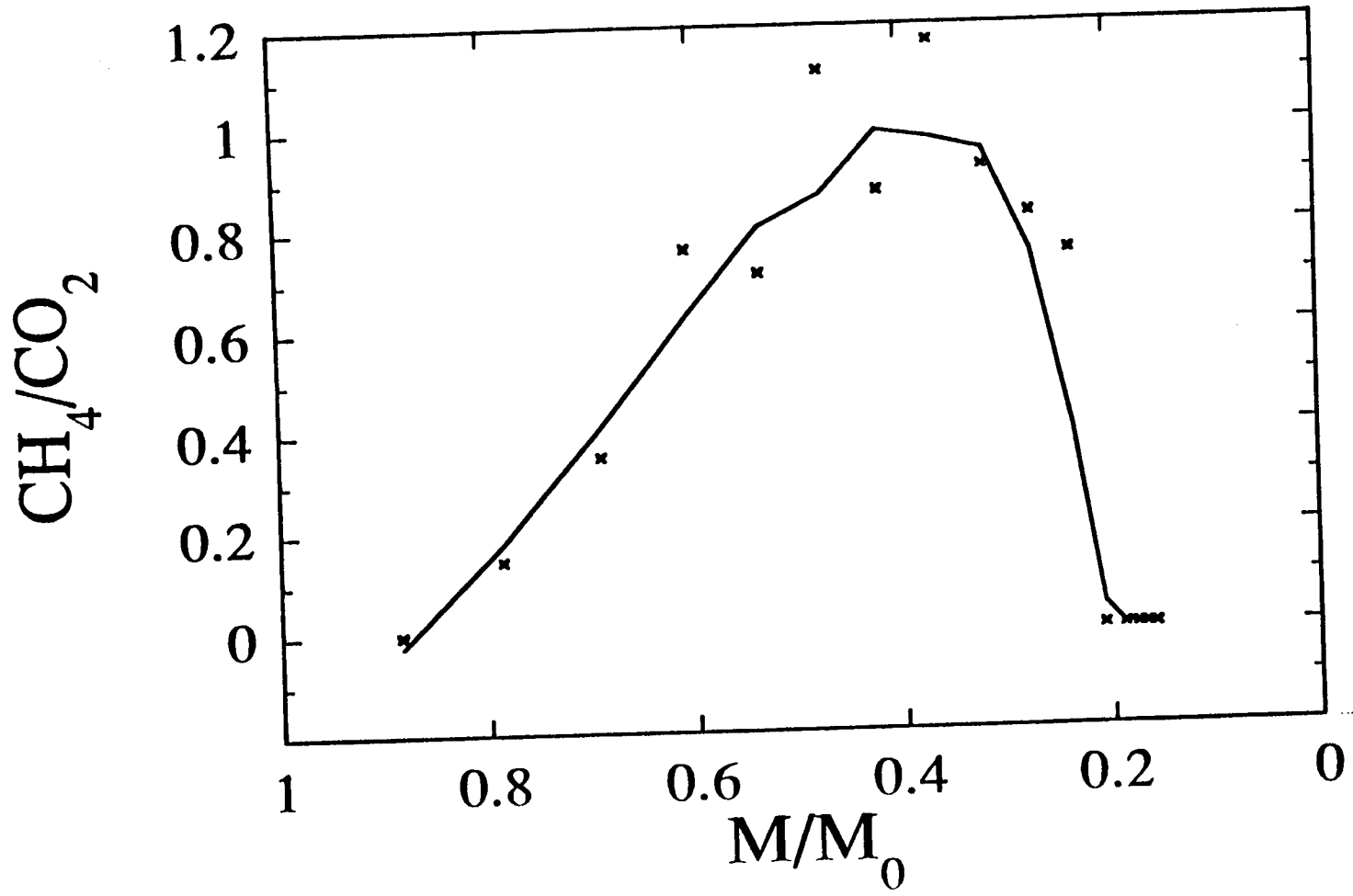

Figure 5.29e: Methane to carbon dioxide molar ratio from low density (0.458 g/cm^3) samples of cellulose, subject to a nominal heat flux of 60 kW/m^2. These are the data of Figure 5.29a, replotted against remaining sample mass

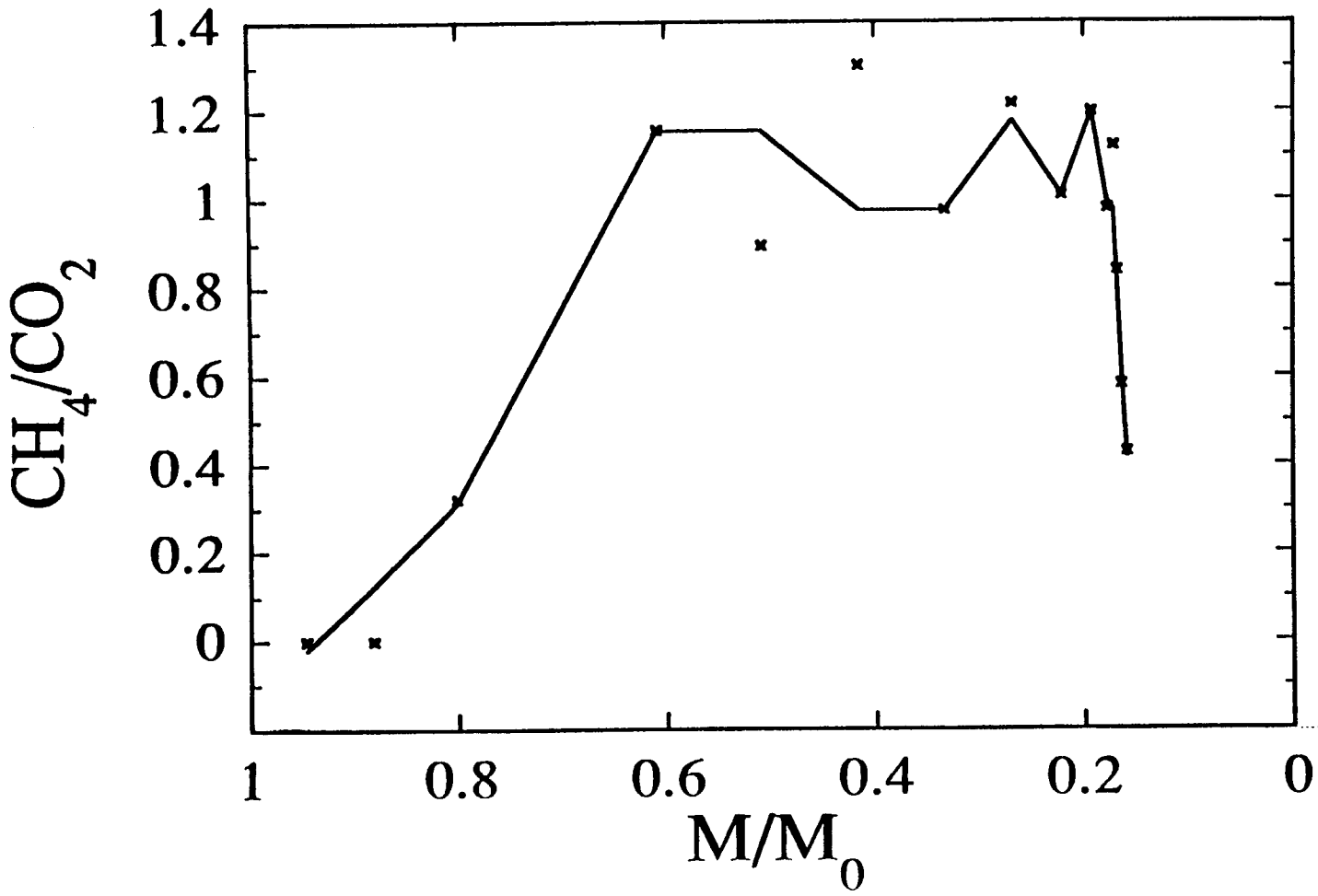

Figure 5.29f: Methane to carbon dioxide molar ratio from middle density (0.691 g/cm^3) samples of cellulose, subject to a nominal heat flux of 60 kW/m^2. These are the data of Figure 5.29b, replotted against remaining sample mass

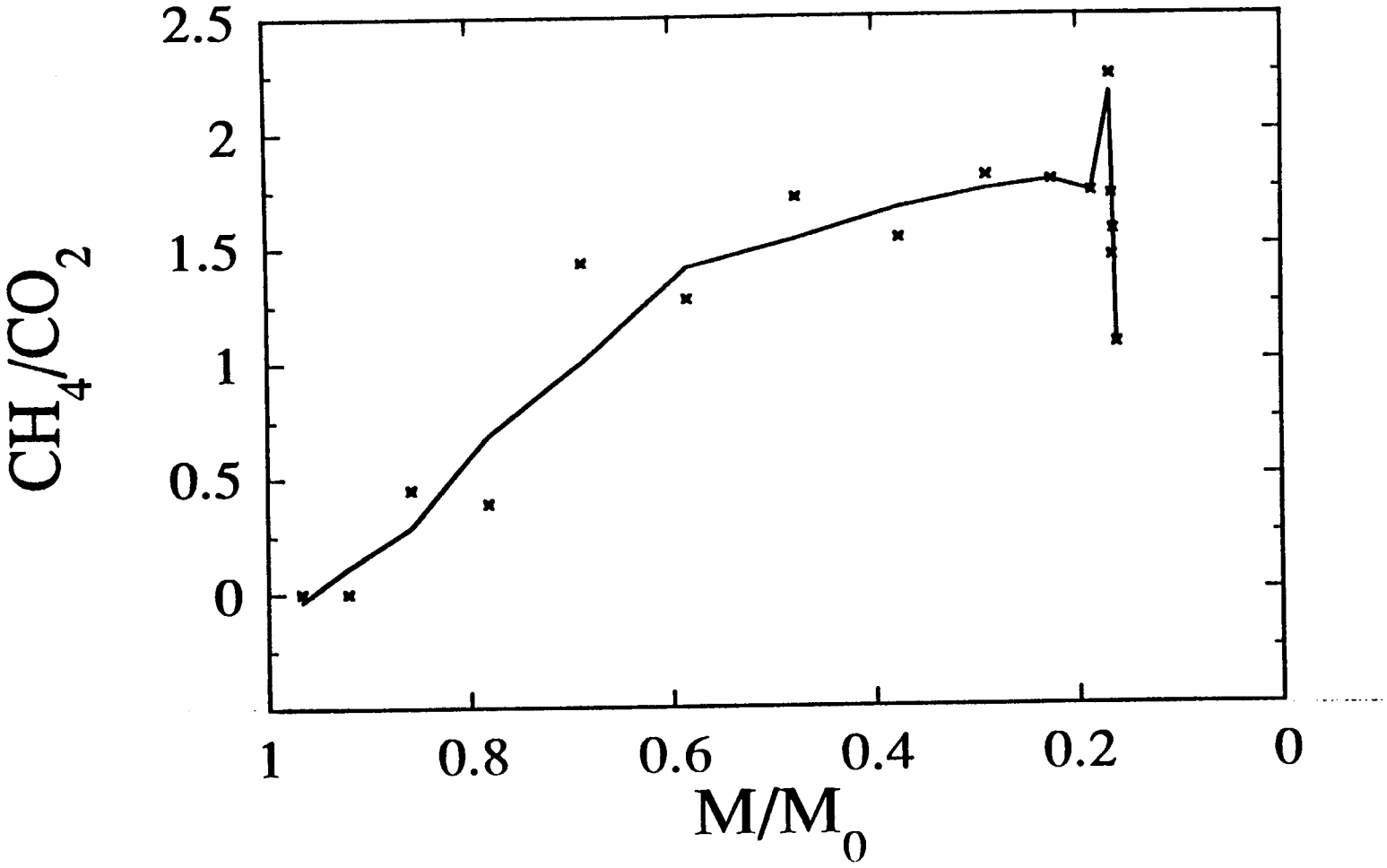

Figure 5.29g: Methane to carbon dioxide molar ratio from high density (0.965 g/cm^3) samples of cellulose, subject to a nominal heat flux of 60 kW/m^2. These are the data of Figure 5.29c, replotted against remaining sample mass

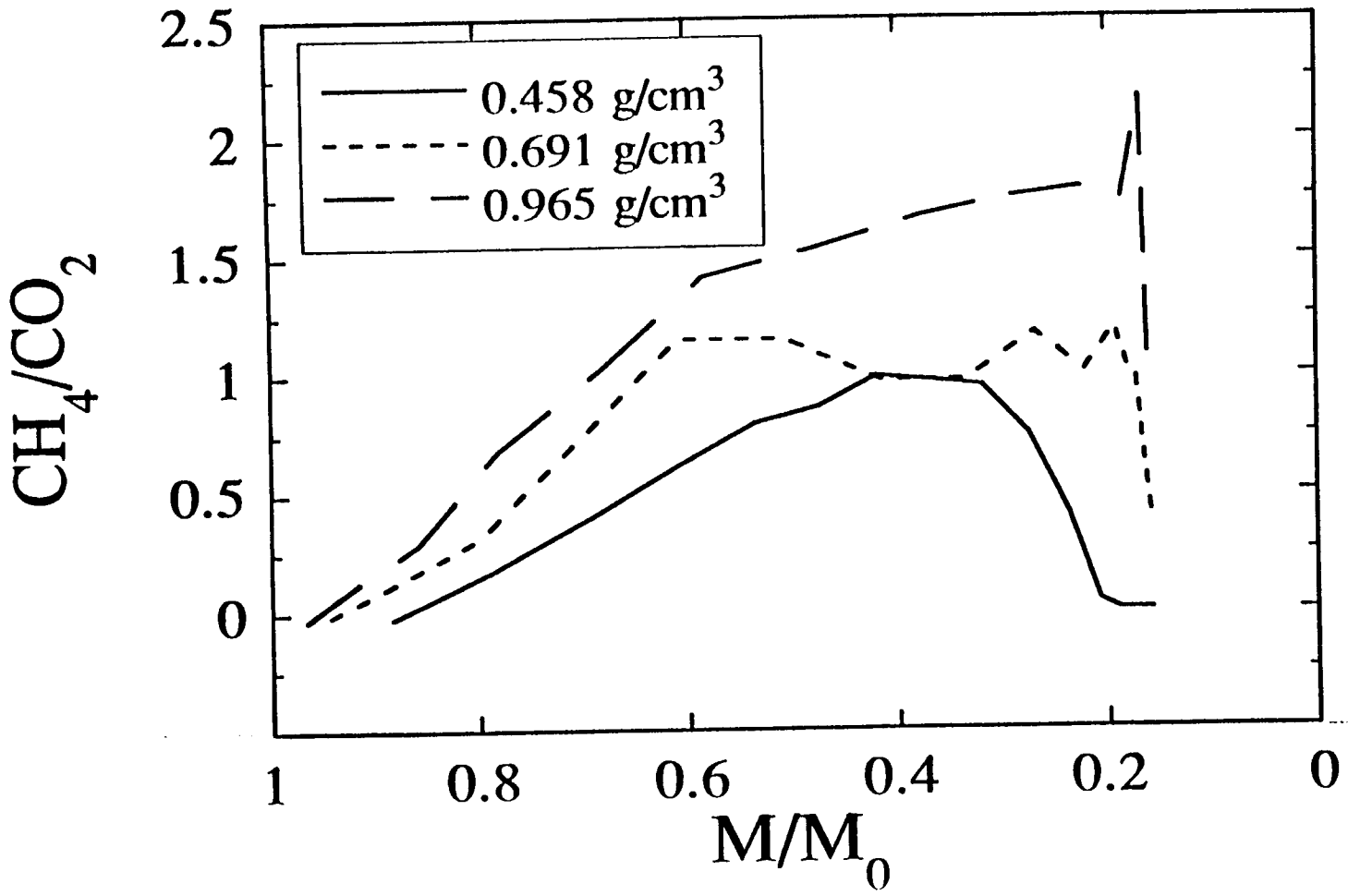

Figure 5.29h: Comparison of results for methane to carbon dioxide molar ratio for different density samples. Data are those shown in Figures 5.29e, 5.29f and 5.29g, with data points omitted for clarity. These are the data of Figure 5.29d, replotted against remaining sample mass

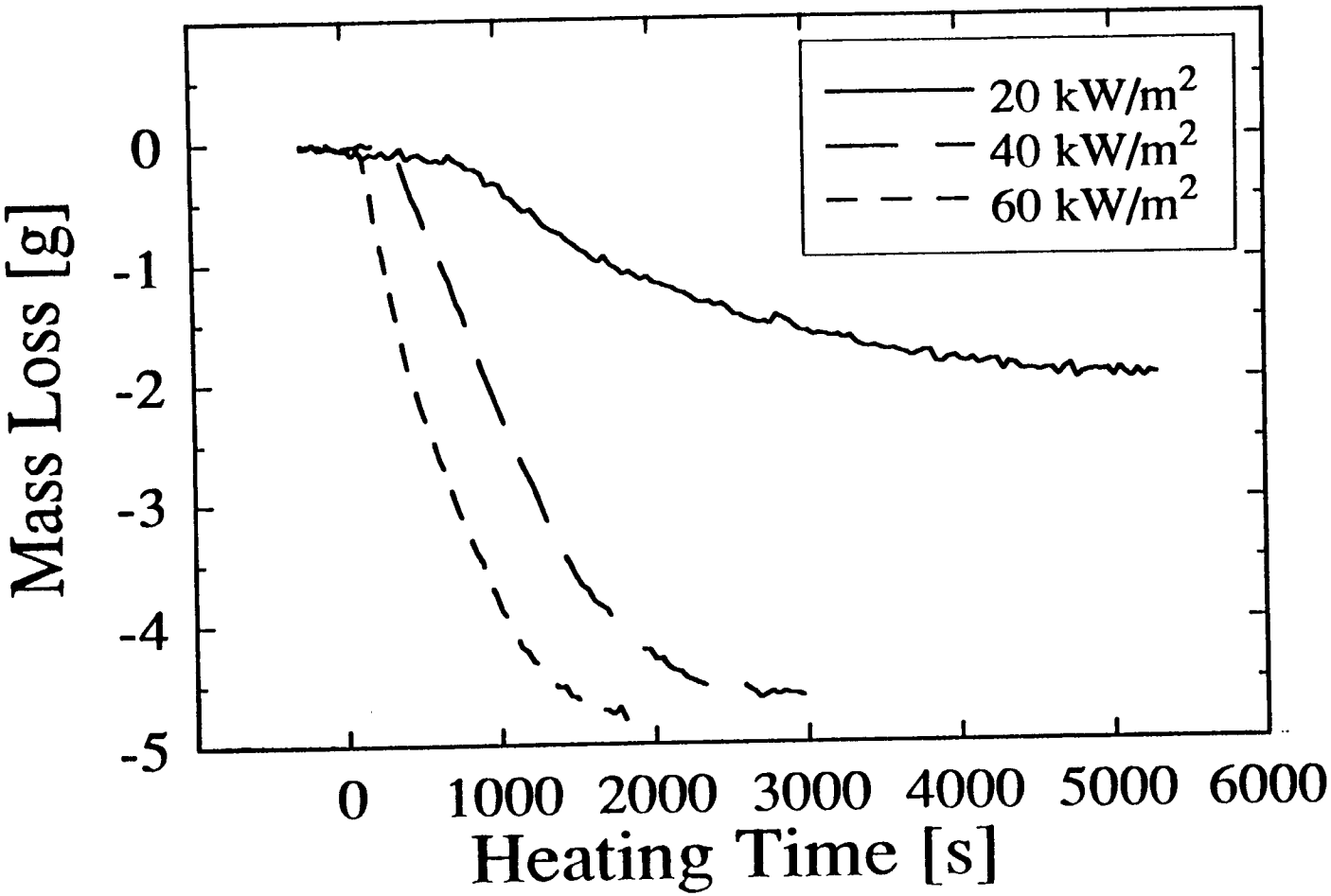

Figure 5.30a Mass loss during pyrolysis of a low density (0.458 g/cm^3) sample as a function of time for three different incident heat fluxes

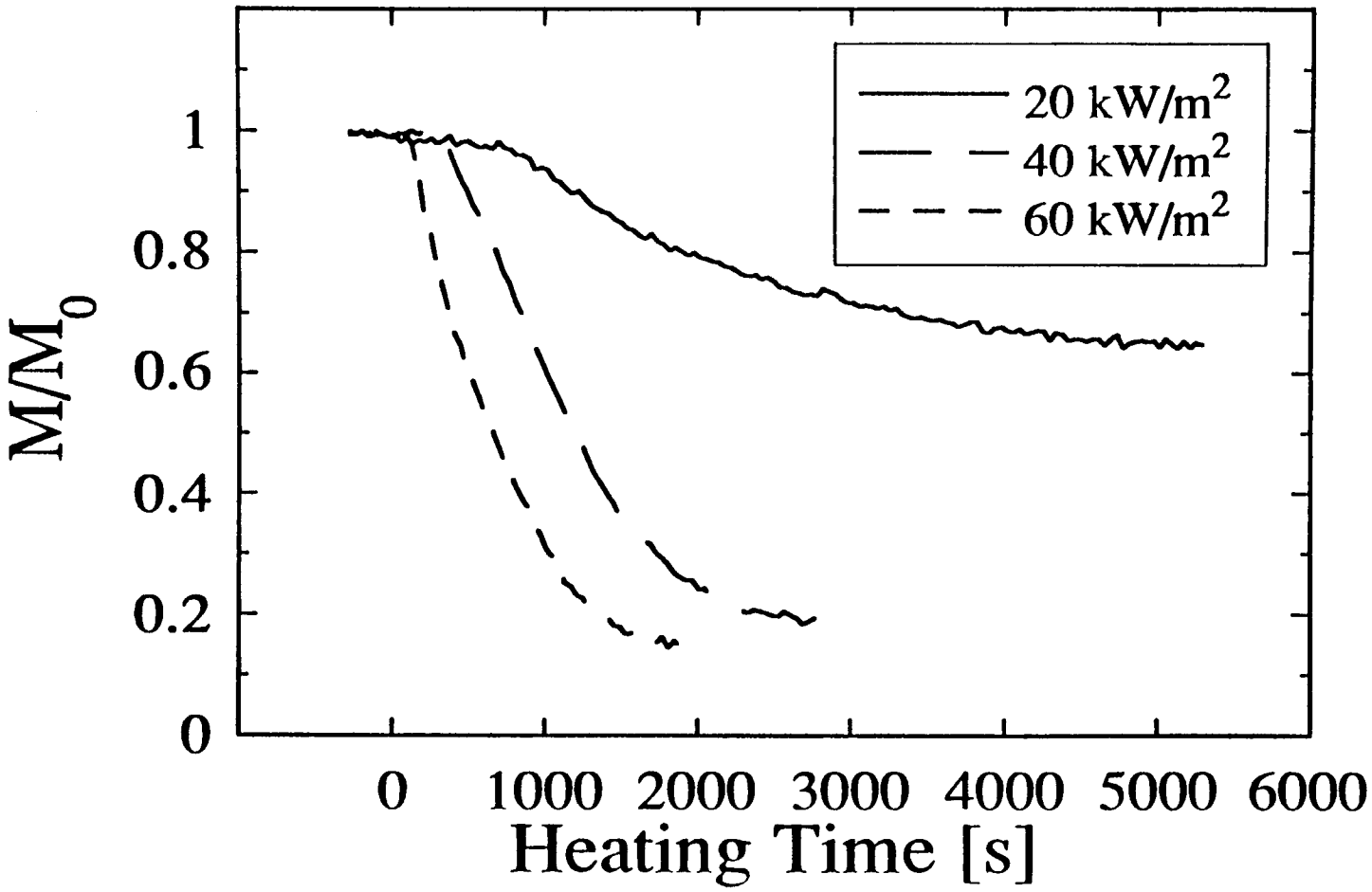

Figure 5.30b Fractional mass loss during pyrolysis of a low density (0.458 g/cm^3) sample as a function of time for three different incident heat fluxes

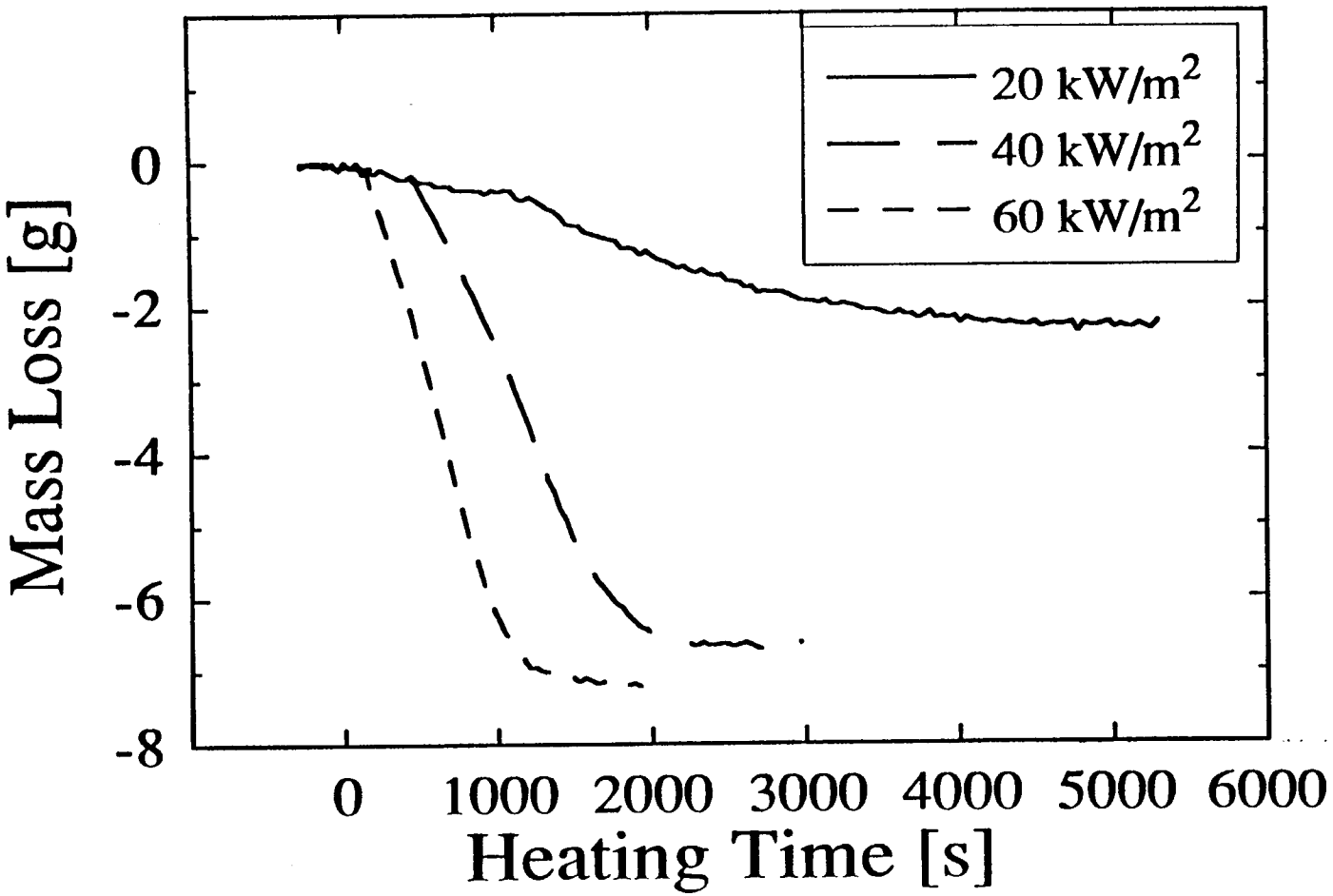

Figure 5.31a Mass loss during pyrolysis of a medium density (0.691 g/cm^3) sample as a function of time for three different incident heat fluxes

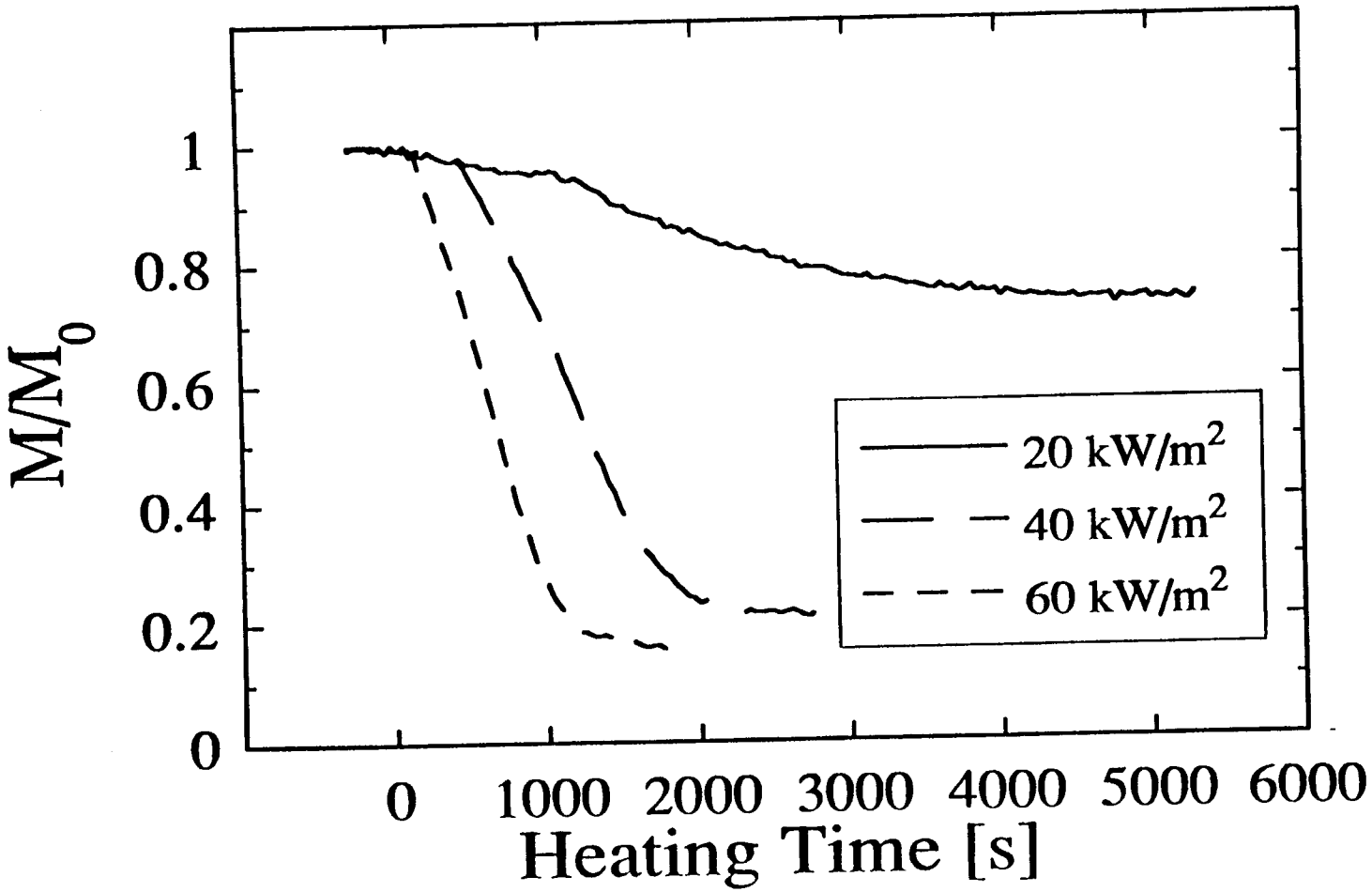

Figure 5.31b Fractional mass loss during pyrolysis of a medium density (0.691 g/cm^3) sample as a function of time for three different incident heat fluxes

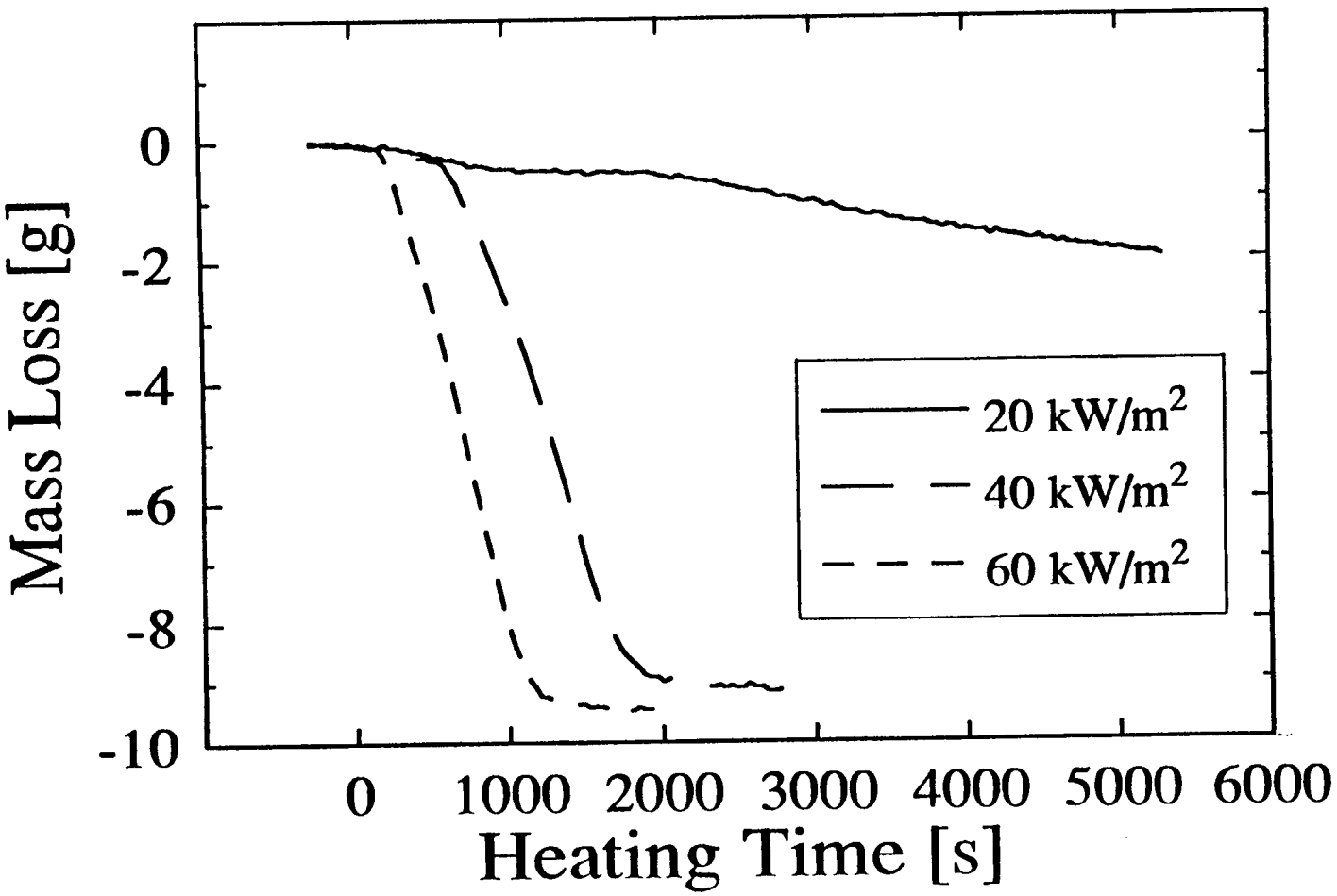

Figure 5.32a Mass loss during pyrolysis of a high density (0.965 g/cm^3) sample as a function of time for three different incident heat fluxes

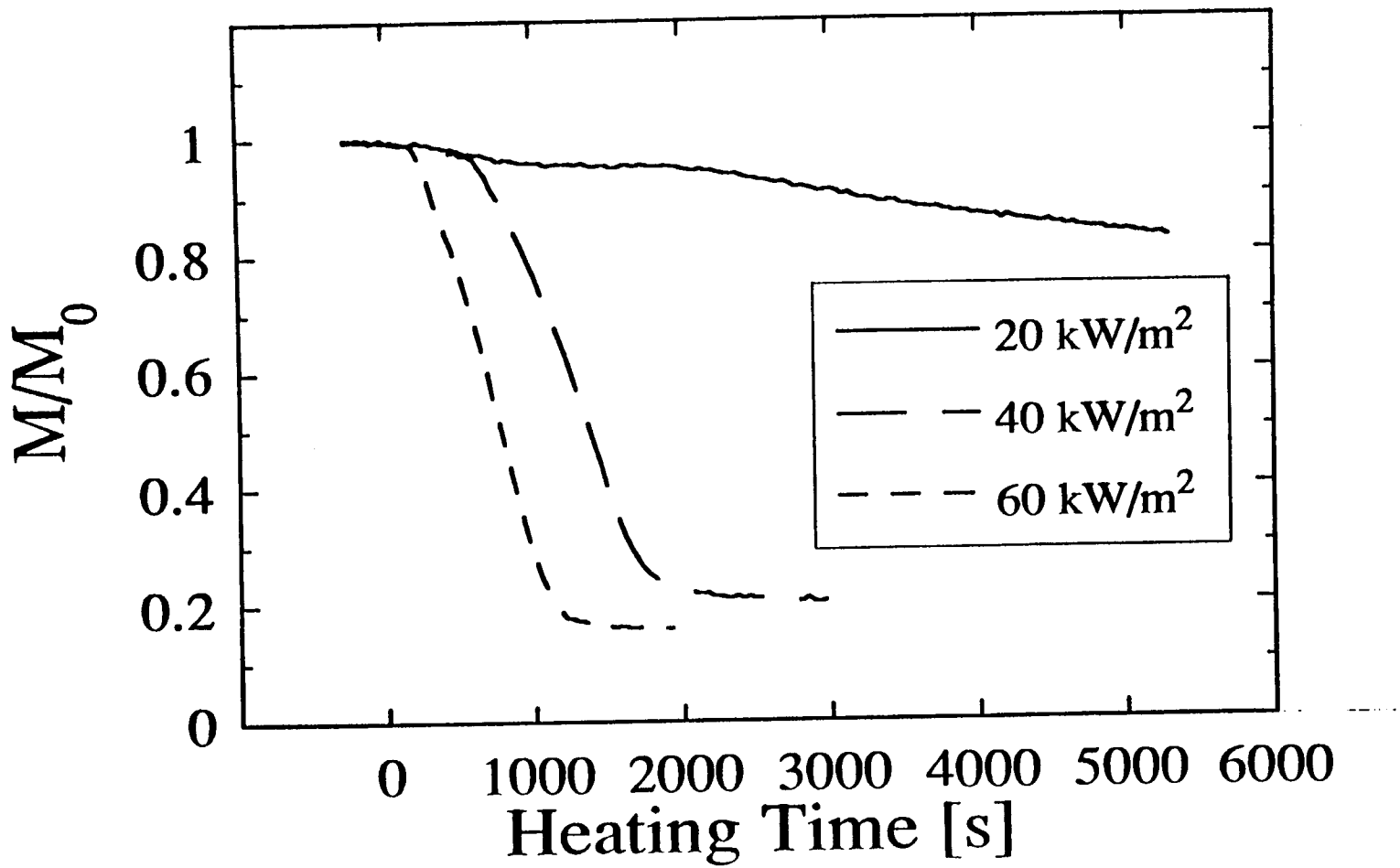

Figure 5.32b Fractional mass loss during pyrolysis of a high density (0.965 g/cm^3) sample as a function of time for three different incident heat fluxes

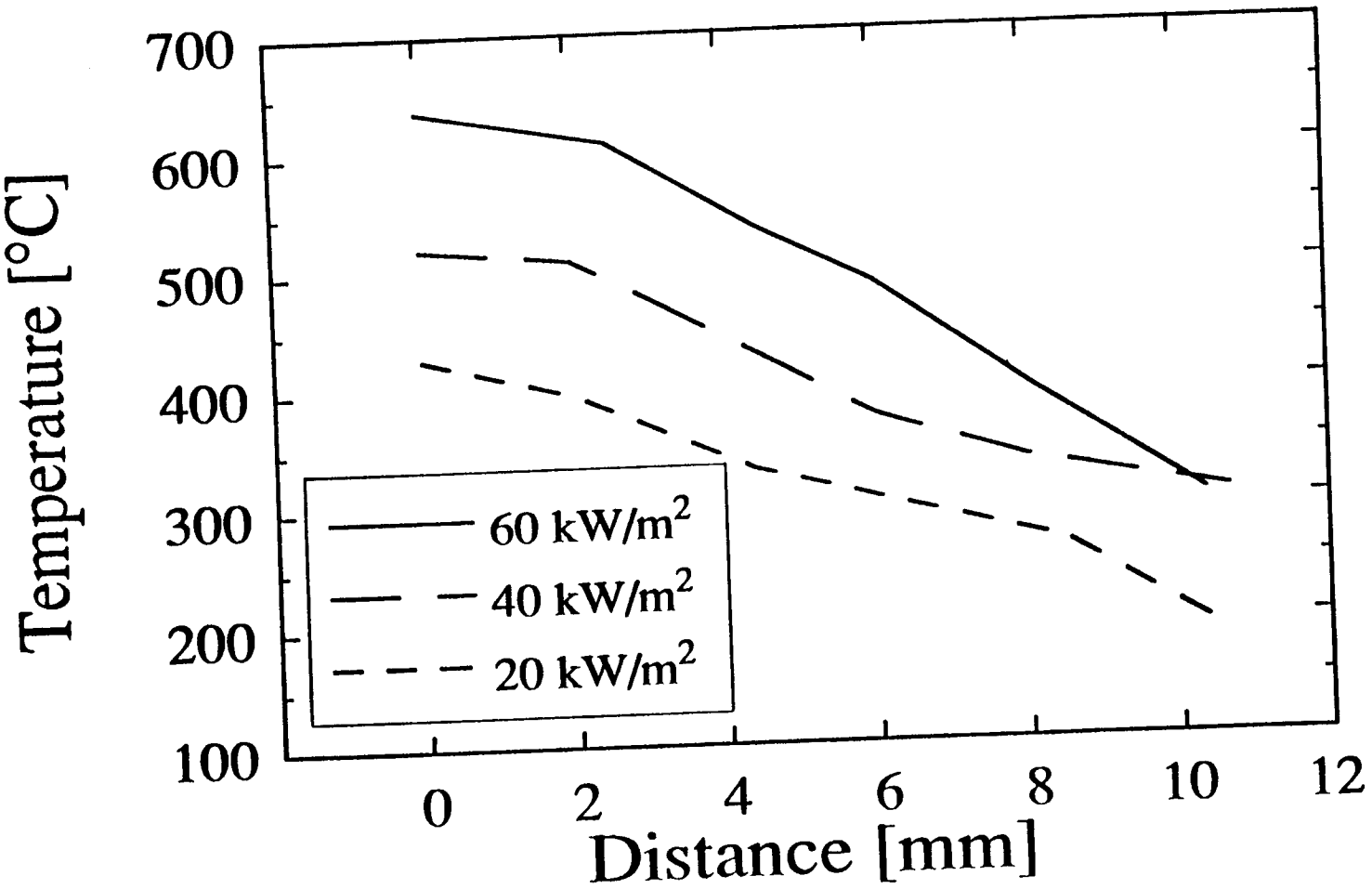

Figure 5.33a Steady state axial temperature profiles (char temperature profiles) in a high (0.965 g/cm^3) density sample and three different incident heat fluxes

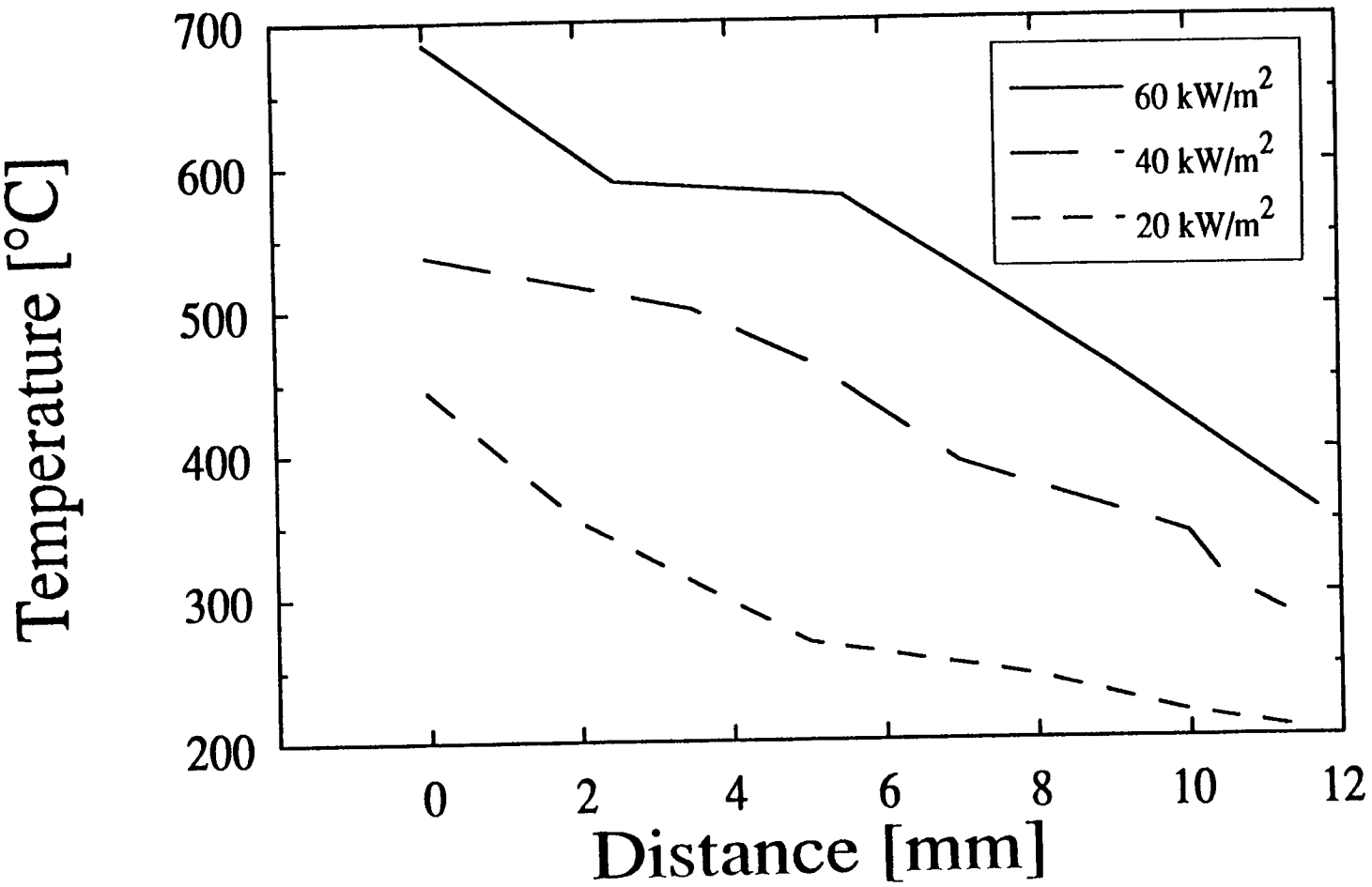

Figure 5.33b Steady state axial temperature profiles (char temperature profiles) in a medium (0.691 g/cm^3) density sample and three different incident heat fluxes

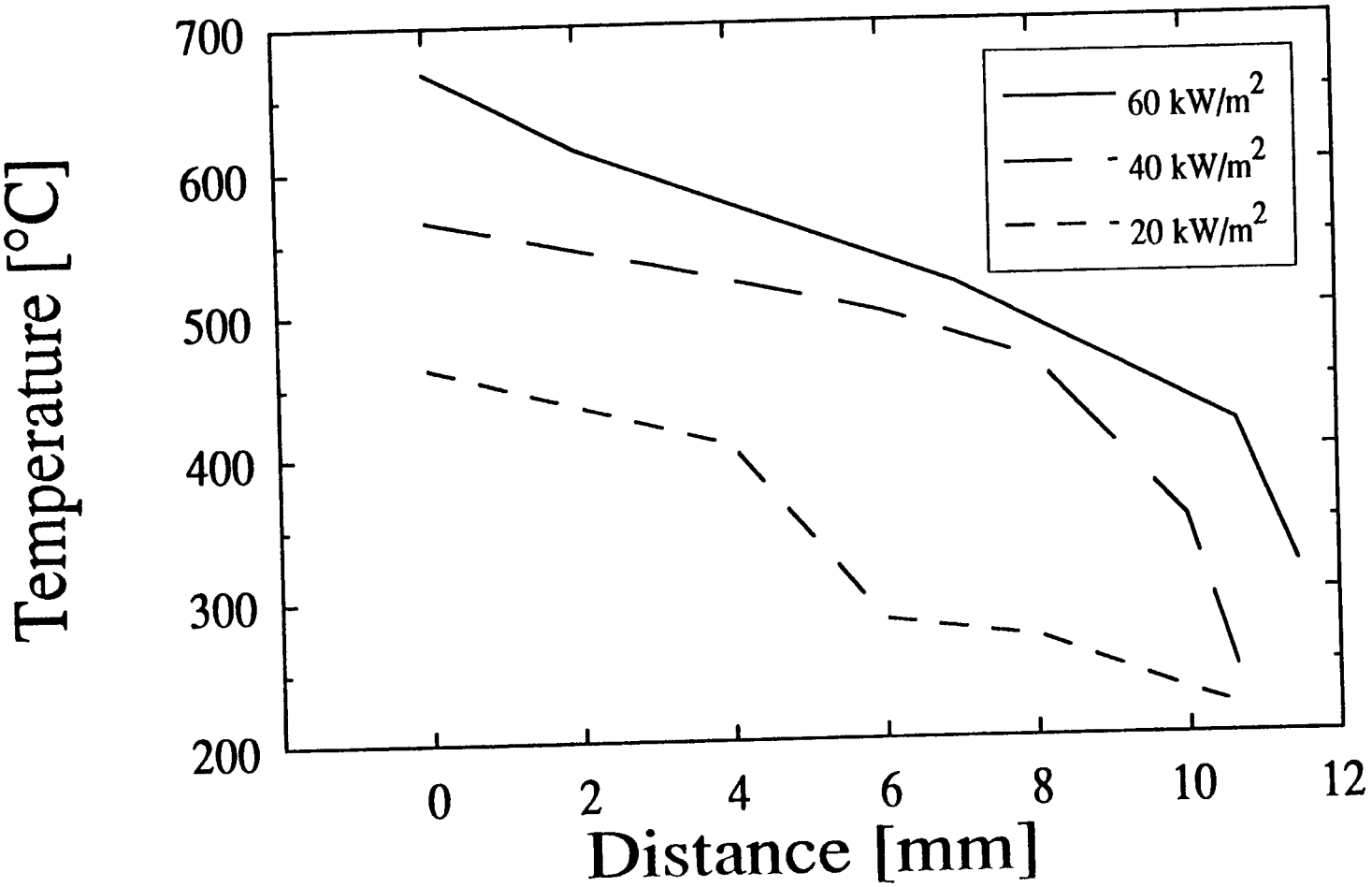

Figure 5.33c Steady state axial temperature profiles (char temperature profiles) in a low (0.458 g/cm^3) density sample and three different incident heat fluxes

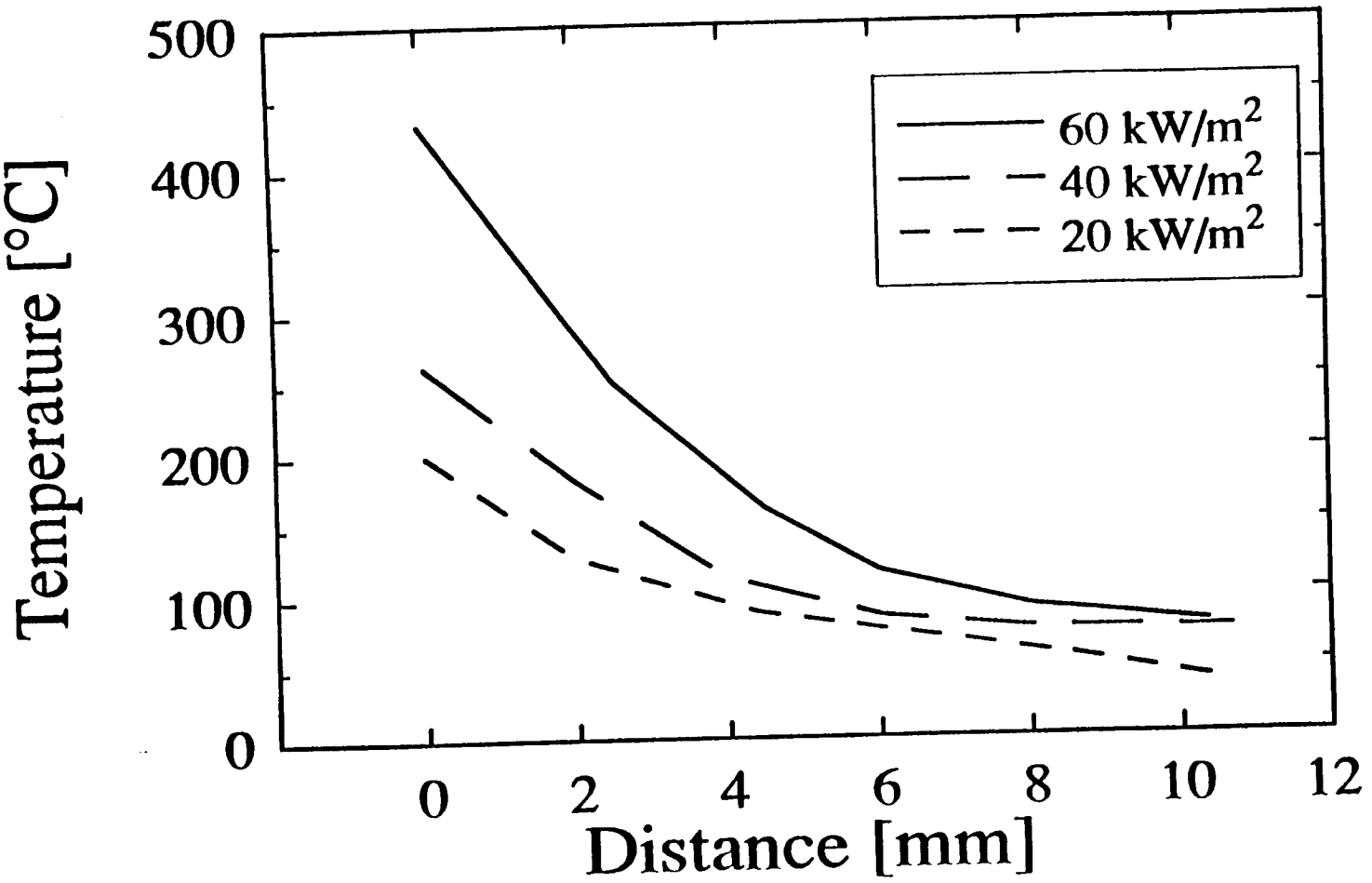

Figure 5.34a A comparison of temperature profiles in a high density sample (0.965 g/cm^3), heated for 200 s (cellulose temperature profile) under different incident heat fluxes

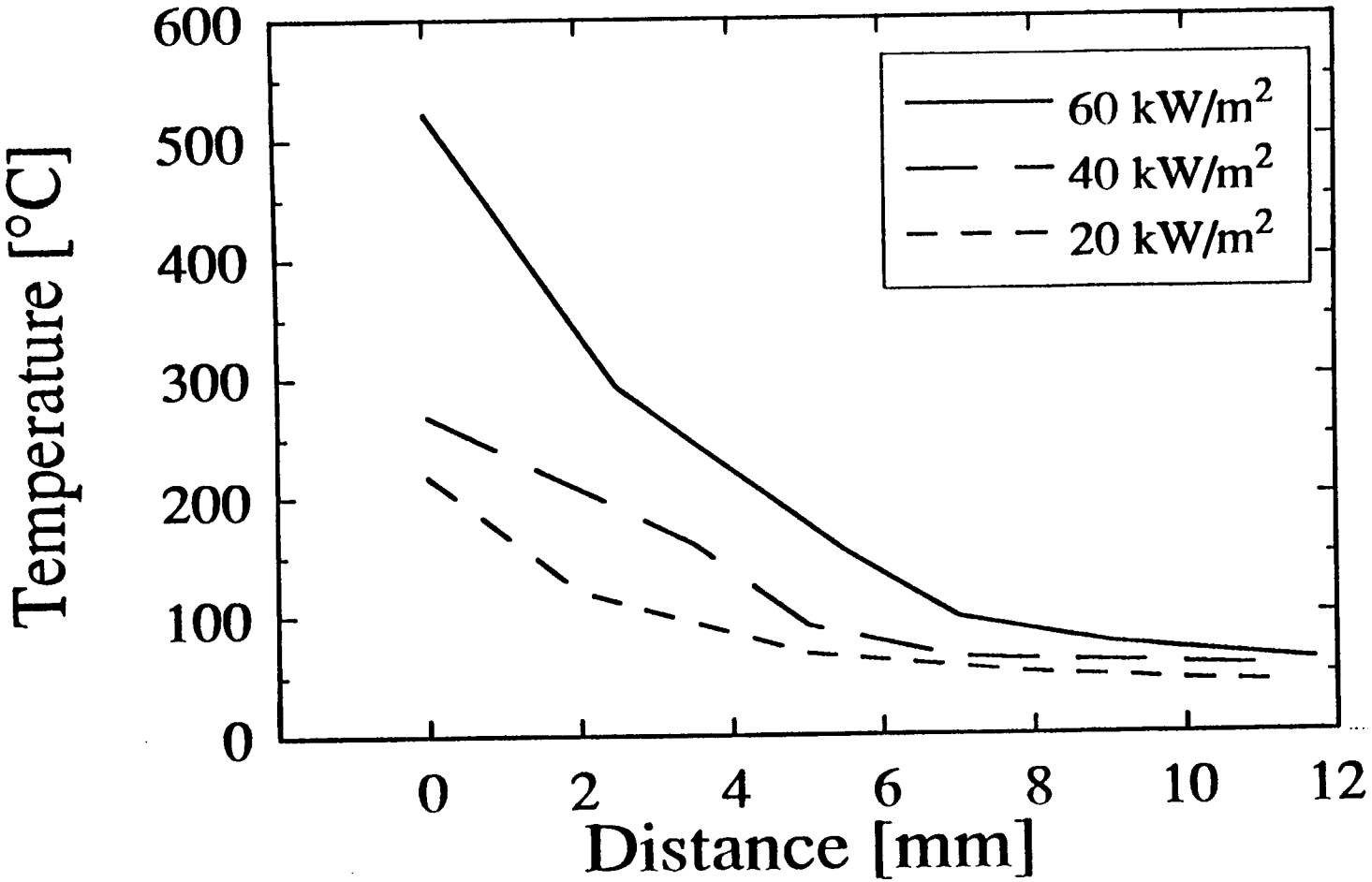

Figure 5.34b A comparison of temperature profiles in a medium density sample (0.691 g/cm^3), heated for 200 s (cellulose temperature profile) under different incident heat fluxes

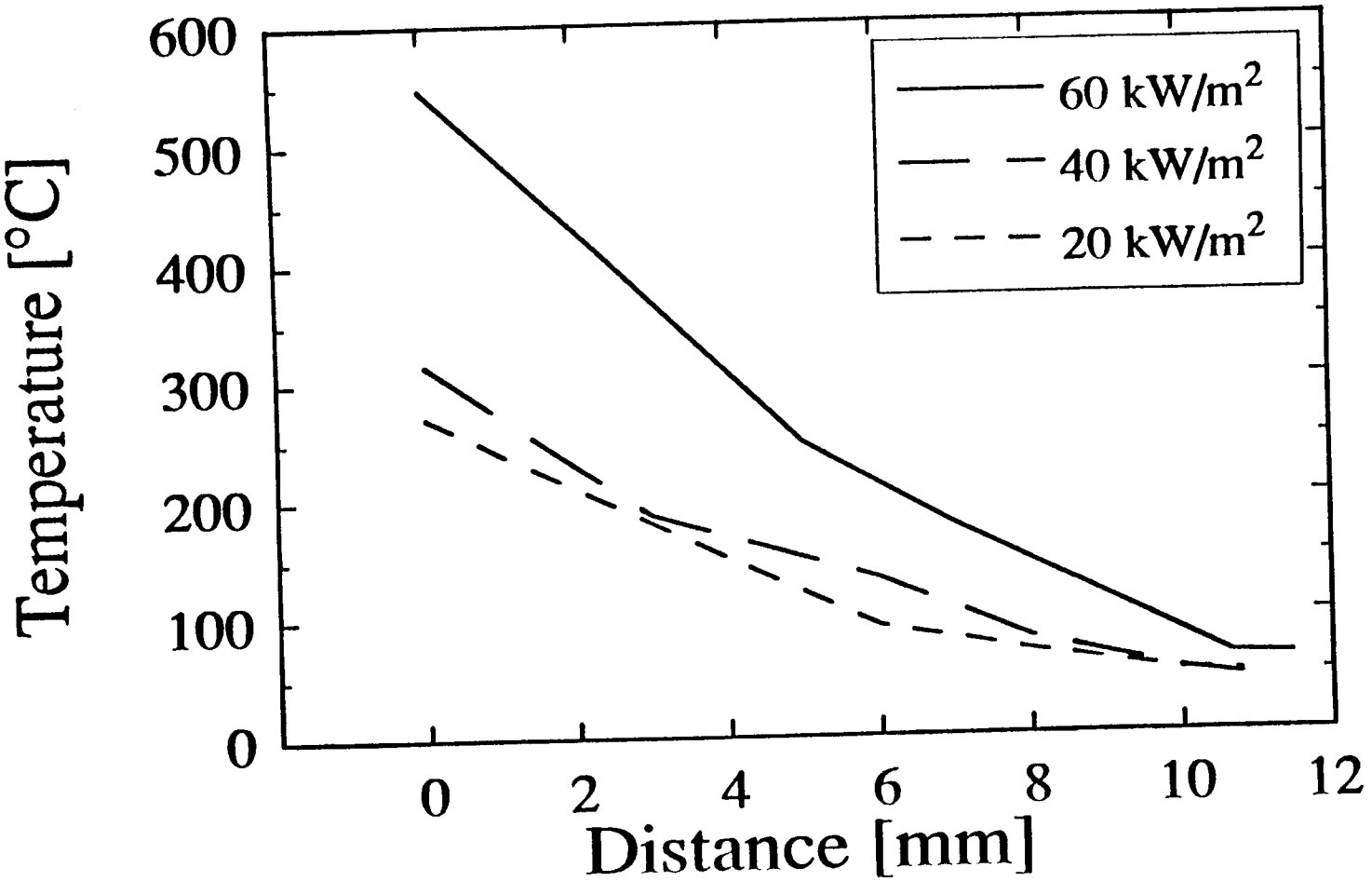

Figure 5.34c A comparison of temperature profiles in a low density sample (0.458 g/cm^3), heated for 200 s (cellulose temperature profile) under different incident heat fluxes

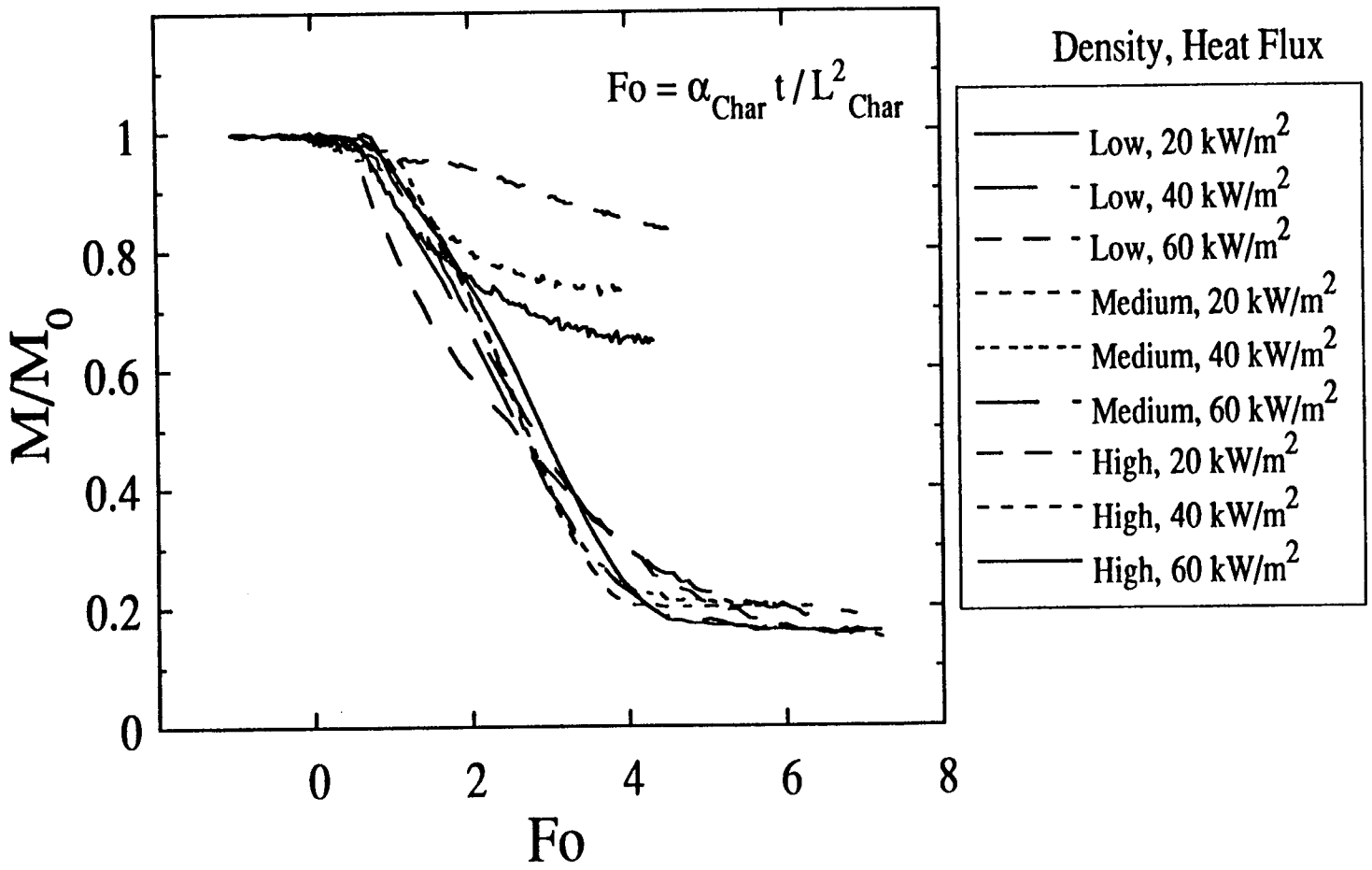

Figure 5.35 Fractional sample mass remaining as a function of Fourier number (defined with respect to char properties) for three different density samples and three different incident heat fluxes (defined with respect to char properties)

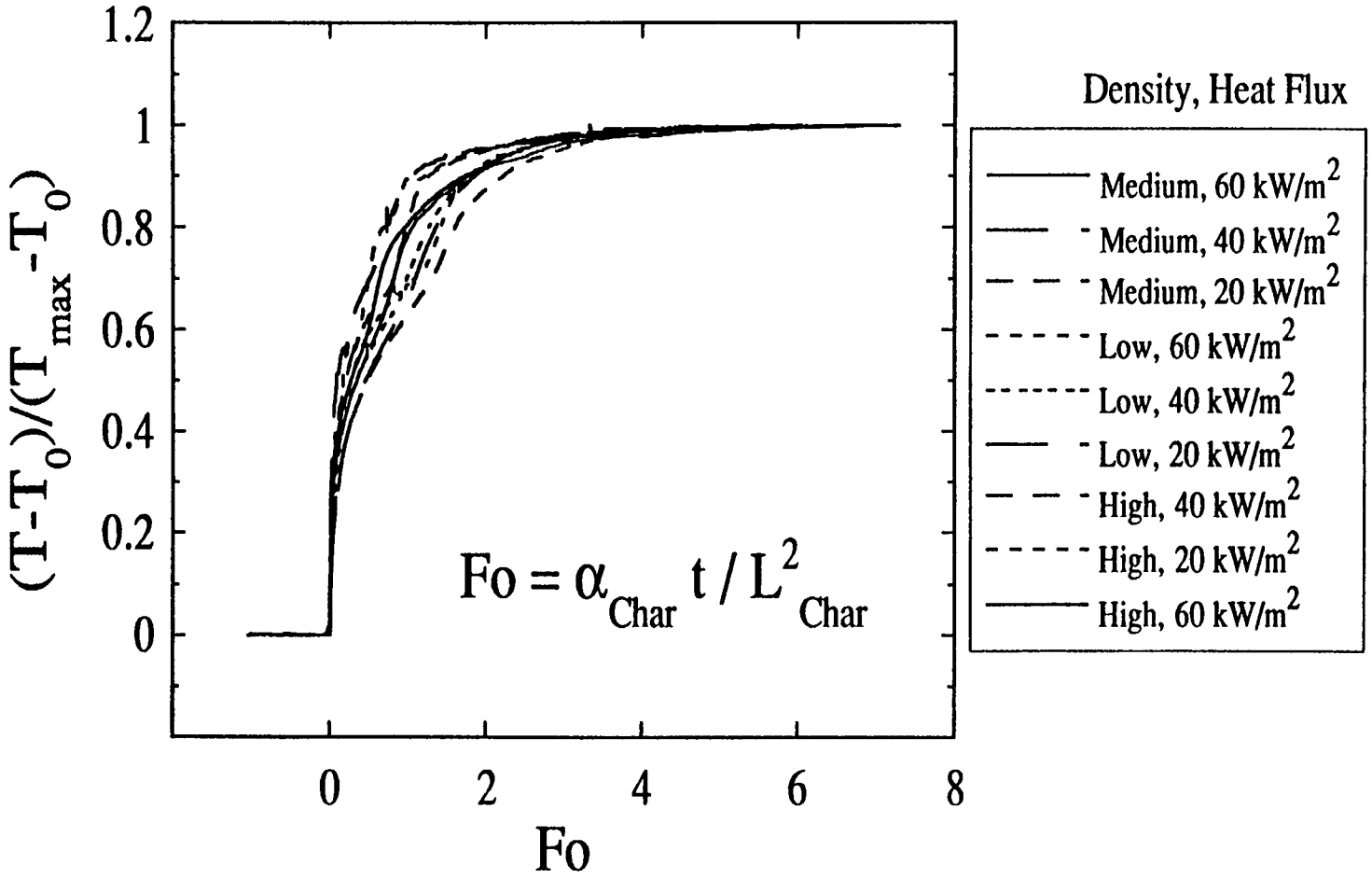

Figure 5.36a Dimensionless front surface temperatures as a function of Fourier number (defined with respect to char thermal diffusivity and final thickness) for three different density samples and three different incident heat fluxes

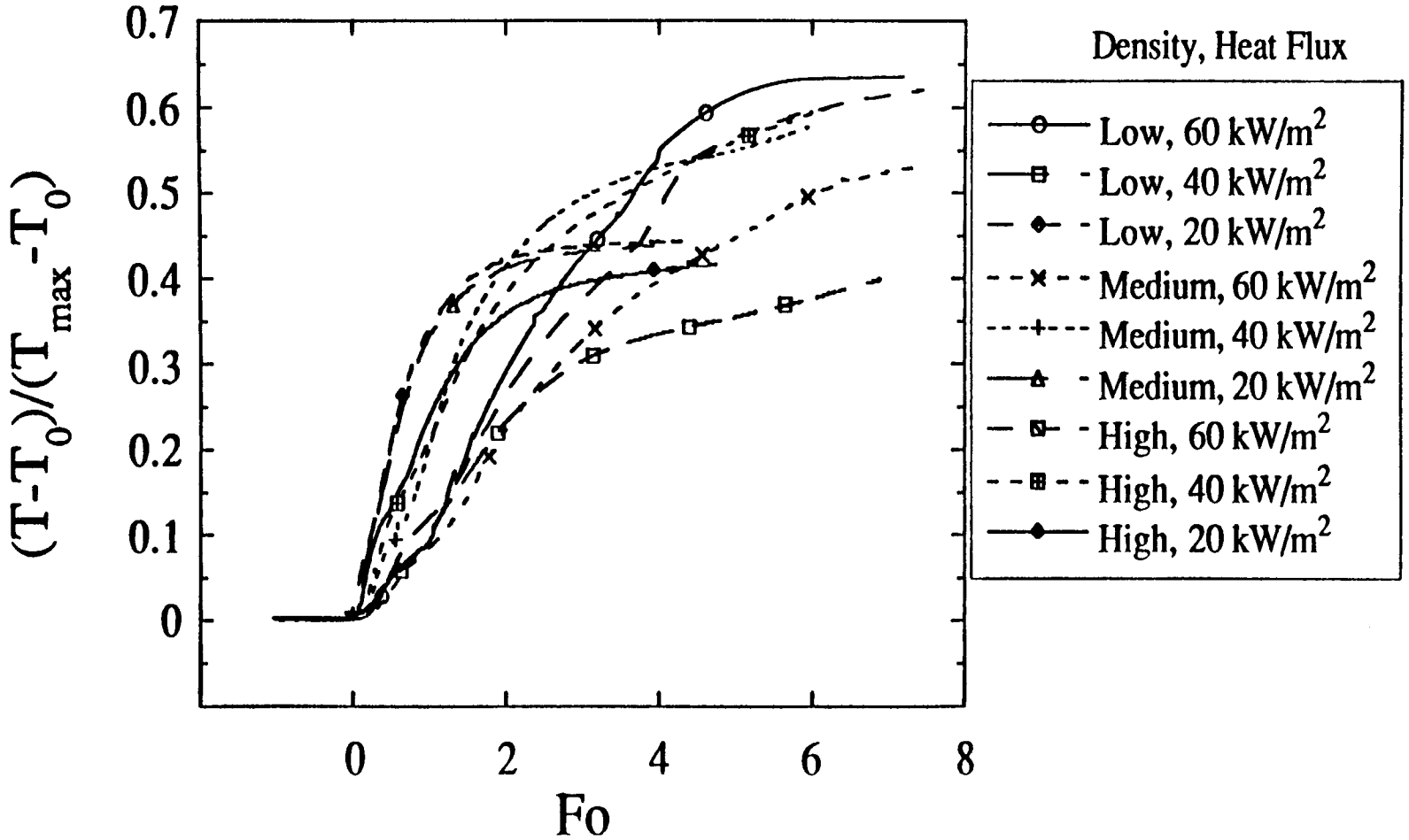

Figure 5.36b Dimensionless back surface temperatures (T_{max} is a maximum front surface temperature) as a function of Fourier number (defined with respect to char thermal diffusivity and final thickness) for three different density samples and three different incident heat fluxes

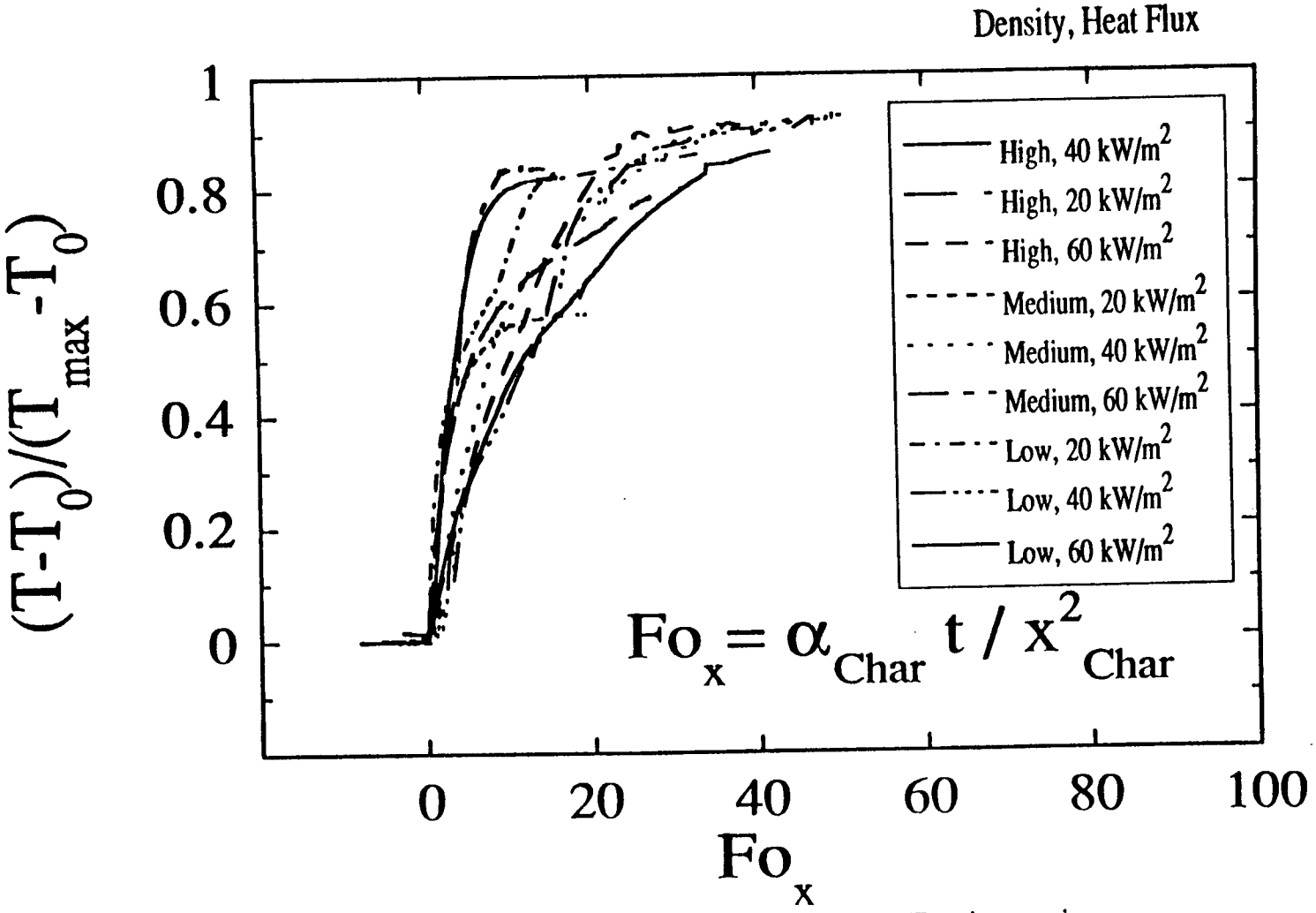

Figure 5.36c Dimensionless interior temperatures (T_{max} is a maximum front surface temperature) as a function of Fourier number (defined with respect to char thermal diffusivity and distance up to a thermocouple) for three different density samples and three different incident heat fluxes

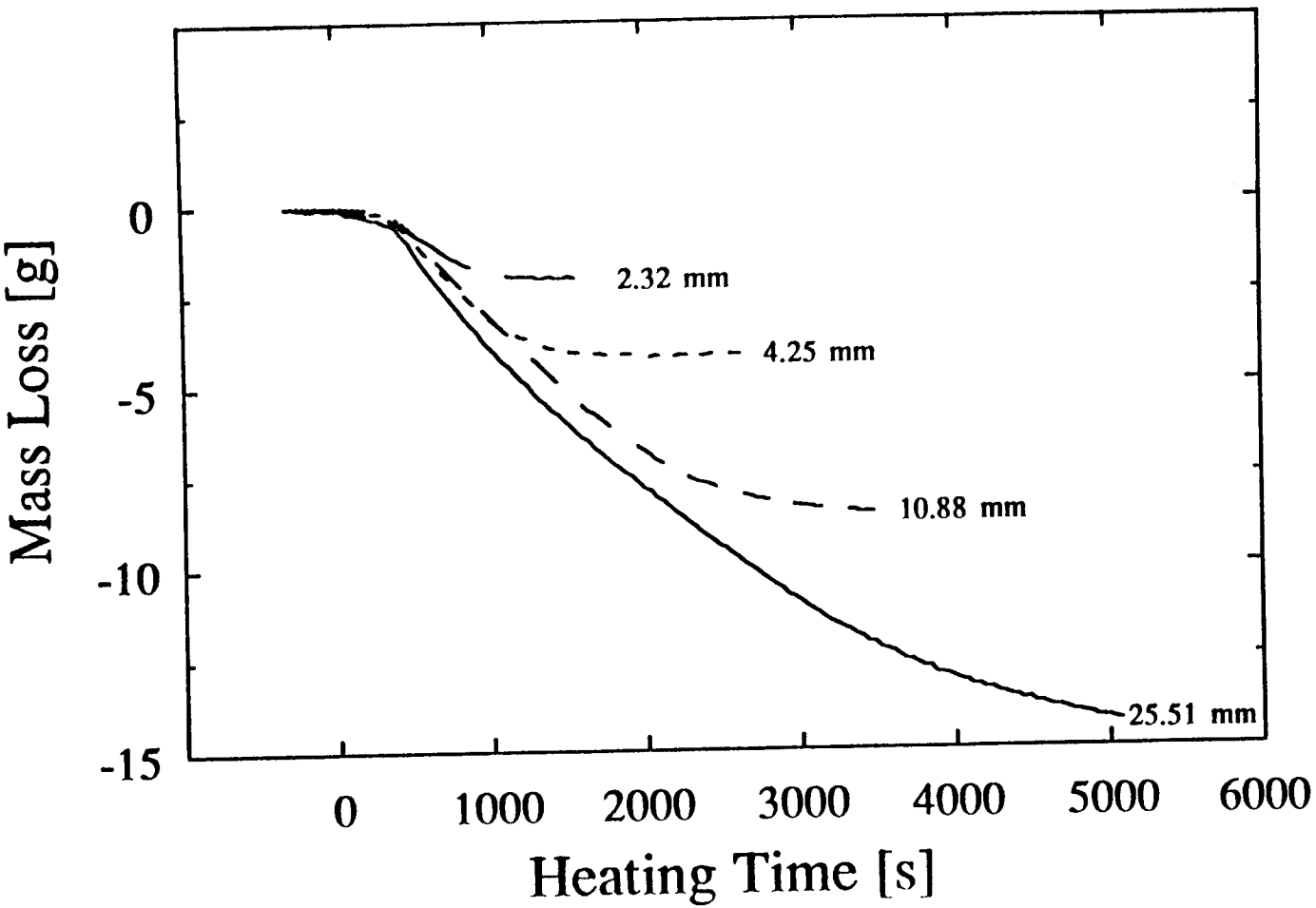

Figure 5.37 Mass loss as a function of time for high density samples of different thickness (incident heat flux of 40 kW/m^2)

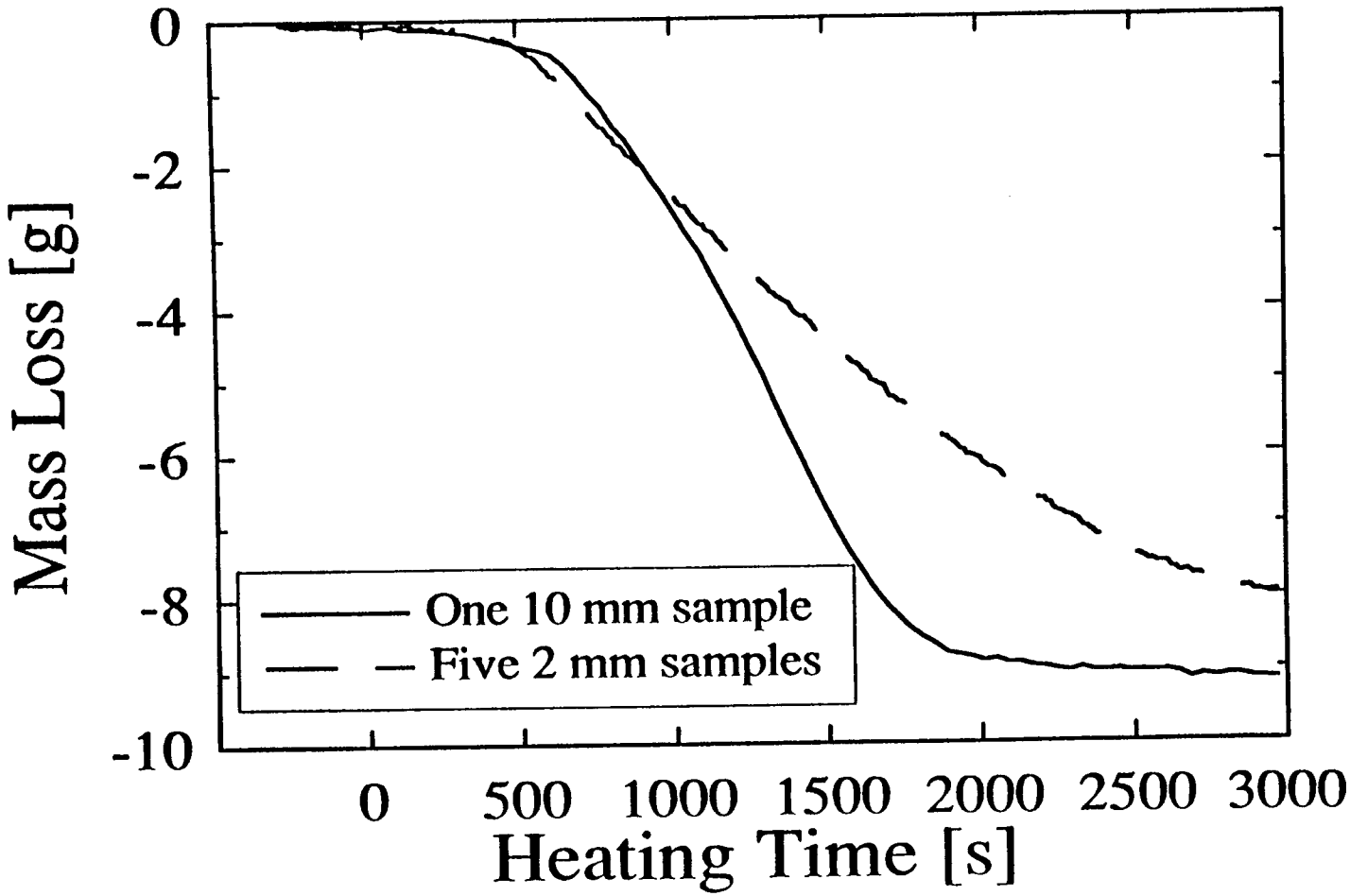

Figure 5.38 A comparison of mass loss as a function of time for five high density samples stacked together and a single high density, 10 mm sample (incident heat flux of 40 kW/m^2)

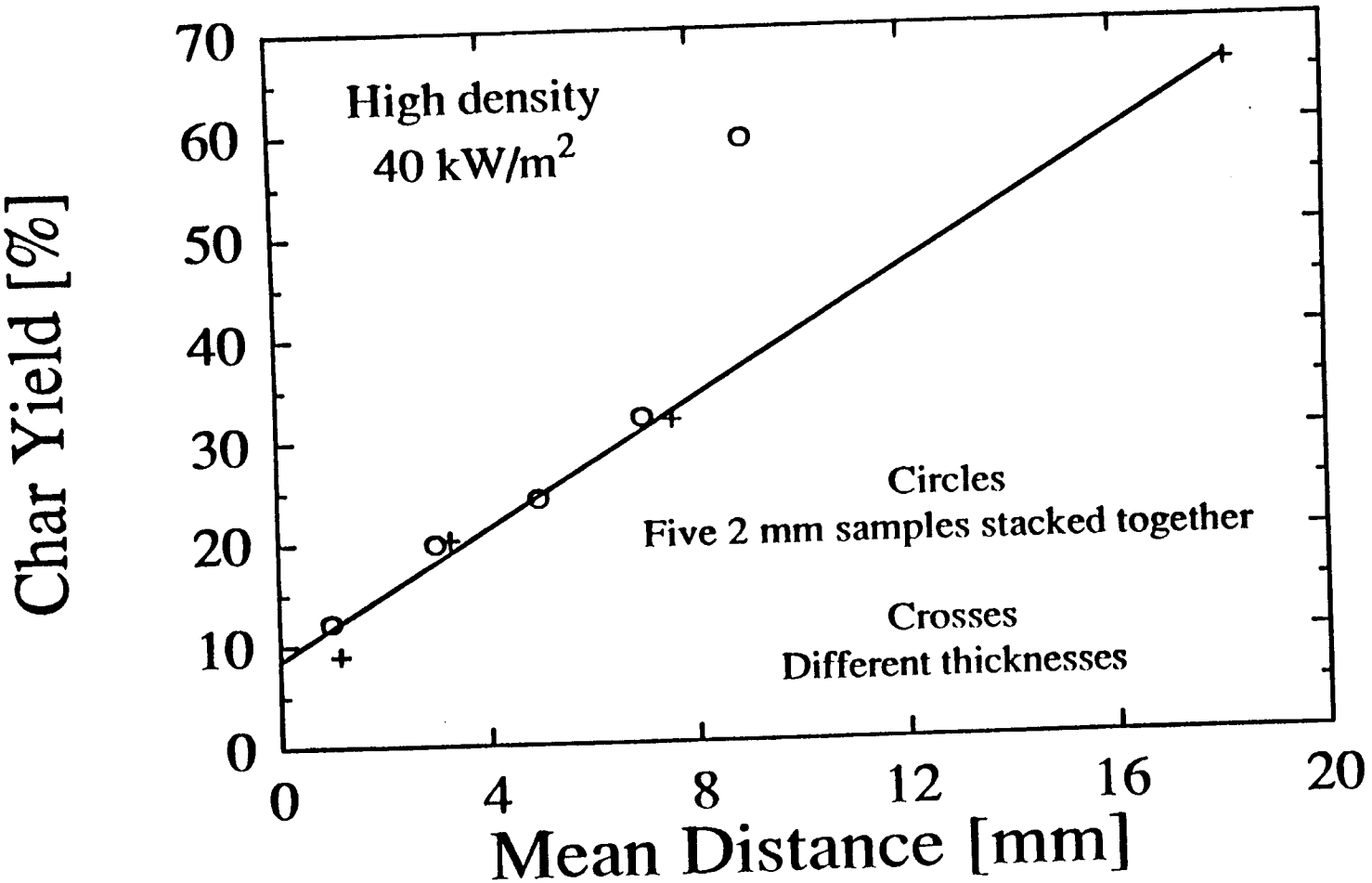

Figure 5.39 Char yield profiles obtained from composite sample (five 2 mm samples) and from different thickness samples (incident heat flux of 40 kW/m^2)

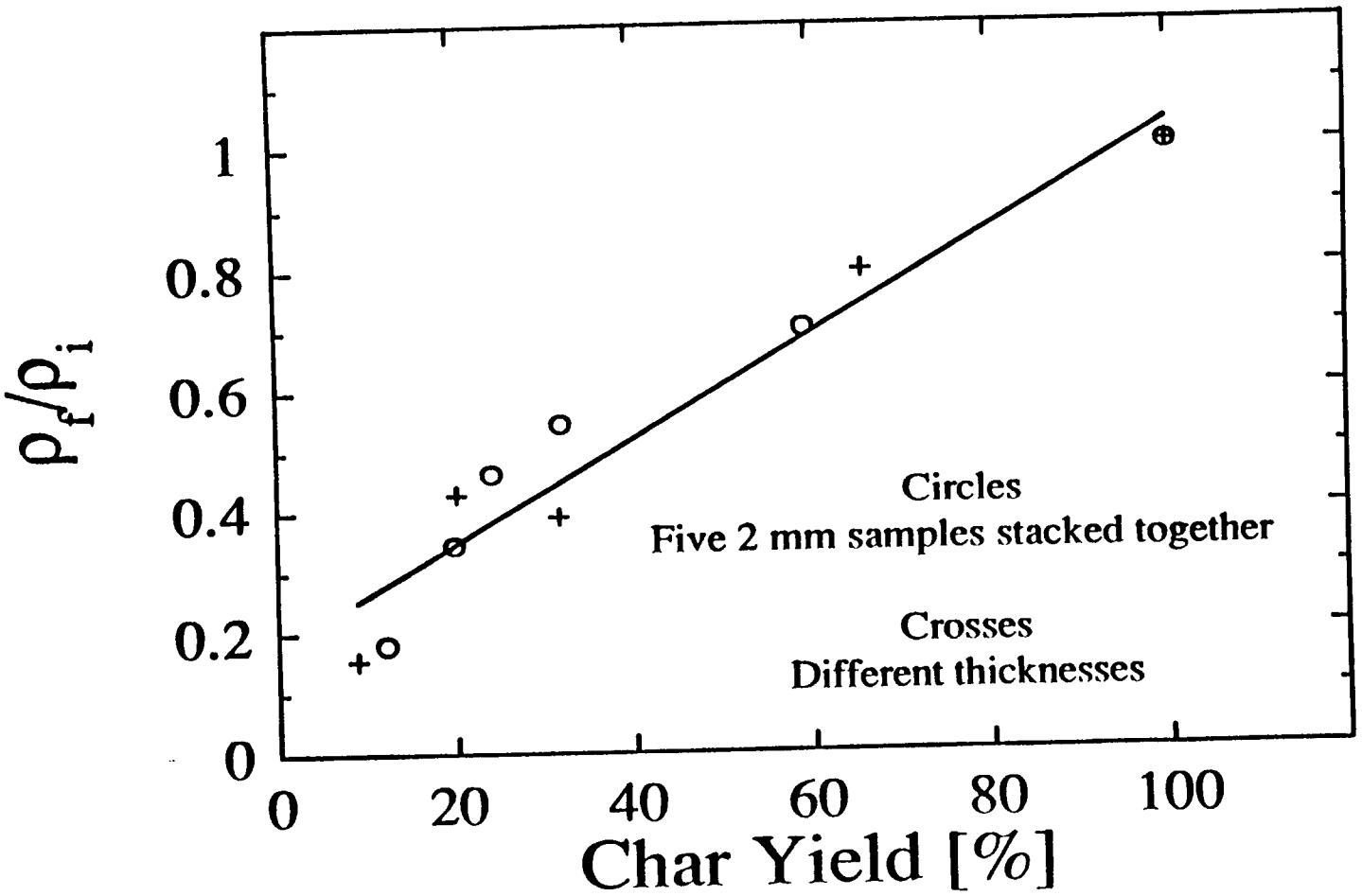

Figure 5.40 Density profiles obtained from composite sample (five 2 mm samples) and from different thickness samples (incident heat flux of 40 kW/m^2)

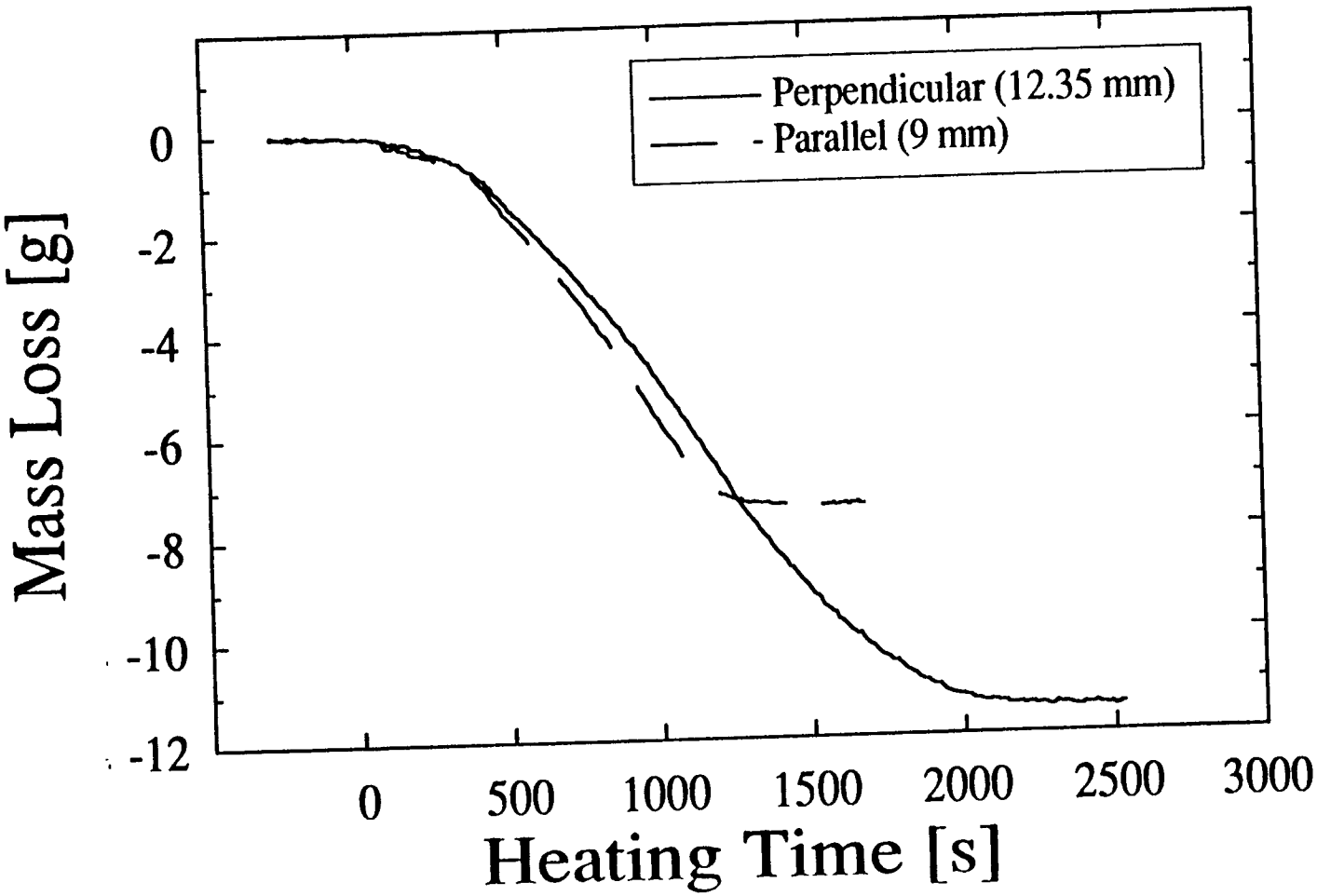

Figure 5.41a Mass loss as a function of time from different grain orientation samples of high density (incident heat flux of 40 kW/m^2)

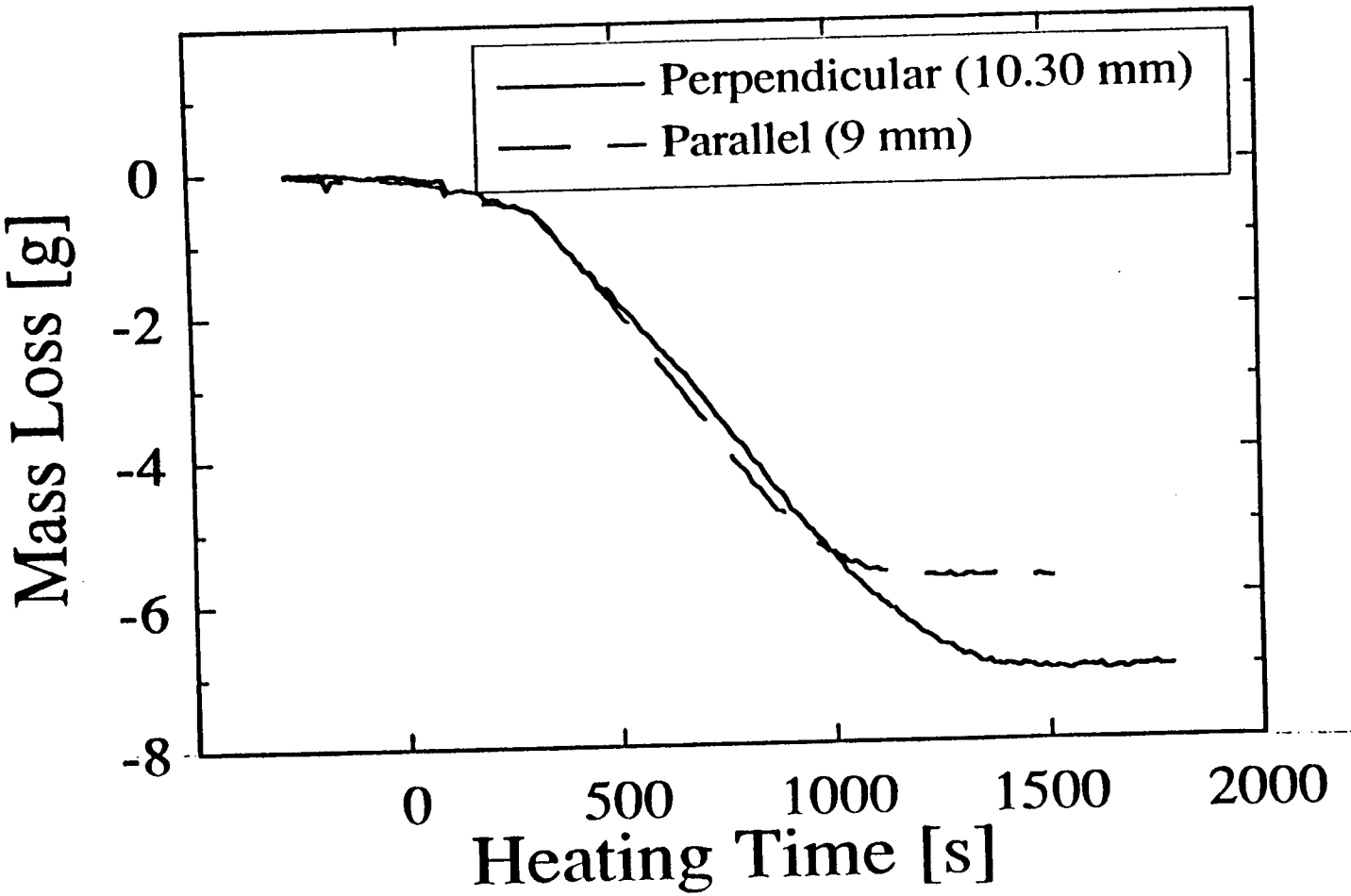

Figure 5.41b Mass loss as a function of time from different grain orientation samples of medium density (incident heat flux of 40 kW/m^2)

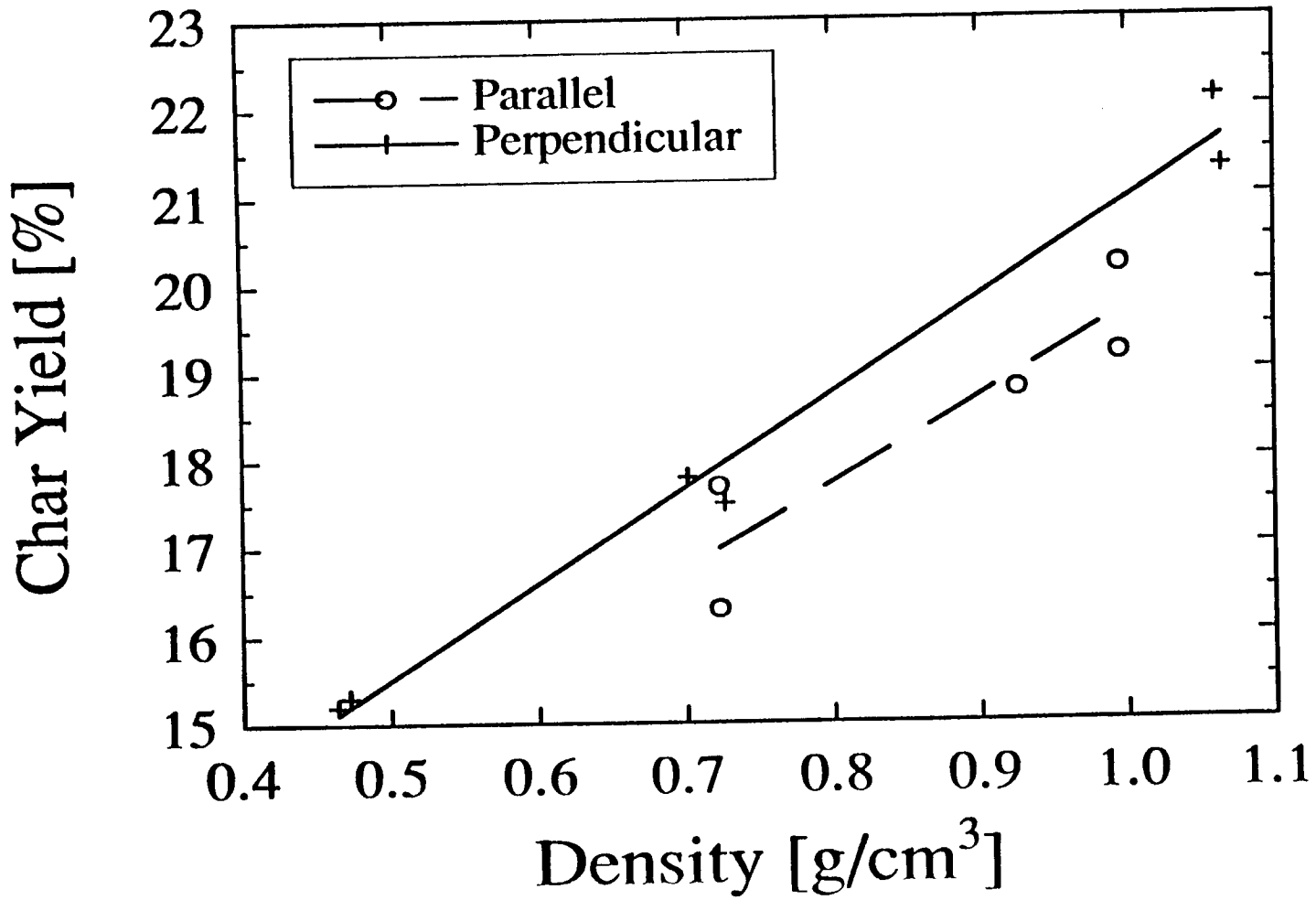

Figure 5.42 Char yield as a function of density from different grain orientation samples (incident heat flux of 40 kW/m^2)

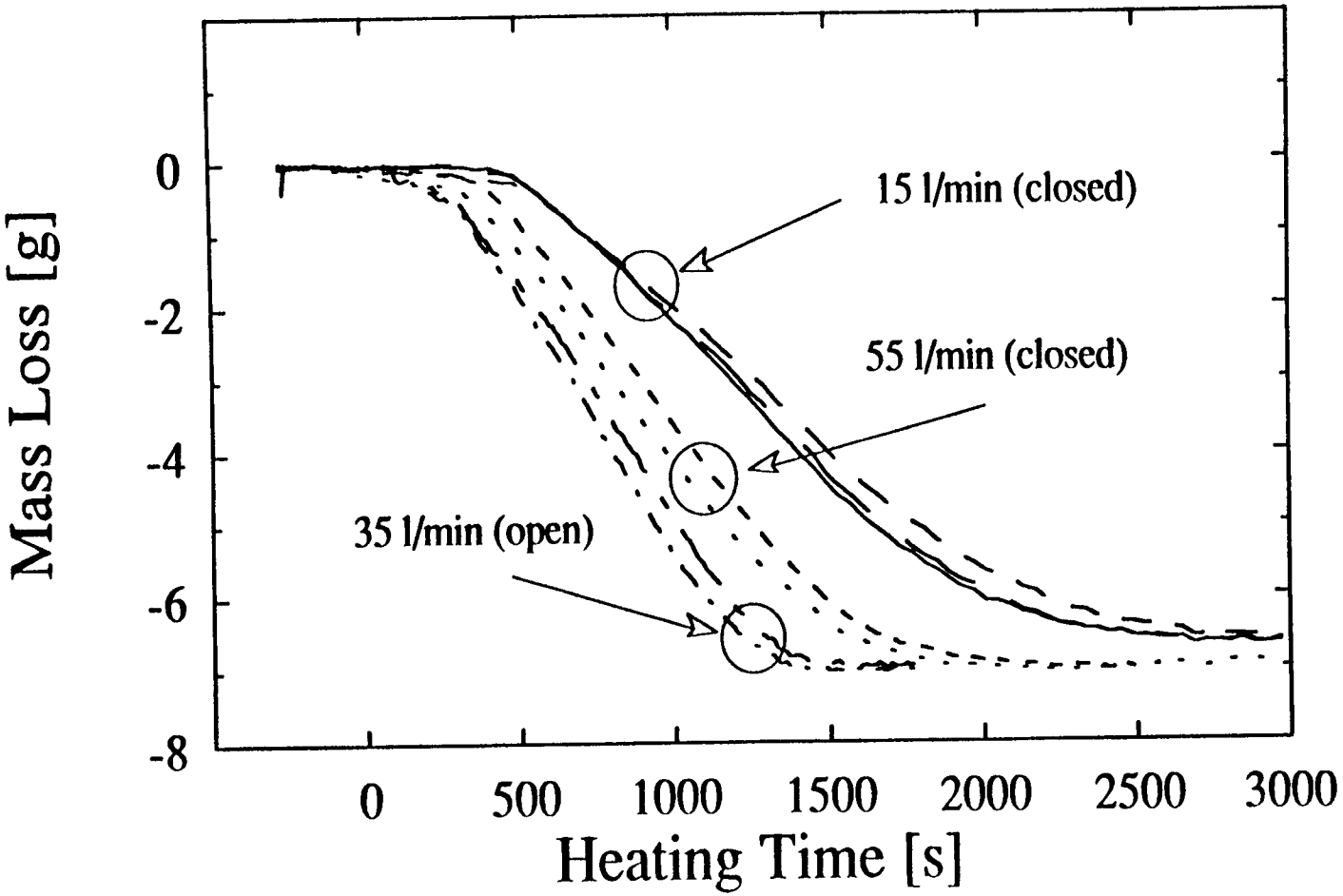

Figure 5.43 The effect of purge gas flowrate on mass loss during pyrolysis of a medium density sample under an incident heat flux of 40 kW/m^2.
The extent of reproducibility is also shown (duplicate samples)

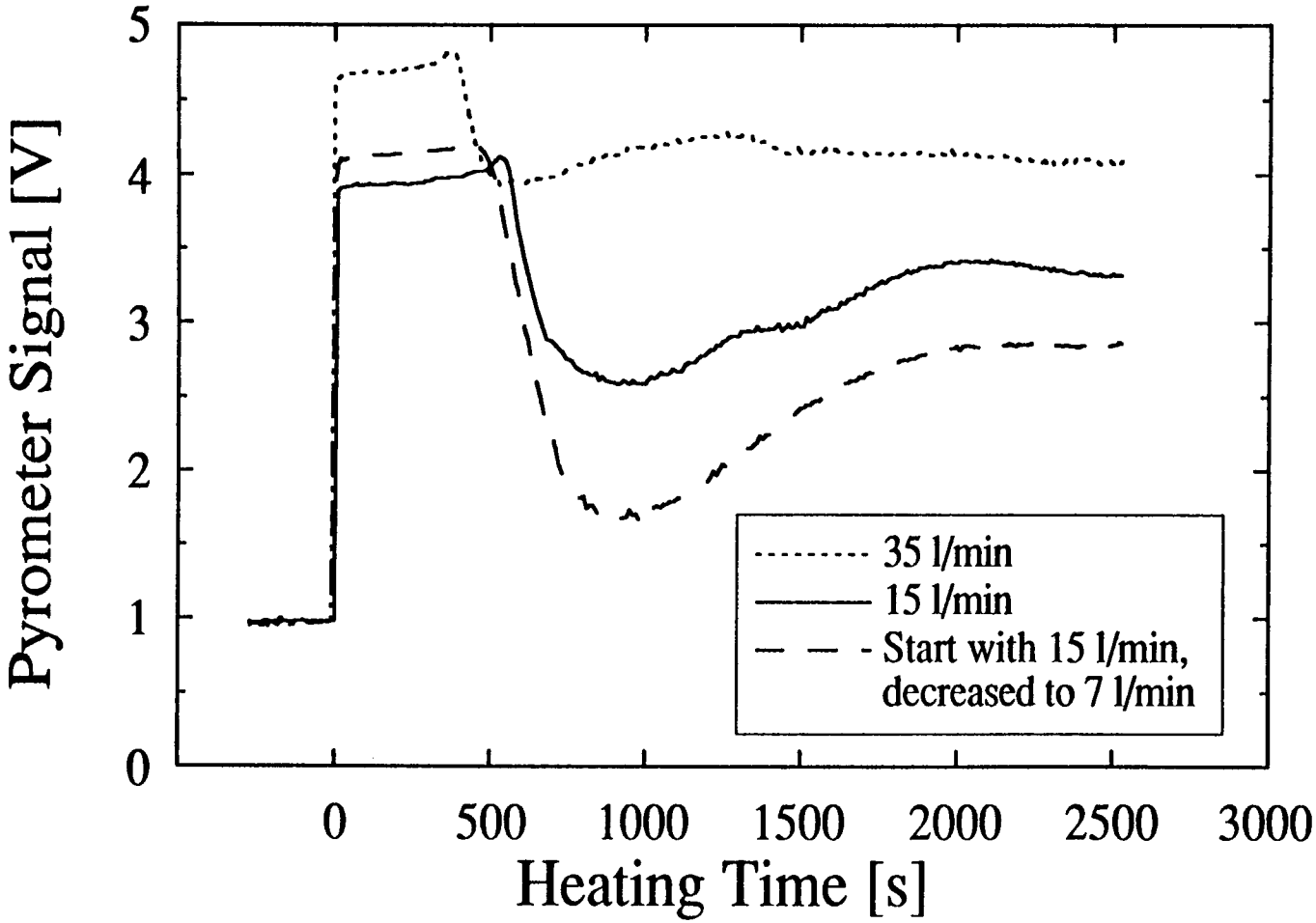

Figure 5.44 The effect of purge gas flowrate on the optical pyrometer signal

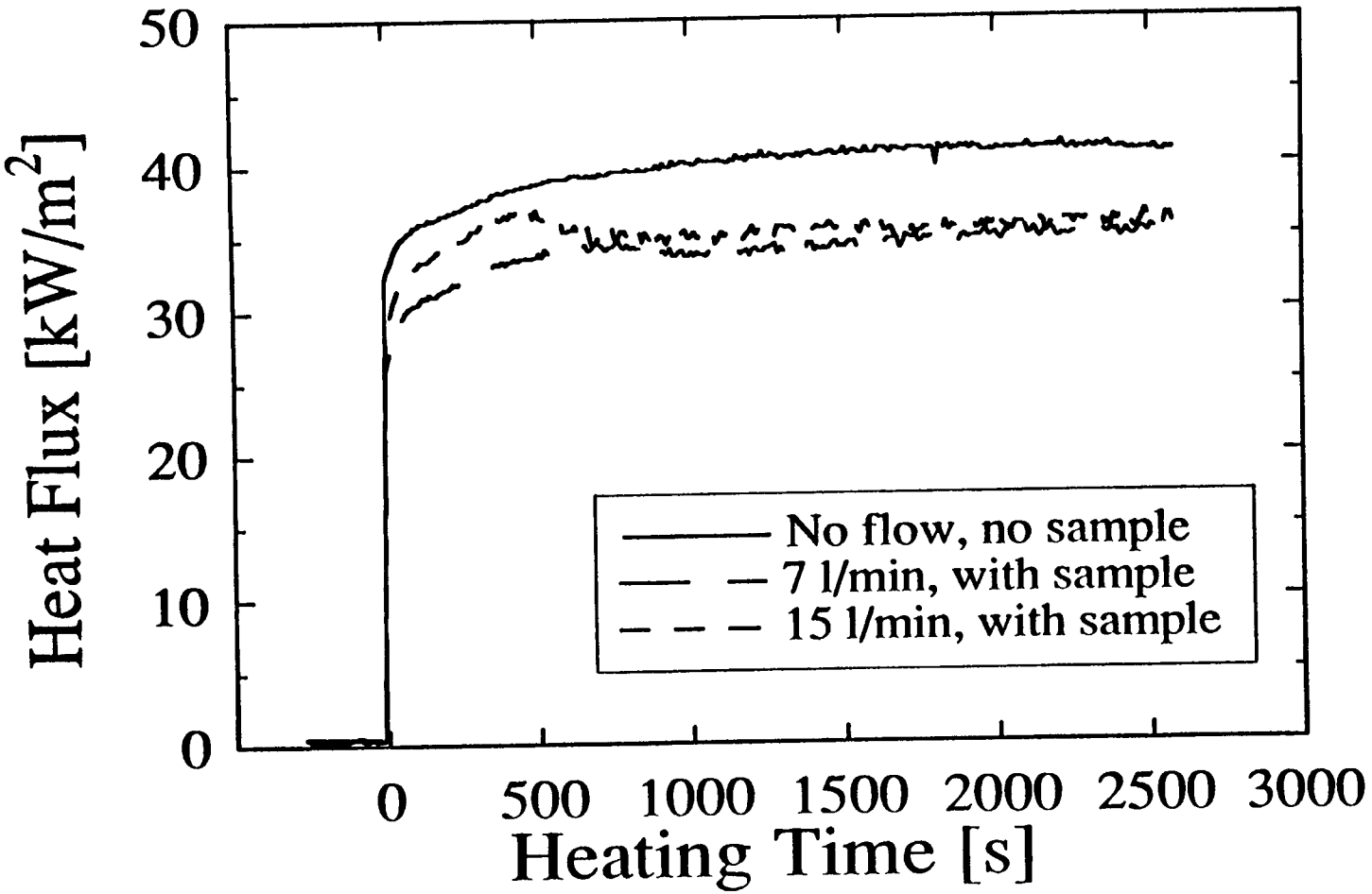

Figure 5.45 The effect of purge gas flowrate on heat flux

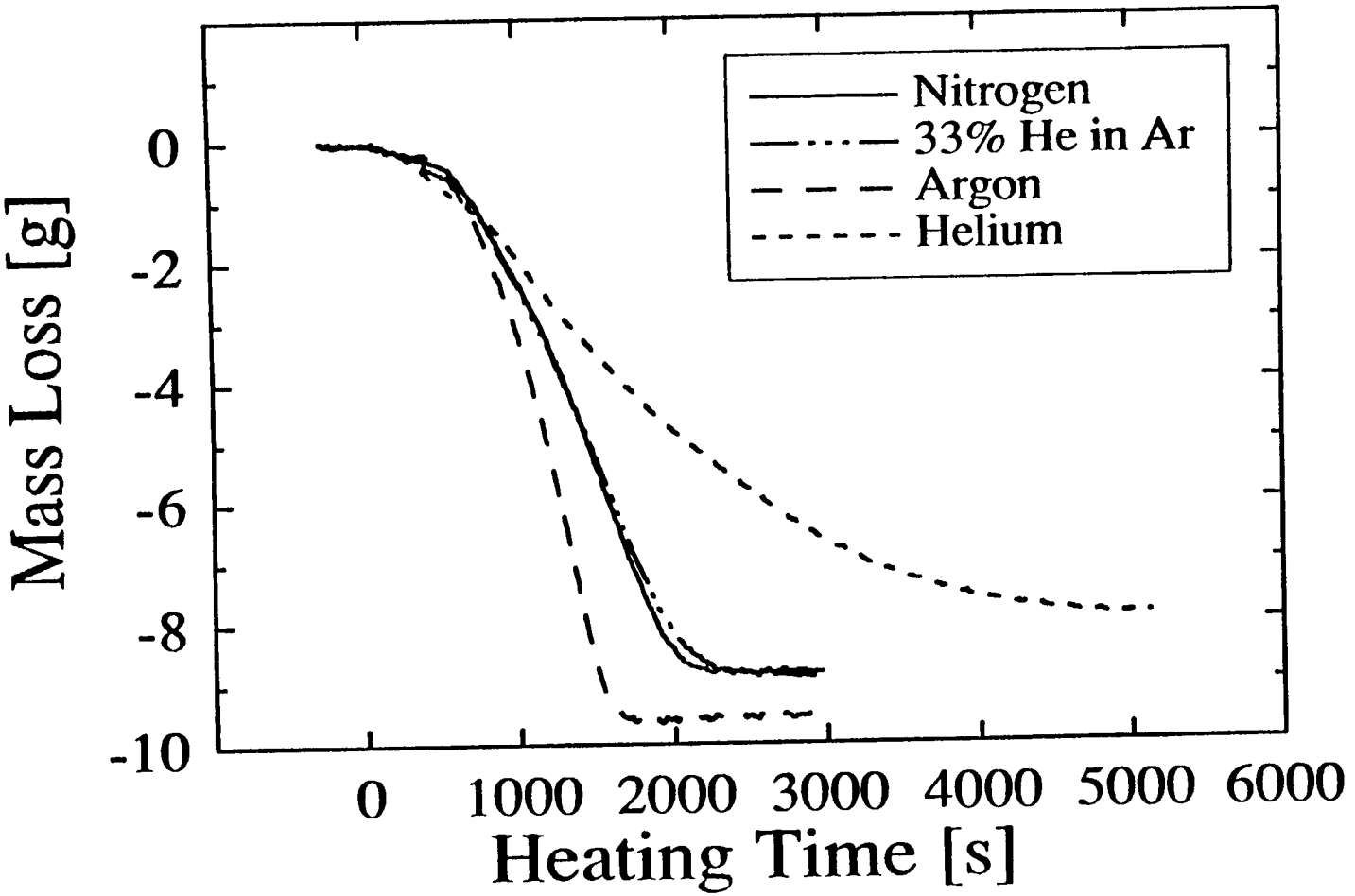

Figure 5.46 The effect of purge gas type on mass loss during pyrolysis of a high density sample under an incident heat flux of 40 kW/m^2

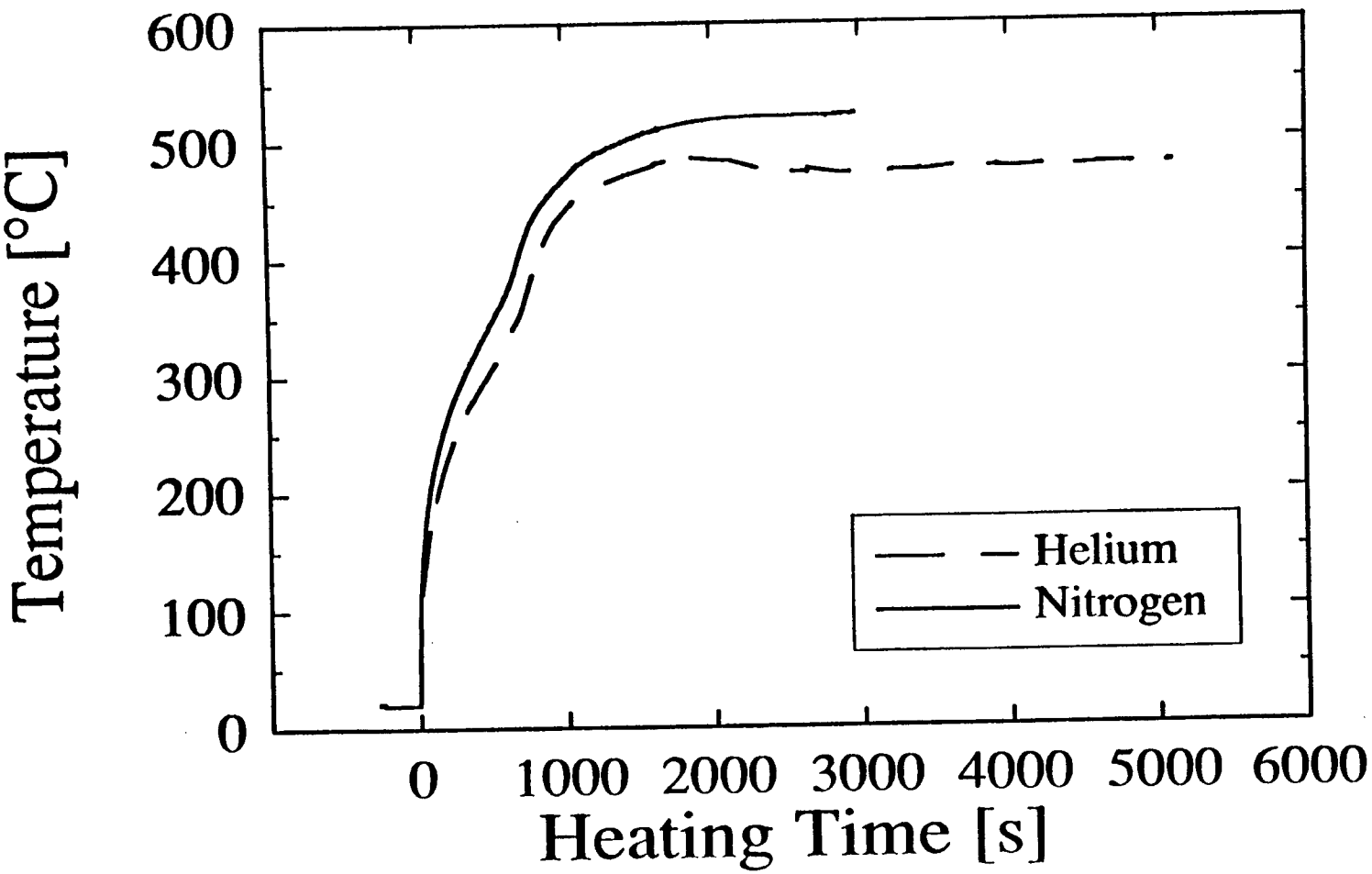

Figure 5.47 A comparison of front surface temperatures of a high density sample pyrolyzed when helium and nitrogen were used as purge gases under an incident heat flux of 40 kW/m^2

Figure 5.48a A micrograph of the front surface of a pyrolyzed cellulose sample (high density, incident heat flux of 40 kW/m^2)

Figure 5.48b A micrograph of the back surface of a pyrolyzed cellulose sample (high density, incident heat flux of 40 kW/m^2)

Figure 5.48c A micrograph of the back surface of a pyrolyzed cellulose sample (high density, incident heat flux of 40 kW/m^2)

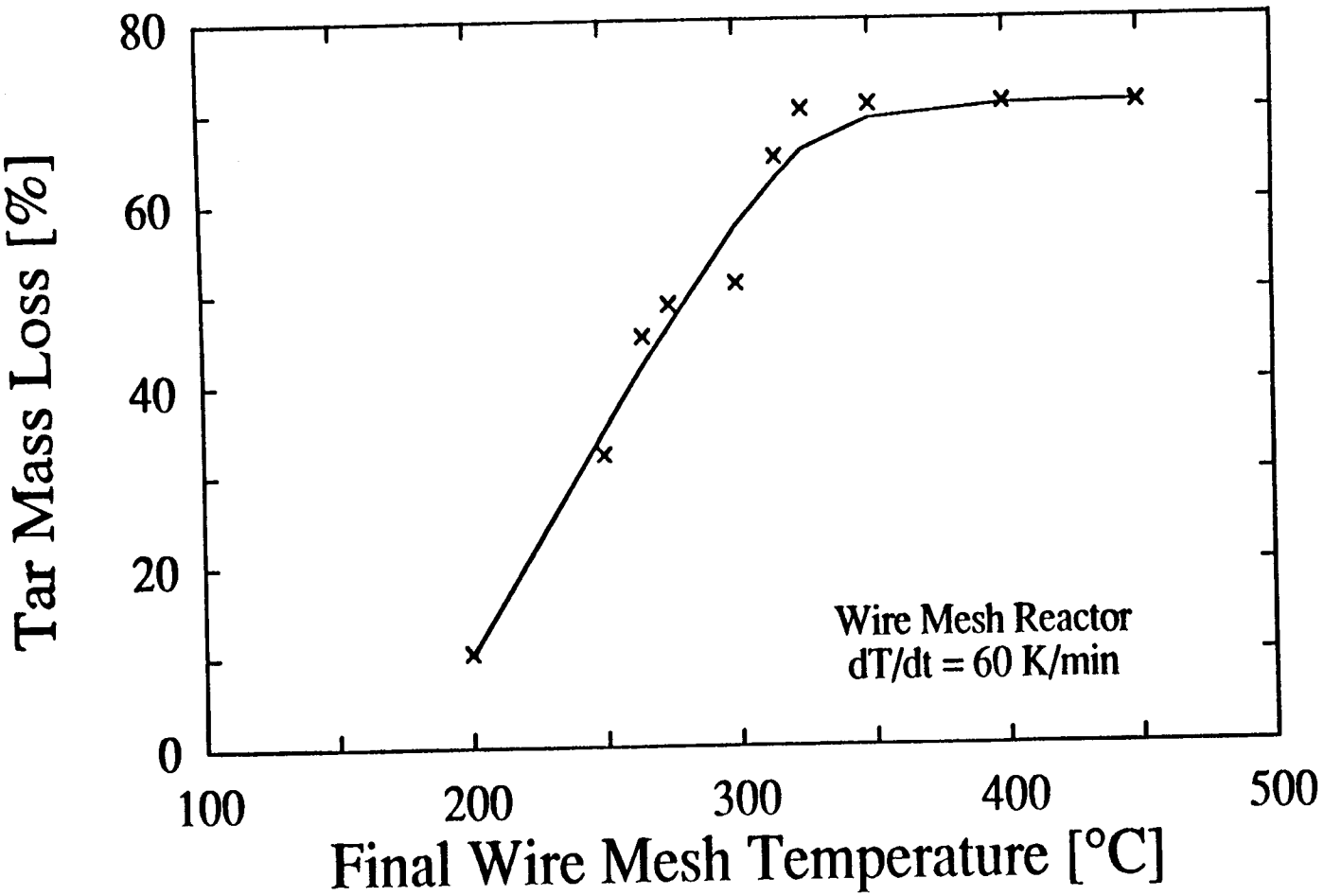

Figure 5.49 Tar mass loss as a function of temperature

6. THE KINETICS AND THERMODYNAMICS OF CELLULOSE PYROLYSIS

Several unanswered questions arose about the course and kinetics of cellulose pyrolysis, in light of the studies on cellulose behavior under simulated fire conditions. The inability to answer questions from those studies was a result of the existence of far too many variables governing cellulose pyrolysis under simulated fire conditions. For that reason the factors governing the wide variation in char yield remained unresolved. Furthermore, there was no means of establishing from the simulated fire results the heat effects of cellulose pyrolysis, mentioned on several occasions. In addition the kinetics of pyrolysis itself were shown to be important under low flux conditions, and these have not yet been discussed.

6.1 CHAR YIELD

One of the main issues of concern in modeling cellulose burning is the correct prediction of char yield. It was noted that char yield varies slightly with initial sample density and with the incident heat flux employed during the pyrolysis. It was demonstrated that the char yield varies significantly with the distance from the front, heated, surface of a sample. Obviously, knowledge of char yield is significant from both fundamental and practical points of view. From the fundamental point of view, char yield information can help in understanding the mechanism of cellulose pyrolysis. From the practical point of view, the char yield is an important piece of information for correctly describing a fire situation.

Obviously keeping more of the original mass of cellulose tied up in the form of solid char reduces the flaming combustion potential of the cellulose. This fact is, of course, what motivates the search for fire retardants to be added to the cellulose. Beyond this, the char itself is important for several reasons. If the cellulose-containing material is a structural,

load-bearing element in a building, the structural properties of the char, and its ability to protect interior portions of the structural element are critical. After the period of flaming combustion ends, the combustion of the char itself may be a significant feature of the fire event. The combustion of char is accompanied with large heat release due to the high heating value of the material. The reactivity of chars towards oxygen is inversely related to pyrolysis temperature, the lower the pyrolysis temperature, the higher its reactivity towards oxygen. That means that the most reactive chars would be in the interior of a char. In a real structure fire, for a vertical wall combustion model, this means that the most reactive char could be on the opposite side of a burning wall, in the area where flaming combustion did not yet occur. Therefore, the effort to identify the parameters that govern the char formation seems well justified.

The effect of density on char yield was studied as a continuation of studies under simulated fire environments. The system employed for these studies was a standard TGA, normally run at a heating rate of 60 K/min up to 550°C (so as to represent heating of the front surface of a sample, heated under 40 kW/m^2 in the simulated fire apparatus). In one case the temperature was raised to 700°C. The atmosphere was nitrogen at a flowrate of 50 ml/min. Samples used in this study were cubes, with sides of either of 3 mm or of 5 mm. They were cut from standard samples used in the simulated fire apparatus in such a way as to preserve the original sample density. Gas analyses were performed by FTIR for samples with sides of 3 mm.

Figure 6.1 presents fractional mass loss as a function of temperature for all three density samples in the form of cubes, 5 mm on a side. The effect of density is seen here on both char yield and kinetics, but for different reasons than in the simulated fire apparatus. The pyrolysis of bulk samples in the simulated fire apparatus was heat conduction-limited. In

the case of the TGA, the sample is uniformly heated and the assumption is that a sample is isothermal. However, in studies with large particles, one has to be cautious about the assumption that a sample is isothermal as will be discussed below.

The reason for the ordering of kinetics by density can be deduced from the data of Figure 6.2, which shows the mass loss of high density sample, the same one as shown in Figure 6.1, together with that for the cellulose powder (the same as used for pressing samples). Also shown in Figure 6.2 are temperature-corrected kinetics for the powder. There were two experiments performed with the powder. During the first experiment, the mass was recorded and during the second experiment, which was in all respects exactly the same as the first one, the temperature was recorded with a thermocouple embedded in the sample. The two experiments were then combined into one, with the corrected temperature applied to the powder mass loss, and these are the data plotted in Figure 6.2. The mass of powder used in these experiments was about 100 mg, depending on a sample density. In ordinary TGA studies, the use of such a large mass of powder would be avoided, for precisely the reason that is apparent. A large mass of powder will increase the likelihood of a heat transfer limitations, as is indeed revealed. Here, the use of a large mass of powder is appropriate, in that it illustrates what can happen with the massive cubes needed to study the effect of density. Clearly, the data show a temperature measurement problem. If it is assumed that a sample is spatially isothermal at the furnace temperature, the real sample temperature might easily be off by as much as 50°C. It should be kept in mind that the pyrolysis proceeds in a temperature range of about 50°C, as seen from Figure 6.2. The reason for the temperature discrepancy is heat absorption by the sample, both because of a pyrolytic endotherm as well as a sensible heat requirements. Both depend on the mass of a sample. In the case of different density samples, with approximately the same volume, the heat sink is larger for a higher density sample. This makes the temperature error larger.

Thus the high density sample mass loss appears to be shifted towards higher temperatures than the low density sample mass loss.

Hence, the conclusion is that the data of Figure 6.1 does not show a density effect on kinetics, due to, essentially, incorrectly measured sample temperature. However, the data of Figure 6.1 is useful for another purpose. It shows that there is an effect of density on the ultimate char yield. Therefore, the char yield is different only due to a density-related phenomenon. Figure 6.3 shows the variation of the ultimate char yield with the initial sample density for 3 and 5 mm cubes. The char yield data for 3 mm cubes are shown for a final temperature of 700°C, as well as for an intermediate temperature of 550°C, and the data for 5 mm cubes are shown for a final temperature of 550°C. The density effect, although not large, can be discerned. In the case of larger samples the difference is about 2% between low and high density samples. A possible explanation for this effect is a mass transfer limitation. As pyrolysis products (presumably the tars) flow outward through the particle, some may be cracked to lighter gases and deposit char as a product. It can be recalled that efforts to re-evaporate tar were only partially successful. As Figure 5.49 illustrated, the tars begin to escape at 180°C, and by 350°C the tar had all either escaped or been transformed to char. If it is assumed that tars might account for about 50% of the products, the amount of tars needed to decompose in order to leave an additional 2% char can be roughly calculated. It was shown that tars, upon complete pyrolysis at temperatures up to 450°C, yield about 30% char (Figure 5.49). That means that about 13% of the original tar should be decomposed in order to increase the char yield by 2%. At a first glance this amount might look a bit high. However, it is in agreement with amounts reported in the literature. Boroson et al. (24) found that for a residence times of about 1 s, homogeneous conversion of tar from wood pyrolysis was 30% at 600°C and 88% at 800°C. For heterogeneous cracking in the presence of carbon, the rates could be even higher. Therefore, it seems plausible that the reason for the increased char yield with

density might be tar decomposition. As in the bulk samples of the simulated fire experiments, the char layer acts as a fixed bed reactor for tar conversion. The higher the sample density, the higher the tar concentration and the better the tar-char matrix contact will be.

As can be seen from Figure 6.1 there is a very small amount of mass loss observed as the temperature is increased above 450°C after the rapid mass loss is complete. The reason for the small mass loss is slow char decomposition (31, 117). Figures 6.4 show cumulative yields of carbon dioxide (6.4a), carbon monoxide (6.4b) and methane (6.4c) on pyrolysis of cubes of 3 mm side. The amounts of light gases appear fairly independent of sample density up to about 450°C, where they start to deviate from each other. However, because of the temperature measurement problem the data can be more correctly viewed as function of remaining fractional masses, shown in Figures 6.5, the combined data of Figure 6.1 and Figures 6.4. Now it becomes clear, from Figure 6.5a that the density does make a difference on the total amount of carbon dioxide generated throughout the pyrolysis process. There is more CO_2 evolved per unit mass of sample when its initial density is higher. This is consistent with the hypothesis that more tars are being decomposed the higher the sample density. Obviously, CO_2 is also a primary pyrolysis product and the product of slow char decomposition. A similar density effect can be discerned from carbon monoxide yields shown in Figure 6.5b. Carbon monoxide also appears as a primary pyrolysis product and the product of slow char decomposition. Since the curves for CO_2 and CO yields from different density samples diverge with increasing mass loss, this indicates an increase in cracking to light gases with increase in temperature. Methane appears mainly as a product of slow decomposition of char (Figure 6.5c), probably during the aromatization of char structure, as a route of dehydrogenation. This late elimination of hydrogen from the structure increases with sample density, presumably because more

hydrogen-rich tar species were incorporated into the structure by the char-depositing reactions. Therefore, it seems likely that higher char yields are observed in higher density samples, due to an increased amount of decomposed tars.

As it became obvious that initial sample density affects the ultimate char yield by affecting the rate of tar escape from the pyrolysis zone, there was a need to determine how the sample size affects char yield. The effects of sample size were already noted in Figure 6.3. The larger the sample, the more char deposition is noted. In terms of the results of the simulated fire apparatus, the thicker the sample, the higher the char yield. It was in connection with the simulated fire apparatus results that another concern arose as well. It was noted that there was a tendency for tarry volatiles to bubble out around the edges of the sample, rather than all issuing directly and uniformly through the front face. This raised a concern about the directionality of the transport of volatiles. It appeared as though transport might be occurring laterally, parallel to the surface of the sample face.

To explore this possibility, a series of experiments was designed to study unidimensional volatiles transport. Thin wafers of pressed cellulose powder, as illustrated in Figure 6.6, were prepared of a constant thickness of 2 mm and a constant length of 20 mm, but of different widths. For that purpose, cellulose was pressed in the same manner as for use in the simulated fire apparatus. Discs of 38 mm in diameter were pressed to high density (about 1 g/cm^3) and to a thickness of 2 mm. From these discs, rectangular samples were cut with one side length fixed to 20 mm. The samples were heated in the same wire mesh reactor as was used for the tar evaporation experiments. In this reactor, once volatiles escape the sample, they are immediately carried out of the reactive zone and do not redeposit on the sample. The 20 mm length was determined as a maximum in order to have a uniform temperature within a sample in that direction and yet to have a large resistance to

the flow of tars in that direction. The only variable was sample width, which was varied from 1 mm to 23 mm. The temperature was measured by a thermocouple, positioned in the mesh in such a manner that the sample was in one mesh fold and the thermocouple in the other. The thermocouple signal was fed to a microcomputer for heating rate control and data logging. The mesh material was stainless steel. The possible catalytic effects of the mesh material were not studied here. However, that effect was addressed by Hajaligol (65) who used a similar system and found that the pyrolysis of cellulose was not affected whether a stainless steel or a gold wire mesh was used. The atmosphere during the pyrolyses was helium, the heating rate was 60 K/min up to the final temperature of 750°C. The char yield was determined by weighing the empty mesh and sample containing mesh before and after an experiment.

Data obtained in experiments in the heated wire mesh reactor are shown in Figure 6.6. The error bars are not included in this figure due to overcrowding. It should be noted that the masses were measured with an uncertainty of ±0.05 mg, which means that the uncertainty in the char yield determination was ±0.13% and less than ±0.01% for samples of 1 mm and 23 mm in width, respectively. Despite the data scatter the trend is obvious. The ultimate char yield is affected by the sample width up to about 9 mm, at which point it seems to level off. Figure 6.6 makes reference to a "grain structure". It was assumed, on the basis of the early simulated fire experiments, that the pressed cellulose samples had a "grain structure" as a result how they were pressed. This was because sample fracture, during pyrolysis, typically occurred in a direction perpendicular to the pressing direction (the pressing direction was normally also co-linear with the direction of incident flux). As was noted in section 5.5 above, however, we now believe that the fracture may have really been more a result of the one-dimensional pyrolysis wave propagation, in which significant sample shrinkage occurred behind the front. By other measures, the samples were fairly isotropic.

The results of Figure 6.6 appear to require reconsideration of the "grain structure" question. Since all samples have the same smallest characteristic dimension, 2 mm, it seems odd that any effect of width should be noted. The results of Figure 6.6 however appear fairly consistent with the data of Figure 6.3 in that the high density 3x3x3 mm cubes of Figure 6.3 gave a char yield of about 5.5%, compared to approximately 4.5-5% for 2x3x20 mm sheets in Figure 6.6. This means that the third, longest, dimension is of little importance, but the second dimension is of importance. When the wafers of Figure 6.6 became wider than 9 mm, the flow of volatiles apparently was forced to choose a route in the direction of the 2 mm dimension, suggesting that the resistance to flow in a direction parallel to the face of the wafer is more than 4 times less than the resistance to flow in a direction perpendicular to the face. These results clearly suggested that there is indeed a subtle role of grain structure in volatiles transport. We reconsider the evidence from the simulated fire experiments, which should higher char yields, but no indication of a role of grain structure.

To address the consistency question the data should be viewed on a comparable basis. A sample in the wire mesh reactor is isothermal, whereas a bulk sample pyrolyzed under simulated fire conditions was non isothermal. It was concluded that in the latter case the ultimate char yield is mainly determined by heating conditions. The ultimate char yield in the experiments in the heated wire mesh reactor were, at most, about 8%, and in the experiments under simulated fire conditions were about 20%, for the same sample density. That indicates a possibility that the ultimate char yield from samples pyrolyzed under simulated fire conditions is affected by the grain orientation but that it might be masked by the more important effects of heat transfer limitations. Indeed, some small differences in the ultimate char yield from different grain orientation samples were seen (see Figure 5.42).

Furthermore, it should be recalled that the surface layer char yield from Figure 5.39 was about 8.5%, similar to the char yield from pyrolysis of large width samples in the heated wire mesh reactor, which is about 7%. The samples in the heated wire mesh reactor were heated to higher temperature and that is probably the reason for slightly lower char yield. In bulk samples the real difference in char yields is seen for layers further from the heated surface, not because of the sample size, but because of the heat transfer effects. Hence, it can be concluded that the char yield data from bulk and thin samples are not inconsistent with each other. When both sets of data are analyzed on the same basis, similar yields are seen. Thus while there is no inconsistency in char yields, there is still a question about the importance of grain structure. We cannot firmly conclude on the basis of the data in hand. It is probable, that just in the simulated fire apparatus, the wafer samples pyrolyze from outside inward. If the heat transfer to the top and bottom faces of the wafer is better than to the sides, because of better contact with the wire mesh heating element, it might be that the process of carbonization itself creates a layered structure in an initially isotropic system. The main conclusion is that different transport effects can be important, to the extent of influencing char yields by several percent.

Some of the chars obtained from wider samples in the wire mesh reactor were cut to approximately one fourth of the original size and repyrolyzed under the same conditions as the original samples. These data are also shown in Figure 6.6. It can be seen that the char yields (which were calculated on the basis of the original sample mass) from repyrolyzed samples are slightly lower than from the original samples. The reason for this is probably due not to pyrolysis but to oxidation. The samples were handled in air and there is a possibility that some oxygen was adsorbed during the handling which subsequently caused char samples to oxidize.

Thus the data obtained so far for char yields from cellulose pyrolysis under controlled conditions can be summarized as follows. The manner in which the tars are transported out of the pyrolysis zone does make a difference. Effects of initial sample density and initial sample size were observed, indicating that the tars might be decomposed in the char structure as they flow out. The char yields obtained are however still, at least, twice as low as those commonly observed in pyrolysis under simulated fire conditions. Thus it might be concluded that, even with the tar transport limitations, the ultimate char yield is nowhere close to the ultimate char yields obtained in pyrolysis under simulated fire conditions and that there must be another effect responsible for the higher char yields in bulk samples. Again, the results for the powdered samples in Figure 6.2 suggest that even with a quite high heating rate of 60 K/min, pyrolysis will be complete by the time samples reach 400°C. On this basis, the in-depth pyrolysis of the bulk samples should be "complete" when a temperature of 400°C is reached, and yet, char yields are still much higher.

The heating rate might have an impact on the ultimate char yield from pyrolysis of cellulose (65, 68). To study this effect, cellulose powder was heated in a TGA at five heating rates up to 550°C in nitrogen at a flowrate of 50 ml/min. The heating rates employed were: 0.1, 1, 6, 15 and 60 K/min. The three higher heating rates represent an average heating rate to pyrolysis temperature of the front (60 K/min), middle (15 K/min) and back parts of a high density sample, pyrolyzed under an incident heat flux of 40 kW/m^2 in the simulated fire apparatus. The sample size was about 30 mg in all cases and the sample pan (platinum, 11 mm in diameter and 3 mm deep) was open. The data are represented in Figure 6.7. It should be noted that the temperature in Figure 6.7 is the corrected temperature; i.e., measured by a thermocouple in the sample, as noted above. Since the sample holder was fairly large it had to be confirmed that there were no temperature gradients, due to nonuniform heating, present within the sample holder. The ultimate char yields were

observed to be similar for all heating rates and they are shown in Figure 6.8, where the logarithmic axis was used for representing heating rate in order to emphasize the effect at low heating rates. The effect is clear, the ultimate char yield increases with decrease in heating rate. As in the cases of different density samples and different sample sizes the effect is obvious but the char yields are still at least twice lower than observed in case of bulk sample pyrolysis under simulated fire conditions.

The ultimate char yields were also measured following heating in a differential scanning calorimeter (DSC). Only the char yield data obtained from DSC measurements will be shown here; the heat flow data will be presented below. The sample holders used for DSC measurements were standard covered aluminum pans. The pans were 7 mm in diameter and 2 mm deep (emphasis is made here concerning preparation of sample holders because they play an important role, as will be seen below). Sample pan covers were 1 mm deep, which means that the active sample holder was 7 mm in diameter and 1 mm deep. The pyrolysis of cellulose involves large mass loss and, for that reason, the sample pans were not hermetically closed (crimped). In addition to leaving the pan cover loose, there were two to ten pinholes made in the pan cover to allow for volatiles escape. Also, in order to compare the mass loss with the heat flow during pyrolysis, several experiments were performed in a TGA using the same sample holders as in the DSC. The experiments with the DSC sample holders were done with cellulose powder at heating rates of 1, 6, 15 and 60 K/min. Two sample sizes were used: about 10 mg and about 1mg. The atmosphere was nitrogen at a flowrate of 50 ml/min.

A summary of the data is shown in Figure 6.9, which also includes the data of Figure 6.8. The error bars are not included in order not to crowd the plot. Again, the uncertainty in sample mass was 0.005 mg (a more precise balance was used, due to the smaller mass measured), which gives an uncertainty in char yield of 0.6% (about 13% of the char yield

value) and of 0.06% (about 4% of the char yield value) from samples of initial mass of about 1 mg and from samples of initial mass of about 10 mg respectively. The sample size effect can be seen by comparing the data at the same heating rate (note that the heating rate was normalized by 60 K/min). The smaller the sample size the lower its char yield on pyrolysis. There is an effect of number of pinholes, a higher char yield was observed for two as opposed to ten pinholes. That result is somewhat similar to the data of Figure 6.3. The sample with lower initial density can be viewed as a sample with more "holes" in its structure.

Finally, it can be seen how the char yields of about 20% were achieved in the bulk samples, pyrolyzed under simulated fire conditions. When the effect of low heating rate is combined with mass transfer limitations, as exist in pans with only two pinholes the char yield quickly approaches 20%. Therefore, it is obvious from Figure 6.9 that resistance to volatiles escape, coupled with low heating rate, can be responsible for high char yields, of the order of 20%. The situation studied in the DSC pans with holes is of course different than seen in the pyrolysis of bulk samples. Wherever the tar decomposition takes place, however, the important conclusion is that it happens and that it is greatly amplified by the effect of heating rate.

This reasoning leads to a better understanding of the roles of heat and mass transport during the pyrolysis of bulk samples. The process, as seen before, is heat conduction limited, which gives rise to temperature gradients in a sample. These cause different parts of a sample to be heated at different heating rates. The tars are forced to flow out of the pyrolysis zone through the char layer, which is at higher temperature than the temperature in the pyrolysis zone. Tars tend to leave more char behind, in lower temperature zones deep within a sample. The front surface of a sample does not experience much of either heat or

mass transport limitations and its char yield is typical of those seen in small particle pyrolysis. Summarizing the above conclusions, it appears that in pyrolysis of bulk samples under simulated fire conditions, a char yield gradient can be expected within the sample.

This is an important conclusion from the point of view of numerical modeling. Although there are some attempts in the literature to predict the char yield (31, 41, 176) it does not seem to be a simple process. The references cited all deal with "four carbon residue" model, which predicts that four carbons from each cellulose ring unit undergo aromatization. Under that model the char yield is 48/162 or 29.6% which is clearly quite different from many char yields reported here. Even the "four carbon residue" model, as simplified as it is, contains several dehydration and depolymerization steps. Obviously, each one of them would proceed at a certain rate, with certain kinetics, which probably would not be an easy task to model numerically. Unfortunately, this means that the mathematical model will likely have to incorporate an empirical char yield. The problem is dealt with here, as will be seen later, by artificially creating a char yield profile, in agreement with the experimentally observed char yield profile.

6.2 HEAT EFFECT OF PYROLYSIS

The heat effect of pyrolysis was studied in a standard differential scanning calorimeter, at heating rates of 1, 6, 15 and 60 K/min up to 550°C. The atmosphere was nitrogen at a flowrate of 50 ml/min. The samples were in the form of cellulose powder, with a typical sample load of about 10 mg. The samples were placed in a loosely covered standard aluminum pan, with two pinholes in the pan cover. In light of the results of Figure 6.9 it is clear that the processes in a DSC might be less transport limited when small samples and a large number of pinholes are used. However, it should be borne in mind that the reason for

this part of the study was to gain a better understanding of processes taking place during pyrolysis of bulk samples under simulated fire conditions. The DSC work was performed in a transport-limited arrangement of the sample pan, recognizing that it is difficult to completely characterize the transport limitations under any circumstances, but knowing that they are important in real systems.

Variation of heat flow with the sample temperature is shown in Figures 6.10a, b, c and d for heating rates of 60, 15, 6 and 1 K/min, respectively. The heat flow is presented with respect to the initial sample mass. It is also represented in units of heat per unit time, which makes the data at different heating rates non comparable as such (the heating rate affects the measured signal). A more comparable basis can be found by dividing by the heating rate, as the resulting values will be in the units of heat per unit temperature. However, that type of representation is not much more useful, except that it gives a comparable graphic impression of the peaks. The data will be reworked onto a more useful basis below.

There are several features of the data of Figures 6.10 that need consideration. An endotherm, due to moisture evaporation, is observable at temperatures near 100°C. The endotherm shifts to higher temperatures with heating rate, as might be expected for a transport-limited evaporative process. The integration of the heat flow versus temperature curve for the moisture evaporation endotherm gives a value of 70±6J/g. That means that if moisture is held in cellulose with a ΔH for adsorption comparable to the latent heat of evaporation of pure water, the moisture content in the cellulose is 3.2±0.3%. This is a little bit lower than the value specified by the manufacturer (7.68%). It should be recalled that cellulose moisture content depends on the relative humidity. The DSC experiments were done over two days, during the heating, low relative humidity, season. Another reason for low moisture content is that all samples were kept in a flow of dry nitrogen at the starting temperature of an experiment (30°C) for five minutes. However, for the instrument to start

isothermal hold, it was necessary for a temperature equilibrium to be achieved, which took no less than 10 minutes. That means that, in total, the samples were actually pre-dried in a stream of dry nitrogen for at least 15 minutes, at temperatures close to 30°C. The relatively high 8.6%, uncertainty in the total heat of moisture evaporation is due to the poorly defined evaporation peak onset. The moisture evaporation starts at such low temperatures that the initial transient, due to the beginning of heating, overlaps the start of the moisture evaporation peak. This problem can be easily solved, by starting a scan at sub-ambient temperatures, so that two effects, initial transient and moisture evaporation, can be separated. However, the moisture evaporation was not of the main concern here and the separation of the effects was not performed. The more important effects of concern, namely the heat effects of pyrolysis, are not affected by the initial transient.

As a sample pyrolyzes, aside from the mass loss and the heat effect, there is a continuous change in its heat capacity. This is partly due to the change in specific heat capacity, and more importantly, to the change in total mass in the sample pan. For this reason, the baseline in a DSC thermogram changes. The effect can be seen in Figures 6.10. Just before the pyrolysis onset the heat flow can be predicted by the variation of cellulose heat capacity with temperature (Chapter 4), taking into account the rate of heating and the DSC cell calibration coefficient. Likewise, the heat flow after the pyrolysis is finished can be predicted knowing the char heat capacity (Chapter 4), heating rate and the char mass at the temperature where the pyrolysis was finished. It should be noted that the heat flow during pyrolysis depends upon the relative amounts of cellulose and char in an unknown way. From the TGA data, it was established that the mass of a sample changes in a sigmoidal fashion between cellulose and char. If the heat capacity per mass were constant, that means that the thermogram baseline would change in a sigmoidal fashion. This would also be true if the heat capacity depends linearly on relative amounts of cellulose and char in material

that undergoes pyrolysis. Unfortunately, there are no means to accurately correct the baseline during pyrolysis, since the pyrolysis is always accompanied by large mass loss. The simplest baseline shift during pyrolysis was thus assumed, a linear change of baseline, and this was used during the integration of peaks.

The data of Figures 6.10 are useful for recognizing the complexity of heat effects of pyrolysis. At the highest heating rate (60 K/min) it can be seen that the pyrolysis proceeds as a completely endothermic process. As the heating rate decreases, there is evidence of another, exothermic, process which follows after the endothermic process is complete in cases of heating rates of 15 and 6 K/min. For the lowest heating rate (1 K/min) the exothermic process started before the endothermic process was complete, as indicated by a sharp change from endotherm to exotherm in Figure 6.10d. The nature of these endothermic and exothermic shifts with heating rates can be explored by a crude kinetic analysis. Of course, a shift with heating rate means that a process is activated. The higher the activation energy the greater the shift. The kinetics of the process will be analyzed in more detail below, here the point is made only that there is a difference in activation energy of endothermic and exothermic process, what cause them to overlap at low heating rates and to move from each other at high heating rates.

The endothermic process probably represents a depolymerization process. It cannot be said, based on the DSC data alone, how the depolymerization takes place. The data obtained here can be compared to the physical model proposed by Mok and Antal (122), presented in Figure 6.11. According to their model depolymerization may take place either to yield tar or through anhydrocellulose to yield volatile intermediate. Under both routes the exothermic process is associated with the char formation. The existence of two endotherms was not seen in this work, unless they perfectly overlap at all heating rates. Similarly, there

were not two exotherms seen. The exotherms seen here may be due to carbon oxides desorption and/or to char forming reactions and, as can be seen from Figures 6.10, they cannot be termed strong, except in the case of the lowest heating rate. Therefore, from the DSC data alone a kinetic model cannot be postulated.

An analogy can be made between the heat needed for decomposition and the mass loss. For that purpose the data from Figures 6.10 were integrated up to a certain temperature (units WK/g), divided by the heating rate (units K/s) and the resulting variation of heat per unit initial sample mass (units J/g) with temperature was combined with the mass loss data. Figure 6.12 shows how the net heat absorption due to reaction (corrected for heat capacity variation) varies with mass loss at different heating rates. Obviously, the total heats of pyrolysis are endothermic for all heating rates, as indicated by the last point on each curve. For fractional remaining mass up to between 75 and 80%, the net heats are fairly similar for all heating rates. This indicates a similar course of pyrolysis to that point, regardless of heating rate. Thereafter, depending on heating rate, the curves follow different paths. After 20-25% mass loss, the exothermic process starts to be significant and the curves deviate from each other and from the near linear behavior of the 60 K/min curve. Although the DSC thermogram for heating rate of 60 K/min, in Figure 6.10a, seemed to suggest that there was no evidence of the exothermic process, the data of Figure 6.12 show a slight deviation from linearity, suggesting that even in that case there are competing processes involved.

The data of Figure 6.12 is in the agreement with the findings in the literature. It is well established in studies of the effect of impurities and flame retardants on cellulose pyrolysis that such pyrolysis leads to more char than in the absence of impurities, and also that the heat of pyrolysis is exothermic (e.g. 29, 40). That observation is corroborated with the data

of Figure 6.13 which shows the heat of pyrolysis as a function of char yield. The data obtained in this work is compared to that of Mok and Antal (122). It can be seen that the higher the char yield, the less exothermic the heat of pyrolysis. That means either that the char formation reactions proceed with a significant degree of exothermicity or that they preclude the endothermic process leading to more tar and less char formation. The slopes of the results, from this work and from (122) agree well, they are -3.4 kJ/g of char deposited and -3.6 kJ/g of char deposited, respectively. That means if the char yield is increased for 1% when the observed heat of pyrolysis was about 400 J/g and the char yield was 10% (0.1 g of char/g of cellulose) the heat of pyrolysis will change for -34 J/g or 8.5%.

The process of char formation was earlier noted to correlate with increased yields of gases. The "ideal" char formation process would involve the reaction:

$$(C_6H_{10}O_5)_n \rightarrow 6n\ C + 5n\ H_2O$$

In this reaction, the maximum theoretical limit of char formation, 44%, is implied. Cracking to CO_2, CH_4 would decrease the amount of char deposited. It has been reported that the heat of combustion of cellulose itself is approximately 16.7 kJ/g (higher heating value-from 177). Using this value the heat of formation of cellulose may be estimated from:

$$\Delta H_{f,cellulose} = \Delta H_{f,products} - \Delta H_{combustion}$$

The products of combustion are assumed to be those for complete combustion:

$$C_6H_{10}O_5 + O_2 \rightarrow 6\ CO_2 + 5\ H_2O(l)$$

and $\Delta H_{f,CO_2}$ = -393.6 kJ/mol, $\Delta H_{f,H_2O(l)}$ = -285.8 kJ/mol, $\Delta H_{f,O_2}$ = 0. The heat of combustion, on a comparable basis, is $\Delta H_{combustion}$ = -2705.4 kJ/eq($C_6H_{10}O_5$). The value of $\Delta H_{f,cellulose}$ is calculated to be -1085 kJ/eq($C_6H_{10}O_5$). Returning to the calculation of the heat of formation, the enthalpy is:

$$\Delta H_{char\ formation} = \Delta H_{f,H_2O(g)} - \Delta H_{f,cellulose} =$$

$$= 5(-241.8)kJ/mole - (-1085)kJ/eq(C_6H_{10}O_5) = -124\ kJ/eq(C_6H_{10}O_5)$$

or $\Delta H_{char\ formation}$ = -1.7 kJ/g C.

This process is in fact exothermic, but inconsistent with the observed magnitude of the char-forming process. But it should be remembered that char formation implies that some tars could not escape. Extrapolation of the correlation of Figure 6.13 back to zero char yield will result in an apparent ΔH of pyrolysis of about 758 J/g. For each gram of tar cracked, there is a "loss" of this amount of endothermicity. Each gram of tar cracked yields only 0.44 g carbon, so the actual "loss" per gram of extra char is 758/0.44=1.7 kJ/g C. Thus the change in net heat of reaction will be 1.7 + 1.7 = 3.4 kJ/g C, in agreement with what is derived from the slope of Figure 6.13. The assumption of the form of the char forming reaction is not particularly important. For example, had the reaction been consistent with the deposition of four carbons per glucose residue, if it was assumed that the gas products consisted only of carbon dioxide, water and methane, it could be shown that:

$$C_6H_{10}O_5 \rightarrow 4\ C + CO_2 + 3\ H_2O + CH_4$$

For this reaction, given that $\Delta H_{f,CH_4}$ = -74.9 kJ/mole, the enthalpy of this reaction would be:

$$\Delta H_{\text{char formation}} = -153\ \text{kJ/eq}(C_6H_{10}O_5) = -2.1\ \text{kJ/g C deposited}$$

Then the change in the net heat of reaction is in this case 3.8 kJ/g C deposited. This calculated value is also close to the measured value of Figure 6.13.

It is clear, then, that the effect of char deposition on the net heat of reaction derives from the reduction of a strong endotherm associated with tar evolution and the exotherm associated with the cracking of the tars.

Since the actual DSC spectra show little separation of the endo- and exothermic processes at heating rates of 6, 15 and 60 K/min, and give only a hint of separation at 1 K/min, then it is clear that the kinetics of the tar evolution and deposition processes must be quite similar. There is no clear separation of these two competing processes under most conditions of

relevance in fire situations. The fact that the exotherm occurs at a very slightly higher temperature than the endotherm in the 1 K/min case, but is practically coincident at higher heating rates means that the endothermic processes are probably characterized by a very slightly higher activation energy than the exothermic, but a firm conclusion in this regard requires a discussion of reaction order as well.

The data of Figure 6.13 are also significant from the point of view of mathematical modeling of pyrolysis. Since it was observed that the char yield changes as a function of distance from the front, heated, surface in bulk samples and since the heat of pyrolysis correlates well with the char yield heat sink will be a function of depth in the sample.

The path dependence of cellulose pyrolysis was addressed in an experiment that involved heating a sample at a heating rate of 1 K/min to 275°C, at which time the heating rate was changed to 60 K/min. The temperature of 275°C was chosen to get as close as possible to the pyrolysis onset at a heating rate of 1 K/min. The two step heating thermogram is compared to the thermogram of single step heating, at a heating rate of 60 K/min, in Figure 6.14. There is a baseline shift due to the change of heating rate, at a temperature where the heating rate was changed. Apart from the effect of heating rate on a baseline, which is apparently different, the endothermic peaks are very similar. It can be, therefore, concluded that slow heating up to the temperature just before the pyrolysis onset does not make any difference in overall pyrolysis thermodynamics, it appears as though the sample was always heated fast. This question was pursued further, now with the change in heating rates right in the middle of the exotherm, observed at a heating rate of 1 K/min. The heating rate was changed from 1 K/min to 60 K/min at a temperature of 327°C and the comparison with single step fast (60 K/min) heating is shown in Figure 6.15. There is the usual first part of an endotherm, associated with heating at a rate of 1 K/min, observed, since that part

was not affected with the heating rate change. The appearance of the endotherm after the heating rate switch is interesting. As expected it is at much lower temperature than commonly seen in the case of 60 K/min heating rate. This is because the decomposition process is already well under way at the time of the heating rate switchover. The relative "delay" of the endotherm in the straight 60 K/min heating is a predictable consequence of activated kinetics. Apparently, the magnitude of the endotherm observed after the heating rate change is significantly lower than the endotherm observed at 60 K/min (83 J/g versus 344 J/g). Furthermore, the endotherm is followed by an exotherm not usually seen in the 60 K/min case. The first of these changes is expected, since a significant extent of conversion had already taken place at low temperatures due to the 1 K/min heating, the subsequent endotherm at 60 K/min could not be expected to be as strong. The second of the changes-occurrence of a small exotherm following the 60 K/min heating period-gives another indication of what is responsible for the exotherms. The deposition of tars during the low heating rate period gives rise to structures in the char which, while themselves no longer volatile, can further exothermically decompose to light gases at higher temperatures.

The data thus suggests that heating at a low rate involves promotion of the tar deposition and cracking processes. The tar evolution processes are favored at higher heating rates, because the higher temperatures that favor evolution are attained more quickly. Interestingly, because the pyrolysis process follows the same generally endothermic pathway initially, regardless of heating rate (see Figure 6.12), there is more to the issue than a simple competition between high and low activation routes. It is easy to appreciate that without the insights provided by such thermal data, there has been much controversy as to the kinetics of pyrolysis.

6.3 KINETICS OF PYROLYSIS

The kinetics of cellulose pyrolysis were studied in a TGA. Two approaches were taken. The first involved isothermal pyrolysis after ramping at a specified heating rate to that isothermal temperature. There were two heating rates used, 1 K/min and 60 K/min and four isothermal temperatures examined: 265°C, 288°C, 311°C and 334°C after 1 K/min ramping and 286°C, 311°C, 334°C and 371°C after 60 K/min ramping. The second, more common TGA approach involved heating at a constant heating rate to 550°C. The heating rates employed were 0.1, 1, 6, 15 and 60 K/min. A typical sample mass of 30 mg and a nitrogen purge at a flowrate of 50 ml/min were used in both approaches .

Figures 6.16a and 6.16b respectively show the remaining fractional mass as a function of time for 1 K/min and 60 K/min ramping to isothermal conditions. The time on the abscissa of Figure 6.16 is the real time of an experiment, it includes ramping as well as the isothermal period. It should be noted that each curve in Figures 6.16 represents a separate experiment, with a fresh sample used for each experiment.

The analysis of the data of Figures 6.16 requires extreme caution. It is very important to determine a consistent basis for kinetic parameter calculations using data from different conditions. The calculations were performed here for the same fractional remaining mass. That was done in order to avoid ambiguities about the order of reaction and the final mass. There is evidence in the literature that cellulose pyrolysis might proceed with different order at different extents of reaction. The assumption was also made here that the final char mass is comparable in all cases, although it was shown before that it is not true. However, it will be justified below that this assumption is valid in this case, in that the calculation does not seem to be very sensitive to the final char mass.

The Arrhenius equation for a general, n-th order, reaction reads:

$$\frac{d\left(\frac{M-M_f}{M_0-M_f}\right)}{dt} = -\left(\frac{M-M_f}{M_0-M_f}\right)^n A \exp\left(-\frac{E_a}{RT}\right) \qquad (6.1)$$

where:

t - time

M - mass at time t

M_0 - initial mass

M_f - final mass

n - order of reaction

A - pre-exponential factor

E_a - activation energy

R - gas constant

T - temperature

Taking the logarithms of both sides of equation (6.1) gives:

$$\ln\left\{-\left[\frac{d\left(\frac{M-M_f}{M_0-M_f}\right)}{dt}\right]\right\} = \ln\left[A\left(\frac{M-M_f}{M_0-M_f}\right)^n\right] - \frac{E_a}{RT} \qquad (6.2)$$

The activation energy can be obtained in a usual manner, by taking the derivative with respect to reciprocal temperature of equation (6.2) if the activation energy is evaluated at a constant value of conversion $(M-M_f)/(M_0-M_f)$, i.e.:

$$E_a = -R \frac{d \ln\left\{-\left[\frac{d\left(\frac{M - M_f}{M_0 - M_f}\right)}{dt}\right]\right\}}{d\left(\frac{1}{T}\right)} \qquad (6.3)$$

The importance of eliminating the reaction order is apparent. By performing each experiment with a fresh sample and by performing the calculations for the same fractional remaining mass, the order of reaction became irrelevant.

The mass loss rates were obtained from the mass loss data at different temperatures. Again, the time derivatives were taken at the same fractional mass loss for all data sets. With those derivatives, either from different isothermal experiments or from different heating rate experiments, the Arrhenius plot was constructed and the activation energy was determined from the slope of the curve.

To determine the sensitivity of the calculation to the final mass of a sample equation (6.3) can be rearranged to get:

$$E_a = -R \frac{d \ln\left\{-\left[\frac{1}{1 - M_f/M_0}\right]\left[\frac{d(M/M_0)}{dt}\right]\right\}}{d\left(\frac{1}{T}\right)} = -R \frac{d \ln\left[-\frac{d(M/M_0)}{dt}\right]}{d(1/T)} \qquad (6.4)$$

The second equality applies only if (M_f/M_0) is a true constant. The derivative of mass with respect to time was measured in the TGA. Therefore, all the variables in equation (6.4) were measured except the final mass. Figure 6.17 shows an example how the activation energy was determined from the data of Figure 6.16a, at a remaining fractional mass of 40%. The slope of the line, determined by least squares linear fit, which is essentially the

graphical analog of equation (6.4) at equal masses for different isothermal experiments, is -25.5 kK, which gives an activation energy of 212 kJ/mole.

The sensitivity of the activation energy determined from equation (6.4) to the char mass was checked for the case of isothermal pyrolysis after heating at a heating rate of 1 K/min (the data shown in Figure 6.16a). The final mass (or char yield) was varied by ±2%, the final mass of a sample pyrolyzed at 311°C was fixed at 10% of the initial mass and the final masses of samples pyrolyzed at 288°C and 328°C were assumed to be 12% and 8% of the initial mass respectively. From equation (6.4) the activation energy, for a remaining mass of 40% (M/M_0=0.4) was calculated to be 209 kJ/mole. Again if the final char mass is assumed to be the same, it drops out of the calculation, since in that case it represents a constant in equation (6.4). The value for activation energy with the constant final mass was 212 kJ/mole (Figure 6.17), or about 1.4% more than the one calculated with the different final mass. The difference between calculated activation energies with and without the final char mass increases as the difference between char yields increase. The difference was calculated if the final mass of a sample pyrolyzed at 311°C were 20%, and the final masses of samples pyrolyzed at 288°C and 328°C were assumed to be 30% and 10% of the initial mass respectively. With these, clearly distorted values, an activation energy (again for M/M_0=0.4) of 195 kJ/mole was calculated, or about 8% less than the activation energy calculated with the constant final mass. This calculation shows that the difference attributable to assuming M_f/M_0 constant is not large. Furthermore, since the temperatures at which the pyrolyses were performed were so close, there is no reason to believe that the ultimate char yield would be much different than ±2%, relative to some middle temperature. That means that the activation energy should be certain to within ±1.4%, at least as far as the error due to the ignoring variations in char yields are concerned.

Activation energies were determined from the data shown in Figures 6.16, in a manner

similar to that shown in Figure 6.17, at several values of remaining mass. An interesting feature was observed for isothermal pyrolysis after heating at a 60 K/min heating rate. An example of the Arrhenius plot is shown in Figure 6.18, for a remaining fractional mass loss of 40%. It can be seen that the linear regression through all four experimental points is not as good as the regression observed in Figure 6.17. The activation energy determined from the regression was 190 kJ/mole. This value is not much different from the value reported by Lipska and coworkers of 176 kJ/mole (110, 111). However, if the temperature range is divided in two regions, below and above 600 K, and if the activation energy is calculated for those two regions, it can be seen that the values at low and high temperature are 226 kJ/mole and 152 kJ/mole, respectively. These two values are very close to the two values most frequently cited in the literature (see Chapter 2.2.4). Of course, the conclusion based only on two pairs of points is highly dangerous, but it will be shown below that the conclusion about the existence of two activation energies is supported by other data.

A summary of the activation energy data is shown in Table 6.1. The very beginning of pyrolysis is not included in Table 6.1 due to the presence of transient, the temperature was not stable during the early mass loss. For the reasons noted above, the data for isothermal pyrolysis after heating at 60 K/min heating rate was divided in two parts, below and above 600 K. The data for isothermal pyrolysis after heating at 1 K/min heating rate was below the threshold level of 600 K for all experiments, except for the one performed at highest temperature of 601 K. It can be seen from Table 6.1 that the activation energies from the 1 K/min and 60 K/min experiments agree very well in the low temperature region and the mean value is 221 kJ/mole with a standard deviation of ±6 kJ/mole. In the high temperature region, however, the activation energy increases with the mass loss (conversion). These data are also graphically presented in Figure 6.19. As it is evident from both Table 6.1 and Figure 6.19 the increase in activation energy is beyond the standard deviation of ±6

kJ/mole seen in low temperature region.

Table 6.1 also shows pre-exponential factors. They were calculated from the intercept of the linear regression, as shown in equation (6.2). It is obvious that the calculation of pre-exponential had to include a reaction order, which was here assumed to be unity. The char yield (final mass) was assumed to be 20%, except for the remaining mass of 20%, where it was taken to be 10%. It is clear from equation (6.2) that the largest fluctuations in calculations of pre-exponentials are seen when the remaining mass is small. Since the final char yield was not determined, due to the interruption of experiments before the mass loss ceased, it can be pointed out that the pre-exponential values are of somewhat less reliability than are the activation energies. The values are similar to many reported in the literature.

The kinetic parameters of pyrolysis were also determined from the separate non-isothermal data of Figure 6.7. Non-isothermal experiments were performed at nominal heating rates of 0.1, 1, 6, 15 and 60 K/min while the actual heating rates respectively were: 0.092, 0.92, 5.8, 14.7 and 68.3 K/min. Determination of kinetic parameters from the non-isothermal TGA data was accomplished in a similar manner as in the case of the isothermal data. The only difference was that the temperature was varying in a course of an experiment.

A summary of the kinetic parameters determined from non-isothermal data is shown in Table 6.2. There are two groups of kinetic parameters, for lower (0.1, 1 and 6 K/min) and higher (15 and 60 K/min) heating rates, analogous to low and high temperature regions in the case of isothermal data. Also shown in Table 6.2 is another set of kinetic parameters, for two lowest heating rates (0.1 and 1 K/min). The reason for calculation of kinetic parameters without the data for 6 K/min heating rate is evident from Figures 6.20. It can be seen that at low conversion (80% of total mass remaining, Figure 6.20a) the point for 6

K/min heating rate is in between the regression lines for data from 0.1 and 1 K/min heating rates on one and 15 and 60 K/min heating rates on the other side. As the conversion increases, the point for 6 K/min heating rate becomes closer (Figure 6.20b, 60% of total mass remaining) and closer (Figure 6.20c, 40% of total mass remaining) to the regression line for high (15 and 60 K/min) heating rates. The reason that the data for this particular heating rate shows an "unusual" behavior is that the pyrolysis at a heating rate of 6 K/min starts before the threshold of 600 K, mentioned above, and finishes above 600 K, as can be seen from Figure 6.7. That means that the data for pyrolysis at a heating rate of 6 K/min is in the middle of some transition temperature, where the activation energy changes.

The questions about the existence of a transition temperature and two activation energies was further addressed by summarizing a broad spectrum of data on a single Arrhenius plot. The data that were used included points obtained by TGA experiments on samples in a DSC pan, as well as the data obtained from DSC measurements themselves. The kinetic analyses of the DSC data were done by making an analogy between the heat flow and mass loss. The working equation was:

$$\frac{\dot{Q}}{(Q_\infty - Q)} = A \exp\left(-\frac{E_a}{RT}\right) \tag{6.5}$$

$$\ln\left(\frac{\dot{Q}}{Q}\right) - \ln\left(\frac{Q_\infty}{Q} - 1\right) = \ln A - \frac{E_a}{RT} \tag{6.5a}$$

where:

$\dot{Q}$ - heat flow at temperature T

Q_∞ - total heat flow

Q - integrated heat flow up to temperature T

A - pre-exponential

E_a - activation energy

R - gas constant

T - temperature

In equation (6.5) the heat flow and the heat up to a certain mass were taken from the different heating rate experiments data at the same fractional mass loss, analogous to the kinetic analyses from mass loss data. On Figure 6.21, the results from the DSC are plotted using (6.5), plotting $\ln(\dot{Q}/Q)$ as ln k.

Figure 6.21 shows a comparison of rate constants, from the data obtained in DSC and TGA in this work under different experimental conditions. Also shown is a comparison to the data of Lewellen et al. (108) and Cooley and Antal (42). Data points were calculated from Lewellen's parameters, while that for Cooley and Antal were determined directly from the original data given in the article (42), using the above described calculation technique. All rate constants in Figure 6.21 refer to 60% of the initial mass left. Clearly, the data of Lewellen et al. is very similar to the data obtained here. The rate constants obtained from (42) are higher than those obtained in this work. However, the slope, that determines the activation energy, is very similar. It can be seen from Figure 6.21 that there are two different activation energies. It should be noted that the transport limitations cannot be the reason for behavior seen in Figure 6.21, as confirmed by the data point obtained by pyrolysis in a TGA of very small sample (0.83 mg), in a DSC pan with 10 pinholes in the cover. As it seems, it is the temperature that determines the pertinent kinetics, rather than the heating rate. The exact temperature of the transition is arguable, but it seems that it is

about 600 K. Furthermore, the assignment of a particular point to one region or the other does not represent an easy task. In other words, if the regression lines in Figure 6.21 are extrapolated to higher or lower temperature there can be found at least one other point that belongs to the other region and still can be extrapolated from different region. Therefore, the data suggest that there is a possibility that sets of experiments might be done in a broad temperature range and yet the effect, seen in Figure 6.21, can be masked. There is, however, little doubt about the existence of two regions, with different kinetic parameters, since the data of Figure 6.21 represents a summary of several different experimental techniques.

There was an attempt made to determine the reaction order of pyrolysis. For that purpose the results of the isothermal experiments were used. The pyrolysis can be mathematically represented as a sum of p reactions, each one with its rate constant, k_i, and reaction order n_i, viz:

$$\frac{d\left(\frac{M-M_f}{M_0-M_f}\right)}{dt} = -\sum_{i=1}^{p} k_i \left(\frac{M-M_f}{M_0-M_f}\right)^{n_i} \tag{6.6}$$

where the rate constant has an Arrhenius form:

$$k_i = A_i \exp\left(-\frac{E_{a_i}}{RT}\right) \tag{6.7}$$

If it is assumed that one of the reactions in equation (6.6) dominates than equation reduces to:

$$\frac{1}{\left(\frac{M-M_f}{M_0-M_f}\right)^{n_1}} \frac{d\left(\frac{M-M_f}{M_0-M_f}\right)}{dt} = -k_1 \tag{6.8}$$

If the temperature is constant (isothermal experiment) equation (6.8) can be integrated to give:

$$\text{for } n_1 = 0 \Rightarrow \frac{M-M_f}{M_0-M_f} = -k_1 t + C_1 \tag{6.9}$$

$$\text{for } n_1 = 1 \Rightarrow \ln\left(\frac{M-M_f}{M_0-M_f}\right) = -k_1 t + C_2 \tag{6.10}$$

$$\text{for } n_1 = 2 \Rightarrow \frac{1}{\left(\frac{M-M_f}{M_0-M_f}\right)} = k_1 t + C_3 \tag{6.11}$$

The reaction orders were determined by the linearity of the curves whose mathematic expressions are given in equations (6.9), (6.10) and (6.11). The linearities were compared by plotting the isothermal data on same set of axes. For that purpose, a normalization parameter was introduced:

$$f(M/M_0) = \frac{F - F_{min}}{F_{max} - F_{min}} \tag{6.12}$$

where F represents the lefthand sides of equations (6.9), (6.10) and (6.11) and subscripts "min" and "max" refer to the minimum and maximum value in a particular data set. The normalization parameter of equation (6.12) does not have any physical significance, it was

introduced as a mathematical tool for convenient graphical data comparison only and should be viewed as such.

A comparison of different orders is shown in Figures 6.22 (isothermal pyrolysis at 288°C in Figure 6.22a and at 311°C, after heating at a heating rate of 1 K/min) and Figures 6.23 (isothermal pyrolysis at 286°C in Figure 6.22a and at 311°C, after heating at a heating rate of 60 K/min). The char yield was assumed to be 13% for all data sets. Clearly, the pyrolysis cannot be represented with a single second order reaction. However, the choice between zero and first order reaction is not as easy as ruling out second order reaction. It does seem from the figures that the pyrolysis proceeds with a (pseudo) first order reaction in the second part of pyrolysis. On the other hand, it appears that a (pseudo) zero order reaction gives a better linearity of the plot at the beginning of the pyrolysis.

Generally, the pyrolysis of cellulose has been modeled with a pseudo-first order dominating reaction. However, there are studies that report data fitting with orders different than unity. Antal's group (see various references by Antal et al., eg. 187) developed a data fitting procedure that gives an apparent order of pyrolysis as well as apparent kinetic parameters (eg. activation energy of 234 kJ/mole and pre-exponential of 3.98×10^{17} s^{-1}). Kashiwagi and Nambu (87) report the apparent order of pyrolysis reaction of 1.8. Suuberg and Dalal (171) found that fitting the data with single kinetic parameters fails at the beginning of pyrolysis for heating rate of 5 K/min. Lipska and Parker (110) and Tang and Neill (177) report that cellulose starts to decompose with pseudo zero order reaction and changes to pseudo first order reaction later, depending on pyrolysis temperature.

Although from the data of Figures 6.22 and 6.23 it cannot be positively stated what the pseudo order of decomposition reaction is it is clear that the cellulose pyrolysis cannot be described by a single pseudo order reaction. The reason might be dramatic changes in

material as it starts to pyrolyze. Broido and Weinstein (27) found that decrystallization of cellulose by action of liquid ammonia improves the data fitting with a single pseudo first order decomposition reaction over 90% of the weight loss range. Basch and Lewin (12) found that the apparent activation energy of pyrolysis changes with the crystallinity. Furthermore, Bacon (11) reported that the mechanical properties of rayon (tensile strength and elongation at break) decrease approximately by a factor of five during the initial 5% of the mass loss, exactly where the destruction of crystalline cellulose takes place. Therefore, it might be possible that the pyrolysis of cellulose follows the destruction of crystalline regions. This is consistent with the hypothesis of "cellulose activation", postulated by Bradbury et al. (26), who discovered it by measuring the degree of polymerization of cellulose pyrolyzed to different extents.

The agreement between the determined kinetic parameters and experiments was checked by comparison of mass loss from numerical integration of the Arrhenius equation and the experimental data. The integrations were performed for heating rates of 0.1 K/min and 60 K/min using a single, first order reaction and with single set of calculated parameters and also for a two-step model involving "activation". Several sets of parameters were used in integration including 224 kJ/mole (pre-exponential of 4.12×10^{16}) and 139 kJ/mole (pre-exponential of 7.76×10^{9}). The "activation" was assumed to have the higher activation energy, i.e. 224 kJ/mole (pre-exponential of 4.12×10^{16}). For the "activation" Bradbury et al. (26) proposed 243 kJ/mole. Figures 6.24a and 6.24b respectively show the comparison for heating rates of 0.1 K/min and 60 K/min. Obviously, the activation energy of 224 kJ/mole fits the data very well and the activation energy of 139 kJ/mole does not predict the pyrolysis at all. If the activation step is included and the activation energy is changed after 20% of the mass loss, the fit is improved but it still does not predict the pyrolysis behavior nearly as well as when it completely proceeds with higher activation energy. This is

consistent with the data of Figure 6.21.

The comparison of models and data is more interesting for a heating rate of 60 K/min. It seems that the best fit is obtained for the activation energy of 224 kJ/mole, not for the activation energy that was determined for that range, of 139 kJ/mole. This is inconsistent with the data of Figure 6.21. However, the fit is significantly improved by adding an "activation" step involving 20% mass loss (the mass loss where DSC curves diverge from each other, see Figure 6.12), with an activation energy of 224 kJ/mole. This might be the source of confusion in the literature about the kinetic parameters for cellulose pyrolysis. It was concluded before that there is little argument about the existence of two temperature regions of cellulose pyrolysis, each one with different activation energy associated with it. On the other hand, from the comparison shown in Figure 6.24b, it seems that the high activation energy works as well in the high temperature region as it does in the low temperature region. When the "activation" step is included they work comparably well. This argues in favor of the existence of "activation" of some kind, not in favor of single activation energy. Again, the data of Figure 6.21 was obtained by many experiments and there is no doubt that it is more general. Furthermore, it is evident from Tables 6.1 and 6.2 that the kinetic compensation effect takes place here and that is the reason that the comparison presented in Figure 6.24b shows small difference.

The potential existence of the "activation" step could explain the behavior shown in Figure 6.21. If the pyrolysis at high temperatures cannot proceed before the crystalline structure is destroyed that means that the low activation energy process cannot be seen at lower temperatures, although it would be seen if the competitive reactions are involved. Hence, the pyrolysis might proceed through some activation step.

The numerical integration was done for two different orders of reaction. Figures 6.25a and 6.25b respectively show a comparisons of experimental mass loss at heating rates of 0.1 and 60 K/min with those obtained by integration, with first order reaction throughout and with zero order reaction initially (up to the fractional remaining mass of 0.75) and with first order reaction afterwards. As it is evident from Figures 6.25 there is almost no difference between the mass losses calculated with single reaction order and when reaction order changes.

The kinetic analysis can help in discussion about physical model, postulated by Mok and Antal (122), that was shown in Figure 6.11. The results from this work indicate that the pyrolysis might follow a path through anhydrocellulose at low temperatures, with high activation energy, while at high temperatures it might follow a path through tar intermediate, with low activation energy. This is also consistent with the DSC data. Thus, the results obtained here are in agreement with the postulated physical model.

6.4 SUMMARY

Three significant variables in cellulose pyrolysis were characterized under well controlled experimental conditions: the ultimate char yield, the heat effect and the pyrolysis kinetics. The data obtained is of crucial importance for understanding bulk cellulose pyrolysis under simulated fire conditions.

The char yield varies with initial sample density, sample size, heating rate and mass transport limitations. There is no single effect that influences the char yield in such a manner so that it can reach the values obtained by bulk samples pyrolysis under simulated fire conditions. It was found that the heating rate effect and the mass transport limitations

combined can result in char yields of magnitude seen in the bulk samples pyrolysis under simulated fire conditions. The initial sample density and the sample size effects are related to mass transport limitations.

Overall, the pyrolysis of cellulose proceeds with endothermic heat effect, under conditions studied. There is an exothermic process observed, especially at lower heating rates. The heat of pyrolysis correlates well with the fractional sample mass and with the char yield.

Depending on the temperature of interest, the pyrolysis of cellulose can proceed with high (221 kJ/mole) or low (139 kJ/mole) activation energy. It was determined that the low temperature pyrolysis proceeds with the high activation energy and the high temperature proceeds with the low activation energy. Since the trend is opposite of what would be seen if there were competitive reactions involved, the existence of an "activation" step, with high activation energy seems plausible. The numerical integration supports the existence of the "activation" step. Seemingly, there are two pseudo orders of pyrolysis reaction: initially pseudo zero order and pseudo first order afterwards. However, the numerical integration did not reveal large differences between the two.

The findings obtained here are in agreement with the physical model in the literature, at least for the part that has been studied here.

Table 6.1: Kinetic parameters determined from isothermal TGA (after heating at a heating rate of 1 K/min or 60 K/min); in calculations for pre-exponential char yield of 20% was used, except where noted

a: after heating at a heating rate of 1 K/min

Remaining Mass [%]	E_a [kJ/mole]	A [s^{-1}]
80	225	4.82×10^{16}
70	215	5.77×10^{15}
60	224	5.39×10^{16}
50	215	8.80×10^{15}
40	212	5.59×10^{15}
30	214	1.15×10^{16}
20[1]	225	4.69×10^{16}

b: after heating at a heating rate of 60 K/min

	BELOW 600 K		ABOVE 600 K	
Remaining Mass [%]	E_a [kJ/mole]	A [s^{-1}]	E_a [kJ/mole]	A [s^{-1}]
70	226	8.83×10^{16}	128	2.23×10^{8}
60	219	2.02×10^{16}	136	1.32×10^{9}
50	224	5.76×10^{16}	145	7.36×10^{9}
40	226	9.07×10^{16}	152	3.21×10^{10}
30	234	4.16×10^{17}	160	1.60×10^{11}
20[1]	217	8.08×10^{15}	177	5.28×10^{12}

[1] 10% char yield used in calculations

Table 6.2: Kinetic parameters determined from non-isothermal TGA (at heating rates of 0.1, 1, 6, 15 and 60 K/min); in calculations for pre-exponential char yield of 20% was used, except where noted

	0.1, 1 and 6 K/min		15 and 60 K/min		0.1 and 1 K/min	
Remaining Mass [%]	E_a [kJ/mole]	A [s^{-1}]	E_a [kJ/mole]	A [s^{-1}]	E_a [kJ/mole]	A [s^{-1}]
90	253	9.32×10^{18}	180	5.28×10^{12}	238	4.12×10^{17}
80	224	4.12×10^{16}	149	2.48×10^{10}	205	6.79×10^{14}
70	229	1.39×10^{17}	143	8.96×10^{9}	207	1.45×10^{15}
60	232	2.91×10^{17}	137	3.88×10^{9}	206	1.21×10^{15}
50	236	8.43×10^{17}	142	1.10×10^{10}	211	3.97×10^{15}
40	253	7.48×10^{18}	142	1.53×10^{10}	216	1.17×10^{16}
30	245	6.62×10^{18}	144	3.76×10^{10}	220	3.96×10^{16}
20[1]	293	3.65×10^{22}	146	4.32×10^{10}	252	9.23×10^{18}

[1] 10% char yield used in calculations

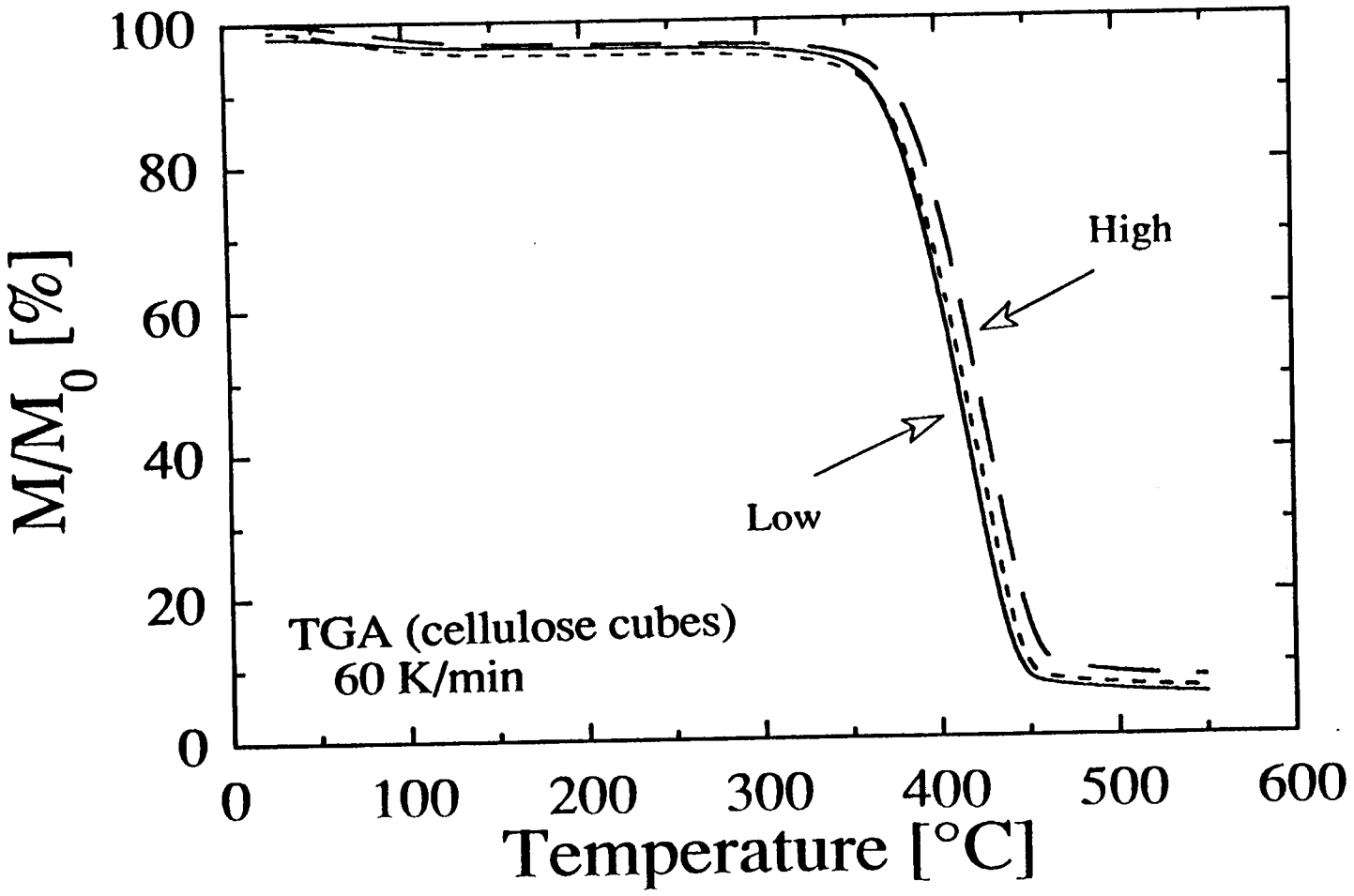

Figure 6.1 Fractional remaining mass as a function of temperature for different density cellulose samples obtained in a TGA

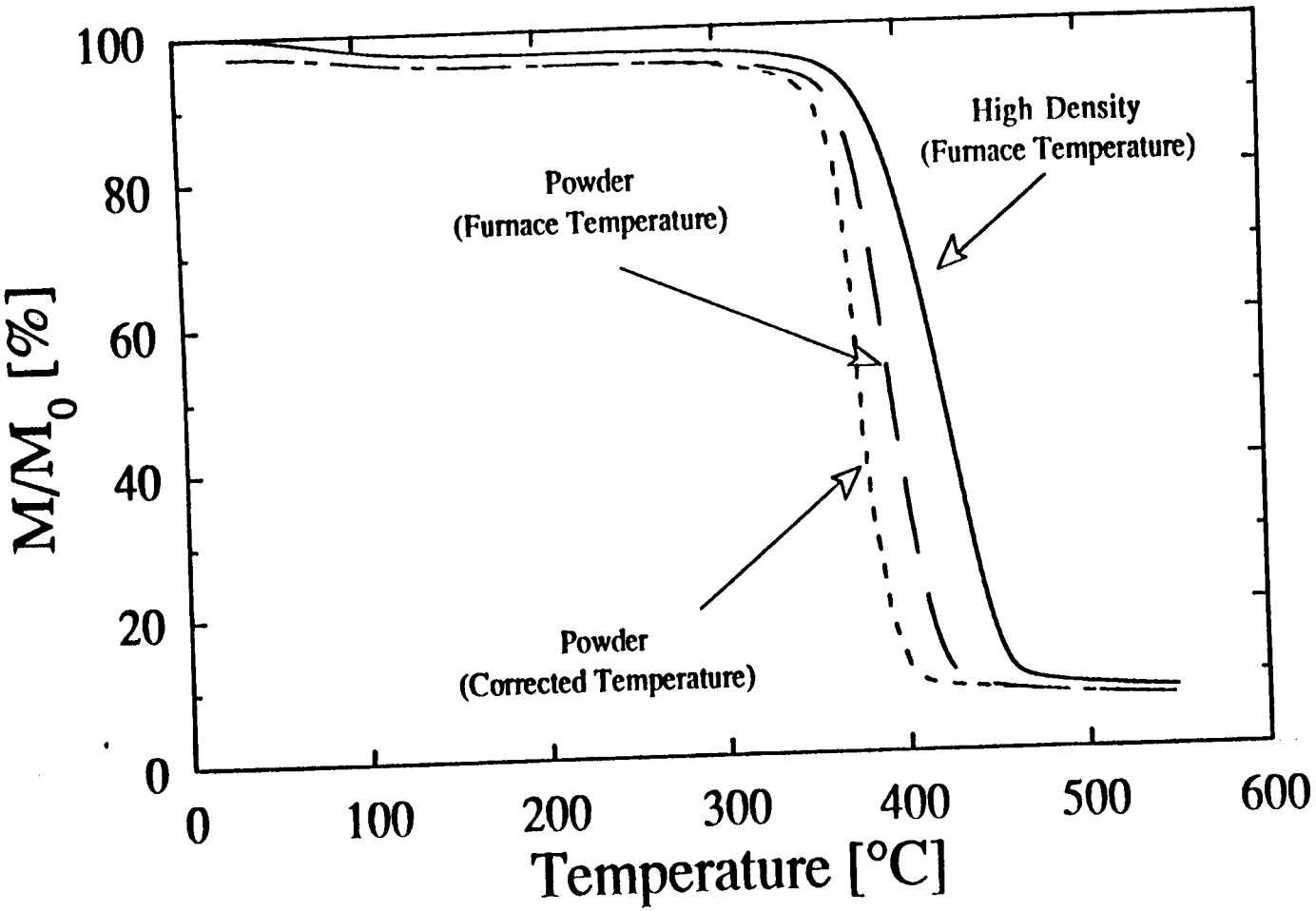

Figure 6.2 Comparison of mass loss for powder and high density cellulose samples. Also shown are the TGA furnace temperature and a temperature measured by inserting a thermocouple into the sample.

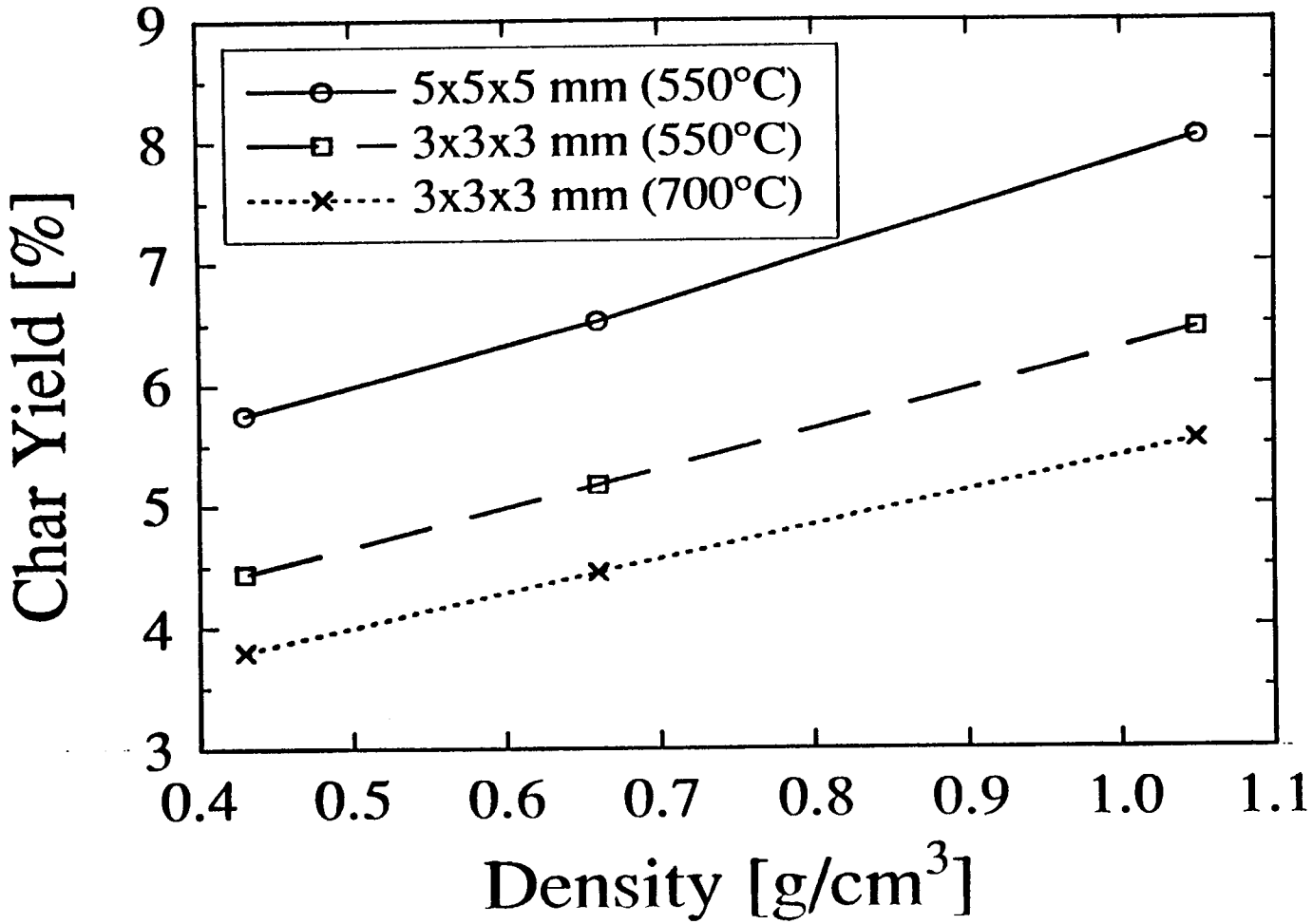

Figure 6.3 Char yield as a function of initial sample density, obtained in a TGA, for two different sample sizes and at two different temperatures

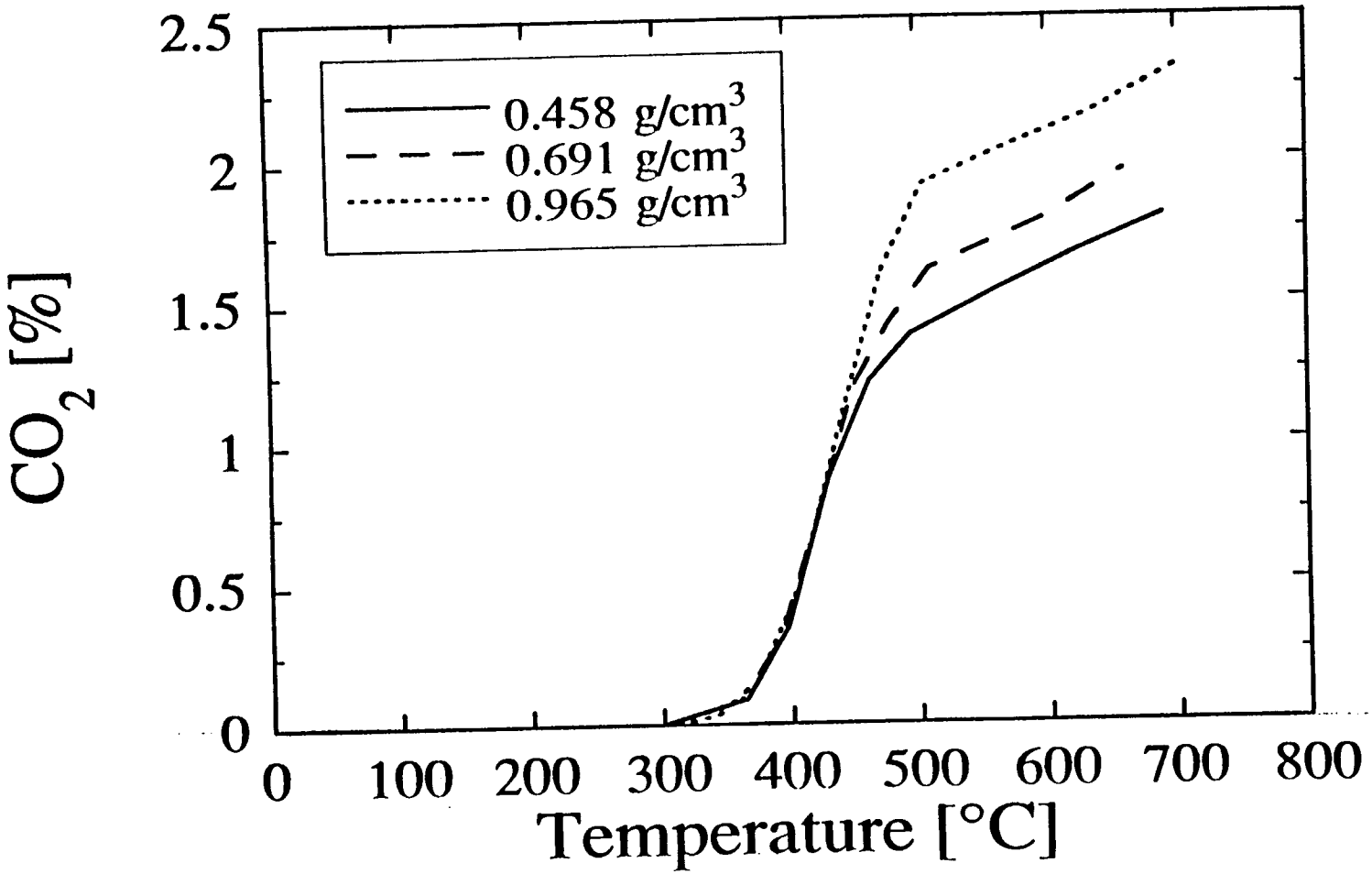

Figure 6.4a Cumulative concentration of carbon dioxide as a function of temperature for different density samples, obtained in a TGA

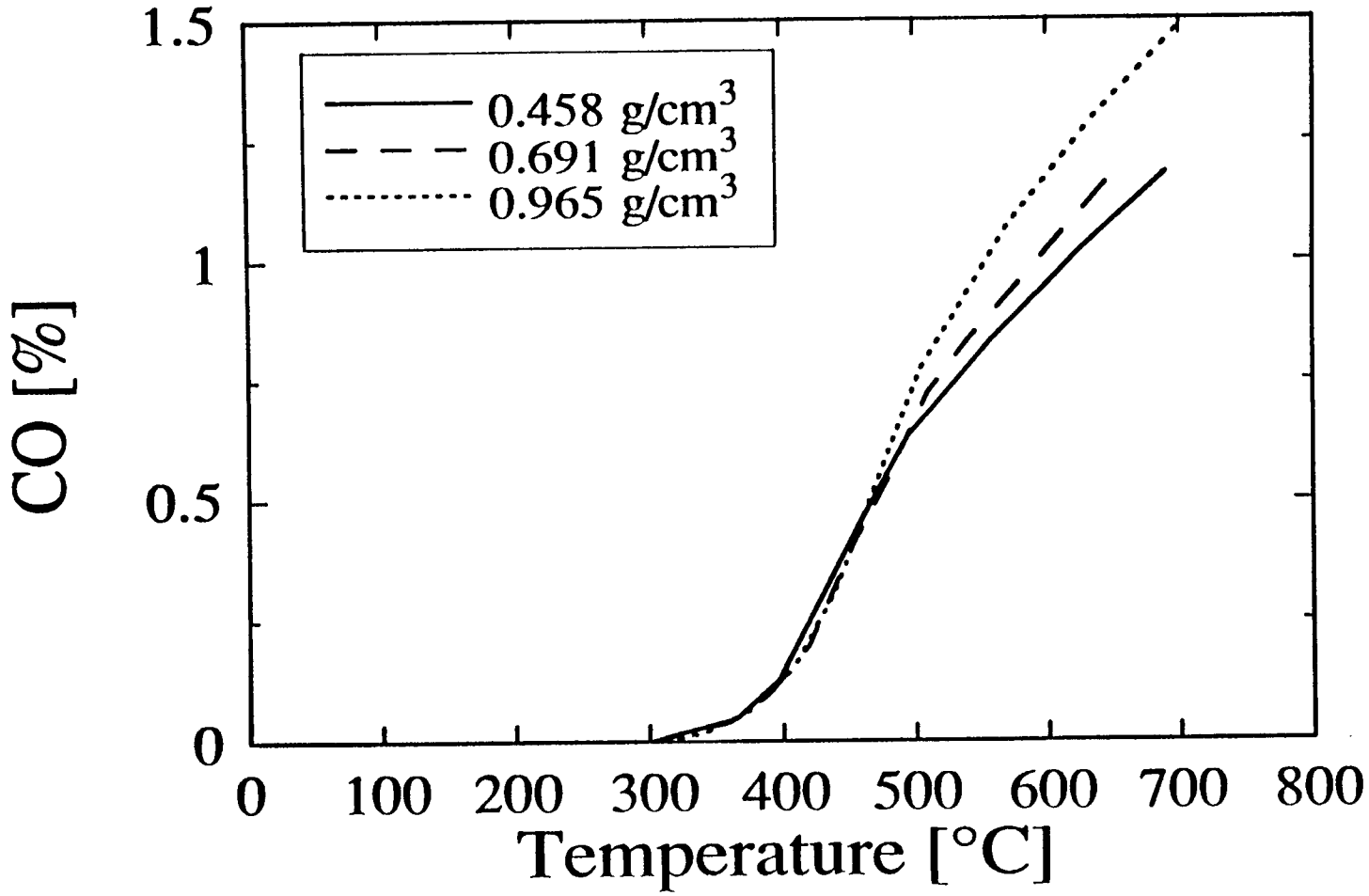

Figure 6.4b Cumulative concentration of carbon monoxide as a function of temperature for different density samples, obtained in a TGA

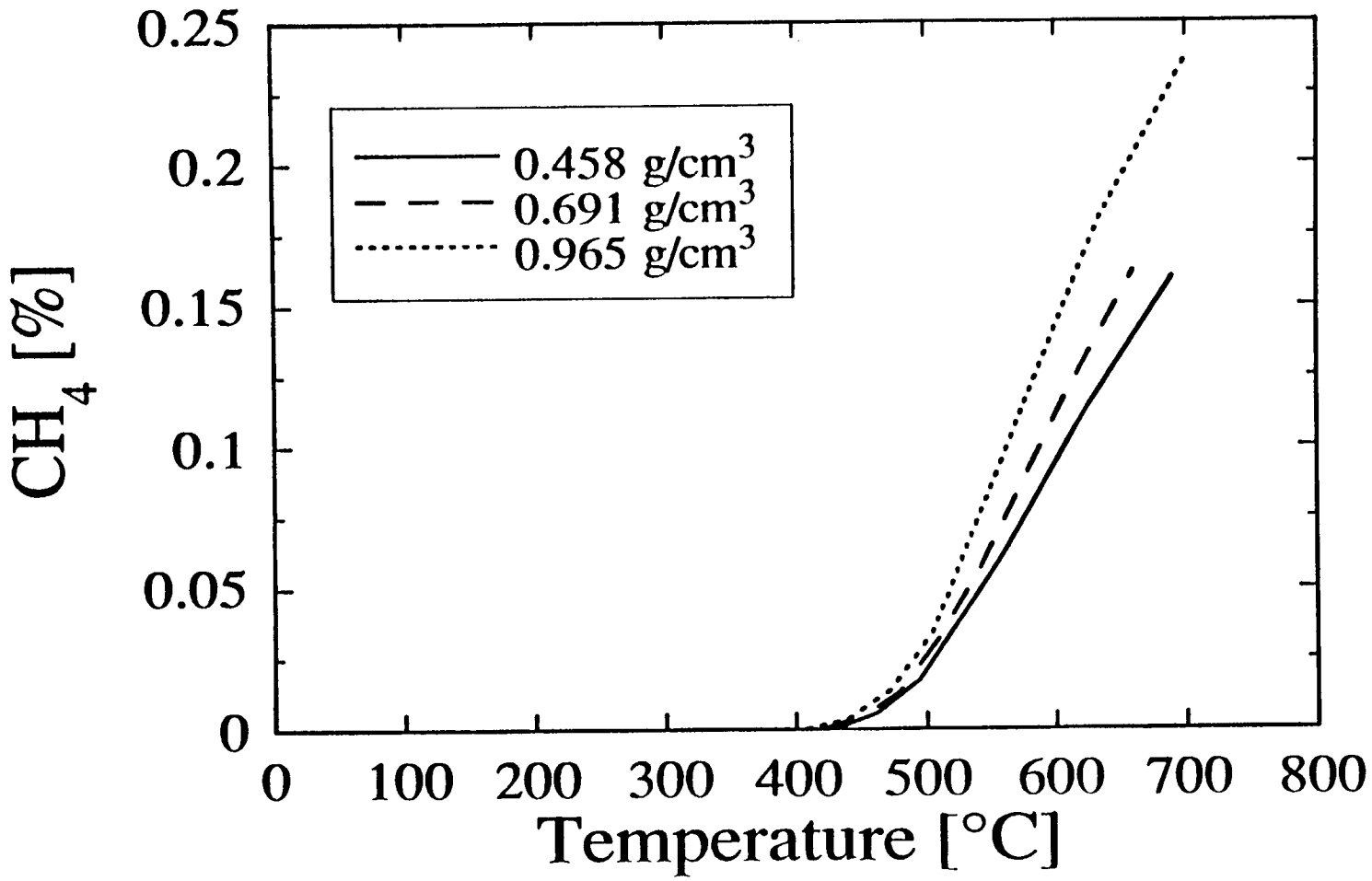

Figure 6.4c Cumulative concentration of methane as a function of temperature for different density samples, obtained in a TGA

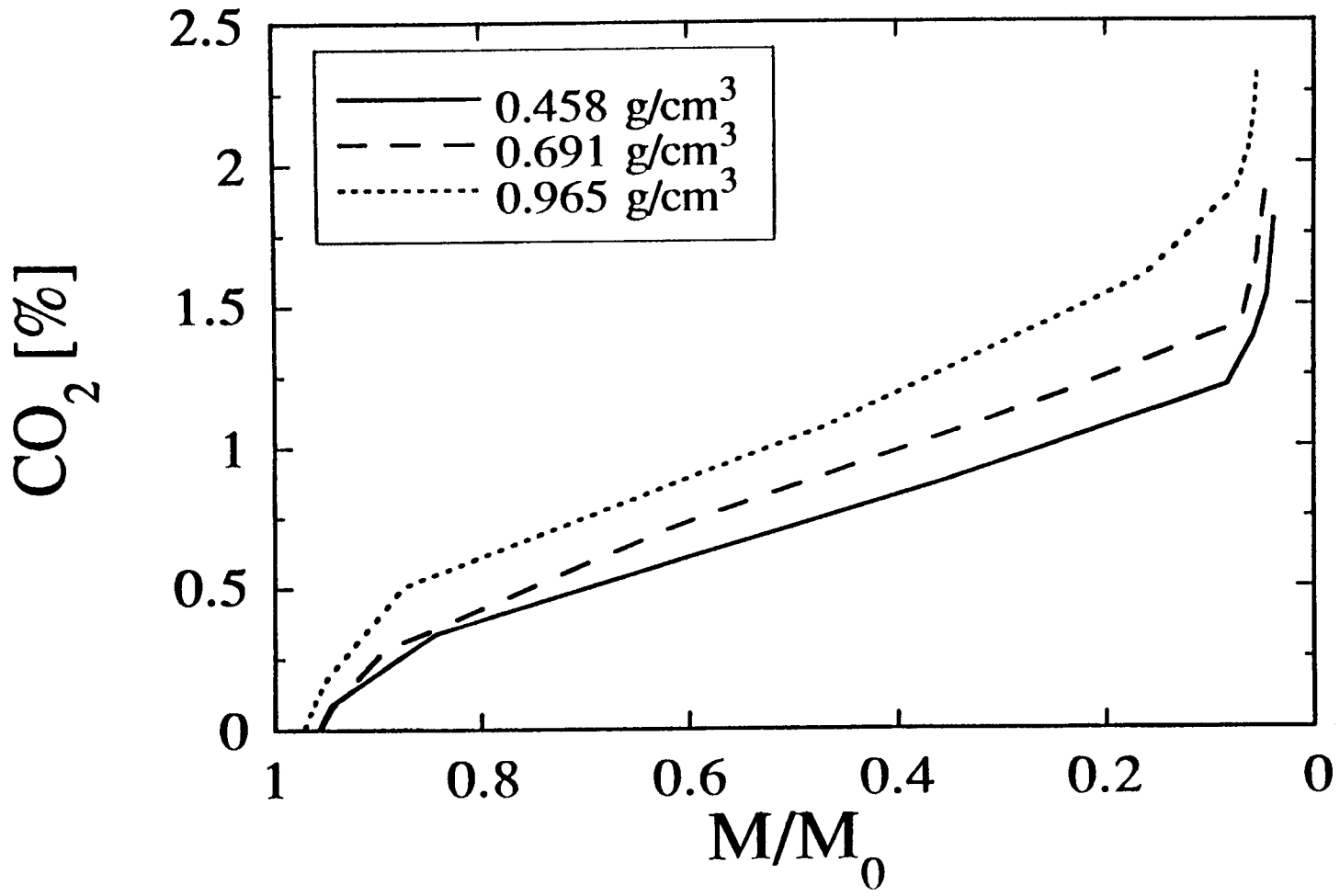

Figure 6.5a Cumulative concentration of carbon dioxide as a function of fractional remaining mass for different density samples, obtained in a TGA

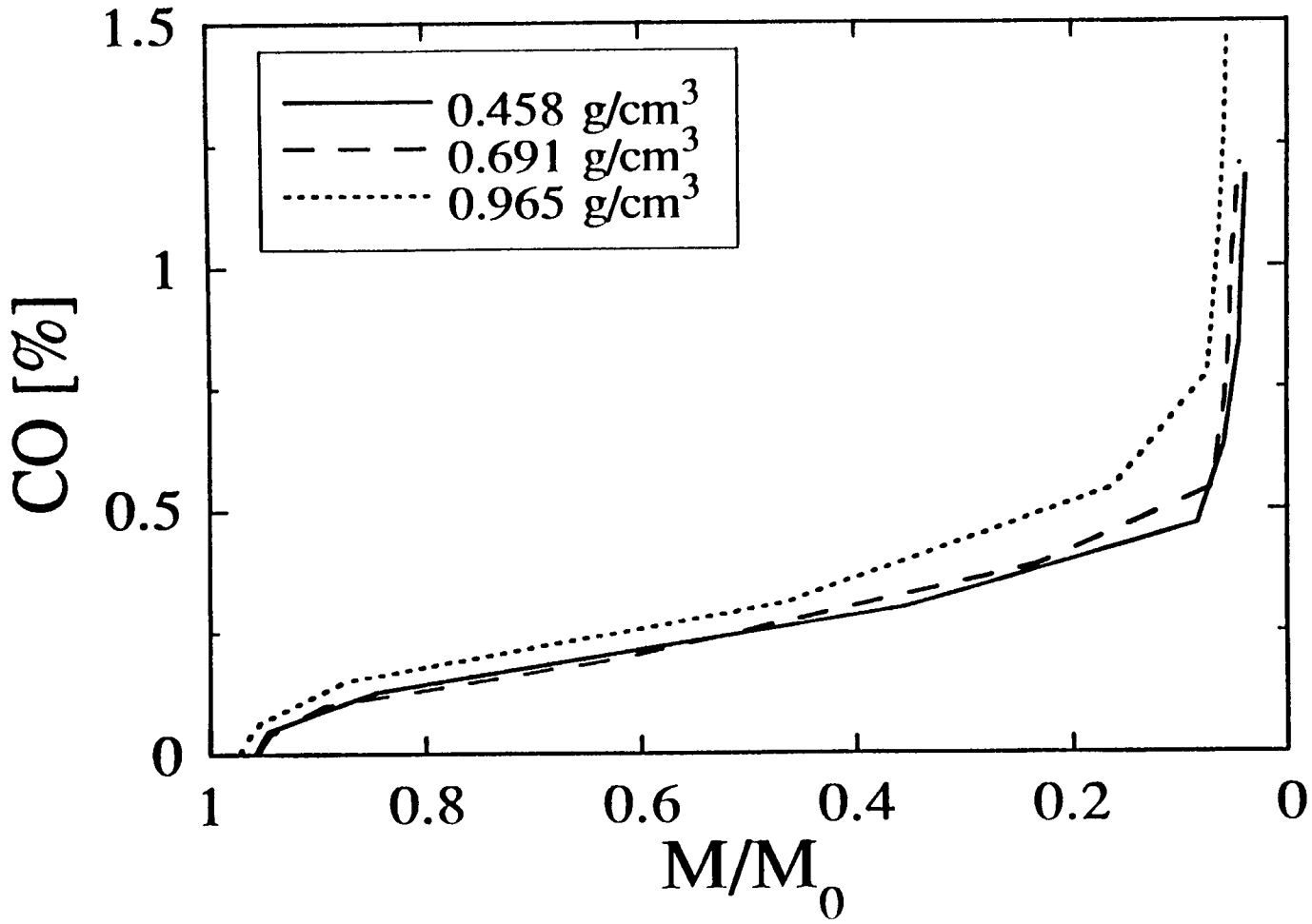

Figure 6.5b Cumulative concentration of carbon monoxide as a function of fractional remaining mass for different density samples, obtained in a TGA

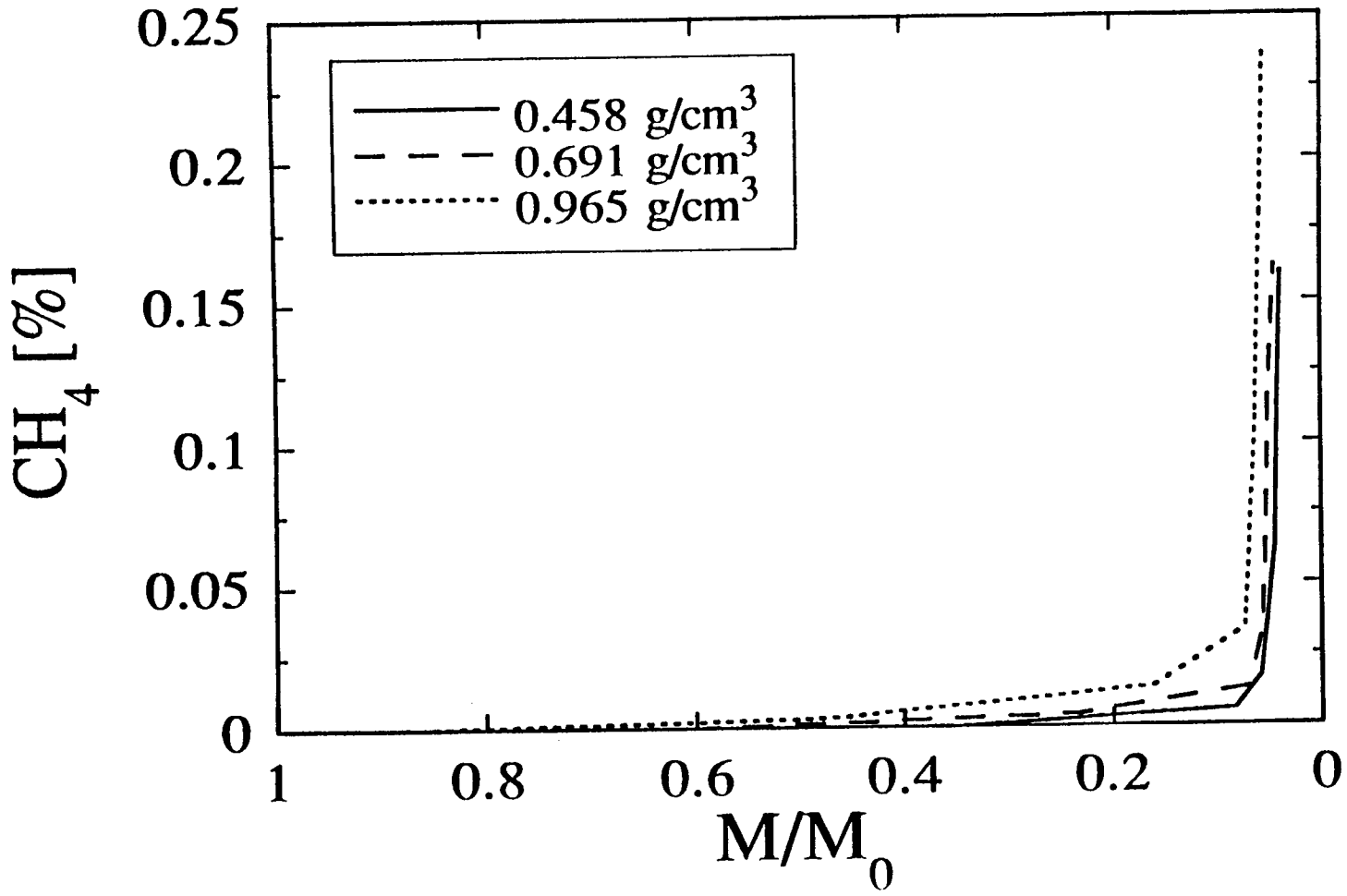

Figure 6.5c Cumulative concentration of methane as a function of fractional remaining mass for different density samples, obtained in a TGA

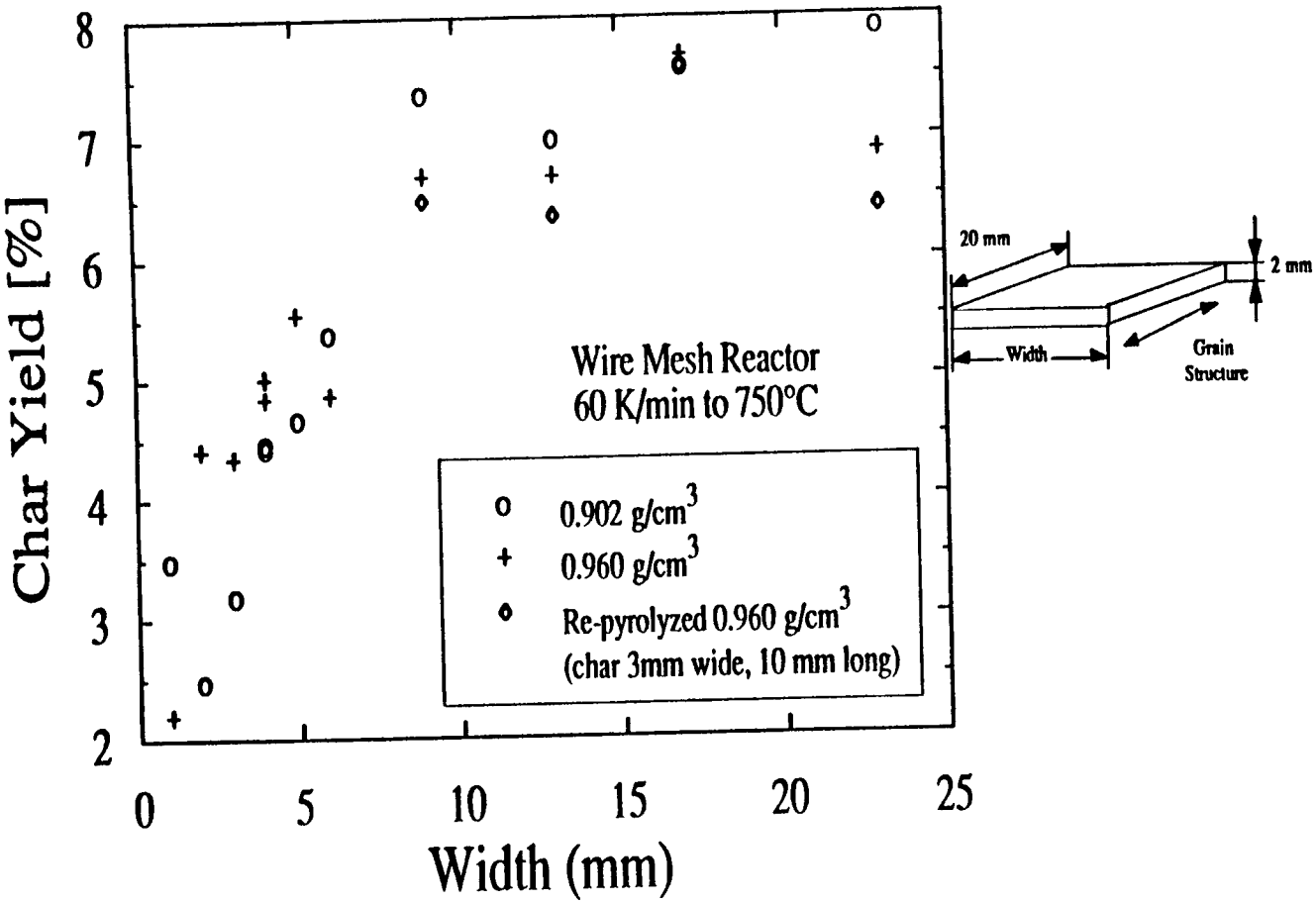

Figure 6.6 Ultimate char yield as a function of sample width for high density samples; length (20 mm) and thickness (2 mm) were the same for all samples

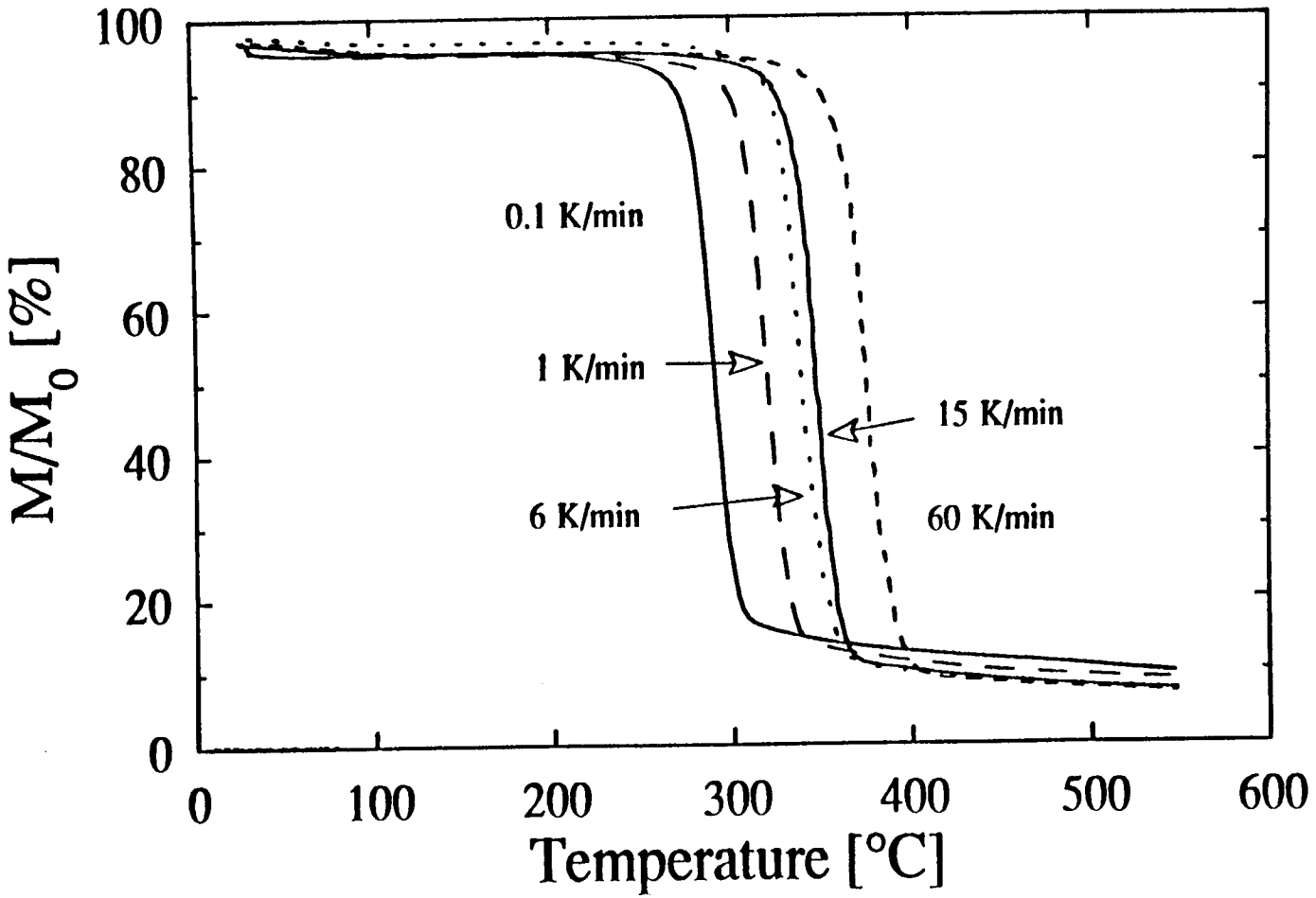

Figure 6.7 Fractional remaining mass as a function of temperature for cellulose powder at different heating rates

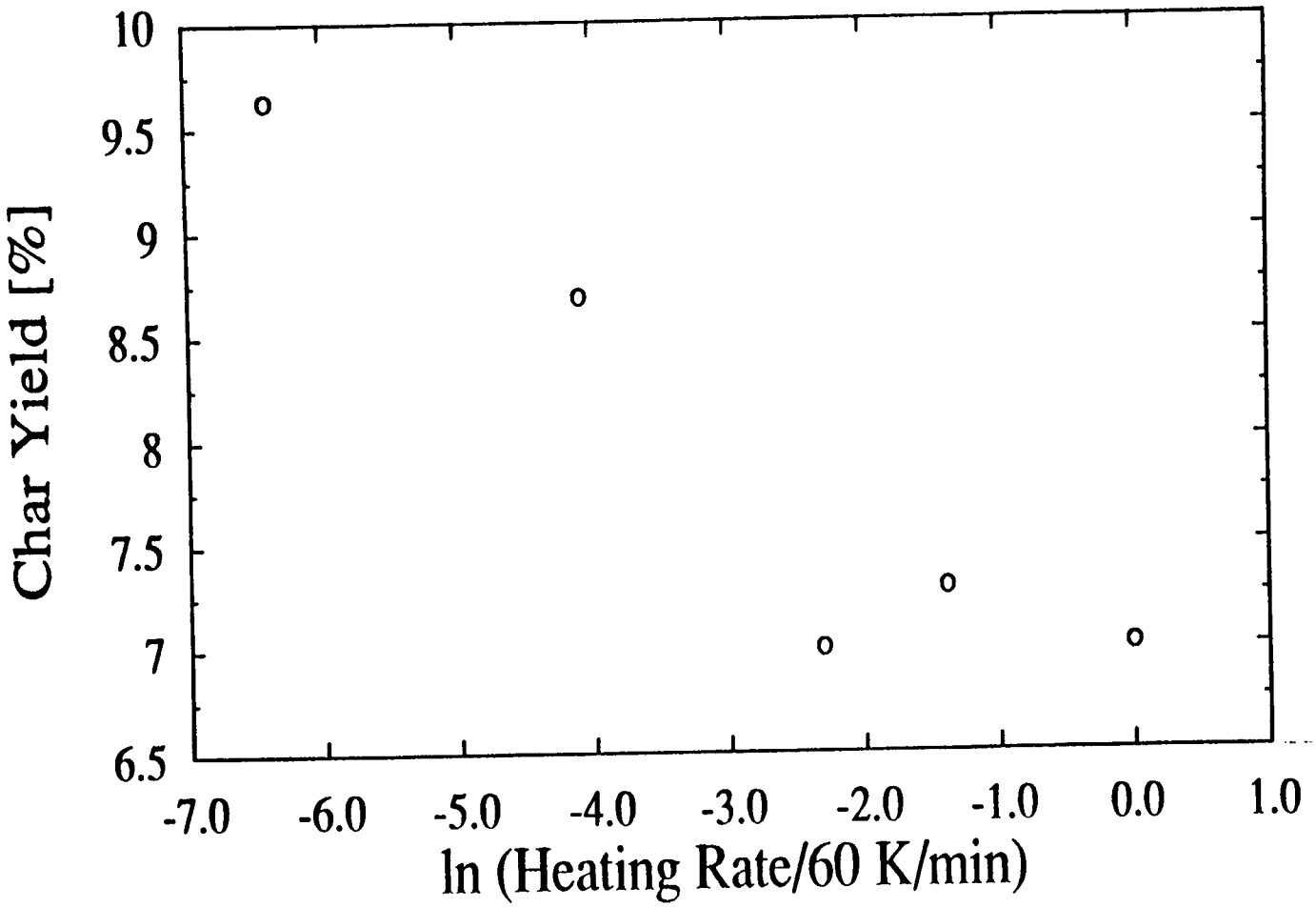

Figure 6.8 Ultimate char yield as a function of heating rate for cellulose powder, obtained in a TGA (data of Figure 6.7)

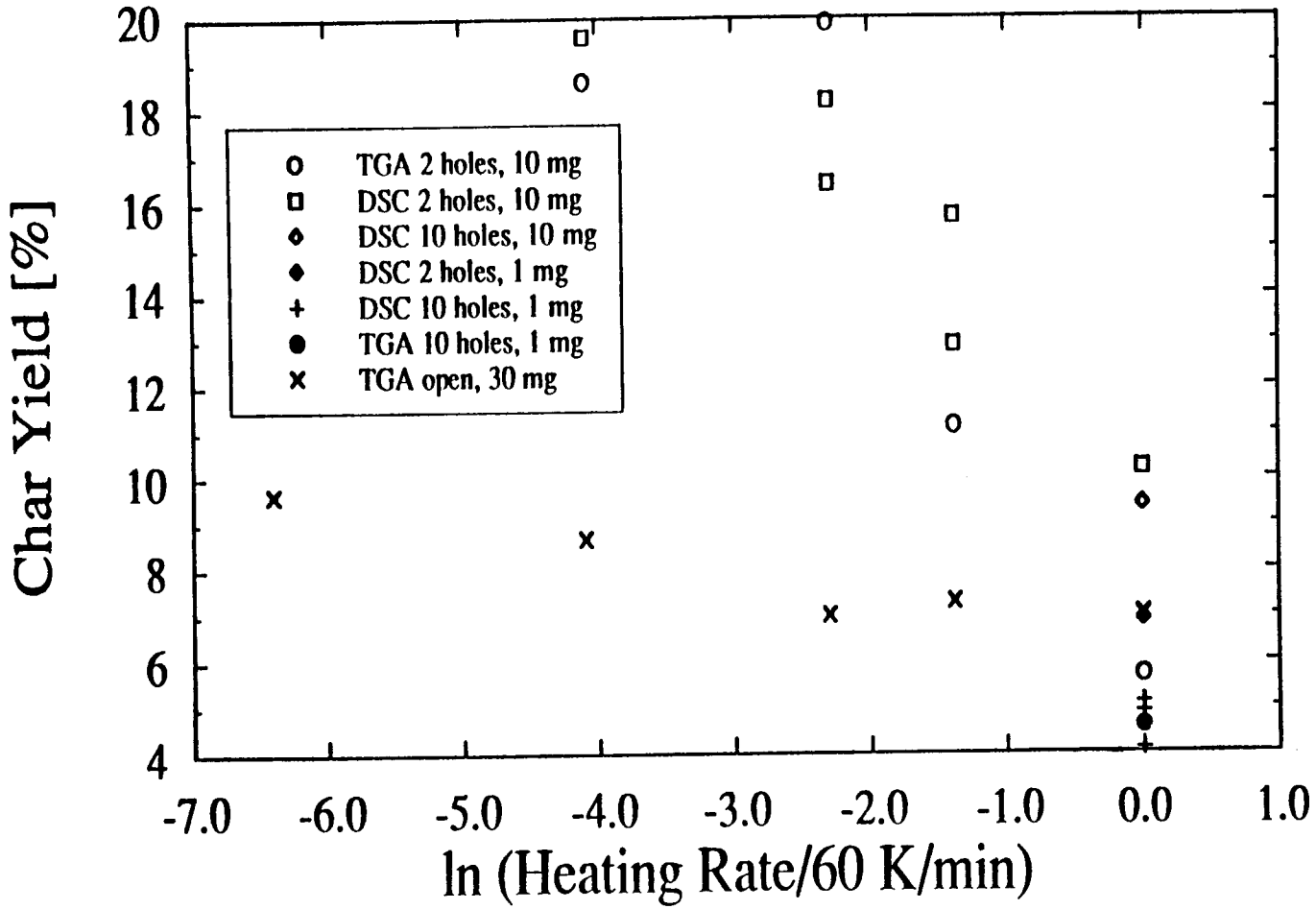

Figure 6.9 Ultimate char yield as a function of heating rate for different amounts of cellulose powder and different transport limitations, obtained in a TGA and in a DSC

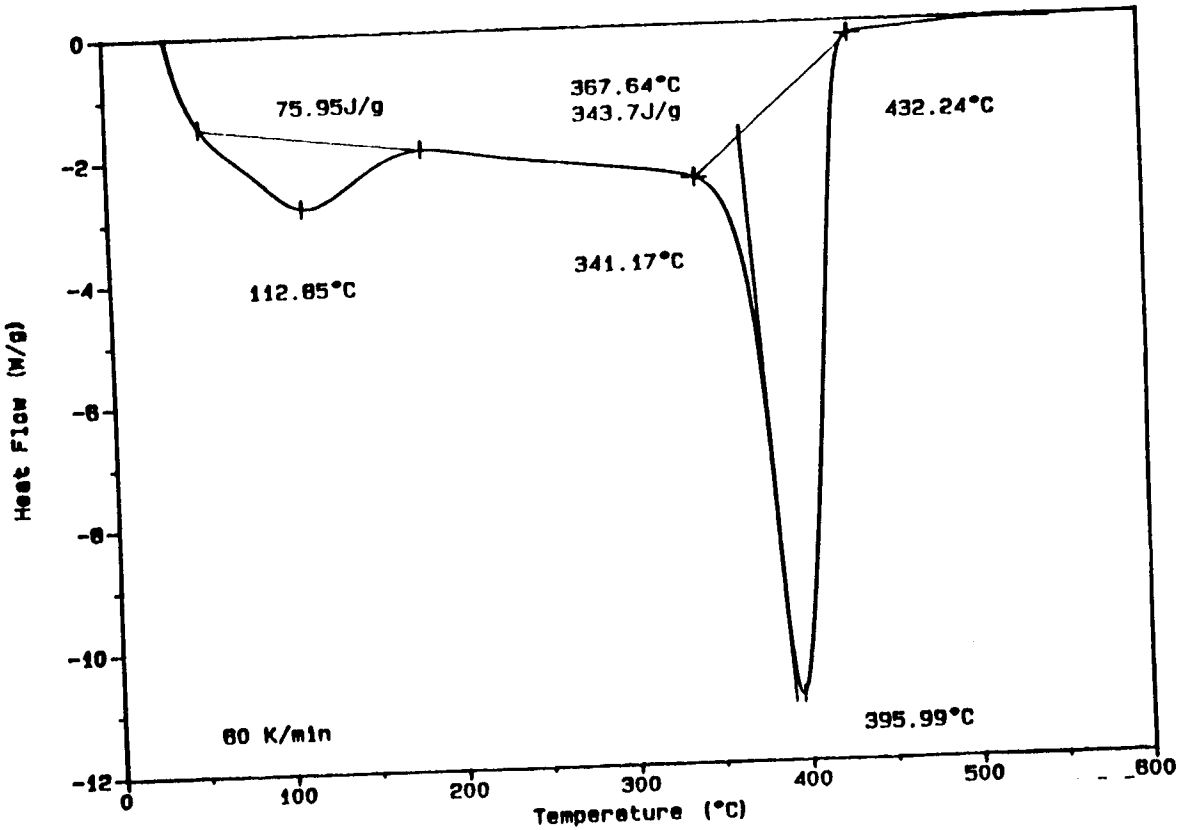

Figure 6.10a DSC of cellulose (powder sample, of about 10 mg; two pinholes in sample pan cover) for heating rate of 60 K/min

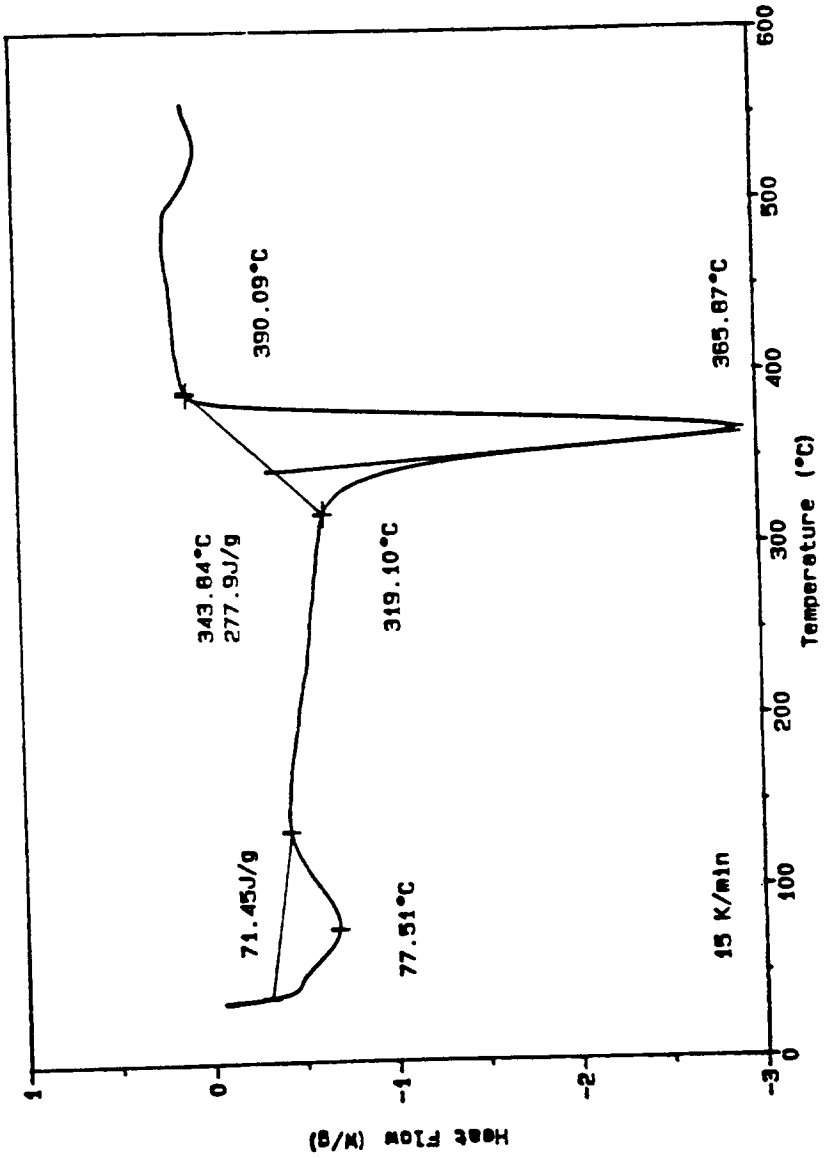

Figure 6.10b DSC of cellulose (powder sample, of about 10 mg; two pinholes in sample pan cover) for heating rate of 15 K/min

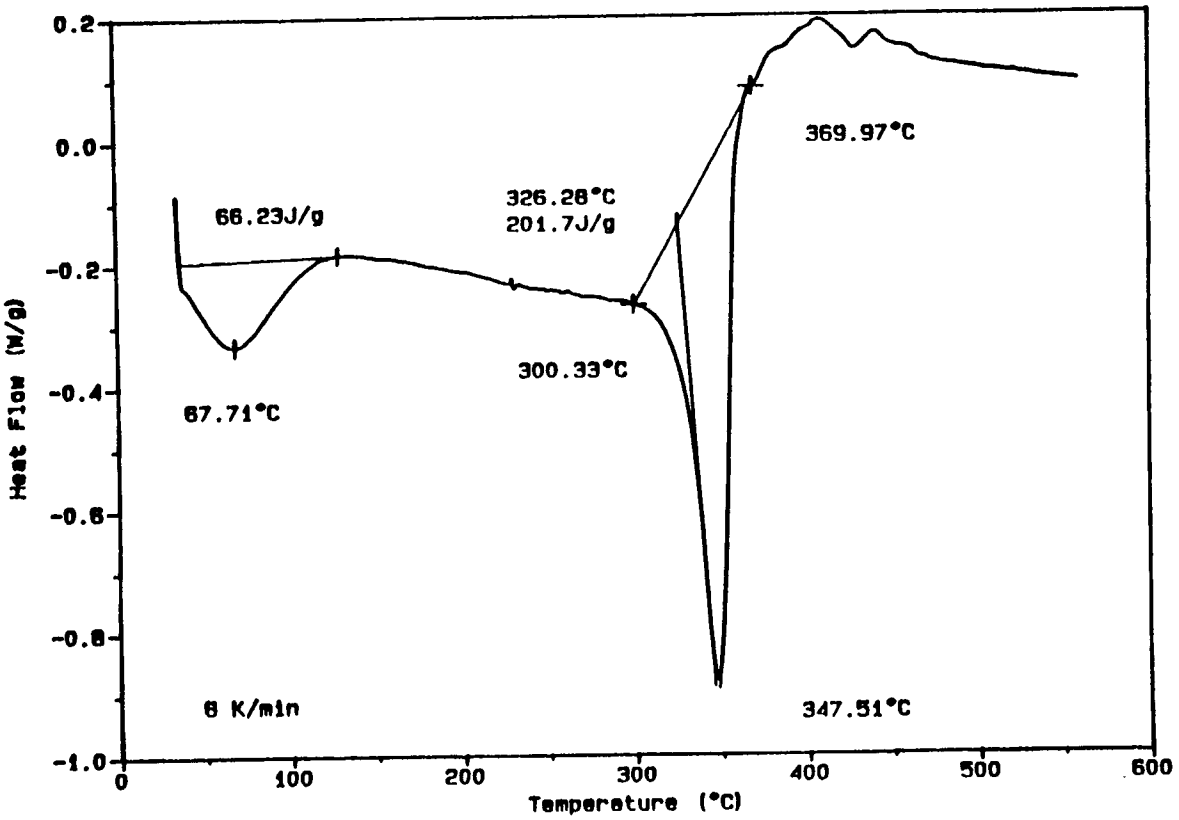

Figure 6.10c DSC of cellulose (powder sample, of about 10 mg; two pinholes in sample pan cover) for heating rate of 6 K/min

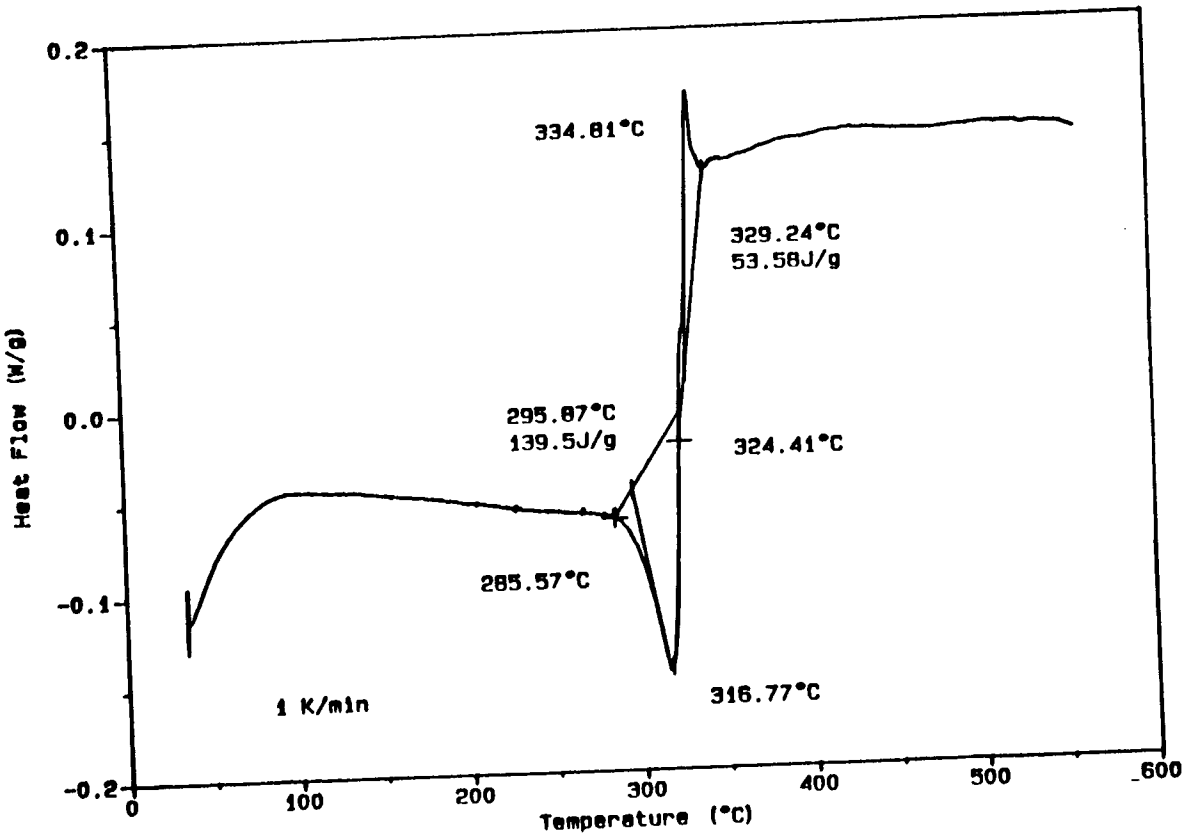

Figure 6.10d DSC of cellulose (powder sample, of about 10 mg; two pinholes in sample pan cover) for heating rate of 1 K/min

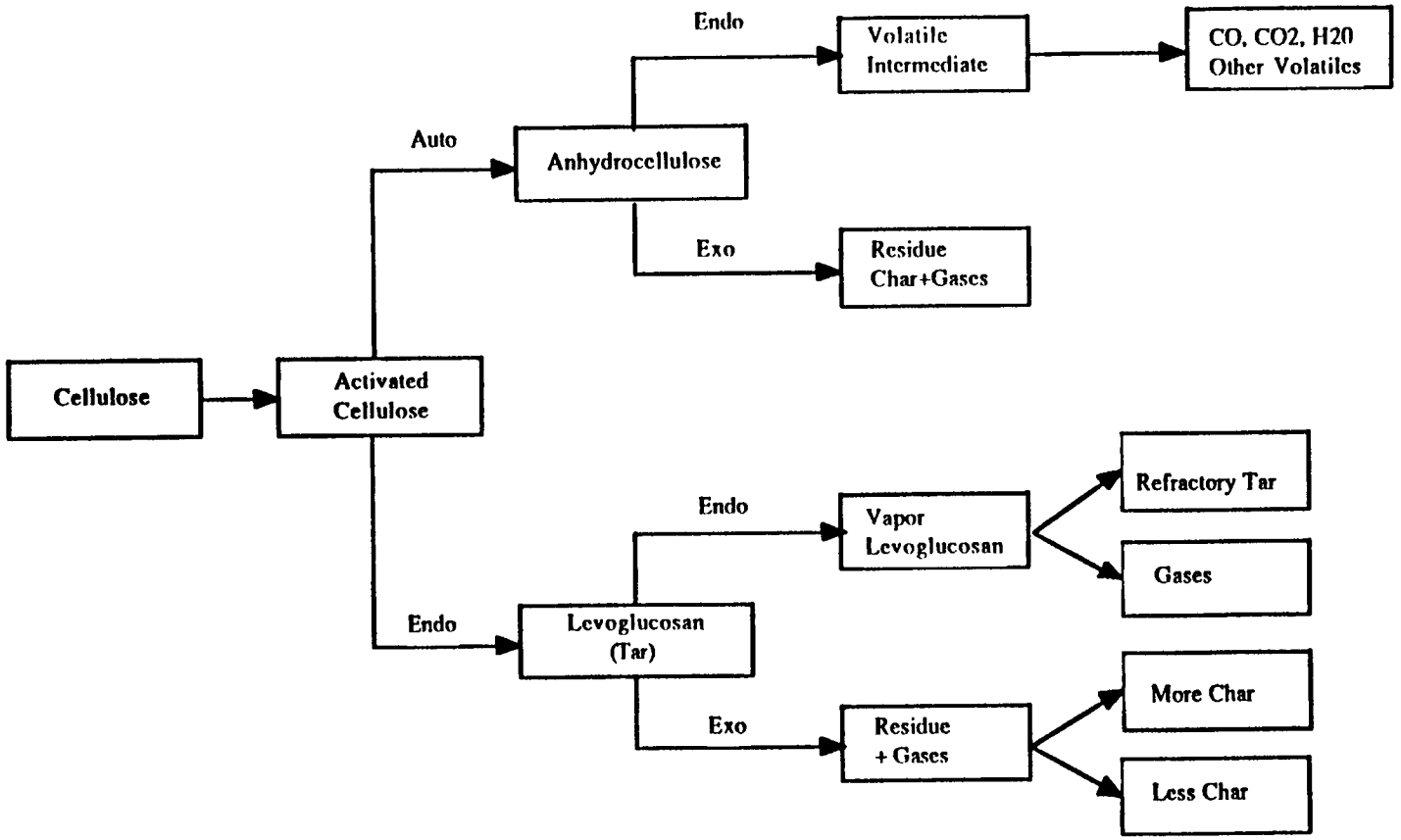

Figure 6.11 Mechanism of cellulose pyrolysis, with proposed endo- and exothermic steps (from 122)

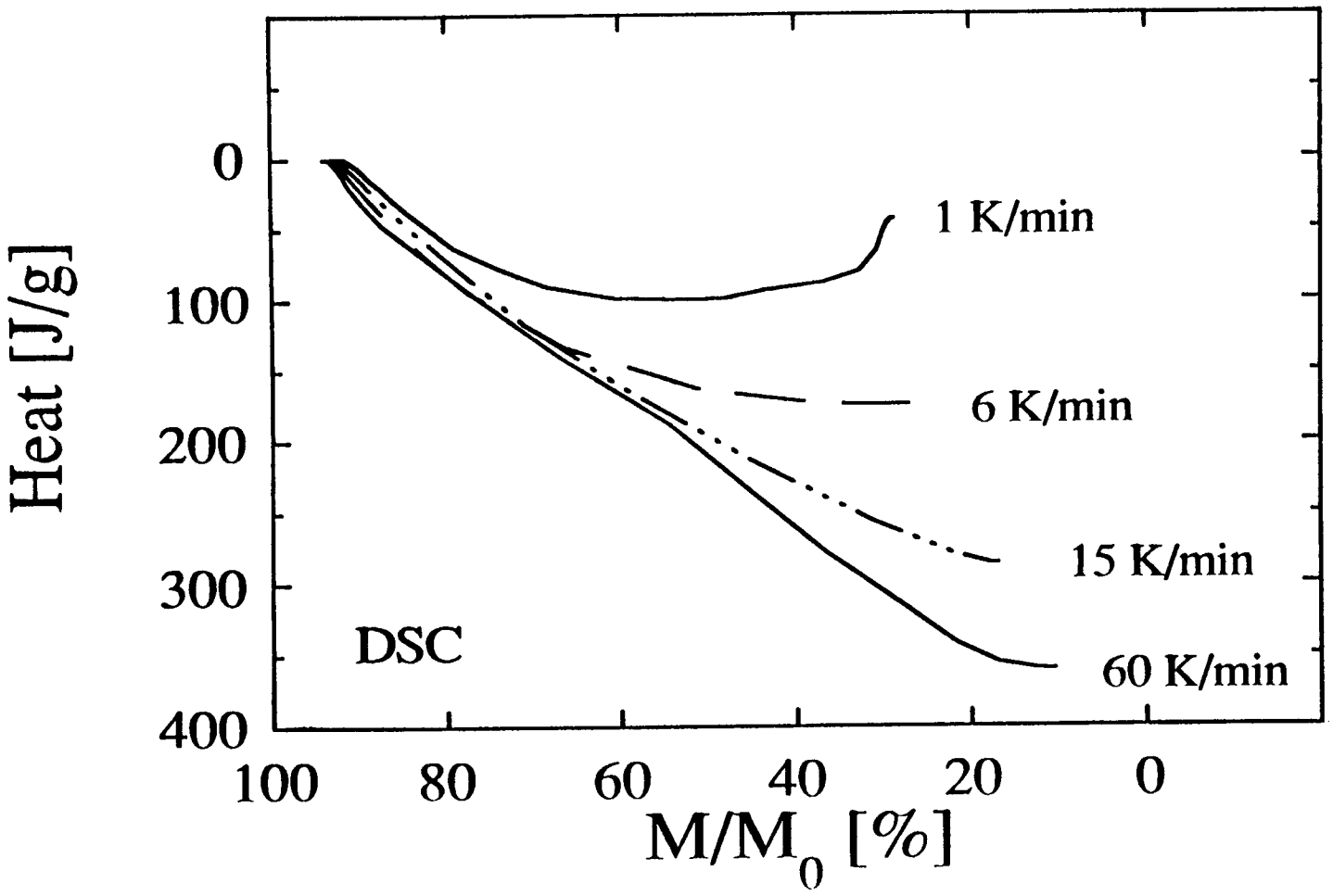

Figure 6.12 Cumulative heat of pyrolysis as a function of remaining fractional mass for different heating rates

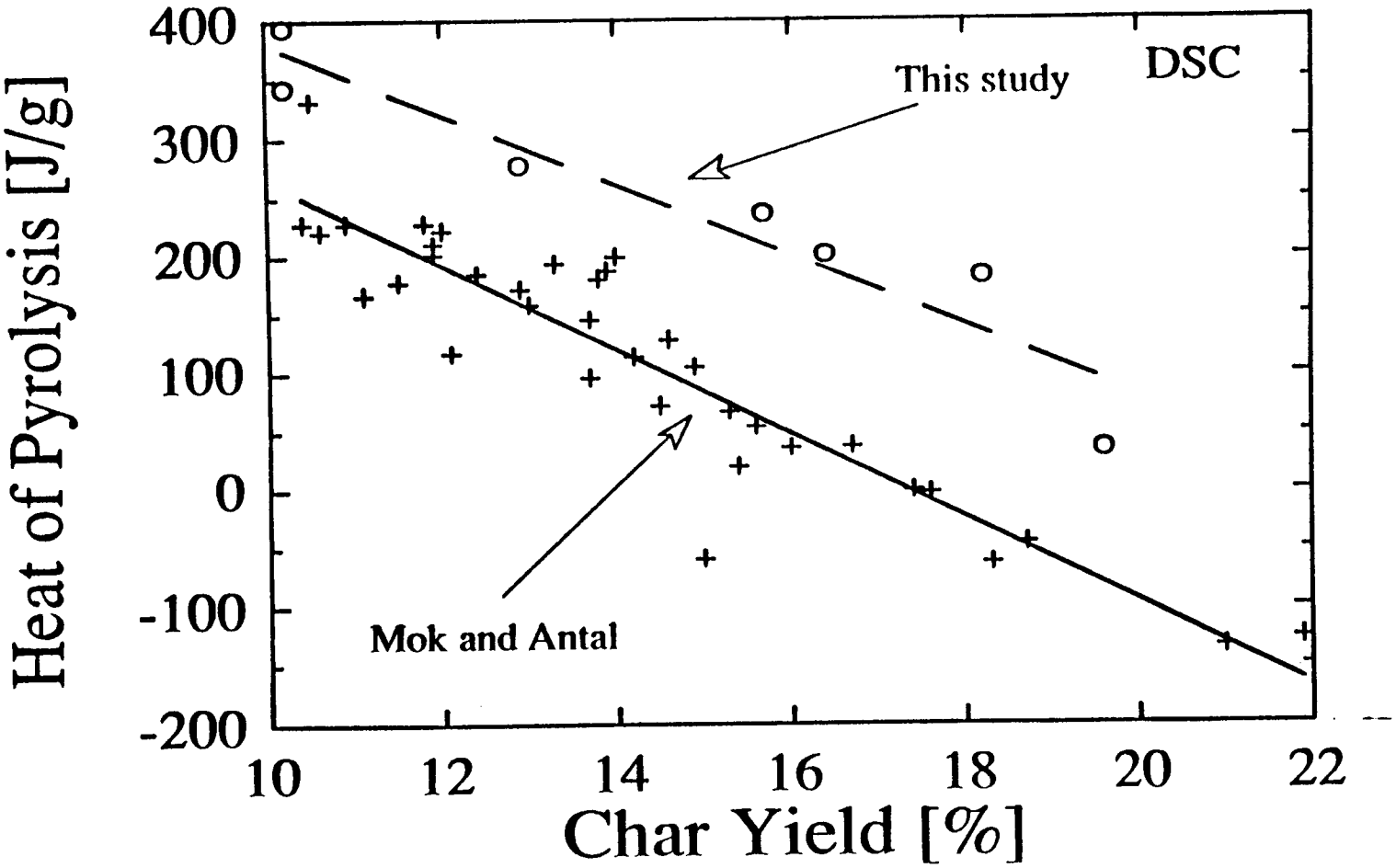

Figure 6.13 Heat of pyrolysis as a function of char yield (different char yields obtained in experiments with different heating rates). Also shown are data of Mok and Antal (122)

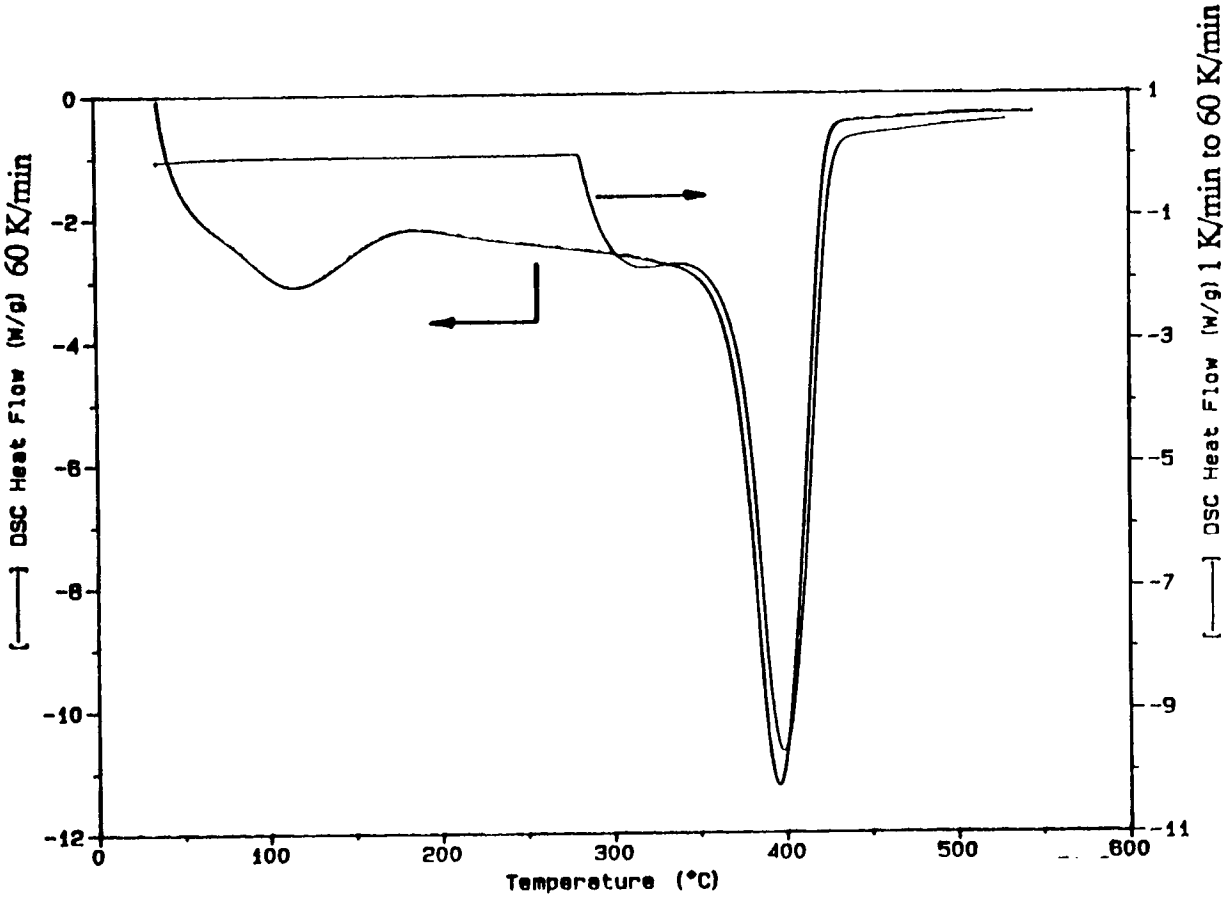

Figure 6.14 Comparison of DSC thermograms obtained at a heating rate of 60 K/min with thermogram from experiment in which the heating rate was changed from 1 K/min to 60 K/min at 280°C (before the 1 K/min main endotherm)

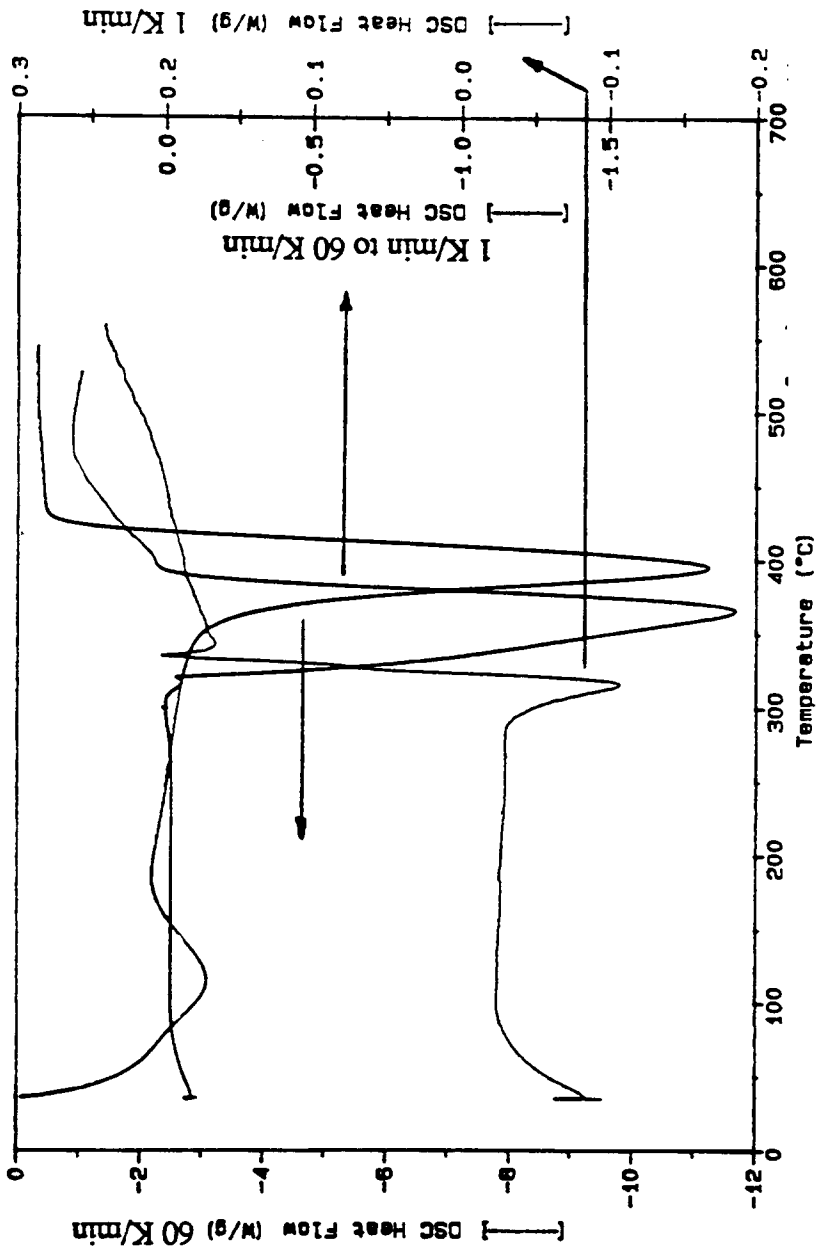

Figure 6.15 Comparison of DSC thermograms obtained at a heating rate of 60 K/min with thermogram from experiment in which the heating rate was changed from 1 K/min to 60 K/min at 327°C (before the 1 K/min exotherm)

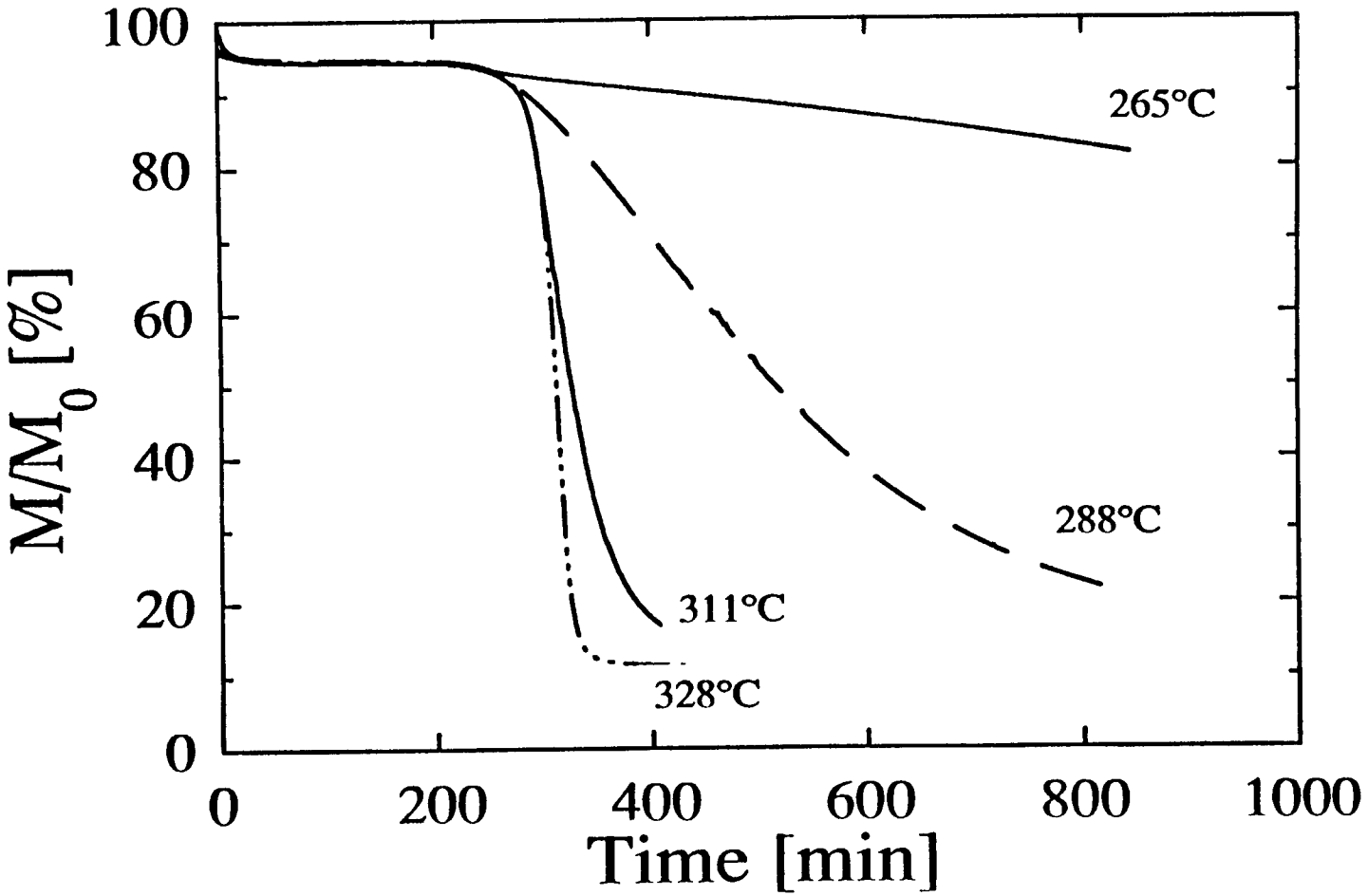

Figure 6.16a Fractional remaining mass, obtained in a TGA as a function of time for isothermal pyrolysis at different temperatures, after heating at a rate of 1 K/min

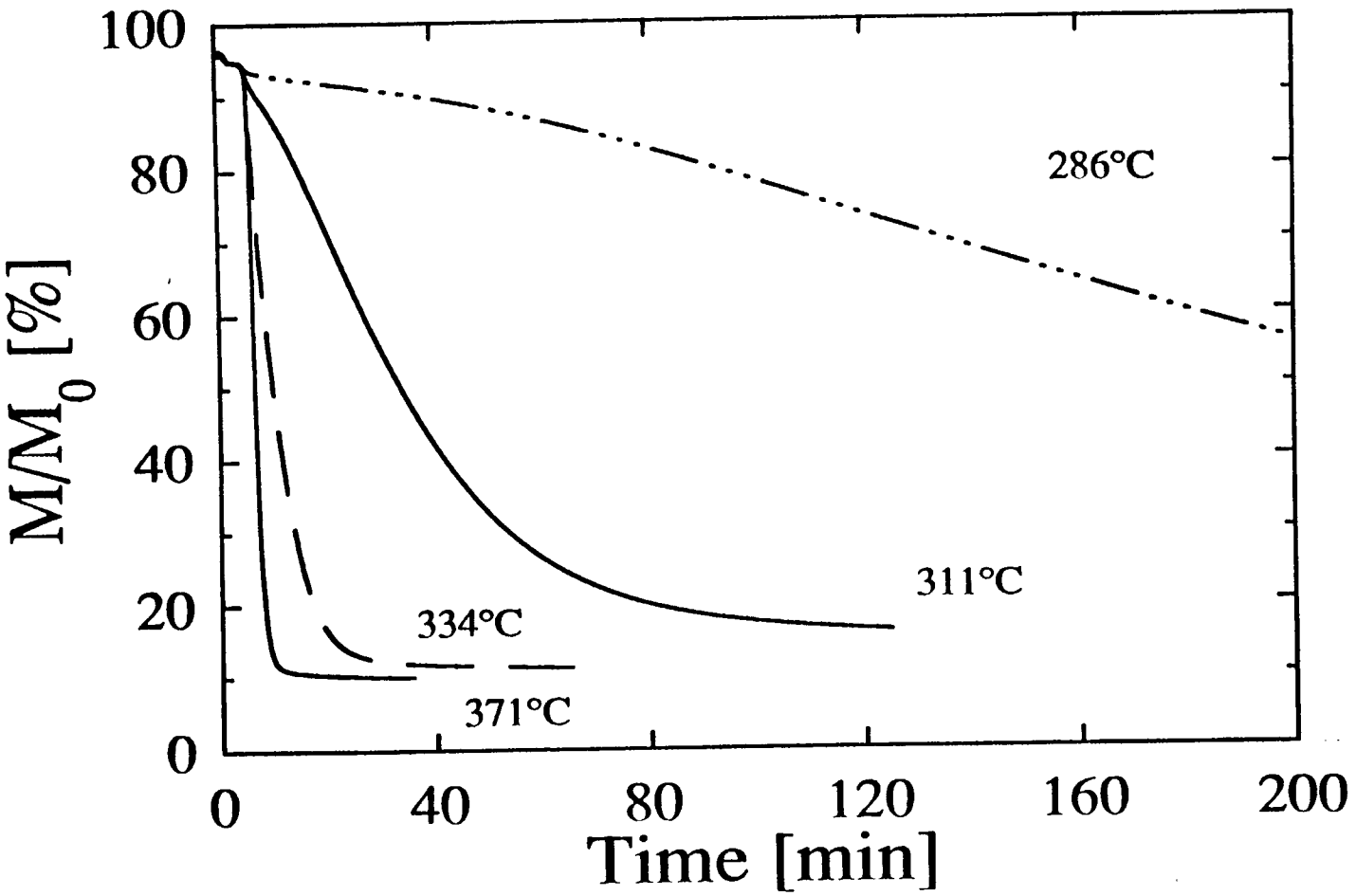

Figure 6.16b Fractional remaining mass, obtained in a TGA as a function of time for isothermal pyrolysis at different temperatures, after heating at a rate of 60 K/min

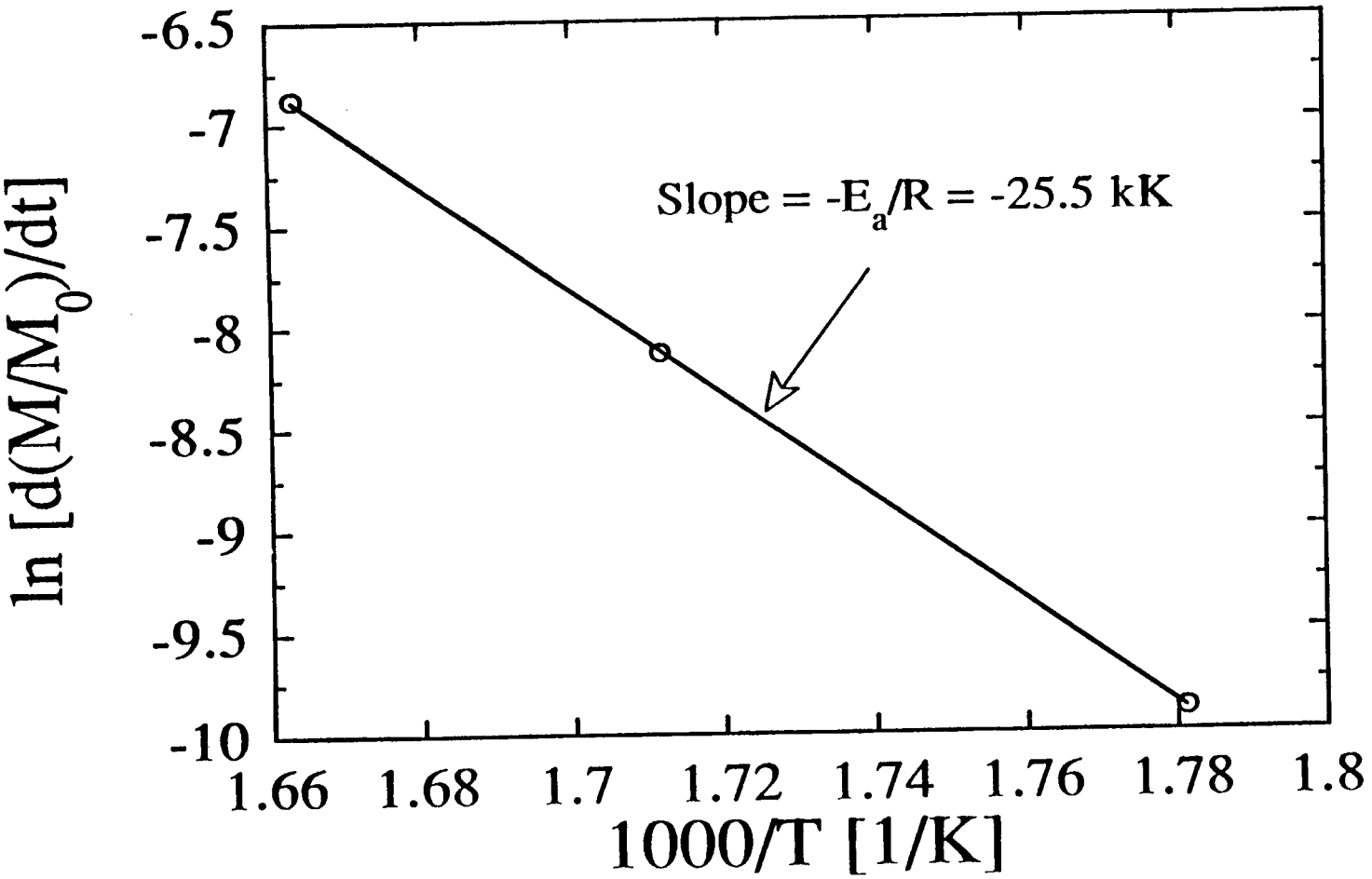

Figure 6.17 The Arrhenius plot for remaining fractional mass loss of 40%, from isothermal pyrolysis, after heating at a rate of 1 K/min (data of Figure 6.16a)

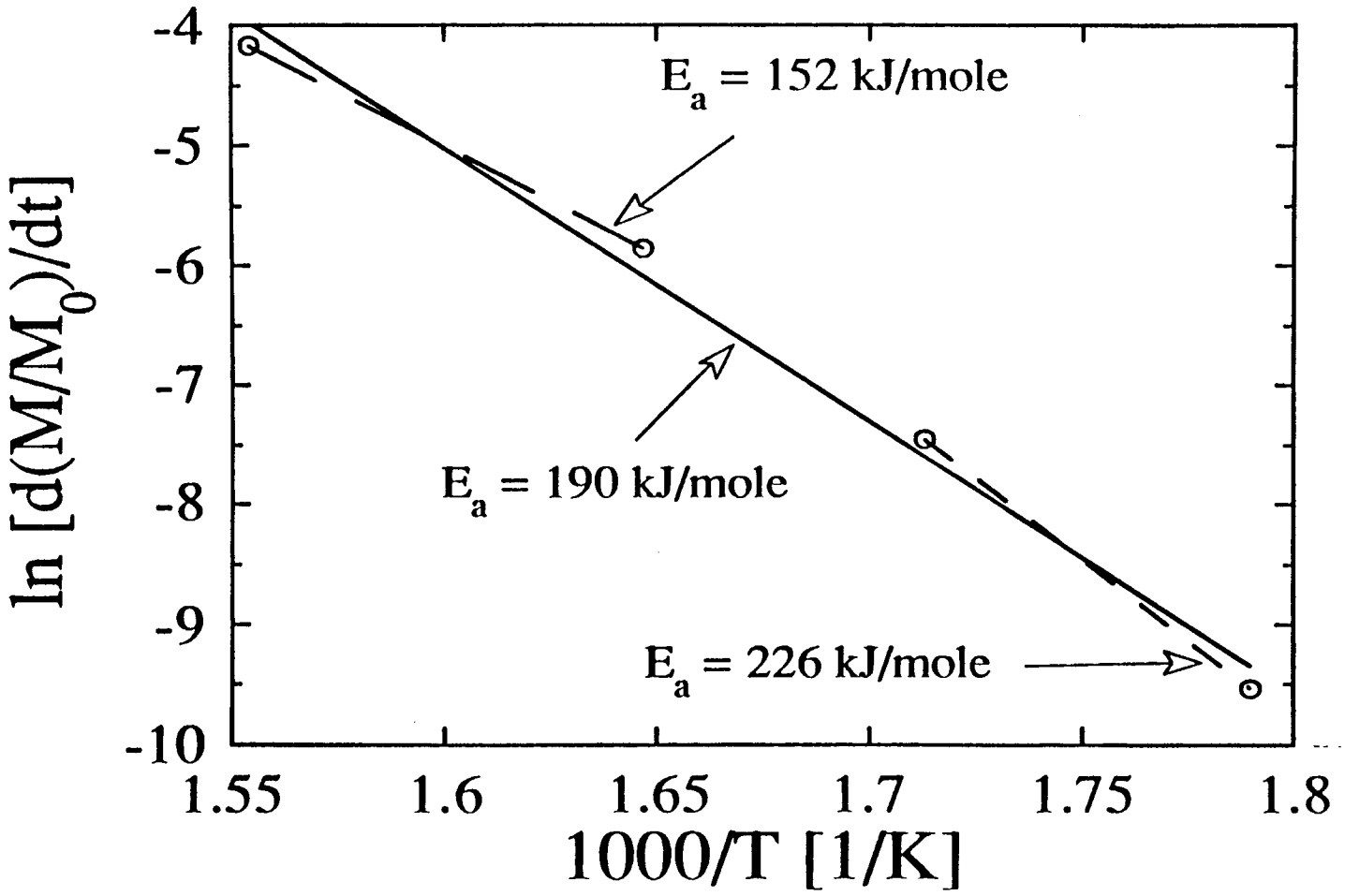

Figure 6.18 The Arrhenius plot for remaining fractional mass loss of 40%, from isothermal pyrolysis, after heating at a rate of 60 K/min (data of Figure 6.16b)

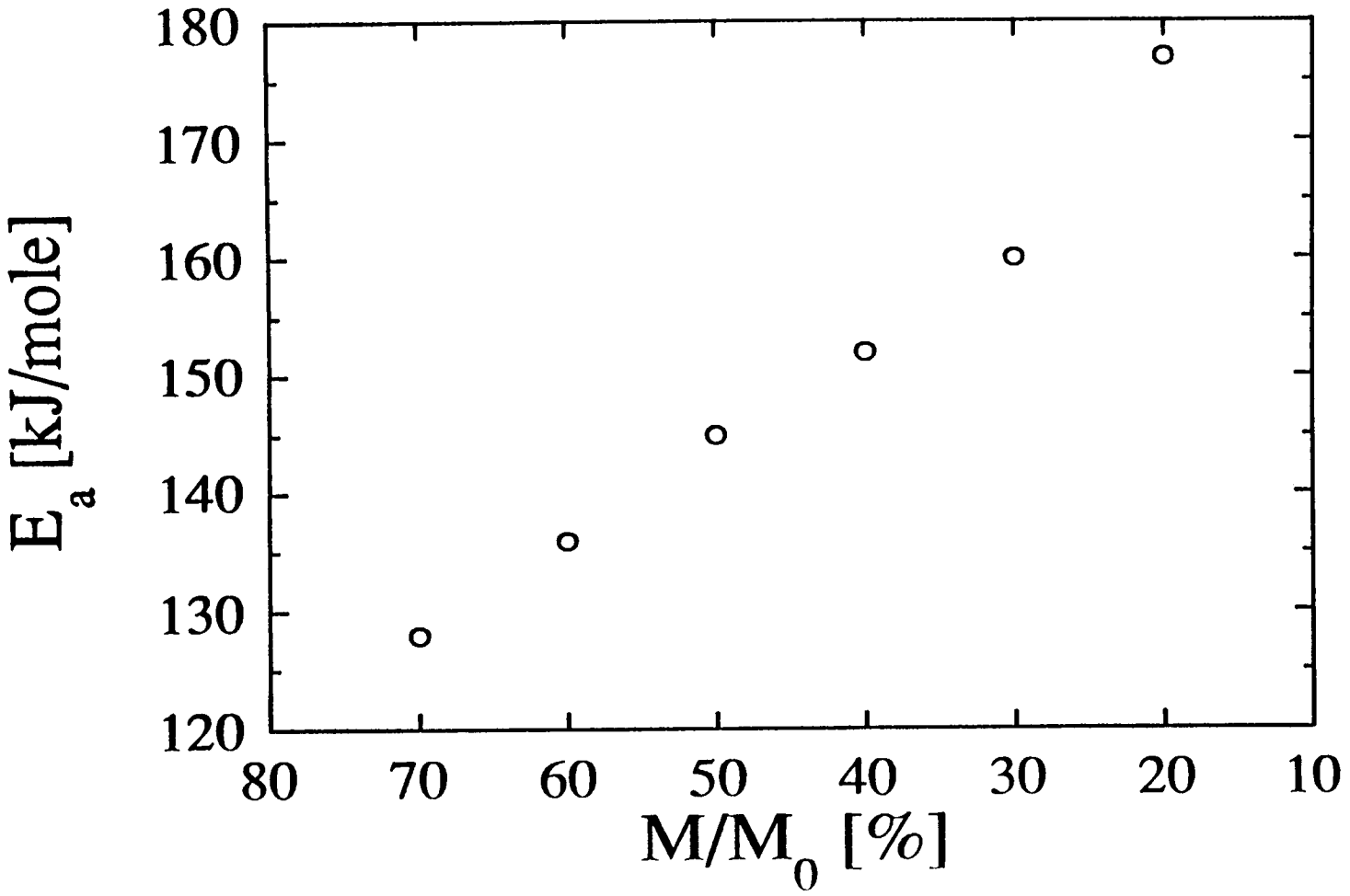

Figure 6.19 Activation energy as a function of fractional remaining mass determined from isothermal experiments after heating at a rate of 60 K/min (data of Figure 6.16b)

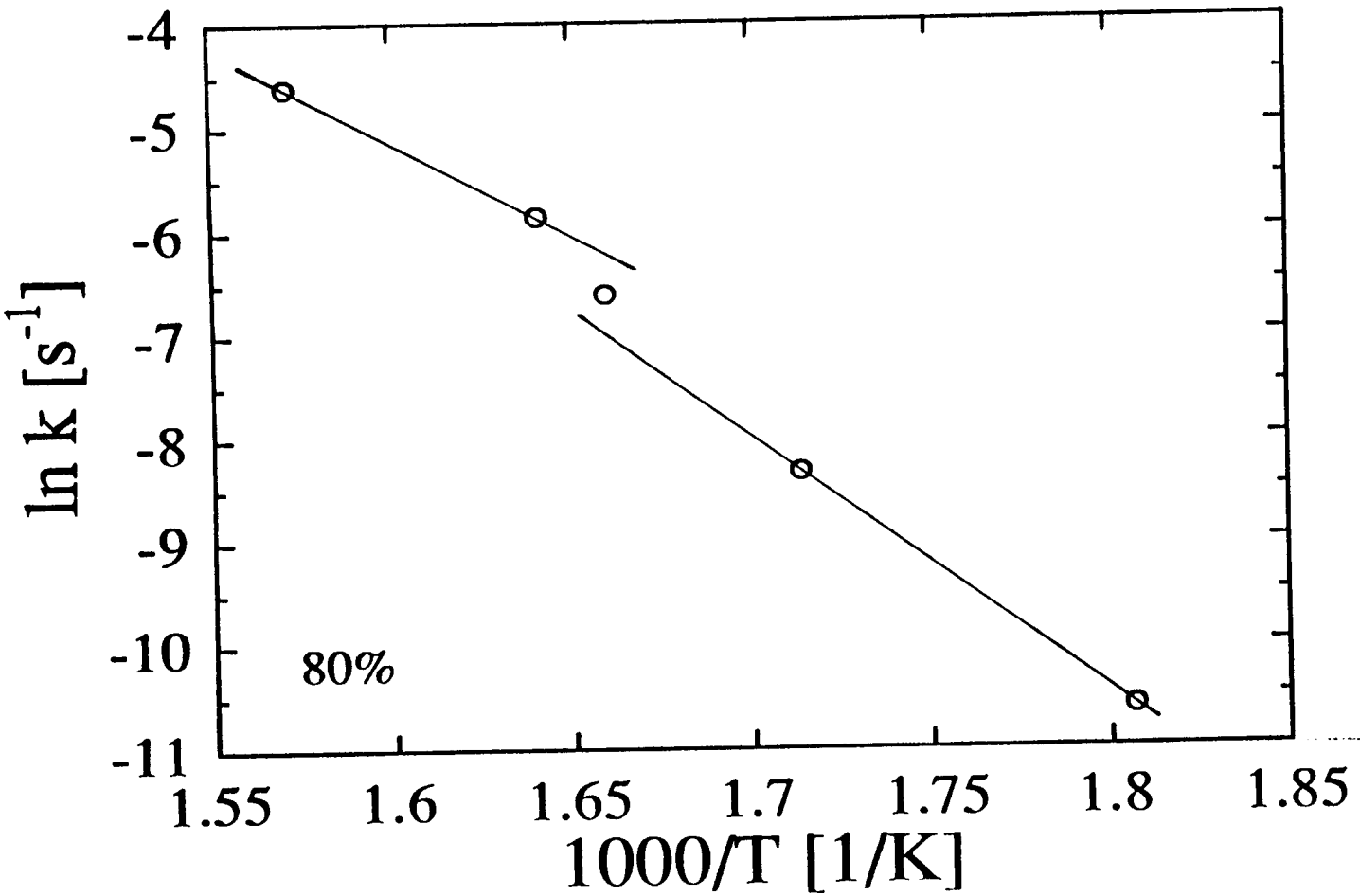

Figure 6.20a The Arrhenius plot for remaining fractional mass loss of 80%, from dynamic pyrolysis in a TGA, at different heating rates (data of Figure 6.7)

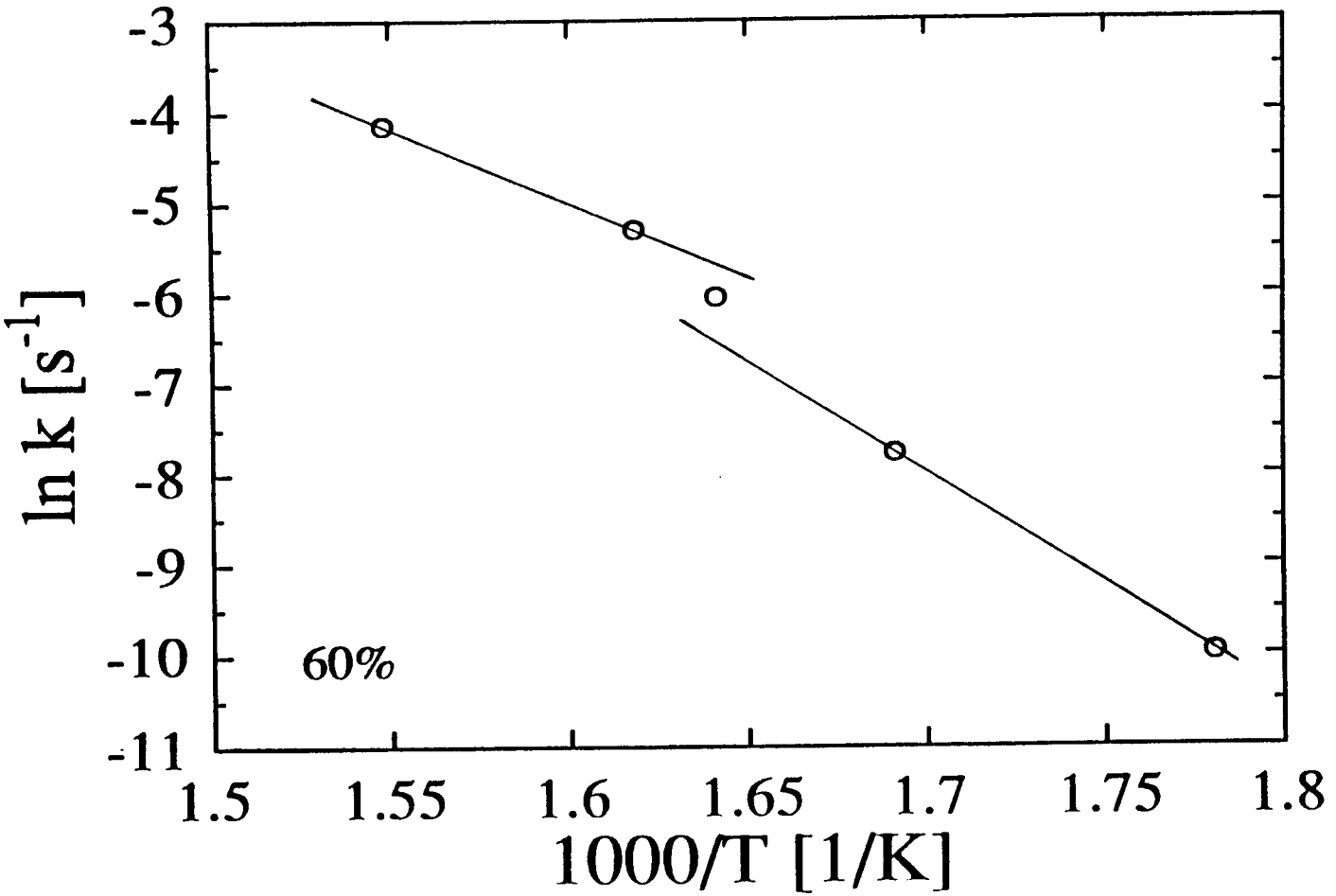

Figure 6.20b The Arrhenius plot for remaining fractional mass loss of 60%, from dynamic pyrolysis in a TGA, at different heating rates (data of Figure 6.7)

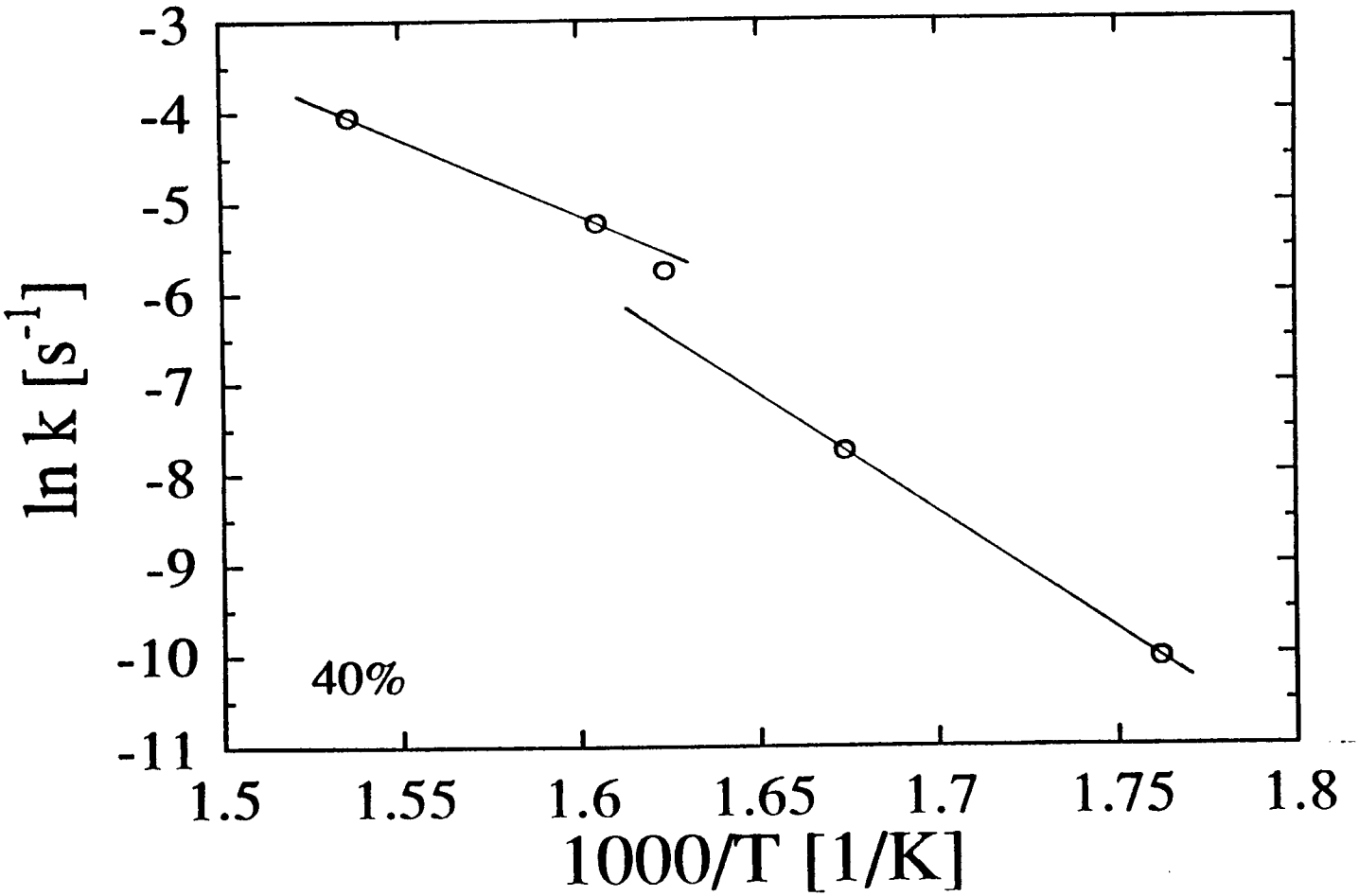

Figure 6.20c The Arrhenius plot for remaining fractional mass loss of 40%, from dynamic pyrolysis in a TGA, at different heating rates (data of Figure 6.7)

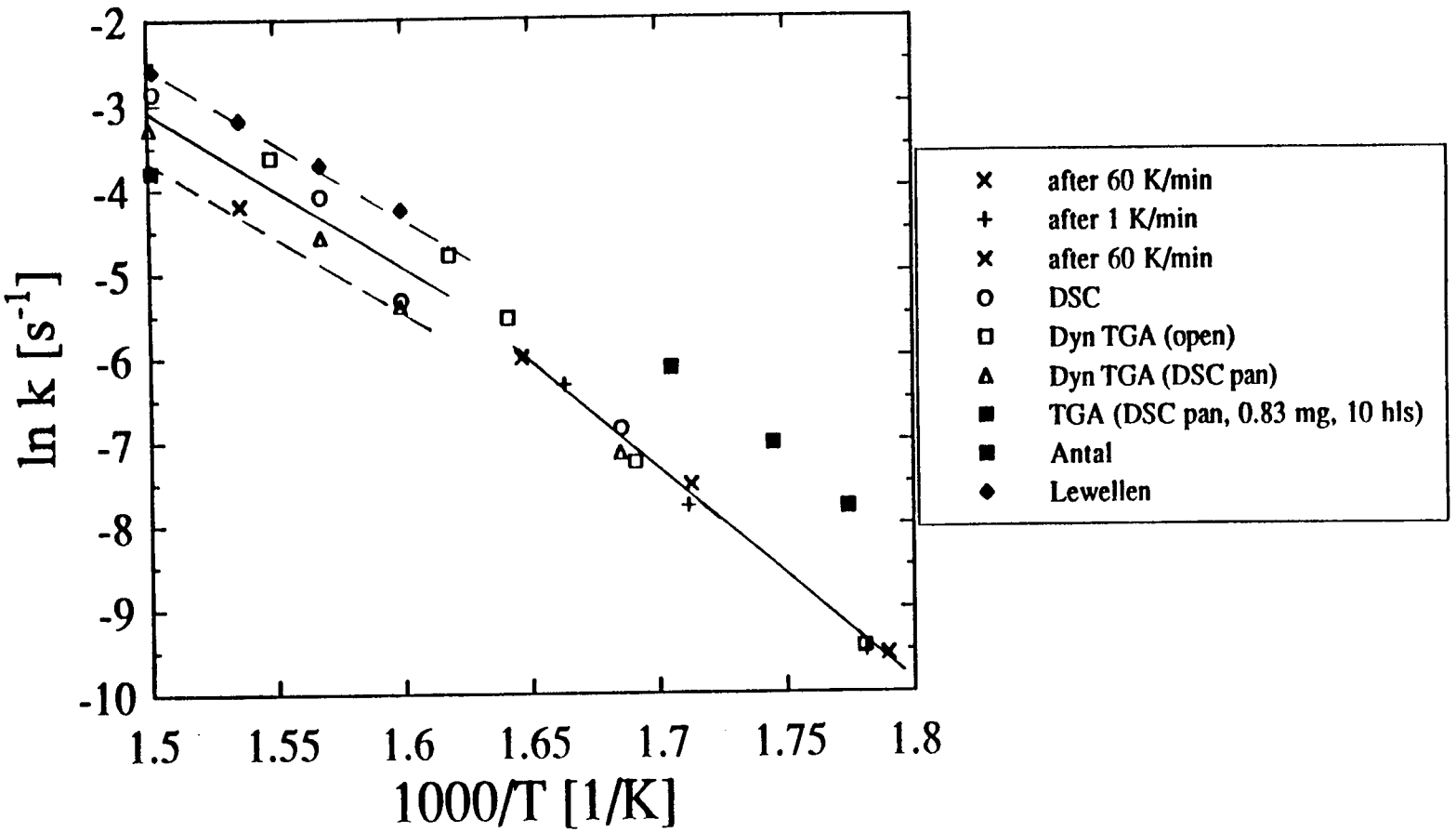

Figure 6.21 The Arrhenius plot for remaining fractional mass loss of 60%, from DSC and TGA (isothermal and dynamic), for different sample sizes and different mass transport limitations. Also shown are data from Lewellen et al. (108) and Cooley and Antal (42)

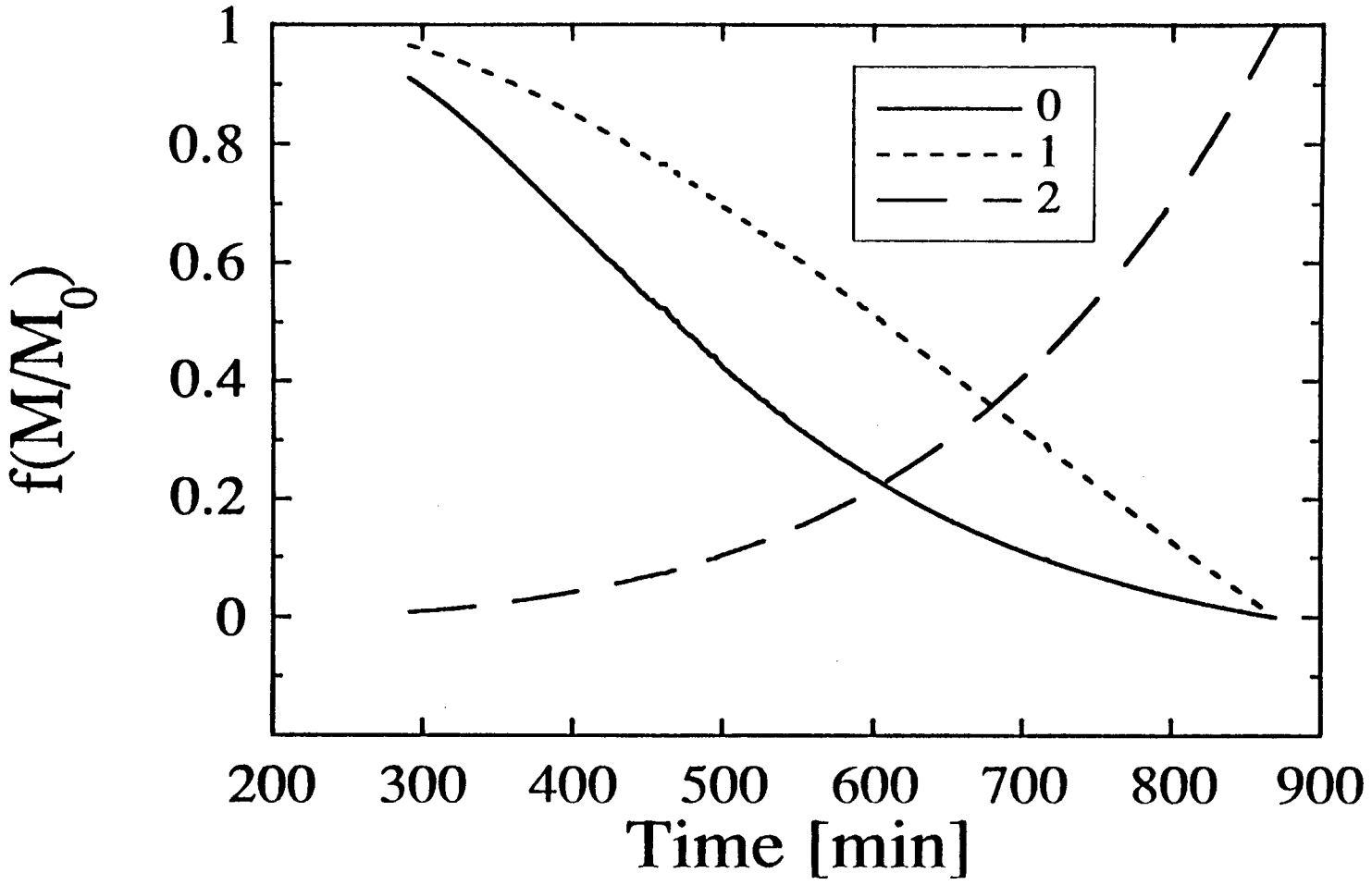

Figure 6.22a Reaction order determination for isothermal TGA at temperatures of 288°C, after heating at a rate of 1 K/min

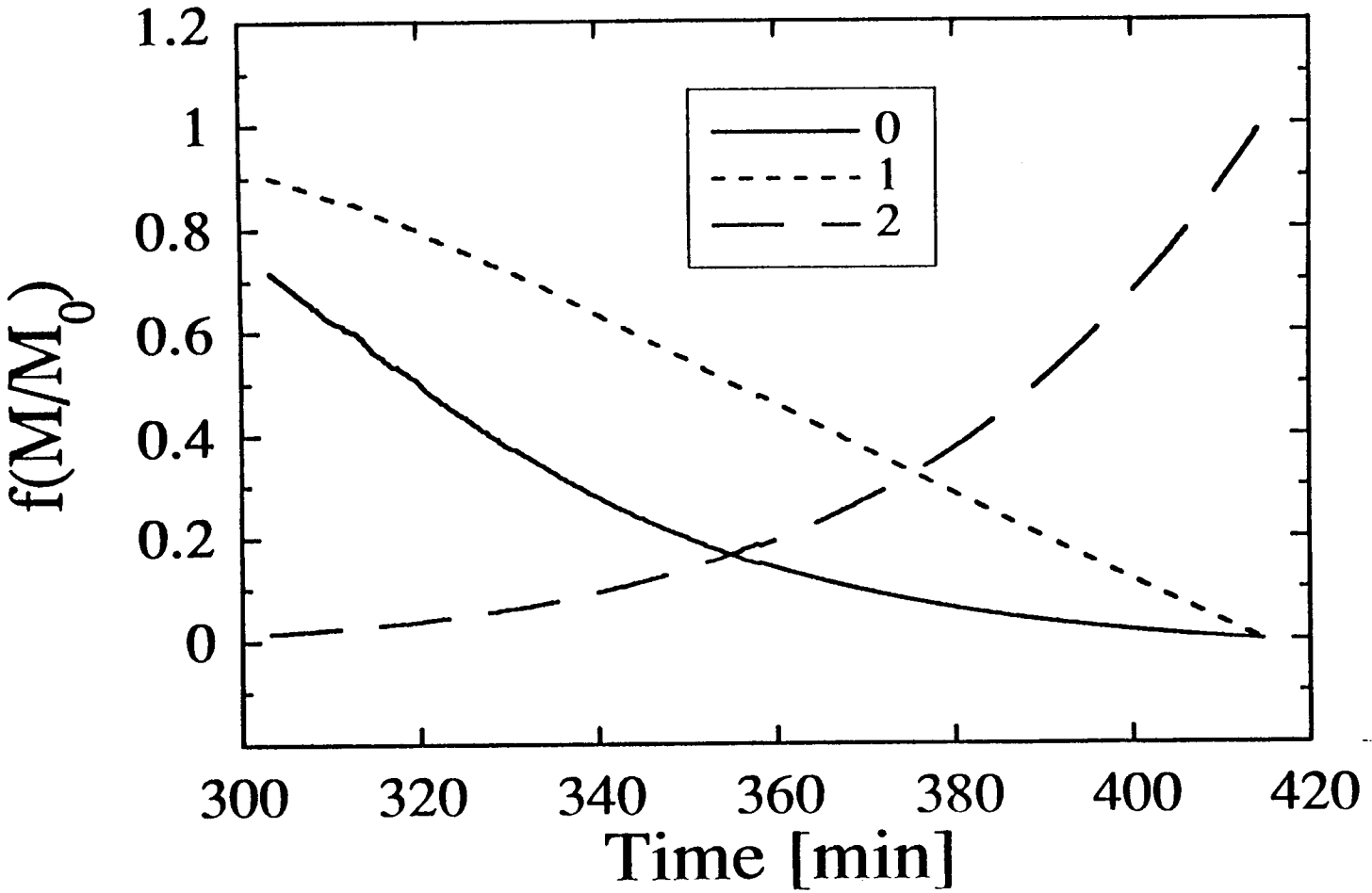

Figure 6.22b Reaction order determination for isothermal TGA at temperatures of 311°C, after heating at a rate of 1 K/min

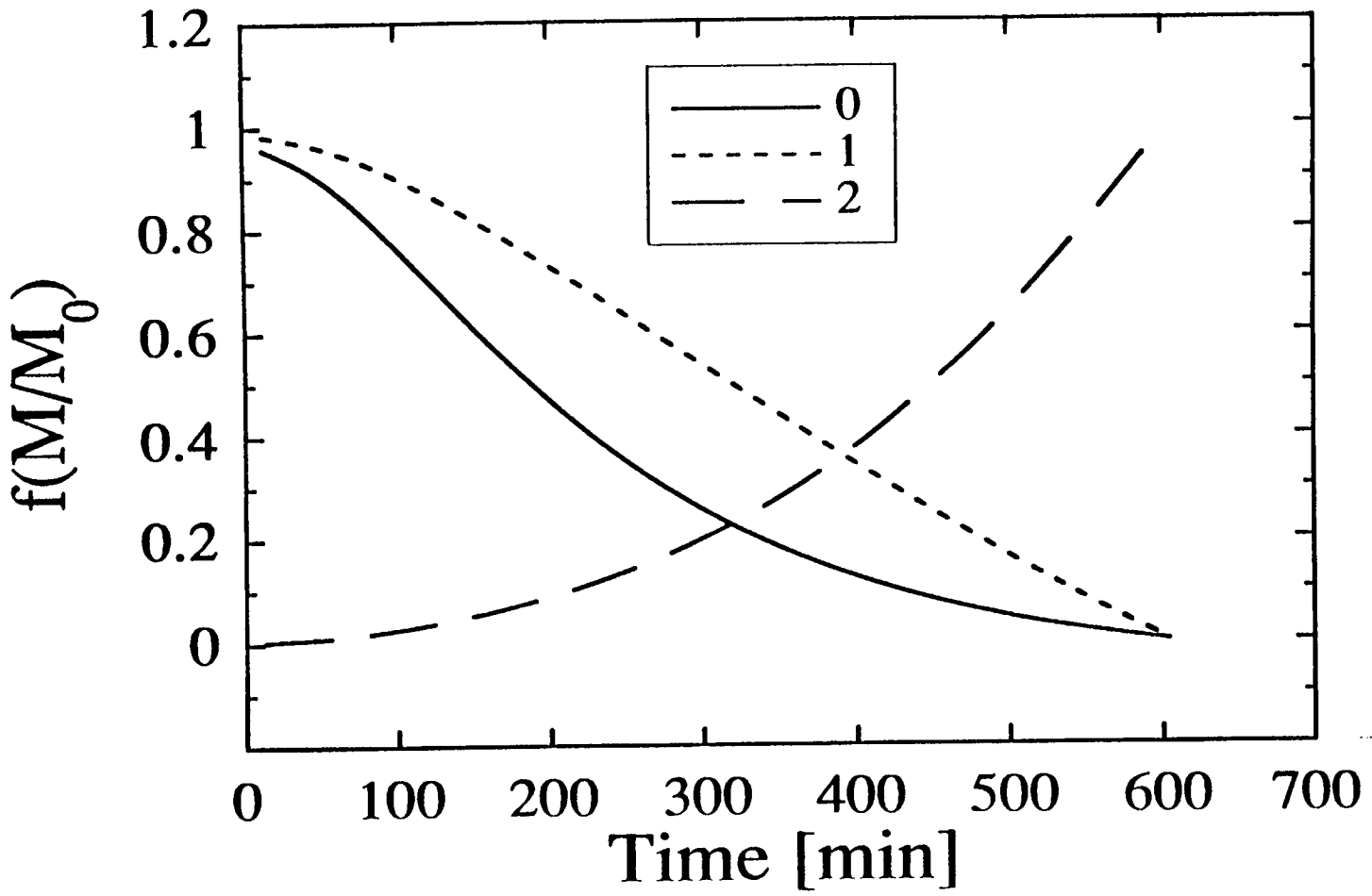

Figure 6.23a Reaction order determination for isothermal TGA at temperatures of 286°C, after heating at a rate of 60 K/min

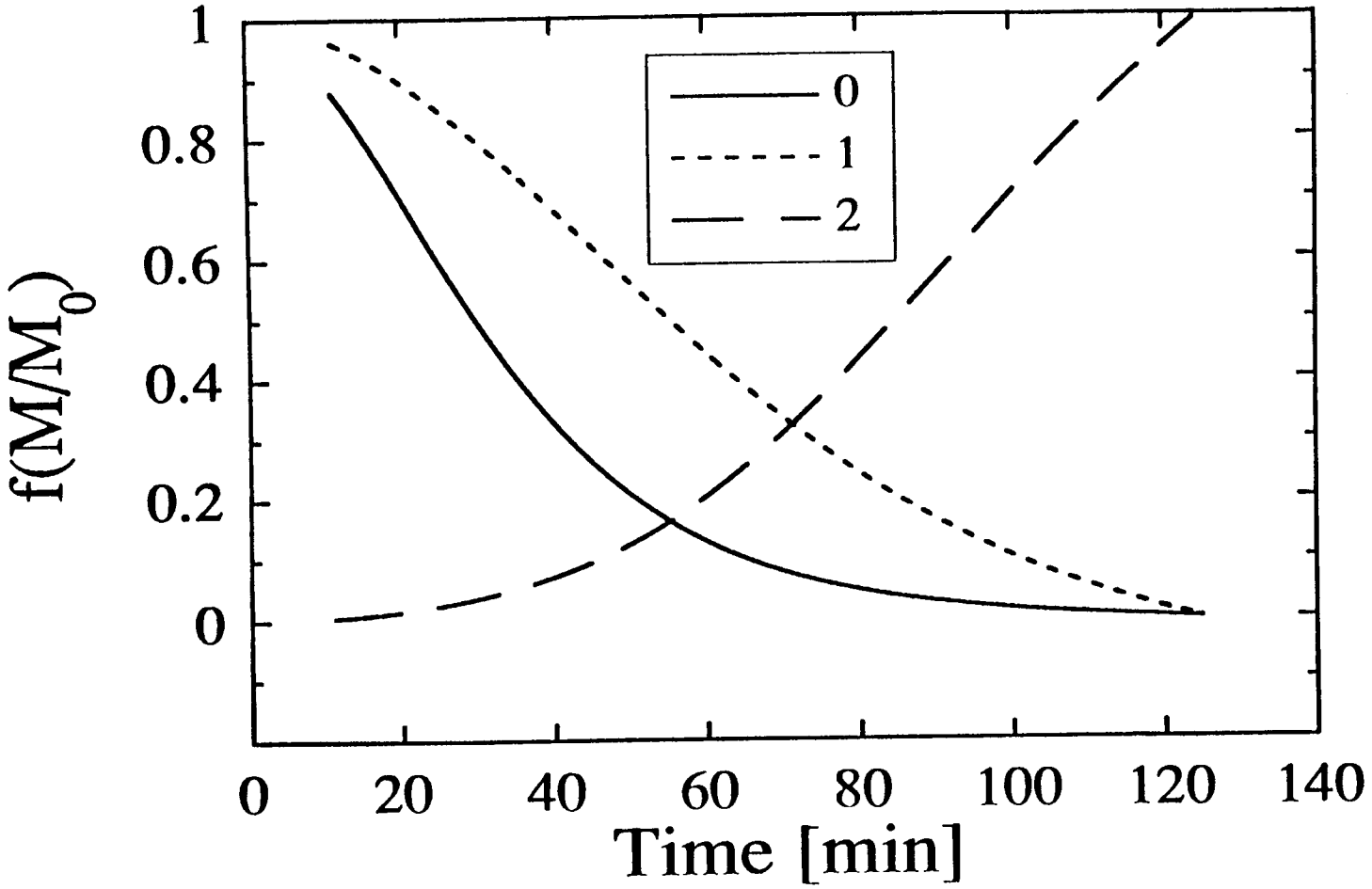

Figure 6.23b Reaction order determination for isothermal TGA at temperatures of 311°C, after heating at a rate of 60 K/min

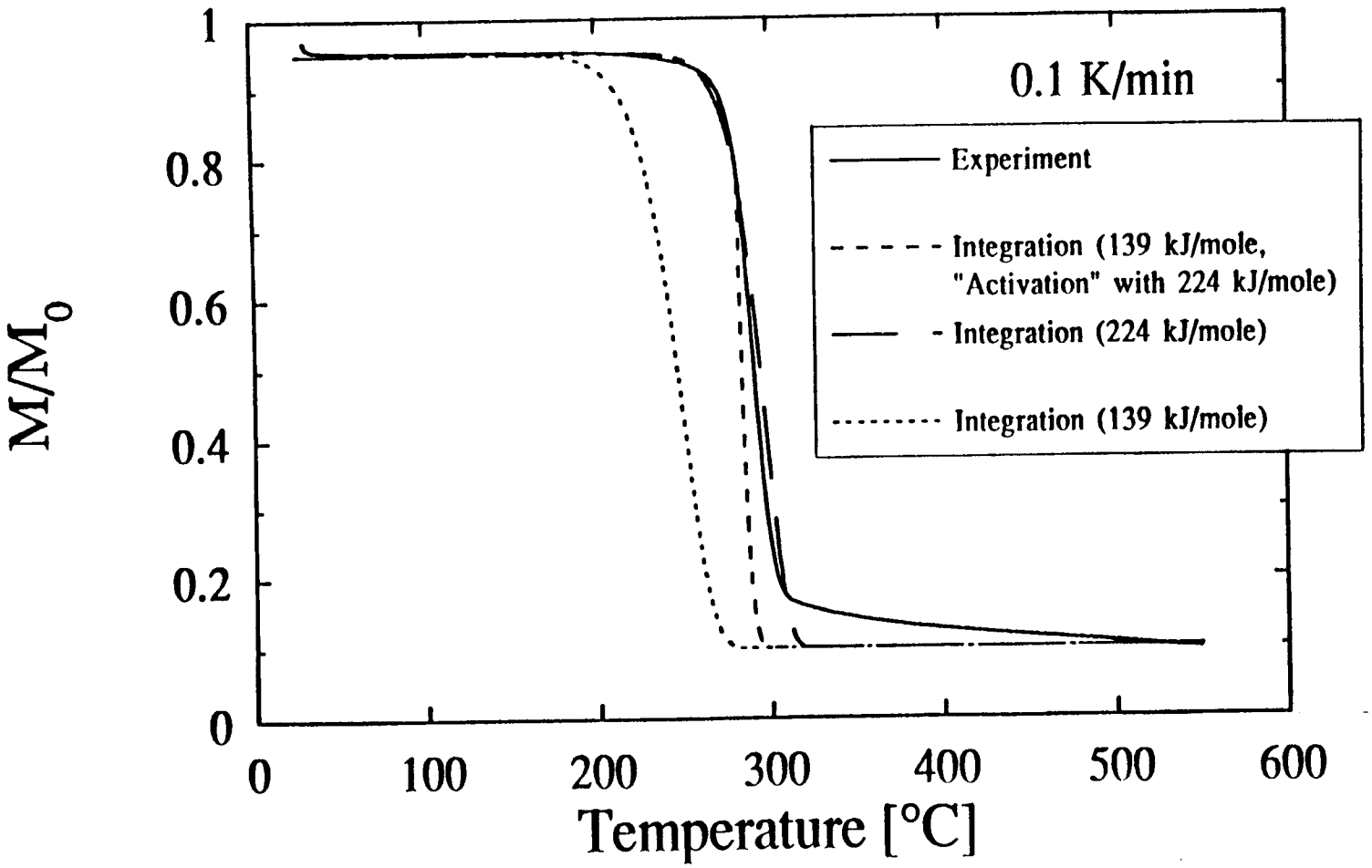

Figure 6.24a Comparison of numerically integrated Arrhenius equation (different kinetic parameters and with activation step) to the experimental fractional remaining mass for the heating rate of 0.1 K/min

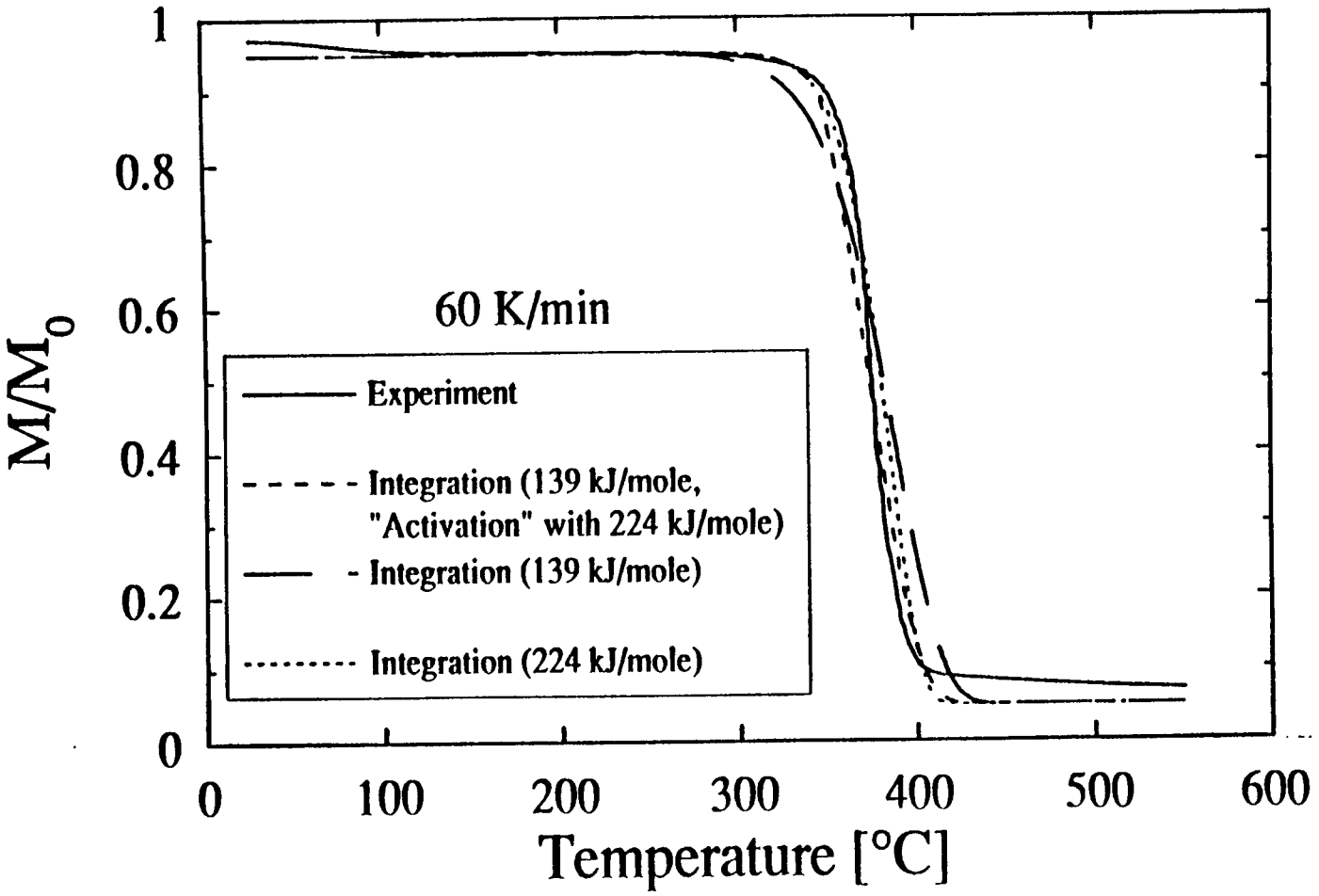

Figure 6.24b Comparison of numerically integrated Arrhenius equation (different kinetic parameters and with activation step) to the experimental fractional remaining mass for the heating rate of 60 K/min

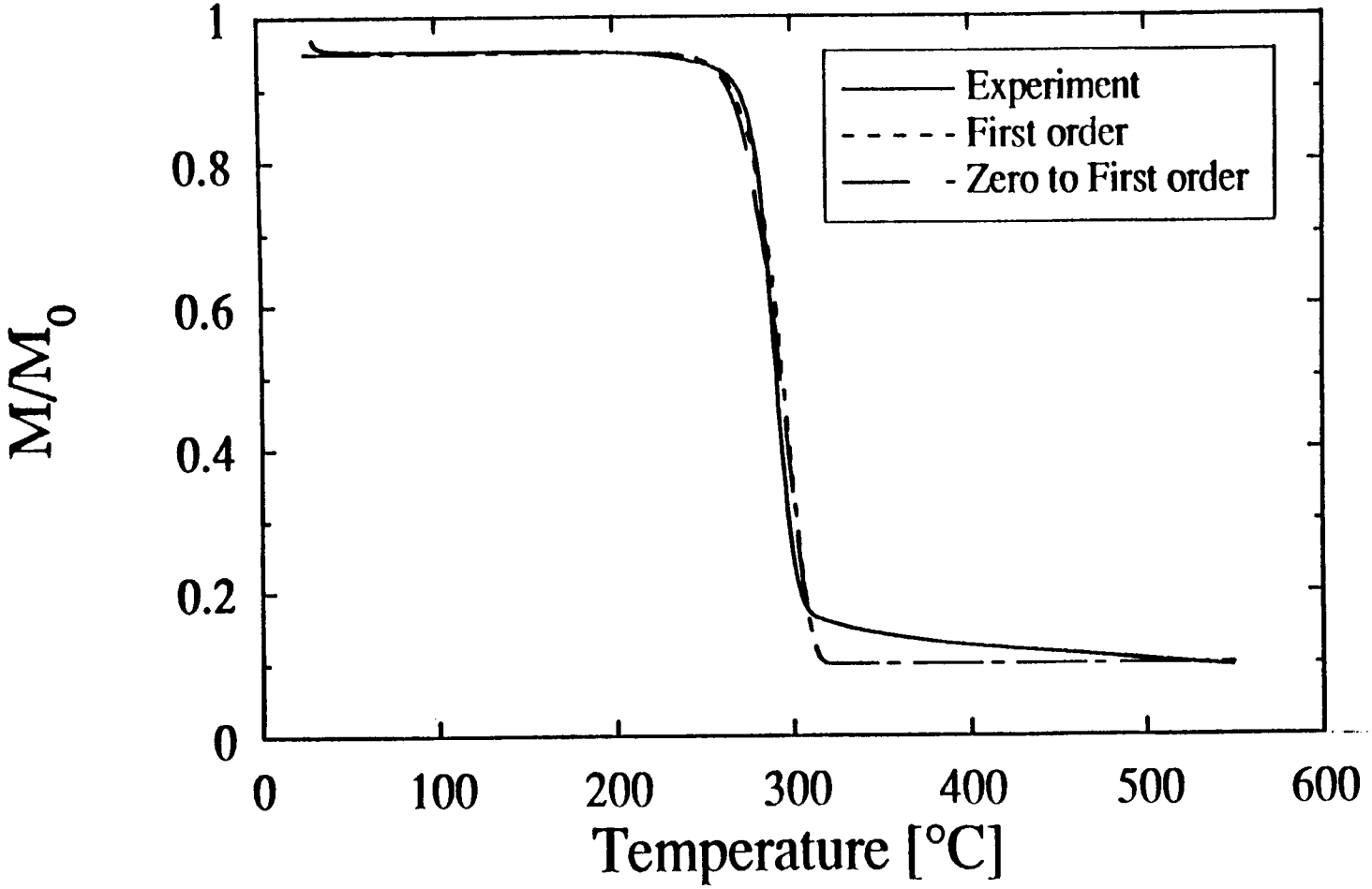

Figure 6.25a Comparison of numerically integrated Arrhenius equation (for change in reaction order from zero to first and for first order reaction) to the experimental fractional remaining mass for the heating rate of 0.1 K/min

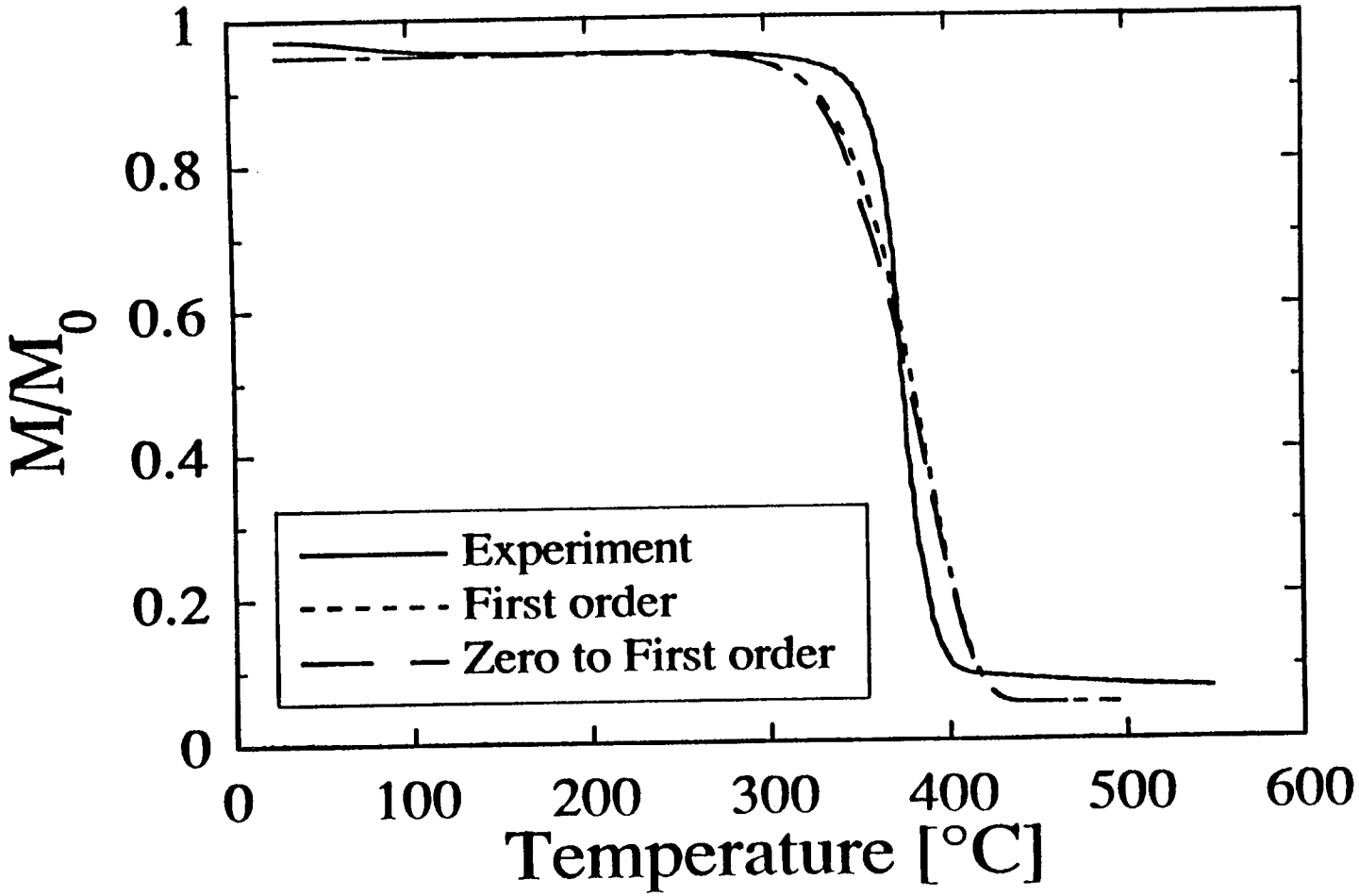

Figure 6.25b Comparison of numerically integrated Arrhenius equation (for change in reaction order from zero to first and for first order reaction) to the experimental fractional remaining mass for the heating rate of 60 K/min

7. MATHEMATICAL MODELING OF INFINITE SLAB PYROLYSIS

The mathematical model used in this work originated from Kung (101) and it was modified by Tamanini (178). It was used by Chen (39), whose version was received by this author from Professor Sibulkin of Brown University.

Several modifications of the model were made in the present work. The modifications were related to the experimental observations described in the preceding chapters. No modifications were made to the original numerical scheme. For that reason, only the changes made in the physical part of the model will be discussed here. The reader is referred to the model documentation by Tamanini (Appendix A in 178) for the part not discussed here. The listing of the program that was used for numerical calculations is presented in Appendix B.

7.1 ASSUMPTIONS

The model is for unsteady heat transfer in one dimension, including reaction kinetics and pyrolytic heat effect. Infinite slab geometry is assumed.

The thermal conductivity and the heat capacity are functions of local temperatures as well as of local fractions of virgin and pyrolyzed material. The linear dependence of the thermal conductivity and the heat capacity on temperature and fractions of virgin and pyrolyzed material is assumed. In light of the results outlined in Chapter 4 it seems that this assumption is well justified.

From the point of view of the present work, a significant disadvantage of the original

model was that it did not take into account the portion of the incident radiation reflected due to non-unity emissivity. Reflection is allowed in the present version. The front surface emissivity is allowed to change as it pyrolyzes. The virgin material and char emissivities are each assumed to be constant. The change of the front surface emissivity is assumed to be linear between virgin material and char, in such a manner that the surface emissivity is completely changed to char emissivity when 15% of the original mass is lost, which is in agreement with the data from pyrolysis under simulated fire conditions. The back, non-heated, surface emissivity was assumed to be constant, and the same as that of the virgin material. This assumption is probably not completely valid. However, the back surface does not completely pyrolyze under simulated fire conditions (Chapter 5) and, therefore, its emissivity might be closer to the virgin material emissivity than to that of char during the pyrolysis.

Pyrolysis follows Arrhenius kinetics. The original model allowed only a first order pyrolysis reaction. The present version allows for any reaction order. Another improvement to the original model is a possibility of two kinetic steps, as in the experimental section (Chapter 6). The first step employs single kinetic parameters, and the second allows for competitive reactions. As a result of decomposition, volatiles are generated and it is assumed that they are in perfect thermal contact with the solid matrix. The accumulation of volatiles within the solid matrix is neglected, it is assumed that they escape toward either or both surfaces as they are generated. The secondary pyrolysis reactions of volatiles are not taken into account. Due to these assumptions, the flux of volatiles from the pyrolyzing slab is governed by the rate of chemical decomposition. Since there was no information about the mechanism of secondary reactions available, this problem had to be treated empirically, in accord with the experimental observations; i.e., the ultimate char yield profile was used as an input.

In the original model, a constant heat of pyrolysis at some reference temperature was assumed. Since in this work the heat of pyrolysis was measured by DSC at reaction temperature, it was included in the present version of the model. Furthermore, the heat of pyrolysis was assumed to be a linear function of local ultimate char yield and it was thus incorporated empirically in the model.

The local shrinkage of the material as it pyrolyzes is taken into account in the present version of the model. It is assumed that the shrinkage is one-dimensional and that it is a function of the local extent of pyrolysis. The final shrinkage is assumed to be a function of the ultimate local char yield and the ultimate local density.

7.2 MODEL EQUATIONS AND BOUNDARY CONDITIONS

The unsteady heat transfer equation including convective heat transfer between the solid and the volatiles and pyrolytic heat effect is:

$$\frac{\partial(\rho_s h_s)}{\partial t} = \frac{\partial}{\partial x}\left(k_s \frac{\partial T}{\partial x}\right) + \frac{\partial}{\partial x}(M_g h_g) - Q\frac{\partial \rho_s}{\partial t} \qquad (7.1)$$

where:

t - time

x - distance from the front, heated, surface

ρ - density

k - thermal conductivity

h - enthalpy

M_g - mass flux of volatiles (positive in the negative x direction)

Q - heat of pyrolysis (positive when reaction is exothermic)

In equation (7.1) subscripts "s" and "g" refer to the solid matrix and volatiles, respectively. The enthalpy is defined as:

$$h = \int_{T_0}^{T} c_p\,(T)\,dT \tag{7.2}$$

where the heat capacity is a linear function of local temperature:

$$c_p(T) = c_p^0 + c_p^* (T - T_0) \tag{7.3}$$

The mass flux of the volatiles is calculated from:

$$\frac{\partial M_g}{\partial x} = \frac{\partial \rho_s}{\partial t} \tag{7.4}$$

The density of the solid matrix is calculated by assuming that it is composed of char and active, as yet not pyrolyzed, material and that each contributes a fraction to the total density:

$$\rho_s\,(t,x) = \left(1 - \frac{\rho_f}{\rho_i}\right) \rho_a\,(t,x) + \rho_f \tag{7.5}$$

where the subscripts "f", "i" and "a" respectively refer to final, initial and active material property, density in particular, in equation (7.5).

The char density is calculated from the density of solid matrix and active material:

$$\rho_c\,(t,x) = \rho_s\,(t,x) - \rho_a\,(t,x) \tag{7.6}$$

The pyrolysis rate is calculated from an nth order kinetics, Arrhenius temperature dependent expression with a single set of kinetic parameters:

$$\frac{\partial \rho_s}{\partial t} = - A \, \rho_a^n \exp\left(-\frac{E_a}{RT}\right) \tag{7.7}$$

or for parallel competitive reactions:

$$\frac{\partial \rho_s}{\partial t} = -\left[A_1 \exp\left(-\frac{E_{a1}}{RT}\right) + A_2 \exp\left(-\frac{E_{a2}}{RT}\right)\right] \rho_a^n \tag{7.8}$$

Equation (7.8) obviously requires the same reaction order for both competitive reactions. For the more general case of different reaction orders for competitive reactions, separate density (ρ_a) terms are required for each reaction.

The contribution from the char and the active material to the energy content of the solid is expressed as:

$$\rho_s h_s = \rho_a h_a + \rho_c h_c \tag{7.9}$$

Equation (7.9) can be used for obtaining the mean heat capacity as a function of the heat capacities of active material and char and the local density:

$$c_{ps} = \frac{\rho_a}{\rho_s} c_{pa} + \frac{\rho_c}{\rho_s} c_{pc} \tag{7.10}$$

where the densities of active material and char are related through equation (7.5).

The thermal conductivities are linear functions of the local temperature:

$$k = k^0 + k^* (T - T_0) \tag{7.11}$$

and the solid matrix thermal conductivity is calculated by assuming a linear variation between thermal conductivities of active material and char through:

$$k_s = \frac{\rho_a}{\rho_i} k_a + \frac{\rho_c}{\rho_f} k_c \tag{7.12}$$

When equation (7.9) is substituted in (7.1) the equation that is to be solved by the model is obtained:

$$(\rho_a c_{pa} + \rho_c c_{pc}) \frac{\partial T}{\partial t} = \frac{\partial}{\partial x}\left(k_s \frac{\partial T}{\partial x}\right) + \frac{\partial}{\partial x}(M_g h_g) - \frac{\partial \rho_s}{\partial t} Q \tag{7.13}$$

with the boundary condition at the front, heated, surface of the slab:

$$-\left(k_s \frac{\partial T}{\partial x}\right)_{x=0} = \varepsilon_{FS} \dot{q}''_L - h(T_{FS} - T_\infty) - \varepsilon_{FS}\sigma(T_{FS}^4 - T_\infty^4), \tag{7.14}$$

where the respective terms have the following general significance: the first term on the right hand side includes the incident heat flux ($\dot{q}''_L$, where the subscript "L" refers to lamps from the simulated fire apparatus) and the reflection of the portion of the radiation due to the non unity emissivity ($(1-\varepsilon_{FS})\ \dot{q}''_L$, where the subscript "FS" refers to the front surface of

the slab); the second term is the convective heat loss (h is the heat transfer coefficient, assumed here to be constant) and the third term is the radiative heat loss. Subscript "∞" refers to both the initial temperature and the temperature of the surfaces far from the slab that might be engaged in the radiative heat transfer with the front surface of the slab. The back surface boundary condition has the form of equation (7.14) without the first term.

7.3 MODIFICATIONS TO THE ORIGINAL MODEL

In this section the principal modifications that were made to the original model will be outlined. A complete listing of the program is given in Appendix B. Listings of the parts of the program will be presented here to aid the description. In the complete listing the lower case letters were used for modified parts, while what is retained from the original code is shown in upper case letters.

The front surface boundary condition was modified to include the reflected radiation from the surface and it is as represented in equation (7.14). In addition to the heat loss by immediate reflection of the portion of the incident radiation the model allows the surface emissivity change between virgin material and char emissivities. The part of the code where the surface emissivity is being calculated and, eventually, changed is (from CHAPTER 5 of the program):

```
      if(rhobar.lt..8)go to 511
      epsl=epscell+(epschar-epscell)*(1-rhobar)/.15
      if(epsl.gt.epschar)epsl=epschar
      epsl=epsl*5.669e-8
511 ...
```

As shown in this partial listing if the average density of the slab (rhobar) is less than 0.8 the calculation is skipped. The entire emissivity change takes place up to the point where 15% of the mass is lost. The emissivity is changed linearly between virgin material (epscell) and char emissivity (epschar).

Another modification of the original model was to allow for char yield profile, heat of pyrolysis to be function of local ultimate char yield and the slab shrinkage. The relevant part of the code is (from CHAPTER 4 of the program):

```
      if(tbar(i).lt.tl.or.ind(i).eq.1)go to 403
      hrate(i)=(tbar(i)-t0k)/time
      if(hrate(i).gt.2.)hrate(i)=2.
      cy(i)=.13-.07*alog(hrate(i))
      qp0(i)=-7.58e5+3.424e6*cy(i)
      rhof(i)=0.066+0.934*cy(i)
      if(rhof(i).lt.rhoff)rhof(i)=rhoff
      shrf(i)=cy(i)/rhof(i)
      rhofml(i)=1-rhof(i)
      ind(i)=1
403   if(rhoa(i).lt.rhof(i))rhoa(i)=rhof(i)
      shr(i)=(shrf(i)-rhof(i)+rhoa(i)*(1-shrf(i)))/rhofml(i)
      if(shr(i)*rhoa(i)-cy(i).le.0.)go to 404
      ...
404   ...
```

The local heating rate (hrate(i)) is calculated. Following the heating rate calculation an

empirical expression is used to determine the local ultimate char yield (cy(i)). With the local ultimate char yield known, the local heat of pyrolysis (qp0(i)), local final density (rhof(i)) and the local ultimate shrinkage (shrf(i)) are calculated, all based on the experimental findings and all expressed as functions of local ultimate char yield. Following those calculations an indication parameter (ind(i)) is set to unity in order not to repeat the calculation for the same position twice, since the ultimate values were meant to remain constant for the rest of the calculations. Next the current local shrinkage parameter (shr(i)) is calculated by linear variation between virgin material (shr(i)=1) and char (shr(i)=shrf(i)). It should be noted that the shrinkage parameter represents a reducing factor and as such it is dimensionless. However, in the expression for shrinkage parameter all densities are non dimensionalized and, thus, there are no conflicts with units. On the other hand the expression represents an equation for straight line and that is where the mixing of shrinkage parameter and densities took place. The current local shrinkage parameter is used further in the model to reduce the size of the grid in the x direction (i.e. DX is replaced by shr(i)*DX, where DX is the grid size in the x direction).

The mass loss rate, or density decrease per time step in the model, is calculated from Arrhenius equation. The part of the code where the calculations take place is (from CHAPTER 4 of the program):

```
      onoff=rhobar-switch
      if(onoff)402,402,401
401   DRHO(I)=-(DTIME*PF*((shr(i)*RHOA(I)-cy(i))**order)
     1  *EXP(TRNEG/TBAR(I)))/rhofml(i)
      go to 404
402   drho(i)=-(dtime*(pf*((shr(i)*rhoa(i)-cy(i))**order)*
```

```
     1 exp(trneg/tbar(i))+pf2*((shr(i)*rhoa(i)-cy(i))**order2)
     2 *exp(trneg2/tbar(i))))/rhofml(i)
404   IF(RHO(I)+DRHO(I).LT.RHOF(i)) DRHO(I)=RHOF(i)-RHO(I)
405   RHOA(I)=RHO(I)+.5*DRHO(I)
```

First it is checked what kinetics should be used by comparing the current average density (`rhobar`) to the preset average density (`switch`) where the change in kinetics takes place. Next the corresponding local density change (`drho(i)`) is calculated. It should be noted that the shrinkage is taken into account for calculation of the remaining material to be pyrolyzed. When the model calculates the density change through competitive reactions it allows for two different orders of reactions (`order` and `order2`). Finally, the local density is reduced for the amount of density change.

The present version of the model allows for incident heat flux screening by the volatiles that are flowing out of the solid matrix. The portion of the code where the heat flux reduction due to the screening is calculated is (from CHAPTER 5 of the program):

```
      reduc=1.
      if(rhobar.eq.1.) go to 535
      if(rhobar.lt.rmaxred) go to 532
      reduc=(.8*rhomaxr+.2*rhobar-rmaxred)/(rhomaxr-rmaxred)
      go to 535
532   reduc=(rmaxred-.8*redback-.2*rhobar)/(rmaxred-redback)
535   if(reduc.gt.1.)reduc=1.
      bc(1)=reduc*bc(1)
      fepsl=epsl/5.669e-8
```

```
BT(1)=BT(1)+fepsl*BC(1)
```

The above calculation represent an approximation to the signal given by optical pyrometer in the simulated fire apparatus. Essentially, it represents an assymetric saw tooth, a mathematical simplification of the pyrometer signal. The reducing factor (`reduc`) starts from unity (no reduction of incident heat flux), when there are no density changes and it starts to change at a desired mean density (`rhomaxr`). It is preset that the maximum reducing factor can be 0.8 at a desired mean density of maximum reduction (`rmaxred`), it decreases from unity to 0.8 until the value of (`rmaxred`) is reached and than increases. The increase is back to unity, when the desired mean density is achieved (`redback`). In this part of the code the reduction of the incident heat flux due to the non unity emissivity (`fepsl`) takes place.

In order to compare the results obtained by model calculations to the experimental results the densities calculated by the model should be put on the similar bases with the experiment. The model operates with non dimensional densities and it is analogous of fractional mass from the experiment, provided that the volume of the slab does not change. In one dimension that means that there is no shrinkage. All calculations were performed with the shrinkage taken into account except for the mean density of the slab, which was actually used for comparison with the experiments, since the mass of the entire slab was experimentally measured. The mean density of the slab is not used for heat transfer or kinetic calculations and there was no need to correct it for shrinkage. However, since the calculations were performed with the shrinkage parameter there is a need to correct the mean density of the slab as well, otherwise it will not correspond to the calculations. The part of the program where the mean density is corrected for the shrinkage is (from SUBROUTINE OUTPUT of the program):

```
      RHOBAR=1.
      rhobar1=1.
      IF(RHOA(1).EQ.1..AND.RHOA(NP1).EQ.1.) GO TO 20
      RHOBAR=.5*RHOA(1)
      rhobar1=.5*rhoa(1)*shr(1)
      DO 21 I=2,N
      RHOBAR=RHOBAR+RHOA(I)
      rhobar1=rhobar1+rhoa(i)*shr(i)
21    CONTINUE
      RHOBAR=RHOBAR+.5*RHOA(NP1)
      rhobar1=rhobar1+.5*rhoa(np1)*shr(np1)
      RHOBAR=RHOBAR/FLOAT(N)
      rhobar1=rhobar1/float(n)
20    CONTINUE
```

The mean density with the shrinkage taken into account (`rhobar1`) should be viewed as a non dimensional mass per unit area of the slab. It is easily seen that the mean density decreases when the shrinkage parameter is introduced, the opposite of what would be expected if (`rhobar1`) were the real mean density. However, the so-called mean density, had to be compared with the actual experimental data, where the non dimensional mass and non dimensional density are not the same due to the shrinkage. Furthermore, if the expression for the mean density with the shrinkage is compared to the expression for the calculation of char yield it can be seen that they are analogous and the char yield is per mass basis, even though it is non dimensional.

7.4 MODEL PREDICTIONS

In this section comparisons between the model predictions and the experimental data will be outlined. The computations were performed with the model that included all the modifications presented in the preceding section. Thermal and material properties and kinetic parameters were used for cellulose, as measured in experimental sections and they are shown in the DATA file in Appendix B.

Figures 7.1a through 7.1f show the comparison of experimentally determined and computed temperatures at various depths in a slab, for an incident heat flux of 40 kW/m^2. The computations were carried for a slab of 10 mm in thickness. In order to make a comparison with the experiments the temperatures at various positions were not corrected for the shrinking distance. Similar to the experiments, the slab is modeled to shrink upon pyrolysis. However, even though it is possible to calculate the temperature at a fixed distance from the surface, despite the shrinkage, it was not done in order to compare the computed values to the experimental values. In other words, the positioning error, as seen in temperature measurements in Chapter 5, was deliberately introduced in the calculations for the purposes of comparison. That means that the experiments and computations can be compared on the same basis. Computed temperatures are recorded in a file for six different positions, similarly to the experiments. The first position is at the front, heated surface, and the other five are 20% of the slab thickness apart from each other. As is evident from Figures 7.1 the agreement between measured and computed temperatures is very good. Some discrepancies exist during the time when the char layer is formed in the front part of a slab. However, the differences are small and it cannot be judged whether they are due to incorrect statement of the physical problem or to the measurement errors. The model predicts the inflection point in the temperature traces. That disturbance propagates and

attenuates into the slab. The noise observed at about 650 K in the surface temperature prediction is due to relatively large error between successive iterations in temperature calculations. The error that was specified was 1 K. That value was chosen for two reasons: first, an error of 1 K is similar to measurements and second, and probably more importantly is the program execution time, which significantly increases with the decrease of allowed error.

Figure 7.2 shows a comparison between predicted and measured mass loss. Overall, the agreement is fair, although not as good as for the temperatures. The reason is probably, given the relatively correct temperature prediction and experimentally determined kinetic parameters, that the shrinkage parameter is not correctly determined. The evidence for that explanation can be seen from Figures 7.3 and 7.4, which show a comparison of predicted temperature with and without shrinkage taken into account. The calculations were performed for an incident heat flux of 40 kW/m^2. As is evident from Figures 7.3a through 7.3f, which are the temperatures at different positions of a slab, differences exist, but they are not very large. However, if the mass losses calculated with and without shrinkage are compared (Figure 7.4) it can be seen that the difference is larger than might be expected if only the temperature difference were important. Actually the behavior is to be expected. The reason is that char yield is quite sensitive to temperature in the back parts of the sample, and that temperature is clearly higher with shrinkage.

Figures 7.5a through 7.5f show a comparison between calculated and measured temperatures at different distances from the front, heated, surface for an incident heat flux of 60 kW/m^2. The calculations were performed using the same parameters as in the case incident heat flux of 40 kW/m^2, the only difference being the incident heat flux. The computed temperatures are lower than the measured temperatures in the middle portion of pyrolysis. The reason for this is the incorrect assumption that the surface emissivity

changes completely from that of virgin material to that of char when 15% of the mass is lost. The comparison of surface temperatures from Figure 7.5a suggest that the change in surface emissivity takes place for much lower mass loss. This is reasonable, bearing in mind that for higher incident heat flux the pyrolysis front is thinner, the layer close to the surface pyrolyzes faster, and the change of optical properties at the surface occurs more rapidly. In the later stages of pyrolysis the surface temperature exhibits the same behavior as in the case of lower (40 kW/m^2) incident heat flux. Similar to the case of lower incident heat flux, the noise can be seen in the calculated surface temperature, at about 750 K, for the same reasons noted above. Although the temperature is under-predicted, the mass loss rate, shown in Figure 7.6, for the incident heat flux of 60 kW/m^2 appears to be well predicted. The reason for this is related to the velocity of thermal wave propagation. The slab, in the case of an incident heat flux of 60 kW/m^2, is being heated faster, the temperatures are higher and, therefore, the change in kinetics, from single kinetic parameters to competitive reactions parameters, should take place later. Indeed, when the calculations were performed for the surface emissivity change between cellulose and char emissivity during 5% of the mass loss, much better agreement between the experiment and the model was obtained, as seen from Figures 7.7 and 7.8.

The predicted temperatures and the mass loss were compared to the experimental data for the incident heat flux of 20 kW/m^2 in Figures 7.9 (a through e) and 7.10a, respectively. The computations were performed for the same parameters as in the case of the incident heat flux of 40 kW/m^2. Similarly to the case of higher incident heat flux (60 kW/m^2) the model does not reasonably predict temperatures within the slab and, therefore, the mass loss from the slab. Once again, the sensitivity as to the assumptions about emissivity change is evident. The agreement is improved (shown in Figures 7.9f through h and 7.10b) by decreasing the heat transfer coefficient (from 10 to 5 W/m^2 K) which is

reasonable, bearing in mind that the surface temperature is lower than in the higher heat flux cases (see Figure 4.9). Also, the pyrolysis is assumed to follow single reaction with higher activation energy. This assumption is in agreement with the data of Figure 6.21, the pyrolysis takes place in lower temperature region.

7.5 MODEL SENSITIVITY

The model sensitivity to some parameters was checked by their variation from the base case values, shown in Table 1 and Figures 7.1 and 7.2.

Figures 7.11 and 7.12 show a comparison between computed temperatures and mass loss, respectively, for virgin material and char emissivity set to unity in one case and measured values in another. As is evident from the figures the prediction with the unity emissivities is not as good as for the measured emissivities. Although the predicted temperatures calculated with two sets of parameters, are not very different, the mass loss prediction is completely wrong, the onset of pyrolysis is off, the shape of the curve is different, and finally the char yield is off. Clearly, the surface emissivity is an important parameter for correctly predicting the temperatures and the mass loss from the slab. This has not been recognized in the literature.

It was somewhat surprising that a factor of two increase in both virgin material and char thermal conductivities did not produce much of an effect, as seen from Figures 7.13 (temperatures) and 7.14 (mass loss). As a matter of fact, the mass loss is even better predicted, partly because the temperatures in the back part of a slab were overpredicted compared to the base case and this compensated for a problem in the kinetics. However, it seems that the calculations are not very sensitive to large changes in thermal conductivities.

It was explored how the change in heat transfer coefficient affects the calculations. The heat transfer coefficient was set to three times higher than in the base case (to reflect roughly the ratio of heat transfer coefficients in nitrogen and helium). The result is shown in Figures 7.15 (temperatures) and 7.16 (mass loss). From the comparison it seems obvious that the heat losses to convection are fairly important. It should be noted that while the incident radiative flux is 40 kW/m^2, only 65% or 26 kW/m^2 is absorbed. The heat losses from the surface by convection are apparently about (10 W/m^2 K)(800-300)= 5kW/m^2 in nitrogen and about 15 kW/m^2 in helium, so the sensitivity to the heat convection coefficient is not surprising, considering these magnitudes. Also, this result supports the hypothesis outlined in Chapter 5 that the very different mass loss rates in helium and nitrogen are primarily due to difference in thermal conductivities and, hence, heat transfer coefficients.

The effect of different kinetic parameters on computations was also studied. In the case of kinetic parameters, the activation energy and the pre-exponential are coupled parameters and independent changes in these were not possible. For that reason only two sets of kinetic parameters were used, the same two obtained experimentally in Chapter 6. The temperatures and mass losses were calculated for those two sets in single reaction and they were compared to the base case in Figure 7.17 and figure 7.18. Only the front surface temperature comparison is shown in Figure 7.17 for the obvious reason, namely the kinetic parameters do not have any significant impact on calculated surface temperatures even if the kinetic parameters influence the temperature at which the endothermic heat of pyrolysis occurs. The mass loss, of course, is calculated to be slightly different, the highest mass loss rate was seen when the kinetic parameters were combined into the competitive reactions form. This is of no surprise. Also of little surprise is the fact that the higher activation energy gave somewhat slower mass loss at lower temperatures.

7.6 SUMMARY

The mathematical model obtained from Professor Sibulkin at Brown University was modified by accounting for several experimentally observed phenomena. The reflection of a portion of the incident radiation due to the non unity surface emissivity is taken into account in the present version of the model. It was experimentally observed that the surface emissivity changes from virgin material to char and that was incorporated in the model. The ultimate char yield profile, heat of pyrolysis dependence on heating rate and slab shrinkage were the empirical inputs in the model. The kinetics of pyrolysis was divided in two steps, the first one with single reaction and the second one with competitive reaction, both of which were taken to be first order.

The present version of the model predicts well the temperatures and the mass loss from a slab undergoing pyrolysis with the incident heat flux of 40 kW/m^2. It can predict well the results for 20 and 60 kW/m^2 only when the emissivity change of the char was assumed to follow a different course than in the 40 kW/m^2 case. The predictions were off for the incident heat flux of 20 kW/m^2, however, it was concluded that with the proper experimental background the model should predict the behavior incident heat flux of 20 kW/m^2.

It was concluded that the calculations are quite sensitive to the surface emissivity and heat transfer coefficient and to the lesser extent to thermal conductivity. The correct values of pyrolysis kinetics and char yields remain an open question.

Table 7.1: Base Case Properties for Mathematical Model

$L = 10$ mm - slab thickness

$\rho_i = 1$ g/cm^3 - initial slab density

$\rho_f = 0.12$ g/cm^3 - final density

$T_0 = 300$ K - initial temperature

$C_p^0 = 2104$ J/kg K - virgin material heat capacity at initial temperature

$C_p^* = 4.19$ J/kg - temperature coefficient of virgin material heat capacity (see eq. 7.3)

$C_{pc}^0 = 1928$ J/kg K - char heat capacity at initial temperature

$C_{pc}^* = 1.98$ J/kg - temperature coefficient of char heat capacity

$C_{pg}^0 = 2000$ J/kg K - gas heat capacity at initial temperature

$C_{pg}^* = 0$ - temperature coefficient of gas heat capacity

$k_a^0 = 0.157$ W/m K - virgin material thermal conductivity at initial temperature

$k_a^* = 3 \times 10^{-4}$ W/m - temperature coefficient of virgin material thermal conductivity

$k_c^0 = 0.084$ W/m K - char thermal conductivity at initial temperature

$k_c^* = 2 \times 10^{-4}$ W/m - temperature coefficient of char thermal conductivity

$h_1 = 10$ W/m^2 K - front surface heat transfer coefficient

$h_2 = 10$ W/m^2 K - back surface heat transfer coefficient

$\varepsilon_{vm} = 0.48$ - virgin material emissivity

$\varepsilon_{char} = 0.72$ - char emissivity

$Q = 300$ J/g - heat of pyrolysis

$\dot{q}_L'' = 40$ kW/m^2 - incident heat flux

$E_{a1} = 145$ kJ/mole ($A_1 = 7.4 \times 10^9$ s^{-1}), $n = 1$

or $E_{a2} = 225$ kJ/mole ($A_2 = 4.8 \times 10^{16}$ s^{-1}), $n = 1$ - kinetic parameters

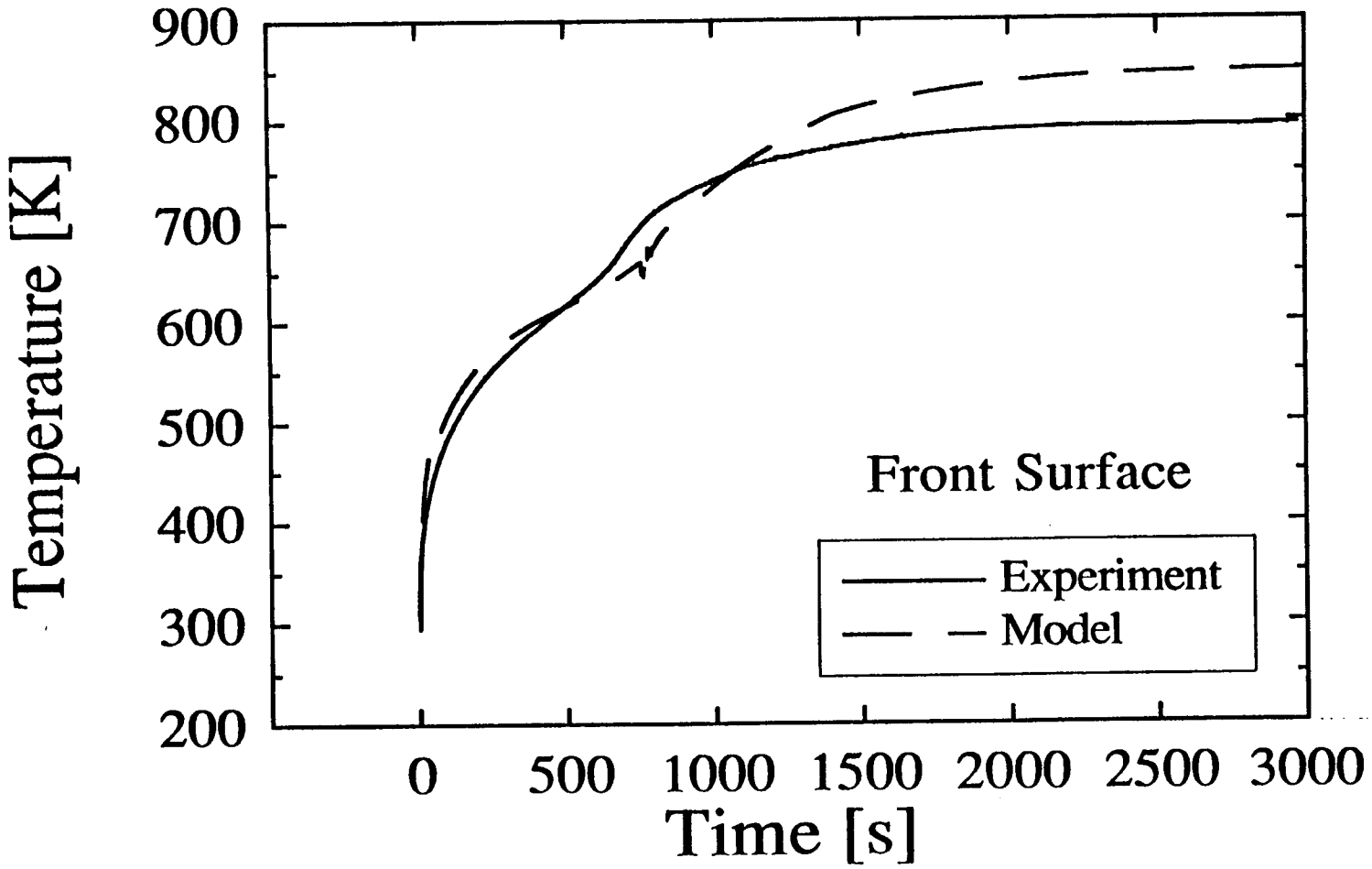

Figure 7.1a Comparison of measured and predicted front surface temperature for high density sample and incident heat flux of 40 kW/m^2

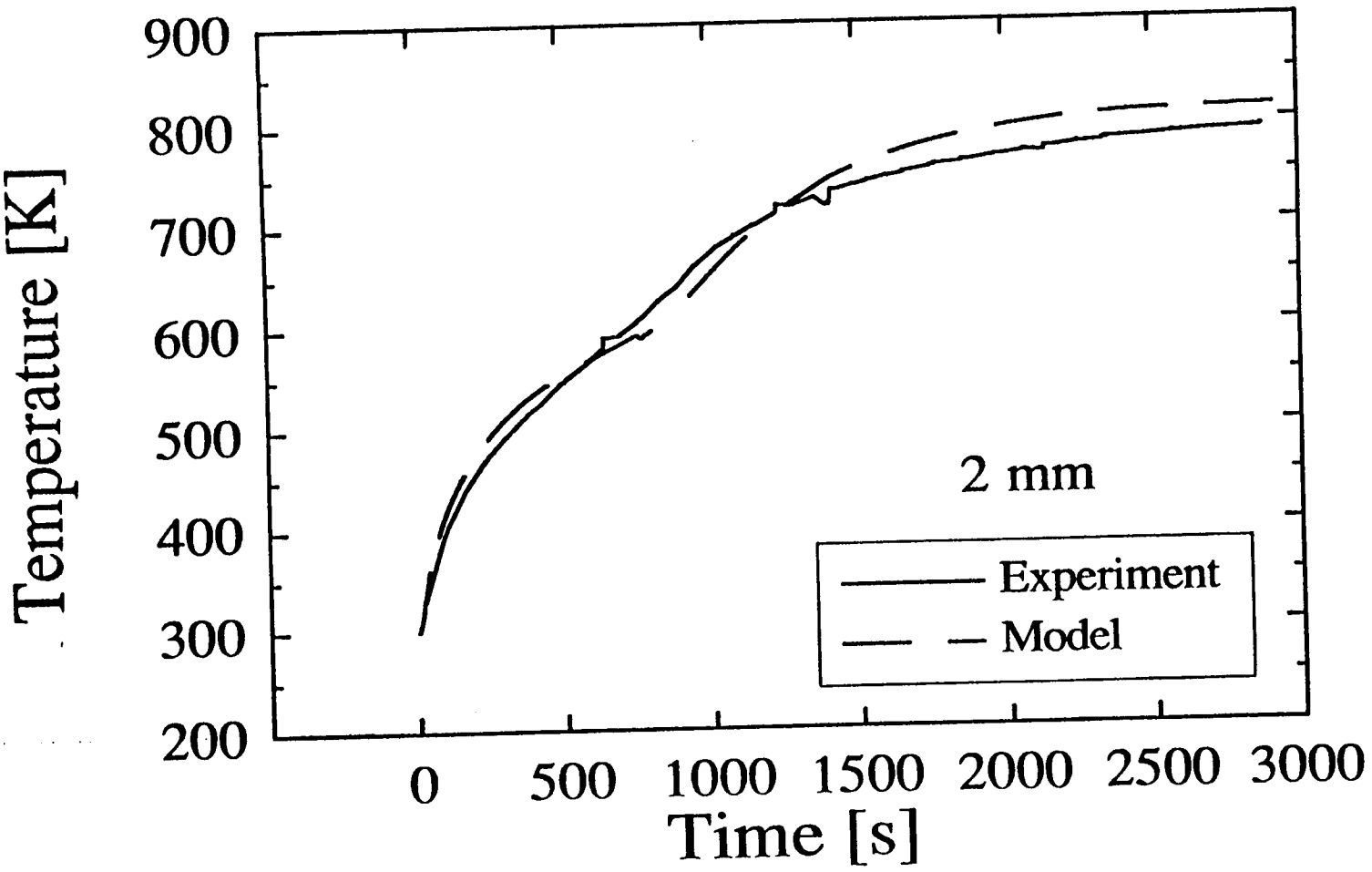

Figure 7.1b Comparison of measured and predicted temperature at 2 mm from the front surface for high density sample and incident heat flux of 40 kW/m^2

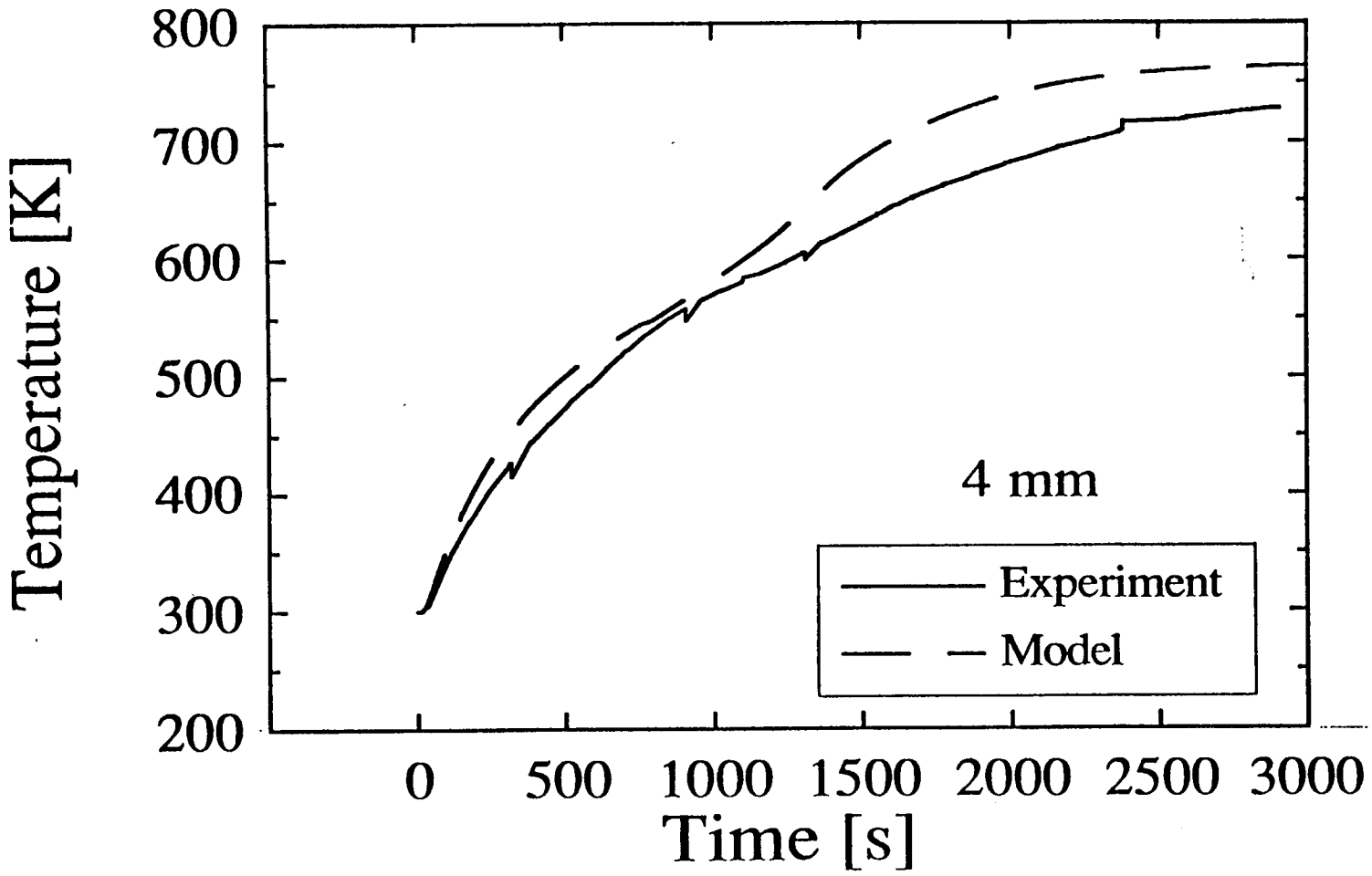

Figure 7.1c Comparison of measured and predicted temperature at 4 mm from the front surface for high density sample and incident heat flux of 40 kW/m^2

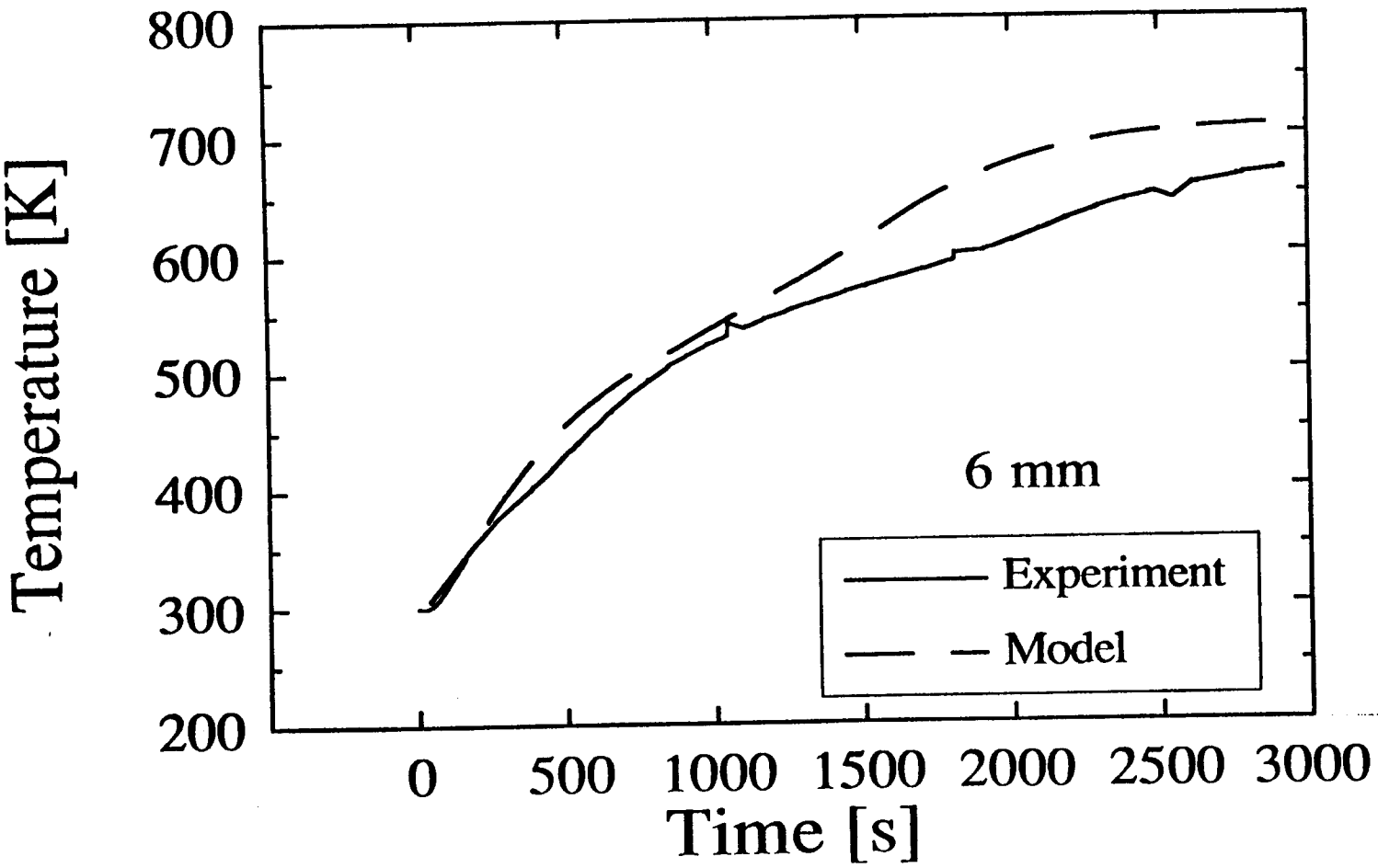

Figure 7.1d Comparison of measured and predicted temperature at 6 mm from the front surface for high density sample and incident heat flux of 40 kW/m^2

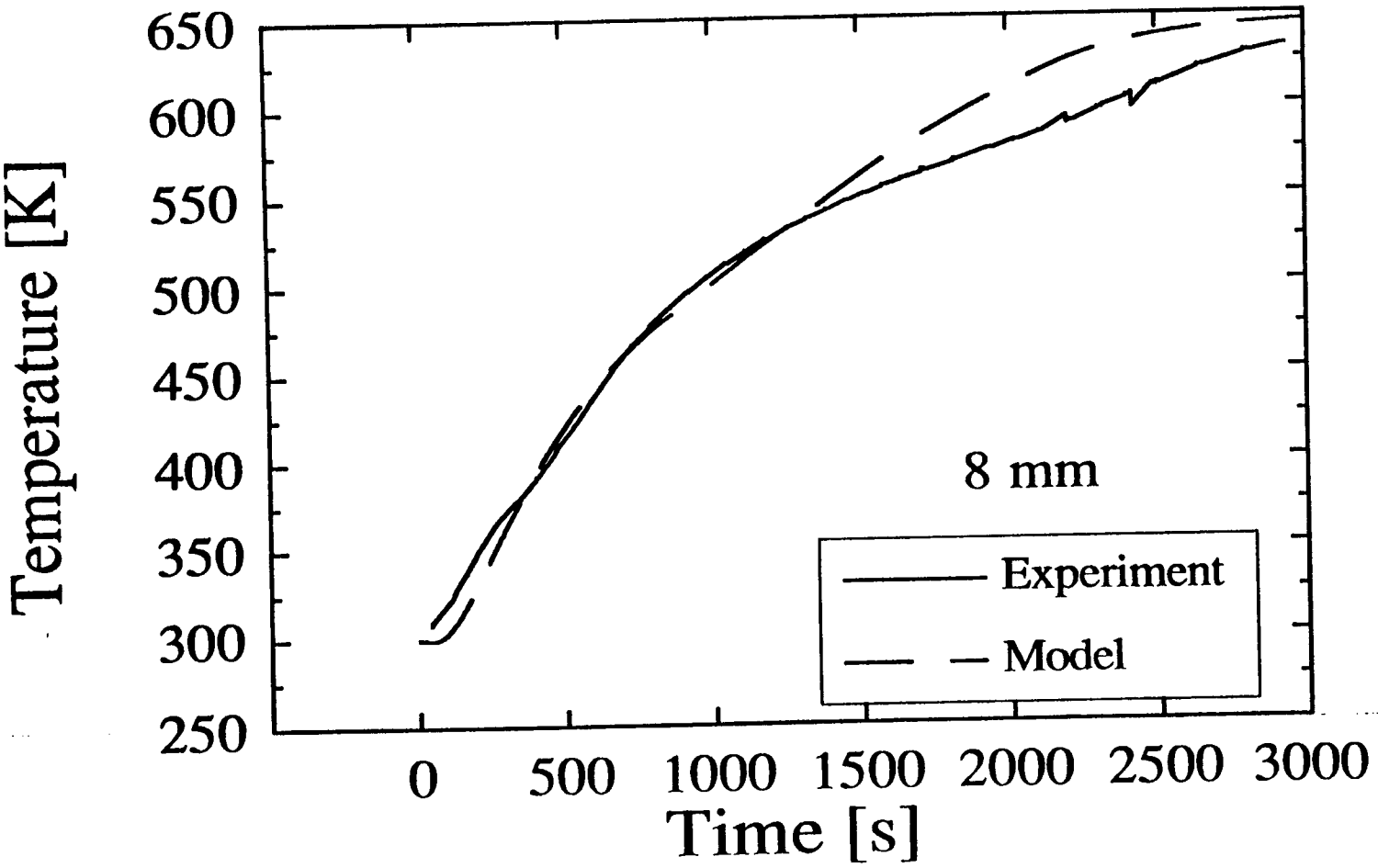

Figure 7.1e Comparison of measured and predicted temperature at 8 mm from the front surface for high density sample and incident heat flux of 40 kW/m^2

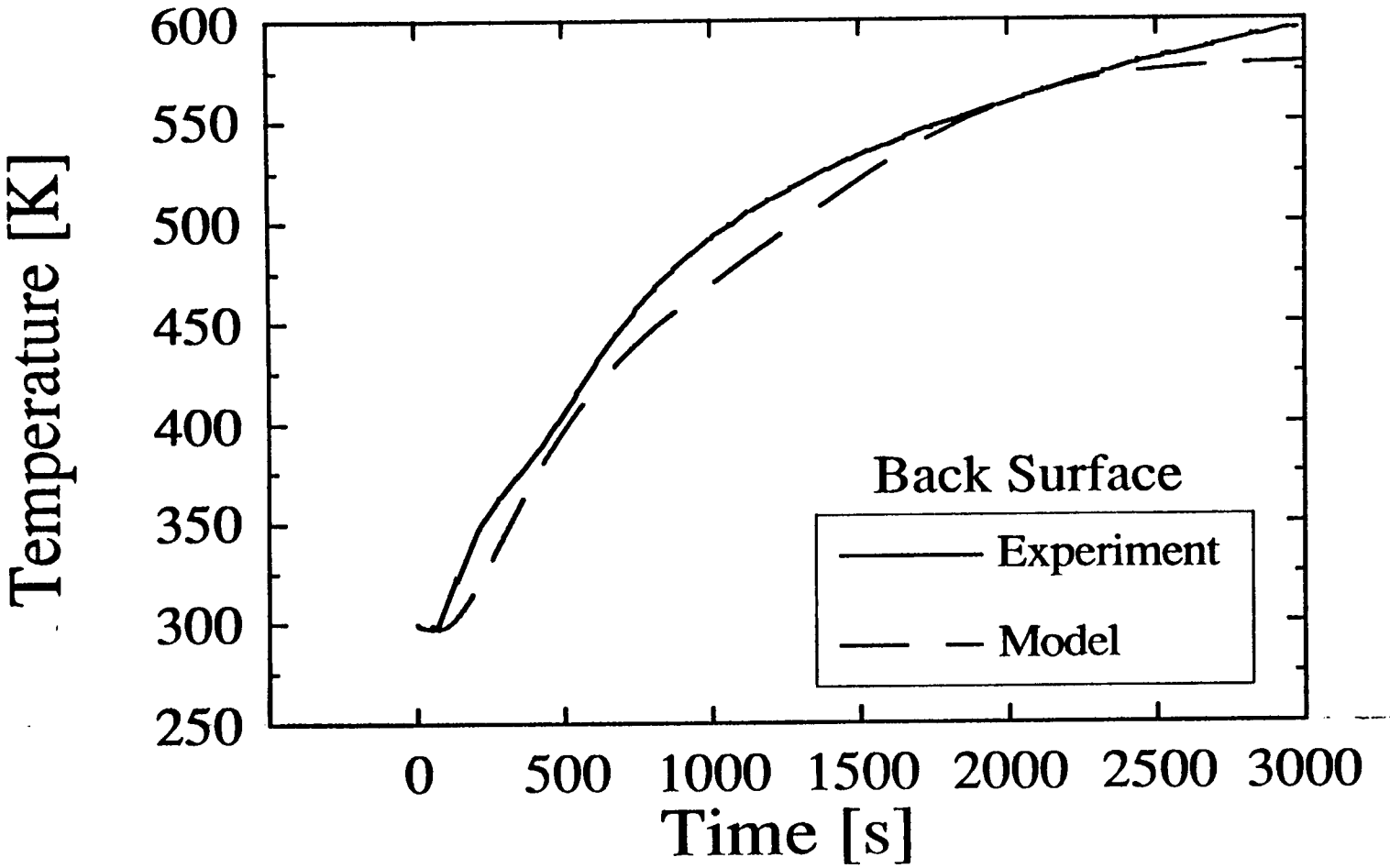

Figure 7.1f Comparison of measured and predicted back surface temperature for high density sample and incident heat flux of 40 kW/m^2

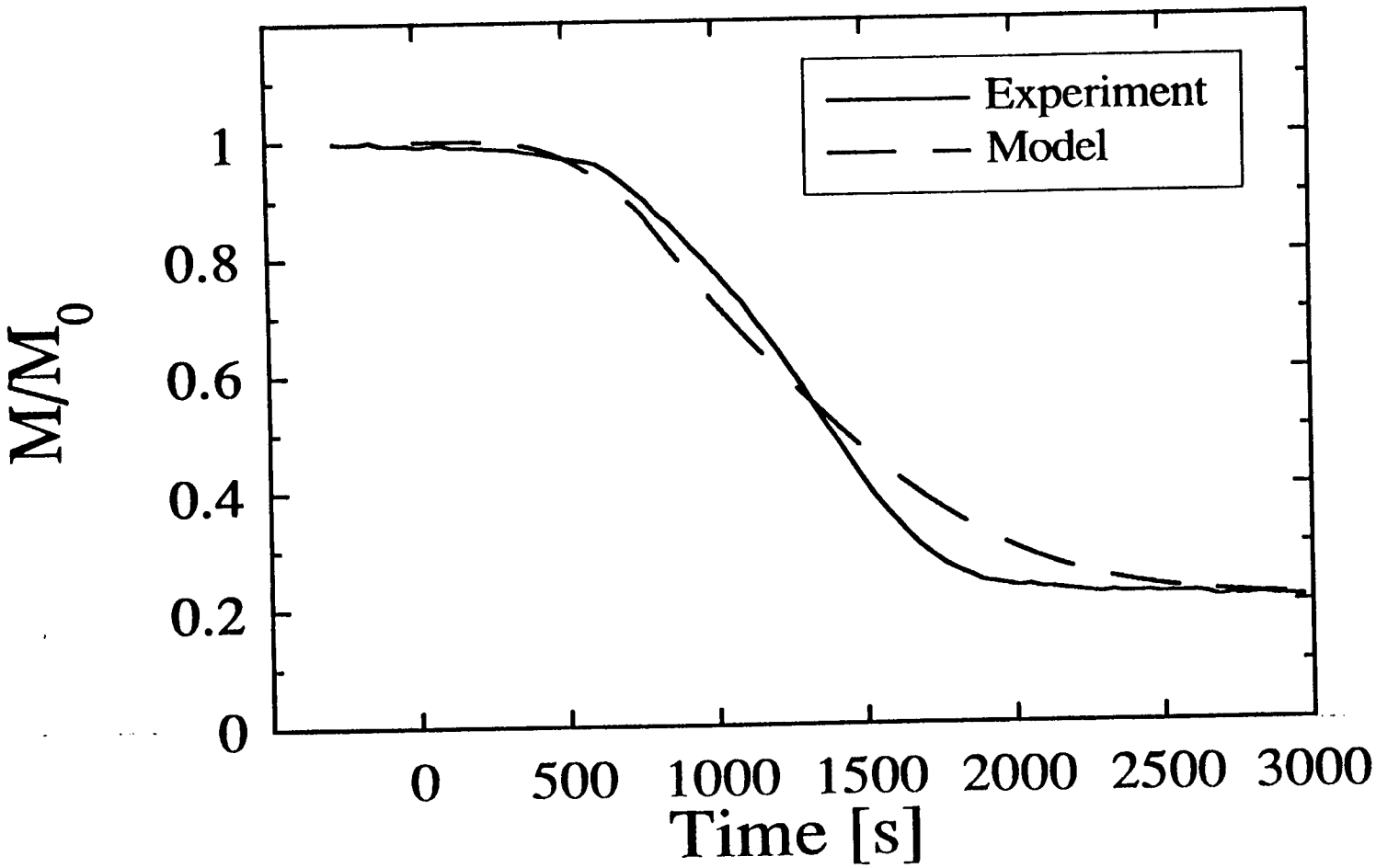

Figure 7.2 Comparison of measured and predicted fractional remaining mass for high density sample and incident heat flux of 40 kW/m^2

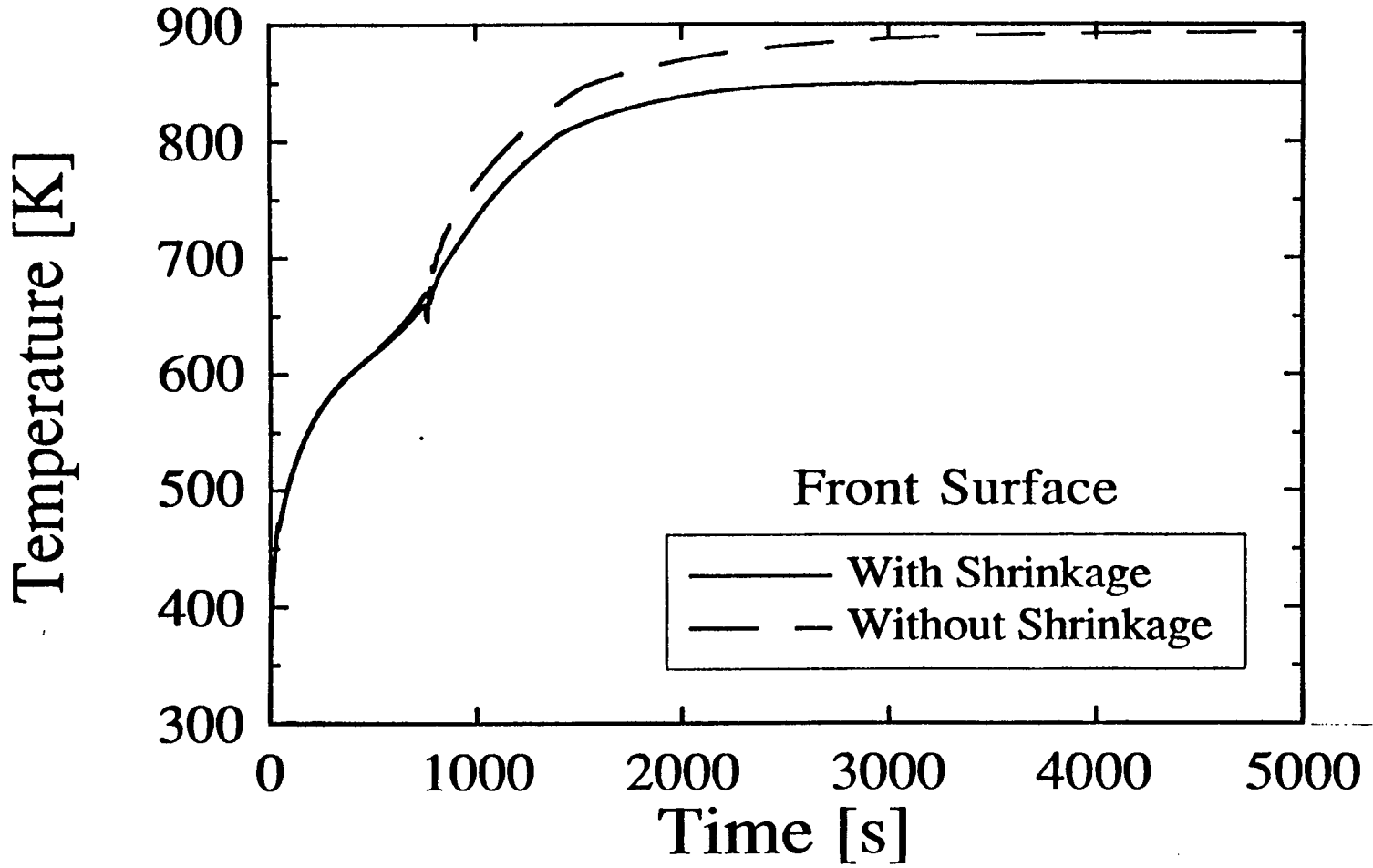

Figure 7.3a Comparison of predicted front surface temperature for high density sample and incident heat flux of 40 kW/m^2 with and without sample shrinkage taken into account

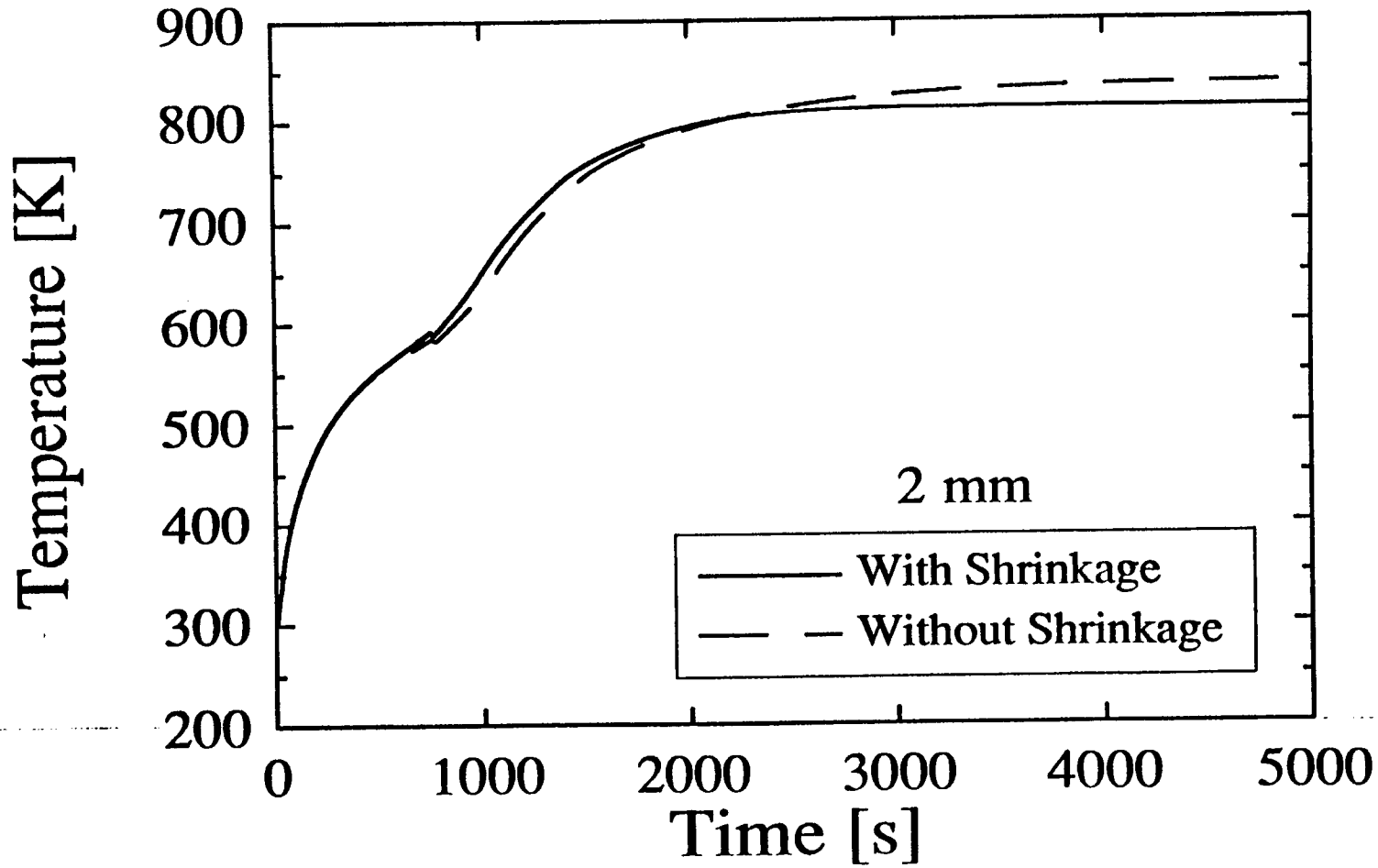

Figure 7.3b Comparison of predicted temperature at 2 mm from the front surface for high density sample and incident heat flux of 40 kW/m^2 with and without sample shrinkage taken into account

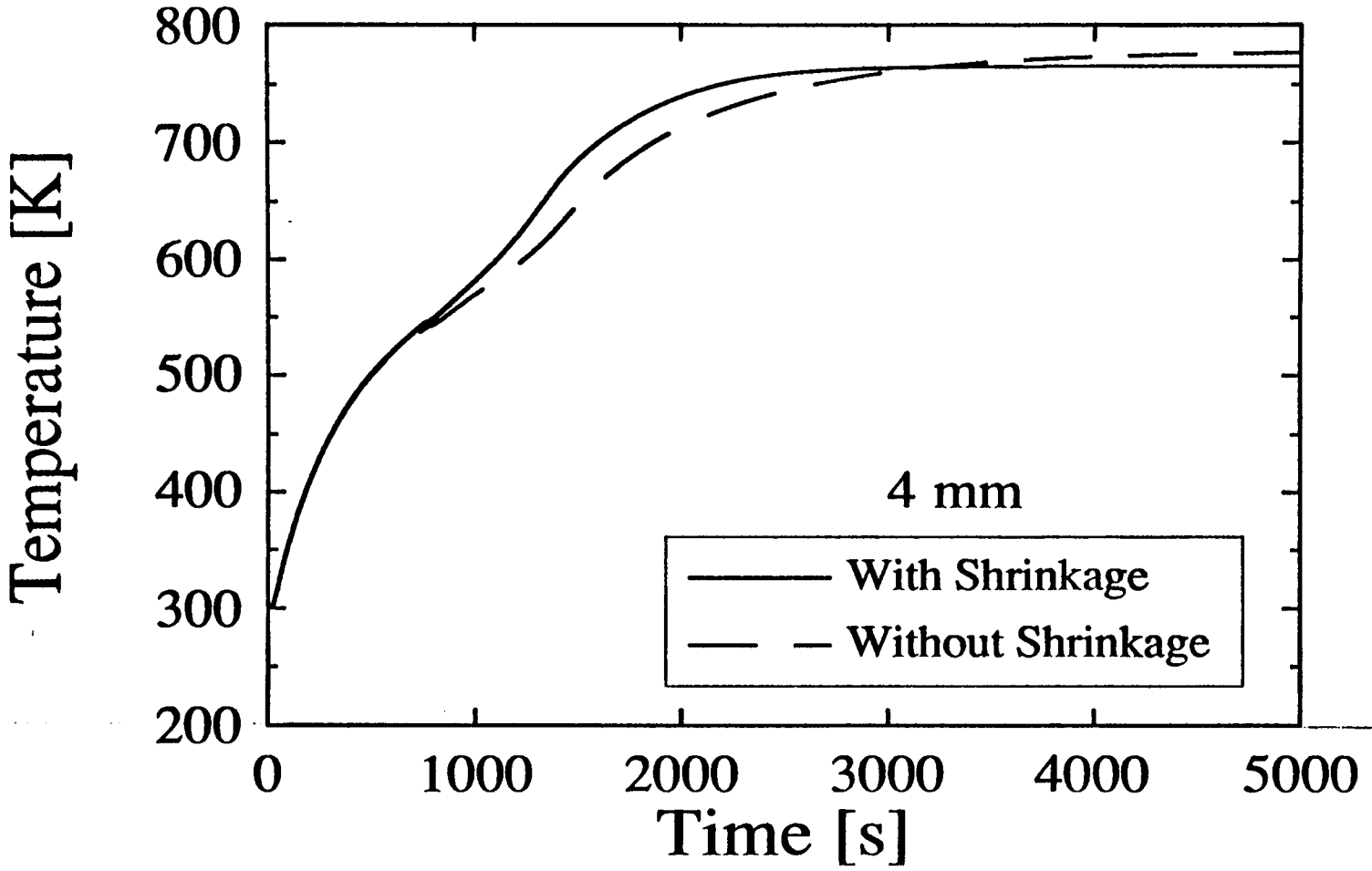

Figure 7.3c Comparison of predicted temperature at 4 mm from the front surface for high density sample and incident heat flux of 40 kW/m^2 with and without sample shrinkage taken into account

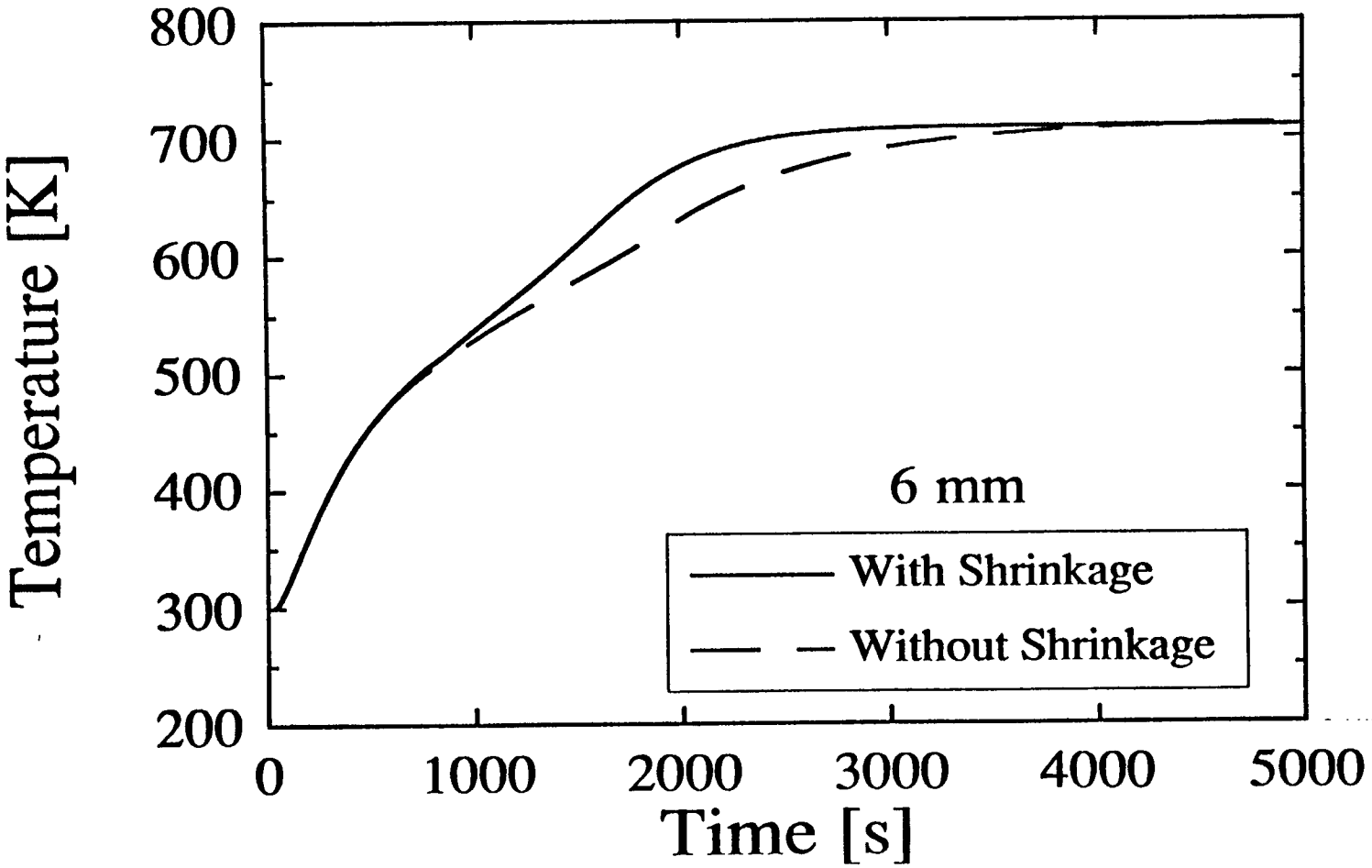

Figure 7.3d Comparison of measured and predicted temperature at 6 mm from the front surface for high density sample and incident heat flux of 40 kW/m^2 with and without sample shrinkage taken into account

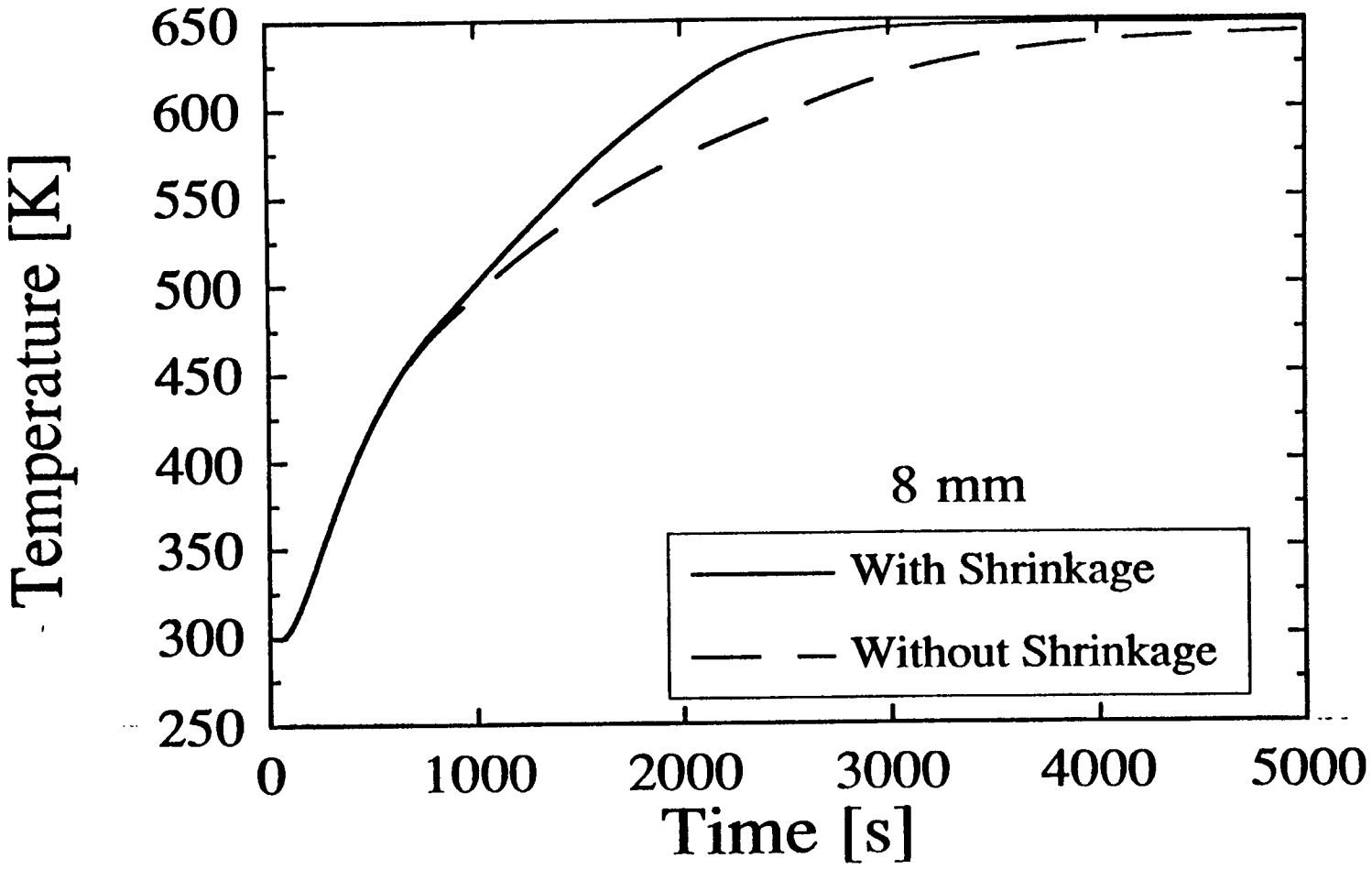

Figure 7.3e Comparison of predicted temperature at 8 mm from the front surface for high density sample and incident heat flux of 40 kW/m^2 with and without sample shrinkage taken into account

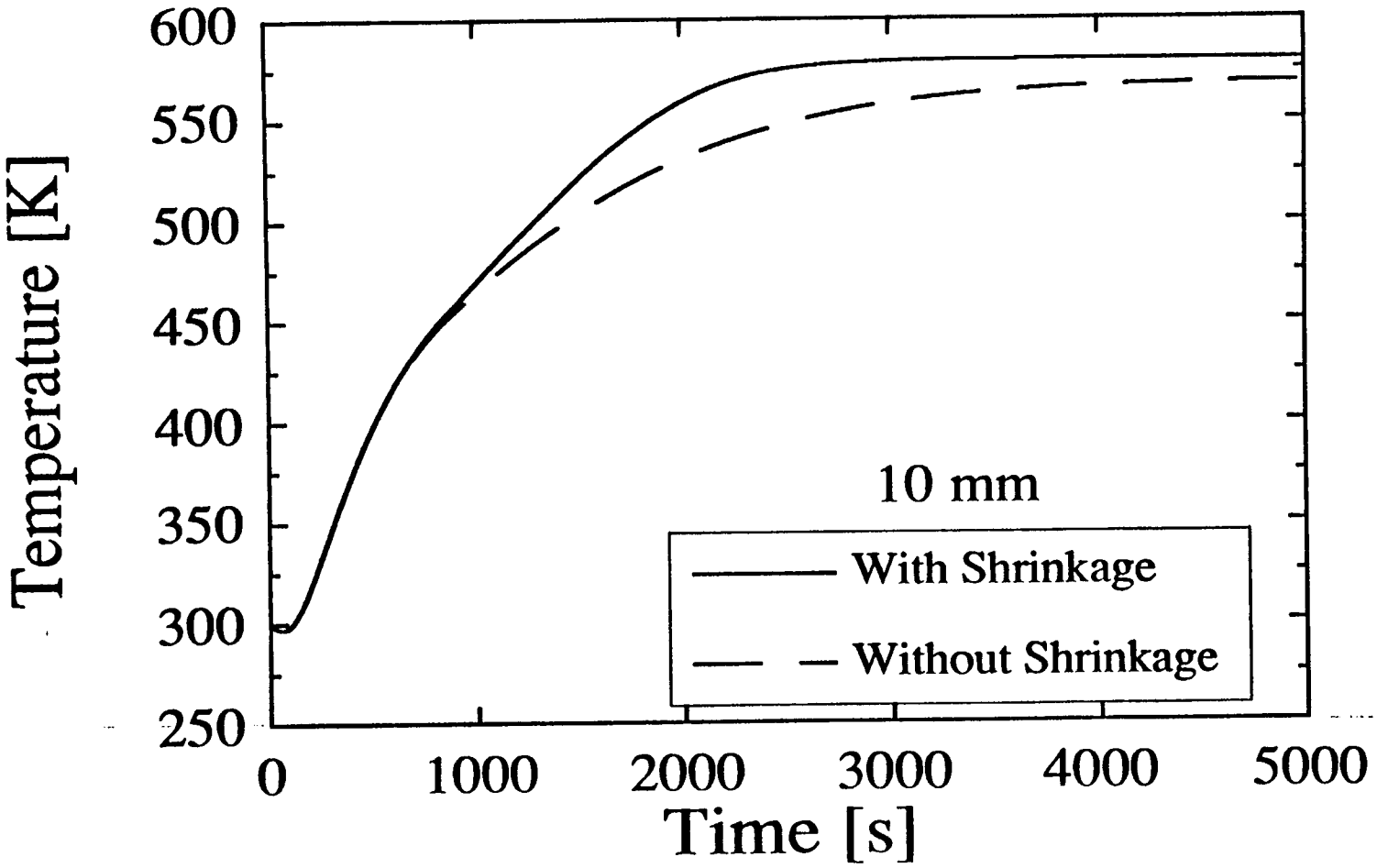

Figure 7.3f Comparison of predicted back surface temperature for high density sample and incident heat flux of 40 kW/m^2 with and without sample shrinkage taken into account

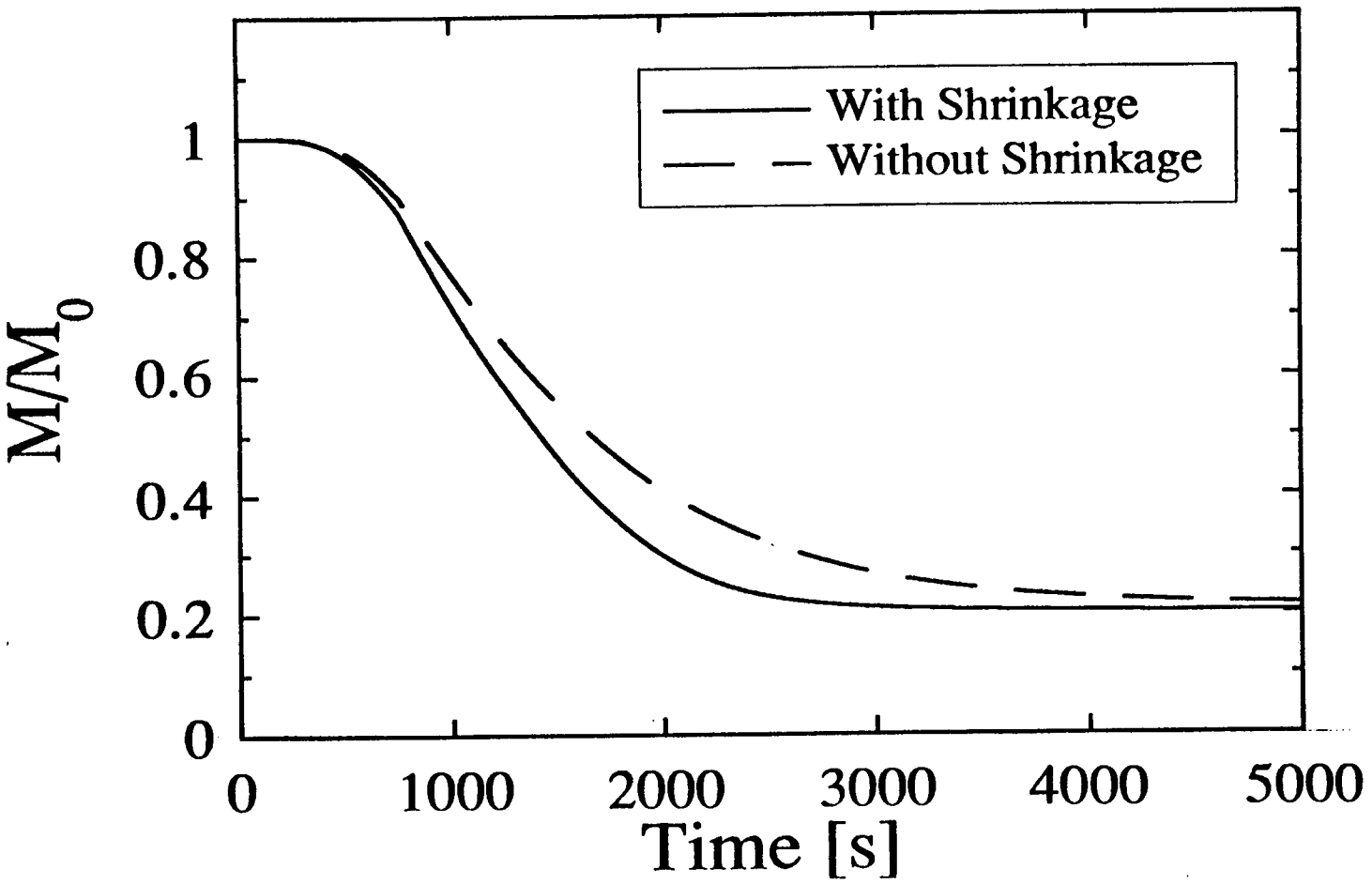

Figure 7.4 Comparison of predicted fractional remaining mass for high density sample and incident heat flux of 40 kW/m^2 with and without sample shrinkage taken into account

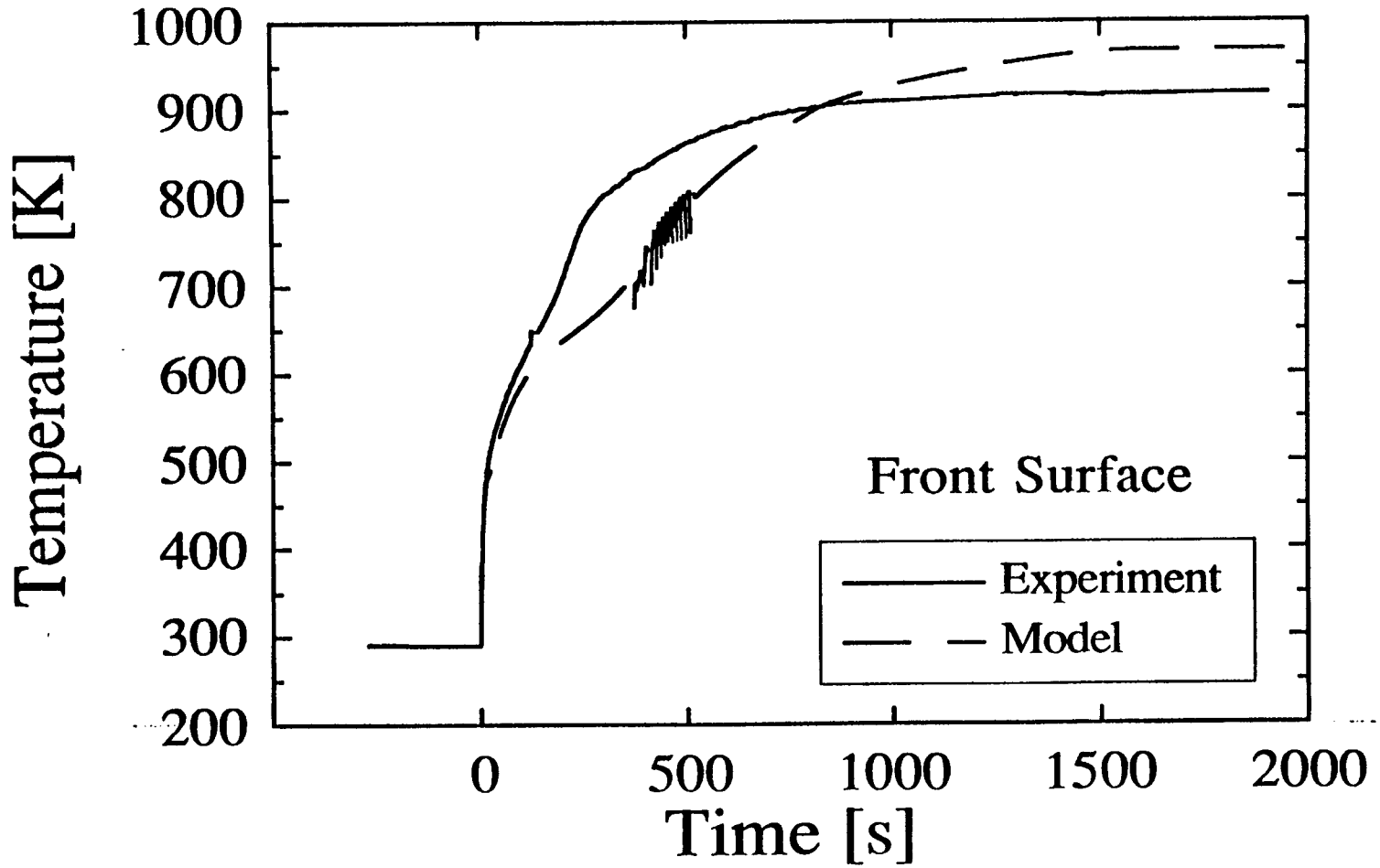

Figure 7.5a Comparison of measured and predicted front surface temperature for high density sample and incident heat flux of 60 kW/m^2 ("base case" values used in computations)

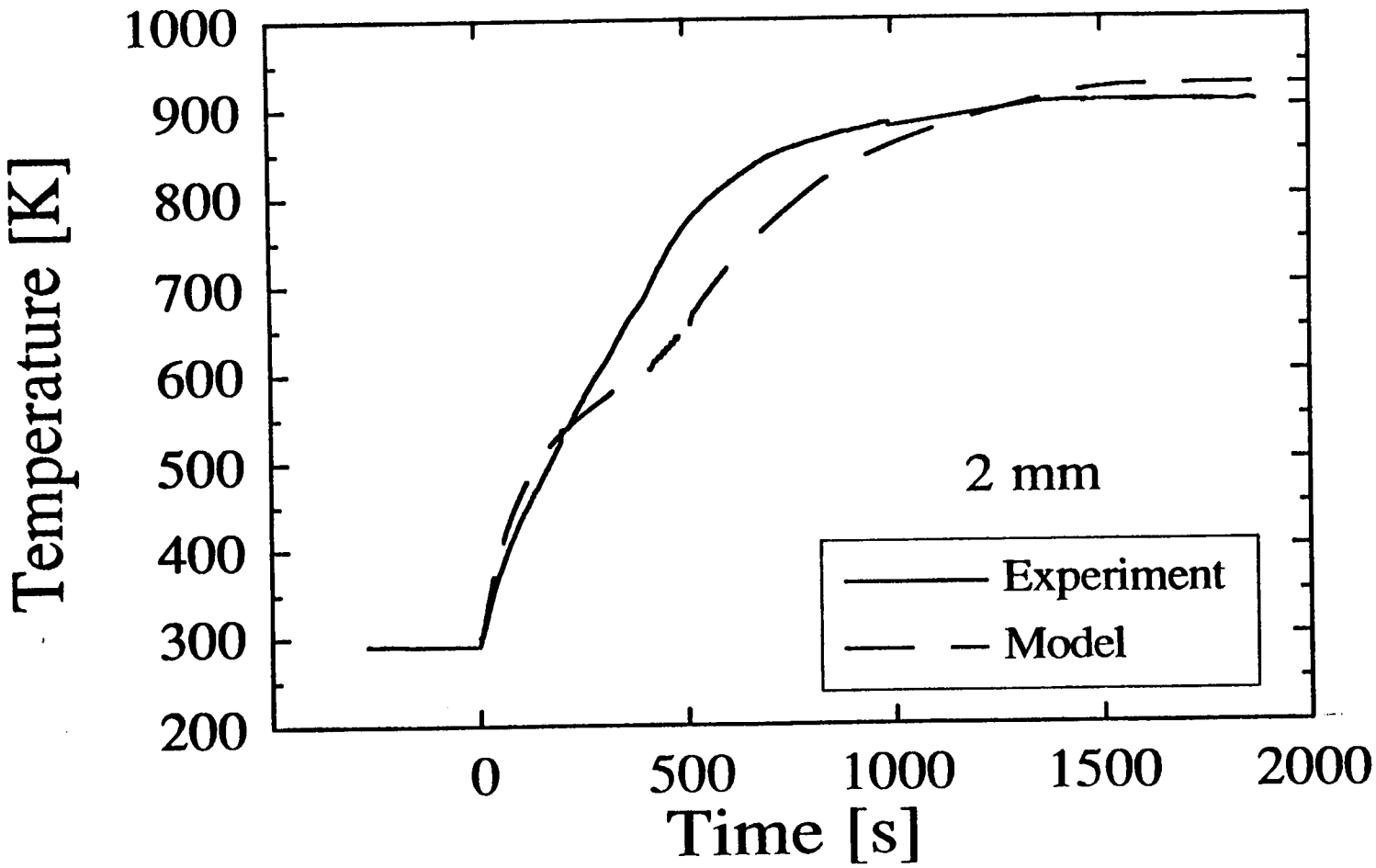

Figure 7.5b Comparison of measured and predicted temperature at 2 mm from the front surface for high density sample and incident heat flux of 60 kW/m^2 ("base case" values used in computations)

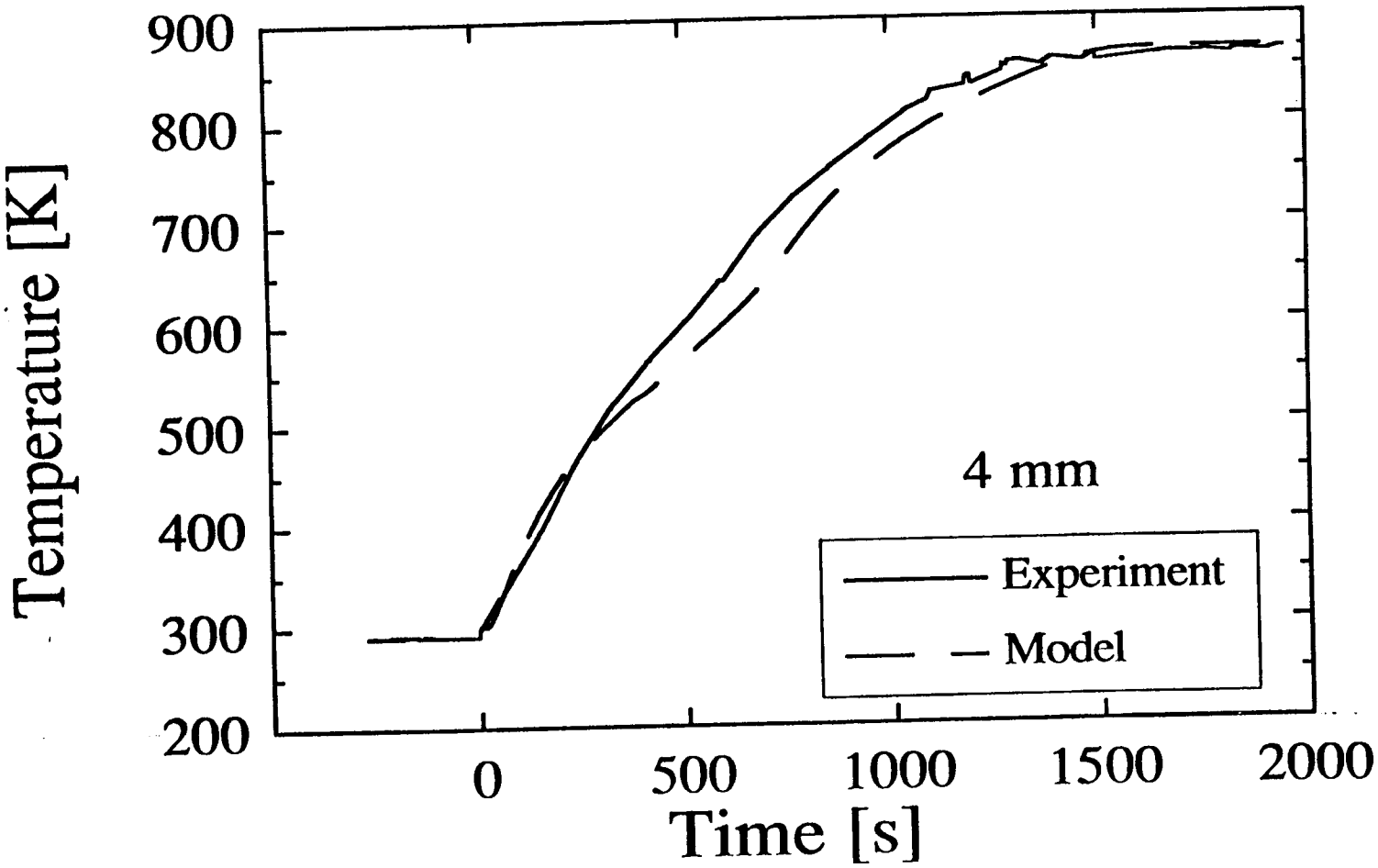

Figure 7.5c Comparison of measured and predicted temperature at 4 mm from the front surface for high density sample and incident heat flux of 60 kW/m^2 ("base case" values used in computations)

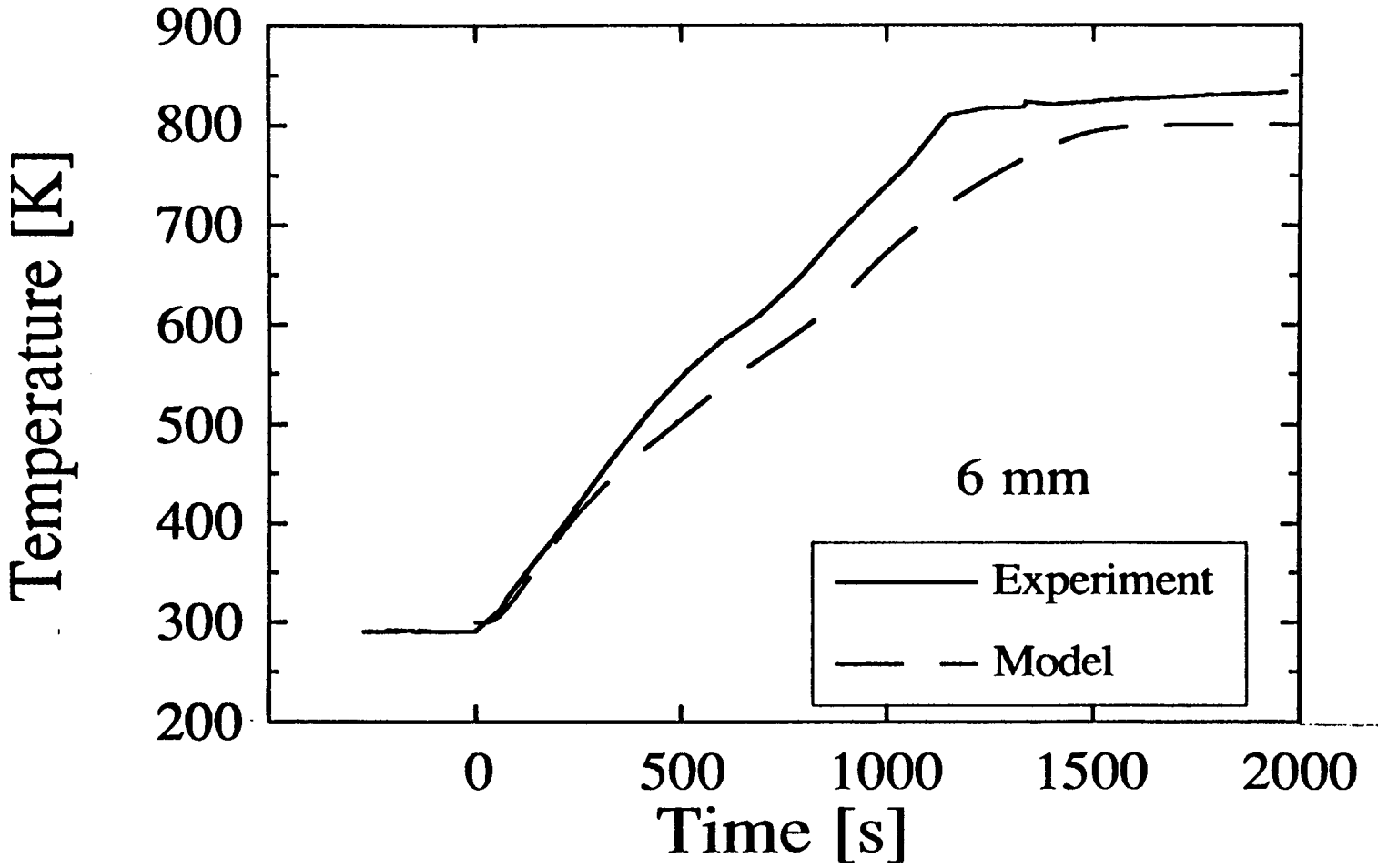

Figure 7.5d Comparison of measured and predicted temperature at 6 mm from the front surface for high density sample and incident heat flux of 60 kW/m^2 ("base case" values used in computations)

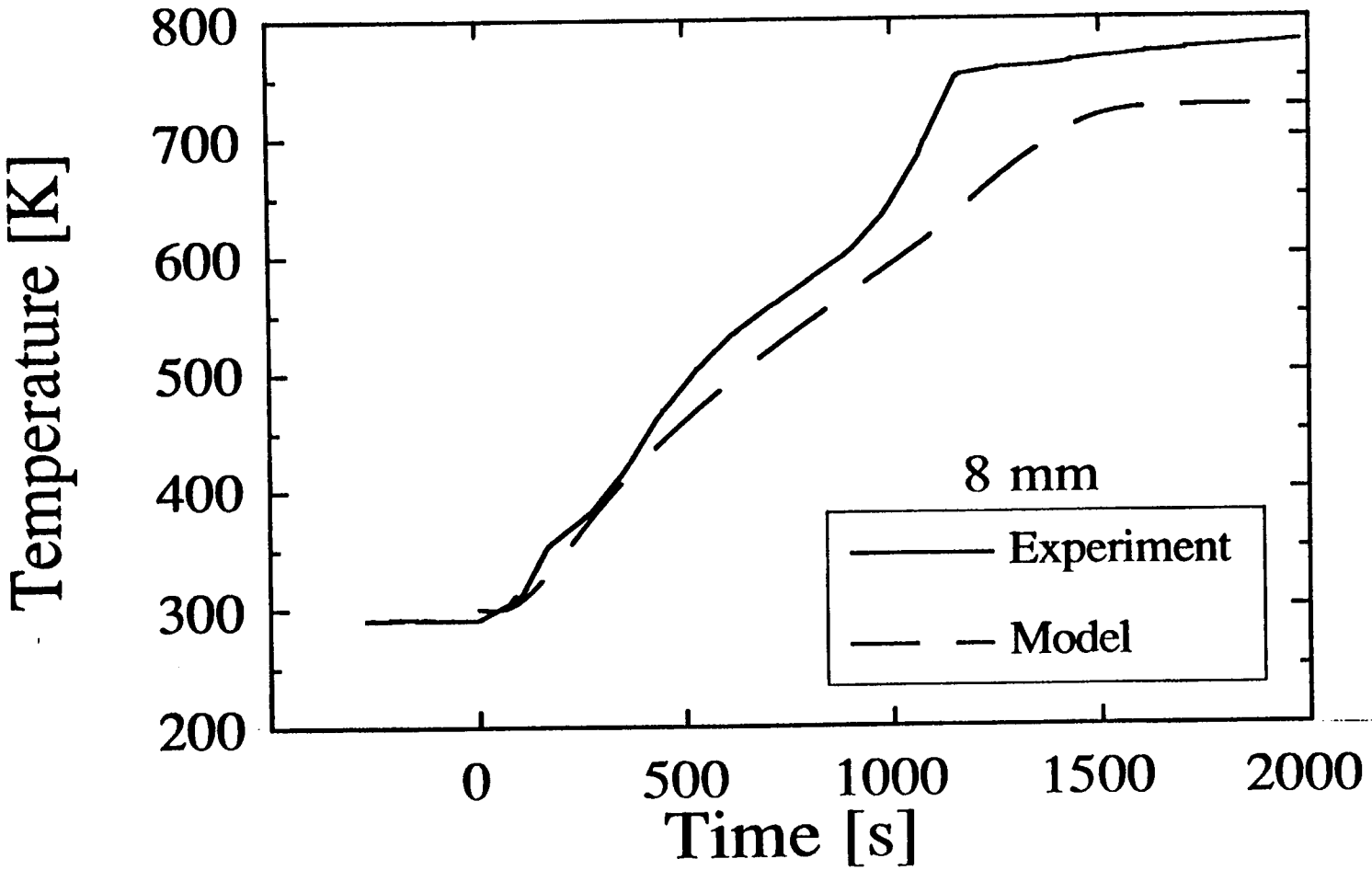

Figure 7.5e Comparison of measured and predicted temperature at 8 mm from the front surface for high density sample and incident heat flux of 60 kW/m^2 ("base case" values used in computations)

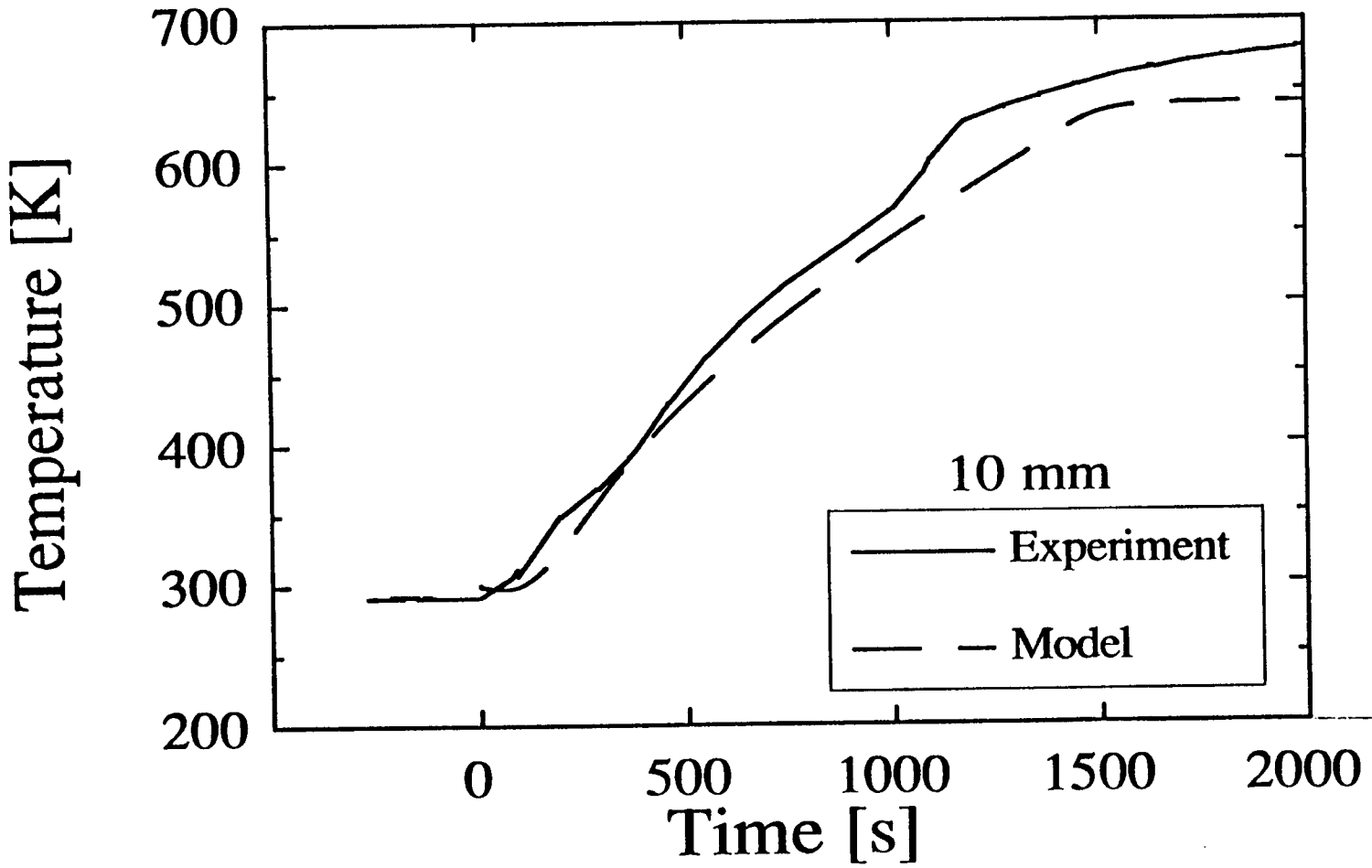

Figure 7.5f Comparison of measured and predicted back surface temperature for high density sample and incident heat flux of 60 kW/m^2 ("base case" values used in computations)

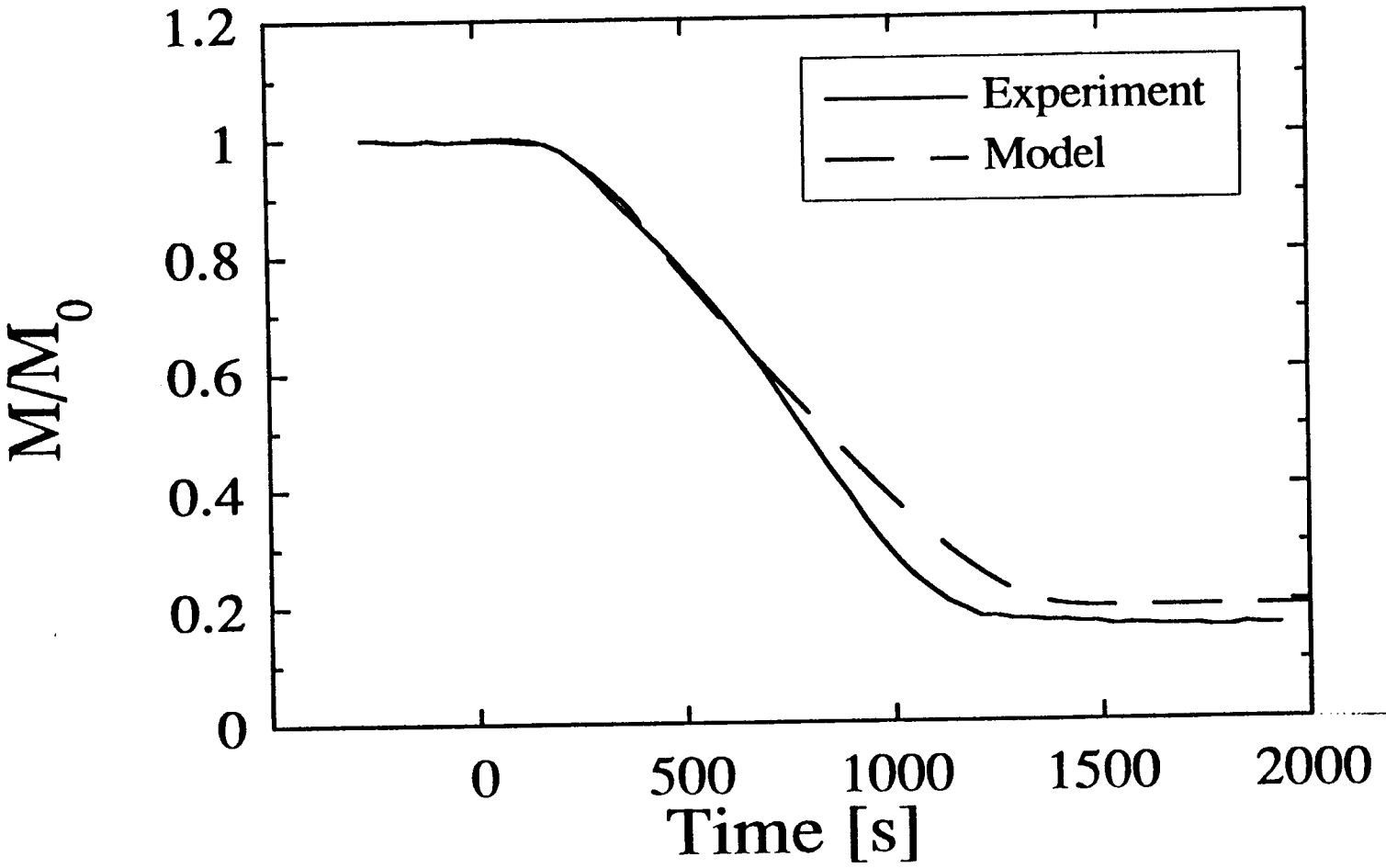

Figure 7.6 Comparison of measured and predicted fractional remaining mass for high density sample and incident heat flux of 60 kW/m^2 ("base case" values used in computations)

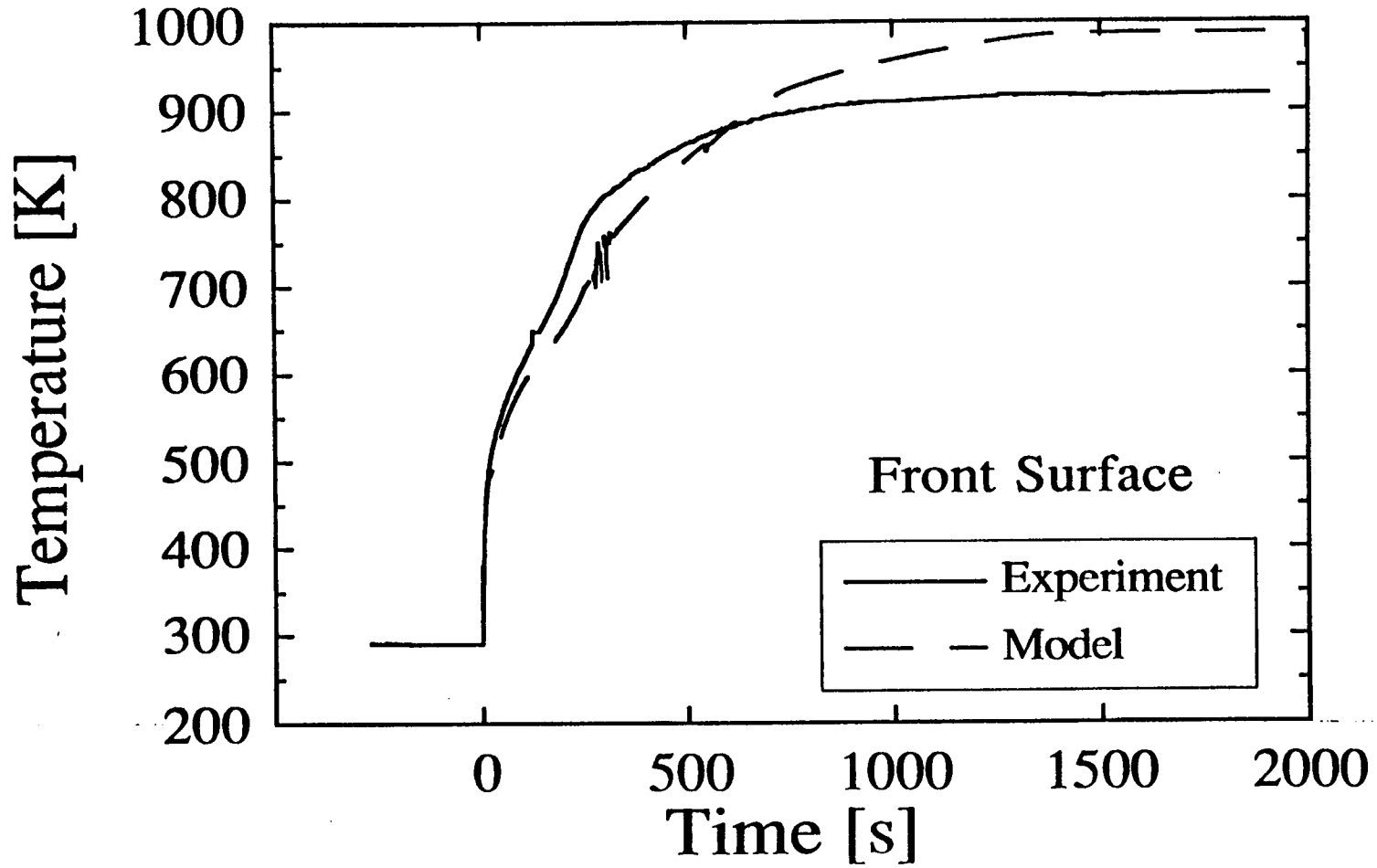

Figure 7.7a Comparison of measured and predicted front surface temperature for high density sample and incident heat flux of 60 kW/m^2 (corrected for faster surface emissivity change)

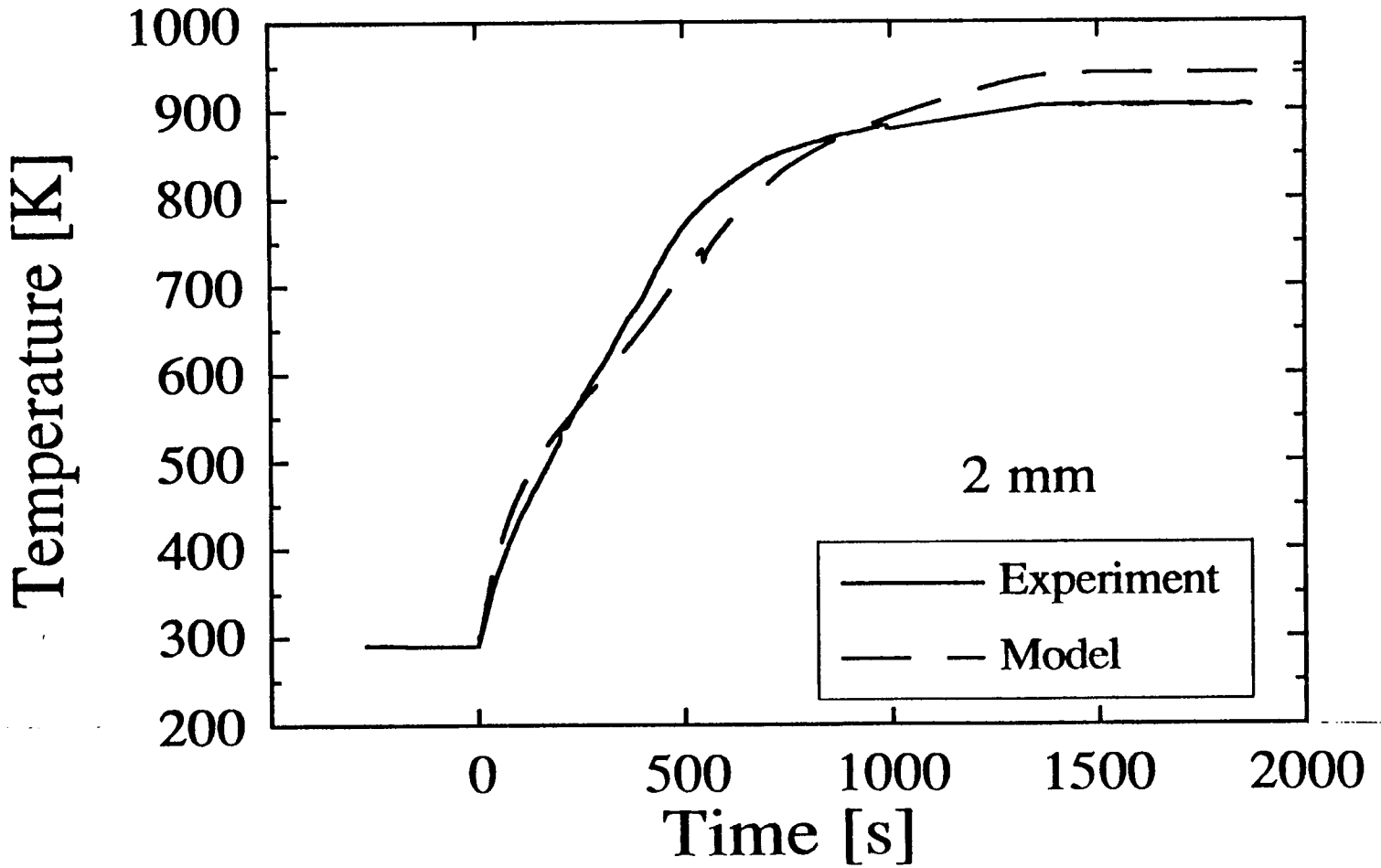

Figure 7.7b Comparison of measured and predicted temperature at 2 mm from the front surface for high density sample and incident heat flux of 60 kW/m^2 (corrected for faster surface emissivity change)

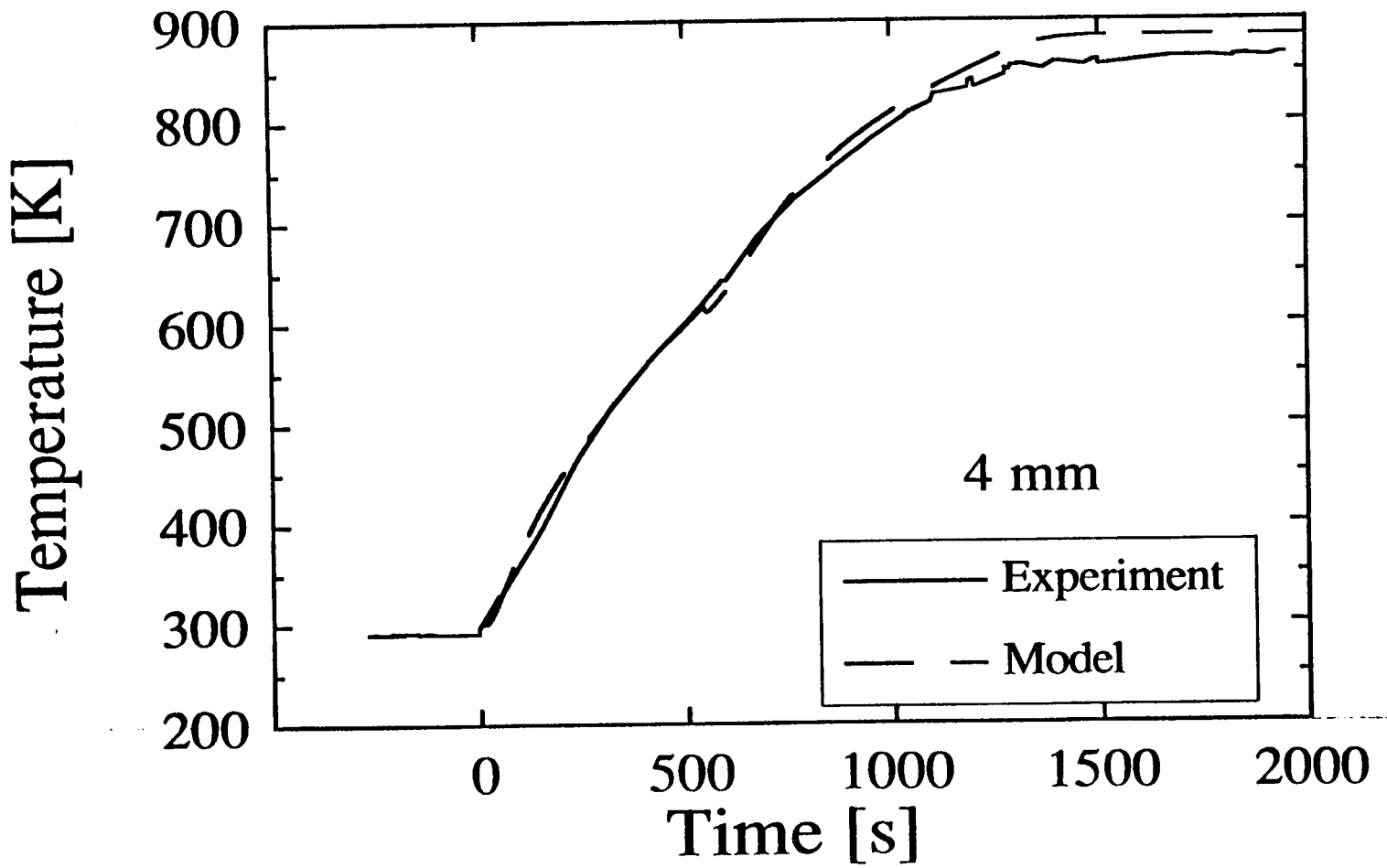

Figure 7.7c Comparison of measured and predicted temperature at 4 mm from the front surface for high density sample and incident heat flux of 60 kW/m^2 (corrected for faster surface emissivity change)

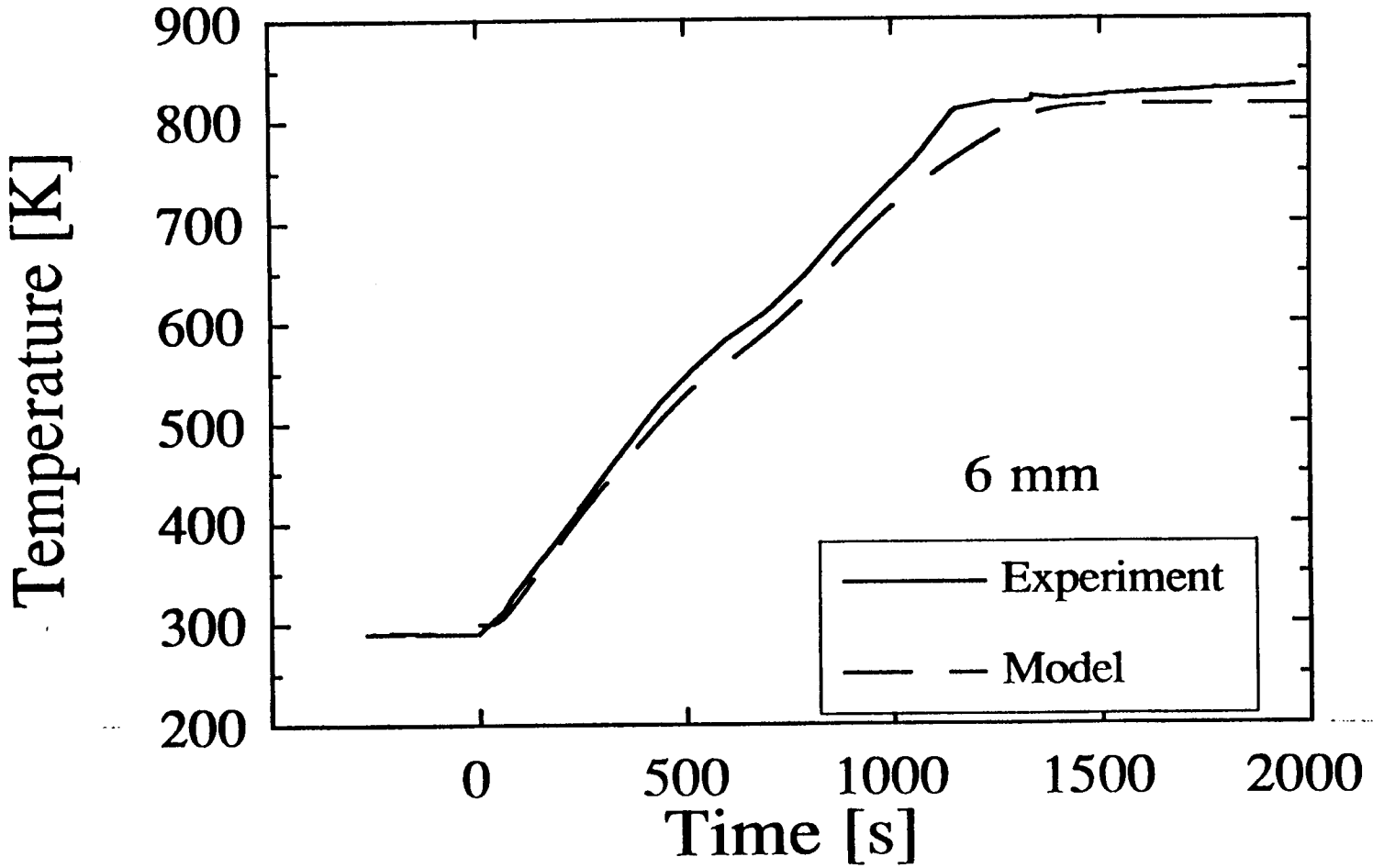

Figure 7.7d Comparison of measured and predicted temperature at 6 mm from the front surface for high density sample and incident heat flux of 60 kW/m^2 (corrected for faster surface emissivity change)

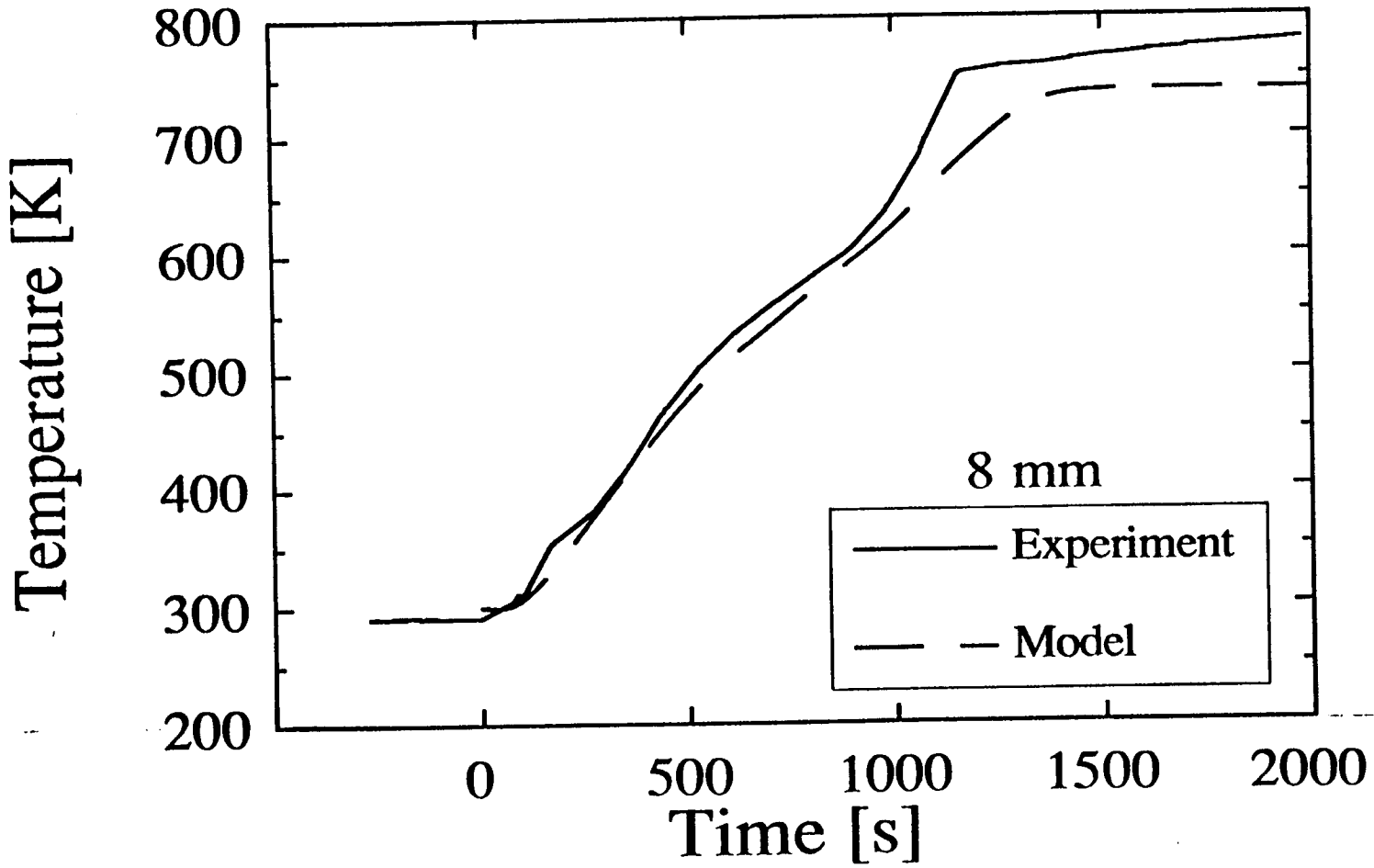

Figure 7.7e Comparison of measured and predicted temperature at 8 mm from the front surface for high density sample and incident heat flux of 60 kW/m^2 (corrected for faster surface emissivity change)

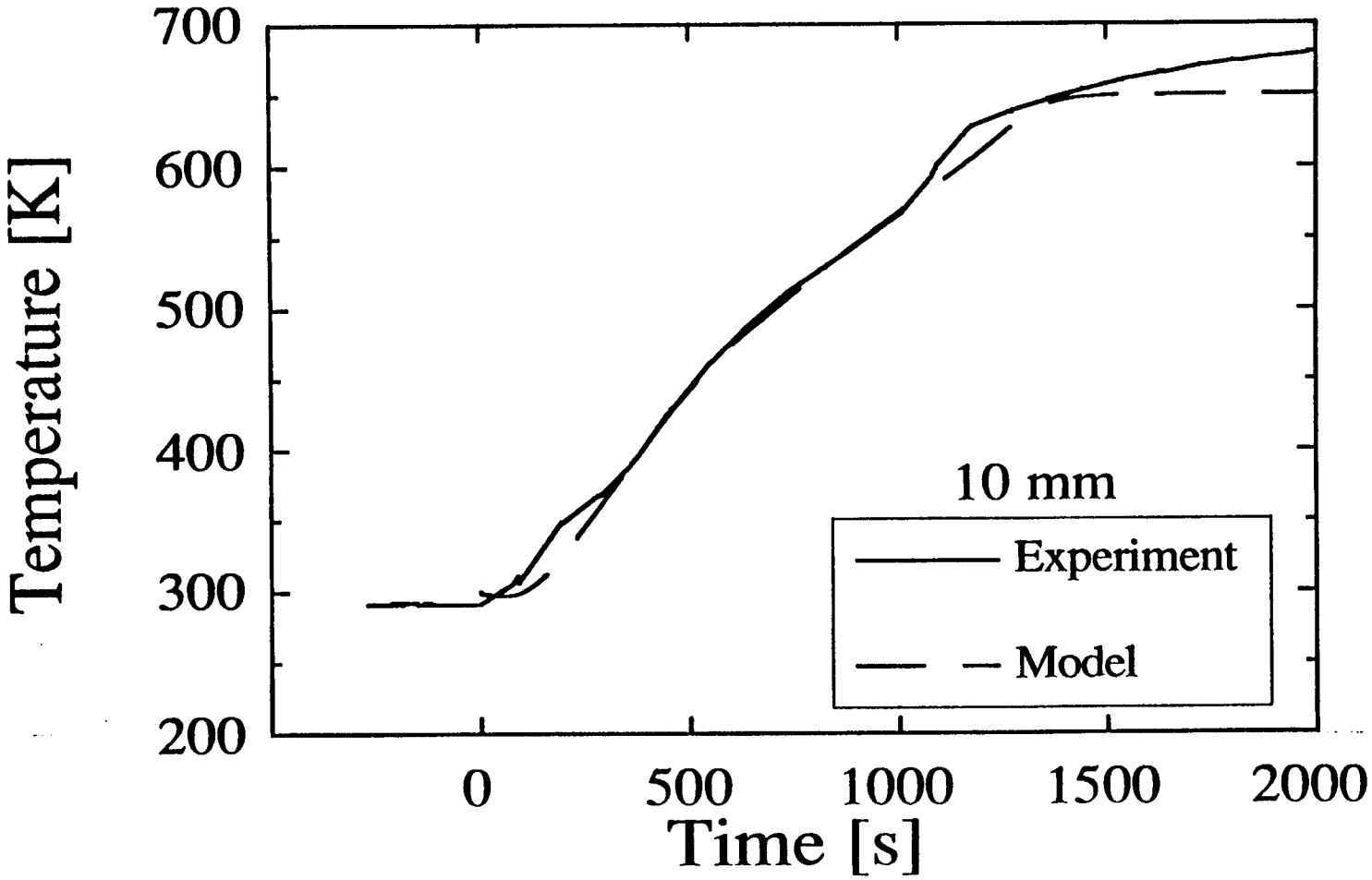

Figure 7.7f Comparison of measured and predicted back surface temperature for high density sample and incident heat flux of 60 kW/m^2 (corrected for faster surface emissivity change)

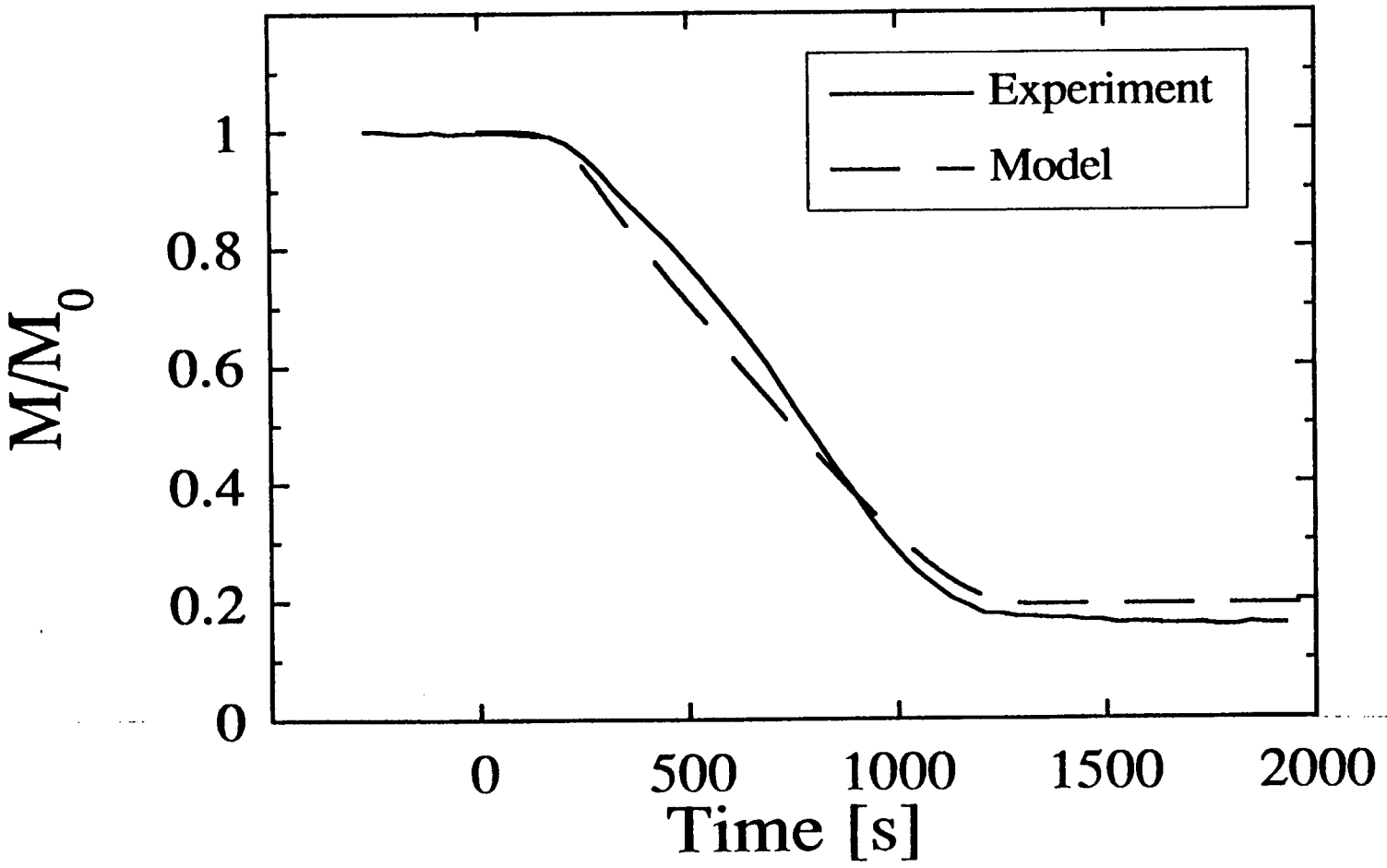

Figure 7.8 Comparison of measured and predicted fractional remaining mass for high density sample and incident heat flux of 60 kW/m^2 (corrected for faster surface emissivity change)

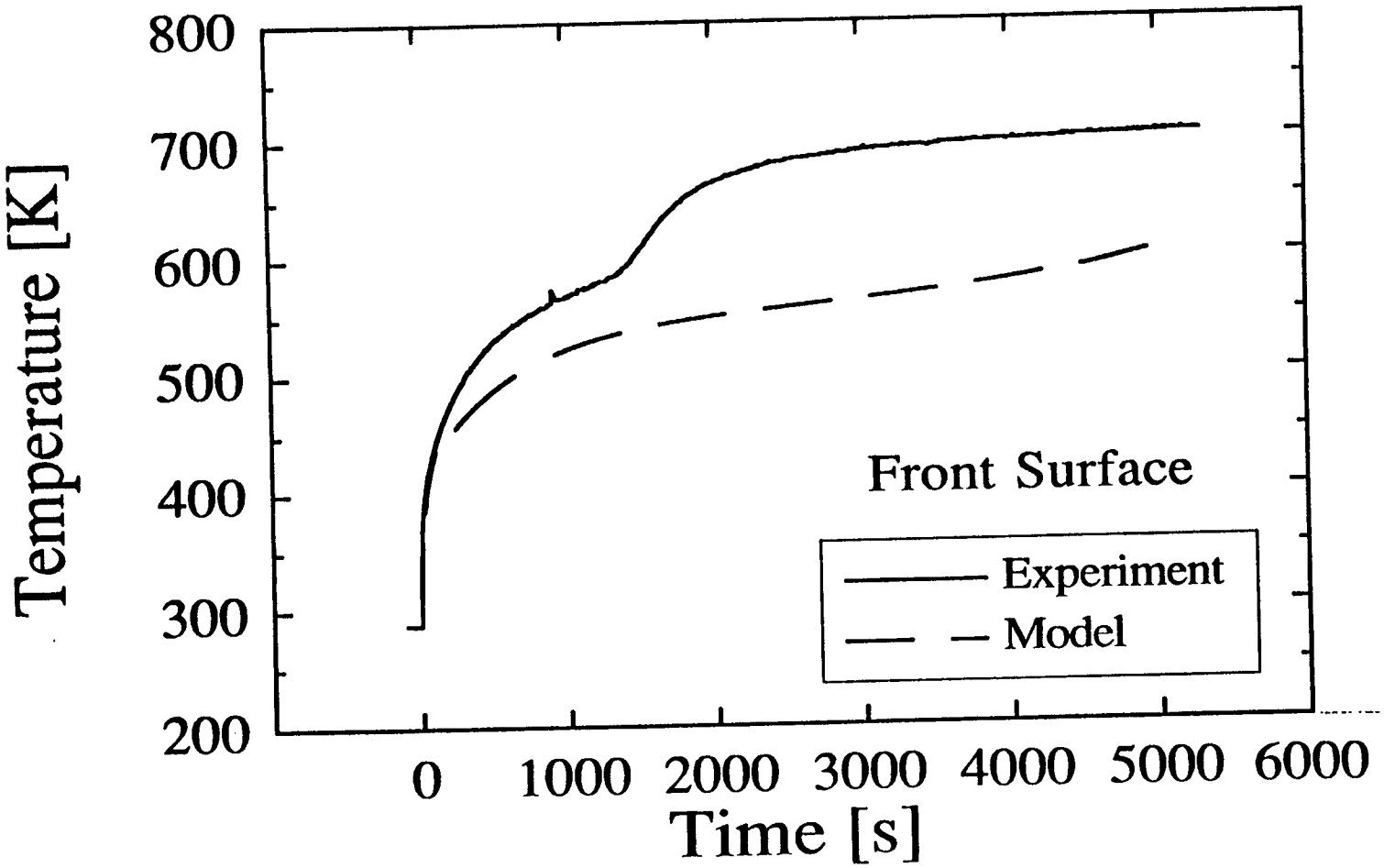

Figure 7.9a Comparison of measured and predicted front surface temperature for high density sample and incident heat flux of 20 kW/m^2 ("base case" values used in computations)

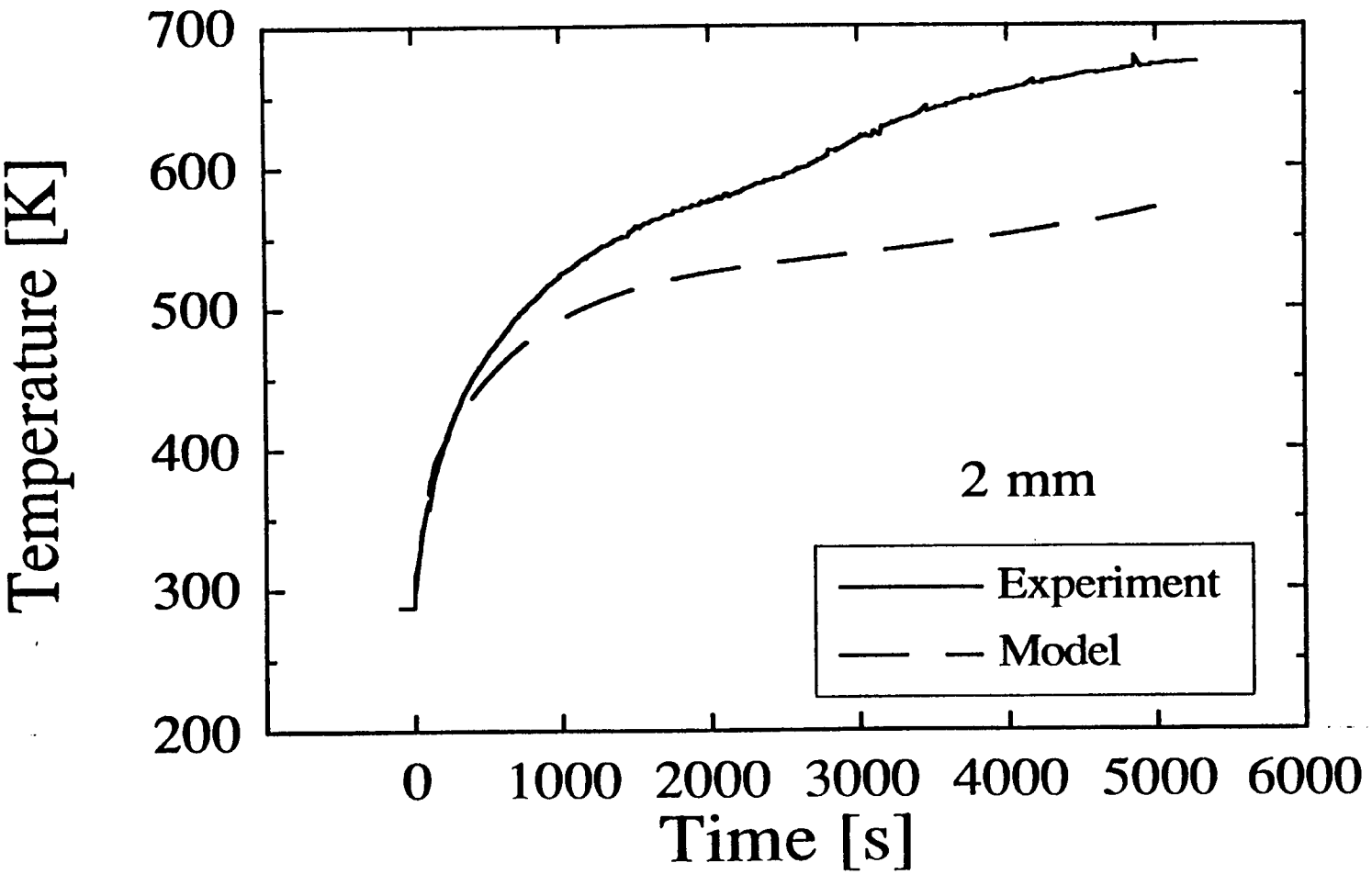

Figure 7.9b Comparison of measured and predicted temperature at 2 mm from the front surface for high density sample and incident heat flux of 20 kW/m^2 ("base case" values used in computations)

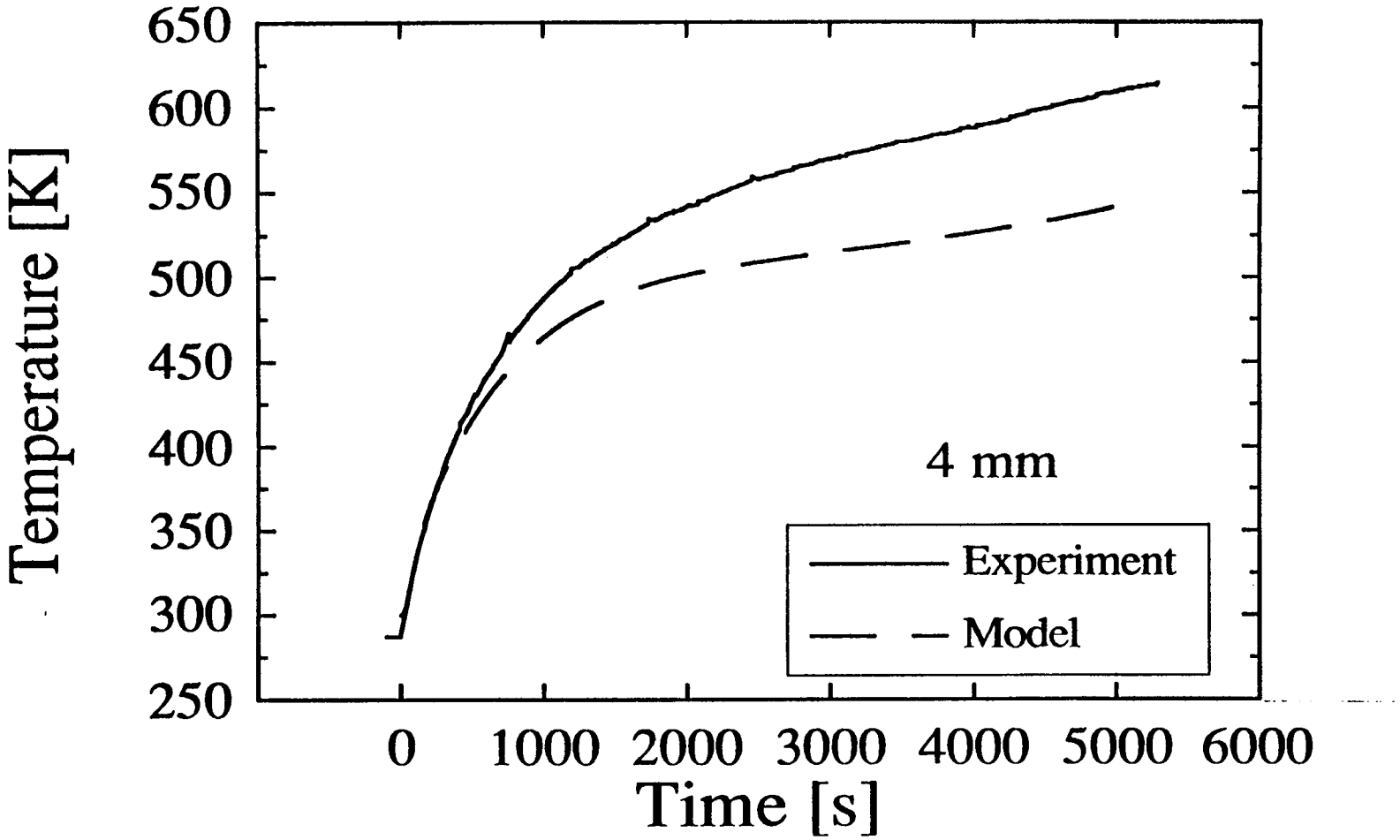

Figure 7.9c Comparison of measured and predicted temperature at 4 mm from the front surface for high density sample and incident heat flux of 20 kW/m^2 ("base case" values used in computations)

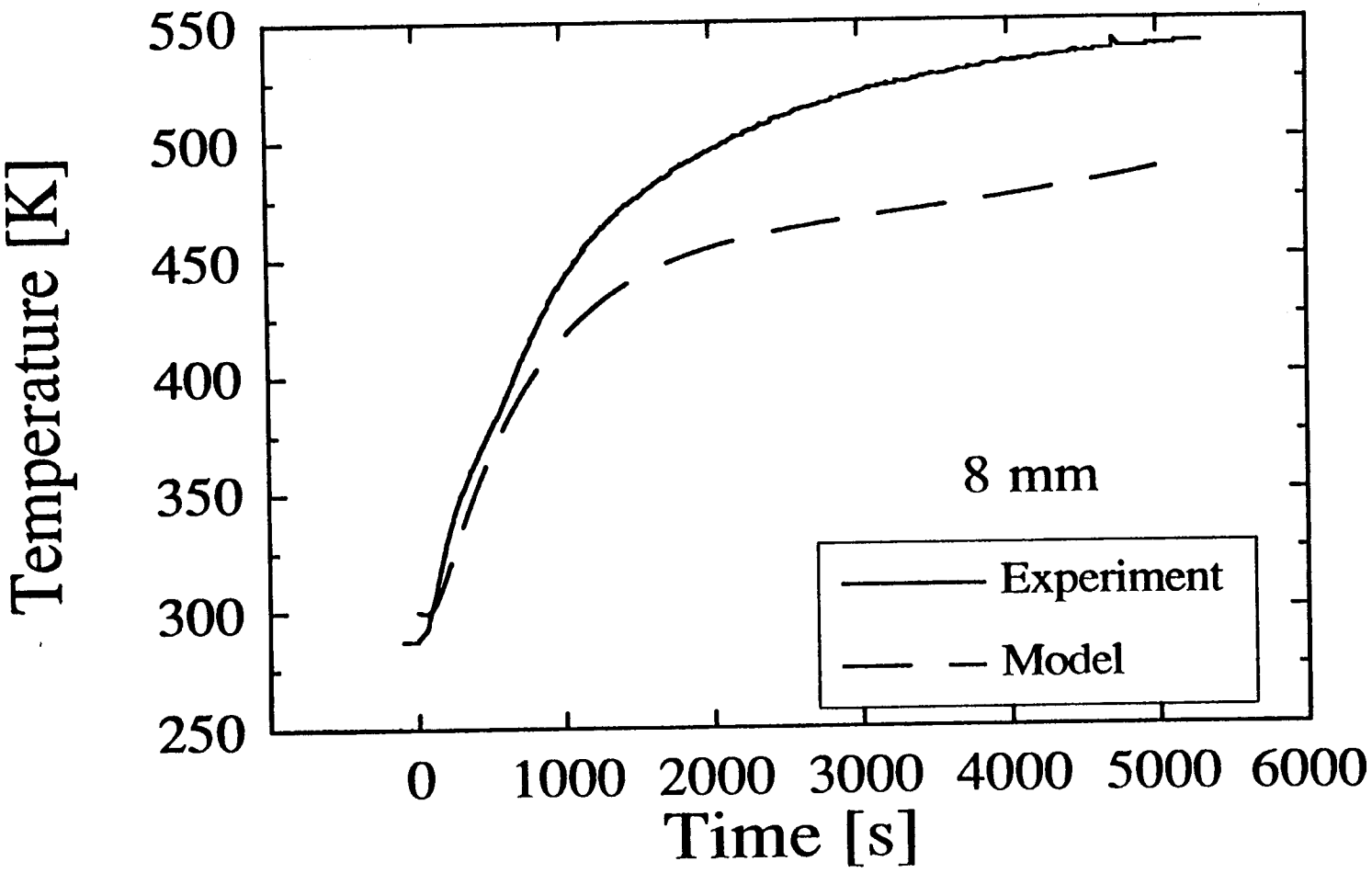

Figure 7.9d Comparison of measured and predicted temperature at 8 mm from the front surface for high density sample and incident heat flux of 20 kW/m^2 ("base case" values used in computations)

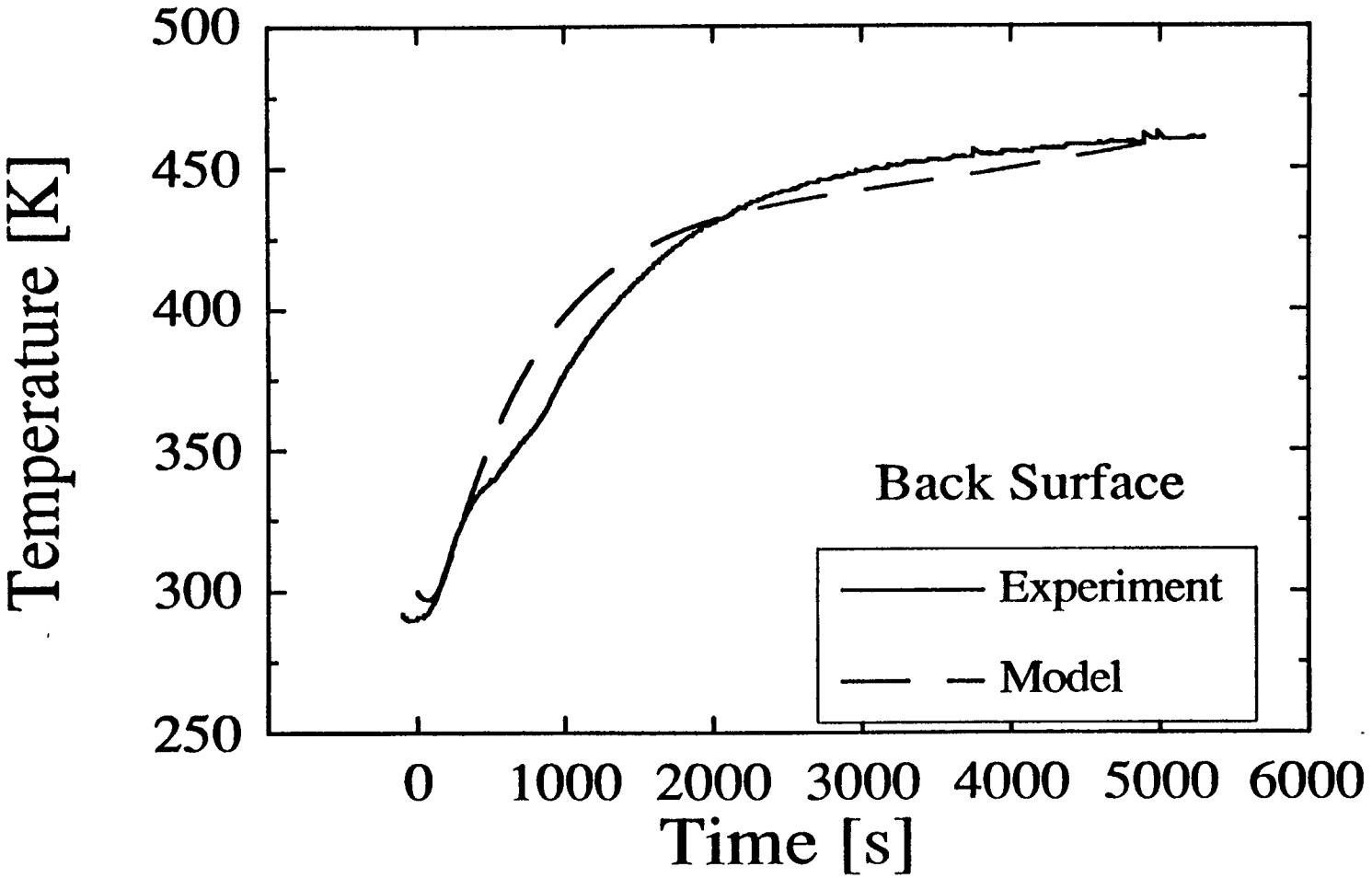

Figure 7.9e Comparison of measured and predicted back surface temperature for high density sample and incident heat flux of 20 kW/m^2 ("base case" values used in computations)

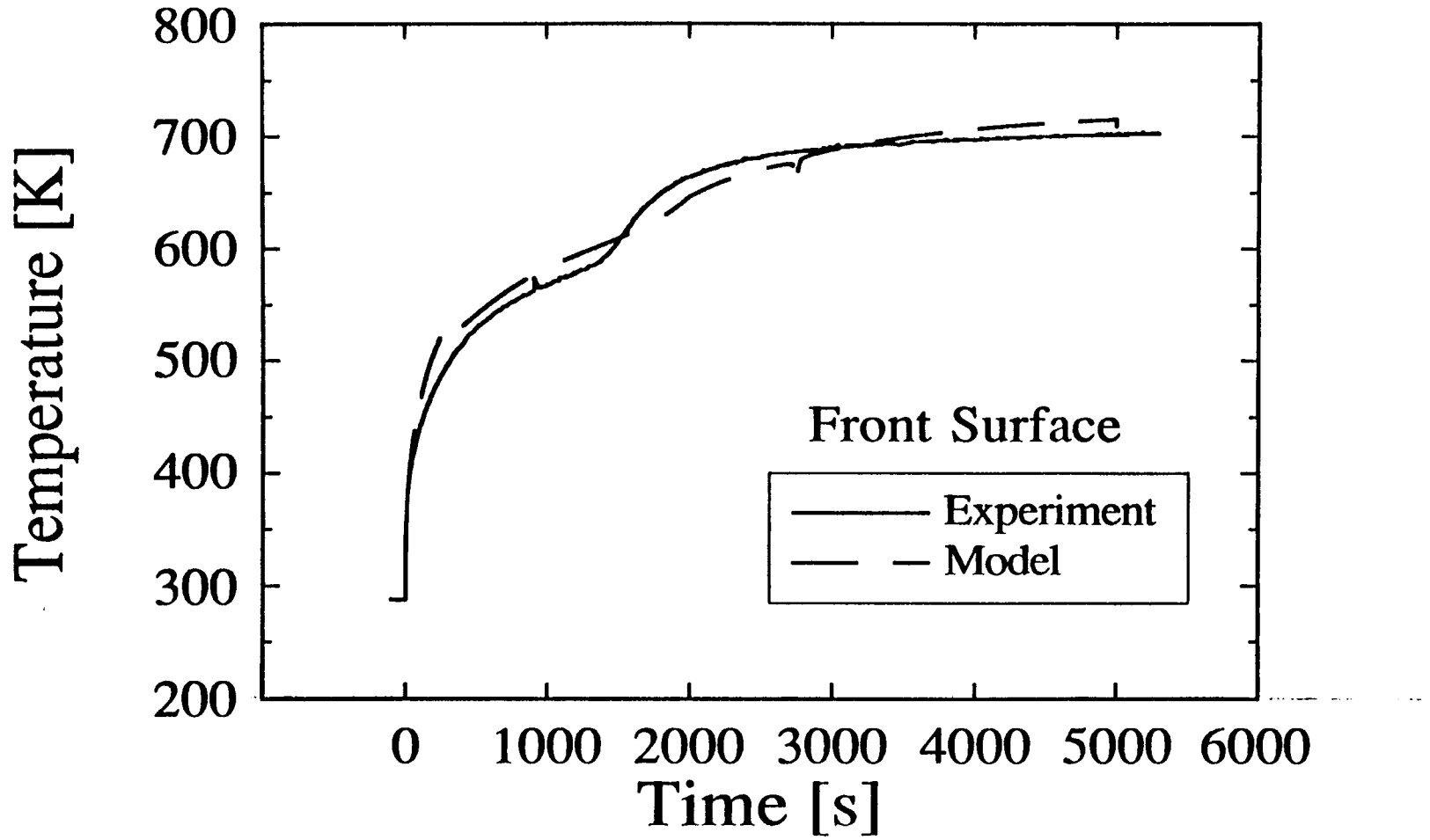

Figure 7.9f Comparison of measured and predicted front surface temperature for high density sample and incident heat flux of 20 kW/m^2 (corrected for slower surface emissivity change, lower heat transfer coefficient and single, high activation energy kinetics)

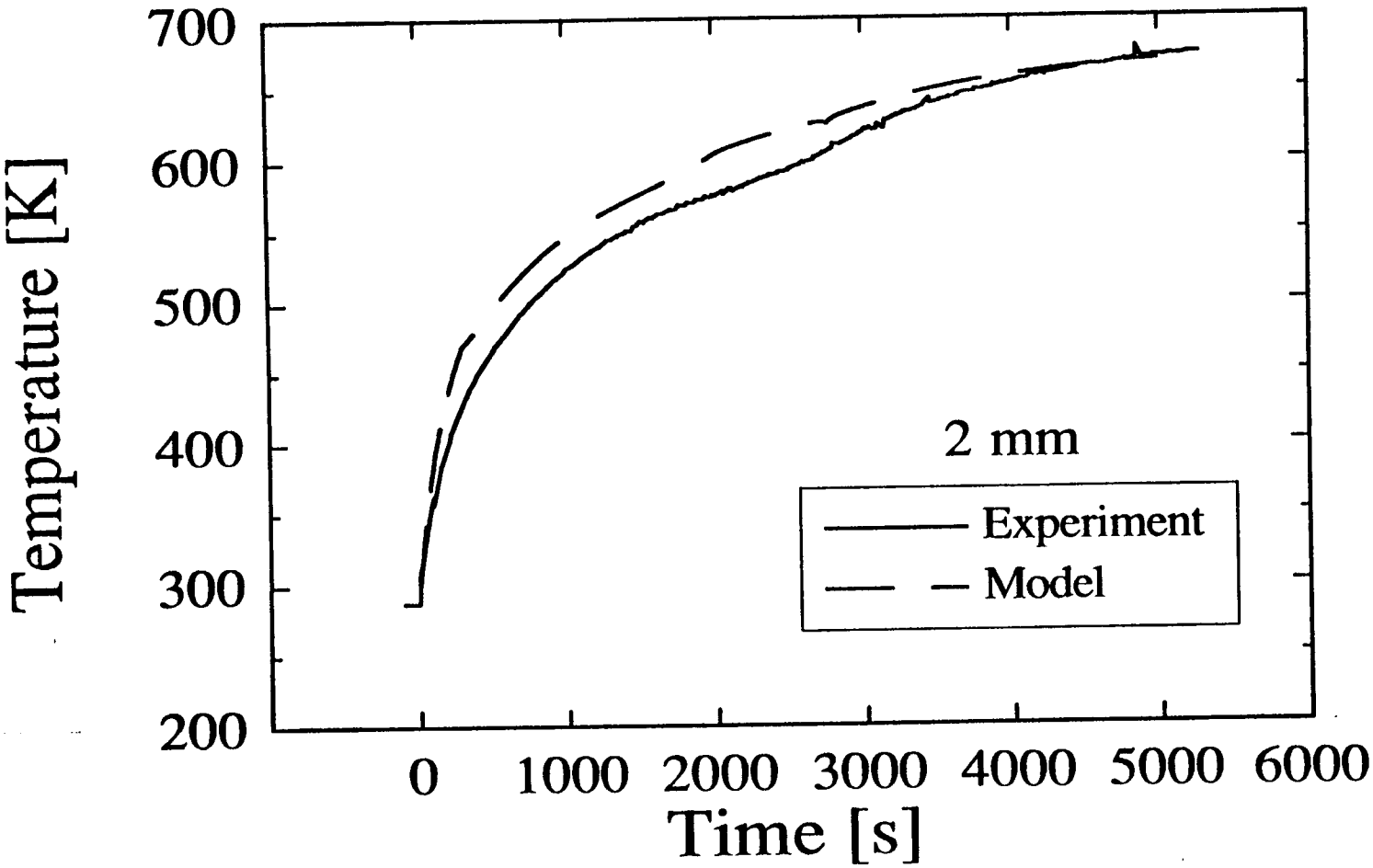

Figure 7.9g Comparison of measured and predicted temperature at 2 mm from the front surface for high density sample and incident heat flux of 20 kW/m^2 (corrected for slower surface emissivity change, lower heat transfer coefficient and single, high activation energy kinetics)

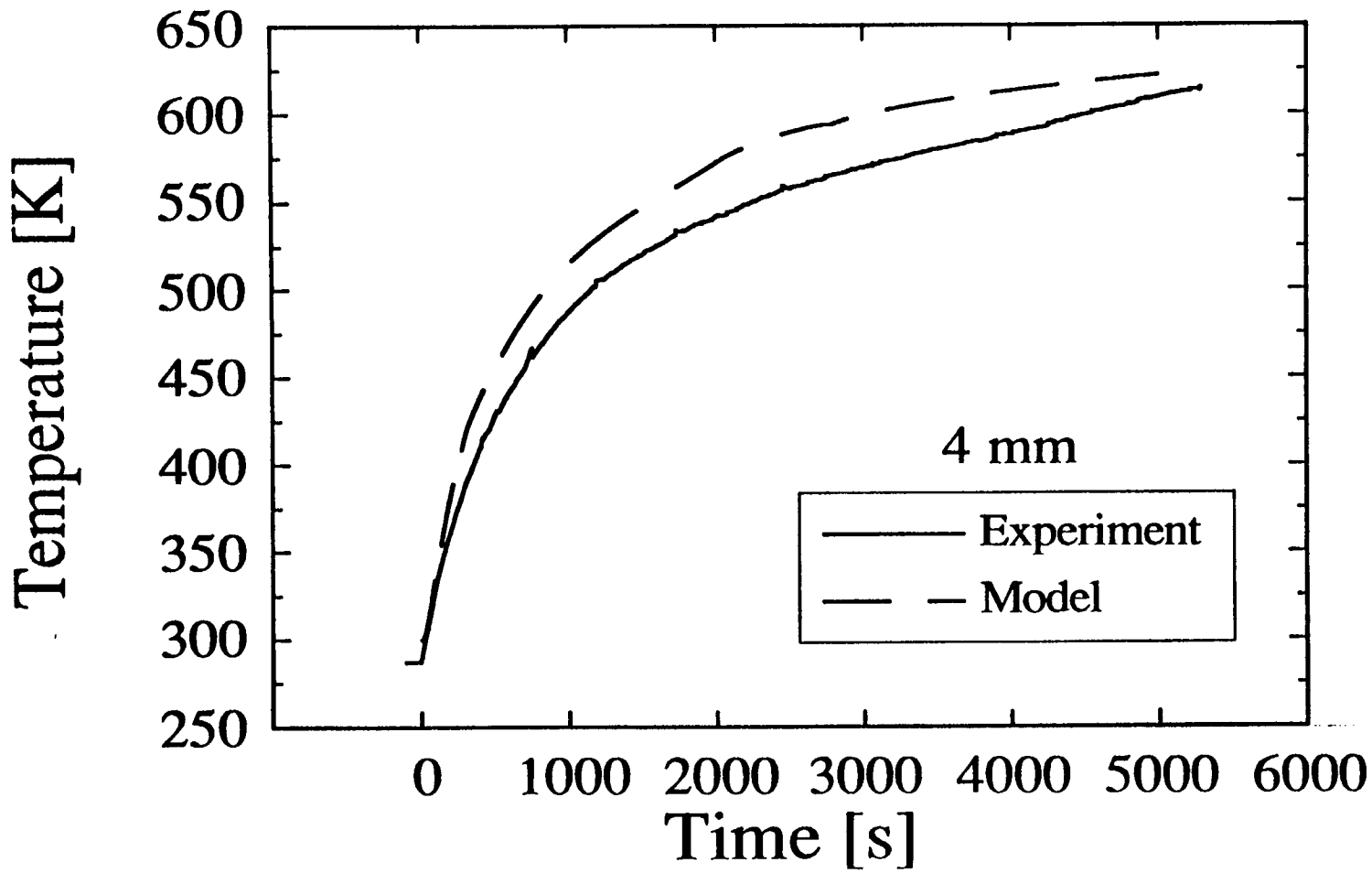

Figure 7.9h Comparison of measured and predicted temperature at 4 mm from the front surface for high density sample and incident heat flux of 20 kW/m^2 (corrected for slower surface emissivity change, lower heat transfer coefficient and single, high activation energy kinetics)

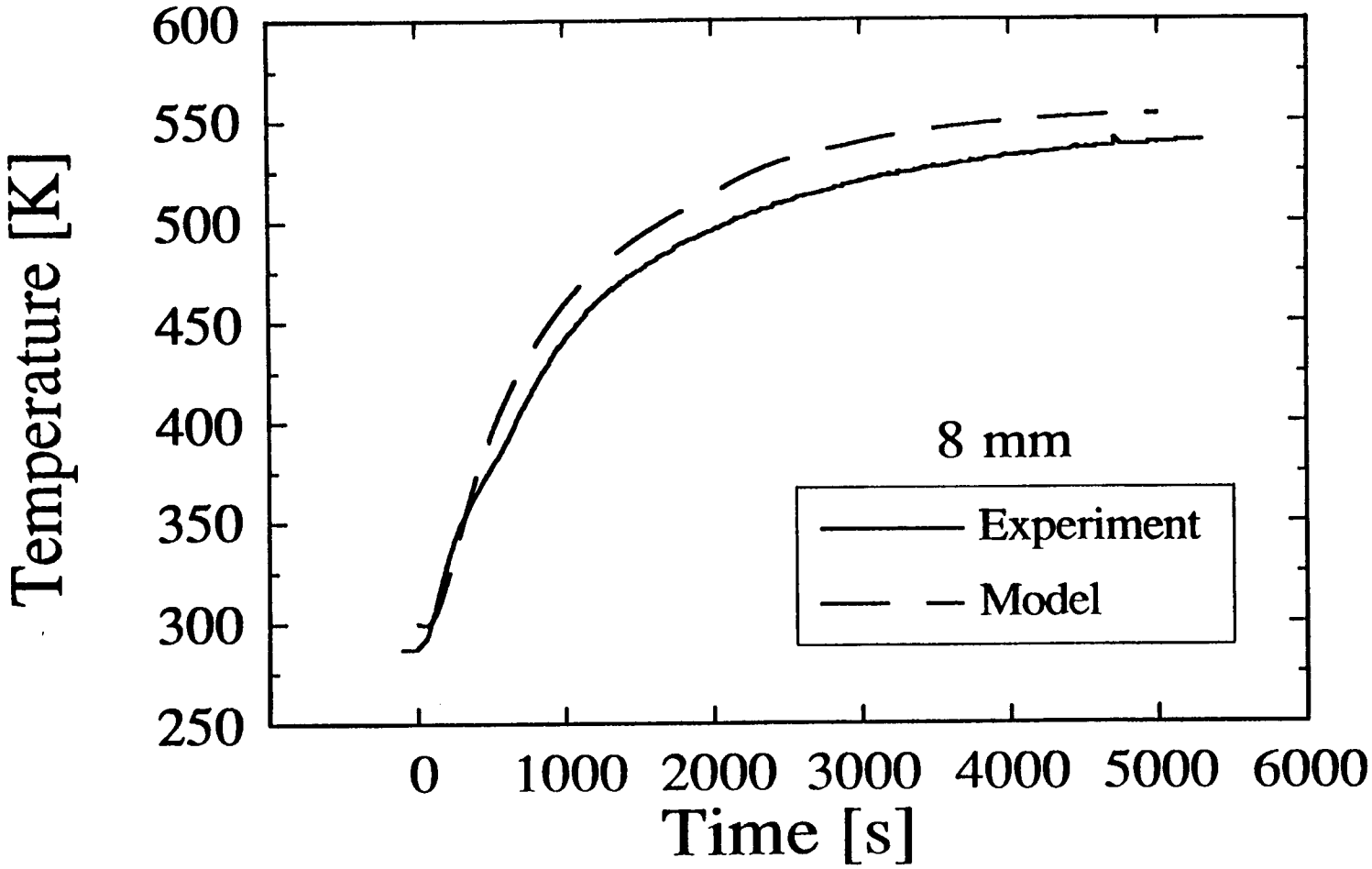

Figure 7.9i Comparison of measured and predicted temperature at 8 mm from the front surface for high density sample and incident heat flux of 20 kW/m^2 (corrected for slower surface emissivity change, lower heat transfer coefficient and single, high activation energy kinetics)

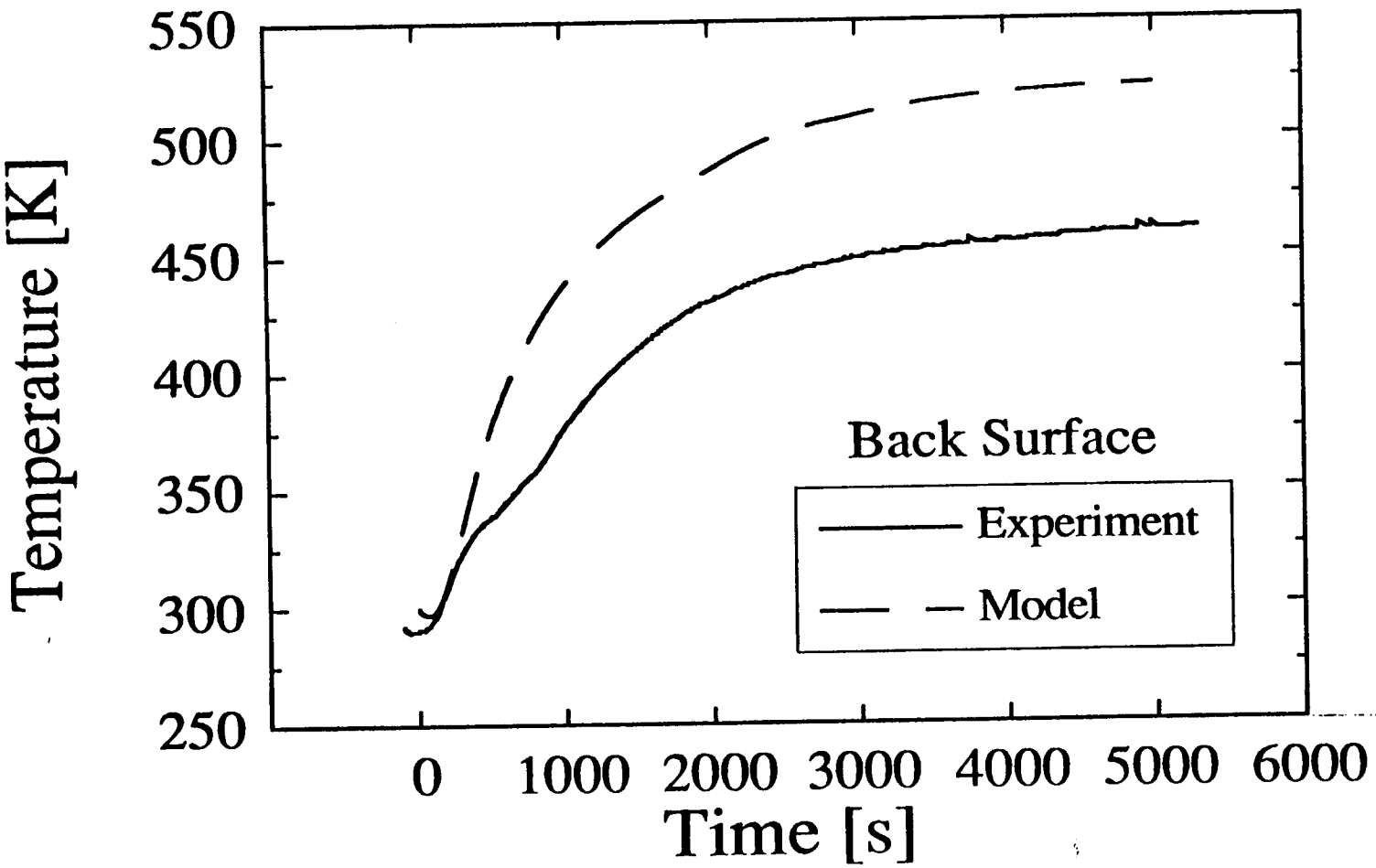

Figure 7.9j Comparison of measured and predicted back surface temperature for high density sample and incident heat flux of 20 kW/m^2 (corrected for slower surface emissivity change, lower heat transfer coefficient and single, high activation energy kinetics)

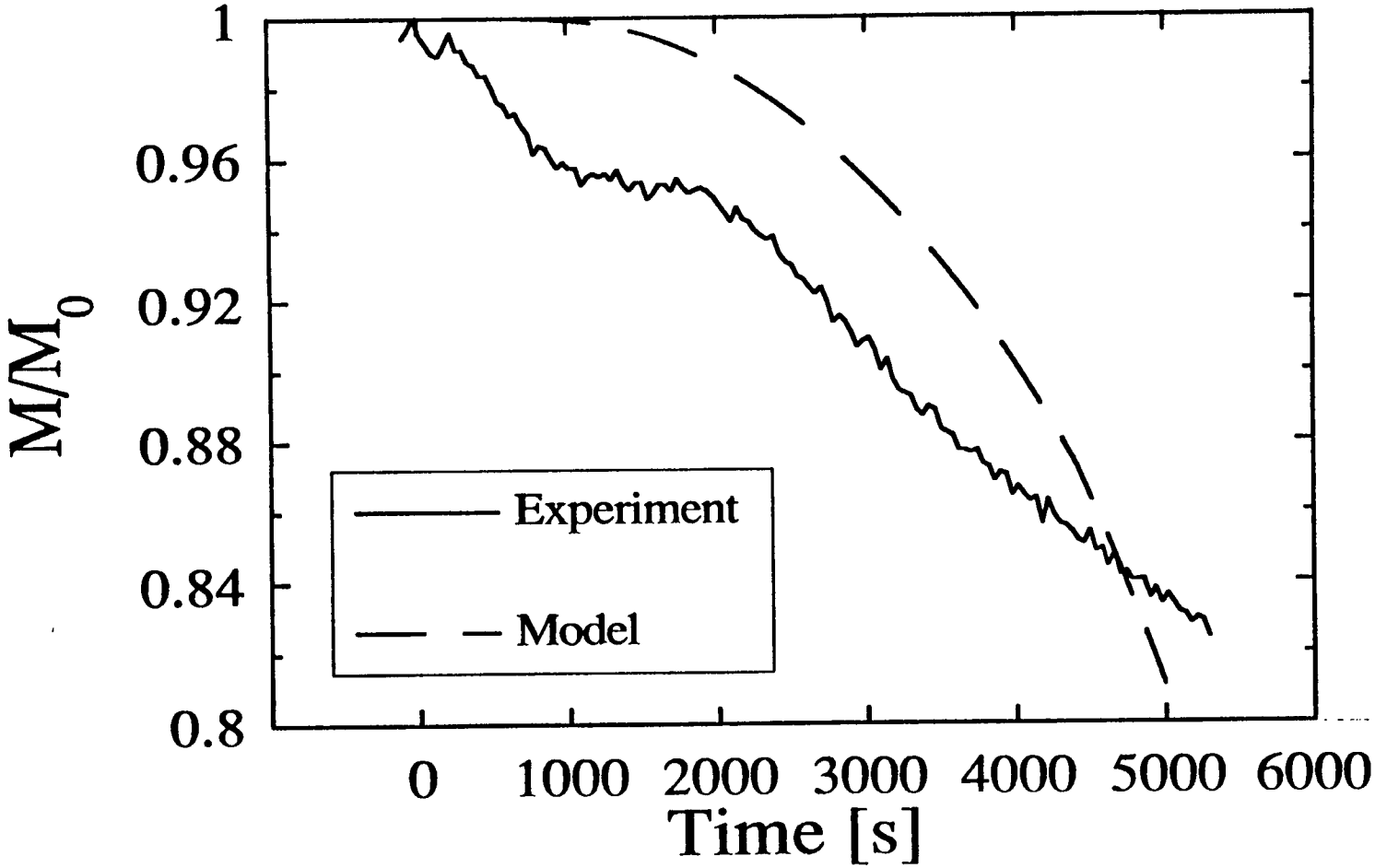

Figure 7.10a Comparison of measured and predicted fractional remaining mass for high density sample and incident heat flux of 20 kW/m^2 ("base case" values used in computations)

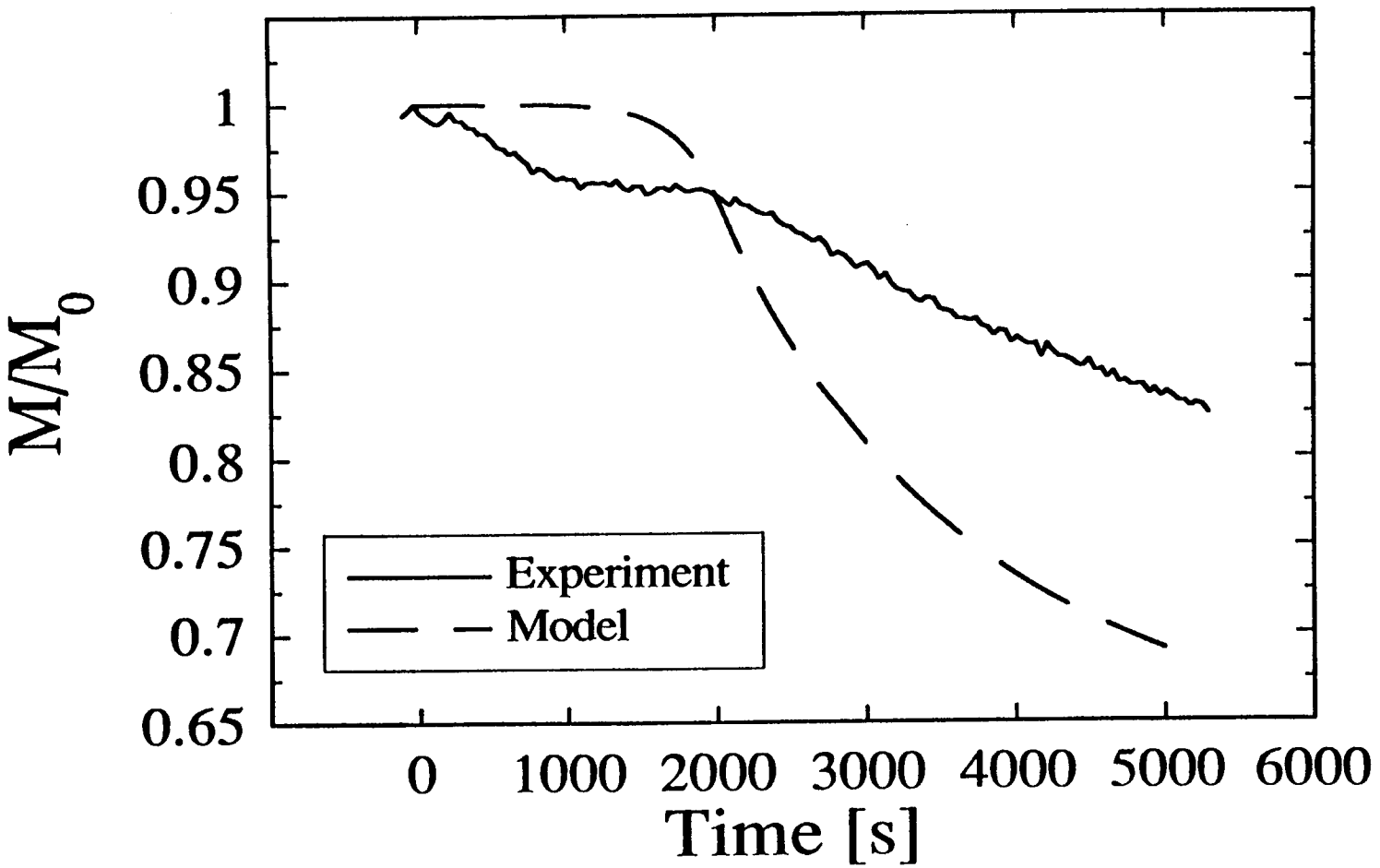

Figure 7.10b Comparison of measured and predicted fractional remaining mass for high density sample and incident heat flux of 20 kW/m^2 (corrected for slower surface emissivity change, lower heat transfer coefficient and single, high activation energy kinetics)

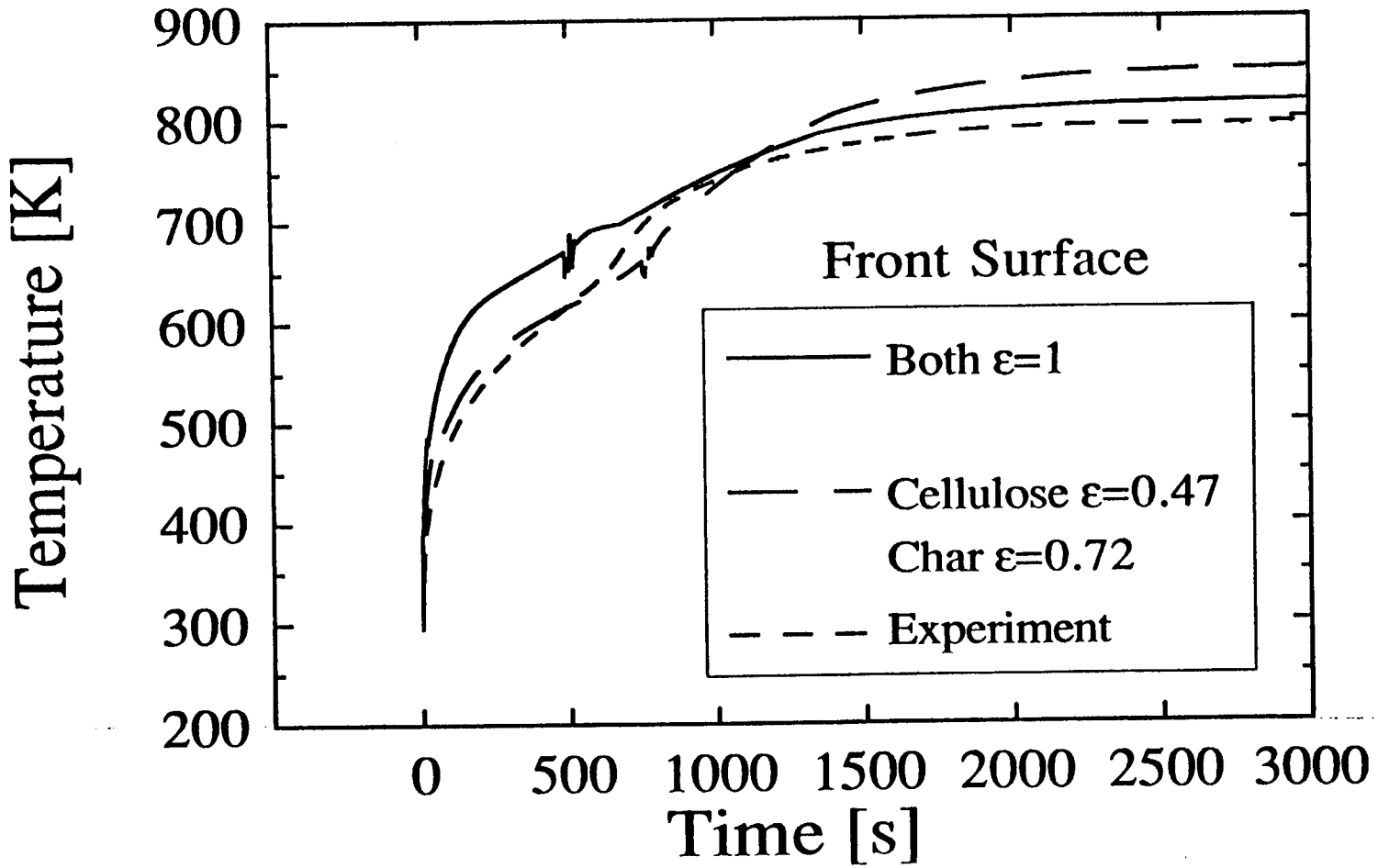

Figure 7.11a Sensitivity of front surface temperature prediction to surface emissivity. Measured surface temperature is also shown

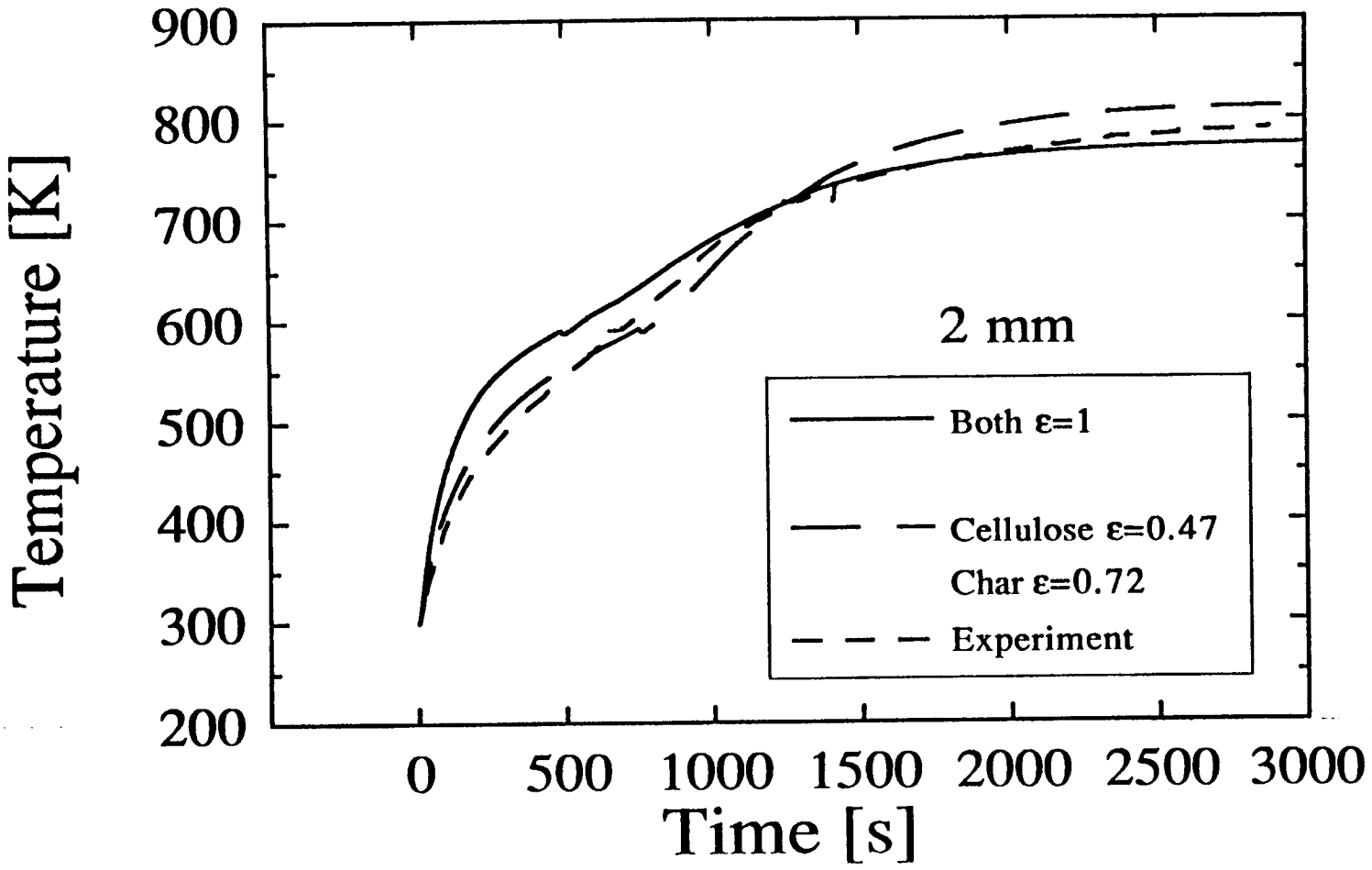

Figure 7.11b Sensitivity of temperature at 2 mm from the front surface prediction to surface emissivity. Measured temperature is also shown

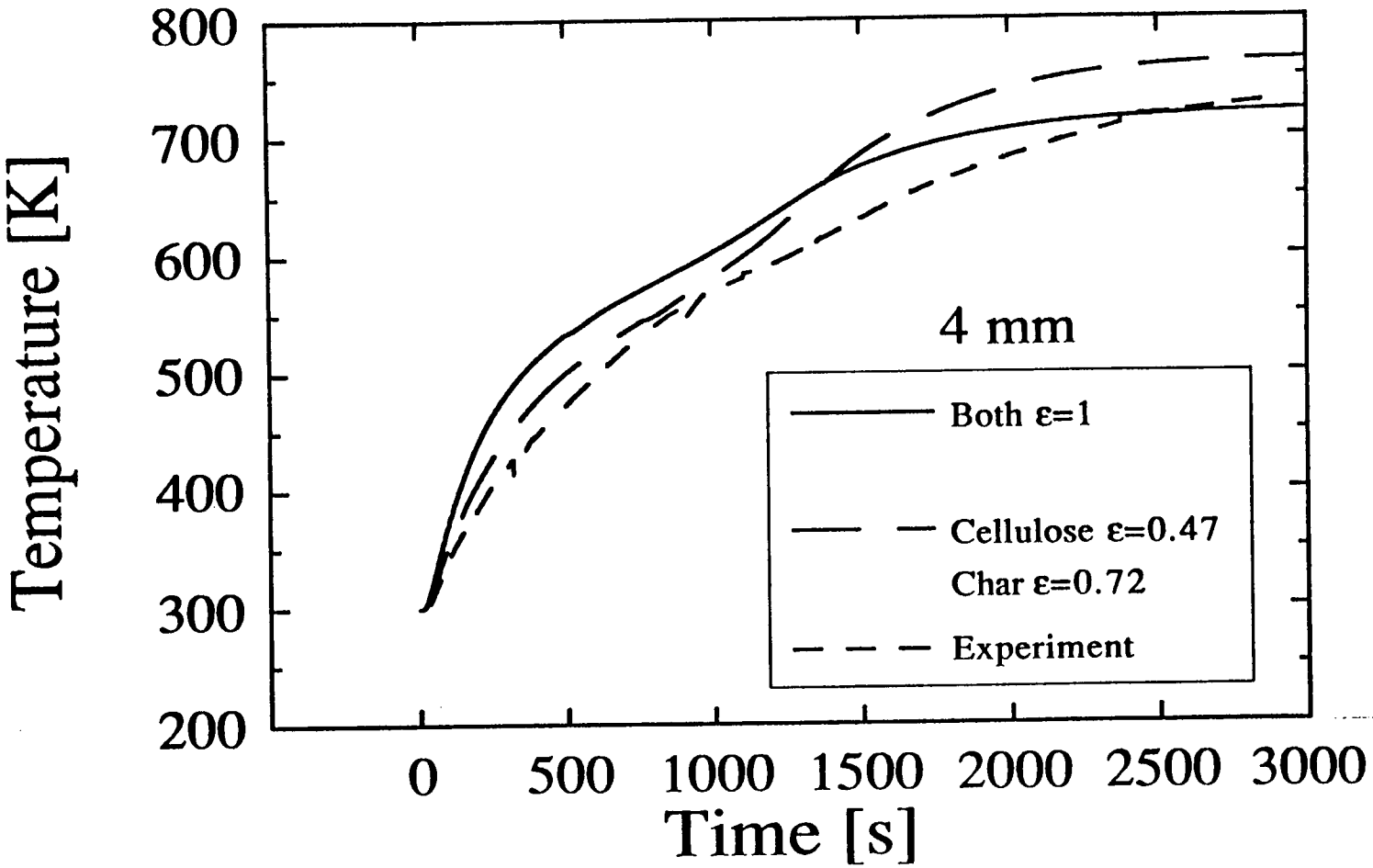

Figure 7.11c Sensitivity of temperature at 4 mm from the front surface prediction to surface emissivity. Measured temperature is also shown

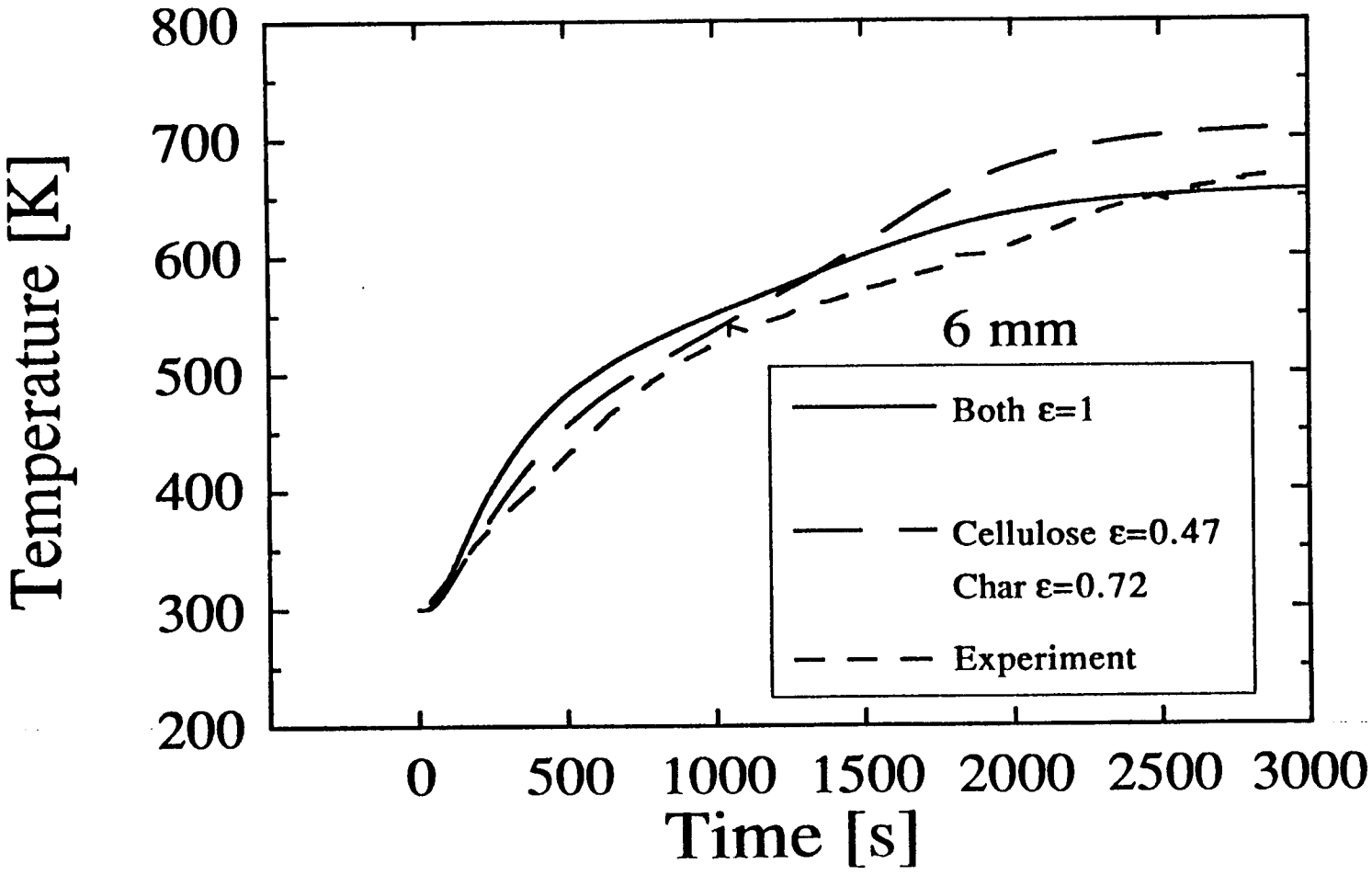

Figure 7.11d Sensitivity of temperature at 6 mm from the front surface prediction to surface emissivity. Measured temperature is also shown

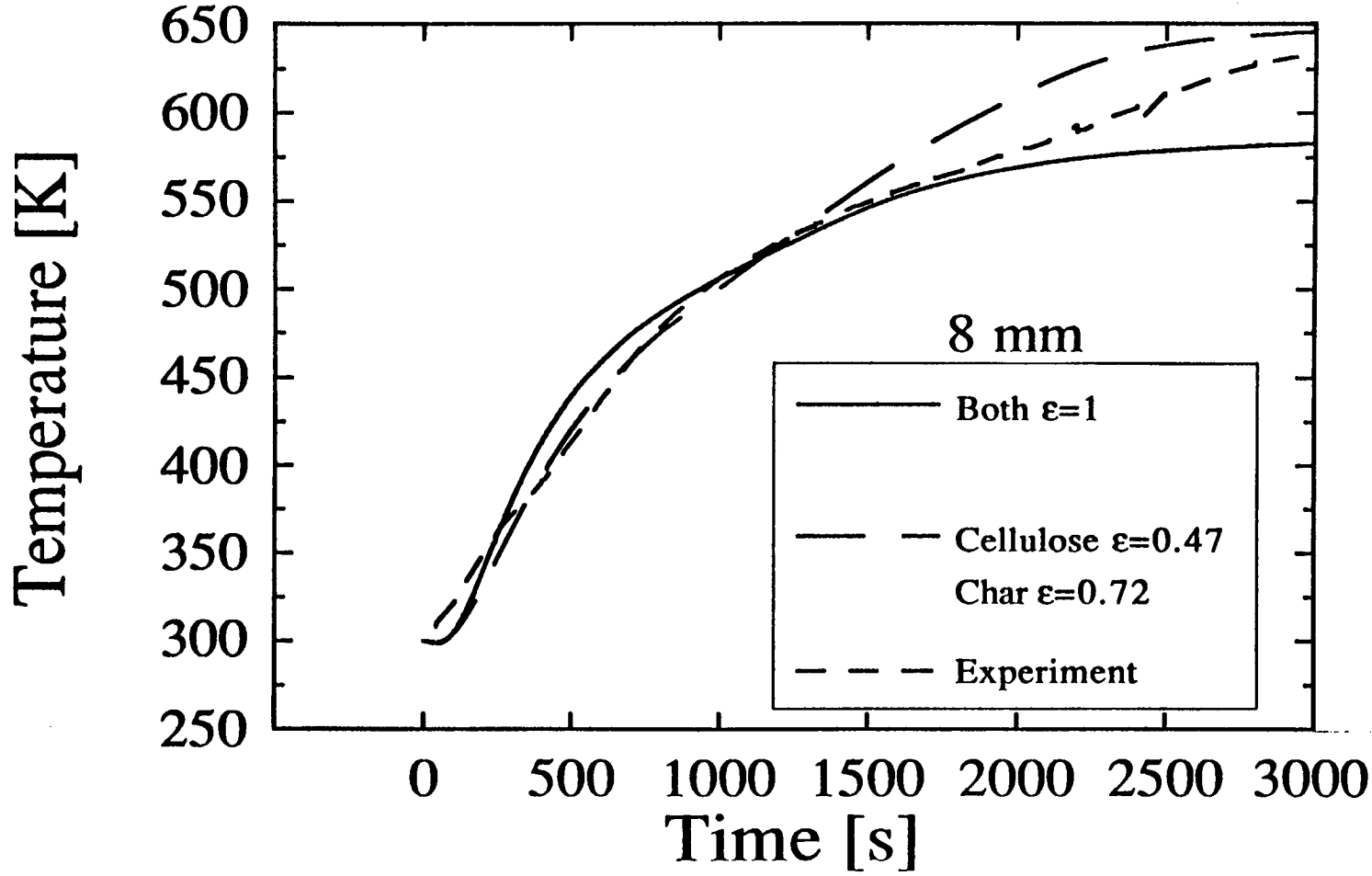

Figure 7.11e Sensitivity of temperature at 8 mm from the front surface prediction to surface emissivity. Measured temperature is also shown

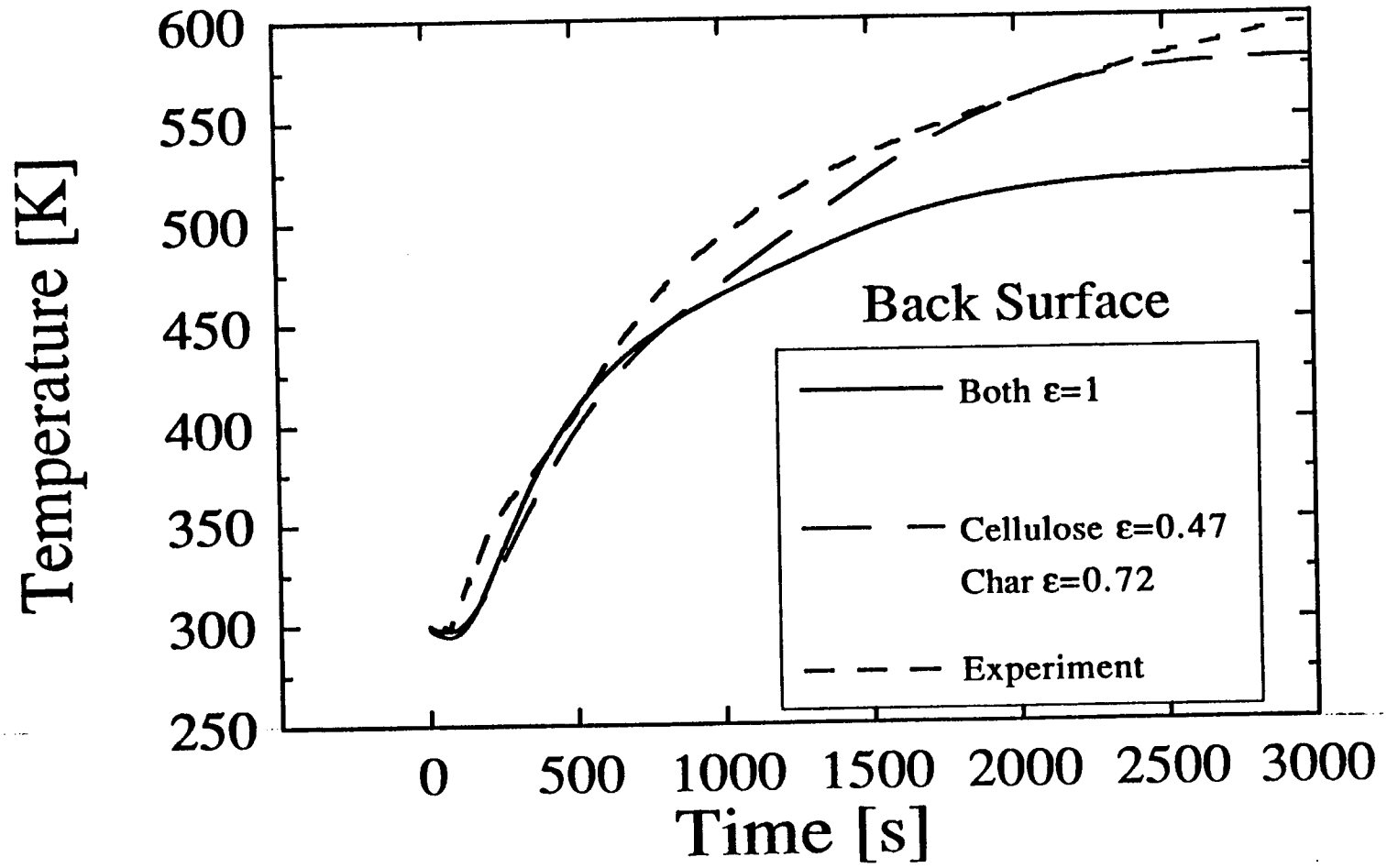

Figure 7.11f Sensitivity of back surface temperature prediction to surface emissivity. Measured temperature is also shown

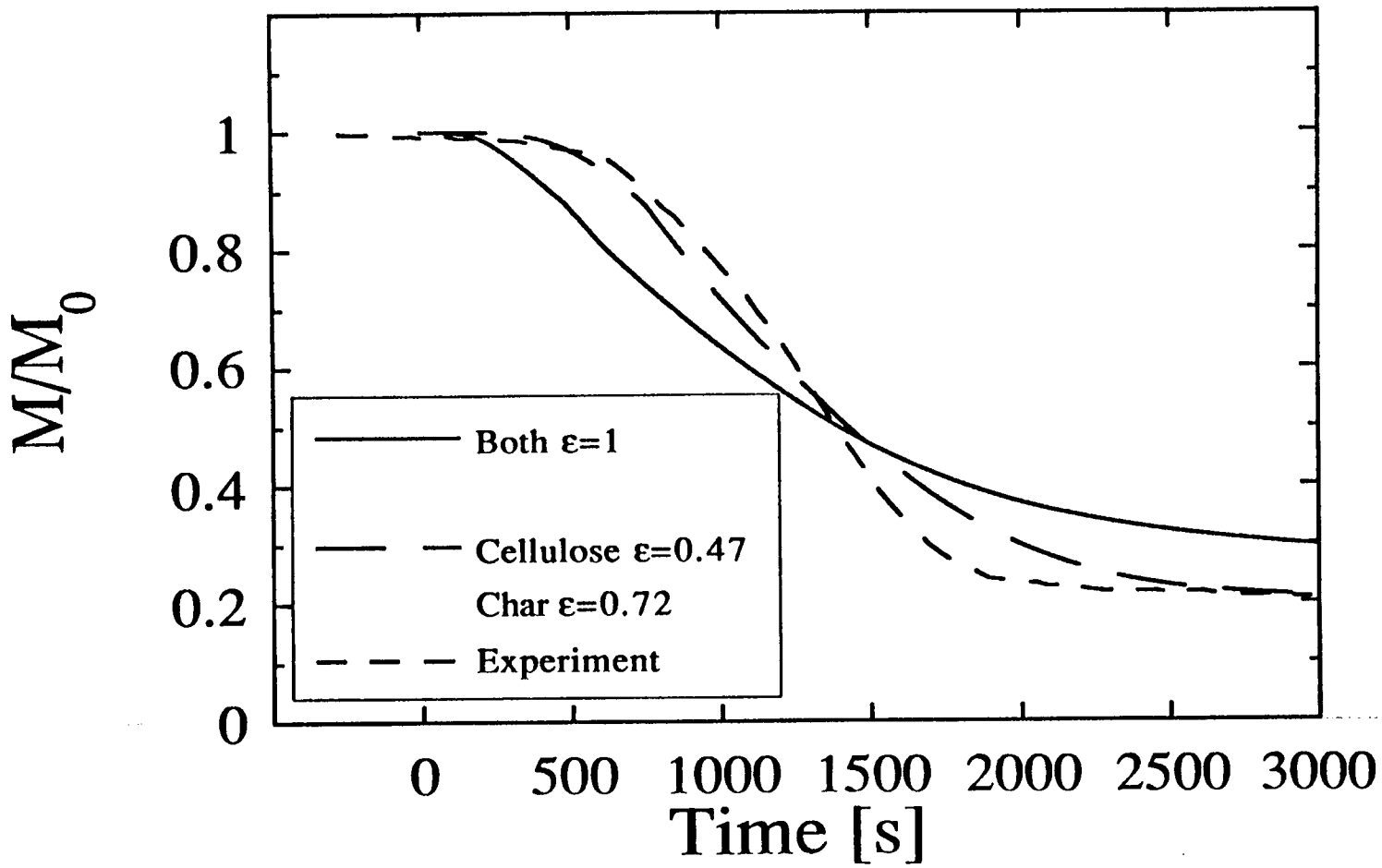

Figure 7.12 Sensitivity of fractional remaining mass prediction to surface emissivity. Measured fractional remaining mass is also shown

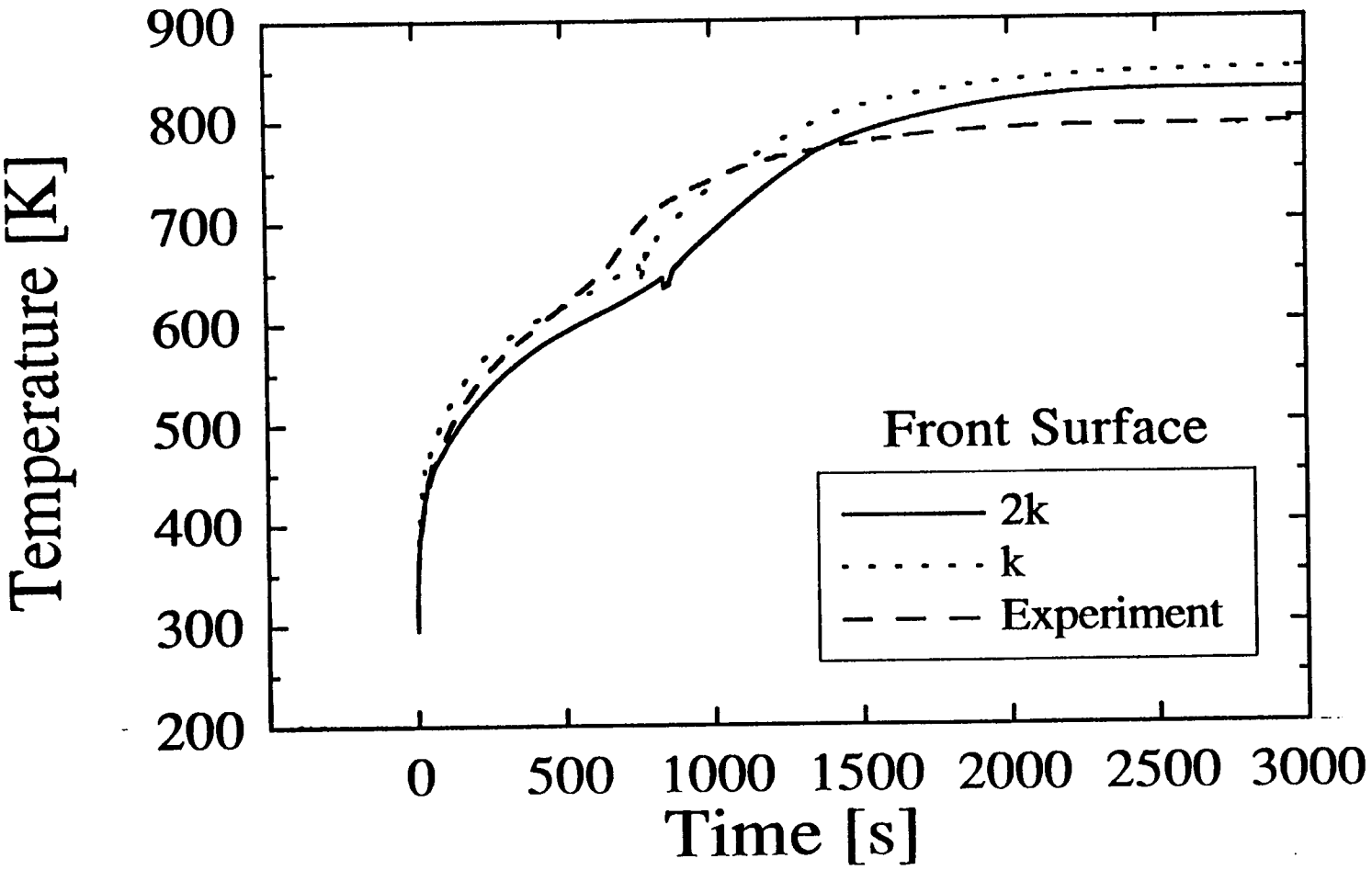

Figure 7.13a Sensitivity of front surface temperature prediction to thermal conductivities. Measured surface temperature is also shown

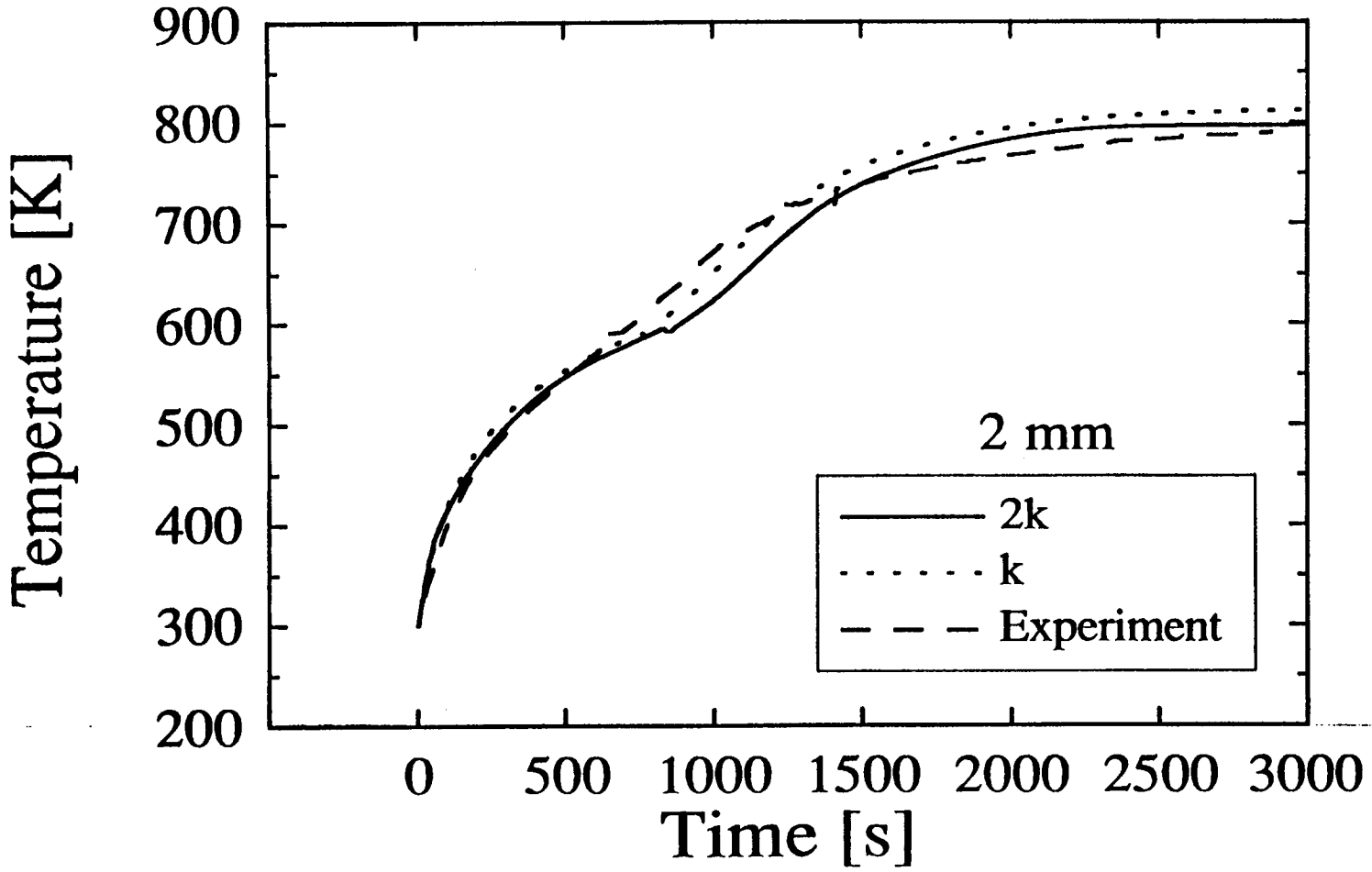

Figure 7.13b Sensitivity of temperature at 2 mm from the front surface prediction to thermal conductivities. Measured temperature is also shown

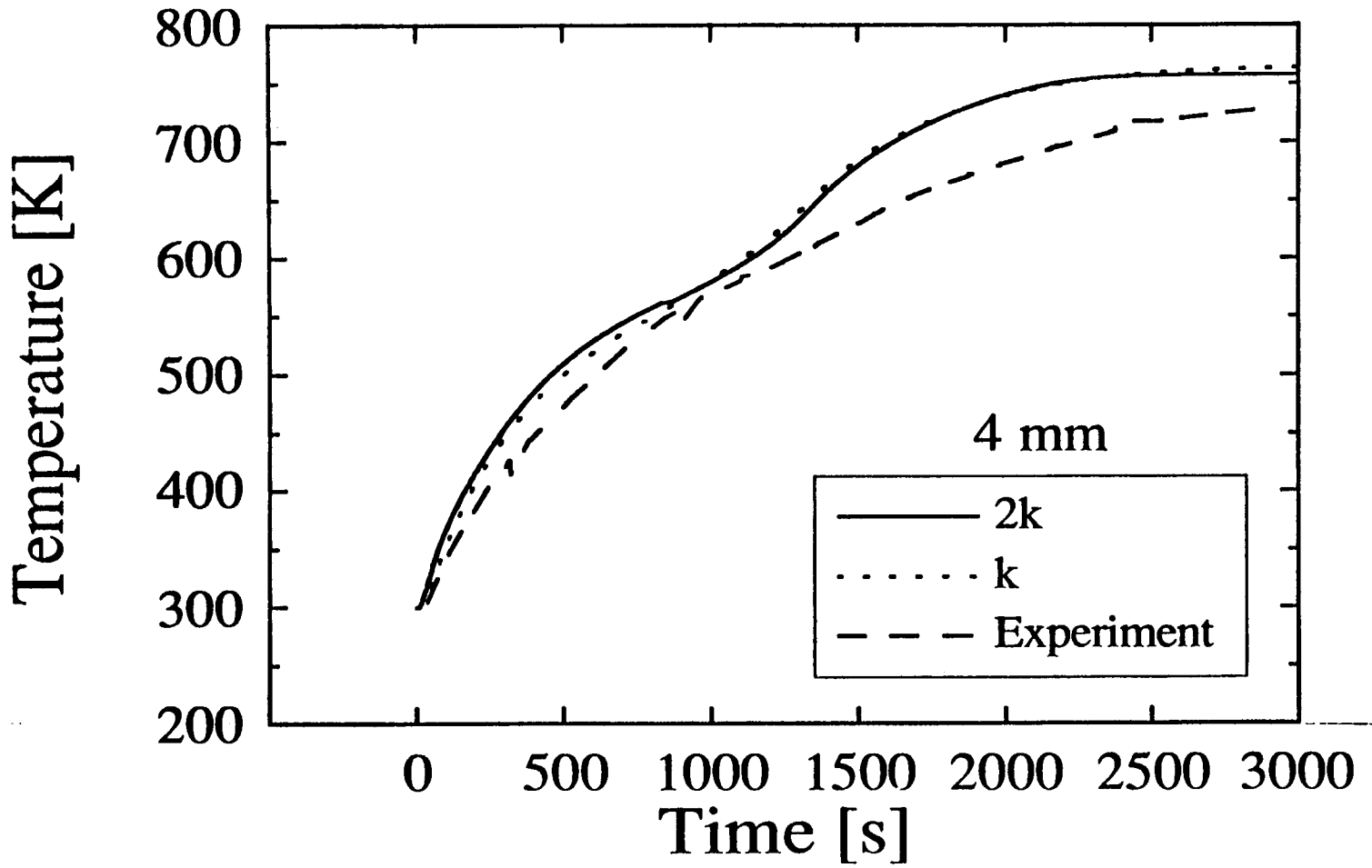

Figure 7.13c Sensitivity of temperature at 4 mm from the front surface prediction to thermal conductivities. Measured temperature is also shown

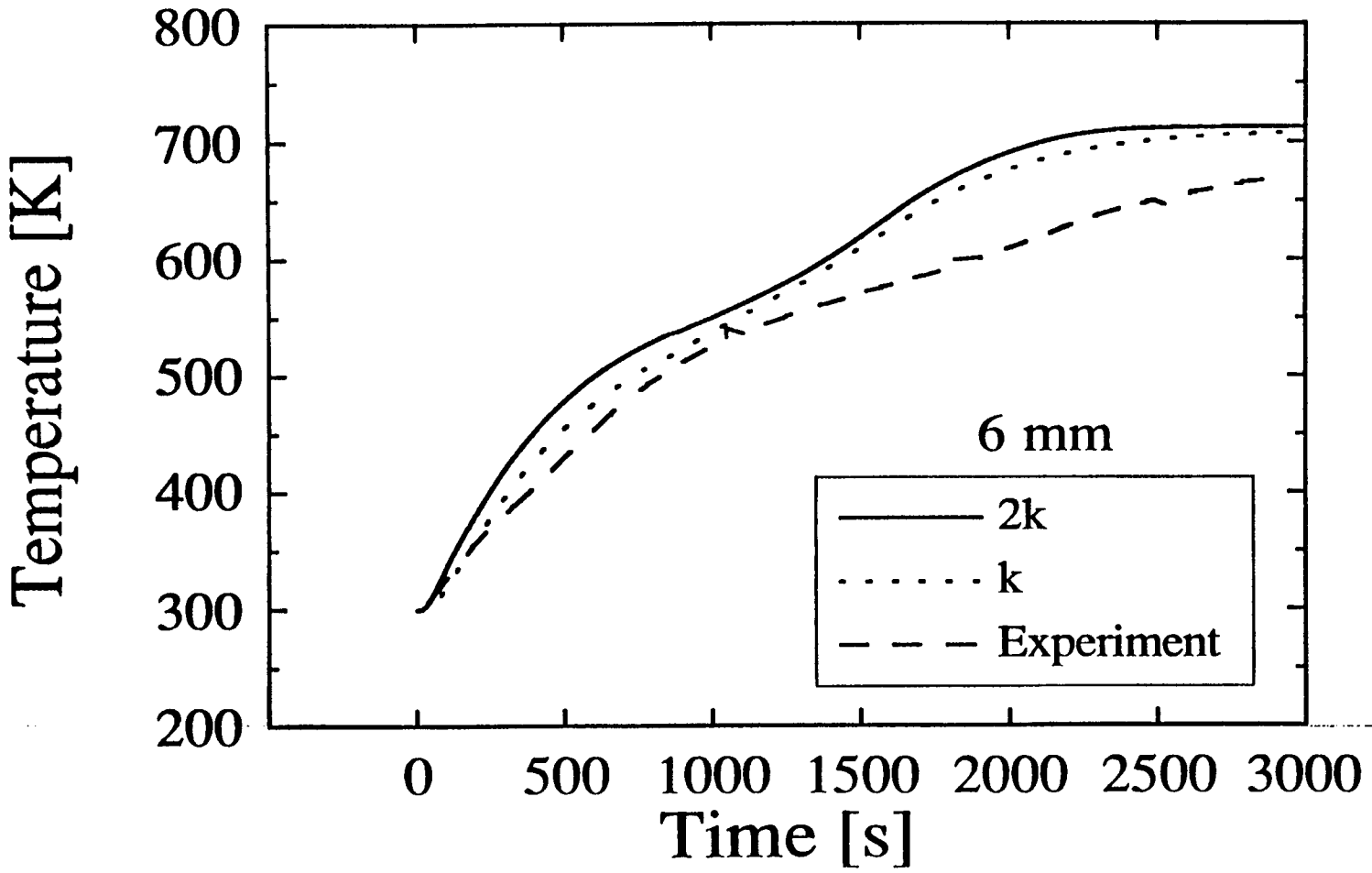

Figure 7.13d Sensitivity of temperature at 6 mm from the front surface prediction to thermal conductivities. Measured temperature is also shown

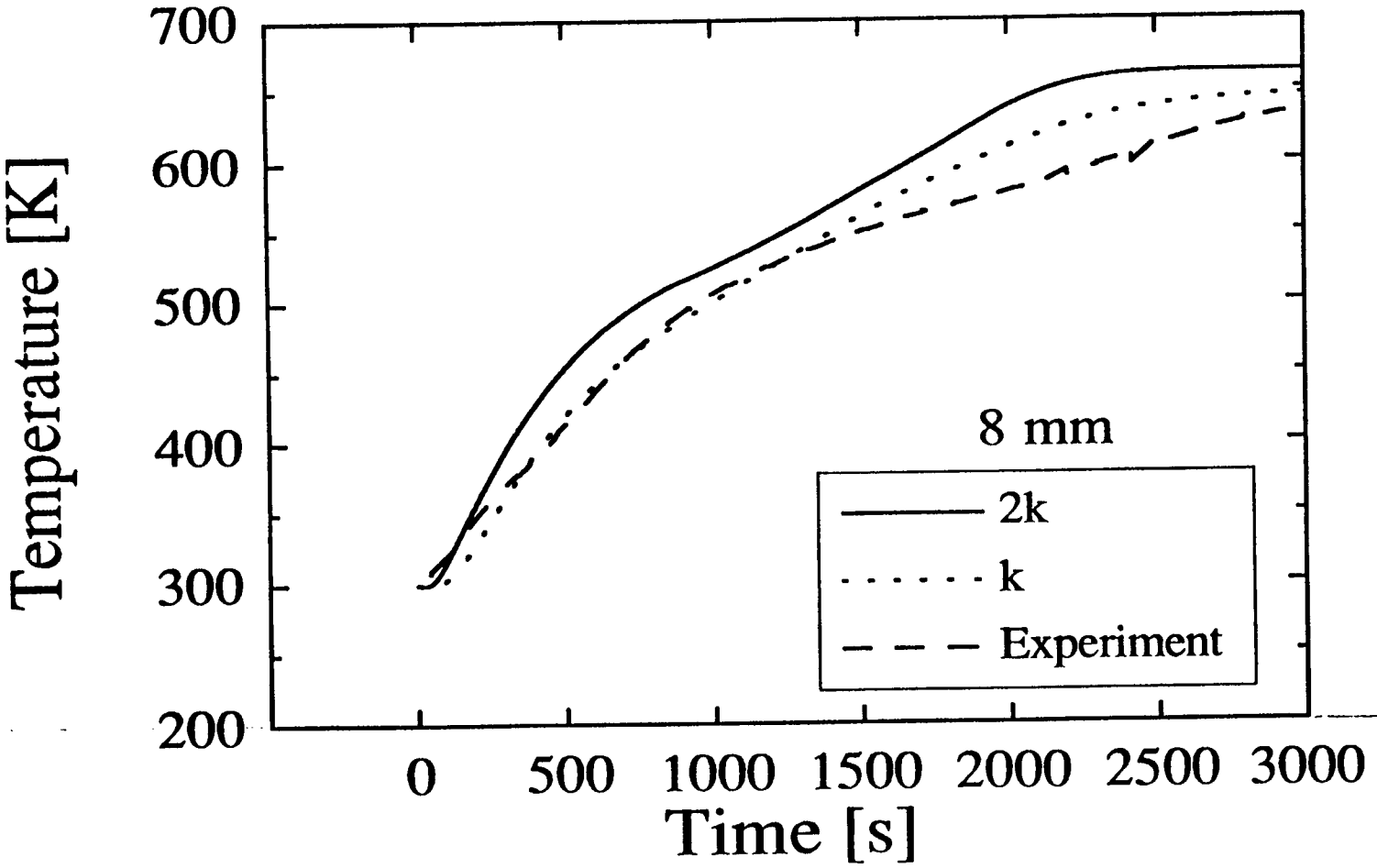

Figure 7.13e Sensitivity of temperature at 8 mm from the front surface prediction to thermal conductivities. Measured temperature is also shown

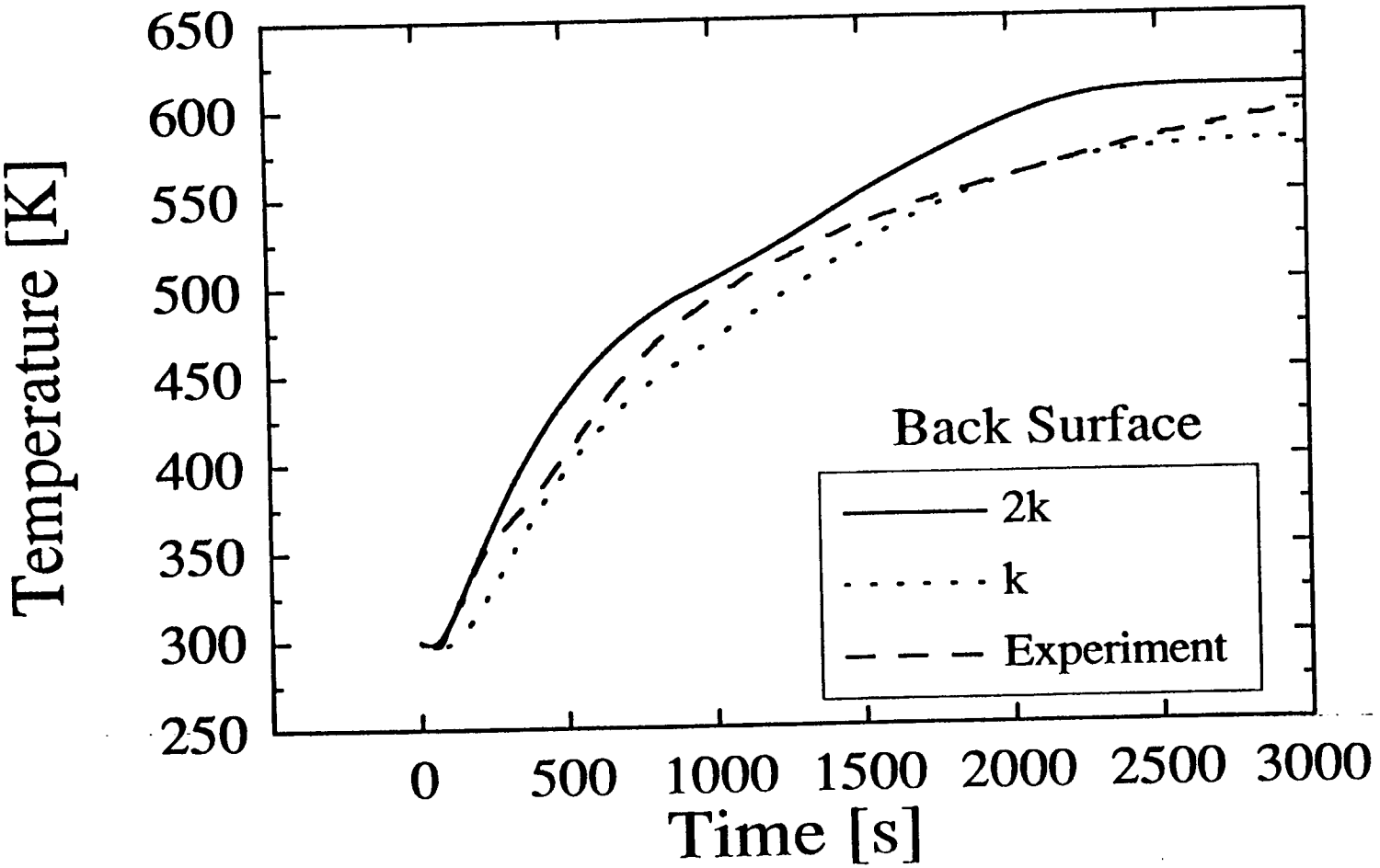

Figure 7.13f Sensitivity of back surface temperature prediction to thermal conductivities. Measured temperature is also shown

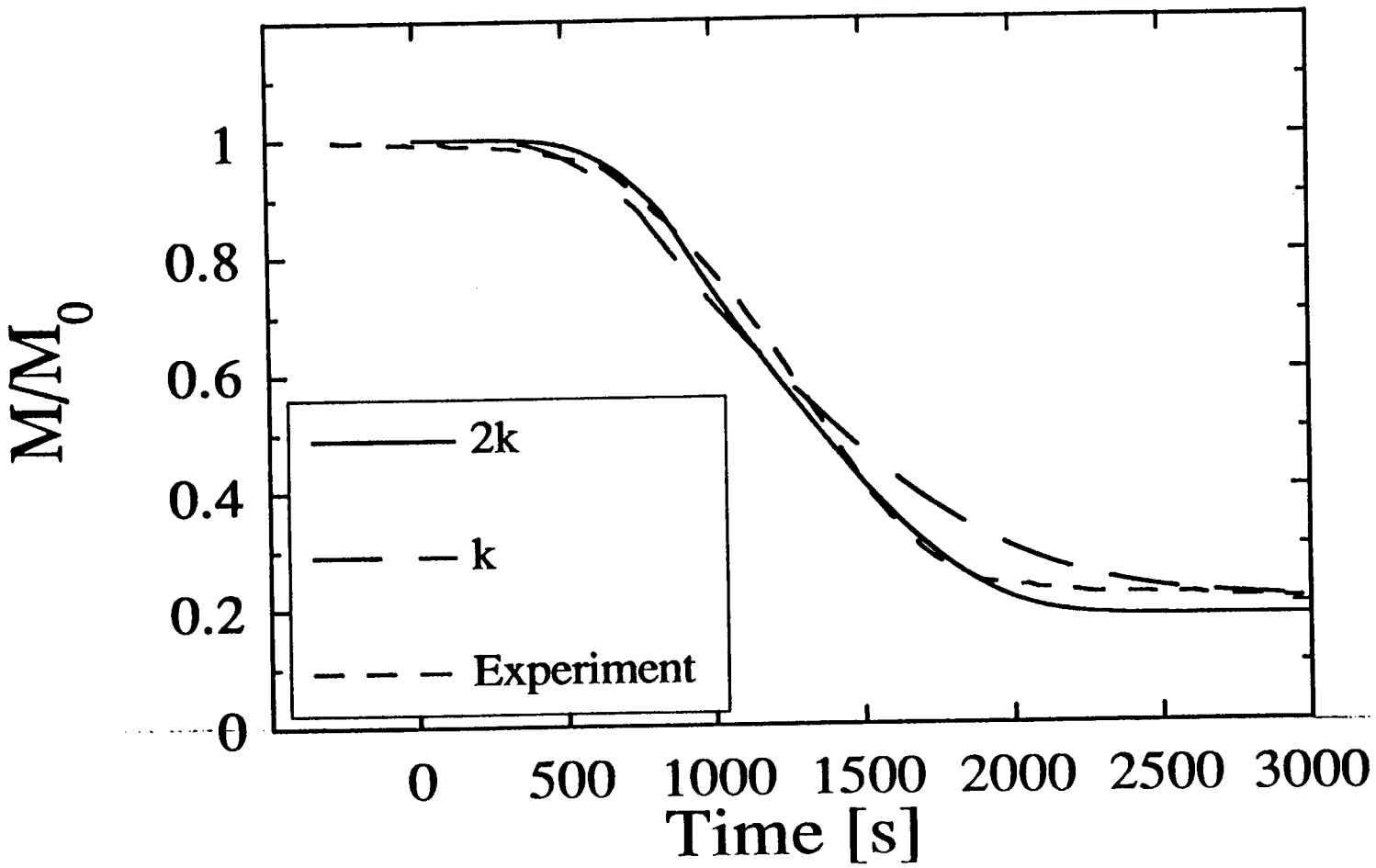

Figure 7.14 Sensitivity of fractional remaining mass prediction to thermal conductivities. Measured fractional remaining mass is also shown

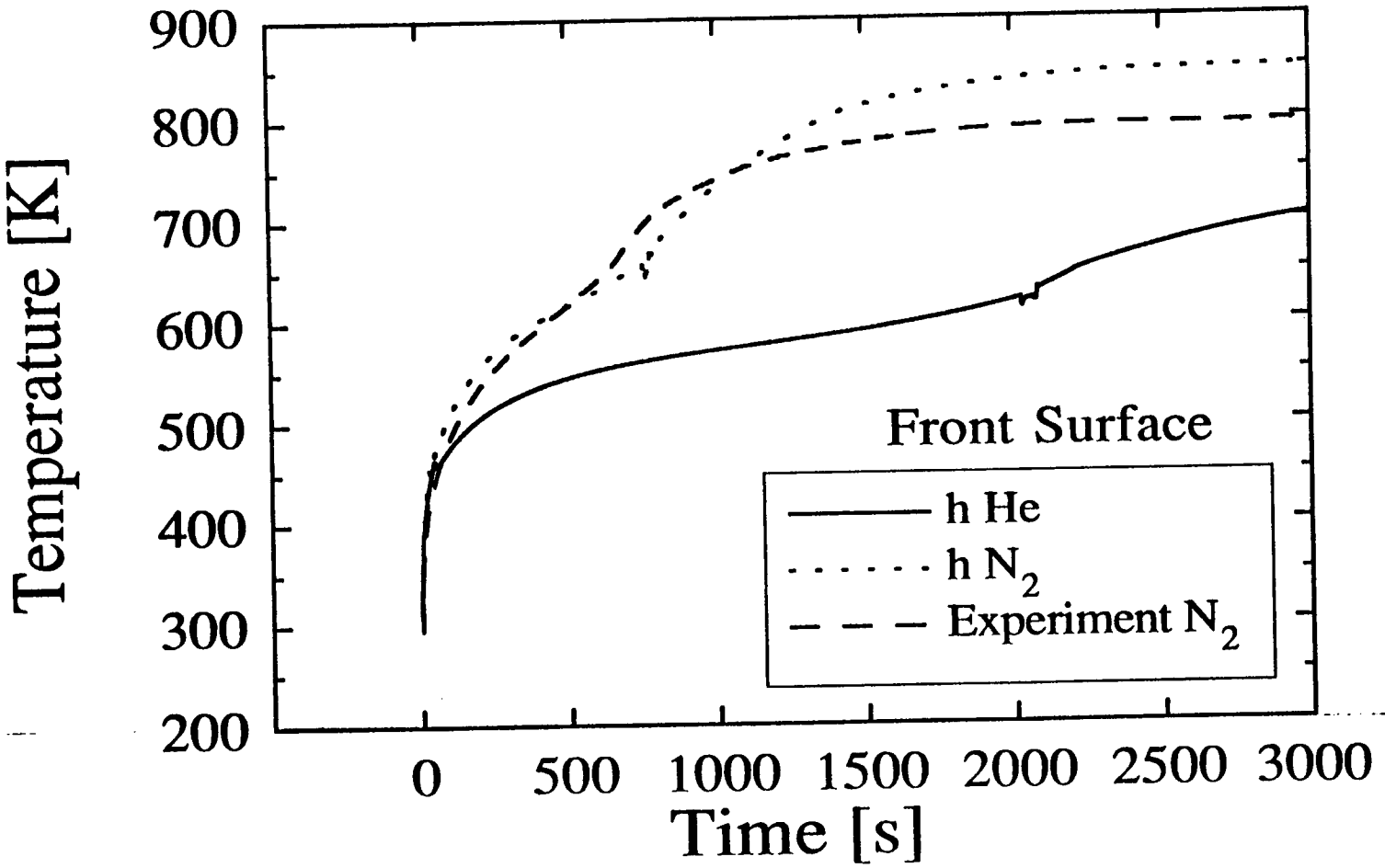

Figure 7.15a Sensitivity of front surface temperature prediction to heat transfer coefficient. Measured surface temperature is also shown

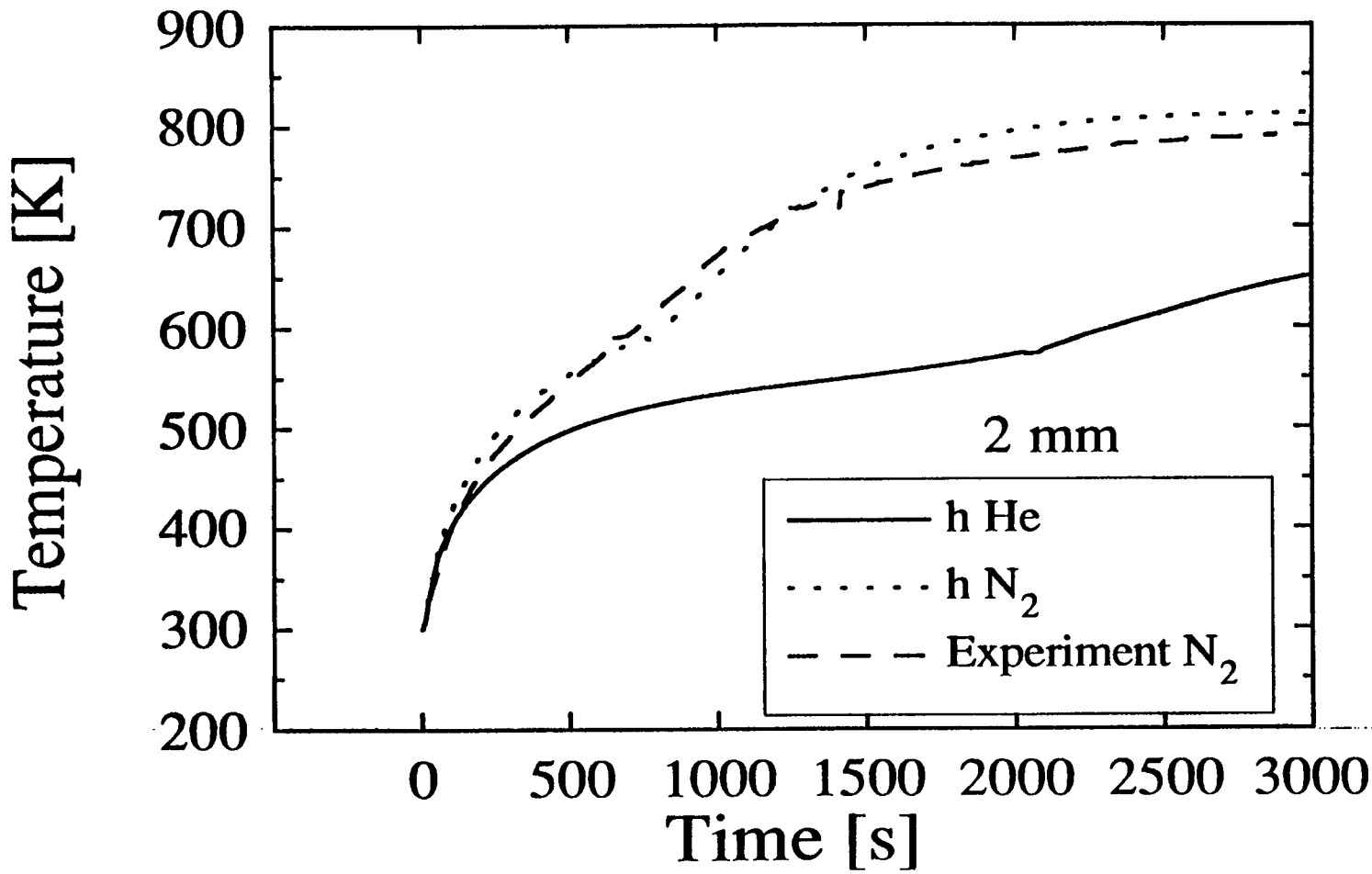

Figure 7.15b Sensitivity of temperature at 2 mm from the front surface prediction to heat transfer coefficient. Measured temperature is also shown

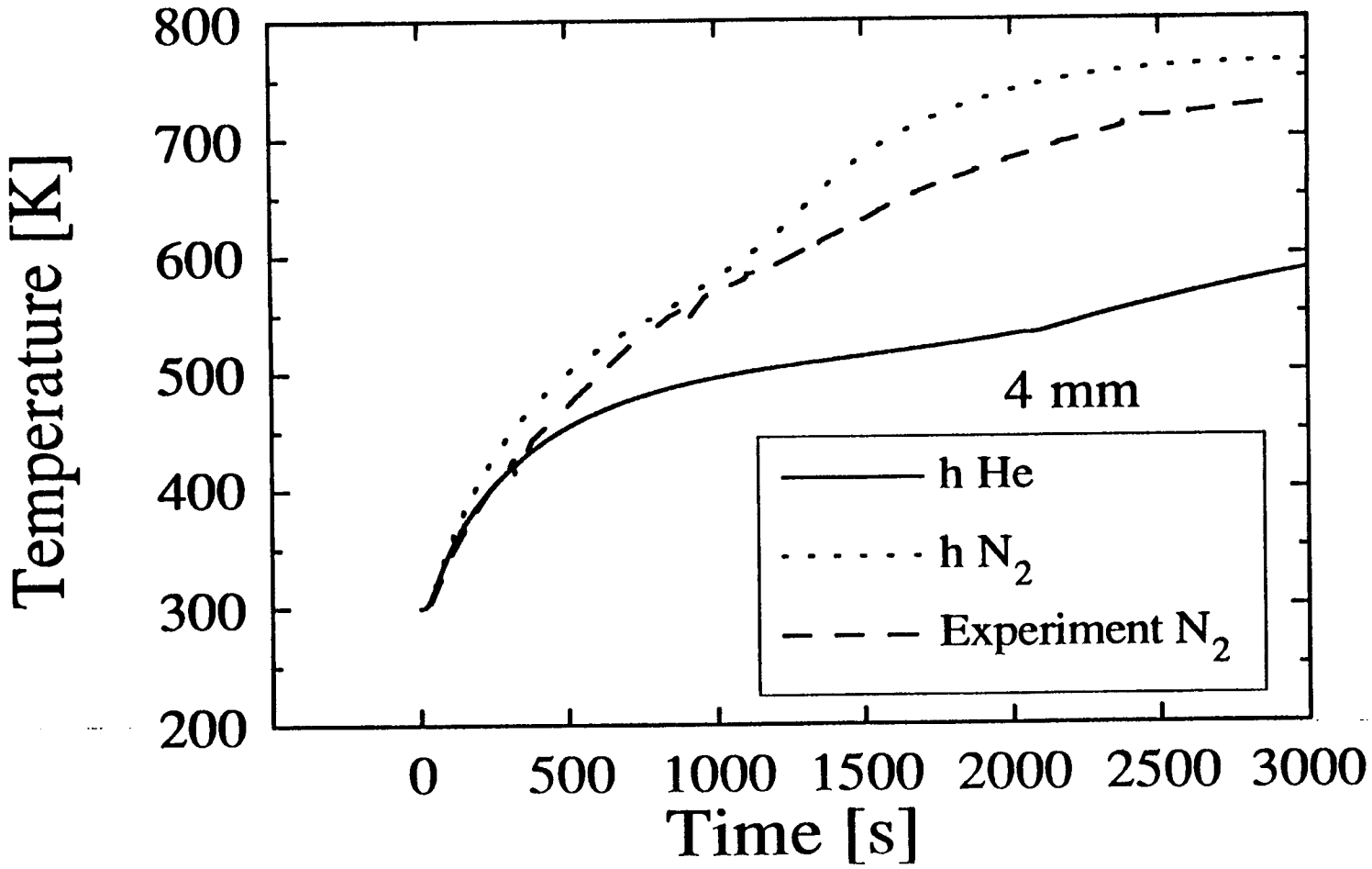

Figure 7.15c Sensitivity of temperature at 4 mm from the front surface prediction to heat transfer coefficient. Measured temperature is also shown

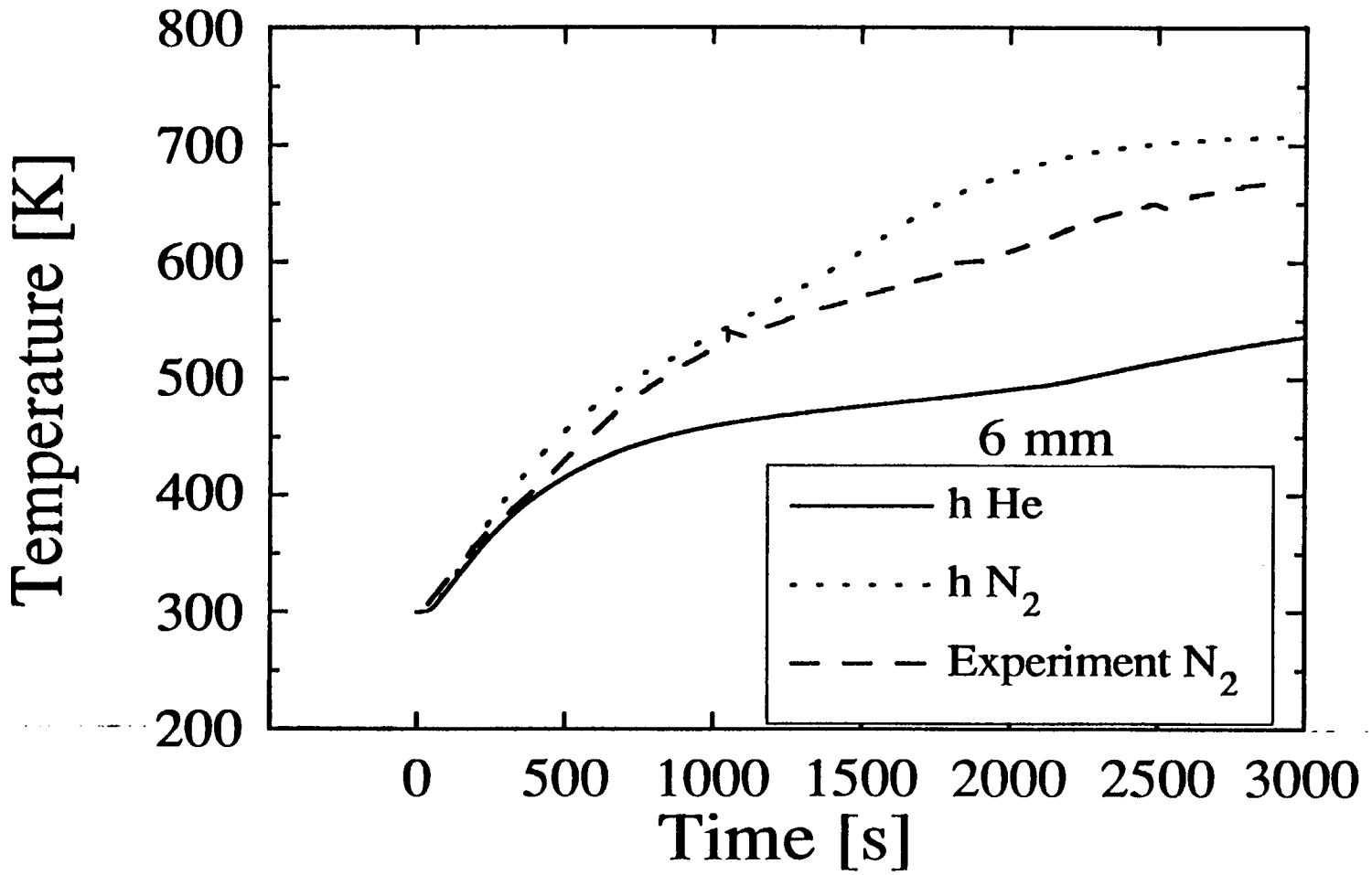

Figure 7.15d Sensitivity of temperature at 6 mm from the front surface prediction to heat transfer coefficient. Measured temperature is also shown

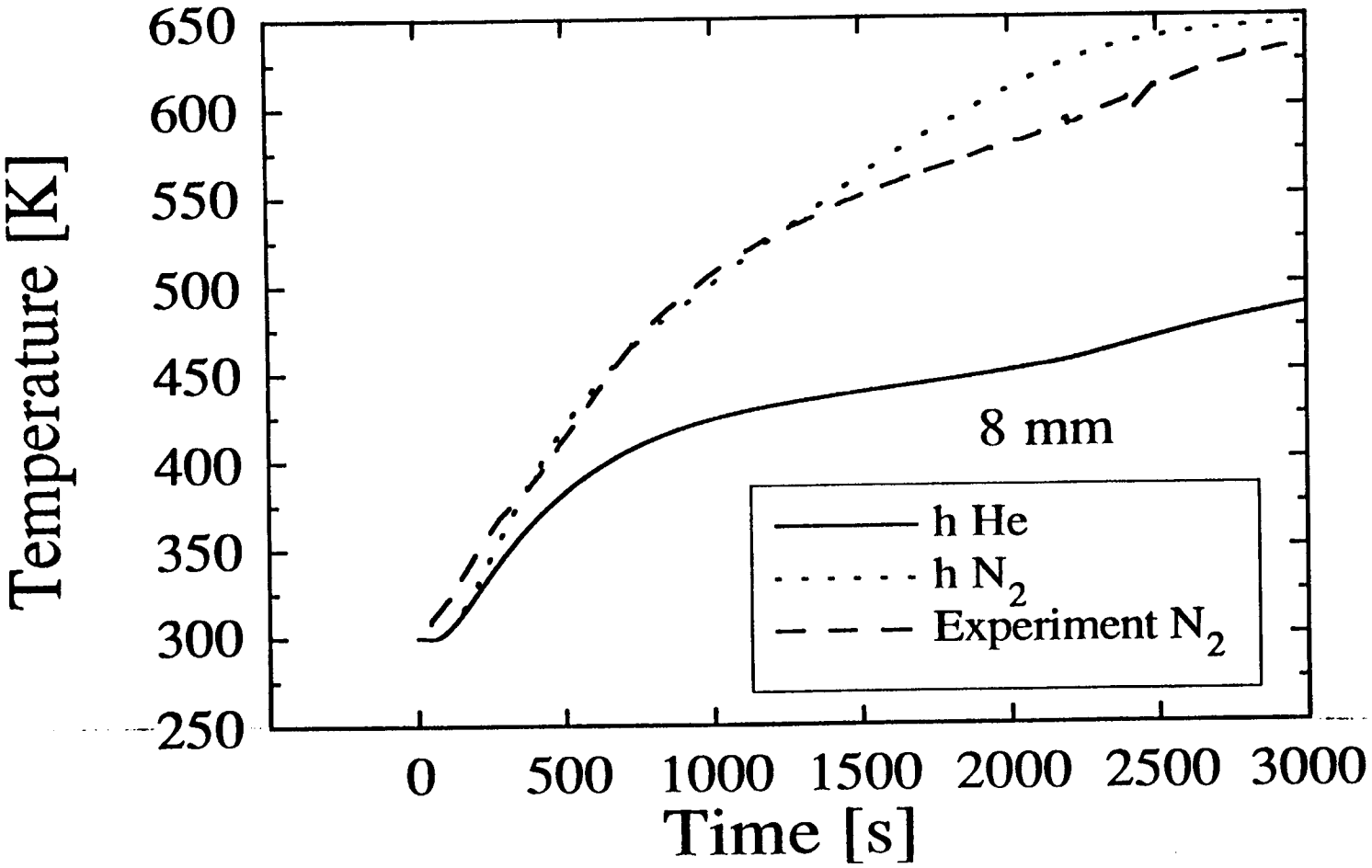

Figure 7.15e Sensitivity of temperature at 8 mm from the front surface prediction to heat transfer coefficient. Measured temperature is also shown

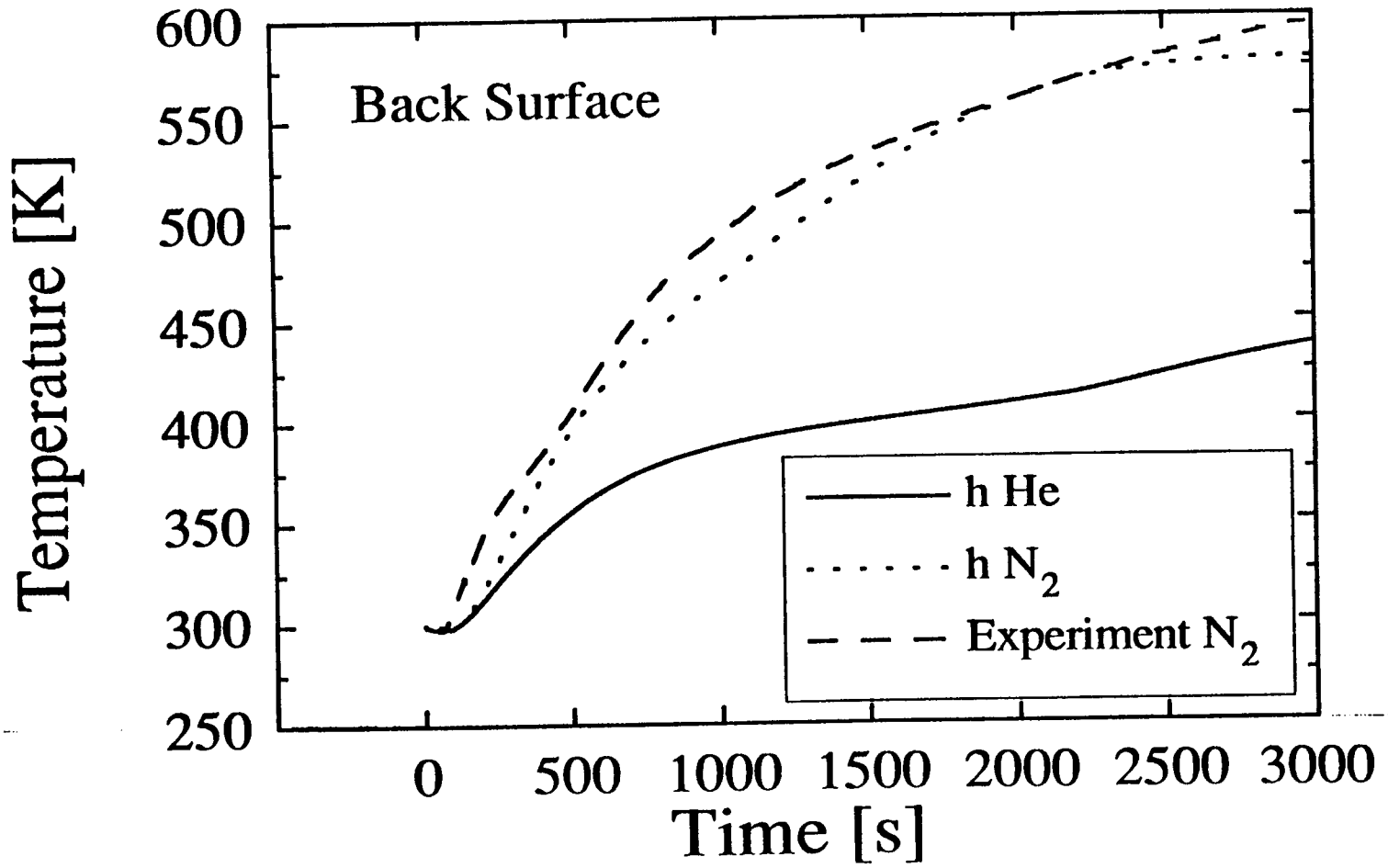

Figure 7.15f Sensitivity of back surface temperature prediction to heat transfer coefficient. Measured temperature is also shown

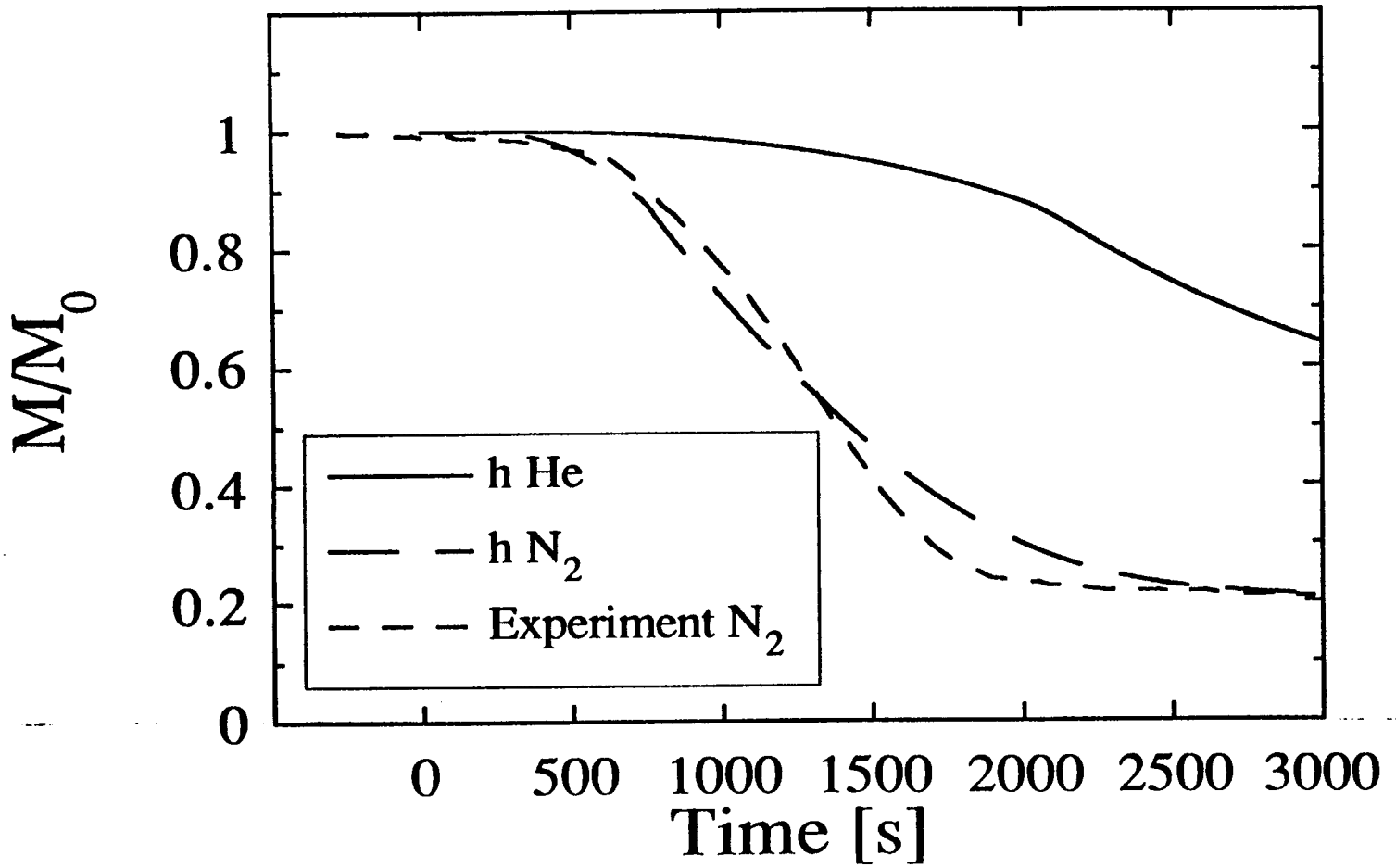

Figure 7.16 Sensitivity of fractional remaining mass prediction to heat transfer coefficient. Measured fractional remaining mass is also shown

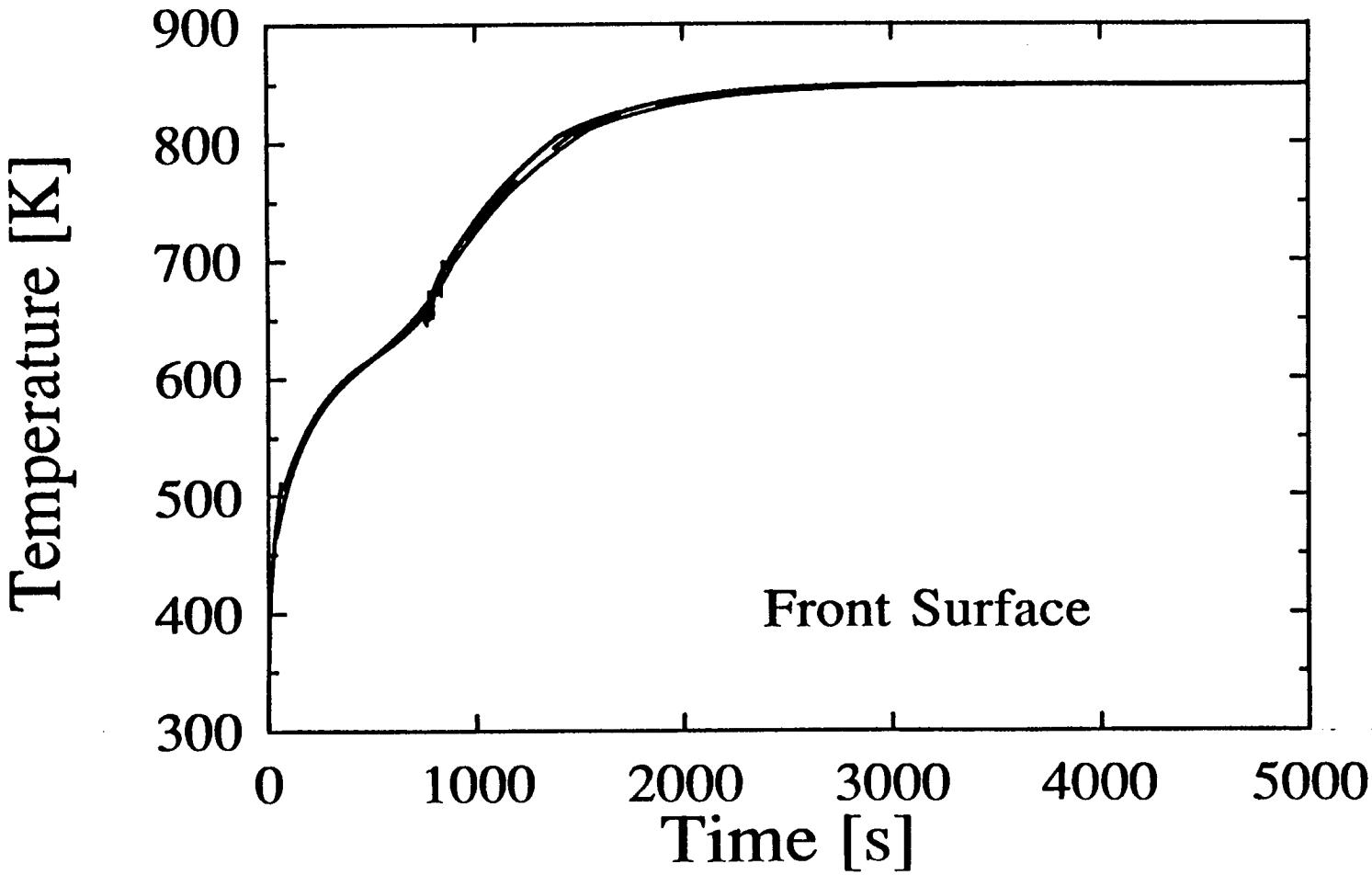

Figure 7.17 Sensitivity of front surface temperature prediction to different kinetic parameters

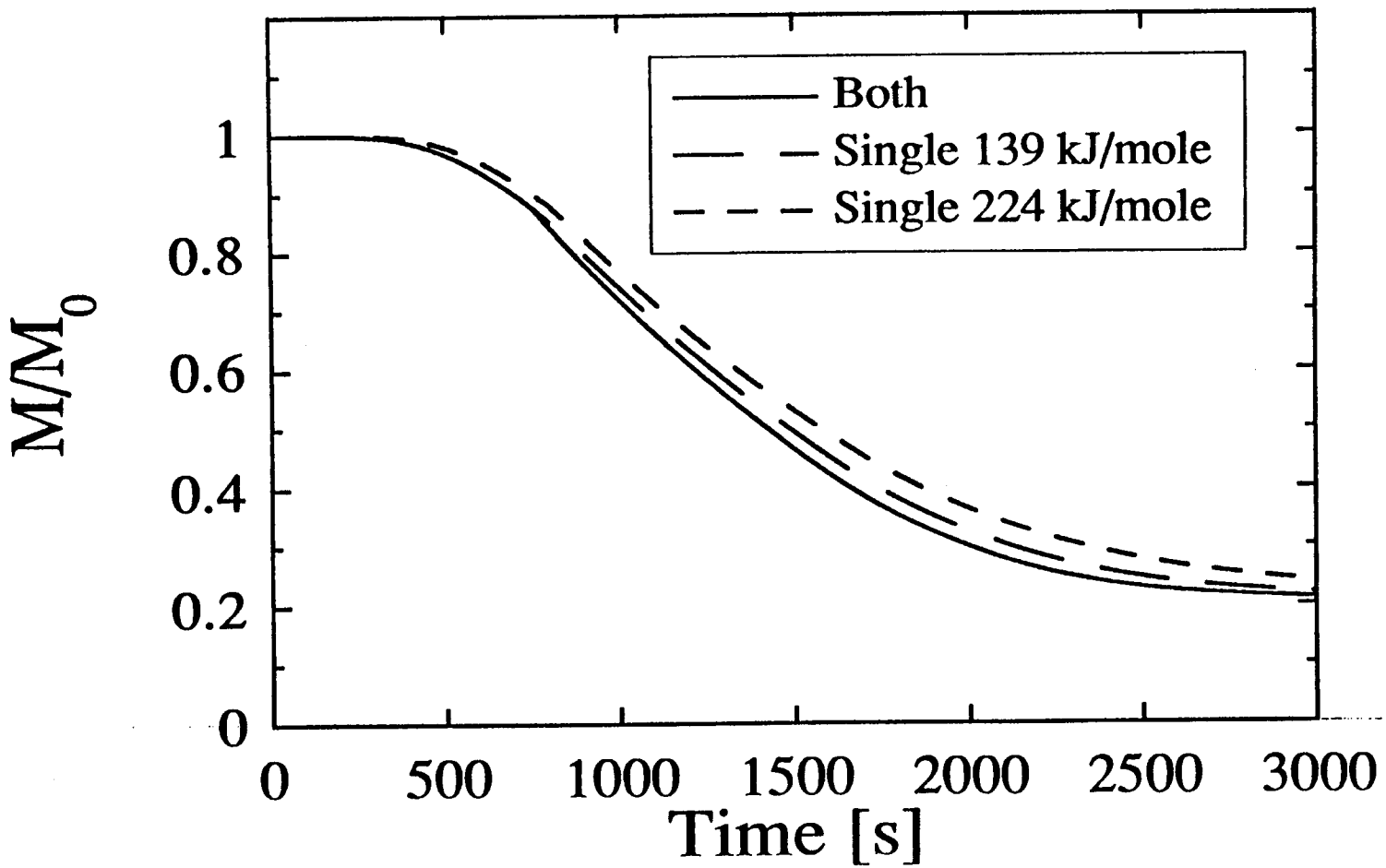

Figure 7.18 Sensitivity of fractional remaining mass prediction to different kinetic parameters

8. FINAL CONCLUSIONS

This project was undertaken in order to improve the state of understanding of bulk solids pyrolysis, as is of relevance in fire modeling. It has for some time been qualitatively understood how a pyrolyzing bulk solid burns-pyrolysis releases fuel vapor which in the act of burning above the solid surface, transfers heat back to the surface, pyrolyzing the solid further and releasing more fuel. Given this understanding of the process, it is not surprising that heat conduction limited pyrolysis models were long ago developed to describe the process. In these models, often little attention was paid to the details of solid decomposition kinetics, partly because the process had a heat transfer limited character, and partly because the details of the kinetics were so poorly understood and hotly debated.

Still, nagging doubts remained about the ability to truly predict the rate of delivery of fuel to the vapor phase. This was a key element of any fire model, since if the rate of delivery of fuel is kept low enough, the fire will be extinguished. From the perspective of accurate prediction of the severity of a fire event, few parameters could be considered more important than the pyrolysis rate. Existing models, though numerous, remained quite "soft" in terms of rigorous testing against data.

The objective here was to carefully examine the behavior of a char-forming material under simulated fire conditions, in order to test many aspects of our understanding. The selection of cellulose as a model material was obvious-not only is it important in its own right, but it is also a good model for wood, but far simpler in terms of the complexity of pyrolysis behavior.

Originally, the goal had been to focus mainly on the changes in composition of volatile

products with time, but it rapidly became apparent how many "holes" there were in basic understanding of many other phenomena. Thus the objective became to define the behavior of cellulose, as a model charring material under simulated fire conditions, in as complete manner as possible. The choice to do so was motivated by the realization that pressed cellulose could in the future serve as a model charring material under a far broader range of conditions than studied here, if only more were understood about its behavior.

Examples of deficiencies in earlier understanding quickly arose and were addressed. The usual assumption of a near unity emissivity of char, made throughout the literature, quickly fell when it was discovered that this can be very poor assumption at certain wavelengths. The smattering of handbook values for the thermal transport properties of cellulose also quickly became suspect. The importance of char shrinkage in accurately predicting mass loss rates also became apparent.

Nowhere more than in the actual kinetic modeling of pyrolysis did the deficiencies of earlier work stand out so clearly. While the problem of fuel release might be conduction controlled for a part of the pyrolysis process, it is inevitable that at some point, the kinetics becomes important. There was never any previous recognition of the fact that the char yields are a strong function of depth in the sample, not because of partial completion of pyrolysis, but because of the combined effect of heating rate and mass transfer limitations on pyrolysis pathways. Nor has it been recognized in fire models how strongly condition-dependent the pyrolysis endotherm can be. Finally, strides have been taken towards resolving a long controversy concerning the "true" kinetics of pyrolysis, by demonstrating that there are apparently two reaction regimes with distinct activation energies, both relevant to fire conditions. Again, this has not ever been really included in previous fire models.

This project is by no means a stopping point for work on this topic. It has pointed out many avenues in need of further examination. The hope is that with this study as background, future workers can explore these avenues with greater confidence, knowing their significance to the overall problem.

9. REFERENCES

1. Agrawal, R. K. and McCluskey, R. J. Fuel, **64**, 1502, 1985
2. Agrawal, R. K., Gandhi, F. and McCluskey, R. J. Journal of Analytical and Applied Pyrolysis, **6**, 325, 1984
3. Aho, M. J., Tummavuori, J. L., Hämäläinen, J. P. and Saastamoinen, J. J. Fuel, **68**, 1107, 1989
4. Antal, M. J. Fuel, **64**, 1483, 1985
5. Antal, M. J., Mok, W. S. L., Varhegyi, G., Szekely, T., Energy and Fuels, **4**, No. 3, 221, 1990
6. Antal. M. J. Div. of Petroleum Chemistry, Inc., ACS, Vol. 24, No. 2, p. 445, 1979
7. Anthony, D. B., Howard, J. B., Hottel, H. C. and Meissner, H. P. Fifteenth (Int) Symposium on Combustion, pp. 1303-1317, 1974
8. Arseneau, D. F. Canadian Journal of Chemistry, **49**, 632, 1971
9. Atreya, A. and Wichman, I. S. J. Heat Transfer, **111**, 719, 1989
10. Bacon, R. and Tang, M. M. Carbon, **2**, 221, 1964
11. Bacon, R. In Chemistry and Physics of Carbon (edited by P. L. Walker, Jr. and P. A. Thrower), Vol. 9, p.1, Marcel Dekker, Ney York, 1973
12. Basch, A. and Lewin, M. Journal of Polymer Science, **11**, 3071, 1973
13. Basch, A. and Lewin, M. Journal of Polymer Science, **11**, 3095, 1973
14. Becker, H. A. and Phillips, A. M. Combustion and Flame, **58**, 255, 1984
15. Becker, H. A. and Phillips, A. M. Combustion and Flame, **58**, 273, 1984
16. Becker, H. A., Phillips, A. M. and Keller, J. Combustion and Flame, **58**, 163, 1984
17. Bennini, S., Castillo, S. and Traverse, J. P. J Anal App Pyrolysis, **21**, 305, 1991
18. Benson, D. F. and Greenberg, J. P. Arch. Neurol., **20**, 82, 1969
19. Berkowitz-Matuck, J. B. and Noguchi, T. J. of Applied Polymer Science, **7**, 709, 1963

20. Bird, R. B., Stewart, W. E. and Lightfoot, E. N. Transport Phenomena, Wiley, New York, 1963
21. Blackadder, W. and Rensfelt, E. in Fundamentals of Thermochemical Biomass Conversion (Edited by R. P. Overend, T. A. Milne and L. K. Mudge), p. 747, Elsevier, 1985
22. Blackshear, P. L. Jr. and Kanury, A. M. Tenth (Int) Symposium on Combustion, p. 911, 1965
23. Bliek, A., van Poelje, W. M., van Swaaij, W. P. M and van Beckum, F. P. H. AIChE Journal, **31**, 10, 1666, 1985
24. Boroson, M. L., Howard, J. B., Longwell, J. P. and Peters, W. A. AIChE Journal, **35**, 1, 120, 1989
25. Boroson, M. L., Howard, J. B., Longwell, J. P. and Peters, W. A. Energy and Fuels, **3**, 735, 1989
26. Bradbury, A. G. W., Sakai, Y. and Shafizadeh, F. Journal of Applied Polymer Science, **23**, 3271, 1979
27. Broido, A. and Weinstein, M. Comb. Sci. Tech. **1**, 279, 1970
28. Broido, A. and Weinstein, M. Thermal Analysis, Volume 3, (H. C. Wiedemann, Ed.), p. 285, Birkhäuser Verlag, Basel, 1972
29. Broido, A. Pyrodynamics, **4**, 243, 1966
30. Browne, F. L. Theories of the Combustion of Wood and its Control, Rep. No. 2136, Forest Service, US Dep. of Agriculture, 1963
31. Brunner, P. H. and Roberts, P. V. Carbon, **18**, 217, 1980
32. Bunbury, H. M. The Destructive Distillation of Wood, Benn Brothers, 1923
33. Byrne, G. A., Gardiner, D. and Holmes, F. H. Journal of Applied Chemistry, **16**, 81, 1966
34. Carslaw, H. S. and Jaeger, J. C. Conduction of Heat in Solids, Clarendon Press, Oxford, 1959

35. Castillo, S., Bennini, S., Gas, G. and Traverse, J. P. Fuel, **68**, 174, 1989

36. Chan, W. R., Kelbon, M. and Krieger, B. B. in Fundamentals of Thermochemical Biomass Conversion (Edited by R. P. Overend, T. A. Milne and L. K. Mudge), p. 219, Elsevier, 1985

37. Chan, W. R., Kelbon, M. and Krieger-Brockett, B. Fuel, **64**, 1505, 1985

38. Chan, W. R., Kelbon, M. and Krieger-Brockett, B. Ind. Eng. Chem. Res., **27**, 2261, 1988

39. Chen, Y. PhD Thesis, Brown University, 1989

40. Chen, Y., Frendi, A., Tewari, S. S. and Sibulkin, M. Combustion and Flame, **84**, 121, 1991

41. Christner, L. G. and Walker, P. L. Jr. Carbon, **31**, 7, 1149, 1993

42. Cooley, S. and Antal, M. J. Jr. J. of An. App. Pyrolysis, **14**, 149, 1988

43. Corte, P., Hérault, V., Castillo, S. and Traverse, J. P. Fuel, **66**, 1107, 1987

44. Cullis, C. F. and Hirschler, M. M. The Combustion of Organic Polymers, Clarendon Press, Oxford, 1981

45. Cullis, C. F., Hirschler, M. M., Townsend, R. P. and Visanuvimol, V. Combustion and Flame, **49**, 235, 1983

46. Cullis, C. F., Hirschler, M. M., Townsend, R. P. and Visanuvimol, V. Combustion and Flame, **49**, 249, 1983

47. Curtis, L. J. and Miller, D. J. Ind. Eng. Chem. Res., **27**, 1775, 1988

48. Delichatsios, M. M. and Delichatsios, M. A. Combustion and Flame, **89**, 5, 1992

49. Di Blasi, C., Crescitelli, S., Russo, G. and Cinque, G. Combustion and Flame, **83**, 333, 1991

50. DiBlasi, C. Comb. Sci. Tech., **90**, 315, 1993

51. Donnot, A., Magne, P. and Deglise, X. J Anal App Pyrolysis, **21**, 265, 1991

52. Drysdale, D. An Introduction to Fire Dynamics, Wiley, 1985

53. Eckert, E. R. G. and Drake, R. M. Jr. Analysis of Heat and Mass Transfer, McGraw Hill, New York, 1972

54. Ernston, M. L. and Rasmuson, A. Fuel, **72**, 1515, 1993

55. Evans, R. J. and Milne, T. A. Energy and Fuels, **1**, No. 2, 123, 1987

56. Evans, R. J. and Milne, T. A. Energy and Fuels, **1**, No. 4, 311, 1987

57. Fraga, A., Gaines, A. F. and Kandiyoti, R. Fuel, **70**, 803, 1991

58. Freeman, E. S. and Carroll, B. J. Phys. Chem., **62**, 394, 1958

59. Friedman, R. First Int. Conf. Fire Sci. (C. E. Grant and P. J. Pagni, Eds), p. 349, Hemisphere 1986

60. Gandhi, P. D. and Kanury, A. M. Comb. Sci. Tech., **57**, 113, 1988

61. Glassman, I. Combustion, Academic Press, 1987

62. Glassner, S. and Pierce, A. R. III Analytical Chemistry, **37**, No. 4, 525, 1965

63. Golova, O. P., Krylova, R. G. and Nikolaeva, I. I. Visokomolekularnie Soedinenia, **1**, No. 9, 1295, 1959

64. Gullett, B. K. and Smith, P. Combustion and Flame, **67**, 143, 1987

65. Hajaligol, M. R. PhD Thesis, MIT, 1980

66. Hajaligol, M. R., Howard, J. B. and Peters, W. A. Combustion and Flame, **95**, 47, 1993

67. Hajaligol, M. R., Peters, W. A. and Howard, J. B. Preprints, ACS Div Fuel Chem. **32**(3), 8, 1987

68. Hajaligol, M., R., Howard, J. B., Longwell, J. P. and Peters, W. A. I&EC Process Design and Development, **21**, 457, 1982

69. Hallen, R. T., Sealock, L. J. Jr. and Cuello, R. in Fundamentals of Thermochemical Biomass Conversion (Edited by R. P. Overend, T. A. Milne and L. K. Mudge), p. 157, Elsevier, 1985

70. Hastaoglu, M. A. and Berutti, F. Fuel, **68**, 1408, 1989

71. Heuser, E. The Chemistry of Cellulose, John Wiley, 1944

72. Heuser, E., West, C. J. and Esselen, G. J. Jr. Textbook of Cellulose Chemistry, McGraw-Hill, 1924

73. Hillis, W. E. in Fundamentals of Thermochemical Biomass Conversion (Edited by R. P. Overend, T. A. Milne and L. K. Mudge), p. 1, Elsevier, 1985
74. Holman, J. P. Heat Transfer, McGraw Hill, New York, 1968
75. Holmes, F. H. and Shaw, C. J. G. Journal of Applied Chemistry, **11**, 210, 1961
76. Holst, L. E., Andersson, L. A. and Bjerle, I. Fuel, **70**, 1017, 1991
77. Holve, D. J. and Kanury, A. M. J. Heat Transfer, **104**, 344, 1982
78. Hshieh, F. Y. and Richards, G. N. Combustion and Flame, **80**, 395, 1989
79. Julien, S., Chornet, E., Tiwari, P. K. and Overend, R. P. Journal of Analytical and Applied Pyrolysis, 19, 81, 1991
80. Kansa, E. J., Perlee, H. E. and Chaiken, R. F. Combustion and Flame, **29**, 311, 1977
81. Kanury, A. M. and Blackshear, P. L. Jr. Comb. Sci. Tech., **1**, 339, 1970
82. Kanury, A. M. and Blackshear, P. L. Jr. Eleventh (Int) Symposium on Combustion, p. 517, 1966
83. Kanury, A. M. and Blackshear, P. L. Jr. Pyrodynamics, **4**, 285, 1966
84. Kanury, A. M. and Holve, D. J. J. Heat Transfer, **104**, 338, 1982
85. Kanury, A. M. Combustion and Flame, **18**, 75, 1972
86. Kanury, A. M. Journal of Fire and Flammability, **2**, 191, 1971
87. Kashiwagi, T. and Nambu, H. Combustion and Flame, **88**, 345, 1992
88. Kashiwagi, T. Comb. Sci. Tech., **8**, 225, 1974
89. Kashiwagi, T. Combustion and Flame, **34**, 231, 1979
90. Kashiwagi, T. Fire Safety Journal, **3**, 185, 1981
91. Kashiwagi, T., Ohlemiller, T. J. and Werner, K. Combustion and Flame, **69**, 331, 1987
92. Kelly, T. A. MSc Thesis, Brown University, 1986
93. Kemp, D. S. and Vellaccio, F. Organic Chemistry, Worth Publishers, New York, 1980
94. Kestin, J., Knierim, K., Mason, E. A., Najafi, B., Ro, S. T. and Waldman, M. J.

Phys. Chem. Ref. Data, **13**, 1, 229, 1984

95. Kilzer, F. J. and Broido, A. Pyrodynamics, **2**, 151, 1965
96. Kindelan, M. and Williams, F. A. Comb. Sci. Tech., **16**, 47, 1977
97. Kissinger, H. E. Analytical Chemistry, **29**, 11, 1702, 1957
98. Kojima, E., Miao, Y. and Yoshizaki, S. Journal of Chemical Engineering of Japan, **24**, 1, 8, 1991
99. Kothari, V. and Antal, M. J. Fuel, **64**, 1487, 1985
100. Kung, H. and Kalelkar, A. S. Combustion and Flame, **20**, 91, 1973
101. Kung, H. Combustion and Flame, **18**, 185, 1972
102. Kung, H. Fifteenth (Int) Symposium on Combustion, p. 243, 1975
103. Lai, W. and Krieger-Brockett, B. Comb. Sci. Tech, **85**, 133, 1992
104. Lede, J., Panagopoulos, J., Li, H. Z and Villermaux, J. Fuel, **64**, 1514, 1985
105. Lee, C. K. and Diehl, J. R. Combustion and Flame, **42**, 123, 1981
106. Lee, C. K., Chaiken, R. F. and Singer, J. M. Sixteenth (Int) Symposium on Combustion, P. 1459, 1976
107. Lentini, J. J., Smith, D. M. and Henderson, R. W. Fire Technology, August 1992, 195
108. Lewellen, P. C., Peters, W. A. and Howard, J. B. Sixteenth (Int) Symposium on Combustion, p. 1471, 1977
109. Lipowicz, P. J. and Rothenberg, S. J. Combustion and Flame, **75**, 217, 1989
110. Lipska, A. E. and Parker, W. J. Journal of Applied Polymer Science, **10**, 1439, 1966
111. Lipska, A. E. and Wodley, F. A. J. of Applied Polymer Science, **13**, 851, 1969
112. Lipska-Quinn, A. E., Zeronian, S. H. and McGee, K. M. in Fundamentals of Thermochemical Biomass Conversion (Edited by R. P. Overend, T. A. Milne and L. K. Mudge), p. 453, Elsevier, 1985
113. Lyons, J. W. Fire, Scientific American Library, New York, 1985

114. Madorsky, S. L. Thermal Degradation of Organic Polymers, Interscience Publishers, 1964

115. Martin, S. B. and Ramstad, R. W. Analytical Chemistry, **33**, No. 8, 982, 1961

116. Martin, S. Tenth (Int) Symposium on Combustion, pp. 877-896, 1965

117. McCarter, R. J. Text. Res. J., **42**, 709, 1972

118. Miller, C. A. and Ramohalli, K. N. R. Comb. Sci. Tech., **46**, 249, 1986

119. Milne, T. A. and Soltys, M. N. in Fundamentals of Thermochemical Biomass Conversion (Edited by R. P. Overend, T. A. Milne and L. K. Mudge), p. 361, Elsevier, 1985

120. Milosavljevic, I. and Suuberg, E. M., ACS Div. Fuel Chem. Prepr., **37** (4), 1567, 1992

121. Mok, W. S. and Antal, M. J. Ind. Eng. Chem. Res., **31**, 1157, 1992

122. Mok, W. S. L. and Antal, M. J. Thermochimica Acta, **68**, 165, 1983

123. Mok, W. S., Antal, M. J. and Varhegyi, G. Ind. Eng. Chem. Res., **31**, 92, 1992

124. Mok, W. S., Antal, M. J., Szabo P., Varhegyi, G. and Zelei, B Ind. Eng. Chem. Res., **31**, 1162, 1992

125. Newsweek Magazine, November 8, 1993

126. Nunn, T. R., Howard, J. B., Longwell, J. P. and Peters, W. A. in Fundamentals of Thermochemical Biomass Conversion (Edited by R. P. Overend, T. A. Milne and L. K. Mudge), p. 293, Elsevier, 1985

127. Ohlemiller, T. J. Comb. Sci. Tech., **26**, 89, 1981

128. Ohlemiller, T. J., Kashiwagi, T and Werner, K. Products of Wood Gasification, NBSIR 85-3127, 1985

129. Ohlemiller, T. J., Kashiwagi, T. and Werner, K. Combustion and Flame, **69**, 155, 1987

130. Oren, M. J., Karunakaran, K. P., Pegg, M. J. and MacKay, G. D. M. Fuel, **66**, 9, 1987

131. Pakdel, H. and Roy, C. Energy and Fuels, **5**, 427, 1991

132. Palmer, R. C. and Cloukey, H. J. Ind. Eng. Chem., **10**, No. 4, 262, 1918

133. Palmer, R. C. J. Ind. Eng. Chem., **10**, No. 4, 264, 1918

134. Palmer, R. C. J. Ind. Eng. Chem., **6**, No. 11, 890, 1914

135. Panton, R. L. and Rittmann, J. G. Thirteenth (Int) Symposium on Combustion, p. 881, 1971

136. Parker, W. J. DSc Thesis, George Washington University, 1988

137. Perry, R.H. and Green, D. Perry's Chemical Engineers' Handbook, McGraw Hill, 1984

138. Phillips, A. M. and Becker, H. A. Combustion and Flame, **46**, 221, 1982

139. Phillips, J., Brown, D. J. and Rothwell, E. Thermal Analysis, Volume 3, (H. C. Wiedemann, Ed.), p. 297, Birkhäuser Verlag, Basel, 1972

140. Pictet, A. and Sarasin, J. Helv. Chim. Acta, **1**, 87, 1918

141. Plunguian, M Cellulose Chemistry, Chemical Publishing, 1943

142. Radlein, D., Piskorz, J. and Scott, D. S. Journal of Analytical and Applied Pyrolysis, **19**, 41, 1991

143. Reid, R. C., Prausnitz, J. M. and Poling, B. E. The Properties of Gases and Liquids, McGraw Hill, 1987

144. Roberts, A. F. Combustion and Flame, **14**, 261, 1970

145. Roberts, A. F. Thirteenth (Int) Symposium on Combustion, p. 893, 1971

146. Rogers, E. and Ohlemiller, T. J. Combustion Science and Technology, **24**, 129, 1980

147. Rosen, S. L. Fundamental Principles of Polymeric Materials, Wiley, 1982

148. Roy, C., de Caumia, B., Brouillard, D. and Menard, H. in Fundamentals of Thermochemical Biomass Conversion (Edited by R. P. Overend, T. A. Milne and L. K. Mudge), p. 237, Elsevier, 1985

149. Samolada, M. C. and Vasalos, I. A. Fuel, **70**, 883, 1991

150. Schorger, A. W. The Chemistry of Cellulose and Wood, Mcgraw-Hill, 1926

151. Schwenker, R. F. Jr. and Beck, L. R. Jr. Journal of Polymer Science C, No. 2, 331, 1963

152. Schwenker, R. F. Jr. and Pacsu, E. Ind. Eng. Chem., Chem. and Eng. Data Series, **2**, No. 1, 83, 1957

153. Scott, D. S., Piskorz, J., Bergougnou, M. A., Graham, R. and Overend, R. P. Ind. Eng. Chem. Res., **27**, 8, 1988

154. Seeker, W. M. R. Twenty-Third (Int) Symposium on Combustion, pp. 867-885, 1990

155. Serio, M. A., Pines, D. S., Bonanno, A. S. and Solomon, P. R. Submitted for Twenty Fifth (Int) Symposium on Combustion, August 1994

156. Shafizadeh, F. Advances in Carbohydrate Chemistry, **23**, 419, 1968

157. Shafizadeh, F. and Bradbury, A. G. W. Journal of Applied Polymer Science, **23**, 1431, 1979

158. Shafizadeh, F. and Fu, Y. L. Carbohydrate Research, **29**, 113, 1973

159. Shafizadeh, F. and Sekiguchi, Y. Combustion and Flame, **55**, 171, 1984

160. Shafizadeh, F. Chapter 13 in The Chemistry of Solid Wood, R. Rowell, editor, Advances in Chemistry Series, 207, ACS, Washington, 1984

161. Shafizadeh, F. in Fundamentals of Thermochemical Biomass Conversion (Edited by R. P. Overend, T. A. Milne and L. K. Mudge), p. 183, Elsevier, 1985

162. Shafizadeh, F., Furneaux, R. H., Cochran, T. G., Scholl, J. P. and Sakai, Y. Journal of Applied Polymer Science, **23**, 3525, 1979

163. Shah, N., Girard, P., Mezerette, C. and Vergnet, A. M. Fuel, **71**, 955, 1992

164. Shreve, R. N. The Chemical Process Industries, McGraw-Hill, 1945

165. Sibulkin, M. First Int. Conf. Fire Sci. (C. E. Grant and P. J. Pagni, Eds), p. 391, Hemisphere 1986

166. Simmons, G. M. and Lee, W. H. in Fundamentals of Thermochemical Biomass Conversion (Edited by R. P. Overend, T. A. Milne and L. K. Mudge), p. 385,

Elsevier, 1985

167. Smith, F. G. III, Pendarvis, R. W. and Rice, R. W. Combustion and Flame 88, 61, 1992

168. Sparr, S. A., Jay, M., Drislane, F. W. and Venna, N. Brain, **114**, 789, 1991

169. Stamm, A. J. Wood and Cellulose Science, Ronald Press, 1964

170. Sundaram, M. S., Steinberg, M. and Fallon, P. T. in Fundamentals of Thermochemical Biomass Conversion (Edited by R. P. Overend, T. A. Milne and L. K. Mudge), p. 167, Elsevier, 1985

171. Suuberg, E. M. and Dalal, V. F., Proc. Eastern States Section, Combustion Institute, 65-1 to 65-4, November, 1987

172. Suuberg, E. M. Comb Flame, **50**, 243, 1983

173. Suuberg, E. M. Energy and Fuels, **2**, No. 4, 593, 1988

174. Suuberg, E. M. Preprints, ACS Div Fuel Chem. **32**(3), 51, 1987

175. Tabatabaie-Raissi, A., Mok, W. S. L. and Antal, M. J. Ind. Eng. Chem. Res. **28**, 856, 1989

176. Tang, M. M. and Bacon, R. Carbon, **2**, 211, 1964

177. Tang, W. K. and Neill, W. K. J. Poly. Sci., C, **6**, 65, 1964

178. Technical Report FMRC Serial No. 21011.7 (A. T. Modak, editor), 1976

179. Teng, H. PhD Thesis, Brown University, 1992

180. Tewarson, A. and Khan, M. M. Twenty Second (Int) Symposium on Combustion, p.1231, 1988

181. Theander, O. in Fundamentals of Thermochemical Biomass Conversion (Edited by R. P. Overend, T. A. Milne and L. K. Mudge), p. 35, Elsevier, 1985

182. Time Magazine, November 4, 1991

183. Tinney, E. R. Tenth (Int) Symposium on Combustion, p. 925, 1965

184. Tsoumis, G. Science and Technology of Wood, Van Nostrand Reinhold, New York, 1991

185. Tsuchiya, Y. and Sumi, K. J. of Applied Polymer Science, **14**, 2003, 1970

186. Tzeng, L. S., Atreya, A. and Wichman, I. S. Combustion and Flame, **80**, 94, 1990

187. Varhegyi, G., Antal, M. J., Szekely, T. and Szabo, P. Energy and Fuels, **3**, 329, 1989

188. Varhegyi, G., Antal, M. J., Szekely, T., Till, F. and Jakab, E. Energy and Fuels, **2**, 267, 1988

189. Varhegyi, G., Antal, M. J., Szekely, T., Till, F., Jakab, E. and Szabo, P. Energy and Fuels, **2**, 273, 1988

190. Ward, S. M. and Braslaw, J. Combustion and Flame, **61**, 261, 1985

191. Weatherford, W. D. Jr. and Sheppard, D. M. Tenth (Int) Symposium on Combustion, pp. 897-910, 1965

192. Weinstein, M. and Broido, A. Comb. Sci. Tech. **1**, 287, 1970

193. White, R. H. and Nordheim, E. V. Fire Technology, Febryary 1992, 5

194. Wichman, I. S. and Atreya. A. Combustion and Flame, **68**, 231, 1987

195. Wise, L. E. and Jahn, E. C. Wood Chemistry, Reinhold Publishing Corporation, 1952

196. Wojtowicz, M. PhD Thesis, Brown University, 1988

197. Zayed, R. S., Oren, M. J., and MacKay, G. D. M. Fuel, **66**, 1166, 1987

198. Zeligman, M. M. Analytical Chemistry, **37**, No. 4, 524, 1965

APPENDIX A: EQUIPMENT

A 1: SIMULATED FIRE APPARATUS

Experimental Chamber Dimensions: 300x400x600 mm

Balance: Mettler PC 220, Top Load Balance

Range 200 g with readability 0.01 g (used)

Range 20 g with readability 0.001 g

Infrared Lamps: Model 5305-5A, Research, Inc. (water cooled; with tungsten filament in quartz envelope; filament emitter reaches 90% of its full operating temperature within 3 seconds)

Optical Pyrometer: Thermalert SL-300C (range 450-1000°C; spectral response 2.1-2.3 μm)

Temperature Indicator: Omega DP80 Digital Indicator (linear output 0-10 V for temperature range from 0-1000°C; maximum error 0.3°C)

Thermocouples: Omega Type K - Chromel Alumel (0.5 mm stainless steel probes; grounded junction; error 2.2°C or 0.75%, whichever is greater)

Gas Chromatograph: Carle Analytical GC Model 111 (columns, all 1/4 inch: 6 feet 80/100 mesh Porapak Q; 5 feet 80/100 mesh Molecular Sieve 5A; reference: 6 feet 8% OV-101 on 80/100 mesh Chromosorb W AW DMCS; oven temperature 50°C isothermal; carrier gas flowrate 27 ml/min)

Sample Pressing: Laboratory Press, Fred S. Carver, Model C

Data Acquisition: Macintosh, 512 K, microcomputer

MacADIOS AD/DA converter, Model 411 GW Instruments

A 2: TEMPERATURE CONTROLLED ENVIRONMENT

TGA: Du Pont Model 951

DSC: Du Pont Model 2910

A 3: OTHER EQUIPMENT USED

- Nicolet 60SX FTIR Spectrometer (for surface reflectivity measurement and char characterization)
- Quantasorb Sorption System (for char total surface area measurements)
- Knauer Vapor Pressure Osmometer (for tar molecular weight measurements)
- Tube Furnace Lindberg, 35 mm ID tube (for char preparation for properties measurement)
- Thermolyne Type 2200 Hot Plate (for thermal diffusivity measurements)

APPENDIX B: COMPUTER PROGRAMMES

B1: COMPUTER PROGRAM FOR DATA ACQUISITION FROM SIMULATED FIRE APPARATUS

The program listed here was made by William Lilly in BASIC programming language for data acquisition from the simulated fire apparatus by Macintosh microcomputer, via MacADIOS AD/DA converter and with frequency of data collection of 1 Hz. It simultaneously records 4 channels. First channel was the balance output, the second one was the output from a digital thermometer, the third channel was the optical pyrometer output and the fourth was an auxiliary channel.

Listing of the program:

```
 REM  Polymer Pyrolysis Application Program - 1Hz
 REM by William D. Lilly, August, 1990
 LIBRARY "MacADIOS Calls":CALL mainit:CALL msinit(9,249,99,1)
 GOTO urt
idle:
 GOTO idle
collect:
 IF i%(nf)>1080*tmerg THEN GOTO astop
 IF MENU(1)=3 THEN GOTO astop
 a%=i%(nf):GOSUB read.it:GOSUB plot.a
 s%=s%+1:IF s%>4 THEN s%=1
 i%(nf)=i%(nf)+1:GOTO collect
read.it:
 CALL
ainx(1,0,1,VARPTR(er%),VARPTR(f%(nf,1,a%)),VARPTR(f%(nf,2,a%)),VARPTR(f%(nf,3,a%
)),VARPTR(f%(nf,4,a%)),0,0,0,0):RETURN
plot.a:
   x=(a%-xos)*xscl:y=120-(yos(s%)+f%(nf,s%,a%))*yscl(s%):PSET(x,y):RETURN
```

```
get.coord:
 vl=3
 WHILE MOUSE(0)<>2
 pt%=INT(xos+MOUSE(1)/xscl): v$=STR$(pt%/10)+"          "
 GOSUB xdat:IF pt%<0 THEN GOTO msskip
 FOR s%=1 TO 4:IF pmd(s%)=-1 THEN GOTO msskip
 v$=STR$(f%(nf,s%,pt%))+"          ":GOSUB ydat
msskip:
 NEXT s%:WEND: v$="
 GOSUB xdat:RETURN
aset:
 MENU 7,2,1:w$="Ready for Acquisition":GOSUB w1
 GOSUB init.plot:RETURN
arun:
 FOR s%=1 TO 6:MENU s%,0,0:NEXT s%:i%(nf)=0:s%=1
 MENU 7,1,0:MENU 7,2,0:MENU 7,3,1:GOTO collect
astop:
 FOR s%=1 TO 6:MENU s%,0,1:NEXT s%:MENU 7,3,0
 FOR s%=4 TO 9:MENU 7,s%,1:NEXT s%
 MENU 1,3,1:MENU 1,6,1:RETURN
mncheck:
 mnum=MENU(0):mitem=MENU(1):MENU
 ON mnum GOSUB utility,stime,smass,sradn,stemp,sconc,acalc:RETURN
acalc:
 ON mitem GOSUB aset,arun,astop,cblc,cpnt,cntl,cmlt,cnvt,cadd:RETURN
utility:
 ON mitem GOSUB ufx,ufl,ufs,usc,ups,ufp,uft,usd,urt,uqt:RETURN
ufx:
 nf=nf+1:IF nf>3 THEN nf=1
  fx$="F"+STR$(nf)+" Active":MENU 1,1,2,fx$
 MENU 7,1,1:RETURN
ufl:
 z$(nf)=FILES$(1,"TEXT"):IF z$(nf)="" THEN RETURN
 OPEN z$(nf) FOR INPUT AS #1:INPUT #1,i%(nf)
 FOR a%=0 TO i%(nf):FOR s%=1 TO 4
```

```
IF NOT EOF(1) THEN INPUT #1,f%(nf,s%,a%)
NEXT s%,a%:CLOSE #1:GOSUB init.plot:GOSUB ufp
FOR s%=4 TO 9:MENU 7,s%,1:NEXT s%:RETURN
ufs:
 z$(nf)=FILES$(0,"Enter output file name:"):IF z$(nf)="" THEN RETURN
 OPEN z$(nf) FOR OUTPUT AS #1:PRINT #1,i%(nf)
 FOR a%=0 TO i%(nf):FOR s%=1 TO 4:PRINT #1,f%(nf,s%,a%)
 NEXT s%,a%:CLOSE #1:RETURN
usc:
 w$="Clear Plot":GOSUB w1:GOSUB init.plot:RETURN
ups:
  pspd=pspd*-1:MENU 1,5,2,"Normal Plot Spd"
  IF pspd<0 THEN MENU 1,5,2,"Quick Plot Spd"
  RETURN
 ufp:
  pst=1:IF pspd=-1 THEN pst=tmerg+1
  FOR s%=1 TO 4:IF pmd(s%)=-1 THEN GOTO dskip
  WINDOW OUTPUT 1:LOCATE 1,13+7*s%:PRINT "   *   ":WINDOW OUTPUT 2
  FOR a%=xos TO i%(nf) STEP pst:IF a%>1080*tmerg THEN RETURN
  GOSUB plot.a:NEXT a%
 dskip:
  NEXT s%:RETURN
  uft:
  RETURN
  usd:
  LCOPY:RETURN
  stime:
   IF mitem=6 THEN GOTO zeroxset
   IF mitem=7 THEN xos=0:RETURN
    FOR s%=1 TO 5:MENU 2,s%,1:NEXT s%:MENU 2,mitem,2:tmerg=mitem
    xscl=.4/mitem:RETURN
  smass:
     d%=1:ON mitem GOTO setmas,setmas,setmas,zeroyset,zeroreset,dataselect
    setmas:
     FOR s%=1 TO 3:MENU 3,s%,1:NEXT s%:MENU 3,mitem,2:GOSUB yset:RETURN
```

```
sradn:
  d%=2:ON mitem GOTO setrad,setrad,setrad,zeroyset,zeroreset,dataselect
 setrad:
 FOR s%=1 TO 3:MENU 4,s%,1:NEXT s%:MENU 4,mitem,2:GOSUB yset:RETURN
stemp:
  d%=3:ON mitem GOTO settmp,settmp,settmp,zeroyset,zeroreset,dataselect
 settmp:
 FOR s%=1 TO 3:MENU 5,s%,1:NEXT s%:MENU 5,mitem,2:GOSUB yset:RETURN
sconc:
  d%=4:ON mitem GOTO setcnc,setcnc,setcnc,zeroyset,zeroreset,dataselect
 setcnc:
 FOR s%=1 TO 3:MENU 6,s%,1:NEXT s%:MENU 6,mitem,2:GOSUB yset:RETURN
zeroxset:
 GOSUB get.coord:xos=xos+MOUSE(5)/xscl
 v$="Z"+STR$(xos/10)+"    ":IF xos>3000 THEN xos=0:v$="
 vl=2:GOSUB xdat:RETURN
yset:
  yscl(d%)=.012*mitem:IF mitem=3 THEN yscl(d%)=.06
 RETURN
zeroyset:
  GOSUB get.coord:yos(d%)=yos(d%)+(120-MOUSE(6))/yscl(d%)
 v$="Z"+STR$(INT(yos(d%)))+"    ":IF yos(d%)>9995 THEN yos(d%)=0:v$="
 s%=d%:vl=2:GOSUB ydat:RETURN
zeroreset:
 yos(d%)=0:RETURN
dataselect:
  pmd(d%)=pmd(d%)*-1:MENU mnum,6,2,"Plot/Calc On"
  IF pmd(d%)<0 THEN MENU mnum,6,2,"Plot/Calc Off"
 RETURN
cblc:
 RETURN
cpnt:
 GOSUB get.coord:RETURN
cntl:
  GOSUB get.coord:x1=MOUSE(5):y1=MOUSE(6)
```

```
 GOSUB get.coord:x2=MOUSE(5):PSET(x1,y1-1):PSET(x1,y1+1)
 CALL MOVETO(x1,y1):CALL LINETO(x2,y1):PSET(x2,y1-1):PSET(x2,y1+1)
  x1=INT(xos+x1/xscl):x2=INT(xos+x2/xscl):vl=1
 FOR s%=1 TO 4:ntg=0:IF pmd(s%)=-1 THEN GOTO ntskip
 FOR a%=x1 TO x2:ntg=ntg+f%(nf,s%,a%)/10:NEXT a%
 v$=STR$(INT(ntg))+"    ":GOSUB ydat
ntskip:
 NEXT s%:s%=5:v$="mv sec    ":GOSUB ydat:RETURN
cmlt:
 RETURN
cnvt:
 FOR s%=1 TO 4:IF pmd(s%)=-1 THEN GOTO nvskip
 nv(s%)=nv(s%)*-1:vl=1:v$="    -       ":IF nv(s%)>0 THEN v$="    +       "
 GOSUB ydat
  FOR a%=0 TO i%(nf):f%(nf,s%,a%)=f%(nf,s%,a%)*-1:NEXT a%
nvskip:
 NEXT s%:MENU 1,3,1:RETURN
cadd:
 FOR s%=1 TO 4:IF pmd(s%)=-1 THEN GOTO adskip
  FOR a%=0 TO i%(1):f%(3,s%,a%)=f%(1,s%,a%)+f%(2,s%,a%):NEXT a%
  i%(3)=i%(1)
adskip:
  NEXT s%:nf=3:MENU 1,1,2,"F 3 Active":MENU 1,3,1:RETURN
w1:
 WINDOW CLOSE 2
  WINDOW 1,"",(0,20)-(530,342),3:CLS:RETURN
xdat:
 WINDOW OUTPUT 1:LOCATE vl,12:PRINT v$
 WINDOW OUTPUT 2:RETURN
 ydat:
  WINDOW OUTPUT 1:LOCATE vl,13+7*s%:PRINT v$
  WINDOW OUTPUT 2:RETURN
 init.plot:
   GOSUB xlabel:WINDOW 2,"",(40,67)-(473,308),3
   FOR y%=0 TO 240 STEP 12:FOR x%=0 TO 432 STEP 36:PSET(x%,y%):NEXT x%,y%
```

```
 FOR x%=0 TO 432 STEP 3:PSET(x%,120):NEXT x%:MENU 1,6,1:RETURN
xlabel:
 LOCATE 4,1: PRINT "Volts":LOCATE 11,3:PRINT "0"
 LOCATE 19,1:PRINT "Min"
 FOR z%=0 TO tmerg*18 STEP tmerg*3:LOCATE 19,4+z%*3/tmerg:PRINT z%:NEXT z%
 RETURN
init.menu:
 MENU 1,0,1,"Utilities":MENU 1,1,2,"F1 Active":MENU 1,2,1,"Load as Active F#"
 MENU 1,3,0,"Save Active F#": MENU 1,4,1,"Setup/Clear Plot":MENU 1,5,2,"Normal Plot
Spd"
 MENU 1,6,0,"Plot Active F#":MENU 1,7,0,"Tabulate Active F#"
 MENU 1,8,1,"Print Screen":MENU 1,9,1,"Reset":MENU 1,10,1,"Quit"
 MENU 2,0,1,"Time":MENU 2,1,2,"18 min":MENU 2,2,1,"36 min"
 MENU 2,3,1,"54 min":MENU 2,4,1,"72 min":MENU 2,5,1,"90 min"
 MENU 2,6,1,"Zero Offset":MENU 2,7,1,"Zero Reset"
 MENU 3,0,1,"Mass":MENU 3,1,2,"±10v Span":MENU 3,2,1,"±  5v Span"
 MENU 3,3,1,"±  2v Span":MENU 3,4,1,"Zero Offset"
 MENU 3,5,1,"Zero Reset":MENU 3,6,2,"Plot/Calc On"
 MENU 4,0,1,"Radiation":MENU 4,1,2,"±10v Span":MENU 4,2,1,"±  5v Span"
 MENU 4,3,1,"±  2v Span":MENU 4,4,1,"Zero Offset"
 MENU 4,5,1,"Zero Reset":MENU 4,6,2,"Plot/Calc On"
 MENU 5,0,1,"Temp":MENU 5,1,2,"±10v Span":MENU 5,2,1,"±  5v Span"
 MENU 5,3,1,"±  2v Span":MENU 5,4,1,"Zero Offset"
 MENU 5,5,1,"Zero Reset":MENU 5,6,2,"Plot/Calc On"
 MENU 6,0,1,"Gas Conc":MENU 6,1,2,"±10v Span":MENU 6,2,1,"±  5v Span"
 MENU 6,3,1,"±  2v Span":MENU 6,4,1,"Zero Offset"
 MENU 6,5,1,"Zero Reset":MENU 6,6,2,"Plot/Calc On"
 MENU 7,0,1,"Acquire/Calc":MENU 7,1,1,"Setup Run"
 MENU 7,2,0,"Start Run":MENU 7,3,0,"Stop Run"
 MENU 7,4,0,"Bsln Correct":MENU 7,5,0,"Evaluate Points"
 MENU 7,6,0,"Peak Integral":MENU 7,7,0,"Multiply"
 MENU 7,8,0,"Invert":MENU 7,9,0,"F3 = (F1+F2)":RETURN
urt:
 CLEAR
  DIM  f%(3,4,5401),i%(3),nv(4),pmd(4),yos(4),yscl(4):er%=0
```

```
 FOR s%=1 TO 4:nv(s%)=1:pmd(s%)=1:yos(s%)=0:yscl(s%)=.012:NEXT s%
  nf=1:pspd=1:tmerg=1:xos=0:xscl=.4
  w$="Pyrolysis  Recorder/Analyzer":GOSUB  w1
 GOSUB init.menu:ON MENU GOSUB mncheck:MENU ON
 GOTO idle
uqt:
 MENU RESET:END
```

APPENDIX B2: MATHEMATICAL MODEL PROGRAM

The code listed here is written in FORTRAN 77. The modifications made in this work are in lower case letters. The program generates files that are in format of columns, separated by commas, so that a file can be readily used by spreadsheet applications. The code itself was ran on Macintosh microcomputer, but it could be also executed in other environments. The size of the code is about 65 Kb, and it requires 384 Kb of RAM for execution. The running time on Macintosh with 68000 (8 MHz) processor is about 30 minutes.

The listing of the program:

```
      program sp5

      COMMON/SPYCOM/BC(2),CPA,CPC,CPG,CPAS,CPCS,CPGS,DARCY,DTIMAX,
     1  DTIME,DTIMIN,DTSTEP,DX,EPS1,EPS2,ERRMX,HFLUX1,HFLUX2,
     2  H1,H2,IBC(2),IFIN,ISTEP,ITER,ITERID,ITERMX,KBC(2),
     3  LASTEP,MG(501),MG1,MG2,N,NP1,PF,Q1DT,Q2DT,RELAX,
     4  RHO(501),RHOA(501),RHOF(501),RHOW,SLIMIT,T(501),TBAR(501),
     5  TBC(2,5000),TCA,TCC,TCAS,TCCS,TIME,TIMEAV,TIMEBC(5000),
     6  TINF1,TINF2,TMLAST,TRNEG,T0K,XBC(2),PTL,PYRO,PPL,
     7  TM(5000),HOLD,HP,HGMAX,T1MAX,MG1MAX,TMMAX,IPLOT,NPLOT

      COMMON/VAPCOM/A(501),B(501),BCTR1(2),BCTR2(2),BT(501),C(501),
     1  D(501),DRHO(501),F(501),ISURF(2),M(501),SLOPE(2),
     2  TP(501),TSLCR(2) ,TSTR1(2),TSTR2(2),U(501),XDEPTH(2),YD(2)

      COMMON/DATAOUT/MG1PLT(5000),HGPLT(5000),T1PLT(5000),T2PLT(5000),
     1  T3PLT(5000),T4PLT(5000),T5PLT(5000),T6PLT(5000),fepsl,
     2  epschar,density(5000),reduc,rhomaxr,rmaxred,redback,
     3  rhobar,tl,order,epscell,pf2,trneg2,qp02,order2,
     4  switch,ind(501),hrate(501),cy(501),shr(501),shrf(501),
     5  qp0(501),rhobarl,rhofml(501),rhoff,qp0f

      REAL MG,MG1,MG2,MG11,MG1MAXMG1PLT

      save/spycom/
      save/vapcom/
      save/dataout/

      OPEN(UNIT=10,FILE='DATA',STATUS='OLD')
      OPEN(UNIT=11,FILE='OUTPUT DATA',STATUS='NEW')
      OPEN(UNIT=12,FILE='M FLUX.KG',STATUS='NEW')
      OPEN(UNIT=13,FILE='TEMPERATURE.KG',STATUS='NEW')
      OPEN(UNIT=14,FILE='HG.KG',STATUS='NEW')
      OPEN(UNIT=15,FILE='DENSITY.KG',STATUS='NEW')
```

```
C-------- INITIALIZATION OF CONSTANTS ---------------------------------

      do 80 I=1,501
       A(I)=0.
       B(I)=0.
       BT(I)=0.
       C(I)=0.
       CY(I)=1.
       D(I)=0.
       DRHO(I)=0.
       F(I)=0.
       HRATE(I)=1.
       IND(I)=0
       M(I)=0.
       MG(I)=0.
       qp0(I)=0.
       RHO(I)=1.
       RHOA(I)=1.
       RHOF(I)=0.
       RHOFM1(I)=1.
       SHR(I)=1.
       SHRF(I)=1.
       T(I)=0.
       TBAR(I)=0.
       TP(I)=0.
       U(I)=0.
80     continue

      do 90 I=1,5000
      density(i)=0.
      HGPLT(I)=0.
      MG1PLT(I)=0.
      T1PLT(I)=0.
      T2PLT(I)=0.
      T3PLT(I)=0.
      T4PLT(I)=0.
      T5PLT(I)=0.
      T6PLT(I)=0.
      TBC(1,I)=0.
      TBC(2,I)=0.
      TM(I)=0.
90    continue

      do 95 I=1,2
       BC(I)=0.
       BCTR1(I)=0.
       BCTR2(I)=0.
       IBC(I)=1
       ISURF(I)=0
       SLOPE(I)=0.
       TSLCR(I)=0.
       TSTR1(I)=0.
       TSTR2(I)=0.
       XBC(I)=0.
       XDEPTH(I)=0.
       YD(I)=0.
```

```
95      continue
        ANPROF=0.
        ANSTAT=0.
        BETA=0.
        BETAM1=0.
        C1=0.
        C2=0.
        CHB=0.
        CHF=0.
        CHG=0.
        CORR=0.
        CPGD4=0.
        CPW=0.
        DBCMN=0.
        DQ1DT=0.
        DQ2DT=0.
        DTIME=0.
        DX=0.
        ERR=0.
        FACT=0.
        fepsl=0.
        epscell=0.
        HFLUX1=0.
        HFLUX2=0.
        HG=0.
        HGMAX=0.
        HOLD=0.
        HP=0.
        ICPL=0
        IPOWHG=0
        IPOWMG=0
        IPOWT1=0
        ISTEP=0
        ISTEPR=0
        ITER=0
        MG1=0.
        MG11=0.
        MG1MAX=0.
        MG2=0.
        N100=0
        onoff=1.
        order=1.
        PPL=0.
        Q1DT=0.
        Q2DT=0.
        QCONV1=0.
        QCONV2=0.
        QNET1=0.
        QP=0.
        RCDX=0.
        RDEN=0.
        RERAD1=0.
        RERAD2=0.
        RHOBAR=1.
        reduc=0.
        rhomaxr=0.
        rmaxred=0.
        redback=0.
        T1MAX=0.
```

```
      TBCC=0.
      TCW=0.
      TCWDHX=0.
      THDIFF=0.
      TIME=0.
      TIMEAV=0.
      TIMEDT=0.
      TL=0.
      TMMAX=0.
      TMX=0.

C-------- THERMAL PROPERTIES
  110 CONTINUE
      read(10,*) RUN
      read(10,*) TMMAX,HGMAX,T1MAX,MG1MAX
      read(10,*) NPLOT
      IPLOT=0
      read(10,*) CPA,CPC,CPG,CPAS,CPCS,CPGS
      read(10,*) TCA,TCC,TCAS,TCCS,RHOW,PTL,PYRO,PPL
C-------- PYROLYSIS CONSTANTS AND SLAB THICKNESS
      read(10,*) ST,RHOFF,PF,TRNEG,QP0F,T0K,DARCY
      HOLD=((RHOFF/(1.0-RHOFF))*CPC)+CPG
      DX=ST
C-------- PARAMETERS FOR BOUNDARY CONDITIONS AND GRID
      read(10,*) KBC(1),KBC(2),N,LASTEP,NSTAT,NPROF,ITERMX,ITERID
      ISTEP=0
      read(10,*) H1,H2,TINF1,TINF2,EPS1,EPS2,XBC(1),XBC(2)
        epscell=eps1
        read(10,*)epschar,rhomaxr,rmaxred,redback,tl,order,hl
        read(10,*)pf2,trneg2,qp02,order2,switch
      read(10,*) DTIMAX,DTIMIN,DTSTEP,TMLAST,ERRMX,RELAX,SLIMIT
      ANSTAT=NSTAT
      ANPROF=NPROF
C-------- INPUT OF BOUNDARY CONDITIONS ------------------------------
      DBCMN=0.
      I=1
  125 CONTINUE
      read(10,*) TIMEBC(I),TBC(1,I),TBC(2,I)
      IF(I.EQ.1) GO TO 155
      IF(TIMEBC(I)+TBC(1,I)+TBC(2,I).EQ.0.) GO TO 150
      IF(TIMEBC(I).GE.TIMEBC(I-1)+TMX) GO TO 155
      IF(ABS(TBC(1,I)-TBC(1,I-1)).LT.DBCMN) GO TO 125
```

```
  155 CONTINUE
      IF(I.EQ.150) GO TO 160
      I=I+1
      GO TO 125
  150 CONTINUE
      I=I-1
  160 CONTINUE
      IR=I
      IF(TMLAST.GT.TIMEBC(IR)) TMLAST=TIMEBC(IR)
      IF(KBC(1).EQ.2.AND.KBC(2).EQ.2) GO TO 170
      DO 165 J=1,2
      DO 165 I=1,IR
      IF(KBC(J).EQ.1) TBC(J,I)=TBC(J,I)+273.
  165 CONTINUE
  170 CONTINUE
C
C-------- OUTPUT OF INITIAL CONDITIONS --------------------------------
       write(11,211)RUN
  211 FORMAT( /'       RUN NO. =  ',A4)
      write(11,210) N,ST,T0K,RHOW,RHOFF,PF,TRNEG,QP0F,DARCY,PTL,PYRO,PPL
  210 FORMAT(//' GEOMETRY, INITIAL CONDITIONS AND PYROLYSIS:'/' N=',
     1  I3,2X,'ST=',1PE10.3,2X,'T0K=',E10.3,2X,'RHOW=',E10.3,2X,
     2  'RHOF=',E10.3,2X,'PF=',E10.3,2X,'TRNEG=',E10.3,2X,'QP0=',
     3  E10.3/' DARCY=',0PF3.0,'  PTL= ',F3.0,'  PYRO= ',F3.0,' PPL=',
     4  F3.0)
       write(11,220) CPA,CPAS,CPC,CPCS,CPG,CPGS,TCA,TCAS,TCC,TCCS
  220 FORMAT(/' THERMAL PROPERTIES:'/' SPECIFIC HEATS:',18X,'CPA=',
     1                          1PE10.3,2X,'CPAS=',
     2  E10.3,2X,'CPC=',E10.3,2X,'CPCS=',E10.3,2X,'CPG=',E10.3,2X,
     3  'CPGS=',E10.3/' THERMAL CONDUCTIVITIES:',10X,'TCA=',E10.3,2X,
     4  'TCAS=',E10.3,2X,'TCC=',E10.3,2X,'TCCS=',E10.3)
       write(11,230) KBC(1),XBC(1),TINF1,H1,EPS1,KBC(2),XBC(2),TINF2,
     1    H2,EPS2
  230 FORMAT(/' BOUNDARY CONDITIONS:'/22X,'KBC',8X,'XBC',11X,'TINF',
     1  12X,'H',13X,'EPS'/' FRONT SURFACE:',I10,1P4E15.3/' BACK SURFACE:
     2' ,I11,4E15.3)
       write(11,250) (TIMEBC(I),I=1,IR)
  250 FORMAT(/' TIME',4X,1P11E11.3/(9X,11E11.3))
      write(11,260) CHF,(TBC(1,I),I=1,IR)
  260 FORMAT(/' CH# ',F4.0,1P11E11.3/' FRONT BC',11E11.3/(9X,11E11.3))
      write(11,270) CHB,(TBC(2,I),I=1,IR)
  270 FORMAT(/' CH# ',F4.0,1P11E11.3/' BACK BC ',11E11.3/(9X,11E11.3))
      write(11,240)DTIMAX,DTIMIN,DTSTEP,ERRMX,SLIMIT,RELAX,ITERMX,ITERID
  240 FORMAT(//' STEP CONTROL PARAMETERS:'/' DTIMAX=',1PE9.2,2X,
     1  'DTIMIN=',E9.2,2X,'DTSTEP=',E9.2,2X,'ERRMX=',E9.2,2X,
     3  'SLIMIT=',E9.2,2X,
     2  'RELAX=',E9.2,2X,'ITERMX=',I3,2X,'ITERID=',I3)
       write(11,241) NSTAT,NPROF,NPLOT
  241 FORMAT(//' OUTPUT CONTROL PARAMETERS:'/' NSTAT=',
     1I5,3X,' NPROF=',I5,3X,' NPLOT=',I5)
       write(11,242) XAXIS,YAXIS,R
  243 FORMAT(' MAXIMUM VALUES:',1X,' TMMAX=',1PE9.3,5X,' HGMAX=',1PE9.3,
     13X,' T1MAX=',1PE9.3,5X,' MG1MAX=',1PE9.3)
```

```
C
C-------- CALL OF SUBROUTINE SPYVAP ----------------------------------
  310 CONTINUE
      IOUT=(ISTEP/NSTAT+1)*NSTAT
      IOUT=MIN0(IOUT,(ISTEP/NPROF+1)*NPROF)
      IOUT=IOUT-ISTEP
      CALL SPYVAP(IOUT,N100)
C-------- CHECK FOR OUTPUT -------------------------------------------
      IPRINT=0
      IF(IPLOT.EQ.NPLOT) IPRINT=1
      IF(FLOAT(ISTEP/NSTAT).EQ.FLOAT(ISTEP)/ANSTAT) IPRINT=2
      IF(FLOAT(ISTEP/NPROF).EQ.FLOAT(ISTEP)/ANPROF) IPRINT=3
      IF(IFIN.NE.0.OR.TIME.GE.TMLAST.OR.ISTEP.EQ.LASTEP) IPRINT=3
      IF(IPRINT.GT.0) CALL OUTPUT(IPRINT,N100)
      IF(IFIN.EQ.0.AND.TIME.LT.TMLAST.AND.ISTEP.NE.LASTEP) GO TO 310
      write(11,200) ISTEP,LASTEP,TIME,TMLAST,IFIN
  200 FORMAT(///' ** TERMINATED WITH ISTEP=',I5,5X,' LASTEP=',I5,5X,
     1' TIME=',1PE11.3,5X,' TMLAST=',E11.3,5X,' IFIN=',I3)

C------------WRITING PROCEDURE-----------------------------------------
      IF(PPL.EQ.0.0)GOTO 320
      DO 710 I=1,N100
        write(15,712)tm(i),density(i)
  710 WRITE(12,712) TM(I),MG1PLT(I)
c  711 FORMAT(F13.8,5X,F13.8)
  712   format(f7.2,',',f13.9)
      DO 810 I=1,N100
  810 WRITE(13,713) TM(I),T1PLT(I),T2PLT(I),T3PLT(I),T4PLT(I),T5PLT(I),
     +  T6PLT(I)
  713   format(f7.2,',',f6.2,',',f6.2,',',f6.2,',',f6.2,',',f6.2
     +      ,',',f6.2)
      DO 910 I=1,N100
  910 WRITE(14,714) TM(I),HGPLT(I)
  714   format(f7.2,',',f13.2)

  320 STOP
      END


      SUBROUTINE SPYVAP(IOUT,N100)
C******* F.TAMANINI, FACTORY MUTUAL RESEARCH CORP., MARCH 1976 ********
C*       MODIFIED BY I. MILOSAVLJEVIC, DECEMBER 1993
C*
C*   THIS SUBROUTINE COMPUTES TEMPERATURE AND DENSITY PROFILES FOR
C*   ONEDIMENSIONAL UNSTEADY HEAT CONDUCTION IN A SOLID SLAB OF
C*   FINITE THICKNESS UNDERGOING PYROLYSIS.
C*
C*   TWO TYPES OF SURFACE BOUNDARY CONDITIONS CAN BE HANDLED:
C*      1) PRESCRIBED TEMPERATURE AT (OR NEAR) THE SURFACE
C*      2) PRESCRIBED SURFACE HEAT FLUX (NOT INCLUDING CONVECTIVE
C*         HEAT TRANSFER OR SURFACE RERADIATION)
C*
C*   THE RATE OF PYROLYSIS IS GIVEN BY AN N ORDER ARRHENIUS REACTIONS
C*   ONE WITH SINGLE KINETIC PARAMETERS, FOLLOWED BY TWO COMPETITIVE
C*   REACTIONS
C*
```

```
C*    PYROLYSIS GASES DIFFUSING THROUGH THE SOLID ARE ASSUMED TO BE
C*    IN PERFECT THERMAL CONTACT WITH THE SOLID AND TO BE MOVING IN
C*    THE DIRECTION OF DECREASING SOLID DENSITIES OR TO MIGRATE
C*    TOWARD BOTH FREE SURFACES IN SUCH A WAY THAT THE NET PRESSURE
C*    DROP ACROSS THE SLAB IS ZERO.
C*
C*    SPECIFIC HEATS (ACTIVE SOLID, CHAR AND PYROLYSIS GASES) AND
C*    THERMAL CONDUCTIVITIES (ACTIVE SOLID AND CHAR) ARE TREATED AS
C*    LINEAR FUNCTIONS OF LOCAL TEMPERATURE.
C*
C*    S.I. UNITS ARE USED THROUGHOUT (KG,M,SEC)
C*
C*************************************************************************
      COMMON/SPYCOM/BC(2),CPA,CPC,CPG,CPAS,CPCS,CPGS,DARCY,DTIMAX,
     1  DTIME,DTIMIN,DTSTEP,DX,EPS1,EPS2,ERRMX,HFLUX1,HFLUX2,
     2  H1,H2,IBC(2),IFIN,ISTEP,ITER,ITERID,ITERMX,KBC(2),
     3  LASTEP,MG(501),MG1,MG2,N,NP1,PF,Q1DT,Q2DT,RELAX,
     4  RHO(501),RHOA(501),RHOF(501),RHOW,SLIMIT,T(501),TBAR(501),
     5  TBC(2,5000),TCA,TCC,TCAS,TCCS,TIME,TIMEAV,TIMEBC(5000),
     6  TINF1,TINF2,TMLAST,TRNEG,T0K,XBC(2),PTL,PYRO,PPL,
     7  TM(5000),HOLD,HP,HGMAX,T1MAX,MG1MAX,TMMAX,IPLOT,NPLOT

      COMMON/VAPCOM/A(501),B(501),BCTR1(2),BCTR2(2),BT(501),C(501),
     1  D(501),DRHO(501),F(501),ISURF(2),M(501),SLOPE(2),
     2  TP(501),TSLCR(2) ,TSTR1(2),TSTR2(2),U(501),XDEPTH(2),YD(2)

      COMMON/DATAOUT/MG1PLT(5000),HGPLT(5000),T1PLT(5000),T2PLT(5000),
     1  T3PLT(5000),T4PLT(5000),T5PLT(5000),T6PLT(5000),fepsl,
     2  epschar,density(5000),reduc,rhomaxr,rmaxred,redback,
     3  rhobar,tl,order,epscell,pf2,trneg2,qp02,order2,
     4  switch,ind(501),hrate(501),cy(501),shr(501),shrf(501),
     5  qp0(501),rhobar1,rhofm1(501),rhoff,qp0f

      REAL M,MG,MG1,MG2,MG11,MG1MAXMG1PLT

      save/spycom/
      save/vapcom/
      save/dataout/

C
CHAPTER 0 0 0 0 0 0 --- PRELIMINARIES --- 0 0 0 0 0 0 0 0 0 0 0 0 0 0 0 0
C
      ISTEPR=ISTEP+IOUT
      IF(ISTEP.GT.0) GO TO 310
C
CHAPTER 1 1 1 ---GEOMETRY, CONTROL INDEXES AND THERMODYNAMIC VARIABLES-
C
      K=1
      IF(N.LT.201) GO TO 125
      write(11,130) N
  130 FORMAT('1DIMENSION OF ARRAYS IS INSUFFICIENT TO HANDLE ',
     1     I3,' GRID POINTS')
```

```
      IFIN=1
      RETURN
  125 CONTINUE
      NP1=N+1
      RDEN=ALOG(1./ERRMX)
      DTIME=DTIMIN
      TIME=TIMEBC(1)
      DX=DX/FLOAT(N)
C
C--------- INDEXES FOR CONTROL OF SURFACE B.C. (J=1,FRONT; =2,BACK) ---
C          KBC(J)=1, TEMPERATURE B.C.; =2, HEAT FLUX B.C.
C          IBC(J): FIRST GRID POINT LEFT OF WHERE TEMP.B.C. IS IMPOSED
C          IBC(J)=0  FOR SURFACE TEMP.B.C.
C
      DO 110 J=1,2
      XDEPTH(J)=XBC(J)
      IF(KBC(J).EQ.2) GO TO 105
      IF(XBC(J).EQ.0.) GO TO 106
      XBC(J)=XBC(J)/DX
      IBC(J)=1+INT(XBC(J))
      XBC(J)=XBC(J)-AINT(XBC(J))
      IF(J.EQ.1) GO TO 110
      IBC(J)=NP1-IBC(J)
      XBC(J)=1.-XBC(J)
      GO TO 110
  105 XBC(J)=0.
  106 IBC(J)=0
  110 CONTINUE
C--------- MINIMUM PYROLYSIS TEMPERATURE ------------------------------
      CPW=CPA
      TCW=TCA
      IF(PF.EQ.0.) GO TO 115
      TRNEG=-TRNEG/8314.
        trneg2=-trneg2/8314.
      IF(PTL.EQ.1.0) GOTO 701
      TL=0.0
  701 write(11,120) TL
  120 FORMAT(//' ***'/' PYROLYSIS CALCULATION IS NOT PERFORMED FOR TEMPE
     1RATURES LESS THAN',F8.2,'  DEGK'/75X,'***'//)
  115 CONTINUE
C
C--------- SPECIFIC HEATS AND THERMAL CONDUCTIVITIES ------------------
      THDIFF=TCW/RHOW/CPW
      RCDX=RHOW*CPW*DX
      CPA=CPA/CPW
      CPAS=CPAS/CPW
      CPC=CPC/CPW
      CPCS=CPCS/CPW
      TCWDHX=.5*TCW/DX
      TCA=TCA/TCW
      TCAS=TCAS/TCW
      TCC=TCC/TCW
      TCCS=TCCS/TCW
      CPGD4=.25*CPG
      IF(CPGS*CPG.NE.0.) CPGS=.5*CPGS/CPG
      EPS1=EPS1*5.669E-8
      EPS2=EPS2*5.669E-8
```

```
C
CHAPTER 2 2 2 -- INITIALIZATION OF ARRAYS AND OTHER VARIABLES --- 2 2 2
      IFIN=0
      DO 210 J=1,2
      TSLCR(J)=1.
      SLOPE(J)=.01
      IF(TBC(J,1).NE.TBC(J,2)) SLOPE(J)=(TBC(J,2)-TBC(J,1))/
     1                         (TIMEBC(2)-TIMEBC(1))
      IF(XBC(J).EQ.0.) GO TO 210
      XD=.5*XDEPTH(J)/SQRT(THDIFF*DTIMAX)
      IF(XD.GT.10.) XD=10.
      SLOPE(J)=SLOPE(J)/(1.+2.*XD*XD)/ERFC(XD)
  210 CONTINUE
      ISURF(1)=1
      ISURF(2)=NP1
      Q1DT=0.
      Q2DT=0.
      DQ1DT=0.
      DQ2DT=0.
      MG1=0.
      MG2=0.
      C1=0.
      C2=0.
      DO 220 I=1,NP1
      T(I)=T0K
      TP(I)=T0K
      RHO(I)=1.
      RHOA(I)=1.
        rhof(i)=rhoff
        qp0(i)=qpof
        rhofm1(i)=1.-rhof(i)
      DRHO(I)=0.
      MG(I)=0.
      C(I)=0.
      D(I)=0.
  220 CONTINUE
CHAPTER 3 3 3 3 3 3 ---EVALUATION OF BOUNDARY VALUES--- 3 3 3 3 3 3 3 3
C--------- LINEAR INTERPOLATION OF BOUNDARY CONDITIONS ----------------
  310 CONTINUE
      TIMEAV=TIME+.5*DTIME
      TIMEDT=TIME+DTIME
      IF(TIMEAV.LE.TIMEBC(K+1)) GO TO 311
      K=K+1
      GO TO 310
  311 CONTINUE
      DO 315 J=1,2
      BC(J)=TIMEDT
      IF(KBC(J).EQ.2) BC(J)=TIMEAV
      BC(J)=(BC(J)-TIMEBC(K))/(TIMEBC(K+1)-TIMEBC(K))
  315 BC(J)=TBC(J,K)+BC(J)*(TBC(J,K+1)-TBC(J,K))
      IF(KBC(1).EQ.1) TP(1)=BC(1)
      IF(KBC(2).EQ.1) TP(NP1)=BC(2)
      HFLUX1=BC(1)
      HFLUX2=BC(2)
      ITER=0
```

```
C
C--------- CALCULATES SURFACE TEMPERATURES (FRONT, J=1; BACK, J=2)
C          WHEN TEMPERATURE NEAR (AND NOT AT) THE SURFACE IS GIVEN
C          AS BOUNDARY CONDITION
  325 CONTINUE
      IF(IBC(1).EQ.0.AND.IBC(2).EQ.0) GO TO 320
      DO 350 J=1,2
      IF(IBC(J).EQ.0) GO TO 350
      IF(ITER.GT.0) GO TO 330
      TSTR1(J)=T(ISURF(J))+SLOPE(J)*DTIME
      TP(ISURF(J))=TSTR1(J)
      GO TO 350
  330 IF(ITER.GT.1) GO TO 340
C
C---- FIRST ITERATION
      BCTR1(J)=TP(IBC(J))+XBC(J)*(TP(IBC(J)+1)-TP(IBC(J)))
      XD=XDEPTH(J)*.5/SQRT(THDIFF*DTIME)
      IF(XD.GT.10.) XD=10.
      IF(XD.LE.1.5) FACT=1.-.6402*XD
      IF(XD.GT.1.5) FACT=.5642*EXP(-XD*XD)/XD
      FACT=(1.+2.*XD*XD)*FACT
      YD(J)=FACT
      IF(FACT.LT..01) FACT=.01
      IF(ISTEP.EQ.0) BCTR1(J)=BC(J)
      IF(BCTR1(J).NE.BC(J)) TSLCR(J)=SLOPE(J)+(BC(J)-BCTR1(J))
     1                                        /DTIME/FACT
      IF(BCTR1(J).EQ.BC(J)) TSLCR(J)=1.1*SLOPE(J)
      IF(SLIMIT.GT.0.) GO TO 331
  329 YD(J)=-SLIMIT*DTSTEP*shr(i)*DX*FLOAT(N)*.5/SQRT(THDIFF*DTIME)
      IF(TSLCR(J)/SLOPE(J).LT.1.) YD(J)=10.*YD(J)
      FACT=ABS(TSLCR(J)-SLOPE(J))*DTIME/YD(J)
      IF(FACT.GT.1.) TSLCR(J)=SLOPE(J)+(TSLCR(J)-SLOPE(J))/FACT
      GO TO 332
  331 CONTINUE
      YD(J)=SLIMIT/(1.-.1*ALOG(YD(J)))
      FACT=TSLCR(J)/SLOPE(J)
      IF(FACT.LT.0..AND.-FACT.GT.YD(J)) TSLCR(J)=-YD(J)*SLOPE(J)
      IF(FACT.GE.0..AND.ABS(FACT-1.).GT.YD(J))
     1        TSLCR(J)=SLOPE(J)*(1.+SIGN(YD(J),FACT-1.))
  332 CONTINUE
      TSTR2(J)=T(ISURF(J))+TSLCR(J)*DTIME
      TP(ISURF(J))=TSTR2(J)
      GO TO 350
C
C---- SECOND ITERATION
  340 BCTR2(J)=TP(IBC(J))+XBC(J)*(TP(IBC(J)+1)-TP(IBC(J)))
      IF(BCTR2(J).NE.BCTR1(J)) TP(ISURF(J))=TSTR2(J)+(TSTR1(J)-TSTR2(J))
```

```
     1       *(BC(J)-BCTR2(J))/(BCTR1(J)-BCTR2(J))
        TSLCR(J)=(TP(ISURF(J))-T(ISURF(J)))/DTIME
        IF(SLIMIT.GT.0.) GO TO 341
        FACT=ABS(TSLCR(J)-SLOPE(J))*DTIME/YD(J)
        IF(FACT.GT.1.) TSLCR(J)=SLOPE(J)+(TSLCR(J)-SLOPE(J))/FACT
        GO TO 342
   341 CONTINUE
        FACT=TSLCR(J)/SLOPE(J)
        IF(FACT.LT.0..AND.-FACT.GT.YD(J)) TSLCR(J)=-YD(J)*SLOPE(J)
        IF(FACT.GE.0..AND.ABS(FACT-1.).GT.YD(J))
     1         TSLCR(J)=SLOPE(J)*(1.+SIGN(YD(J),FACT-1.))
   342 CONTINUE
        IF(ISTEP.GT.0) SLOPE(J)=TSLCR(J)
        IF(SLOPE(J).EQ.0.) SLOPE(J)=.01
        IF(ABS(SLOPE(J)).LT..01) SLOPE(J)=SIGN(.01,SLOPE(J))
        TP(ISURF(J))=T(ISURF(J))+SLOPE(J)*DTIME
   350 CONTINUE
   320 CONTINUE
CHAPTER 4 4 4 4 4 4 4 4 ----BEGINNING OF LOOP ---- 4 4 4 4 4 4 4 4 4 4
C--------- COMPUTES DENSITY INCREMENTS ------------------------------
   400 CONTINUE
        DO 410 I=1,NP1
        IF(ITER.EQ.0) RHOA(I)=RHO(I)+.5*DRHO(I)
        TBAR(I)=.5*(TP(I)+T(I))
        DRHO(I)=0.
        IF(TBAR(I).LE.TL) GO TO 405
        IF(RHO(I).EQ.RHOF(i)) GO TO 405

          if(tbar(i).lt.tl.or.ind(i).eq.1)go to 403
          hrate(i)=(tbar(i)-t0k)/time
          if(hrate(i).gt.2.)hrate(i)=2.
          cy(i)=.13-.07*alog(hrate(i))
          qp0(i)=-7.58e5+3.424e6*cy(i)
          rhof(i)=0.066+0.934*cy(i)
          if(rhof(i).lt.rhoff)rhof(i)=rhoff
          shrf(i)=cy(i)/rhof(i)
          rhofml(i)=1-rhof(i)
          ind(i)=1

   403    if(rhoa(i).lt.rhof(i))rhoa(i)=rhof(i)
          shr(i)=(shrf(i)-rhof(i)+rhoa(i)*(1-shrf(i)))/rhofml(i)
          if(shr(i)*rhoa(i)-cy(i).le.0.)go to 404
          onoff=rhobar-switch
          if(onoff)402,402,401
   401   DRHO(I)=-(DTIME*PF*((shr(i)*RHOA(I)-cy(i))**order)
        1  *EXP(TRNEG/TBAR(I)))/rhofml(i)
          go to 404

   402    drho(i)=-(dtime*(pf*((shr(i)*rhoa(i)-cy(i))**order)*
        1  exp(trneg/tbar(i))+pf2*((shr(i)*rhoa(i)-cy(i))**order2)
        2  *exp(trneg2/tbar(i))))/rhofml(i)
   404    IF(RHO(I)+DRHO(I).LT.RHOF(i)) DRHO(I)=RHOF(i)-RHO(I)
     405 RHOA(I)=RHO(I)+.5*DRHO(I)
     410 CONTINUE
```

```
C
C---------COMPUTES NEW DISTRIBUTION OF GASEOUS FLUX, ASSUMING THAT
C          FLUX IS IN THE DIRECTION OF DECREASING DENSITY (DARCY.NE.1.)
C          OR THAT IT FOLLOWS DARCY'S LAW (DARCY.EQ.1.)
      IF(RHOA(1).EQ.1..AND.RHOA(NP1).EQ.1.) GO TO 435
      J=NP1
      MG(NP1)=0.
      MG2=0.
      DO 420 I=2,NP1
      ICPL=NP1+1-I
  419 MG(ICPL)=MG(ICPL+1)-DRHO(ICPL+1)*shr(i)*DX*RHOW/DTIME
      IF(ICPL.EQ.N) MG(ICPL)=.5*MG(ICPL)
      IF(RHO(ICPL).GT.RHOA(J)) J=ICPL
  420 CONTINUE
  414 MG1=MG(1)-DRHO(1)*.5*shr(i)*DX*RHOW/DTIME
      IF(DARCY) 435,415,418
  418 MG2=.25*(MG1-MG(1)-MG(N)+MG(NP1))
      DO 416 I=1,N
  416 MG2=MG2+MG(I)
      MG2=MG2/FLOAT(N)
      GO TO 417
  415 CONTINUE
      IF(J.EQ.NP1) GO TO 435
      IF(J.NE.1) MG2=.5*(MG(J)+MG(J-1))
      IF(J.EQ.1) MG2=MG1
  417 CONTINUE
      DO 430 I=1,NP1
  430 MG(I)=MG(I)-MG2
      MG1=MG1-MG2
      MG2=-MG(NP1)
  435 CONTINUE
C
C--------- COMPUTES AVERAGE VALUES OF SPECIFIC HEAT ----------
      DO 440 I=1,NP1
      A(I)=RCDX/DTIME
      IF(RHOA(I).EQ.1..AND.CPAS.EQ.0.) GO TO 440
      CORR=CPA+CPAS*(TBAR(I)-T0K)
        if(rhoa(i).eq.1.)go to 441
      CORR=(((RHOA(I)-RHOF(i))*CORR+RHOF(i)*(1.-RHOA(I))*(CPC+CPCS*
     1          (TBAR(I)-T0K)))/RHOFM1(i))*shr(i)
  441 A(I)=CORR*A(I)
  440 CONTINUE
      A(1)=.5*A(1)
      A(NP1)=.5*A(NP1)
C
C--------- COMPUTES AVERAGE VALUES OF THERMAL CONDUCTIVITY ----------
      DO 445 I=1,NP1
      B(I)=TCWDHX
      IF(RHOA(I).EQ.1..AND.TCAS.EQ.0.) GO TO 445
      CORR=TCA+TCAS*(TBAR(I)-T0K)
      IF(RHOA(I).EQ.1.) GO TO 446
      CORR=((RHOA(I)-RHOF(i))*CORR+(1.-RHOA(I))*(TCC+TCCS*(TBAR(I)-
                T0K)))/(RHOFM1(i)*shr(i))
```

```
     1
  446 B(I)=CORR*B(I)
  445 CONTINUE
      DO 450 I=1,N
      B(I)=.5*(B(I)+B(I+1))
  450 CONTINUE
C
C--------- COMPUTES COEFFICIENT OF CONVECTIVE TERM --------------------
      IF(MG1.EQ.0..AND.MG2.EQ.0.) GO TO 460
      DO 455 I=1,N
      C(I)=MG(I)*CPGD4
      IF(CPGS.EQ.0.) GO TO 455
      C(I)=C(I)*(1.+((TBAR(I)+TBAR(I+1))*.5-T0K)*CPGS)
  455 CONTINUE
      C1=MG1*CPGD4*(1.+(TBAR(1)-T0K)*CPGS)
      C2=-MG2*CPGD4*(1.+(TBAR(NP1)-T0K)*CPGS)
  460 CONTINUE
C
C--------- COMPUTES ENERGY SOURCE DUE TO PYROLYSIS IN THE SOLID -------
      IF(PF.EQ.0.) GO TO 470
      DO 465 I=1,NP1
      D(I)=0.
      QP=TBAR(I)-T0K
  464 D(I)=-QP0(I)*DRHO(I)*shr(i)*DX*RHOW/DTIME
  465 CONTINUE
      D(1)=.5*D(1)
      D(NP1)=.5*D(NP1)
  470 CONTINUE
CHAPTER 5 5 5 5 5 5 ---TRIDIAGONAL MATRIX OPERATIONS--- 5 5 5 5 5 5 5 5
C
C--------- COMPUTES COEFFICIENTS: M,U,F AND BT ----------------------
      DO 510 I=1,N
      F(I)=-B(I)-C(I)
  510 CONTINUE
        if(rhobar.lt..8)go to 511
        epsl=epscell+(epschar-epscell)*(1-rhobar)/.15
        if(epsl.gt.epschar)epsl=epschar
        epsl=epsl*5.669e-8
511   U(1)=B(1)-C(1)+2.*C1+.5*(H1+EPS1*TBAR(1)**3)
      DO 515 I=2,N
      U(I)=B(I)+B(I-1)-C(I)+C(I-1)
  515 CONTINUE
      U(NP1)=B(N)+C(N)-2.*C2+.5*(H2+EPS2*TBAR(NP1)**3)
      DO 520 I=2,NP1
      M(I)=C(I-1)-B(I-1)
  520 CONTINUE
      BT(1)=(A(1)-U(1))*T(1)-F(1)*T(2)+4.*T0K*(C1-C(1))+D(1)+H1*TINF1
      DO 525 I=2,N
      BT(I)=-M(I)*T(I-1)+(A(I)-U(I))*T(I)-F(I)*T(I+1)+
     1              4.*T0K*(C(I-1)-C(I))+D(I)
  525 CONTINUE
      BT(NP1)=-M(NP1)*T(N)+(A(NP1)-U(NP1))*T(NP1)+4.*T0K*(C(N)-C2)+
     1              D(NP1)+H2*TINF2
      DO 530 I=1,NP1
      U(I)=U(I)+A(I)
  530 CONTINUE
```

```
C
C--------- MAKES APPROPRIATE CHANGES IN COEFFICIENTS WHEN A SURFACE
C          TEMPERATURE BOUNDARY CONDITION IS GIVEN
C
C---- FRONT SURFACE
      IF(KBC(1).EQ.1) GO TO 540
        reduc=1.
        if(rhobar.eq.1.) go to 535
        if(rhobar.lt.rmaxred) go to 532
        reduc=(.8*rhomaxr+.2*rhobar-rmaxred)/(rhomaxr-rmaxred)
        go to 535
  532   reduc=(rmaxred-.8*redback-.2*rhobar)/(rmaxred-redback)
  535   if(reduc.gt.1.)reduc=1.
        bc(1)=reduc*bc(1)
        fepsl=epsl/5.669e-8
      BT(1)=BT(1)+fepsl*BC(1)
        if(bt(1).lt.0.)bt(1)=0.
      GO TO 545
  540 CONTINUE
      BT(1)=BT(1)-U(1)*TP(1)
        if(bt(1).lt.0.)bt(1)=0.
      BT(2)=BT(2)-M(2)*TP(1)+BT(1)
      U(2)=U(2)+F(1)
      U(1)=-1.
      M(2)=-1.
  545 CONTINUE
C
C---- BACK SURFACE
      IF(KBC(2).EQ.1) GO TO 550
      BT(NP1)=BT(NP1)+BC(2)
      GO TO 555
  550 CONTINUE
      BT(NP1)=BT(NP1)-U(NP1)*TP(NP1)
      BT(N)=BT(N)-F(N)*TP(NP1)+BT(NP1)
      U(N)=U(N)+M(NP1)
      U(NP1)=-1.
      F(N)=-1.
  555 CONTINUE
C
C--------- SOLVES THE TRIDIAGONAL MATRIX AND PUTS NEW TEMPERATURES
C          IN ARRAY BT(I)
      DO 560 I=2,NP1
      M(I)=M(I)/U(I-1)
  560 U(I)=U(I)-M(I)*F(I-1)
      DO 565 I=2,NP1
  565 BT(I)=BT(I)-M(I)*BT(I-1)
      BT(NP1)=BT(NP1)/U(NP1)
      DO 570 I=1,N
      J=NP1-I
  570 BT(J)=(BT(J)-F(J)*BT(J+1))/U(J)
C
C--------- MAKES APPROPRIATE CHANGES IN SURFACE VARIABLES WHEN
C          SURFACE BOUNDARY CONDITION IS ON TEMPERATURE
      IF(KBC(1).EQ.2) GO TO 585
```

```
      HFLUX1=BT(1)
      BT(1)=TP(1)
  585 CONTINUE
      IF(KBC(2).EQ.2) GO TO 590
      HFLUX2=BT(NP1)
      BT(NP1)=TP(NP1)
  590 CONTINUE
C
CHAPTER 6 6 6 ---CONTROL OF NUMBER OF ITERATIONS AND STEP SIZE--- 6 6 6
C
C--------- CHECKS FOR MAXIMUM ERROR BETWEEN SUCCESSIVE ITERATIONS
C          AND UPDATES TP(I) ARRAY
      ERR=0.
      CHG=0.
      DO 610 I=1,NP1
      IF(I.EQ.1.OR.I.EQ.NP1) GO TO 607
      IF(ABS(BT(I)-TP(I)).LT.ERR) GO TO 607
      ERR=ABS(BT(I)-TP(I))
      IER=I
  607 CONTINUE
      BETAM1=TP(I)
      TP(I)=BT(I)
      BT(I)=BETAM1
      CHG=AMAX1(CHG,ABS(TP(I)-T(I)))
  610 CONTINUE
      ITER=ITER+1
C
C--------- DOES 3 PRELIMINARY ITERATIONS WHEN B.C. IS NOT AT THE SURFACE
      IF (IBC(1).EQ.0.AND.IBC(2).EQ.0) GO TO 605
      IF(ITER.LT.3) GO TO 325
  605 CONTINUE
C
C--------- CHECKS FOR REQUIRED ACCURACY (ERRMX) ----------------------
      IF(ISTEP.EQ.0) GO TO 615
      IF(PF+CPAS+TCAS+EPS1+EPS2.EQ.0.
     1     .AND.IBC(1)+IBC(2).EQ.0) GO TO 615
      IF(ERR.LT.ERRMX.OR.ERR.LT.ERRMX*CHG) GO TO 615
      IF(ITER.EQ.ITERMX) GO TO 625
C
C--------- RELAXATION OF ESTIMATED TEMPERATURE PROFILE ---------------
      IF(RELAX.EQ.0.) GO TO 400
      BETA=ERR/ERRMX
      IF(CHG.GT.1.) BETA=BETA/CHG
      BETA=AMIN1(1.,ALOG(BETA)/RDEN)
      BETA=RELAX*BETA
      BETAM1=1.-BETA
      DO 640 I=1,NP1
      TP(I)=BETA*BT(I)+BETAM1*TP(I)
  640 CONTINUE
      GO TO 400
```

```
C
C--------- TIME STEP IS HALVED WHEN TOO MANY (ITERMX) ITERATIONS ARE
C          REQUIRED.  EXECUTION STOPS WHEN DTIME IS LESS THAN DTIMIN
  625 CONTINUE
      ERR=ERR/CHG
      write(11,611) ITER,ISTEP,IER,ERR
  611 FORMAT(' *** MORE THAN',I3,' ITERATIONS REQUIRED AT ISTEP=',I4,
     1 ' / TEMP. RELATIVE ERROR AT I=',I3,' WAS ',1PE11.4)
      DTIME=.5*DTIME
      IF(DTIME.GT.DTIMIN) GO TO 310
      IFIN=2
      GO TO 630
  615 CONTINUE
C
C--------- UPDATES TIME AND DENSITY. CALCULATES NEW STEP SIZE AND
C          MAGNITUDE OF TP(I) AND DRHO(I) AT NEXT STEP
      TIME=TIMEDT
      CHG=0.
      DO 645 I=2,N
      ERR=ABS(TP(I)-T(I))
      CHG=CHG+ERR
  645 CONTINUE
      CHG=CHG/FLOAT(N-1)
      ERR=DTSTEP/CHG
      IF(ERR.GT.1.) ERR=1./ERR
      ERR=1.-ERR
      IF(ITER.GT.ITERID) ERR=ERR*FLOAT(ITERID)/FLOAT(ITER)
      DTIME=AMIN1(DTIMAX,DTIME*(DTSTEP/CHG)**ERR)
      IF(ITER.LE.ITERID) GO TO 635
      DTIME=DTIME*SQRT(FLOAT(ITERID)/FLOAT(ITER))
  635 CONTINUE
      IF(DTIME.GT.DTIMIN) GO TO 630
      IFIN=3
  630 CONTINUE
      IF(TIME+DTIME.GT.TMLAST) DTIME=TMLAST-TIME
      CHG=DTIME/2./(TIME-TIMEAV)
      IF(ISTEP.EQ.0) CHG=0.
      DO 620 I=1,NP1
      TBAR(I)=.5*(TP(I)+T(I))
      ERR=T(I)
      T(I)=TP(I)
      TP(I)=T(I)+CHG*(T(I)-ERR)
      RHO(I)=RHO(I)+DRHO(I)
      DRHO(I)=CHG*DRHO(I)
      IF(DRHO(I)+RHO(I).LT.RHOF(i)) DRHO(I)=RHOF(i)-RHO(I)
      IF(PYRO.EQ.0.0) GOTO 620
      IF(RHO(NP1).LE.RHOF(np1)) IFIN=4
  620 CONTINUE
C
CHAPTER 7 7 7 7 7 7 --- END OF LOOP --- 7 7 7 7 7 7 7 7 7 7 7 7 7 7 7 7 7
C
C--------- CHECKS WHETHER TO RETURN TO MAIN FOR OUTPUT ----------------
```

```
      IPLOT=IPLOT+1
      ISTEP=ISTEP+1
      IF(TIME.GE.TMLAST.OR.ISTEP.EQ.LASTEP) RETURN
      IF(ISTEP.EQ.ISTEPR) RETURN
      IF(IPLOT.EQ.NPLOT) RETURN
      IF(IFIN.NE.0) RETURN
      GO TO 310
      END

      SUBROUTINE OUTPUT(IPRINT,N100)
        COMMON/SPYCOM/BC(2),CPA,CPC,CPG,CPAS,CPCS,CPGS,DARCY,DTIMAX,
     1  DTIME,DTIMIN,DTSTEP,DX,EPS1,EPS2,ERRMX,HFLUX1,HFLUX2,
     2  H1,H2,IBC(2),IFIN,ISTEP,ITER,ITERID,ITERMX,KBC(2),
     3  LASTEP,MG(501),MG1,MG2,N,NP1,PF,Q1DT,Q2DT,RELAX,
     4  RHO(501),RHOA(501),RHOF(501),RHOW,SLIMIT,T(501),TBAR(501),
     5  TBC(2,5000),TCA,TCC,TCAS,TCCS,TIME,TIMEAV,TIMEBC(5000),
     6  TINF1,TINF2,TMLAST,TRNEG,T0K,XBC(2),PTL,PYRO,PPL,
     7  TM(5000),HOLD,HP,HGMAX,T1MAX,MG1MAX,TMMAX,IPLOT,NPLOT

        COMMON/VAPCOM/A(501),B(501),BCTR1(2),BCTR2(2),BT(501),C(501),
     1  D(501),DRHO(501),F(501),ISURF(2),M(501),SLOPE(2),
     2  TP(501),TSLCR(2) ,TSTR1(2),TSTR2(2),U(501),XDEPTH(2),YD(2)

        COMMON/DATAOUT/MG1PLT(5000),HGPLT(5000),T1PLT(5000),T2PLT(5000),
     1  T3PLT(5000),T4PLT(5000),T5PLT(5000),T6PLT(5000),fepsl,
     2  epschar,density(5000),reduc,rhomaxr,rmaxred,redback,
     3  rhobar,tl,order,epscell,pf2,trneg2,qp02,order2,
     4  switch,ind(501),hrate(501),cy(501),shr(501),shrf(501),
     5  qp0(501),rhobar1,rhofm1(501),rhoff,qp0f

        REAL MG,MG1,MG2,MG11,MG1MAXMG1PLT

        save/spycom/
        save/vapcom/
        save/dataout/

C-------- COMPUTES FRACTION OF INITIAL WEIGHT
      RHOBAR=1.
        rhobar1=1.
      IF(RHOA(1).EQ.1..AND.RHOA(NP1).EQ.1.) GO TO 20
      RHOBAR=.5*RHOA(1)
        rhobar1=.5*rhoa(1)*shr(1)
      DO 21 I=2,N
      RHOBAR=RHOBAR+RHOA(I)
        rhobar1=rhobar1+rhoa(i)*shr(i)
   21 CONTINUE
      RHOBAR=RHOBAR+.5*RHOA(NP1)
        rhobar1=rhobar1+.5*rhoa(np1)*shr(np1)
      RHOBAR=RHOBAR/FLOAT(N)
        rhobar1=rhobar1/float(n)
   20 CONTINUE
```

```
C-------- COMPUTES HEAT FLUXES
      N100=N100+1
      HG=0.0
      QCONV1=H1*(TINF1-TBAR(1))
      RERAD1=EPS1*TBAR(1)**4
      QCONV2=H2*(TINF2-TBAR(NP1))
      RERAD2=EPS2*TBAR(NP1)**4
C-------- COMPUTES NET HEAT FLUX INTO FACE 1
      QNET1=eps1*HFLUX1/5.669e-8+QCONV1-RERAD1
        if(QNET1.lt.0.0)QNET1=0.0
C-------- COMPUTES HEAT OF PYROLYSIS
      IF(MG1.EQ.0.0) GOTO 500
      HG= QNET1/MG1




  500 IF(PPL.EQ.0.0)GOTO 502
      HGPLT(N100)=HG
      T1PLT(N100)=TBAR(1)
        T2PLT(N100)=TBAR(11)
        T3PLT(N100)=TBAR(21)
        T4PLT(N100)=TBAR(31)
        T5PLT(N100)=TBAR(41)
        T6PLT(N100)=TBAR(51)
        density(n100)=rhobar1
        chck=float(n100)/10.
        pchck=int(chck)-chck
        if(pchck.eq.0.)print*,rhobar1
      MG1PLT(N100)=MG1
      TM(N100)=TIMEAV
      IF ((HGPLT(N100).GT.HGMAX).OR.(HGPLT(N100).EQ.0.0))
     $   HGPLT(N100)=HGMAX
      IF (T1PLT(N100).GT.T1MAX) T1PLT(N100)=T1MAX
      IF (MG1PLT(N100).GT.MG1MAX) MG1PLT(N100)=MG1MAX
      IF (TM(N100).GT.TMMAX) TM(N100)=TMMAX
      IPLOT=0
  502 return
        end
```

APPENDIX B3: DATA FILE FOR MATHEMATICAL MODEL PROGRAM OF APPENDIX B2

The program listed in Appendix B2 requires data file. That file contains thermal properties, physical properties, kinetic parameters and numerical control parameters. The file is called DATA and is listed below (the file does not contain first listing, it is given here for reference):

```
Run Number
TMMAX    HGMAX    T1MAX    MG1MAX
NPLOT
CPA      CPC      CPG      CPAS     CPCS     CPGS
TCA      TCC      TCAS     TCCS     RHOW     PTL      PYRO     PPL
ST       RHOFF    PF       TRNEG    QPOF     T0K      DARCY
KBC(1)   KBC(2)   N        LASTEP   NSTAT    NPROF    ITERMX   ITERID
H1       H2       TINF1    TINF2    EPS1     EPS2     XBC(1)   XBC(2)
EPSCHAR  RHOMAXR  RMAXRED  REDBACK  TL       ORDER
PF2      TRNEG2   QP02     ORDER2   SWITCH
DTIMAX   DTIMIN   DTSTEP   TMLAST   ERRMX    RELAX    SLIMIT
TIMEBC(I)         TBC(1,I)          TBC(2,I)


Run-1
5000.0   5.0E06   1.0E03   5.0E-02
1
2104.    1928.    2000.    4.190    1.980    0.000
0.157    0.084    0.0003   0.0002   1000.    1.       1.       1.
0.01     0.120    7.4E09   1.45E08  -3.0E05  300.     -1.000
2        2        50       5000     50       200      3        1
10.000   10.000   300.     300.     0.48     0.48     0.000    0.000
0.72     0.99     1.       0.55     320.     1.
4.8e16   2.25e8   0.       1.       0.9
2.000    0.200    5.000    5000.    1.000    0.       0.
0.000    40000.   0.000
5000.    40000.   0.000
0.       0.       0.000
```

NIST-114
(REV. 6-93)
ADMAN 4.09

U.S. DEPARTMENT OF COMMERCE
NATIONAL INSTITUTE OF STANDARDS AND TECHNOLOGY

MANUSCRIPT REVIEW AND APPROVAL

(ERB USE ONLY)	
ERB CONTROL NUMBER	DIVISION
PUBLICATION REPORT NUMBER: NIST-GCR-94- 645	CATEGORY CODE
PUBLICATION DATE: June 1994	NUMBER PRINTED PAGES

INSTRUCTIONS: ATTACH ORIGINAL OF THIS FORM TO ONE (1) COPY OF MANUSCRIPT AND SEND TO THE SECRETARY, APPROPRIATE EDITORIAL REVIEW BOARD.

TITLE AND SUBTITLE (CITE IN FULL)

Behavior of Charring Materials in Simulated Fire Environments

CONTRACT OR GRANT NUMBER: 60NANB0D1042

TYPE OF REPORT AND/OR PERIOD COVERED: Final Project Report 1990 - 1992

AUTHOR(S) (LAST NAME, FIRST INITIAL, SECOND INITIAL)

E.M. Suuberg, I. Milosavljevic, W.D. Lilly
Brown University
Providence, RI 02912

PERFORMING ORGANIZATION (CHECK (X) ONE BOX)

- [ ] NIST/GAITHERSBURG
- [ ] NIST/BOULDER
- [ ] JILA/BOULDER

LABORATORY AND DIVISION NAMES (FIRST NIST AUTHOR ONLY)

SPONSORING ORGANIZATION NAME AND COMPLETE ADDRESS (STREET, CITY, STATE, ZIP)

U.S. Department of Commerce
National Institute of Standards and Technology
Gaithersburg, MD 20899

PROPOSED FOR NIST PUBLICATION

- [ ] JOURNAL OF RESEARCH (NIST JRES)
- [ ] J. PHYS. & CHEM. REF. DATA (JPCRD)
- [ ] HANDBOOK (NIST HB)
- [ ] SPECIAL PUBLICATION (NIST SP)
- [ ] TECHNICAL NOTE (NIST TN)
- [ ] MONOGRAPH (NIST MN)
- [ ] NATL. STD. REF. DATA SERIES (NIST NSRDS)
- [ ] FEDERAL INF. PROCESS. STDS. (NIST FIPS)
- [ ] LIST OF PUBLICATIONS (NIST LP)
- [ ] NIST INTERAGENCY/INTERNAL REPORT (NISTIR)
- [ ] LETTER CIRCULAR
- [ ] BUILDING SCIENCE SERIES
- [ ] PRODUCT STANDARDS
- [X] OTHER NIST-GCR

PROPOSED FOR NON-NIST PUBLICATION (CITE FULLY) [ ] U.S. [ ] FOREIGN

PUBLISHING MEDIUM

- [ ] PAPER [ ] CD-ROM
- [ ] DISKETTE (SPECIFY)
- [ ] OTHER (SPECIFY)

SUPPLEMENTARY NOTES

ABSTRACT (A 2000-CHARACTER OR LESS FACTUAL SUMMARY OF MOST SIGNIFICANT INFORMATION. IF DOCUMENT INCLUDES A SIGNIFICANT BIBLIOGRAPHY OR LITERATURE SURVEY, CITE IT HERE. SPELL OUT ACRONYMS ON FIRST REFERENCE.) (CONTINUE ON SEPARATE PAGE, IF NECESSARY.)

The focus of this study was the behavior of thick charring solids in fire situations. Clearly one of the most important parameters governing the fire phenomenon is the rate of release of combustible volatiles into the gas phase, in which they actually burn. Over the years, fire researchers have learned how to model the processes in the gas phase, so that the rate of heat feedback to the solid surface can be reasonably well predicted. Likewise, there exists the ability to model the heat transfer processes at the solid surface and within the solid itself. Finally, there is a large literature on the laboratory-scale pyrolysis of various charring polymers. It might appear that predicting the course of the fire would involve carefully coupling these different models together. There have unfortunately not been any successful demonstrations of the ability to do this, though in broad stroke, some models capture the key features of the processes.

This study was concerned with the possibility that the inability to come to complete closure on the charring polymer fire problem might derive from difficulties in applying laboratory scale kinetics to actual fire conditions. Specifically, we were concerned about how well small scale laboratory experiments used to derive the kinetics of pyrolysis could be used to predict the behavior of charring solids in fire situations.

KEY WORDS (MAXIMUM OF 9; 28 CHARACTERS AND SPACES EACH; SEPARATE WITH SEMICOLONS; ALPHABETIC ORDER; CAPITALIZE ONLY PROPER NAMES)

cellulose; cellulosic materials; char; char depth; fire research; model studies; pyrolysis

AVAILABILITY

- [X] UNLIMITED
- [ ] FOR OFFICIAL DISTRIBUTION - DO NOT RELEASE TO NTIS
- [ ] ORDER FROM SUPERINTENDENT OF DOCUMENTS, U.S. GPO, WASHINGTON, DC 20402
- [X] ORDER FROM NTIS, SPRINGFIELD, VA 22161

NOTE TO AUTHOR(S): IF YOU DO NOT WISH THIS MANUSCRIPT ANNOUNCED BEFORE PUBLICATION, PLEASE CHECK HERE. [ ]